AD NUMBER

ADB010469

LIMITATION CHANGES

TO:

Approved for public release; distribution is unlimited.

FROM:

Distribution authorized to U.S. Gov't. agencies only; Test and Evaluation; 23 APR 1976. Other requests shall be referred to Supersonic Transport Office, Washington, DC 20590.

AUTHORITY

FAA ltr, 26 apr 1977

REPORT No. FAA-SS-73-29-II

R75AEG362

SUPERSONIC TRANSPORT NOISE REDUCTION TECHNOLOGY PROGRAM

PHASE II

VOLUME II

J.T.BLOZY
V.L.DOYLE
S.B.KAZIN
R.B.MISHLER
R.L.NEBUDA
E.J.STRINGAS
A.R. SIECKMAN

GROUP ENGINEERING DIVISION
Aircraft Engine Group
General Electric Company
Cincinnati, Ohio 45215

FINAL REPORT

SEPTEMBER, 1975

Prepared for:

DEPARTMENT OF TRANSPORTATION
FEDERAL AVIATION ADMINISTRATION
Supersonic Transport Office
Washington, D.C. 20590

The contents of this report reflect the views of the General Electric Company, which is responsible for the facts and the accuracy of the data presented herein. The contents do not necessarily reflect the official views or policy of the Department of Transportation. This report does not constitute a standard, specification, or regulation.

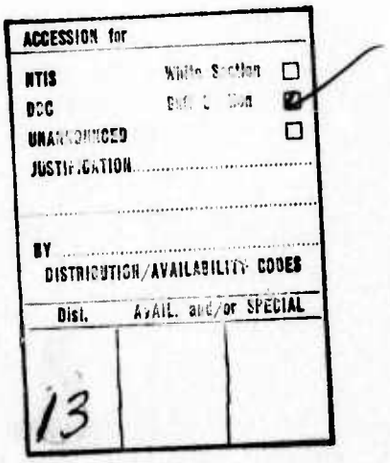

1. Report No.	2. Government Accession No.	3. Recipient's Catalog No.
FAA-SS-73-29-2		

4. Title and Subtitle	5. Report Date
Supersonic Transport Noise Reduction Technology Program - Phase II, Volume 2.	September 1975
	6. Performing Organization Code

7. Author(s)	8. Performing Organization Report No.
S.B. Kazin and E.J. Stringas (Program Technical Directors) J.T. Blozy, V.L. Doyle, R.B. Mahler, R.L. Nebuda, A.R. Sieckman	R75AEG362 - Vol-2
	10. Work Unit No.

9. Performing Organization Name and Address	11. Contract or Grant No.
Group Engineering Division Aircraft Engine Group General Electric Company Cincinnati, Ohio 45215	DOT-FA72WA-2894
	13. Type of Report and Period Covered
12. Sponsoring Agency Name and Address	Final Rept.
Department of Transportation Federal Aviation Administration Supersonic Transport Office Washington, D.C. 20590	14. Sponsoring Agency Code

15. Supplementary Notes

16. Abstract

The Supersonic Transport Noise Reduction Technology Program, sponsored by the Federal Aviation Administration, was conducted as a follow-on effort after cancellation of the SST Program to finalize selected noise technology areas and summarize results of the SST Program. Using initial effects of the SST Program, as summarized in Phase I of The Supersonic Transport Noise Reduction Technology Program, the Phase II contract was issued to the General Electric Company (and Boeing) to continue this important work. The overall program objective was to provide additional acoustic technology necessary to design high speed aircraft systems, recognizing future acceptable noise levels. General Electric's effort was divided into the acoustic technology areas of jet noise reduction, turbomachinery noise reduction, and aircraft system integration.

Jet noise reduction technology work was achieved through analytical studies, model tests, and J79 engine tests. Selected suppression systems identified during the SST Program were further refined (multispoke/chute suppressors or annular plug nozzles). Novel advanced concepts of suppression were identified, and extensive aerodynamic (static and wind-on) performance tests and hot-jet acoustic tests were performed.

Both compressor and turbine noise were studied in the turbomachinery noise reduction areas. A 3-stage low pressure compressor with variable-flap inlet guide vanes was tested at General Electric's outdoor test site. A hybrid inlet, which employs airflow acceleration suppression in combination with wall acoustic treatment, was investigated as the suppression device for all three noise monitoring point operating conditions. The effect of auxiliary inlets on noise leakage and suppression was studied for takeoff mode. Also, variable inlet guide vane flaps were used to reduce area and generate high passage Mach numbers as another means of compressor noise suppression. Turbine noise was studied using a J85 engine with massive inlet suppressor and open nozzle to unmask the turbine. Second-stage turbine blade/nozzle spacing and exhaust acoustic treatment were investigated as means of turbine noise suppression.

The best performing components from noise suppression work performed under the jet and turbomachinery noise reduction tasks were integrated into a viable-type aircraft-engine system study. Overall system noise was evaluated from EPNL estimates of the suppressed and unsuppressed SST systems relating to the current FAR Part 36 Noise Regulations.

17. Key Words (Suggested by Author(s))	18. Distribution Statement
Jet Noise, High Velocity Suppression, Aircraft Engine Suppression, Turbomachinery Noise, Hybrid Inlet Aircraft Engine Suppression Integration	Approved for U.S. Government only. Transmittal of this document outside the U.S. Government must have prior approval of the Supersonic Transport Office.

19. Security Classif. (of this report)	20. Security Classif. (of this page)	21. No. of Pages	22. Price*
Unclassified	Unclassified	849	

403 468 VB

PREFACE

The program technical effort was conducted under the direction of Mr. E.J. Stringas (Jet Noise Technology) and Mr. S.B. Kazin (Turbomachinery Noise Technology).

Many people contributed to the successful completion of this Acoustic Technology Program. Among the significant contributors were: Mr. V.L. Doyle, who conducted the Jet Noise Reduction Technology investigations and much of the Aircraft Systems Integration work, as well as serving as Chief Coordinator for the report; Mr. R.B. Mishler, who supervised the Turbomachinery Noise Reduction Technology effort as well as conducting the Hybrid Inlet investigations and contributed to a major portion of the Systems Integration work; Mr. R.L. Nebuda, who conducted much of the Turbine Noise Reduction effort; and Mr. J. Blozy who performed many of the Compressor Noise Reduction investigations.

Thanks are addressed to Mr. A.R. Sieckman for his efforts in helping to conduct the Aircraft Systems Integration studies, and to Messrs. A.J. Burch and L.S. Paul for their assistance in the report organization and format preparation. Graditude is also extended to all the supporting groups and personnel. In particular, the Exhaust Nozzle and Installed Performance Unit personnel, Messrs. R.W. Whittaker (Manager) and J.J. Schloemer, who performed the Aerodynamic Performance investigations on the Jet Exhaust Nozzle configurations.

TABLE OF CONTENTS

VOLUME I

TABLE OF CONTENTS (continued)

TABLE OF CONTENTS (continued)

TABLE OF CONTENTS (continued)

TABLE OF CONTENTS (concluded)

LIST OF ILLUSTRATIONS

VOLUME I

LIST OF ILLUSTRATIONS (Continued)

LIST OF ILLUSTRATIONS (Continued)

LIST OF ILLUSTRATIONS (Continued)

LIST OF ILLUSTRATIONS (Continued)

LIST OF ILLUSTRATIONS (Continued)

LIST OF ILLUSTRATIONS (Continued)

LIST OF ILLUSTRATIONS (Continued)

LIST OF ILLUSTRATIONS (Continued)

LIST OF ILLUSTRATIONS (Continued)

LIST OF ILLUSTRATIONS (Continued)

LIST OF ILLUSTRATIONS (Continued)

LIST OF ILLUSTRATIONS (Continued)

LIST OF ILLUSTRATIONS (Continued)

LIST OF ILLUSTRATIONS (Continued)

LIST OF ILLUSTRATIONS (Continued)

LIST OF ILLUSTRATIONS (Continued)

LIST OF ILLUSTRATIONS (Continued)

LIST OF ILLUSTRATIONS (Continued)

LIST OF ILLUSTRATIONS (Continued)

LIST OF ILLUSTRATIONS (Continued)

LIST OF ILLUSTRATIONS (Continued)

LIST OF ILLUSTRATIONS (Continued)

LIST OF ILLUSTRATIONS (Continued)

LIST OF ILLUSTRATIONS (Continued)

LIST OF ILLUSTRATIONS (Continued)

LIST OF ILLUSTRATIONS (Continued)

LIST OF ILLUSTRATIONS (Continued)

LIST OF ILLUSTRATIONS (Continued)

LIST OF ILLUSTRATIONS (Continued)

LIST OF ILLUSTRATIONS (Continued)

LIST OF ILLUSTRATIONS (Continued)

LIST OF ILLUSTRATIONS (Concluded)

LIST OF TABLES

VOLUME I

VOLUME II

LIST OF TABLES (Continued)

LIST OF TABLES (Continued)

LIST OF TABLES (Continued)

LIST OF TABLES (Concluded)

NOMENCLATURE

Symbol	Description	Units
A	Area	($in.^2$, ft^2)
A_8	Physical primary nozzle exit (throat) plane area	($in.^2$), (ft^2)
A_{e8}	Effective throat area	($in.^2$), (ft^2)
A_9	Nozzle exit plane area	($in.^2$), (ft^2)
A_{18}	Fan stream exit area	($in.^2$), (ft^2)
A_B	Blocked area	($in.^2$), (ft^2)
AR_d	Area ratio: ratio of total area (annulus for plug nozzles, plane for 2-D nozzles) to physical flow area	- - -
a	Ellipse semimajor axis	(in.)
AST	Advanced supersonic transport	- - -
B	Turbine blade	- - -
BID	Blow-in-door	- - -
BPF	Blade passing frequency	(Hz)
b	Ellipse semiminor axis	(in.)
C	Coefficient	- - -
$C1$, C_2, etc	Compressor rotor	- - -
$C_1 - F_2$	Compressor rotor - 2nd harmonic	(Hz)
C_{fg}	Nozzle gross thrust coefficient (static and wind-on)	- - -
C_D	Nozzle discharge coefficient (ratio of actual to ideal flow rates) or inlet area coefficient (ratio of actual to physical flow area)	
C_x	Axial balance readout	counts
C_{pp}	Normalized cross-correlation function in-jet to far-field	- - -
c	Speed of sound	(ft/sec)
D	Diameter	(in.), (ft)
D_F	Aerodynamic drag force	lb_f
D_o	Nozzle physical outer dia.	(in.)
D_t	Tube internal diameter	(in.)
D_{Td}	Circumscribed tube bundle diameter	(in.)
D_8	Internal diameter of conical primary nozzle at primary exit, plane 8	(in.)
D_9	Internal diameter of nozzle at plane 9	(in.)
dm	Outer shroud diameter	(in.)
dB	Decibel, re 0.0002 dyne/$in.^2$	(dB)
Dv	Discharge valve	- - -
EGT	Exhaust gas temperature	(° R)
EPNL	Effective perceived noise level	(EPNdB)
EPNdB	Unit of effective perceived noise level	
F	Sabbl separation parameter	- - -
Fg, fg	Measured gross thrust (stream)	(lb_f)
F_N	Net thrust	(lb_f)

NOMENCLATURE (Continued)

Symbol	Description	Units
f	Frequency	(Hz)
G	Real-gas stream thrust correlation factor	- - -
H	Axial thrust	(lb)
H_x	Axial balance force	(lb)
H_8	2-D nozzle throat height (normal)	(in.)
H_p	2-D ramp (plug) rize	(in.)
$\bar{H}$	2-D immersion depth parameter	(in.)
HPT	High pressure turbine	- - -
h	Conical ejector annulus height (mean)	(in.)
h_1, h_2	2-D suppressor height	(in.)
h	2-D primary flow passage height	(in.)
H	Height	(in.)
h	Pressure altitude	(ft)
IGV	Inlet guide vane	- - -
j	$\sqrt{-1}$ imaginary number	
$jX/\rho c$	Normalized reactance (imaginary part of complex acoustic impedance)	- - -
K_{cr}	Critical flow factor	$\sqrt{°R}$/sec
K_e	Fan-core (dual-flow) exit plane offset distance ~ 5.75"	(in.)
k	Isentropic ratio of specific heats (1.4)	
L	Calibration load	(lb)
L	Length	in., ft
L_p	Axial length of 2-D ramp	(in.)
L_z	Axial reference location of variable position inlet centerbody	
L_s	Shroud internal length	(in.)
L_t	Tube external diameter	(in.)
LPC	Low pressure compressor	- - -
LPT	Low pressure turbine	- - -
M	Mach number	- - -
M_∞	Freestream Mach number	- - -
M_j	Jet stream Mach number	- - -
$M_{a/c}$	Aircraft Mach number	- - -
MPT	Multiple pure tone	- - -
m	Mass flow rate	(lbm/sec)
M_{th}	Throat Mach number	- - -
N	Nozzle	- - -
N	Rotational speed	rpm
$\%N_c$	Percent corrected speed	%
$N/\sqrt{\theta}$	Corrected speed	rpm
n	Number	- - -
NR	Narrowband	- - -
NOY	Annoyance weight SPL; used to calculate PNL	(NOY)

NOMENCLATURE (Continued)

Symbol	Description	Units
OB	Octave band	- - -
OAPWL	Overall sound power level re 10^{-13} watts	dB
OAJPL	Overall jet pressure level(aero-dynamic pressure, rms)	dB
OASPL	Overall sound pressure level	dB
P	Pressure	psia, psig
P_o	Ambient free stream pressure	psia, psig
P_b	Suppressor base static pressure	psia, psig
P_s	Static pressure (surface)	psia, psig
P_w	Wall surface pressure	psia, psig
P_r	Pressure ratio	- - -
P_{T8}	Nozzle exit total pressure	psia
ΔP	Static pressure difference	psi
PWL	Sound power level, re 10^{-13} watts	dB
$(\Delta P_T/P_T)_{Max.}$	Inlet total pressure distortion =	$\frac{(P_{TMax} - P_{TMin.})}{P_{TAv}}$
PNL	Perceived noise level	PNdB
PNdB	Unit of perceived noise level	- - -
P_F	Sound pressure in far field	(psi)
$P_j(t)$	Sound pressure in jet	(psi)
qc	Compressible dynamic pressure,	$P_T - P_S$
R	Resistance	
R	Radius	(in.)
R_o	Outer flowpath contour radius	(in.)
R_i	Inner flowpath contour radius	(in.)
$R/\rho c$	Normalized resistance (real part of complex acoustic impedance)	- - -
RPM	Revolutions per minute	rpm
R1	Rotor one - 1st stage rotor	- - -
R_N	Reynolds number	- - -
r	Radial distance	(in.)
RH	Relative humidity	%
r_i	Immersion radius	(in.)
r_o	Outer (tip) radius	(in.)
r_h	Hub (inner) radius	(in.)
S	Distance between $\mathcal{L}$ of tube rows	(in.)
S_j	In-jet Strouhal number fD/V	- - -
$S_j^2 \cdot \overline{P_F P_j}(t)$	Source function distribution	- - -
SPL	Sound pressure level	dB
SL	Sideline distance	- - -
SDOF	Single degree of freedom	- - -
SST	Supersonic transport	- - -
SABBL	Stratford and Beavers boundary layer analysis - computer program	- - -

NOMENCLATURE (Continued)

Symbol	Description	Units
SM	Compressor stall margin	%
STC	Streamtube curvature - compressible potential flow computer program	- - -
T	Temperature	° R
T_{T8}	Nozzle exit total temperature	° R
T_1, T_2	Turbine Stage 1, Stage 2, etc.	- - -
U	Rotor tangential velocity	ft/sec
U_t, V_T	Rotor tip speed	ft/sec
$\underline{u}'$	Turbulent particle velocity	ft/sec
u	Mean particle velocity	ft/sec
V, v	Velocity	ft/sec
V_c	Core stream velocity	ft/sec
V_F	Fan bypass stream velocity	ft/sec
V_J, V_j	Fully expanded ideal jet velocity	ft/sec
VSF	Vortex shedding frequency	Hz
W, ω	Weight flow rate	lb/sec
w	Width	(in.)
W_e, W_{ej}	Secondary entrained flow	lb/sec
W_8	Nozzle primary flow	lb/sec
W_T	Total primary and secondary flow	lb/sec
W_2	Induced flow	lb/sec
WFB	Flow width at basis (hub)	(in.)
WFT	Flow width at tip (casing)	(in.)
x	Axial distance	(in.)
X	Reactance	- - -
γ	Ramp normal coordinate direction	(in.)
Z	Axial coordinate from geometric 2-D unsuppressed nozzle throat	(in.)
Z	Aerodynamic axial calculation station	(in.)
10 log ρA	Normalizing factor (SPL and PNL) for size & test condition variance (deg)	
α	Angle of attack	(deg)
β	Bypass ratio	- - -
β	Orifice coefficient	- - -
θ	Angle between a straight line from source to microphone and engine or nozzle $\mathbb{Q}$; ref to inlet or exhaust (acoustic angle)	(deg)
θ	Diffusion angle	(deg)
θ	Corrected total temperature $(\frac{T_{act}}{T_o})$	
δ	Corrected total pressure $(\frac{P_{act}}{P_o})$	
ρ	Jet stream density	lbm/ft^3
∂	Ratio of specific heats	- - -
Δ	Incremental quantity	- - -
λ	Pressure ratio's wave length	(ft)
η_R	Inlet total pressure recovery factor	- - -

NOMENCLATURE (Concluded)

Symbol	Description	Units
Subscripts		
AMB, a	Ambient	
ANN	Annulus	
Av	Average	
B	Blocked	
BID	Blow-in-door	
b	Base	
C	Core	
CH	Chute	
D	Subsonic diffuser	
d	Discharge	
e	Effective	
e	Exit	
EN	Entrance	
EQ	Equivalent	
Ex	Exit	
F	Fan	
I	Inlet	
i	Ideal	
j,	Jet	
H	Hub	
Max.	Maximum	
Min.	Minimum	
O	Freestream or ambient condition	
Overall	Combined primary & BID performance	
PRI	Primary inlet	
SP	Spoke	
S	Static condition	
t,T	Total conditions	
T	Tip	
TE	Trailing edge	
th, TH	Throat	
Total	Sum of primary & BID properties	
Venturi	Venturi-measured flowrate	
w	Wall	
.5	Compressor entrance station	
1	Metering nozzle station - wind tunnel	
2	Diffuser exit (aero-traverse) station	
2.5C	Compressor discharge station	
3	Flexible seal station - wind tunnel	
7	Measurement plane for nozzle throat P_T and T_T	
8	Nozzle throat plane	
9	Nozzle exit plane	
18	Fan bypass exhaust throat plane	

SECTION 4.0

TURBOMACHINERY NOISE REDUCTION TECHNOLOGY

4.1 SUMMARY

4.1.1 Turbine Noise Reduction

Acoustic testing of a YJ85 turbojet engine at Edwards Flight Test Center (EFTC), Edwards, California, was performed to:

- Investigate the acoustic characteristics of turbine noise in the far field.
- Obtain far-field noise reductions
- Verify air turbine rig results from Phase I of this program

The acoustic configurations tested were:

- Baseline
- Increased axial spacing between the turbine 2nd stage stator and turbine blades
- Acoustic treatment (single degree of freedom) in the turbine exhaust

These tests demonstrated that increasing the spacing to 1.0 nozzle tip chord from 0.34 chords resulted in an average turbine tone PWL reduction of 5.6 dB in the far field. The acoustic treatment (L/D = 1 with a splitter) reduced the turbine tone (second stage) PWL an average of 23.5 dB. Both the spacing and the treatment were found to suppress the turbine noise over a wide frequency range. Jet noise and casing radiation created a "floor" in the far field for the J85; this limited the apparent treatment effectiveness in the far field for this vehicle.

The baseline turbine far-field directivities were found to be consistent with prior investigations (such as Smith and Bushel, Reference 8). In addition, the directivities were similar for both the suppressed and unsuppressed turbines.

Scaling studies were performed to indicate the magnitude of the turbine noise in an SST application. The 300-foot sideline peak PNL's for the turbine are summarized below:

Condition	% rpm (J85)	Baseline (SST) Turbine PNdB@110°	Spacing PNdB@110°	Spacing plus Treatment PNdB@110°
Takeoff	100	112.1	103.5	102.9
Approach	80	106.8	102.5	93.4

These perceived noise level results provide a measure of suppression levels with turbine spacing and treatment. It is seen that turbine spacing is quite effective in reducing the turbine noise, yet can be done with relatively small penalties to the engine system. The impact of turbine spacing on engine system noise was studied in more detail in the Systems Integration part of the program reported in Section 5.0.

4.1.2 Compressor Noise Reduction

Acoustic testing was performed at Peebles Site IVB on an advanced three-stage low pressure compressor fitted with a hybrid inlet to determine the noise suppression relative to a cylindrical hardwall baseline at the approach and take-off conditions. This inlet had a design quite similar to the SST/GE4 inlet but had a bellmouth forebody to simulate inflow conditions during flight.

For the approach mode, the hybrid inlet provided 11.5 ΔPNdB noise suppression relative to the baseline cylindrical bellmouth inlet at the SST selected operating point (inlet throat Mach number = 0.78). These results are for a 1045 lbm/sec SST engine.

For the take-off mode, the hybrid inlet was evaluated both with the blow-in doors closed and open. With the blow-in doors (BID) closed, the hybrid inlet provided 15.5 ΔPNdB noise suppression relative to the baseline inlet at an inlet throat Mach number of 0.77.

The auxiliary inlets were designed so that the effect of a high-flow Mach number in the passage on noise leakage through the open doors could be investigated. However, the aerodynamic performance of the blow-in doors was somewhat disappointing in that high throat Mach numbers were not achieved in the BID passages. At the high fan tip speeds, characteristic of the take-off condition, the noise emanating from the BID's dominated the noise spectra and, therefore, the acceleration suppression achieved in the primary inlet did not reduce the noise level. However, at these speeds, up to 15 ΔPNdB noise suppression for this configuration was achieved relative to the baseline inlet. This was attributed to the acoustic treatment between the fan and the doors and the difference in inlet configuration.

The aerodynamic performance of the hybrid inlet with the BID's closed was excellent. The pressure recoveries for both the approach and take-off (BID's closed) mode were 0.98 at the selected operating inlet throat Mach number. There was no performance penalty due to the addition of acoustic treatment to the inlet. The radial pressure distortions were 0.047 and 0.063 (maximum-minimum/average) for the approach and take-off modes, respectively, with about 30% of the flow area adjacent to the tip flowpath below average.

Inlet performance, with the three BID positions investigated, was below the level assumed in sizing the inlet. Overall operating point recoveries were 0.952 to 0.962, with corresponding radial distortions of about 8% and 42 to 66% area extent, increasing with BID throat area. This performance degradation caused the primary/BID flow split to depart significantly from the design intent for the nominal and large BID settings.

Another method of suppressing compressor noise was evaluated: that of using the IGV variable flaps to reduce area and increase Mach number in the IGV passage. For the High Mach IGV Test, significant noise suppression was achieved. A 9 ΔPNdB noise reduction was measured at a 1410 ft/sec tip speed, and a 5.5 ΔPNdB reduction was measured at a 1524 ft/sec tip speed. However, coupled with these noise reductions was a sharp drop in fan performance, i.e., airflow and pressure ratio. The corresponding thrust loss was so great that this suppression technique is rendered impractical for high power flight conditions (i.e., takeoff). It might possibly have an application for the approach mode, where thrust requirements are low, but the penalties involved in its implementation would likely result in a poor trade with noise suppression gains.

4.2 INTRODUCTION

4.2.1 Background

It is well known that the environmental impact on community noise for a supersonic transport system is generally dominated by jet noise at the sideline measuring point during takeoff. This is particularly true for turbojet and low bypass ratio turbofan cycles.

The SST engine turbomachinery components which dominate the generated noise are the first compressor stages and the last turbine stages. Both were studied in the current program. A three-stage low pressure system with variable flap IGVs was used as the source model in the compressor noise investigations. This fan had an overall design pressure ratio of 4 and a Rotor 1 tip speed of 1524 ft/sec. As such, it constituted a valid model for low bypass ($\beta = 0.2$) turbofan SST engine noise studies. This same compressor, or variations thereof, has been used extensively in the Advanced Supersonic Transport (AST) Studies being conducted by General Electric for NASA-Lewis under Contract NAS3-16950, in cooperation with several airframe manufacturers. Two approaches to limiting the propagation of compressor noise were studied: namely a hybrid inlet and high Mach number IGVs.

The YJ85-5 turbojet engine was used for the turbine noise investigations. A large inlet suppressor for compressor noise and an open nozzle for jet noise reduction were used to unmask the far-field turbine noise. The J85 engine has a relatively high pressure two-stage turbine designed for a tip speed of 1181 ft/sec. As such, it represented a valid model for SST engine turbine noise investigations. The details and results of both the compressor and turbine tests are included in the sections which follow. In Section 5, these results, combined with the jet noise reduction results, are applied in a Systems Integration Study to define the level of SST noise technology developed under this program relative to the current FAR-36 regulation.

4.2.2 Turbine Noise Reduction

In the past, the noise generated by the turbine has not been as significant as the noise problems associated with other jet engine components, e.g., the compressor or the jet. With the significant acoustic gains that have been made in controlling the far-field noise from other components, consideration of turbine noise and its reduction becomes an integral part of any systems noise study. Consequently, there is a definite need for turbine noise data and established turbine noise reduction methods.

The Supersonic Transport Noise Reduction Technology program, Phase II, was established with the broad goal of providing the additional acoustic technology necessary to design high speed aircraft systems recognizing future acceptable noise levels. Within this framework, a turbine noise reduction study was established with the following objectives:

- Determine the best methods of minimizing turbine noise
- Demonstrate turbine noise reduction techniques experimentally
- Extend near-field results from Phase I to the far field

Acoustic testing of a YJ85 turbojet engine was performed to demonstrate and evaluate methods of suppressing this turbine noise for the SST.

4.2.3 Compressor Noise Reduction

Testing was performed to evaluate the unsuppressed compressor noise and the use of a hybrid inlet to suppress this noise for both take-off and approach flight conditions. In addition, a pioneering effort to evaluate the effect of blow-in-door auxiliary inlets, a necessary part of any SST inlet, on take-off noise was accomplished with an attempt in the design to suppress the noise leakage through the doors. Finally, the generation of high Mach numbers in the IGV passage was also used to suppress the compressor noise.

The variable geometry inherent in a supersonic transport engine inlet and nozzle makes it well suited to the hybrid inlet concept, which employs moderate airflow acceleration suppression in addition to wall acoustic treatment suppression, and thus avoids the performance problems associated with hard choking the inlet. The variable geometry already present makes it possible to use the same inlet noise suppression scheme at take-off and approach conditions. Approach, of course, is the most important condition with regard to compressor noise, since jet noise dominates at takeoff, although some compressor noise suppression is required at this condition. The hybrid inlet had a basic design quite similar to the SST/GE4 inlet, but had a bellmouth forebody to simulate inflow conditions during flight. Four segments of wall acoustic treatment were used in order to suppress a wide range of frequencies (that is, the blade passing frequency of all three rotors, the first rotor second harmonic, and the lower frequency multiple pure tones). The treatment panels were replaceable with hardwall panels so that acoustic treatment suppression could be isolated. A baseline cylindrical inlet also was tested to evaluate the basic source noise characteristics of the compressor, to isolate the acceleration suppression, and to perform the High Mach Number IGV test.

4.3 TURBINE NOISE REDUCTION

4.3.1 Test Description

4.3.1.1 Vehicle Description

The test vehicle for the turbine tests was a YJ85-5. A cutaway of a J85 is shown on Figure 350. The J85 turbojet engine has an eight-stage compressor (with an air bleed system) and a two-stage turbine. Blade numbers for the rotor stages are presented on Table 12.

The basic J85 turbine is illustrated on Figure 351. For the speed range tested (70% to 100% rpm), the turbine tip speed ranged from 826 ft/sec to 1181 ft/sec; and, the turbine pressure ratio (PT_{in}/PS_{out}) varied between 2.4 and 5.0. The turbine inlet temperature ranged from 1300° to 1670° R.

4.3.1.2 Configuration Selection

There are two methods for reducing the turbomachinery noise emanating from a jet engine: (1) reducing the power of the noise source, and (2) absorbing the acoustic energy before it is radiated to the far field.

It was decided that the turbine source noise reduction methods that were investigated would be applied to the noise generated by the turbine second stage blade. The main reason for selecting the second stage for investigation was that the test results would be more easily interpreted, in that such complexities as blade row attenuation and rotor interaction with both upstream and downstream nozzle blades would be avoided.

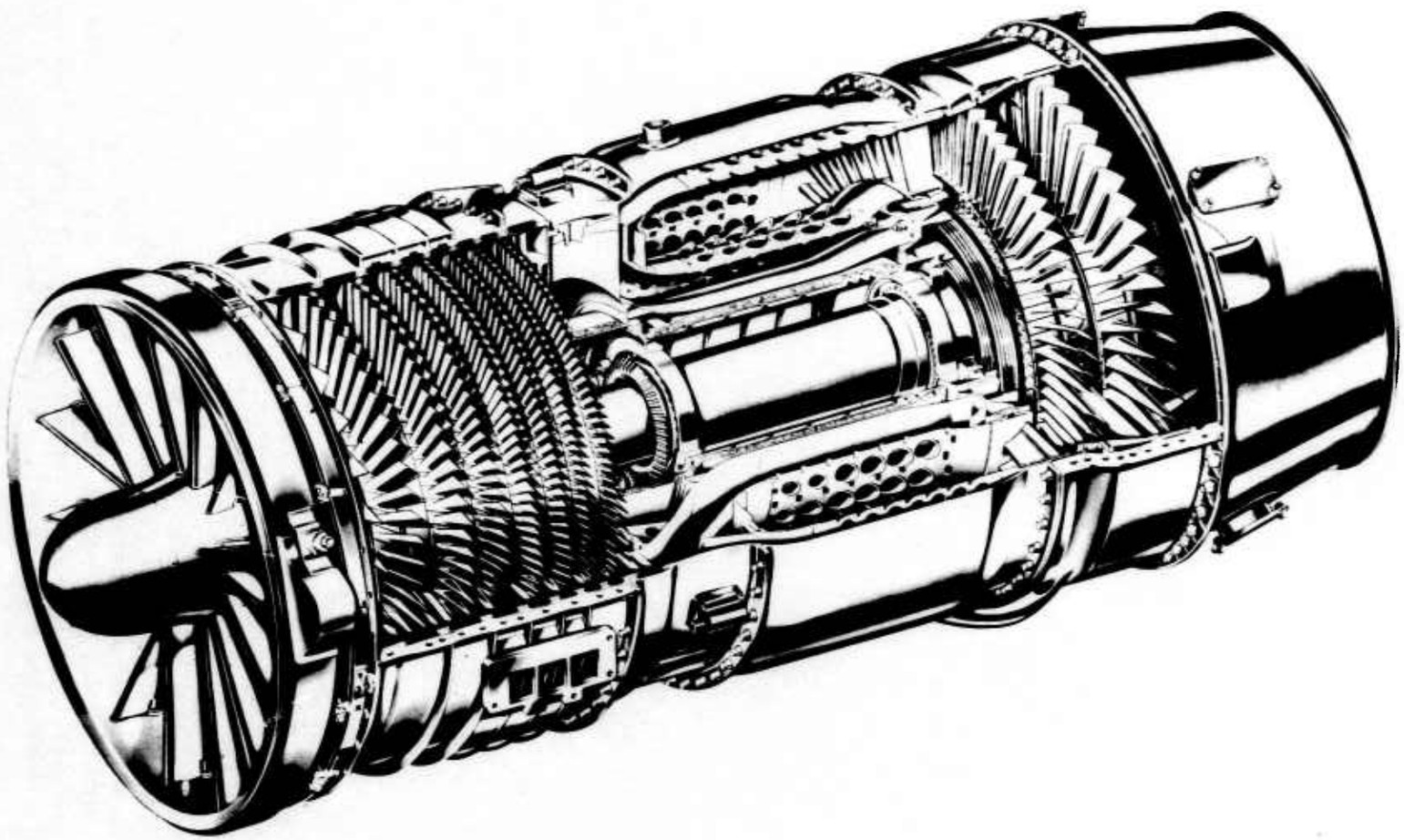

Figure 350. Cross Section of J85 Engine.

Table 12. Blade Numbers for J85 Turbomachinery.

Compressor	
Stage	Number of Blades
1	31
2	60
3	87
4	106
5	131
6	132
7	140
8	120
Turbine	
Stage	Number of Blades
1	75
2	55

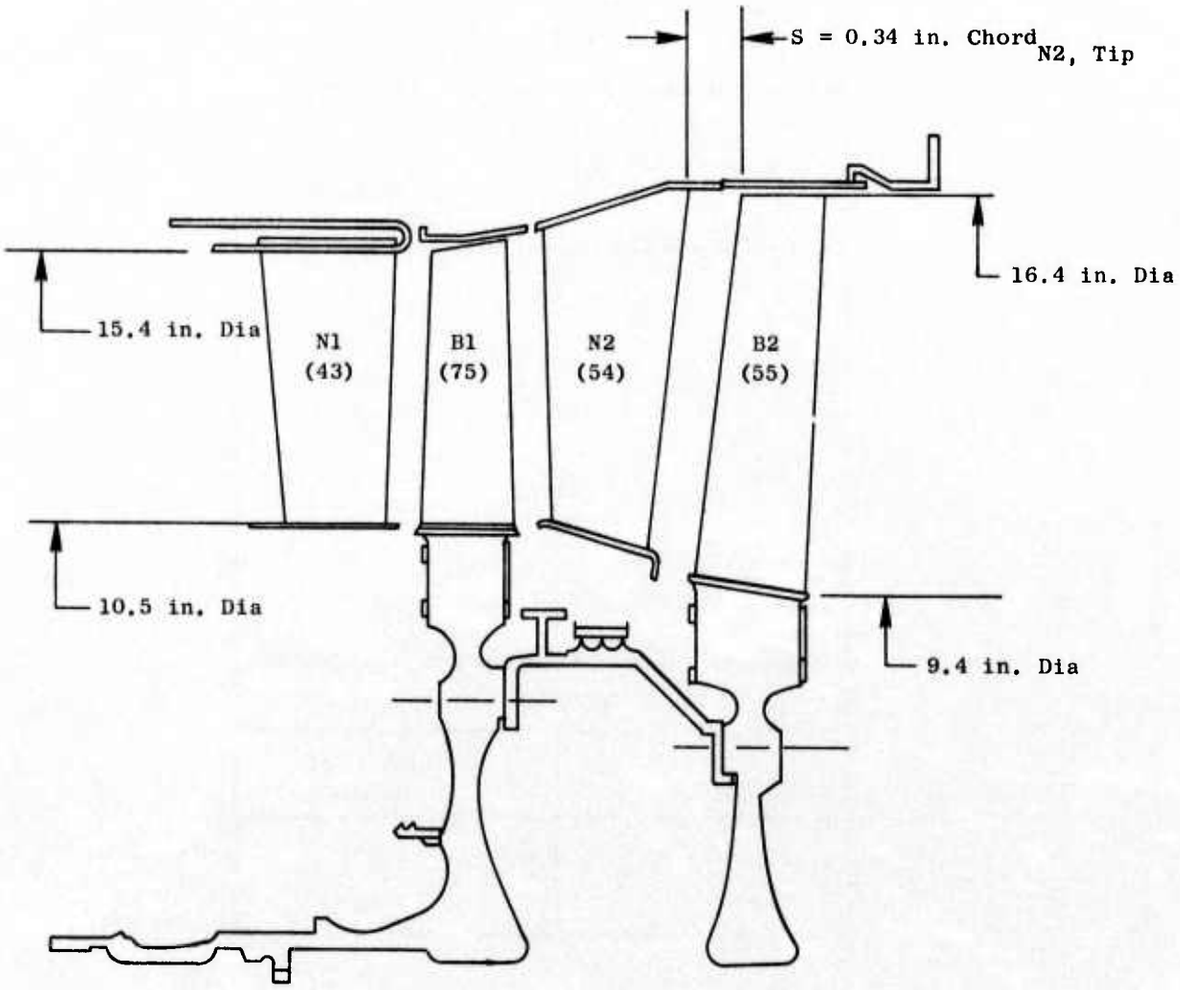

Figure 351. J85-5 Turbine Baseline Configuration.

A systematic investigation of the effects of spacing on high pressure turbine noise was one of the avenues of investigation in Phase I (Reference 3). A schematic of the test turbine from Reference 3 and the spacings tested are presented on Figures 352 and 353, respectively. A summary curve of the acoustic results is presented on Figure 354. As indicated, an increase of the second stage turbine spacing to one nozzle tip chord would result in a significant noise reduction for the J85.

In addition to the spacing tests, the Phase I program investigated problems associated with high temperature treatment design and established criteria necessary to apply acoustic treatment technology to turbine noise reduction studies. A number of candidate materials (Figure 355) were evaluated using the high temperature acoustic duct facility (Figure 356). Typical results are shown on Figures 357 through 359. These studies concluded that Single Degree of Freedom (SDOF) treatment should be used in high temperature applications because of its predictable acoustic behavior in the turbine environment and its superior mechanical characteristics.

Thus, based on Phase I results, the best acoustic configurations for minimizing the turbine noise would be: first, increasing the turbine second-stage axial spacing to reduce the noise generation and, then, adding acoustic treatment in the turbine exhaust duct.

Spacing is not the only method for reducing the source noise in turbomachinery. Other techniques which have been used successfully in the past for fan/compressor modifications include: circumferential lean of the stationary blades to phase the interaction, swept blades to increase the spacing in the tip region, and changing the rotor/stator blade number ratio to create modes which propagate less efficiently. Within the scope of this program, however, the only practical alternative to spacing was to circumferentially lean the second-stage vanes. Analytical studies were made to determine the relative noise reduction of spacing versus leaned vanes. The analysis procedure used was similar to the one presented in Reference 43. Results from these studies are summarized on Figures 360 and 361. For the J85, spacing is the best initial method to reduce the noise generated by the second-stage vane/blade interaction.

Thus, it was decided that the two turbine acoustic configurations that would be tested were: (1) spacing, and (2) SDOF acoustic treatment downstream of the spaced turbine.

A practical upper limit on the amount of treatment that might be utilized in an engine application is "one diameter in length with a treated splitter." Testing the J85 with maximum exhaust treatment thus would provide an estimate of the upper limit for turbine noise suppression. Selection of the amount of treatment required to meet any systems goals could then be determined by interpolation rather than extrapolation. A nominal tuning frequency of 16 KHz was selected in order to: (1) suppress the stage 1 noise (not directly affected by spacing), and (2) utilize the broadband suppression characteristics of SDOF to further reduce the stage 2 noise in the far field. The results of a design study for the J85 showed that a treatment depth of

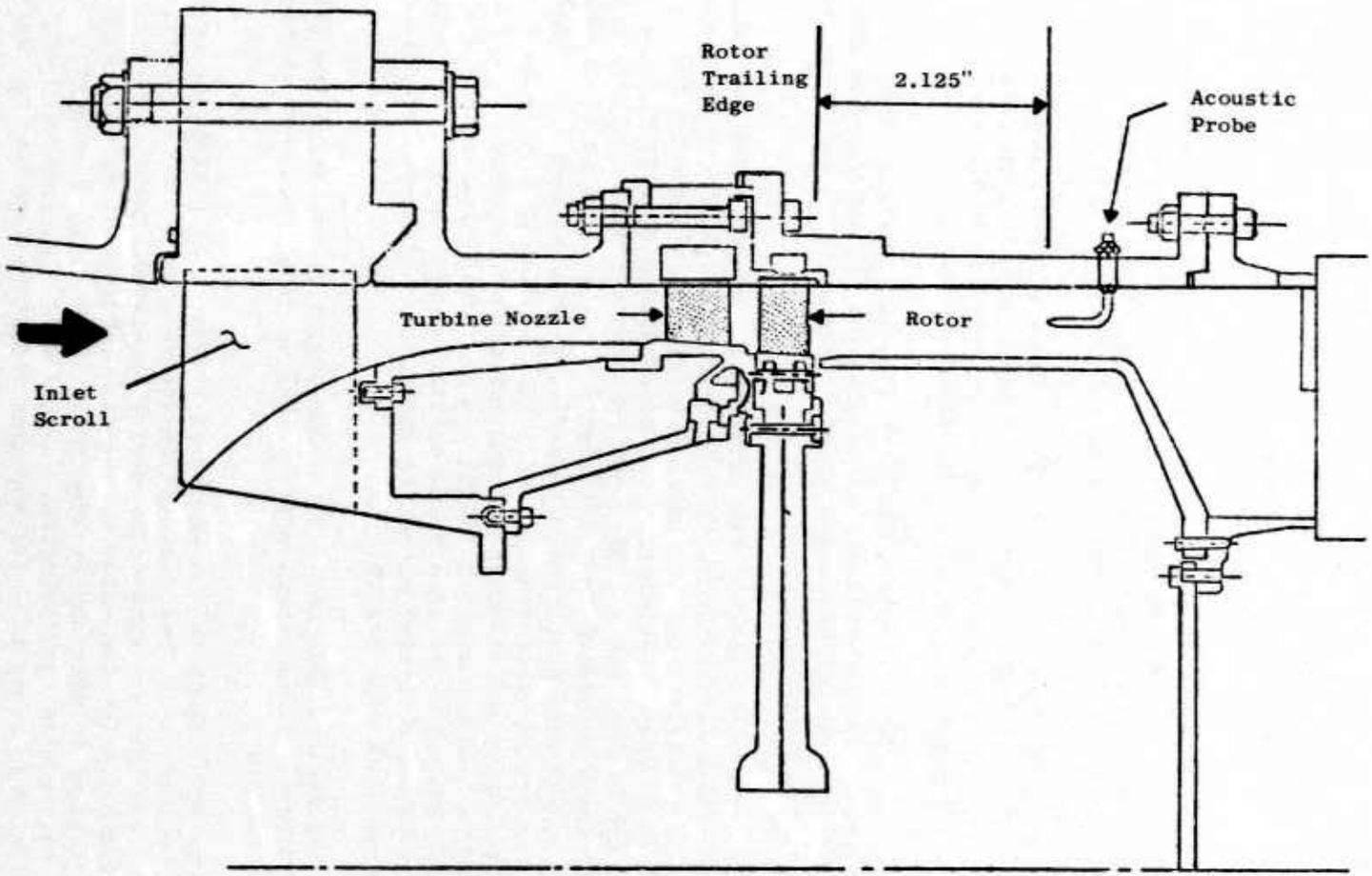

Figure 352. Schematic of Test Turbine.

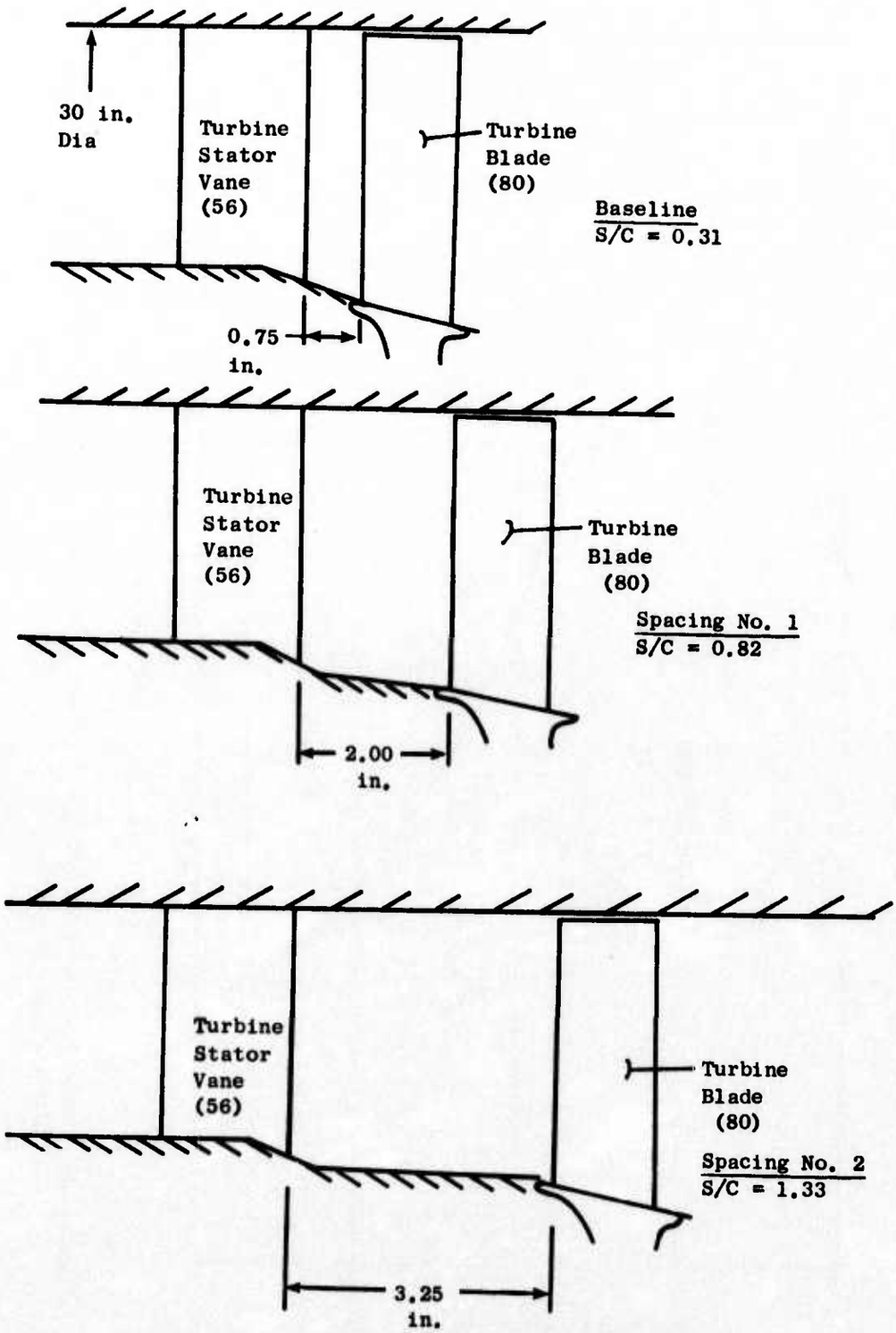

Figure 353. Turbine Schematics and Spacings Tested.

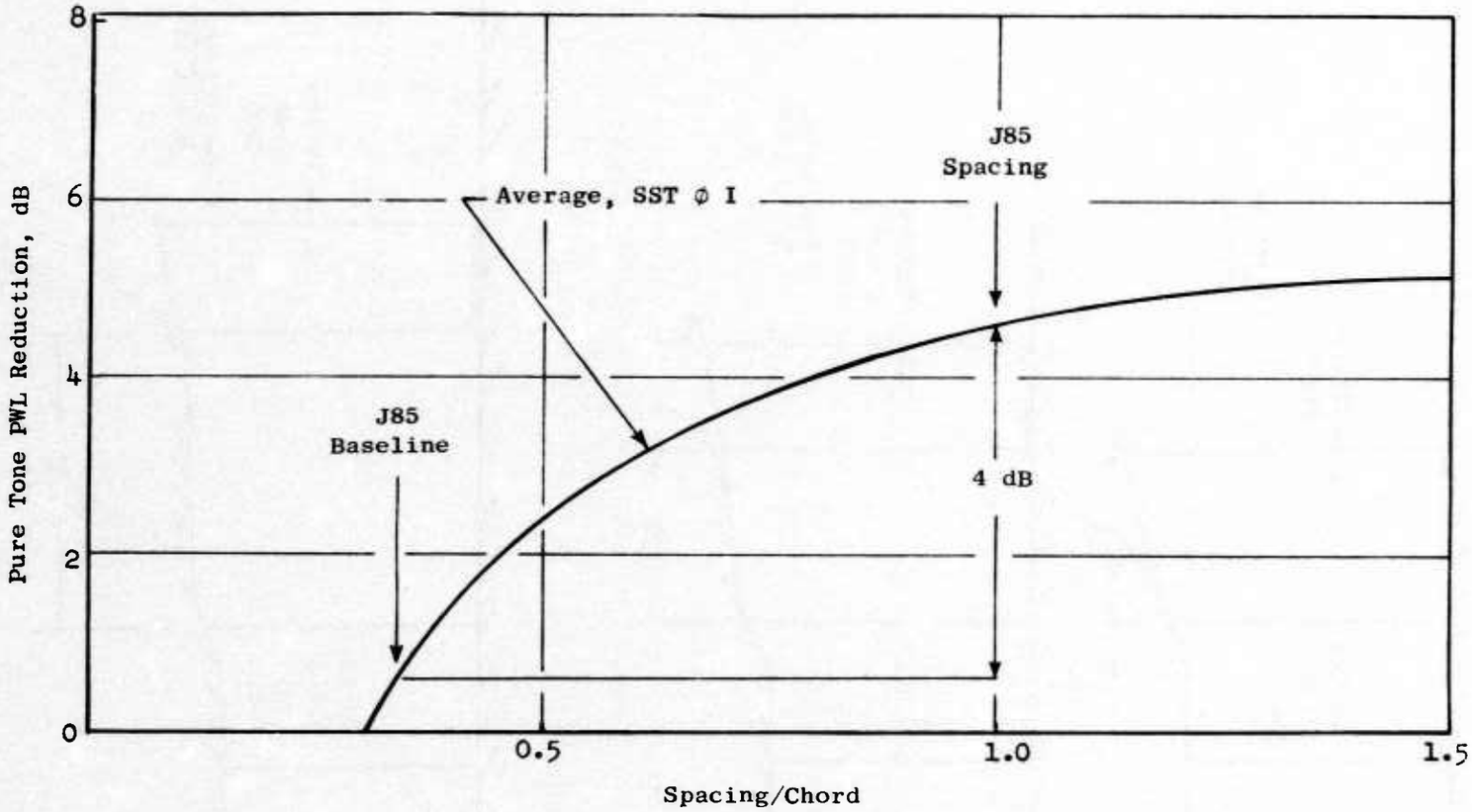

Figure 354. Effect of Spacing on High Pressure Turbine, Supersonic Transport Noise Reduction Technology, Phase I.

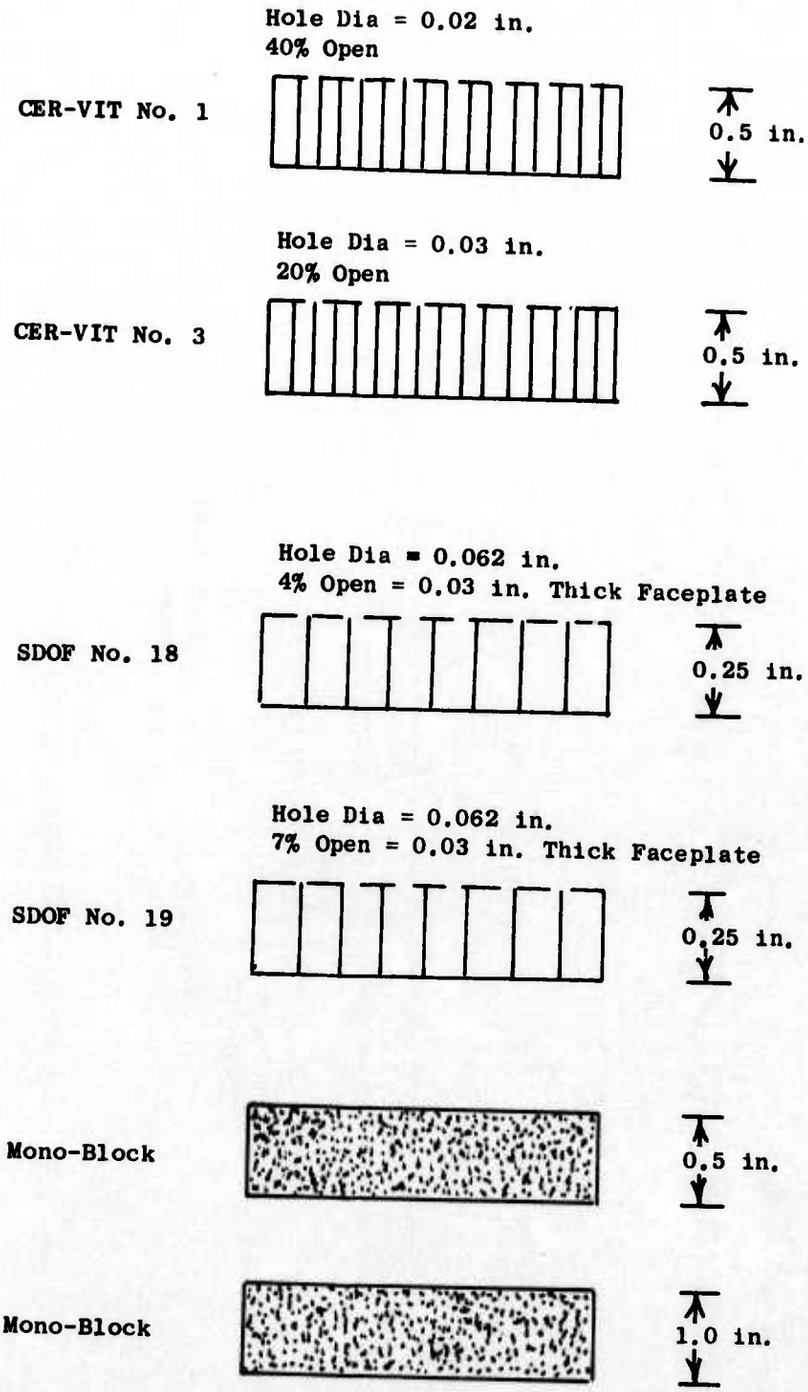

Figure 355. High Temperature Acoustic Treatment, SST Noise Reduction Technology, Phase I.

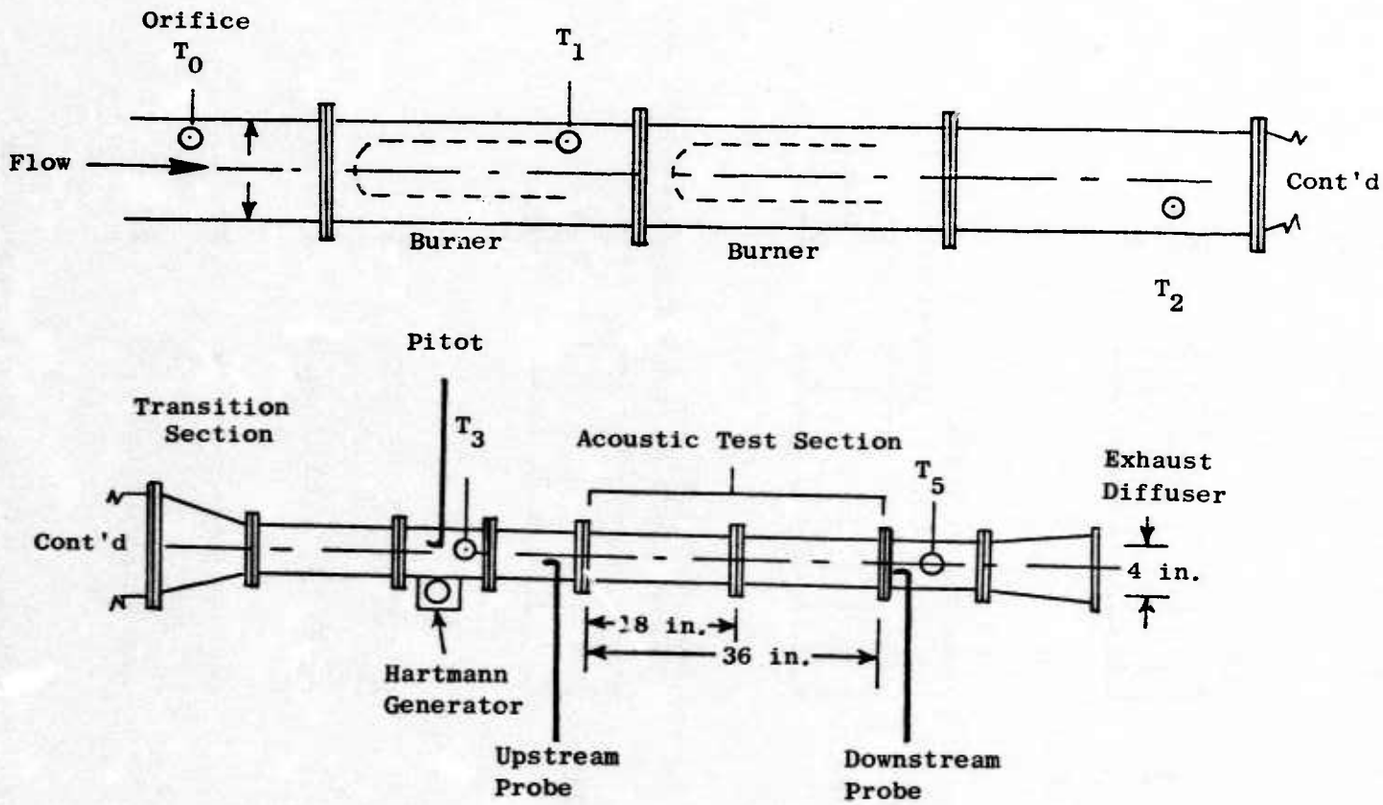

Figure 356. Schematic of High Temperature Acoustic Duct Facility.

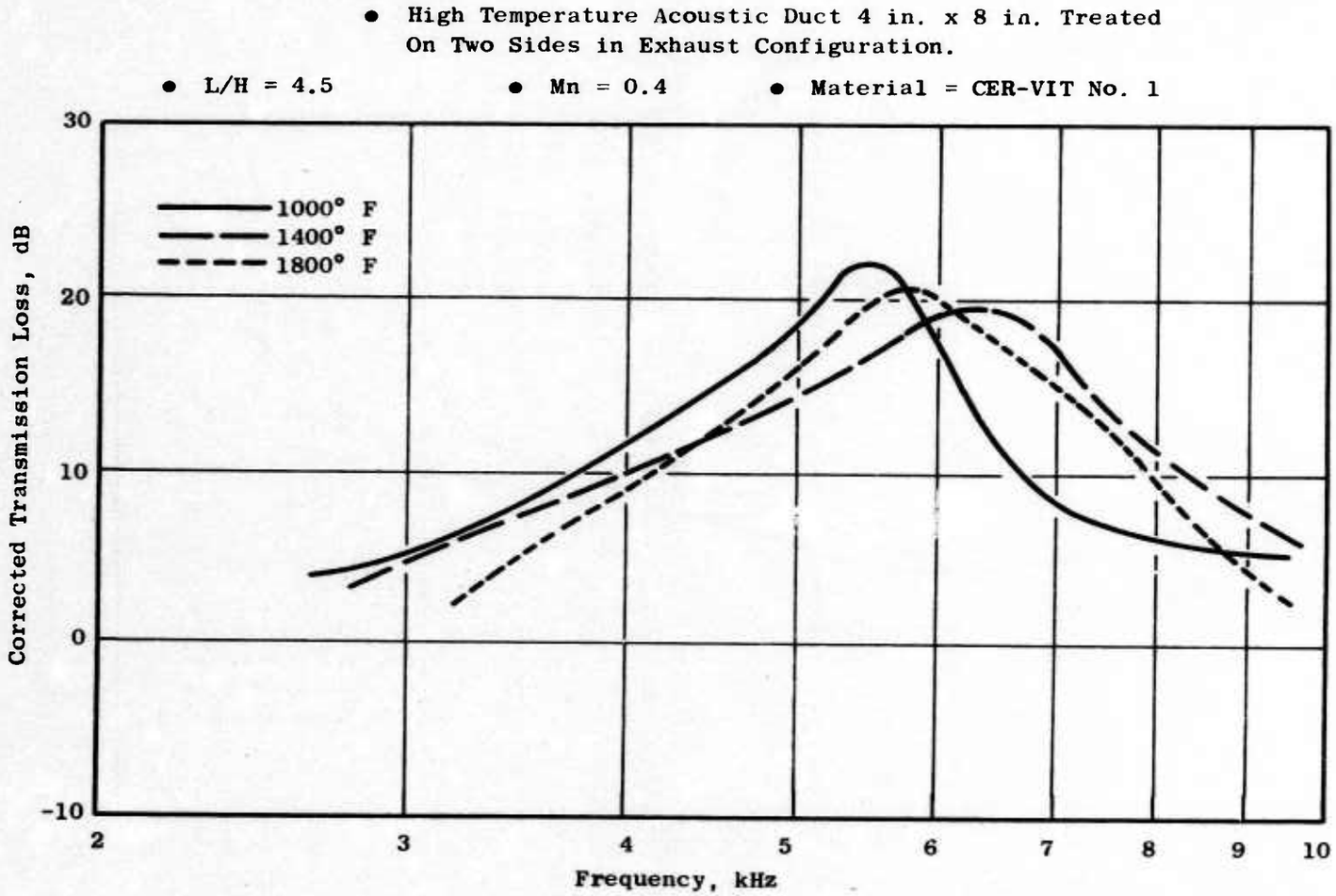

Figure 357. Corrected Transmission Loss Versus Frequency, CER-VIT No. 1, SST Noise Reduction Technology, Phase I.

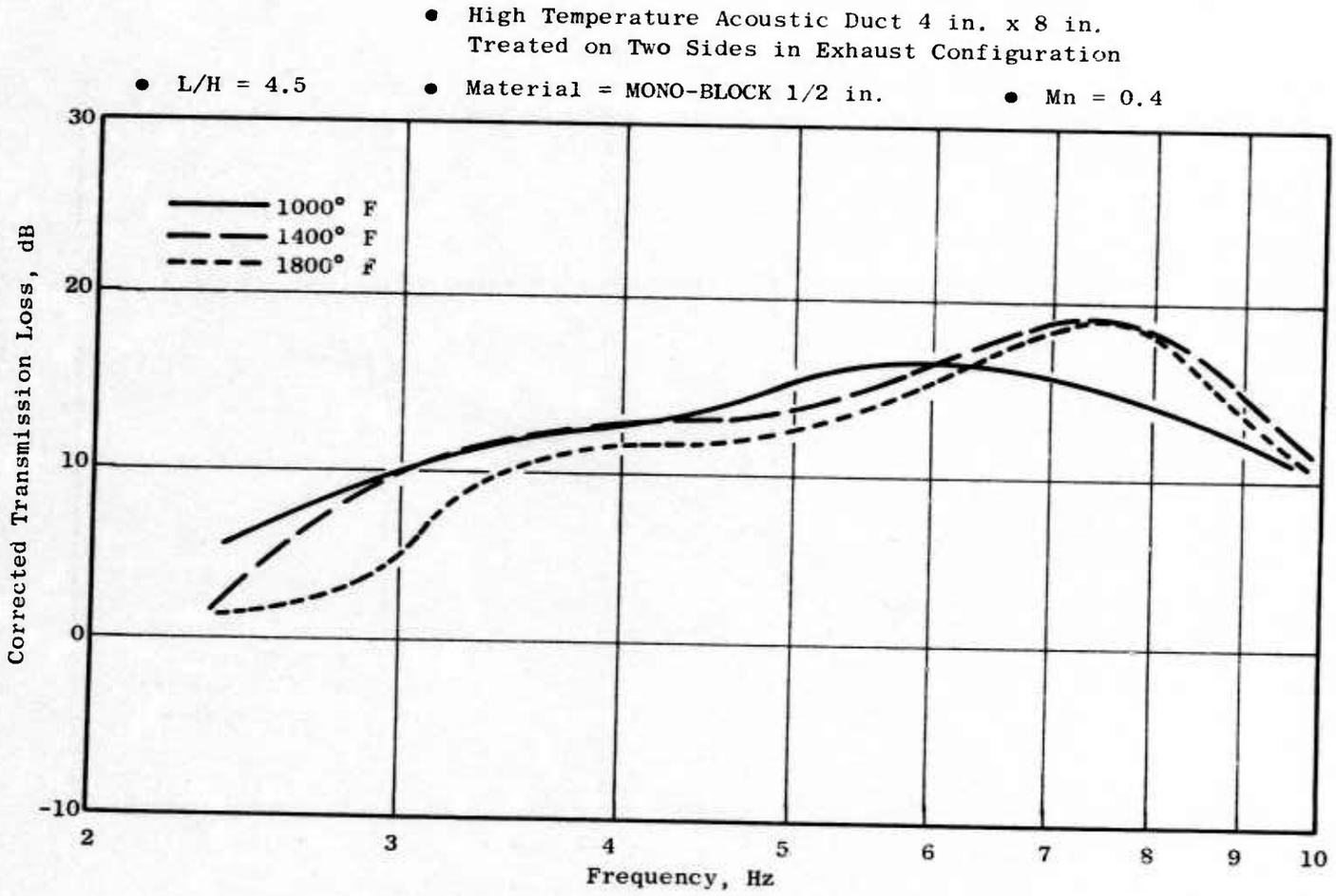

Figure 358. Corrected Transmission Loss Versus Frequency, 1/2" Mono-block, SST Noise Reduction Technology, Phase I.

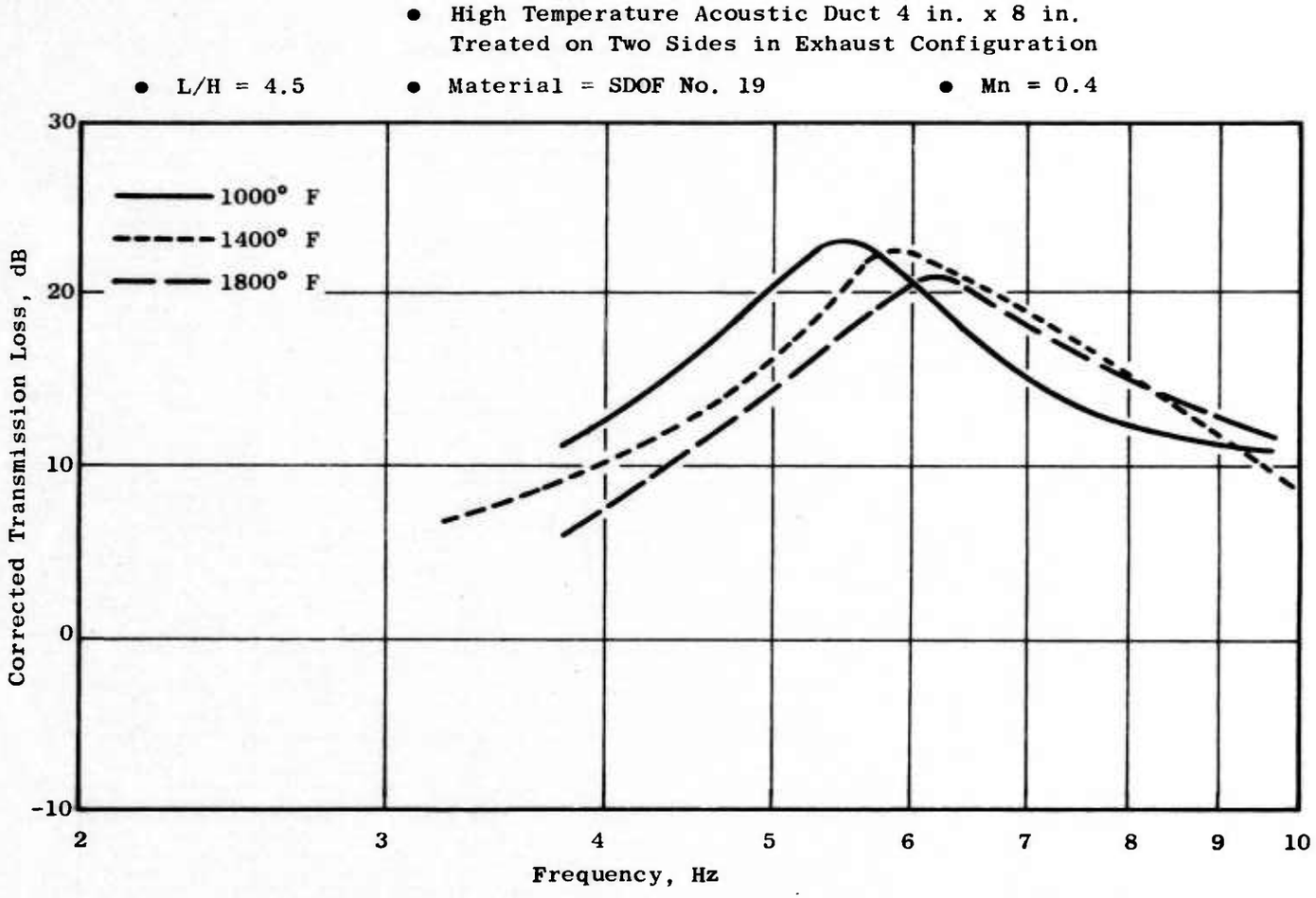

Figure 359. Corrected Transmission Loss Versus Frequency, SDOF No. 19, SST Noise Reduction Technology, Phase I.

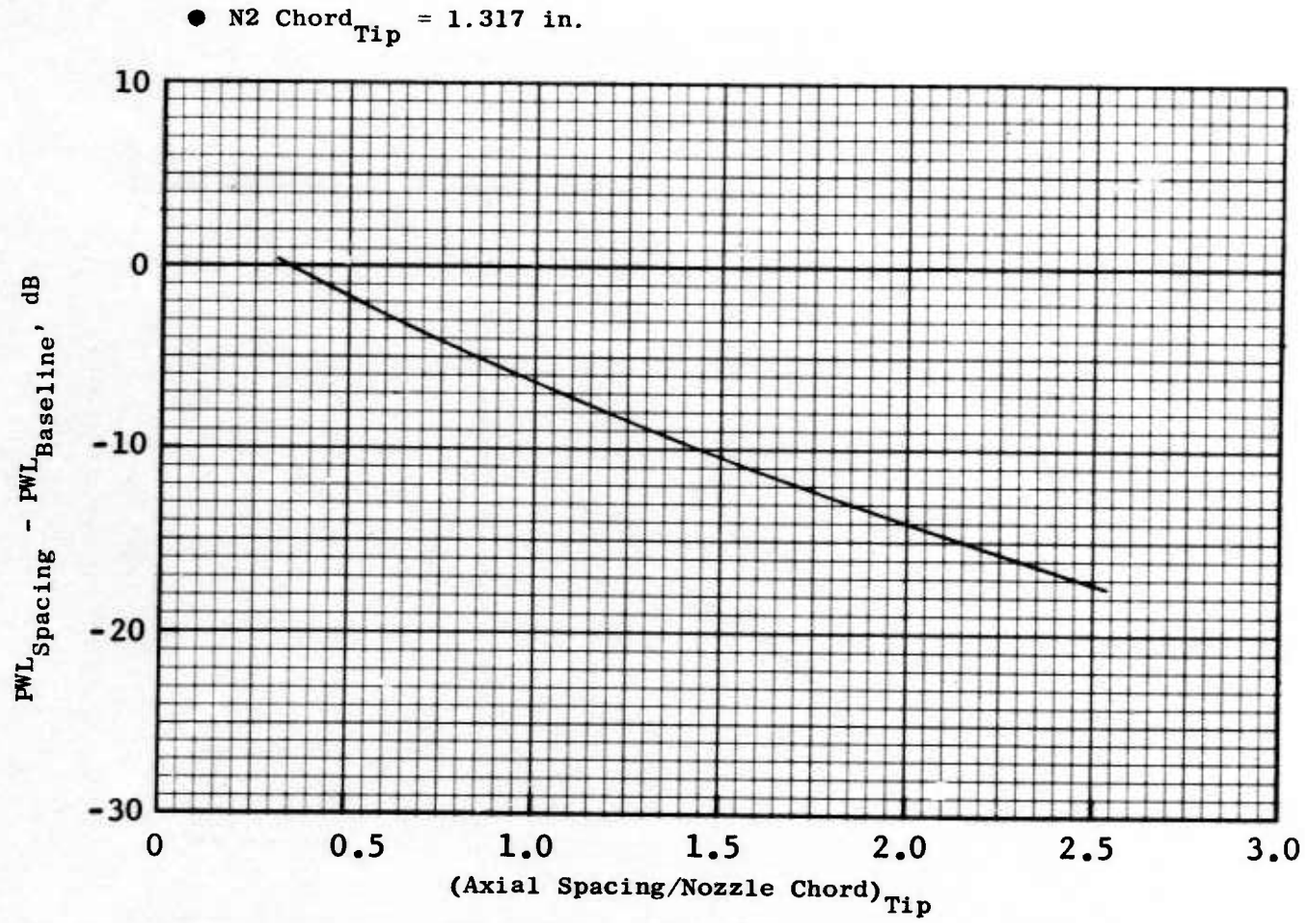

Figure 360. Predicted Noise Reduction with Second-Stage Spacing.

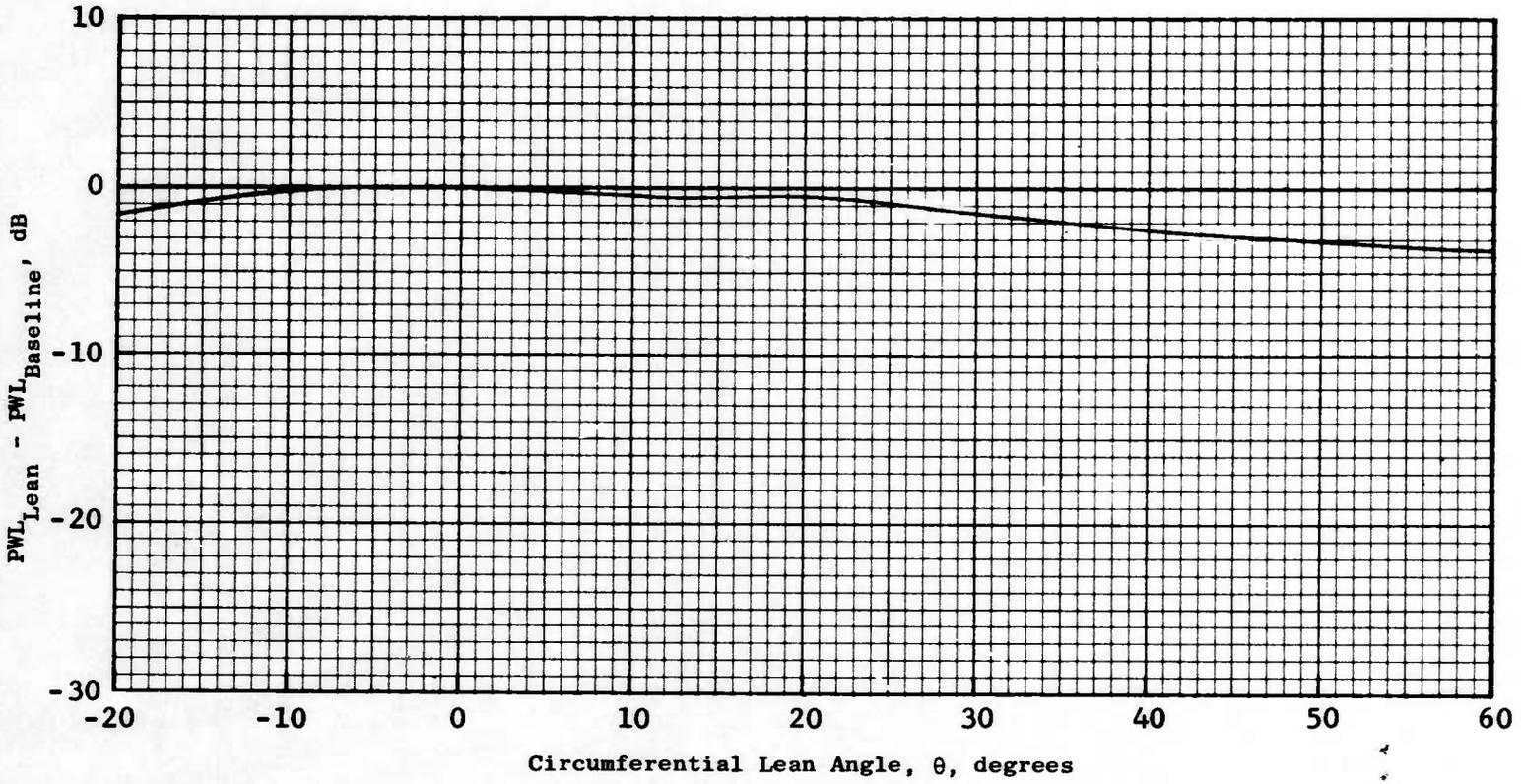

Figure 361. Predicted Noise Reduction with Second-Stage Vane Lean.

0.125 inch, having a peak suppression in the 14.5 KHz to 18 KHz range (approach through takeoff), would provide significant turbine suppression.

The J85 turbine schematic was shown previously on Figure 351. The spaced second-stage turbine and the spacing-plus-treatment configurations are illustrated schematically on Figures 362 and 363. The hardware for the acoustic treatment section is shown on the photograph of Figure 364. The assembled treatment section is shown on Figure 365 (aft looking forward).

4.3.1.3 Isolation of Turbine Noise

In order to minimize the inlet noise radiated to the far field, an inlet suppressor which has been used successfully for J79 testing (Reference 1) was adapted to the J85 (Figure 366).

The J85 engine has a variable area (A_8) exhaust nozzle. For these acoustic tests, jet noise masking of the turbine acoustic signal presented a potential problem. The far-field jet noise could be reduced by opening the nozzle which lowered the jet exit velocity. A review of available J85 data on the engine operating limitations was made, and the maximum nozzle area setting for the acoustic tests was determined to be: 200 $in.^2$ at 70% through 95% rpm and 160 $in.^2$ at 100% rpm. The nominal value of A_8 at 80% speed is, for comparison, 131 $in.^2$.

An analytical study was made to determine the effectiveness of testing at maximum A_8 in order to unmask the turbine. The turbine noise model from Smith and Bushel (Reference 8) and the SAE AIR 876 jet noise model (Reference 44) were used. Typical predicted spectra from these studies are presented on Figures 367 and 368. Also shown for comparison are the predicted jet spectra for the J85 at the nominal area setting. Two important conclusions from this study were:

(1) Opening the exhaust nozzle is necessary in order to avoid masking of the turbine by the jet noise.

(2) Even at maximum A_8, there may still be a potential jet noise masking problem at 95% and 100% rpm.

Because the acoustic effects of the inlet suppressor and operation at maximum A_8 were not known, extra testing was planned for the baseline configuration; i.e., the baseline J85 was tested on a nominal and maximum A_8 schedule both with and without the inlet suppressor. Thus, comparisons could be made to determine the extent of compressor, jet, and turbine noise for the baseline J85, and the effect of the suppressor and maximum A_8 operation on the turbine far-field acoustic signal could be determined.

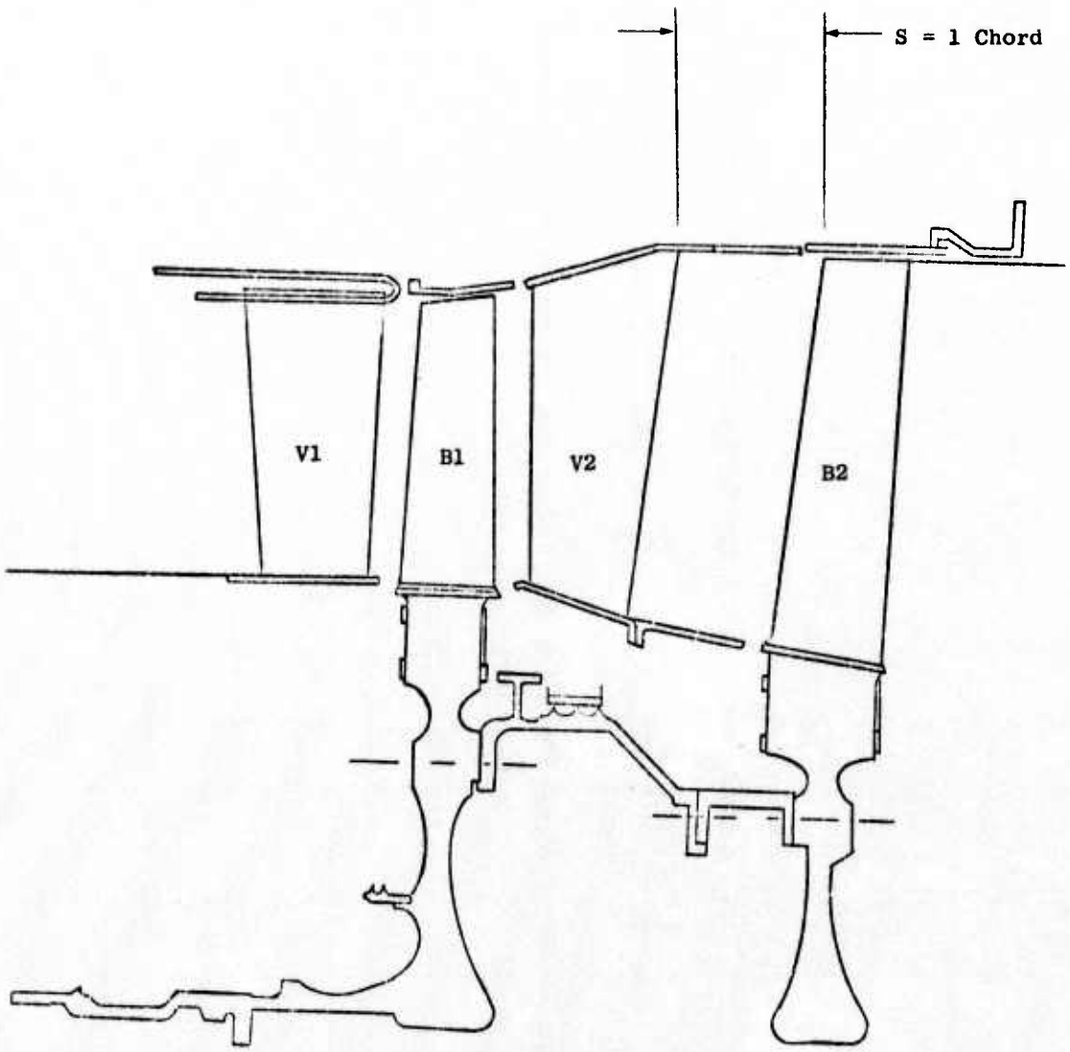

Figure 362. J85-5 Turbine Increased Spacing, V2-B2.

Resonator Depth = 0.125"

Face Plate Porosity = 6.5%

Hole Diameter = 0.04"

Face Plate Thickness = 0.015"

Cell Size = 0.20" - 0.225"

L/D_{tip} = 1.0

L/H = 9.85

Tuning Frequency = 16 KHz (Nominal)

H/λ = 1.39

Treatment Area = 2600 in^2

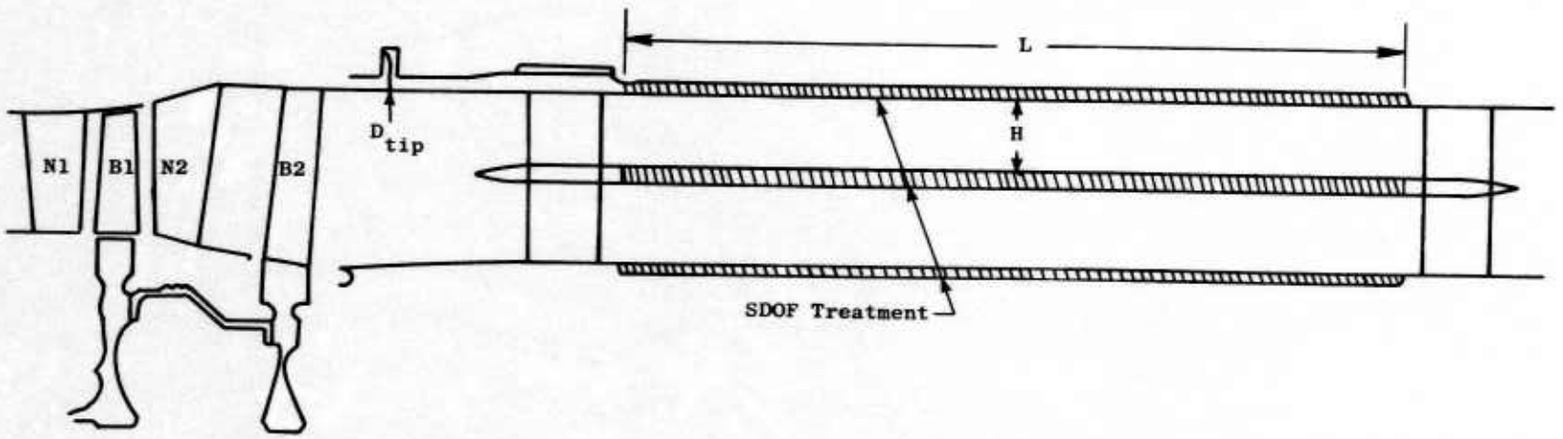

Figure 363. J85 Turbine Spacing + Treatment.

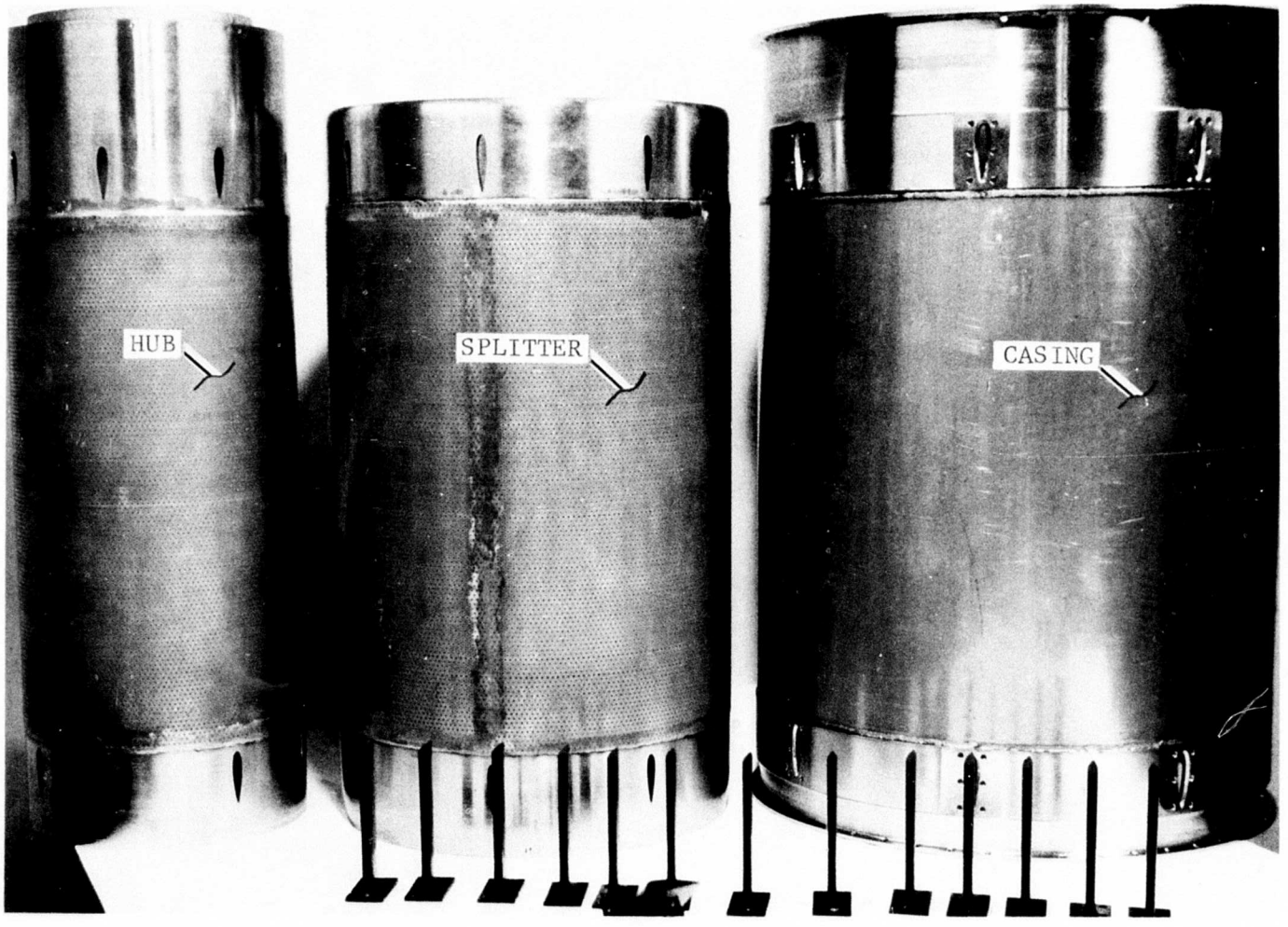

Figure 364. Hardware for Exhaust Acoustic Treatment Section.

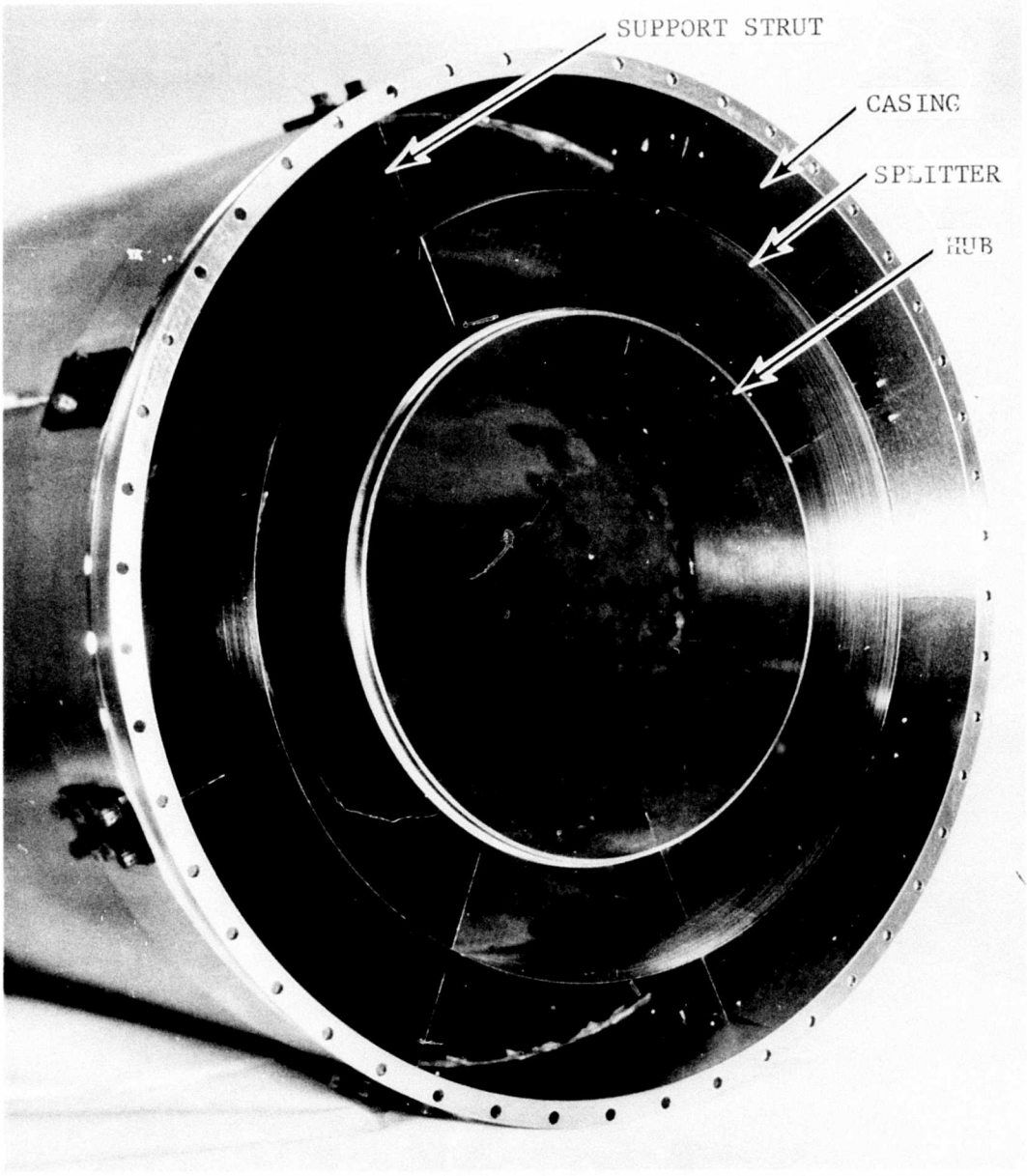

Figure 365. Exhaust Acoustic Treatment Section Assembled, Aft Looking Forward.

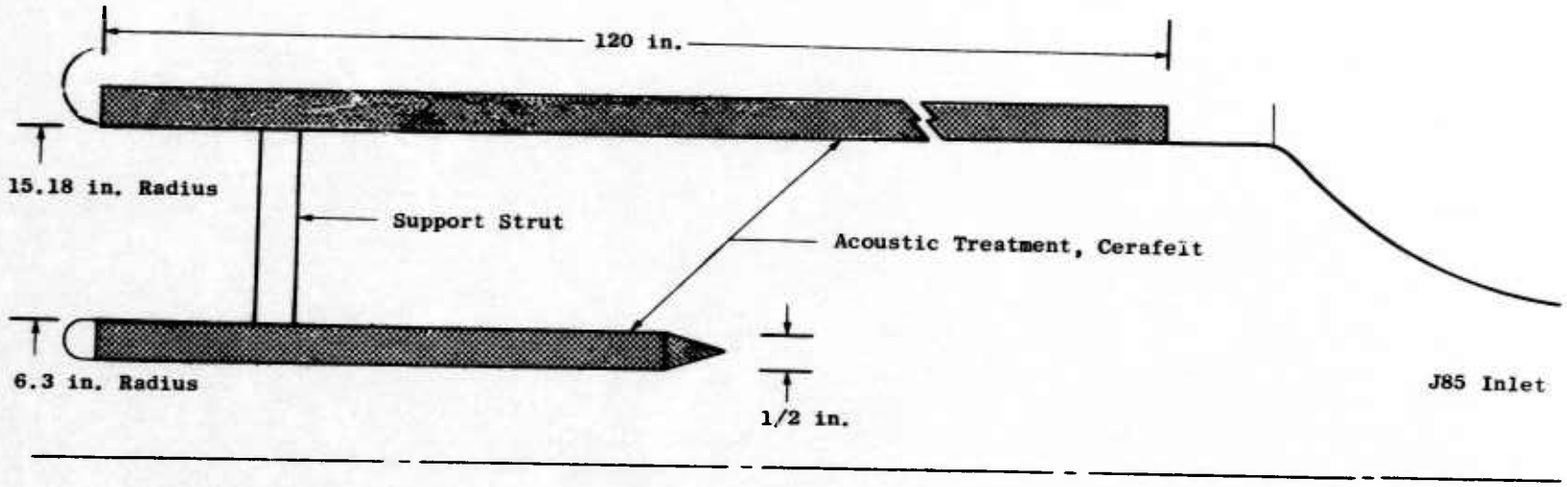

Figure 366. Schematic of Inlet Suppressor Adapted for J85 Tests.

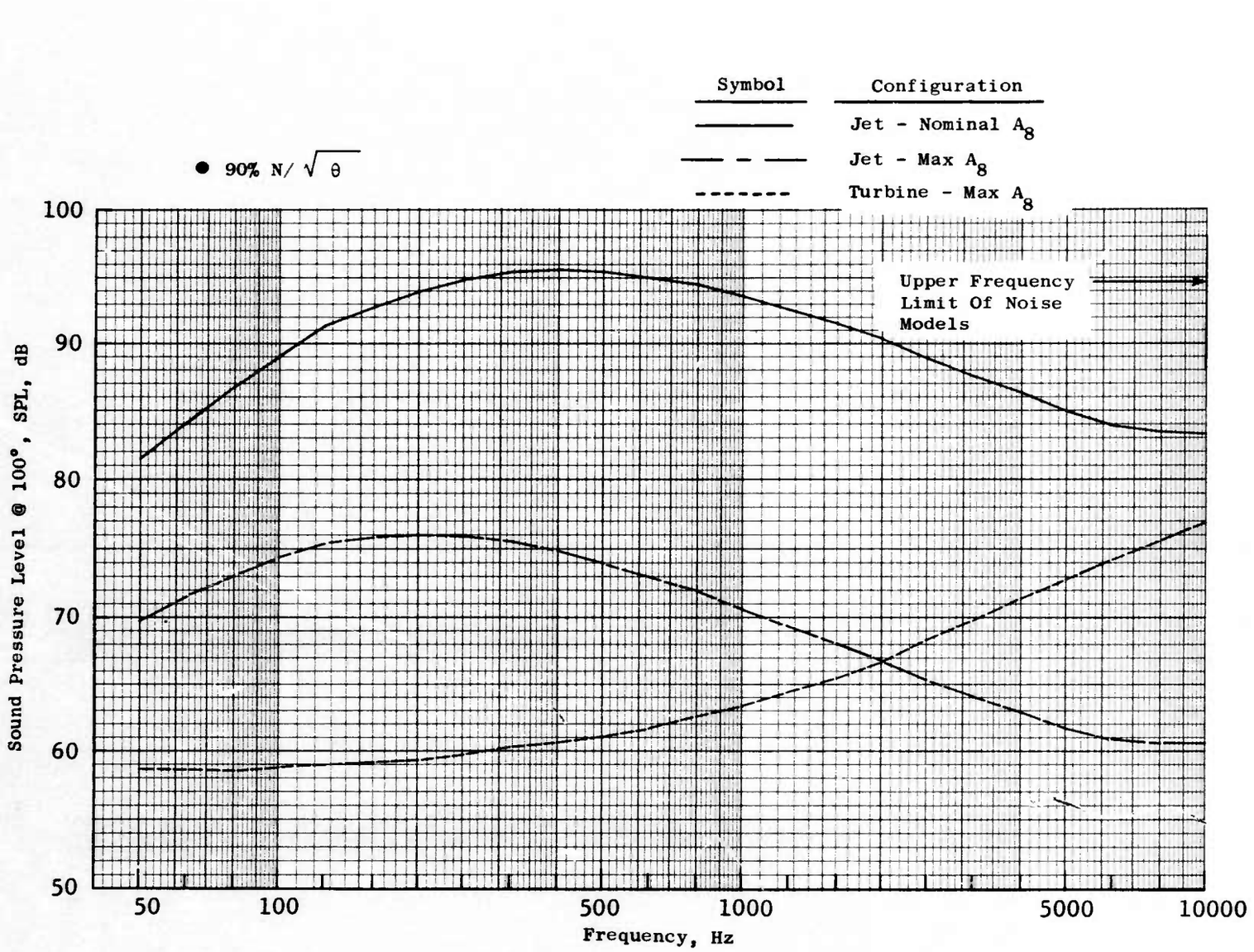

Figure 367. Component Noise Prediction, J85 Baseline, 90% N/√θ.

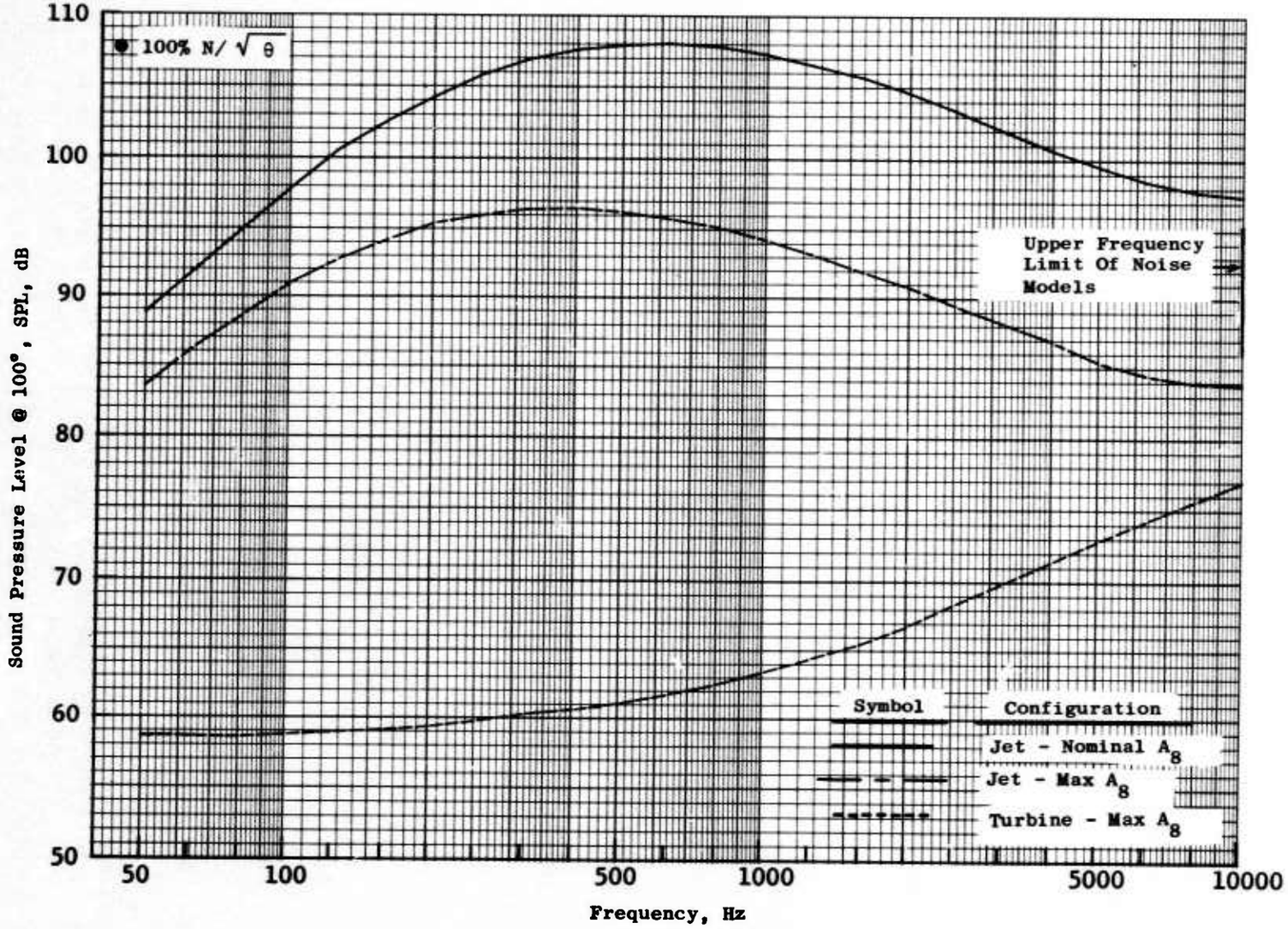

Figure 368. Component Noise Prediction, J85 Baseline, 100% N//θ.

4.3.1.4 Test Program and Results

The test program was performed at the General Electric Flight Test Center facilities, located at Edwards Air Force Base in Southern California. A description of this facility is presented in Appendix A. In Appendix B, the acoustic data reduction system is described.

The acoustic tests of the J85 were performed according to the test matrix presented on Table 13. Summaries of the actual nozzle settings and speeds tested along with the ambient conditions for the baseline (max. A_8 with inlet suppressor), spacing, and spacing plus treatment configurations are presented in Appendix D.

4.3.2 Discussion of Results

4.3.2.1 Identification of Turbine Noise

As has been noted previously, in order to ensure that the turbine noise could be measured in the far field, the tests were performed with an inlet suppressor (minimize inlet noise) and on a maximum exhaust nozzle schedule (low jet noise). Additional points were added to the baseline tests in order to investigate the effects and the effectiveness of these measures.

The approximate peak Strouhal frequency (peak jet noise) is 400 Hz. The jet noise reduction which was achieved is indicated by comparing the 400 Hz 1/3-octave SPL directivities for the nominal A_8 schedule and the maximum A_8 tests, Figure 369 (100% rpm) for example.

Similarly, the effectiveness of the inlet suppressor is shown by comparing the first-stage compressor tone SPL directivities (1/3-octave data) for the bellmouth inlet and the inlet suppressor configurations, Figure 370 (80% rpm).

The combined effect of maximum A_8 operation and the inlet suppressor are shown on Figures 371 through 373 where typical one-third octave spectra at 40° (front max. noise), 110° (turbine max. noise), and 140° (aft max. noise) are shown at approach for the bellmouth/nominal A_8, bellmouth/max. A_8 and inlet suppressor/max. A_8 acoustic tests. In addition to supporting the prior evidence that the inlet suppressor and max. A_8 operation were effective in isolating the turbine far-field noise, these spectra comparisons indicate two other things. First, the "bare" J85 (bellmouth inlet/nominal A_8) far-field noise signature contains significant contributions from the compressor and the jet (i.e., the inlet suppressor and max. A_8 operation were necessary to isolate the turbine noise signal). Second, the turbine 1/3-octave "tone" SPL's increased in level when the exhaust nozzle was opened. This indicates that the engine operating point shifted (increasing the turbine noise that was generated); this shift is shown on Figure 374, where the turbine pressure ratio (PT_{in}/PS_{out}) and energy extraction ($\Delta Tt/Tt_{in}$) are shown versus the turbine speed function. Opening the nozzle caused the turbine to operate at a

Table 13. YJ85-5 Test Point Matrix Turbine Noise Reduction.

Corrected Speed, %	Bellmouth		Baseline w/ Inlet Suppressor		Spacing (Max. A_8)	Treatment (Max. A_8)
	Cycle A_8	Max. A_8	Cycle A_8	Max. A_8		
70	X	X	X	X	X	X
75	X			X	X	X
80	X	X	X	X	X	X
85	X			X	X	X
90	X	X	X	X	X	X
95	X			X	X	X
100	X	X	X	X	X	X
Run and repeat at each point.						

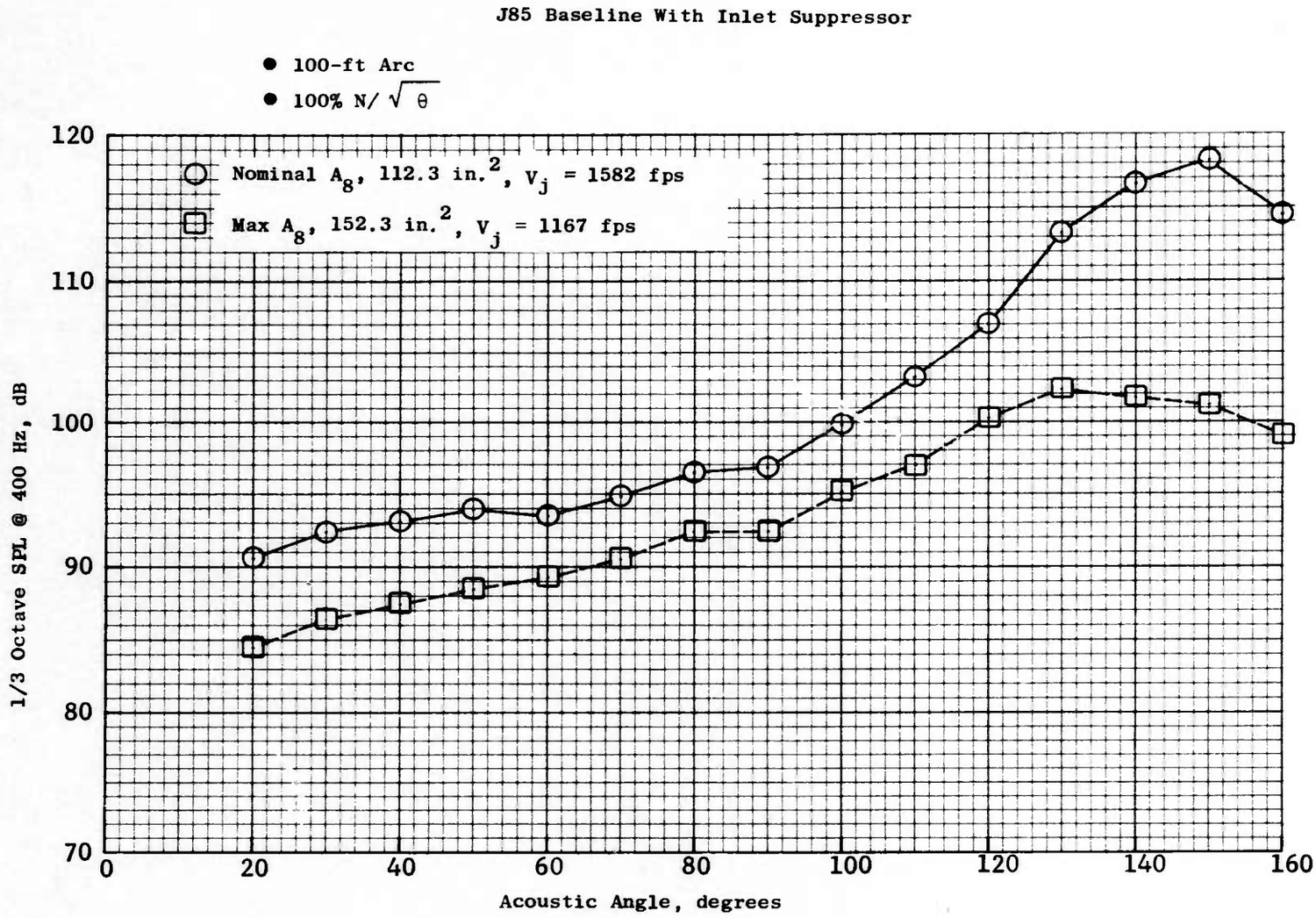

Figure 369. Effect of Maximum A_8 on J85 Jet Noise.

J85 Baseline

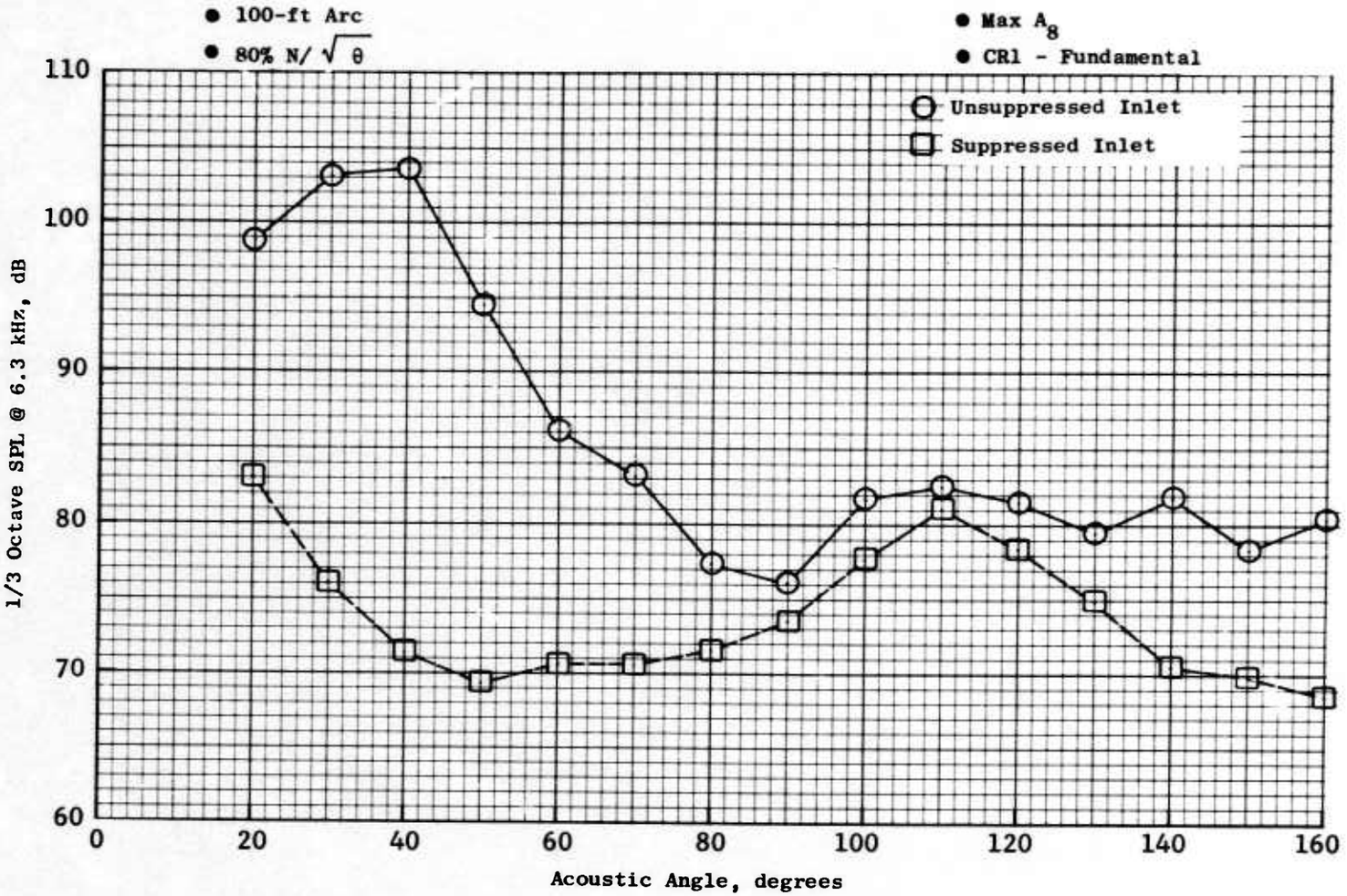

Figure 370. Effect of Inlet Suppressor on Compressor Noise.

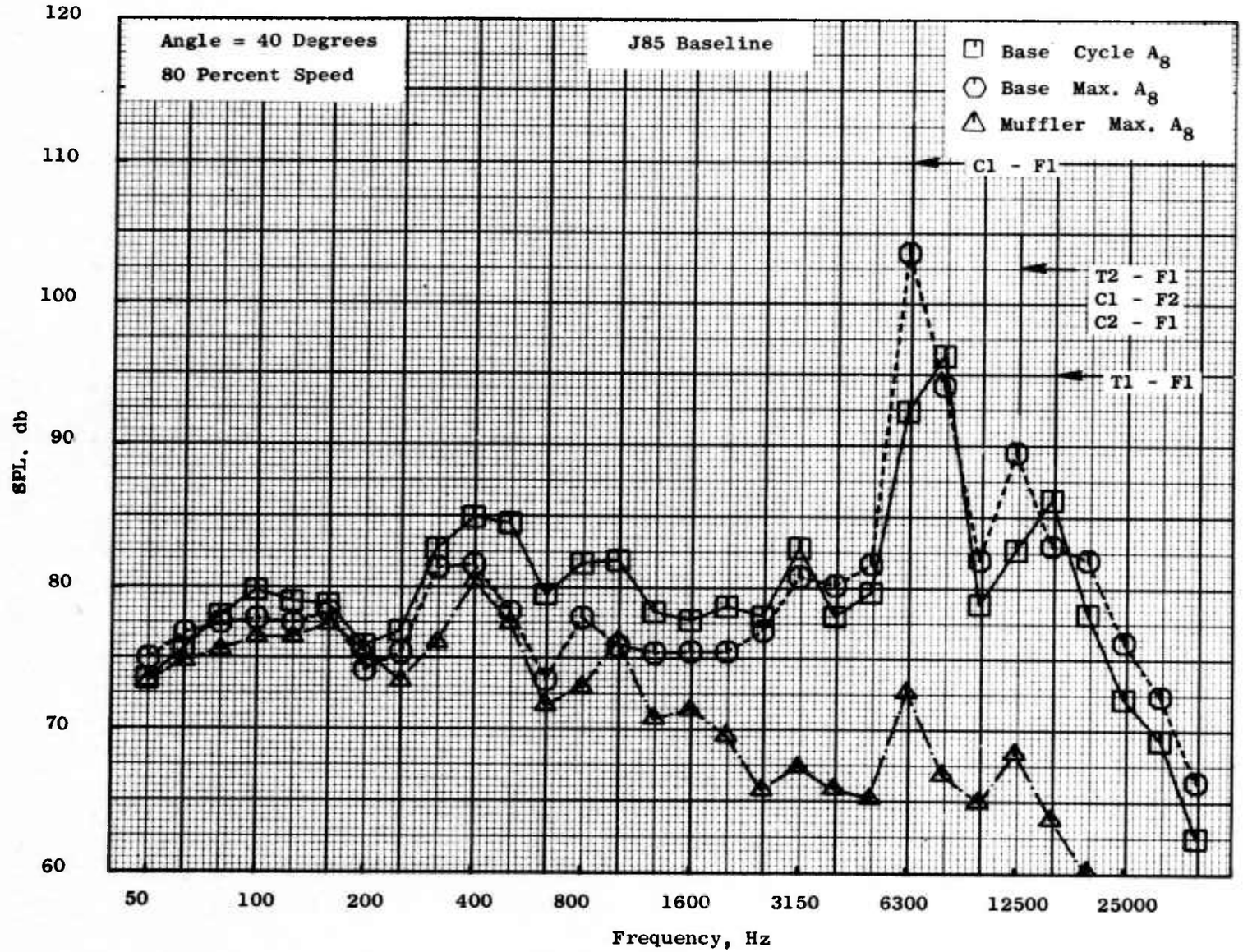

Figure 371. Approach Condition, Maximum Front Noise (40°), 1/3-Octave Spectra.

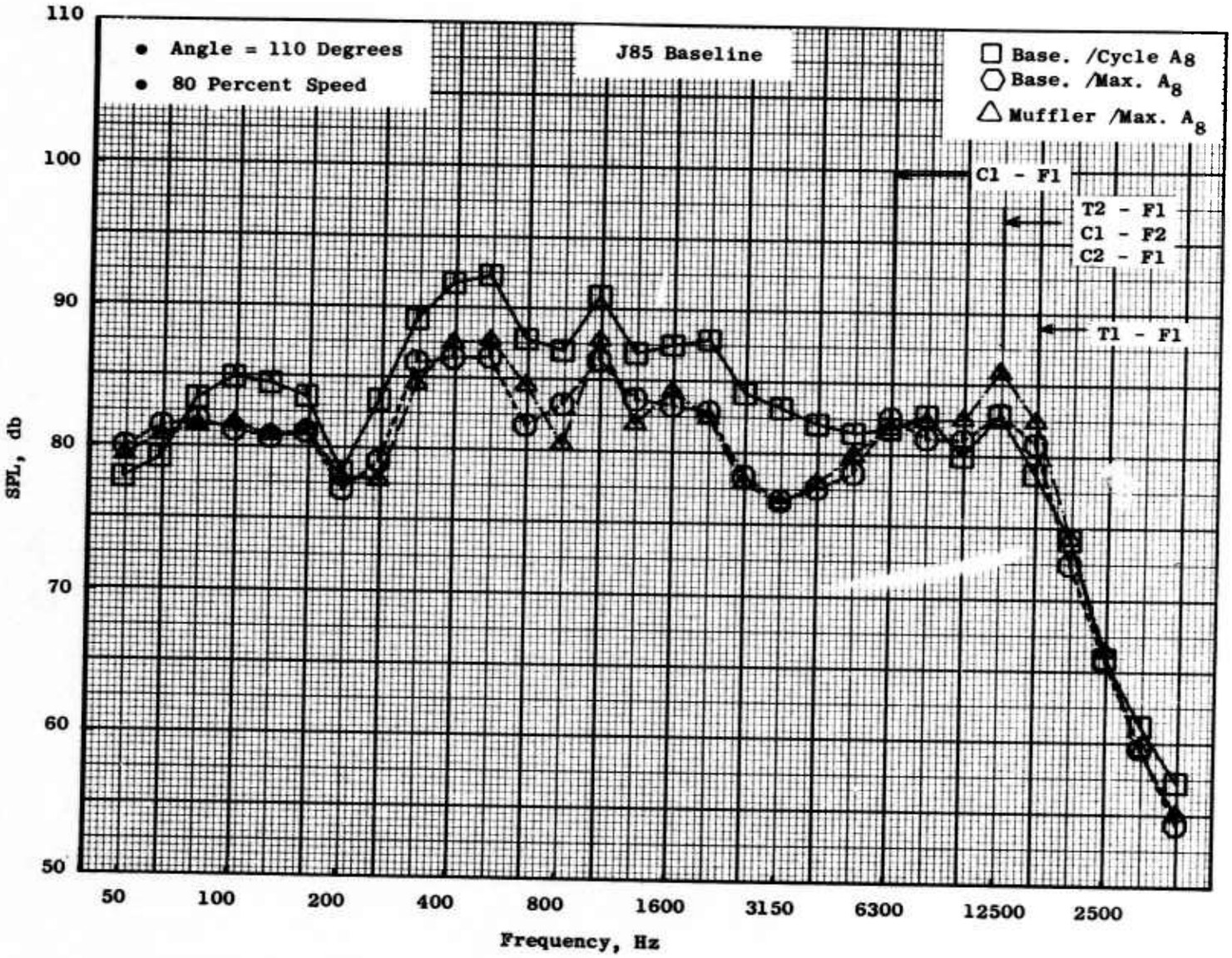

Figure 372. Approach Condition, Maximum Turbine Noise (110°), 1/3-Octave Spectra.

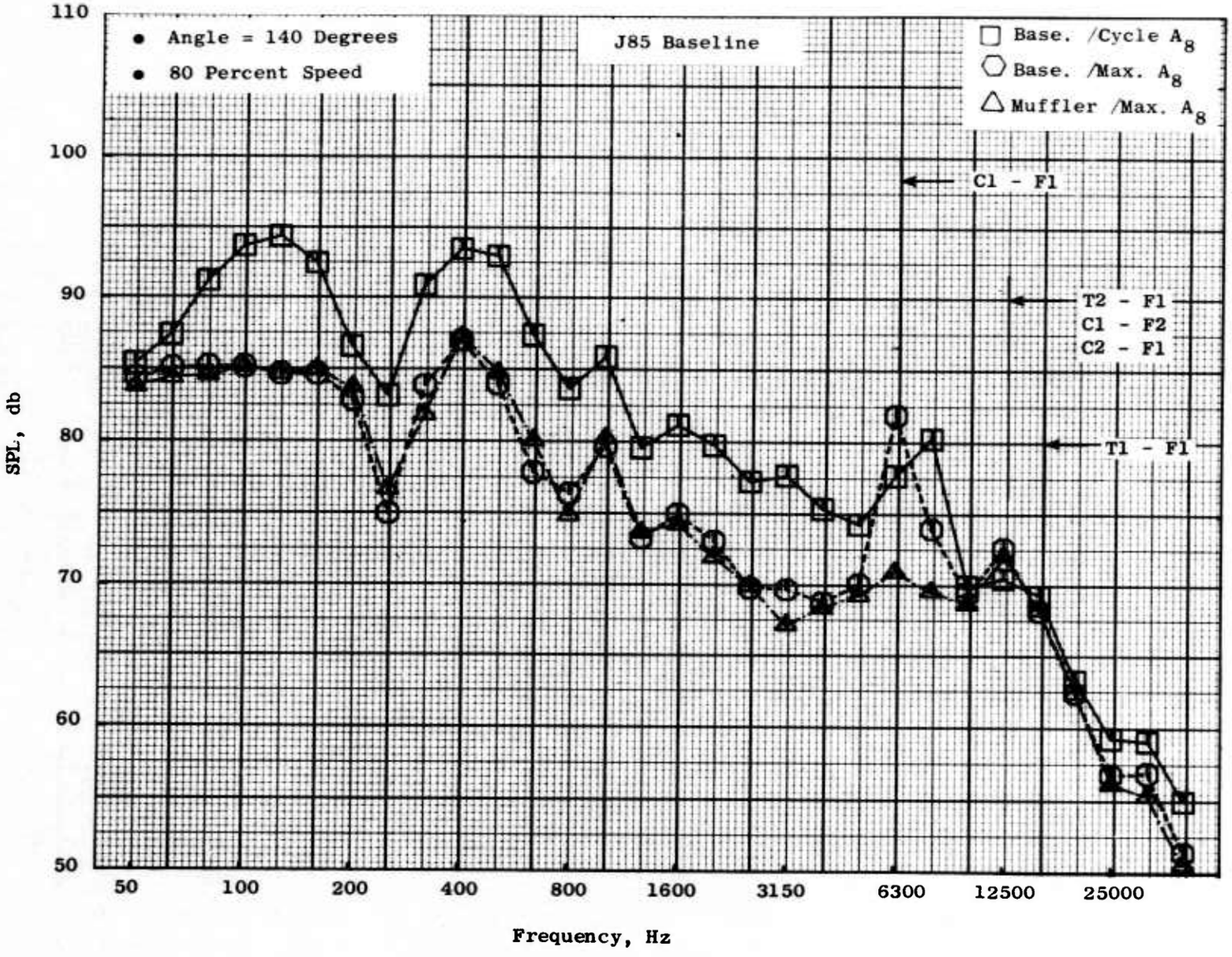

Figure 373. Approach Condition, Maximum Aft Noise (140°), 1/3-Octave Spectra.

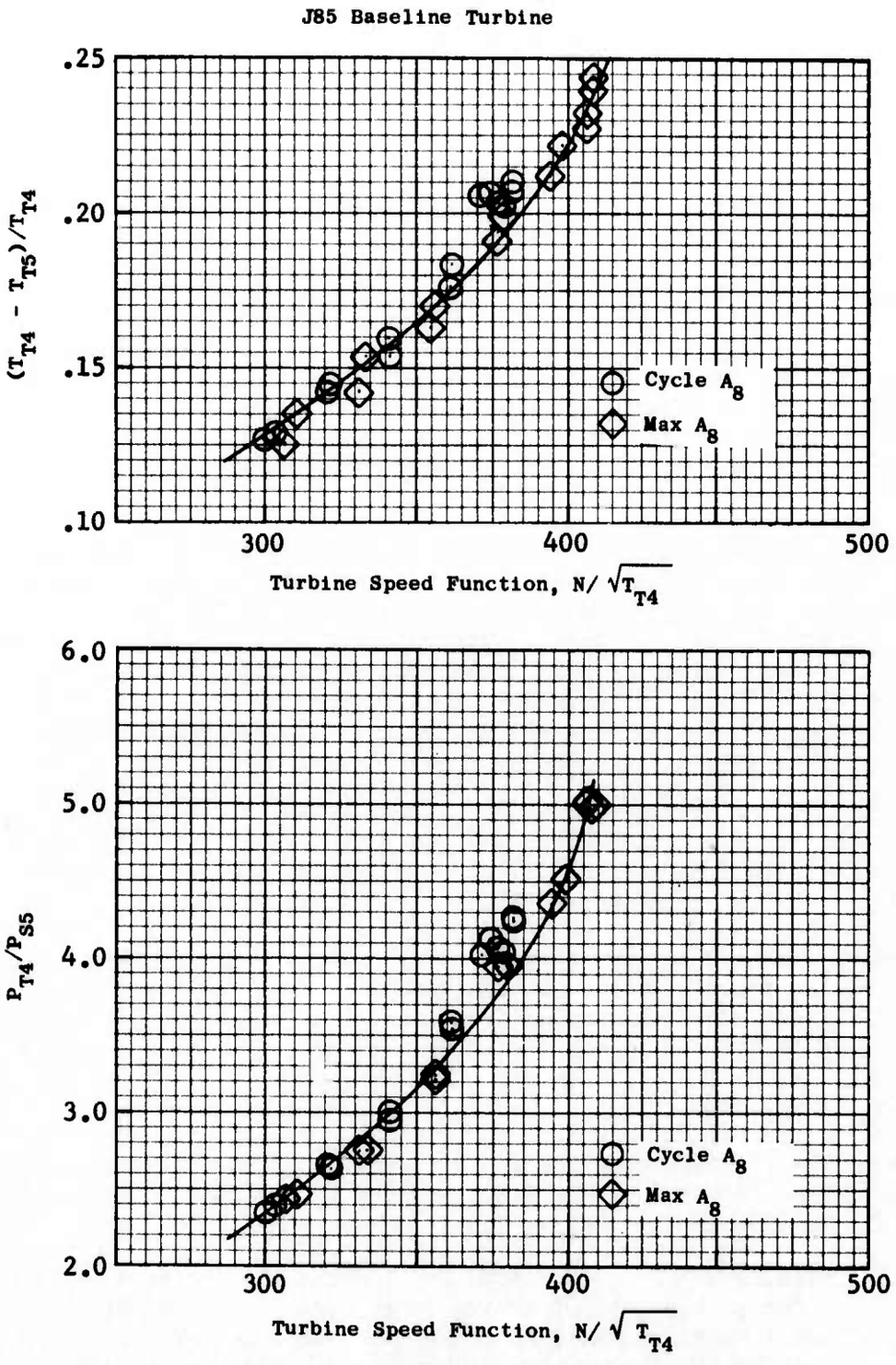

Figure 374. Effect of Open A_8 on Turbine Performance.

higher speed function and, consequently, at a higher pressure ratio and higher loading; this resulted in the turbine noise increase in the far-field data.

As noted on the one-third octave spectra, the band which contains the turbine second-stage blade passing frequency also would contain the compressor tones from the stage 2 fundamental and stage 1 second harmonic. The far-field narrowband spectrum at 80% speed, 110° to the inlet, Figure 375, shows that with the inlet suppressor there were no significant contributions from the compressor tones at 110°. A comparison between the far-field narrowband and one-third octave turbine stage 2 directivities, Figure 376, shows that the influence of the residual compressor tones was negligible for acoustic angles 40° through 160°. For this reason, one-third octave PWL's used in the analysis of the test results do not include the data at 20° and 30°. Comparisons of the far-field narrowband spectra from the configurations tested indicated that 8 KHz should be used as a lower frequency bound for calculating an overall turbine PWL. Both of these results have been factored into the PWL and OAPWL's tabulated in Appendix D.

A second feature which is evident in the far-field narrowbands is that, rather than having a distinct tone at turbine blade passing in the far field, there is a rather broad hump or haystack of noise in the far field around the blade passing frequency. Examination of the baseline probe narrowbands (Figures 377-380) reveals that in the duct the turbine noise is indeed a tone. The mechanism behind this modulated tone (haystack) in the far field is thought to be the effect of radiation of the turbine tones through the turbulent jet. The total "tone" energy in the far field is then the integrated value across the frequency range of the haystack; this integration is approximated by using the 1/3-octave PWL's in this report. A comparison between the far-field one-third octave PWL's and the duct (probe) PWL's is shown on Figure 381. Considering the unknowns (i.e., transmission from the duct to the far field) the agreement is quite good.

The J85 baseline turbine directivity (stage 2) is compared with the directivities from Smith and Bushell's work (Reference 8) on Figure 382. The good agreement in the aft quadrant shows that operation at maximum A_8 did not create a turbine directivity pattern untypical of a turbojet.

In summary then:

- The J85 turbine noise was discernable in the far field when the inlet suppressor was used, and the exhaust nozzle was at the maximum area setting.

- Opening the exhaust nozzle shifted the turbine to a higher point on its operating line. This resulted in a higher turbine noise level at max. A_8, which suggests a strong dependence of turbine noise on the turbine pressure ratio and/or energy extraction.

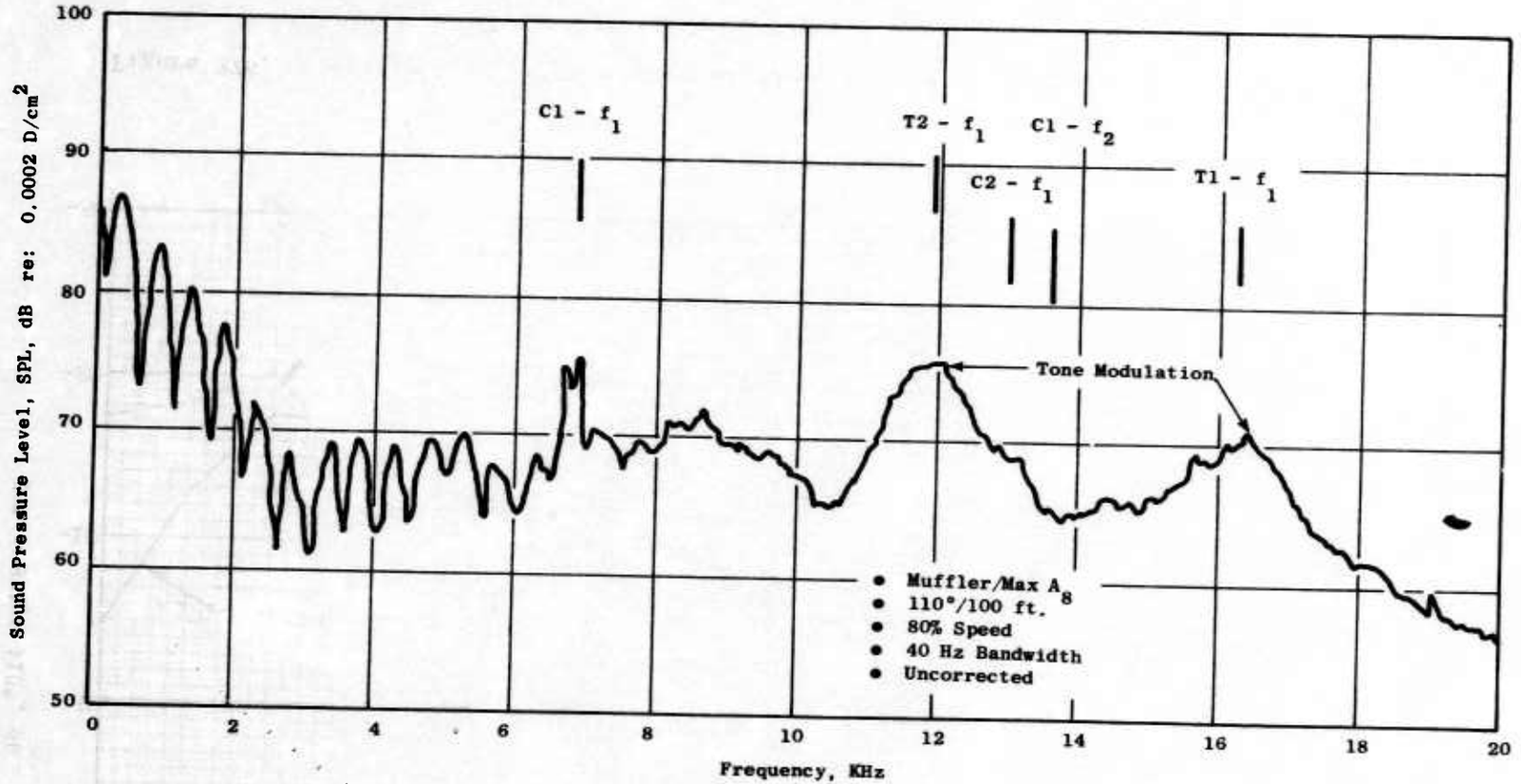

Figure 375. Far-Field Narrowband Spectrum Inlet Suppressor/Max. A_8.

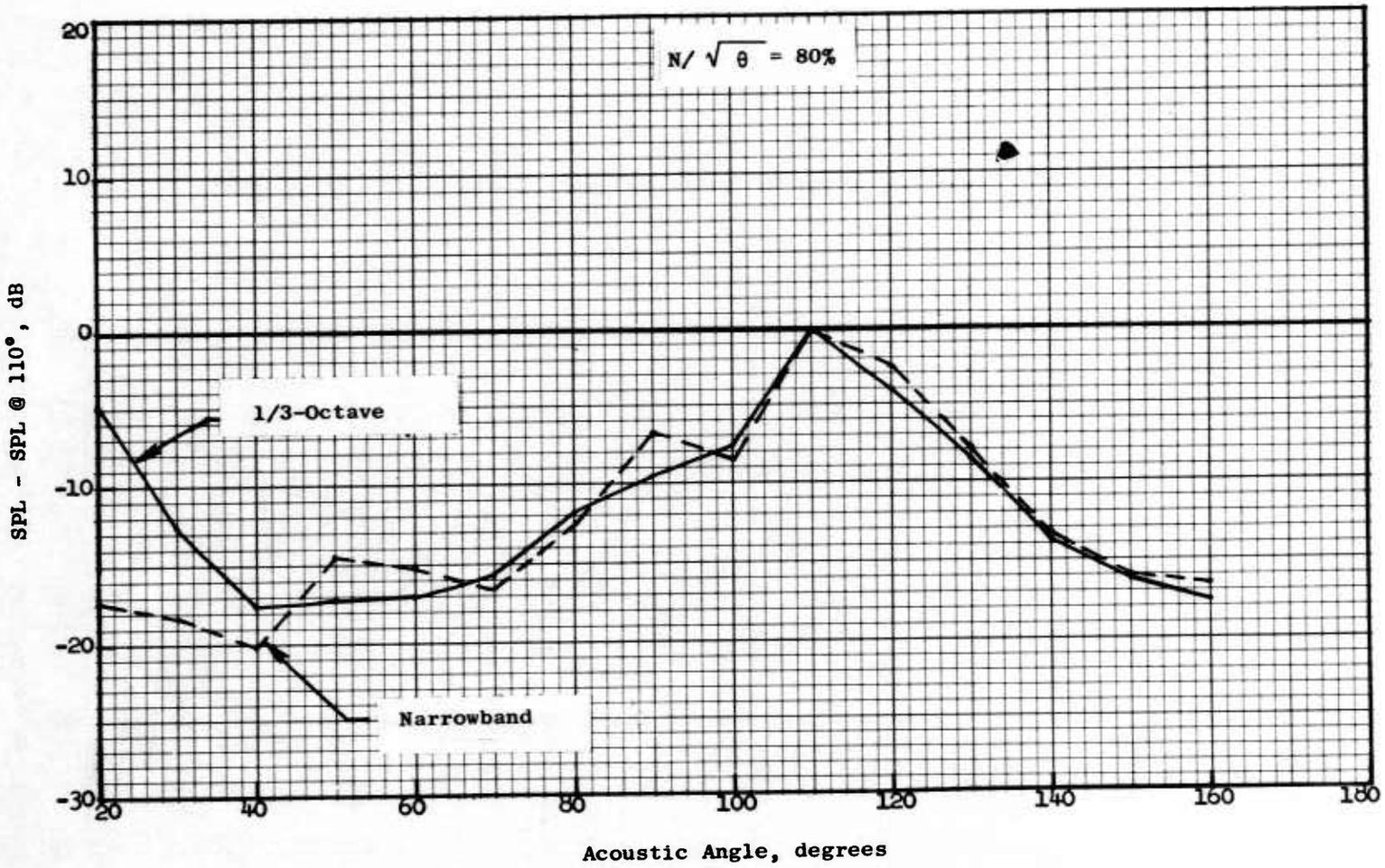

Figure 376. Comparison of Turbine Directivities, 1/3-Octave Versus Narrowband Data.

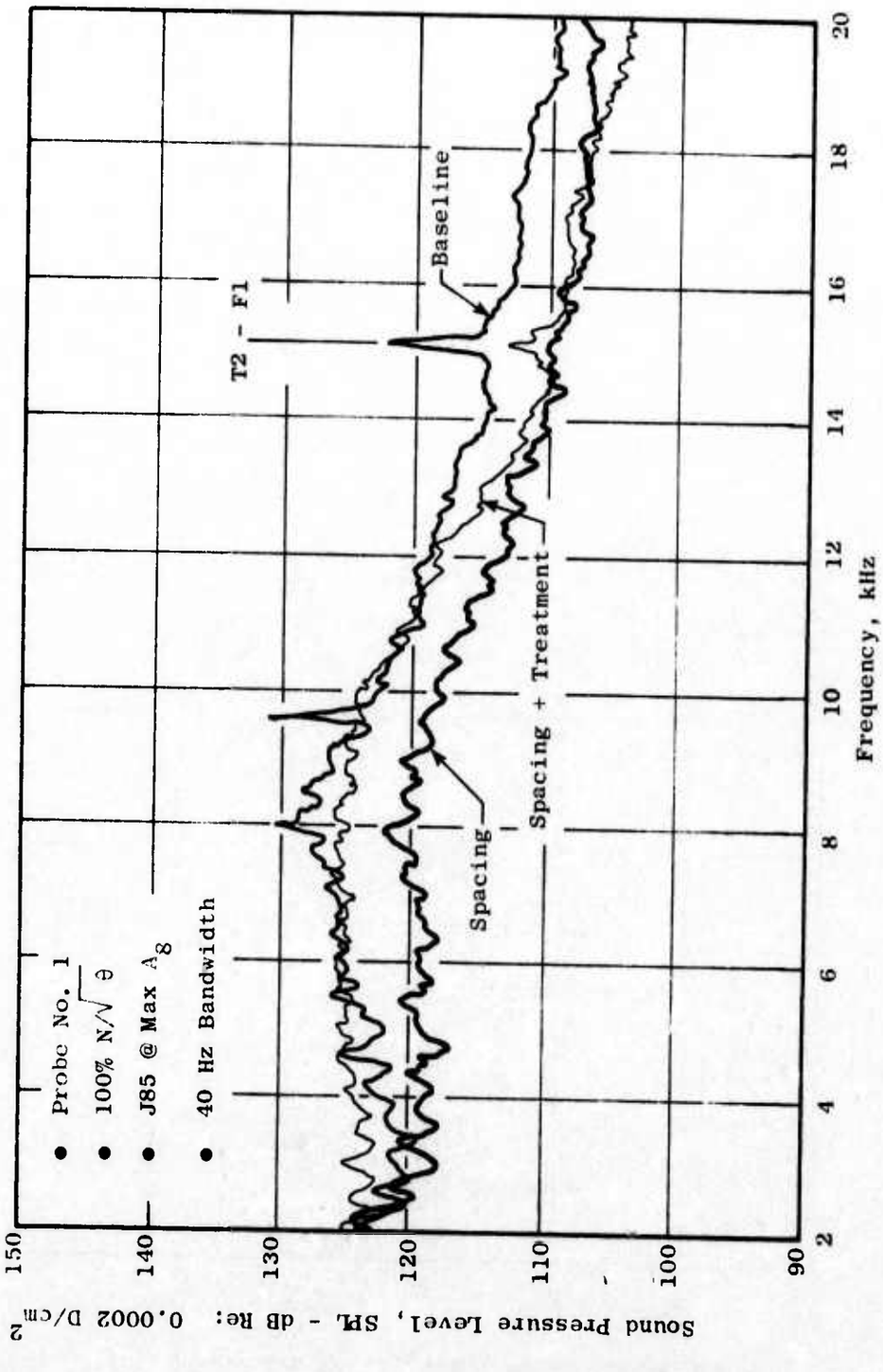

Figure 377. Probe Narrowband Comparison, Uncorrected, Probe No. 1, 100% N/√θ.

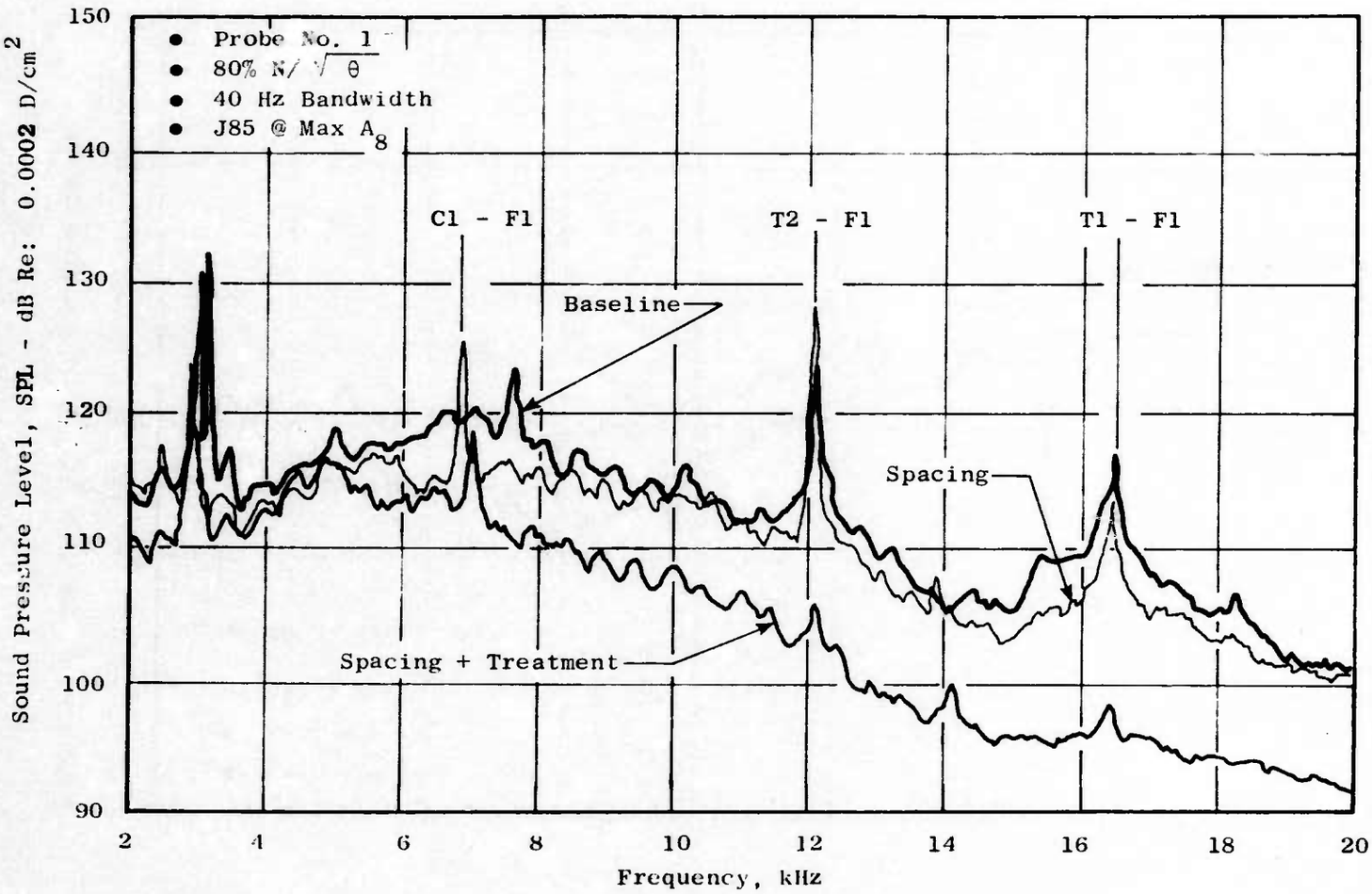

Figure 378. Probe Narrowband Comparison, Uncorrected, Probe No. 1, 80% N/√θ.

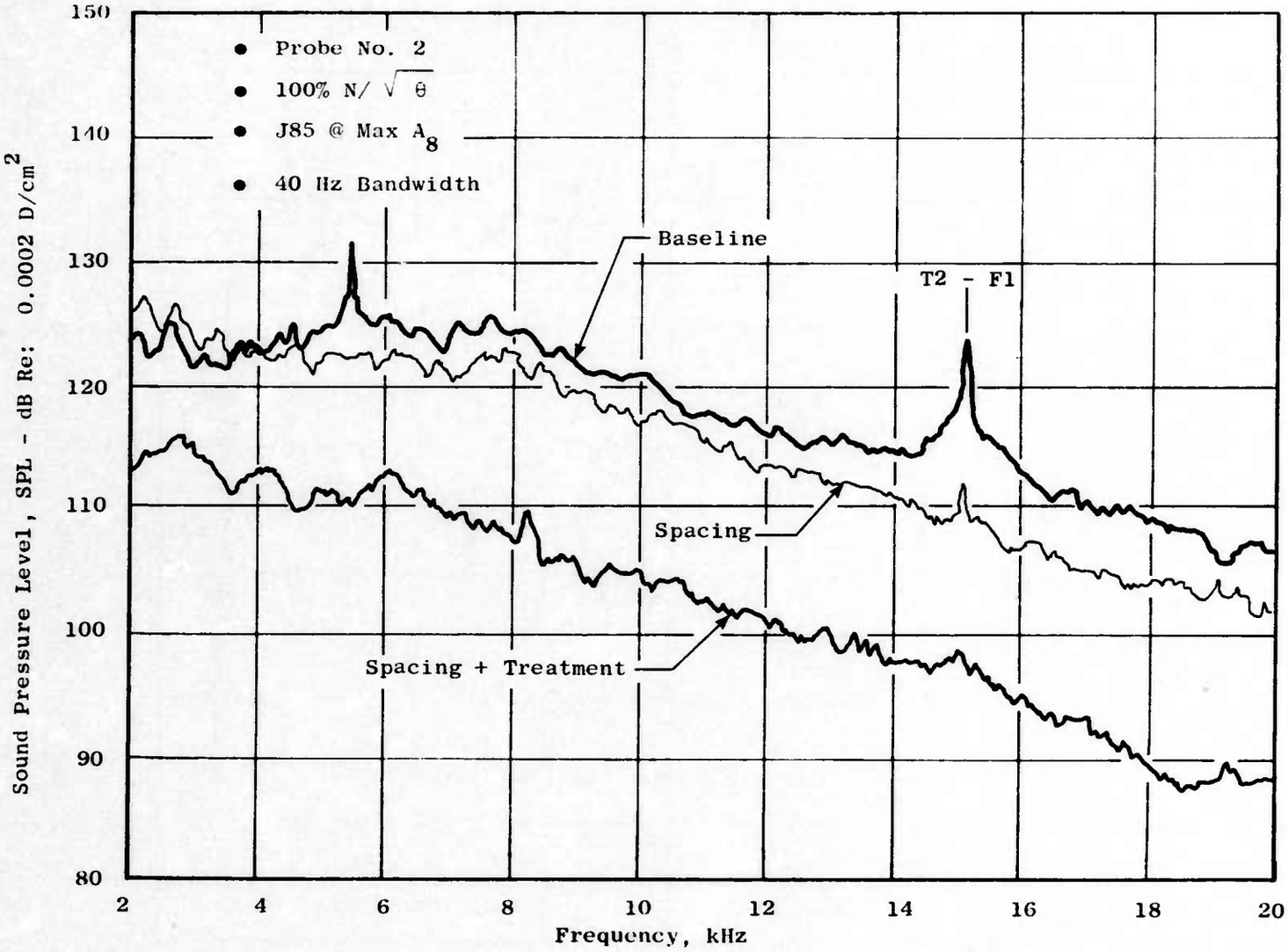

Figure 379. Probe Narrowband Comparison, Uncorrected, Probe No. 2, 100% N//θ.

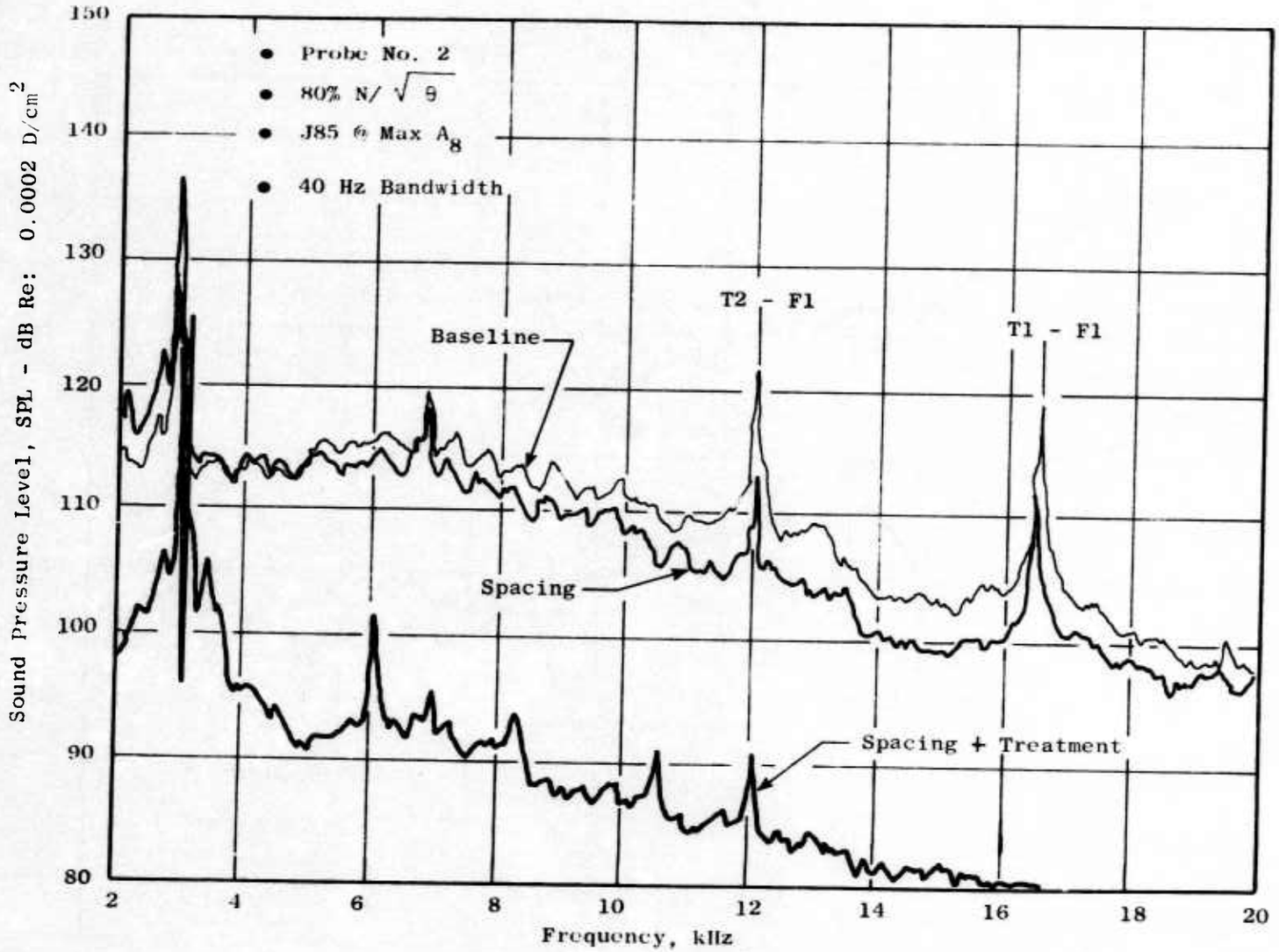

Figure 380. Probe Narrowband Comparison, Uncorrected, Probe No. 2, 80% N/√θ.

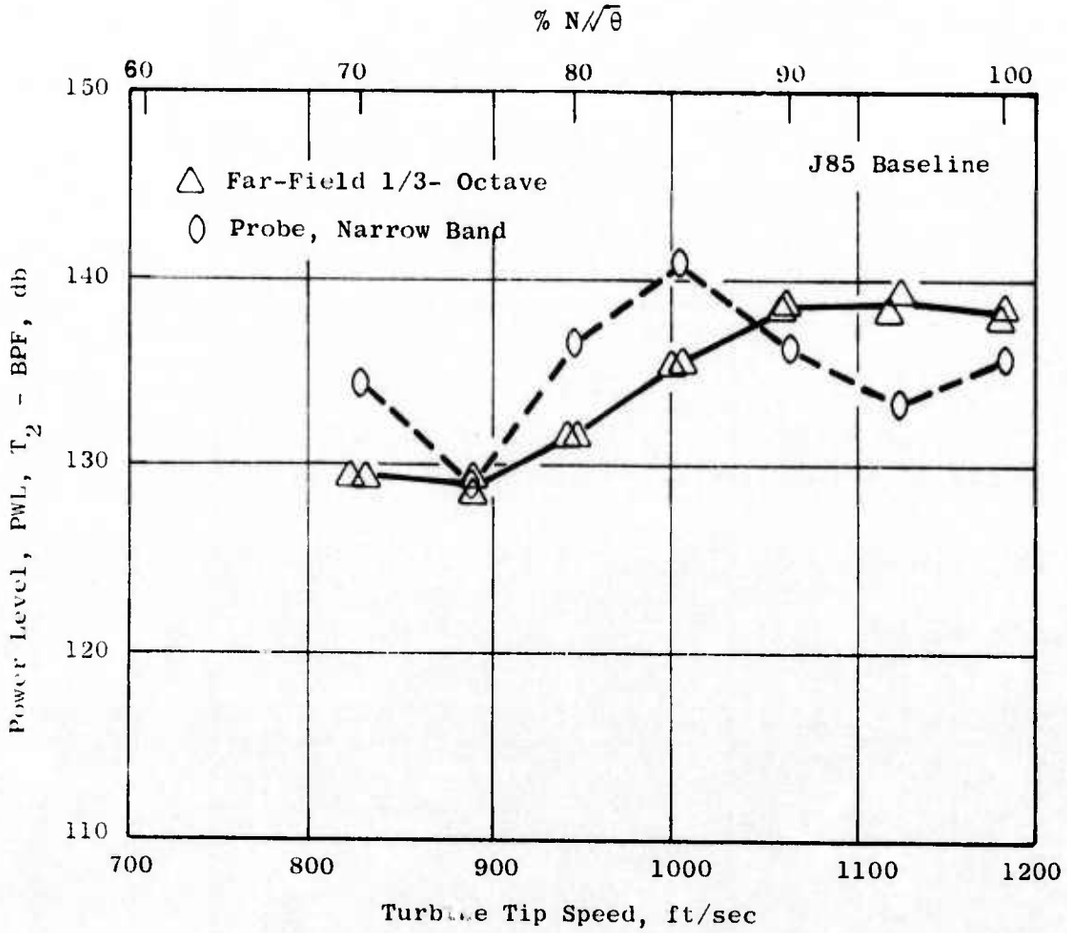

Figure 381. Comparison Between Duct and Far-Field Measurements.

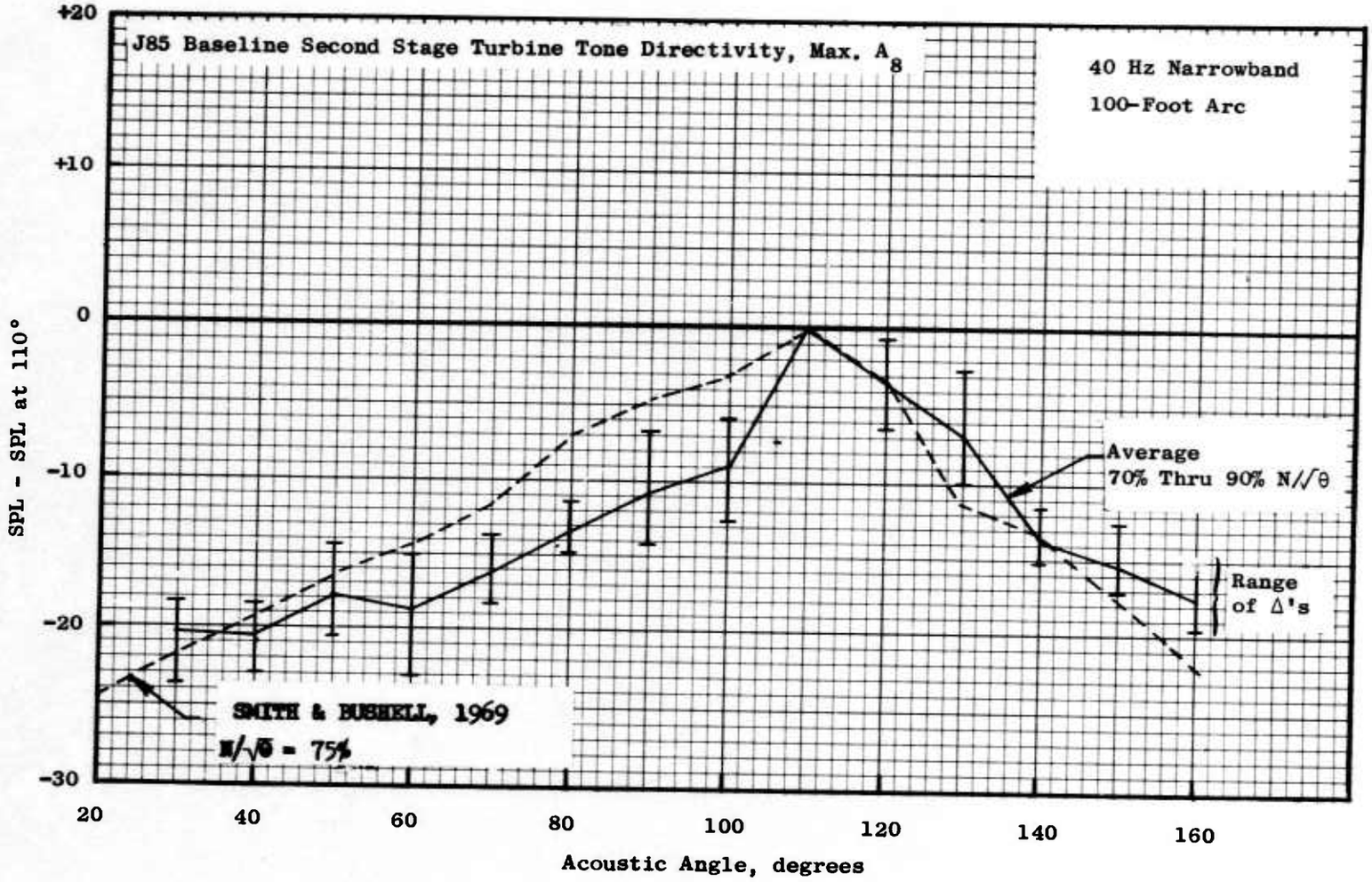

Figure 382. J85 Directivity Compared with Prior Results.

- The inlet suppressor effectively eliminated the influence of compressor tones on the 1/3-octave turbine data at acoustic angles of 40° through 160°.

- The baseline turbine noise in the far field was a modulated tone.

- The duct measurements (tone PWL's) were in agreement with the far-field one-third octave PWL's.

- Measured turbine directivities were consistent with previously published results.

4.3.2.2 Effects of Spacing and Treatment

The one-third octave SPL directivities for the band containing the stage 2 blade passing frequency at 80% speed are presented on Figure 383 for the baseline, spacing, and spacing-plus-treatment configurations. There appears to be a "noise floor" at approximately 65 dB. Except for the influence of this floor, the directivities are similar for all three configurations. The one-third octave spectra at 110° are compared on Figure 384. In addition to the large noise reduction at blade passing which was evident in the directivities, this spectral comparison demonstrates that both the treatment and the spacing resulted in a significant noise reduction over a wide frequency range. This broadband suppression, associated with spacing and treatment, is also evident in the far-field narrowband spectrum comparison (110°) of Figure 385. In addition to the previous observations, two other features are evident. First, for the fully suppressed configuration (spacing-plus-treatment), a tone appeared at 3 KHz. The source of this tone is unknown; it is peculiar to this speed/point configuration. Second, for the fully suppressed configuration, tones rather than haystacks appeared in the far field. This suggests that either: (1) the far-field tones are the result of casing radiation (unaffected by the jet), or (2) the haystacking phenomena are amplitude-dependent, hence the fully suppressed tones are not "strong enough" to have modulation occur.

The far-field tone directivity, one-third octave spectra at 110°, and far-field narrowband spectra at 110° are compared on Figures 386, 387, and 388 for the three configurations at the 90% speed point. As with the 80% data, the far-field turbine noise reduction is quite significant not only at blade passing frequency but also over a broad frequency range; the directivities are similar, and tones reappeared in the far field.

As with the baseline results, the comparison is good between the probe tone PWL's and the far-field one-third octave PWL's for the spacing configuration, Figure 389. For the fully suppressed configuration, however, the far-field tone (narrowband, no haystacking) PWL's were generally 10 dB higher than the probe PWL's, Figure 390. This indicates that the primary transmission path is not out the exhaust duct but, rather, that casing radiation is

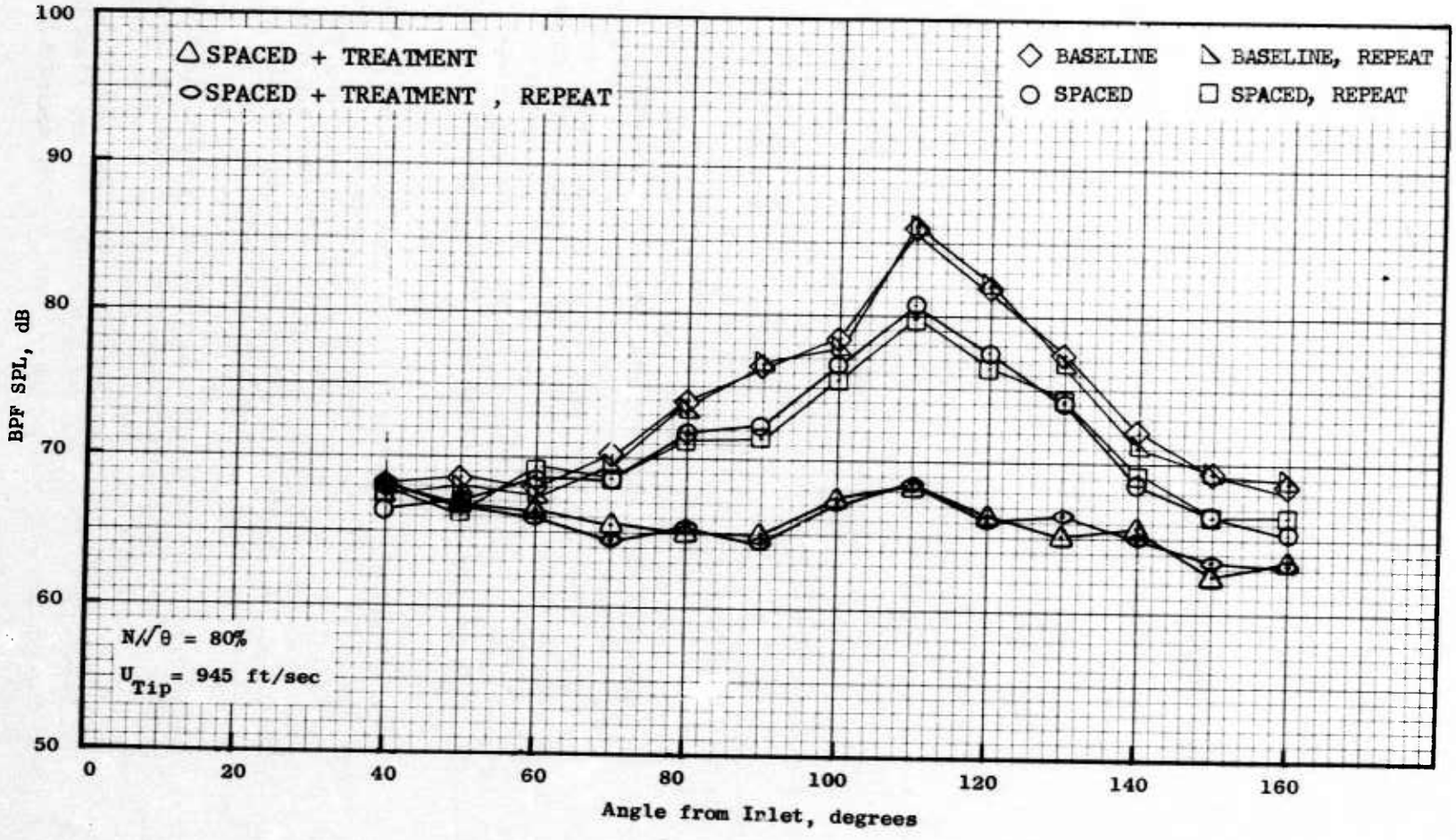

Figure 383. 1/3-Octave Second-Stage Turbine Tone Directivity, N//θ = 80%.

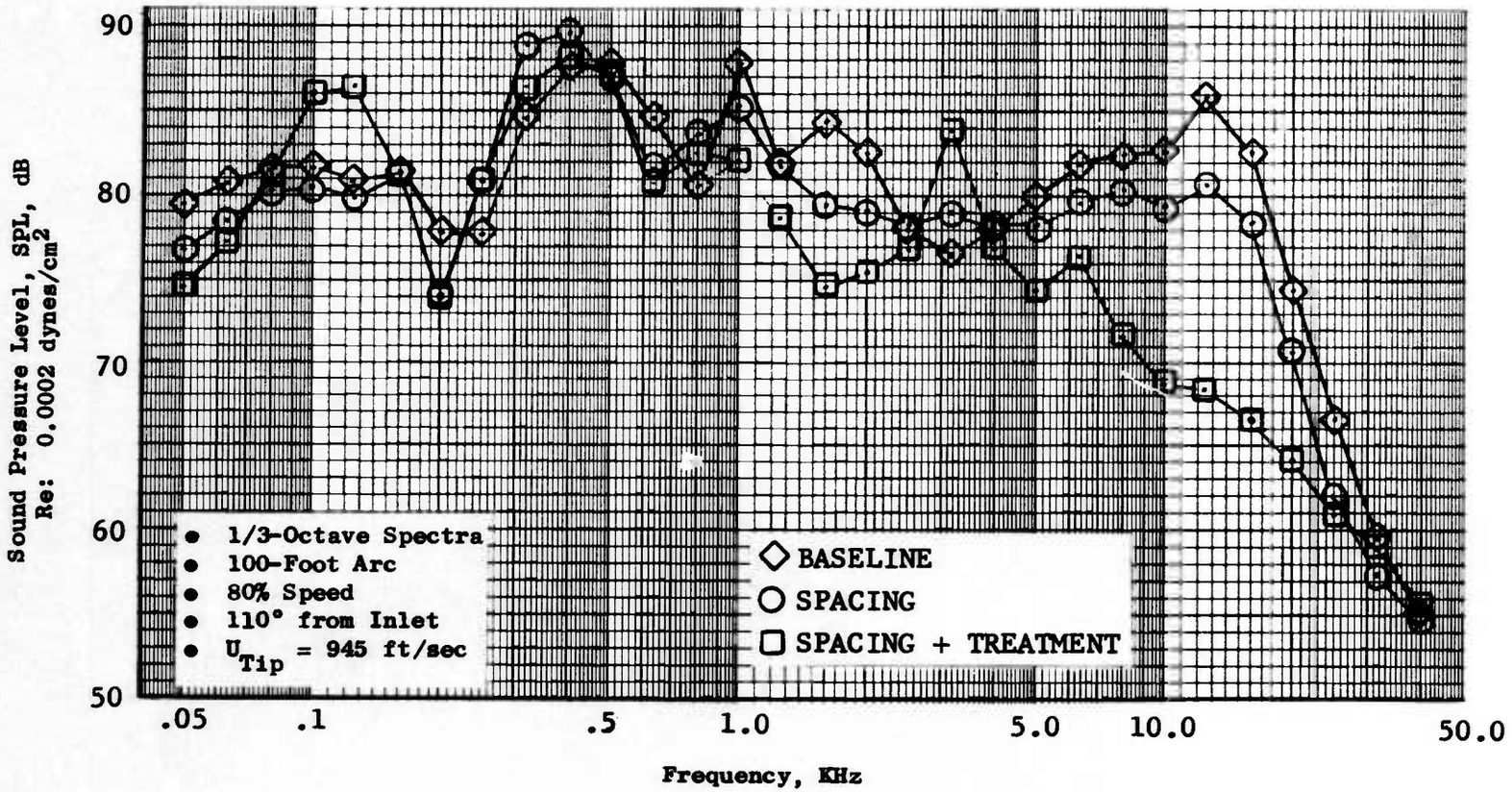

Figure 384. J85 Turbine Tests, Spectra Comparison, $N/\sqrt{\theta}$ = 80%.

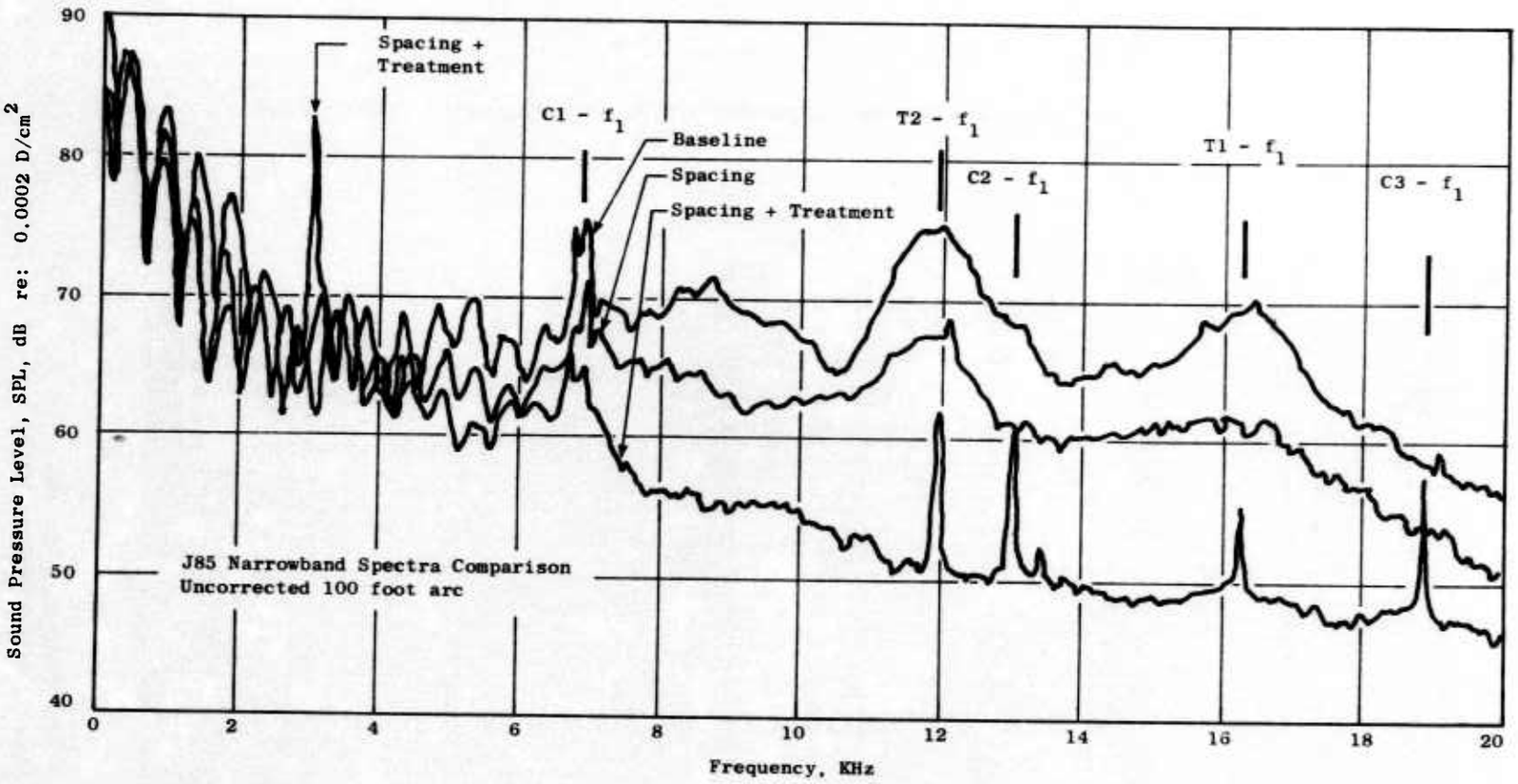

Figure 385. J85 Turbine Test, 80% Speed, 110° to Inlet, U_{Tip} - 945 ft/sec.

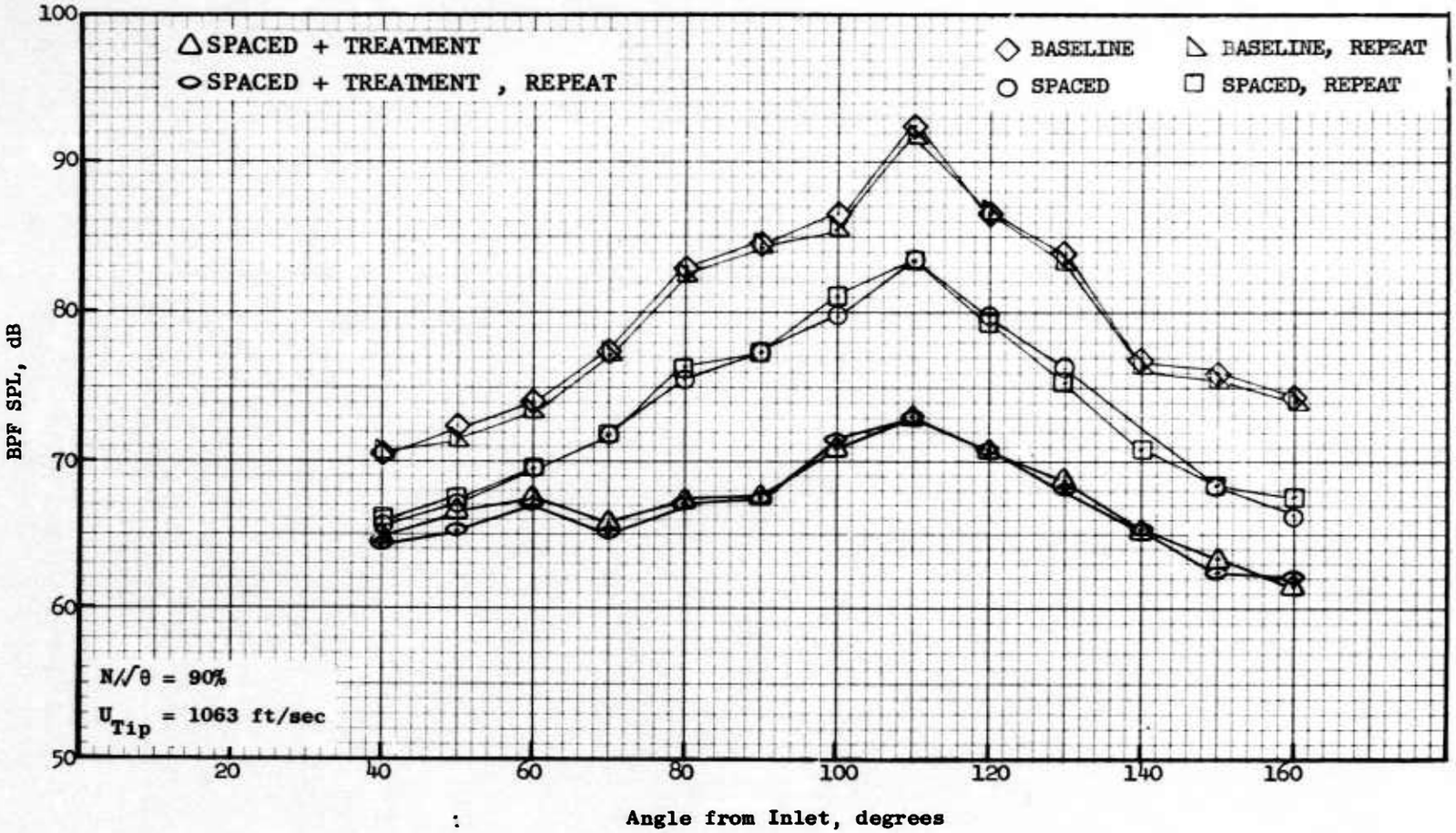

Figure 386. 1/3-Octave Second-Stage Turbine Tone Directivity, N//θ = 90%.

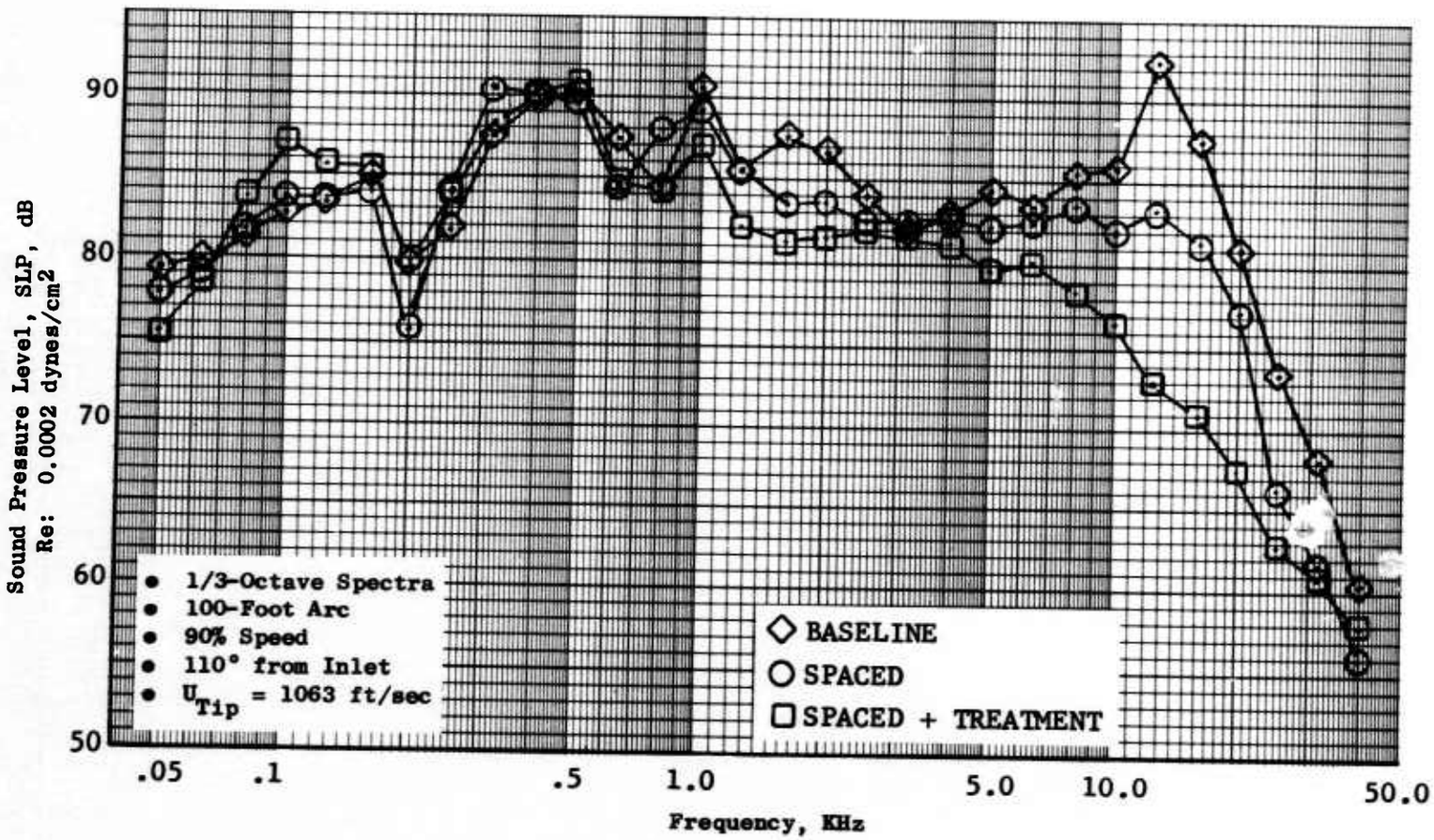

Figure 387. J85 Turbine Tests, Spectra Comparison, $N/\sqrt{\theta}$ = 90%.

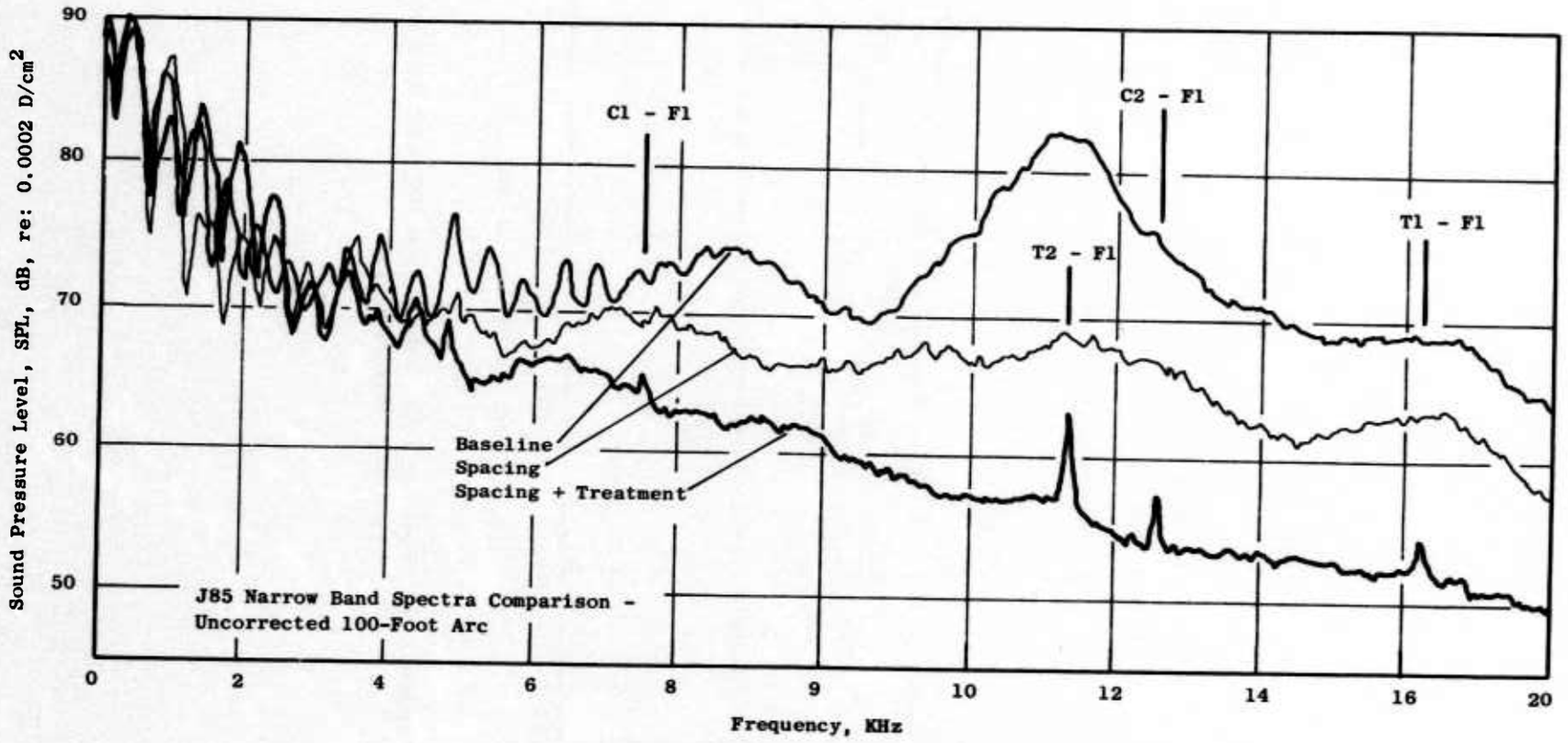

Figure 388. J85 Turbine Test, 90% Speed, 110° to Inlet, U_{Tip} = 1063 ft/sec.

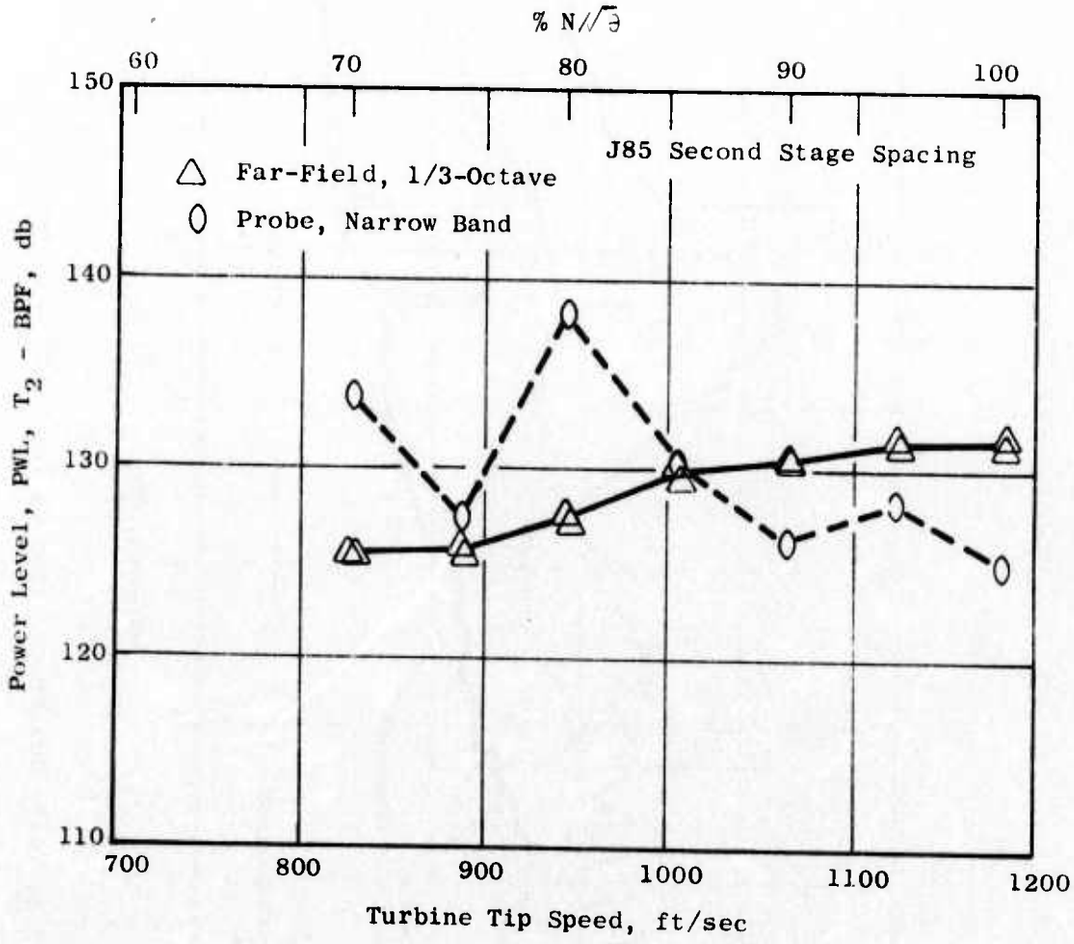

Figure 389. Spacing Test, Comparison Between Duct and Far-Field Measurements.

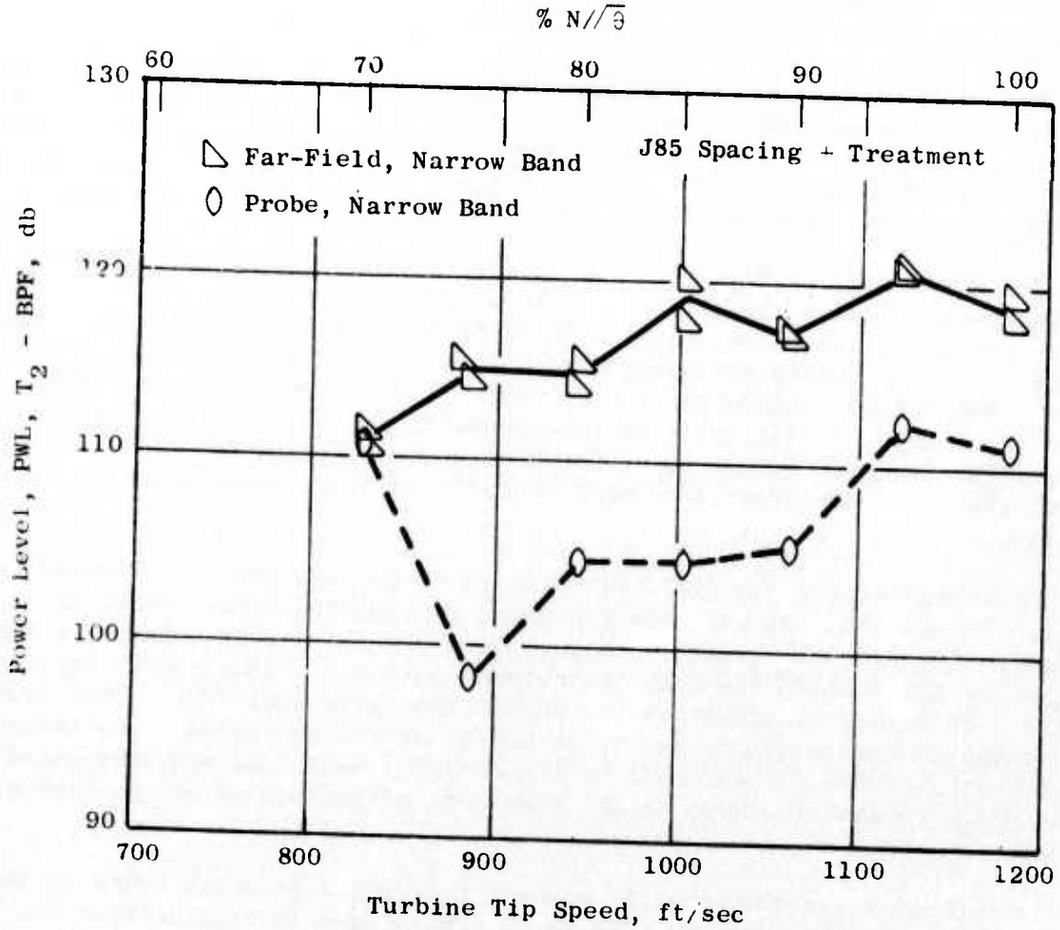

Figure 390. Fully Suppressed Turbine, Comparison Between Duct and Far-Field Measurements.

dominant in the far field for the fully suppressed configuration. This supports the hypothesis that casing radiation is the source of far-field tones for the fully suppressed configuration.

One other feature of the fully suppressed probe data (Figures 377 through 380) is that the broadband noise for the outer acoustic probe (Probe No. 1) was 10 dB above the tone level at the inner probe (Probe No. 2). For purposes of calculating the PWL's, it was assumed that the tone at Probe No. 1 was the same level as at Probe No. 2 but masked by the broadband noise.

The reductions in far-field PWL at the turbine stage 2 blade passing frequency are shown on Figure 391. Also shown, is the projected PWL reduction which would have been achieved if there were no casing radiation "floor" in the far field (using the probe results) for the fully suppressed configuration. These tests demonstrated that the turbine noise in the far field could be reduced significantly by incorporating spacing and/or treatment in the turbine design. Furthermore, for the levels of noise reduction achievable, casing radiation considerations must be factored into acoustic design decisions.

One-third octave far-field PWL spectra at 80% and 90% rpm are shown on Figure 392 and 393. As with the SPL data, the turbine noise reduction occurred over a broad frequency range. On a one-third-octave basis, a broadband noise floor holds the fully suppressed data at a higher level (approximately 5 dB higher at blade passing versus the narrowband PWL). This broadband noise is attributed to jet noise and/or casing radiation. The reductions in the turbine OAPWL's are shown on Figure 394; again, the apparent broadband noise floor causes the decay in the treatment effectiveness at the high speed points.

As previously noted, the J85 spacing that was tested was based on results from Phase I of this program. The average reduction in turbine tone PWL's from the J85 spacing test is compared with the Phase I results on Figure 395. The PWL reductions derived from the duct probe data are shown versus engine speed on Figure 396 for the J85. The variation in the ΔPWL's is consistent with the variations in the Phase I component test data (Reference 3). A comparison between the two turbines tested in Phase I and Phase II is made on Table 14. The primary differences between these turbines are the PWL's and the stage pressure ratio's. The difference in PWL for these two turbines at different pressure ratios, along with the change in turbine tone level which was observed in the J85 baseline data when the exhaust nozzle was opened (changing the turbine pressure ratio), leads to the conclusion that pressure ratio should be a prime factor in turbine noise correlation work and/or scaling studies.

The design goal for the turbine acoustic treatment was 20 dB. The test results, excluding casing radiation, show that the average suppression was 23.5 dB (probe data). This confirms the conclusion made in the Phase I program, that, for high temperature applications, SDOF acoustic treatment has predictable acoustic behavior.

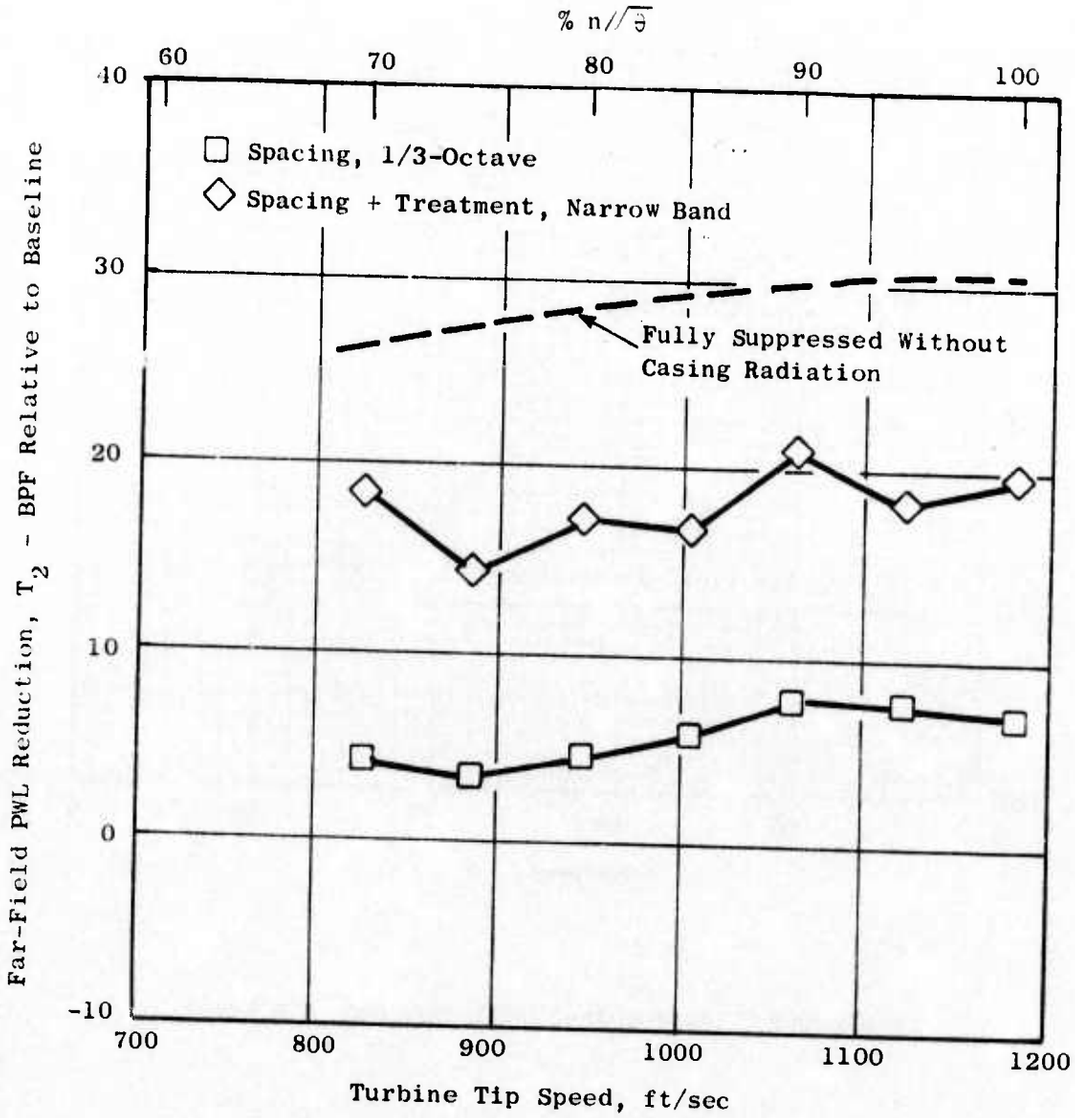

Figure 391. Far-Field Reduction in T2 PWL, Spacing and Treatment Tests, J85.

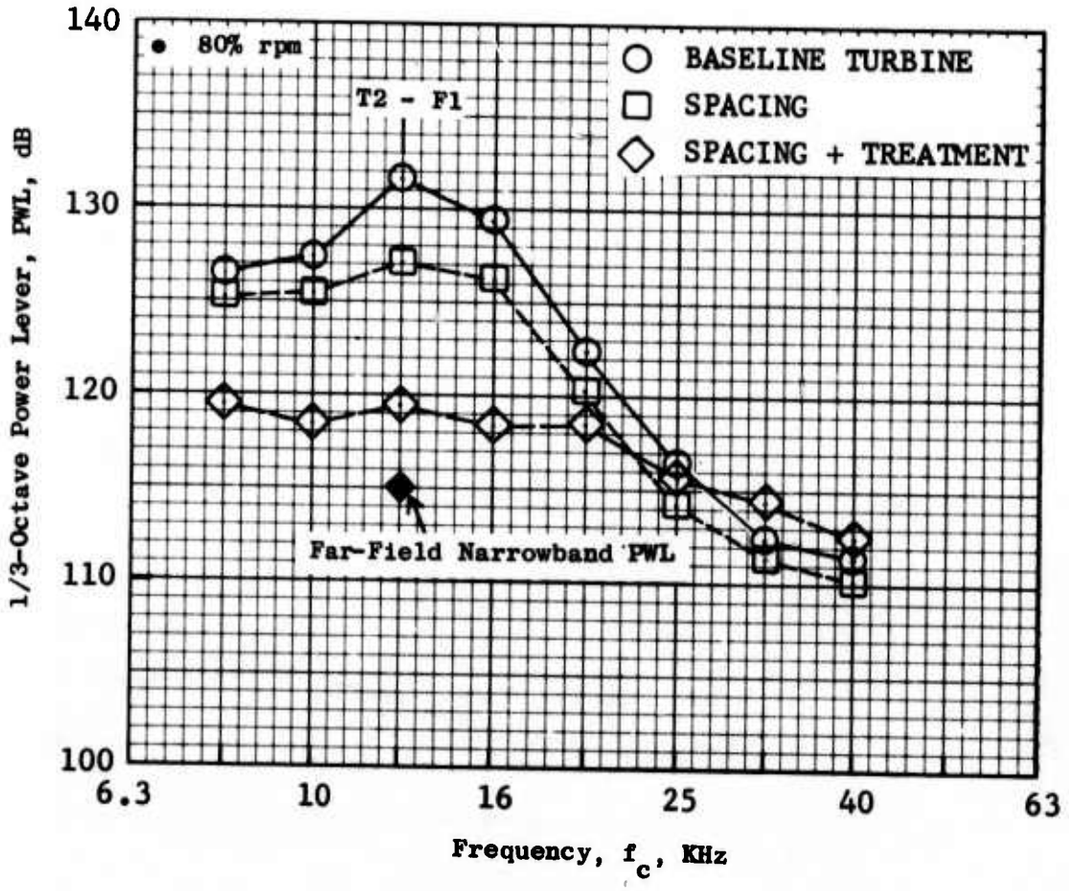

Figure 392. J85 Far-Field PWL Spectra, 80% Speed.

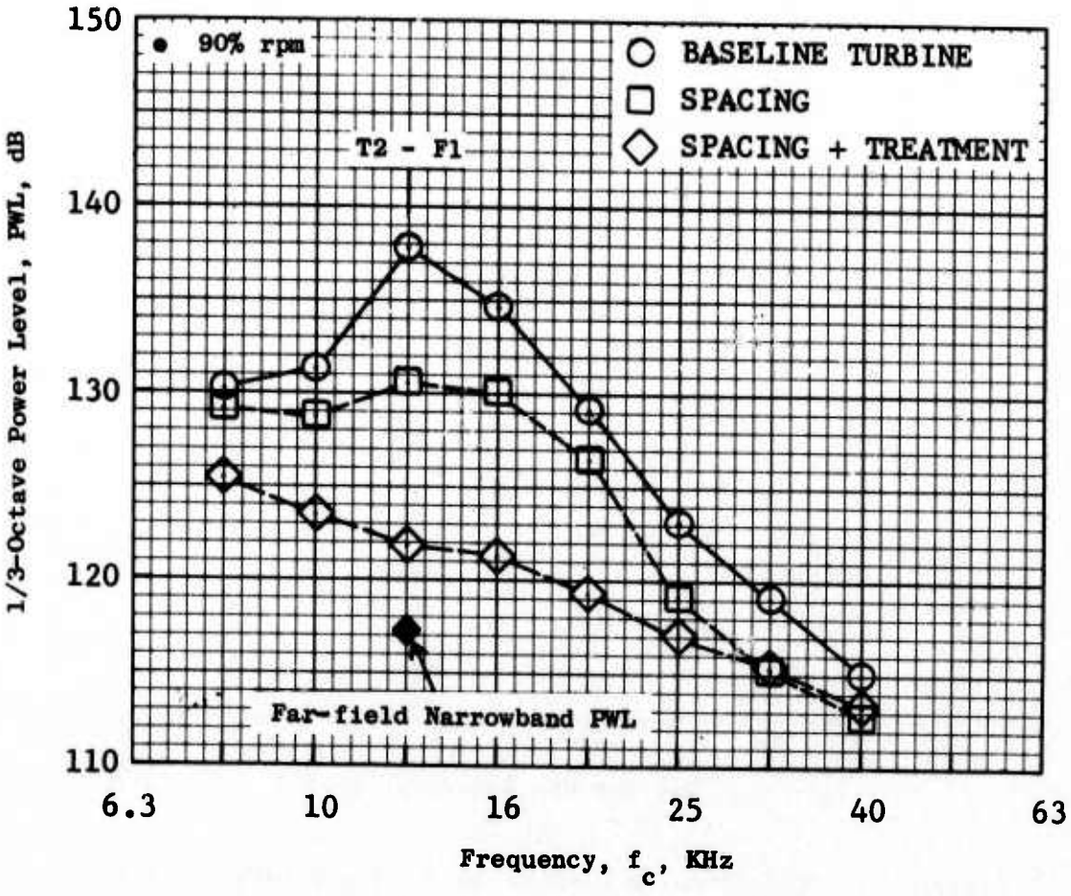

Figure 393. J85 Far-Field PWL Spectra, 90% Speed.

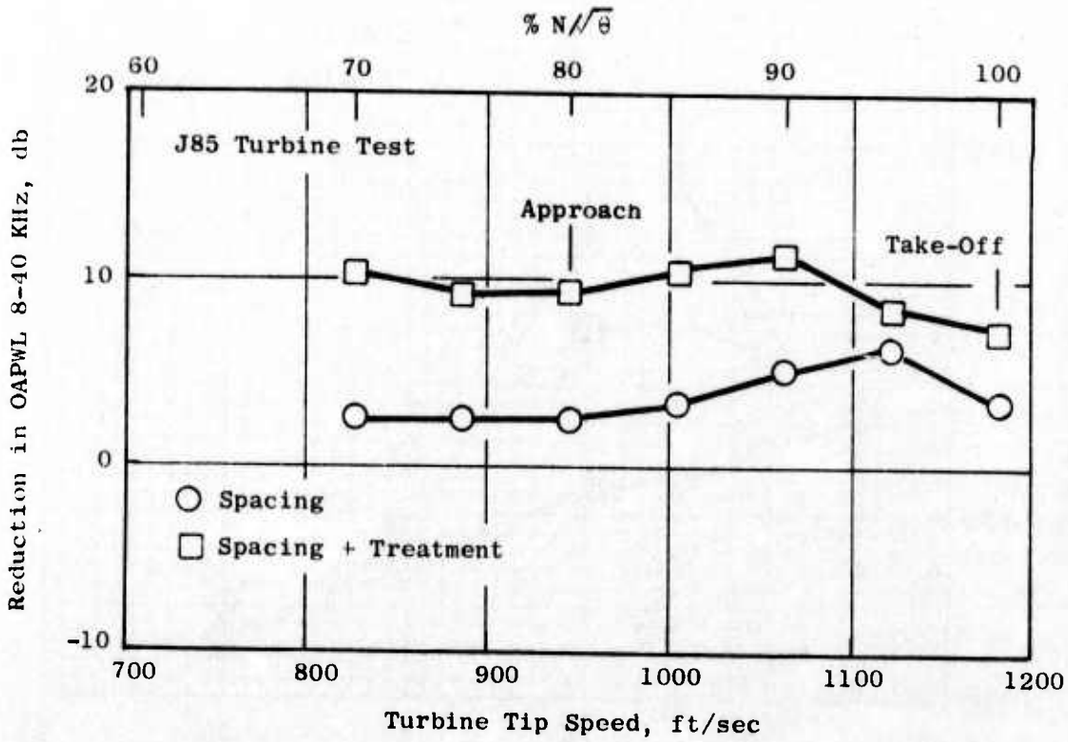

Figure 394. Reduction in Turbine OAPWL, J85 Far-Field Data.

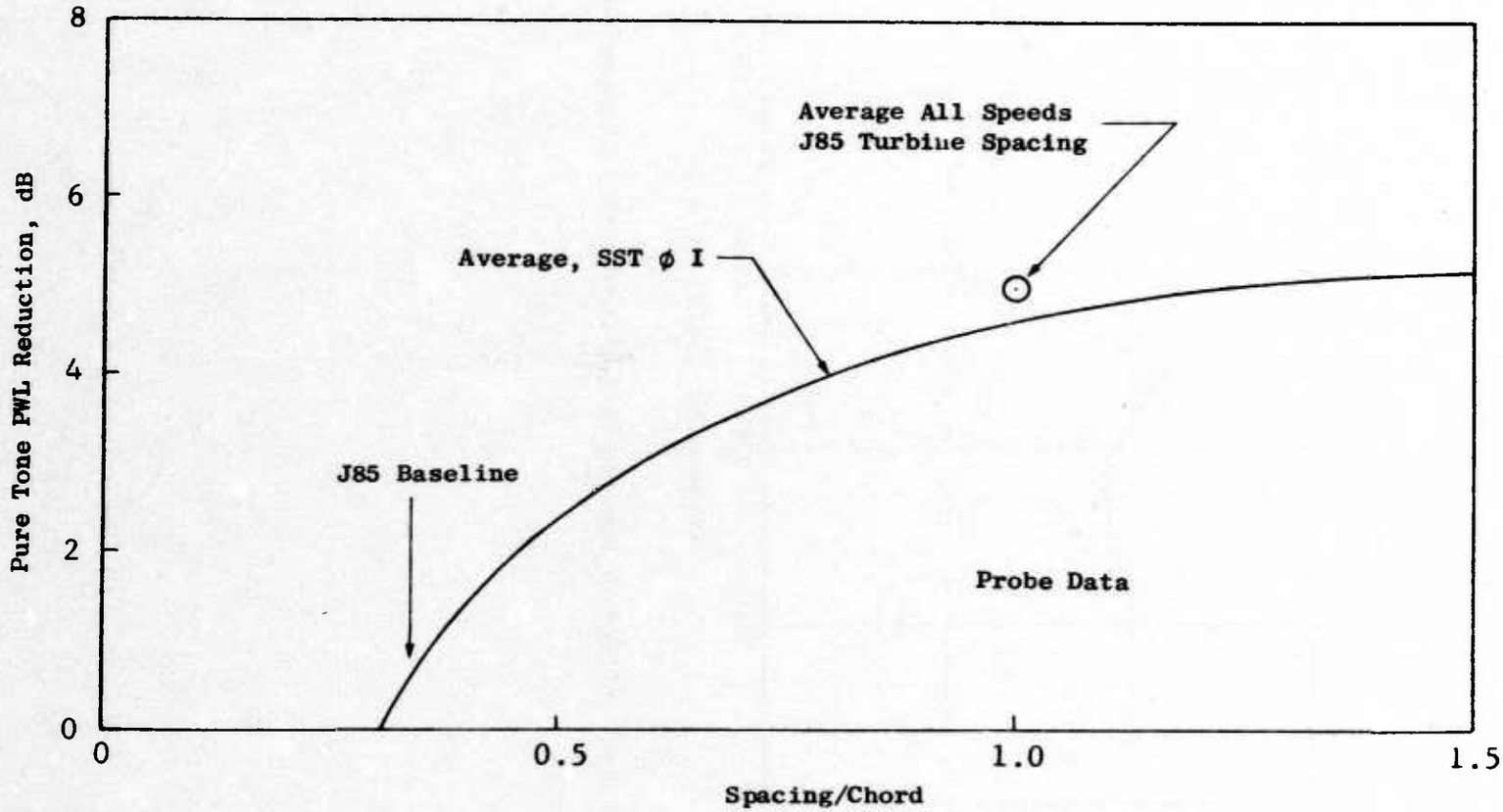

Figure 395. Effect of Spacing on High Pressure Turbine Noise, J85 and Phase I.

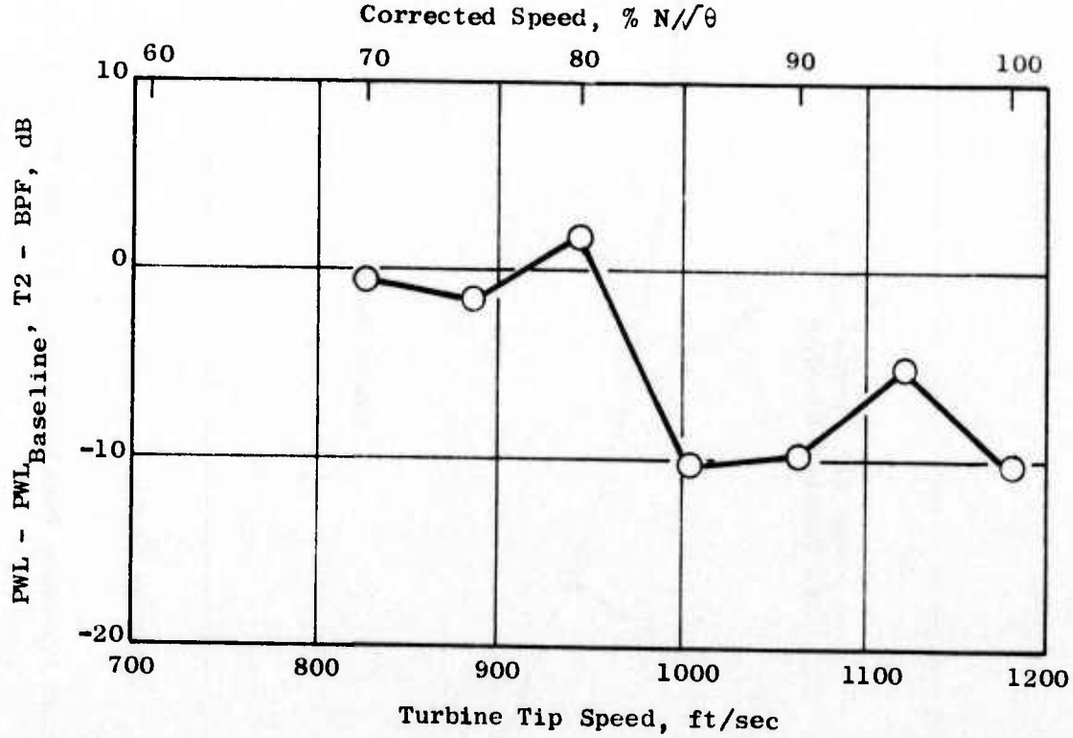

Figure 396. Effect of Spacing on Turbine Noise in Exhaust Duct.

Table 14. Comparison of HPT Acoustic Test Probe Data.

	Single-Stage HPT (Phase I)	J85 2nd Stage (Phase II)
PWL (dB)	149.5	135.9
No. Turbine Blades	80	55
Spacing/Tip Chord	0.306	0.341
U_{tip}, ft/sec	966	1181
Mach No. (Tip)	0.847	0.714
Stage Loading	0.7114	0.879
Stage Pressure Ratio (P_T/P_S)	5.11	2.702

For a given treatment configuration (in this case SDOF as specified on Figure 363 with treatment on the hub, splitter, and outer casing), the suppression is (to a first-order approximation) directly proportional to the treatment length. Thus, the suppression achievable for varying lengths of treatment can be drawn for the J85, Figure 397. Also shown on Figure 397 is the casing radiation floor experienced in this test, and the projected suppression which would be observed in the far field in a test for the effect of treatment length.

The effect of eliminating the splitter from the treatment section would be to lower the ideal suppression by roughly a factor of 4. This is illustrated on Figure 398.

While the effects of spacing and the effects of treatment are functions of the specific design under consideration, the turbine noise suppression curves of Figures 395 (spacing) and 397 or 398 (treatment) can be used to estimate what acoustic modifications are required to meet systems noise goals for preliminary design studies.

4.3.2.3 Full-Scale Results

In order to provide a basis for the assessment of full-scale (SST size) turbine noise, the J85 far-field data were scaled on a weight-flow basis to the SST size. This scaling resulted in a downward frequency shift of approximately 7 1/3-octave bands. Generally the J85 data below 8 KHz were omitted; however, each case was examined individually, and the lower frequency limit was adjusted. PNL directivities (300-foot sideline) at 80%, 90%, and 100% are shown on Figures 399 through 403. The PNL reductions at 110° are shown versus engine speed on Figure 402. Again, the jet noise floor, and the casing radiation, hold the fully suppressed turbine data at a higher PNL value to the extent that no reduction is seen at takeoff. Comparing the J85 PWL reductions at blade passing, Figure 391, with the full-scale PNL reduction, Figure 401, for the spacing configuration shows the delta's to be nearly the same, i.e., $\Delta PWL_{J85} \simeq \Delta PNL_{SST}$. Thus, without the effects of the jet noise floor and casing radiation, a PNL reduction on the order of 25 to 30 PNdB could be achieved for the turbine by including spacing and treatment in the design.

4.3.2.4 J85 Performance

A comparison between engine performance of the J85 for the baseline engine (nominal and maximum A_8) and the engine with the increased turbine second-stage spacing is presented on Table 15. Opening the exhaust nozzle for the baseline J85 moved the operating point(s) considerably, relative to the nominal nozzle performance. Operating so far "off-design" essentially eliminates the possibility of extrapolating the performance results directly to other engines. However, from an acoustic standpoint, opening the nozzle was necessary. When the turbine spacing was increased, the flow apparently

- Constant Annular Height
- No Jet Floor

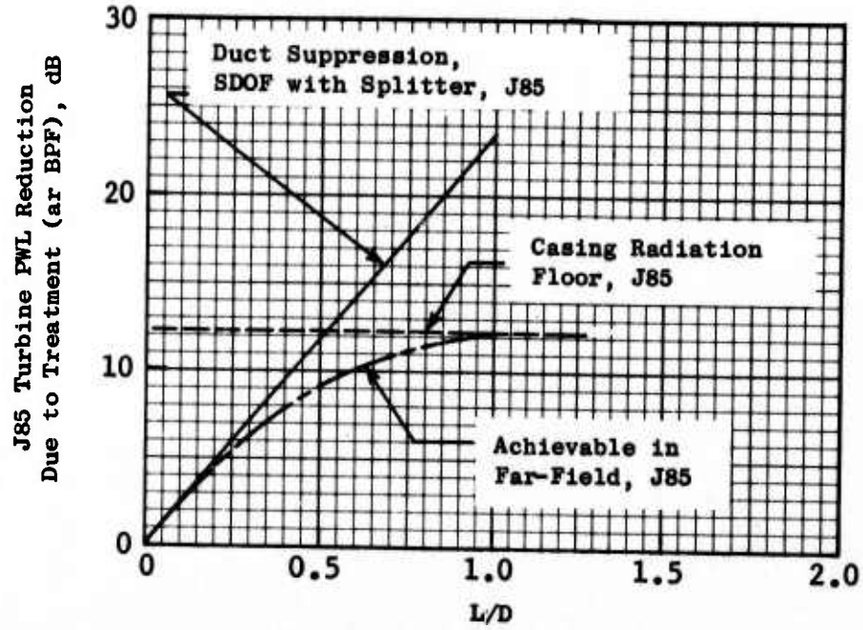

Figure 397. Effect of Acoustic Treatment (with Splitter) on Turbine Far-Field Noise.

- Constant Annular Height
- No Jet Floor

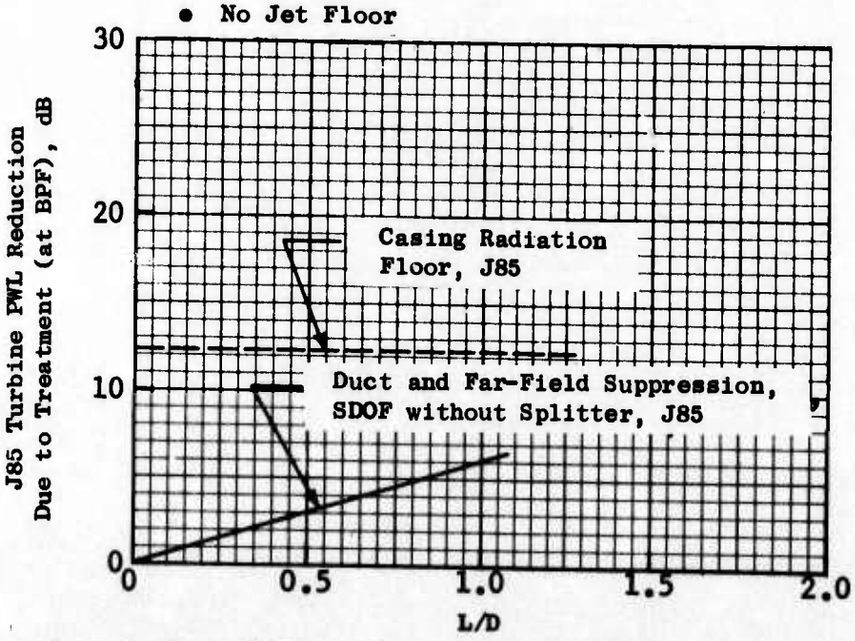

Figure 398. Effect of Acoustic Treatment (without Splitter) on Turbine Far-Field Noise, J85.

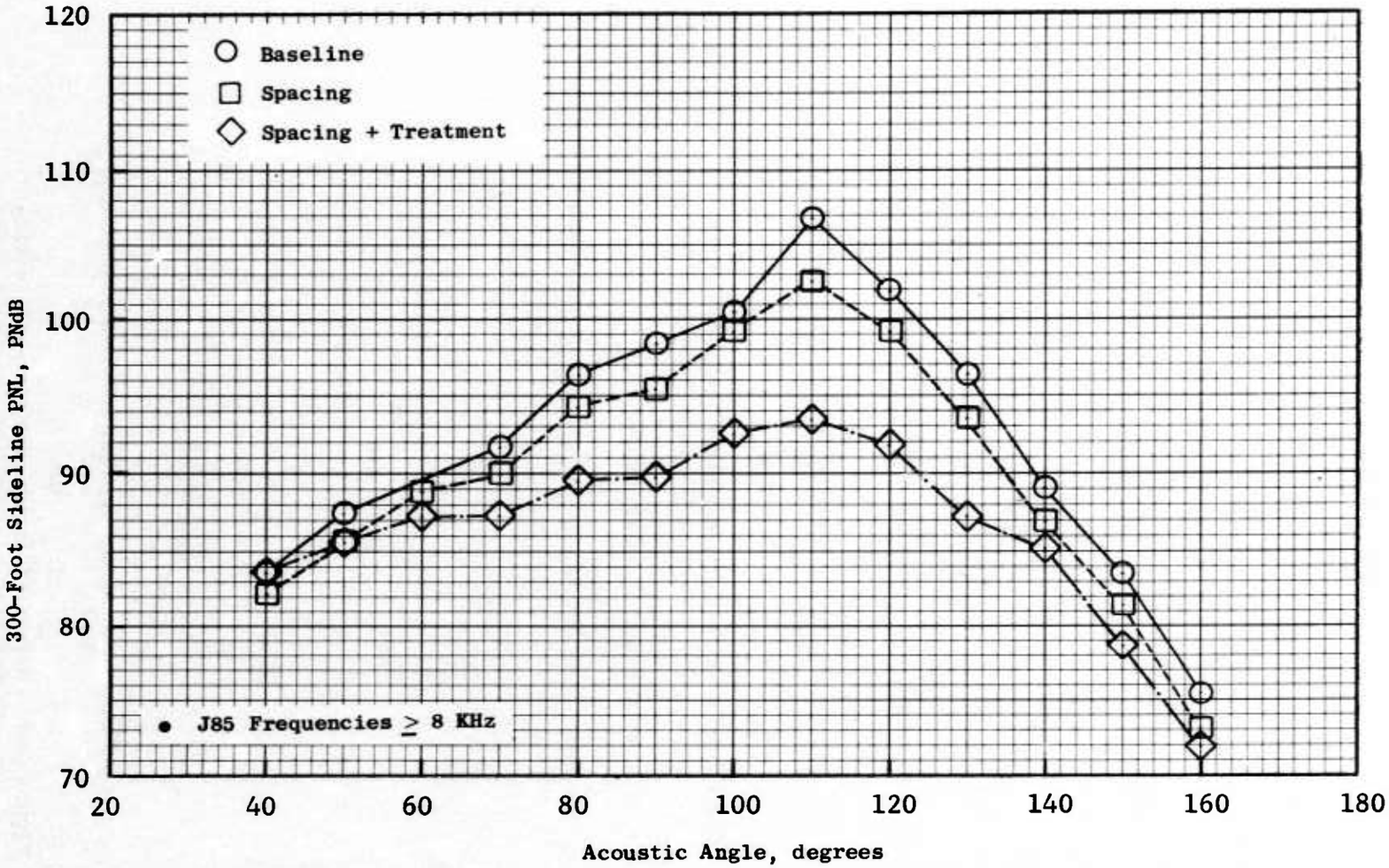

Figure 399. PNL Directivity, 80% N//θ, J85 Scaled to SST Weight Flow.

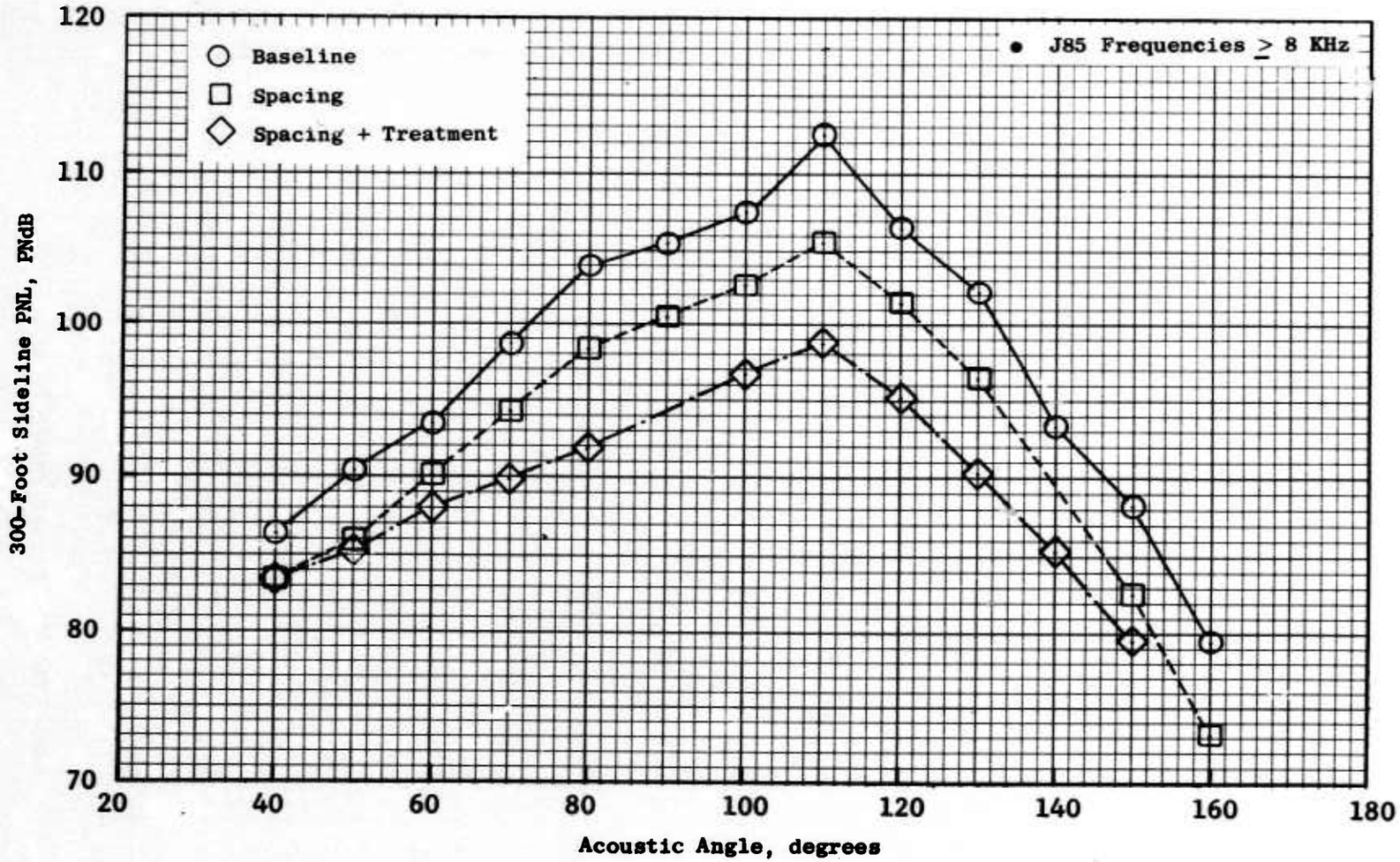

Figure 400. PNL Directivity, 90% N$\sqrt{\theta}$, J85 Scaled to SST Weight Flow.

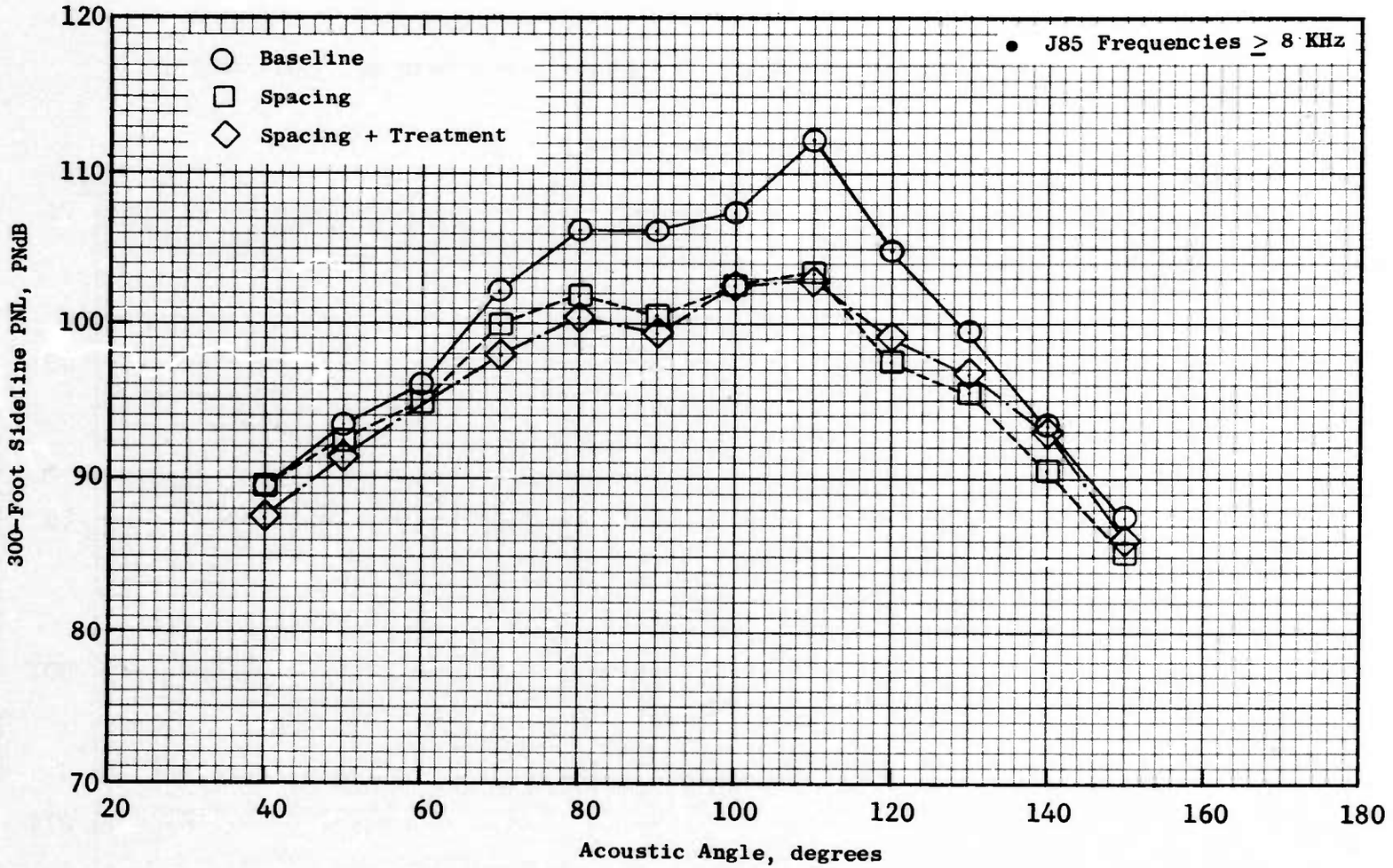

Figure 401. PNL Directivity, 100% N//θ, J85 Scaled to SST Weight Flow.

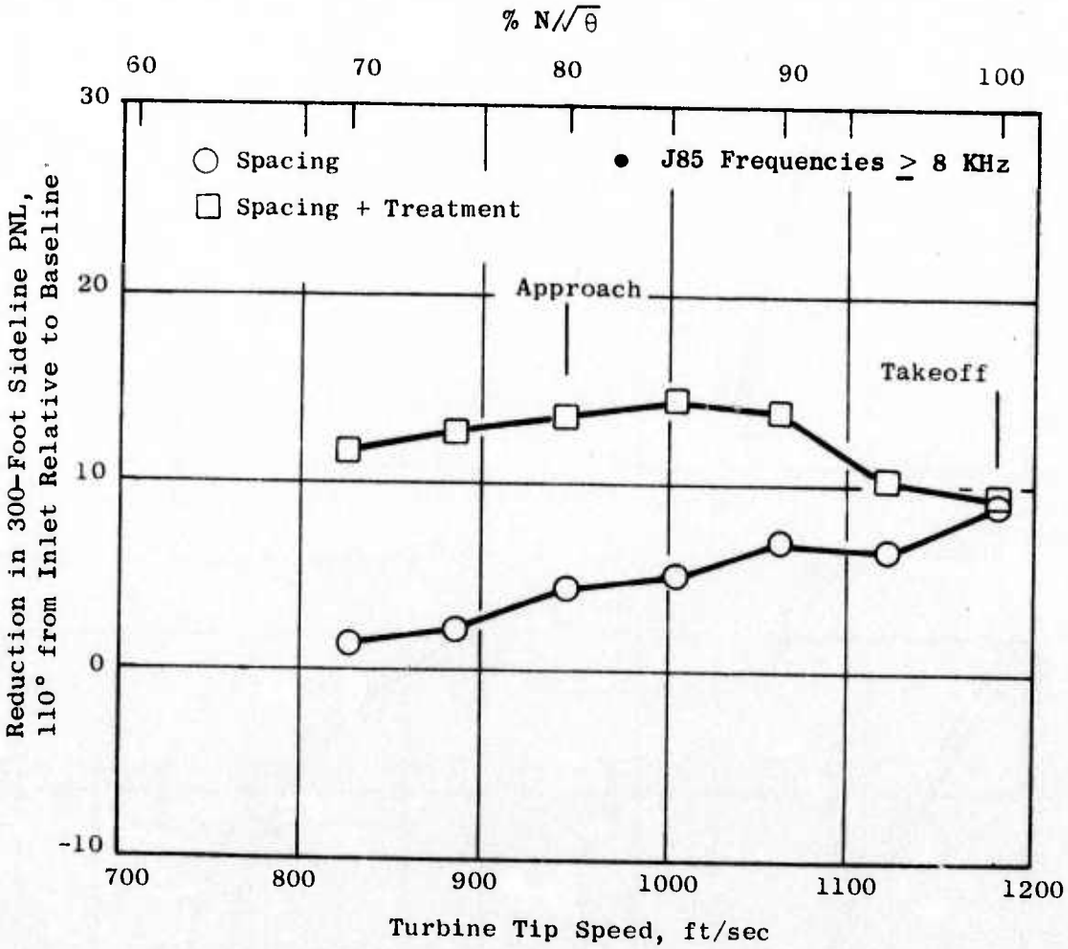

Figure 402. PNL Reduction, J85 Scaled to SST Weight Flow.

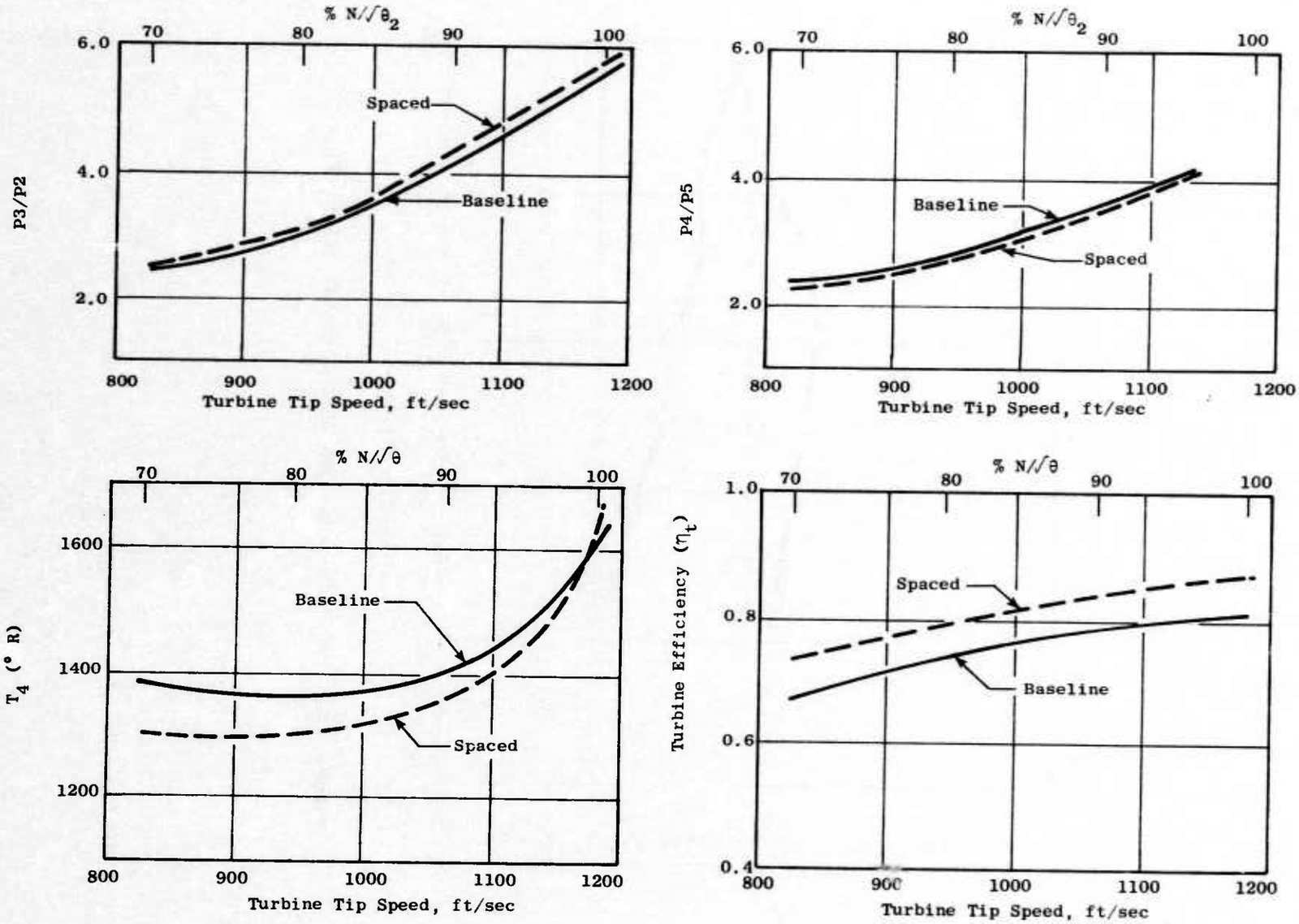

Figure 403. Performance Comparison for the J85, Maximum A_8.

Table 15. Performance Comparison.

Takeoff	16,500 rpm				
Test Vehicle	Airflow, lb/sec	$\frac{P3}{P2}$	EGT, ° F	$\frac{P5.1}{P2}$	V_{jet}, ft/sec
Base/Cycle A_8	40.3	6.18	1027	1.74	1582
Base/Max. A_8	40.9	5.89	821	1.42	1167
Turbine Spacing	42.72	5.70	749	1.50	1239
Approach	13,200 rpm				
Test Vehicle	Airflow, lb/sec	$\frac{P3}{P2}$	EGT, ° F	$\frac{P5.1}{P2}$	V_{jet}, ft/sec
Base/Cycle A_8	27.0	3.16	790	1.17	736
Base/Max. A_8	27.2	3.04	680	1.07	410
Turbine Spacing	29.9	3.17	596	1.12	393

had a chance to "straighten itself out," e.g., the pitchline analysis indicates that the relative air angle into the second-stage turbine blades was ∿18° for baseline nominal A_8, ∿24° for baseline max. A_8, and ∿21° for spacing max. A_8. Summary curves showing pertinent operating parameters are shown on Figure 403.

While it is recommended that these results should not be applied quantitatively to other turbines, they do point out that spacing does not necessarily impose a severe performance penalty.

4.3.3 Summary and Conclusions

1. Both spacing and treatment are quite effective methods for suppressing turbine noise in the far field.

2. Both spacing and treatment suppressed turbine noise over a broad frequency range.

3. The spacing results are consistent with Phase I of this program.

4. Far-field directivities are similar for the suppressed and unsuppressed turbines.

5. Measured directivities are consistent with previously published results.

6. Both jet noise and casing radiation must be considered in setting the noise floor prior to selecting the amount of turbine treatment required.

7. Future turbine noise correlations and scaling studies should consider turbine pressure ratio as a key parameter.

8. Spacing does not necessarily impose a severe performance penalty on the system.

4.4 COMPRESSOR NOISE REDUCTION

4.4.1 Test Description

4.4.1.1 Vehicle Description

The vehicle tested is representative of a low pressure fan for a Supersonic Transport (SST). The design characteristics are listed in Table 16. The low pressure compressor (LPC) test vehicle is a three-stage and has an inlet guide vane system with fixed forward struts and long-chord variable trailing-edge flaps. The rotors are unshrouded with the exception of Rotor 1, which employs a mid-span shroud. All stators are shrouded and have variable stagger. A schematic of the vehicle is shown in Figure 404. Figure 405 and 406 show photographs of the 3-stage compressor.

The measured fan performance map is shown in Figure 407. The two fan operating lines are indicated along with typical constant fan thrust lines. Figure 408 shows the IGV schedule as a function of corrected tip speed.

4.4.1.2 Test Configurations

Two types of inlet systems were tested with the three-stage compressor. A cylindrical inlet with a bellmouth forebody was used for the clean inlet fan aerodynamic evaluation and as the baseline configuration for the acoustic data. A hybrid inlet, which was a scale model of a mixed-compression supersonic inlet designed for cruise flight at Mach 2.5, was also tested.

4.4.1.2.1 Baseline Inlet

The baseline bellmouth cylindrical inlet is shown in Figure 409. It consists of a bellmouth forebody to simulate inflow conditions during flight and a long cylindrical section. The inlet-length-to-fan-diameter ratio (L/D) of the inlet from the fan IGV's is 3.26 fan diameters. This inlet was used to evaluate the unsuppressed noise of the fan.

4.4.1.2.2 Hybrid Inlet - Aerodynamic Design

In the hybrid inlet suppression concept, the noise suppression from moderate airflow acceleration and wall acoustic treatment are combined. In this way, the performance and stability concerns associated with hard-choking the inlet are avoided. This hybrid inlet concept is especially attractive for the SST because the variable geometry and airflow control required by the hybrid inlet concept is inherent in the supersonic inlet and, thus, not a penalty to the system. The hybrid inlet was designed for a 0.75 average throat Mach number at both takeoff and approach. In addition, the design featured a blow-in-door auxiliary inlet system to augment take-off airflow.

Table 16. Low Pressure Compressor Characteristics.

1. Design Characteristics (100% Sea Level Static)

Design Speed	13,266 rpm
Tip Speed	1524 ft/sec
Total Airflow	217 lb/sec
Pressure Ratio	4.1
Bypass Ratio	0.2

2. Compressor Rotors

32 Stage 1 Mid-span Shrouded Blades
42 Stage 2 Blades
52 Stage 3 Blades
26.3 in. Tip Diameter

3. Stators

18 Inlet Guide Vanes
68 Stage 1 Blades
92 Stage 2 Blades
92 Stage 3 Blades

4. Other Characteristics

Vane/Blade Ratio (Stage 1)	2.125	
IGV/Rotor 1 Spacing	0.29 (Tip)	0.05 (Hub)
Rotor 1/Stator 1 Spacing	0.29 (Tip)	0.09 (Hub)

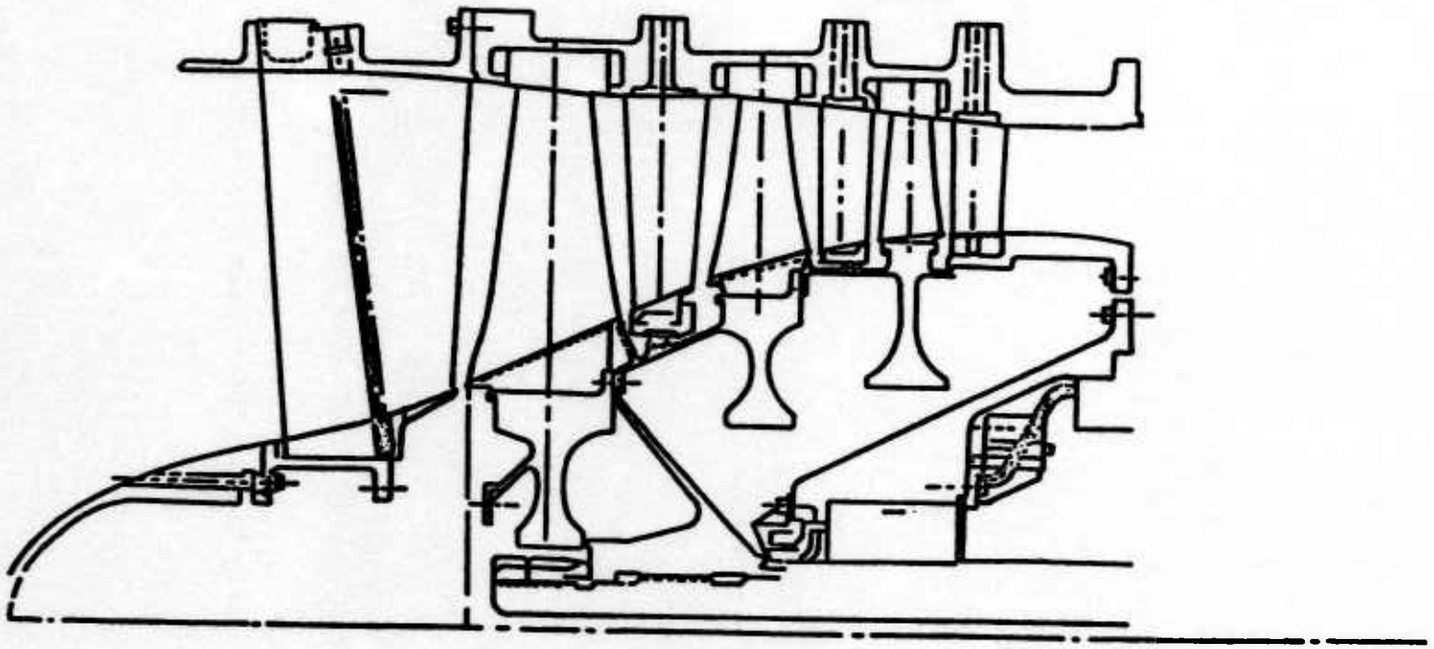

Figure 404. Test Vehicle Schematic.

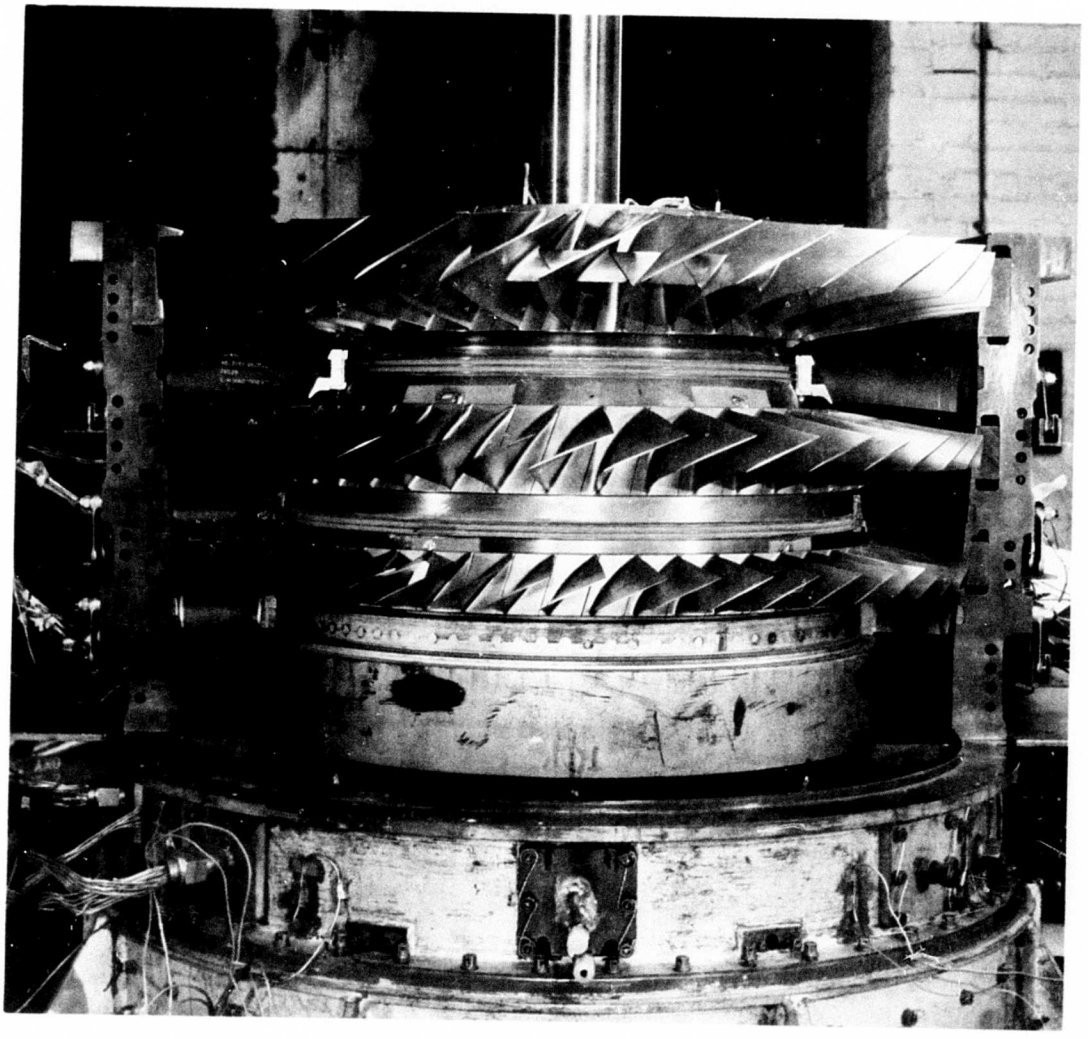

Figure 405. Cutaway View of Three-Stage Compressor.

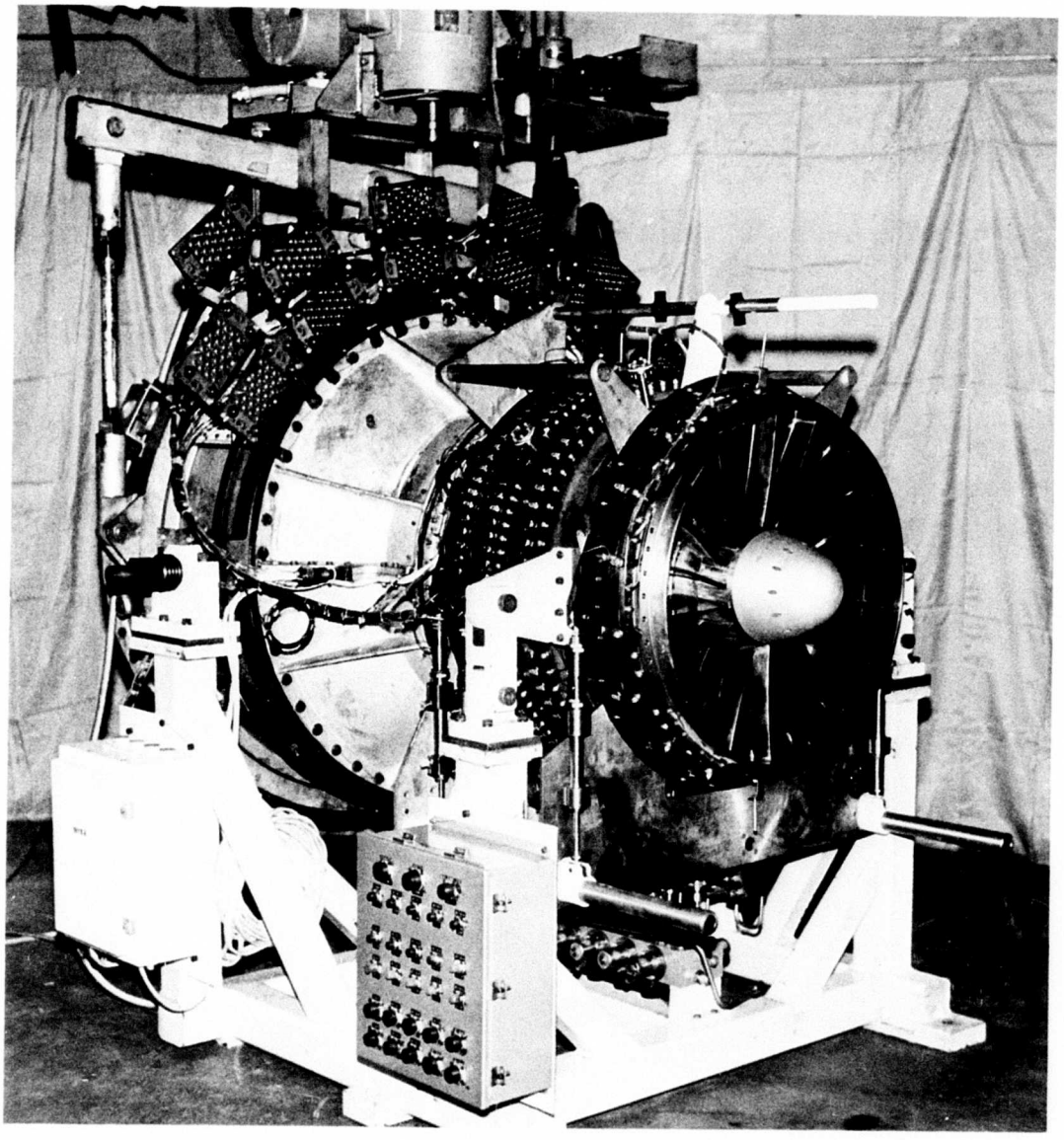

Figure 406. Compressor Installation.

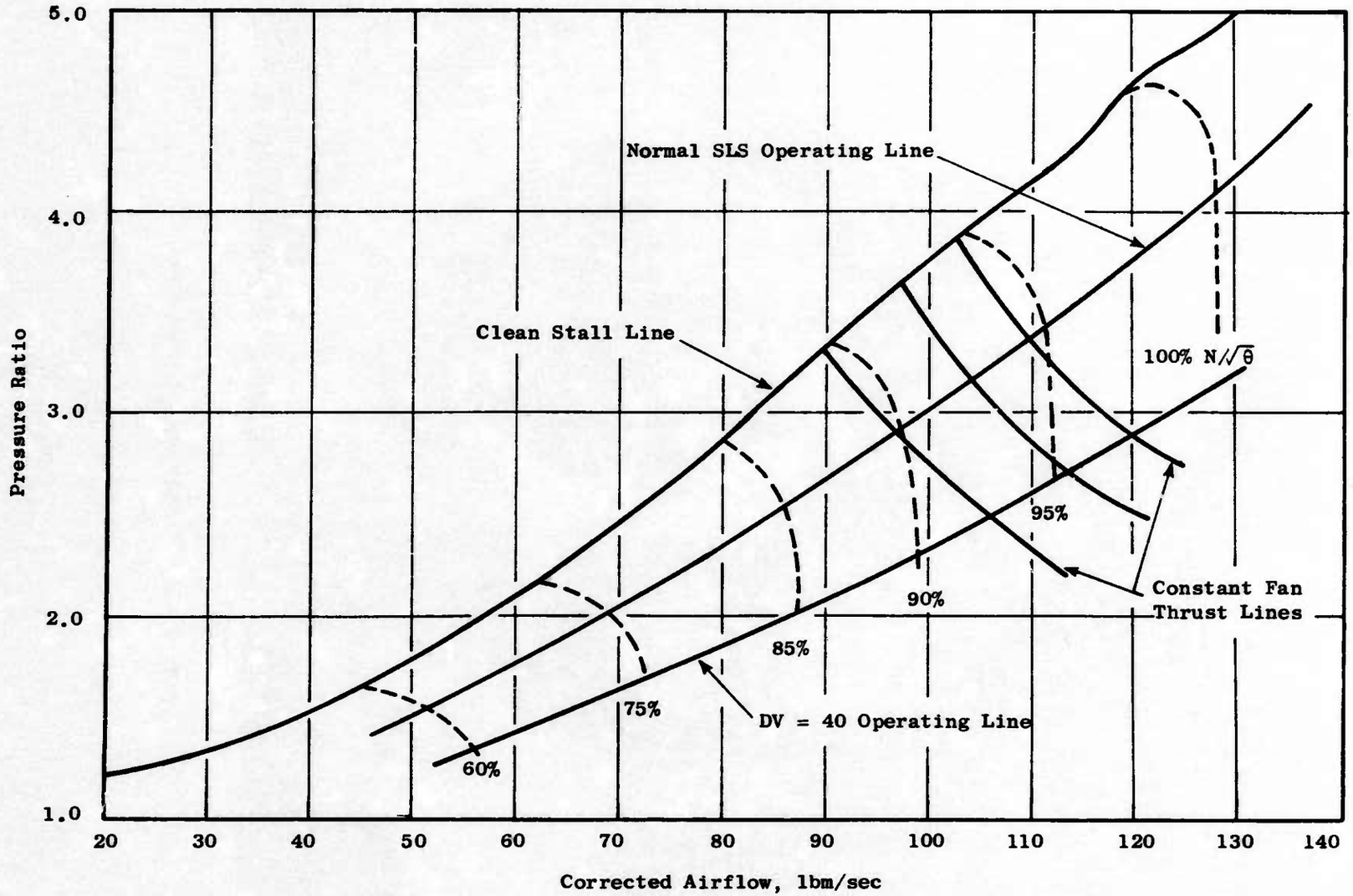

Figure 407. Measured Fan Performance Map.

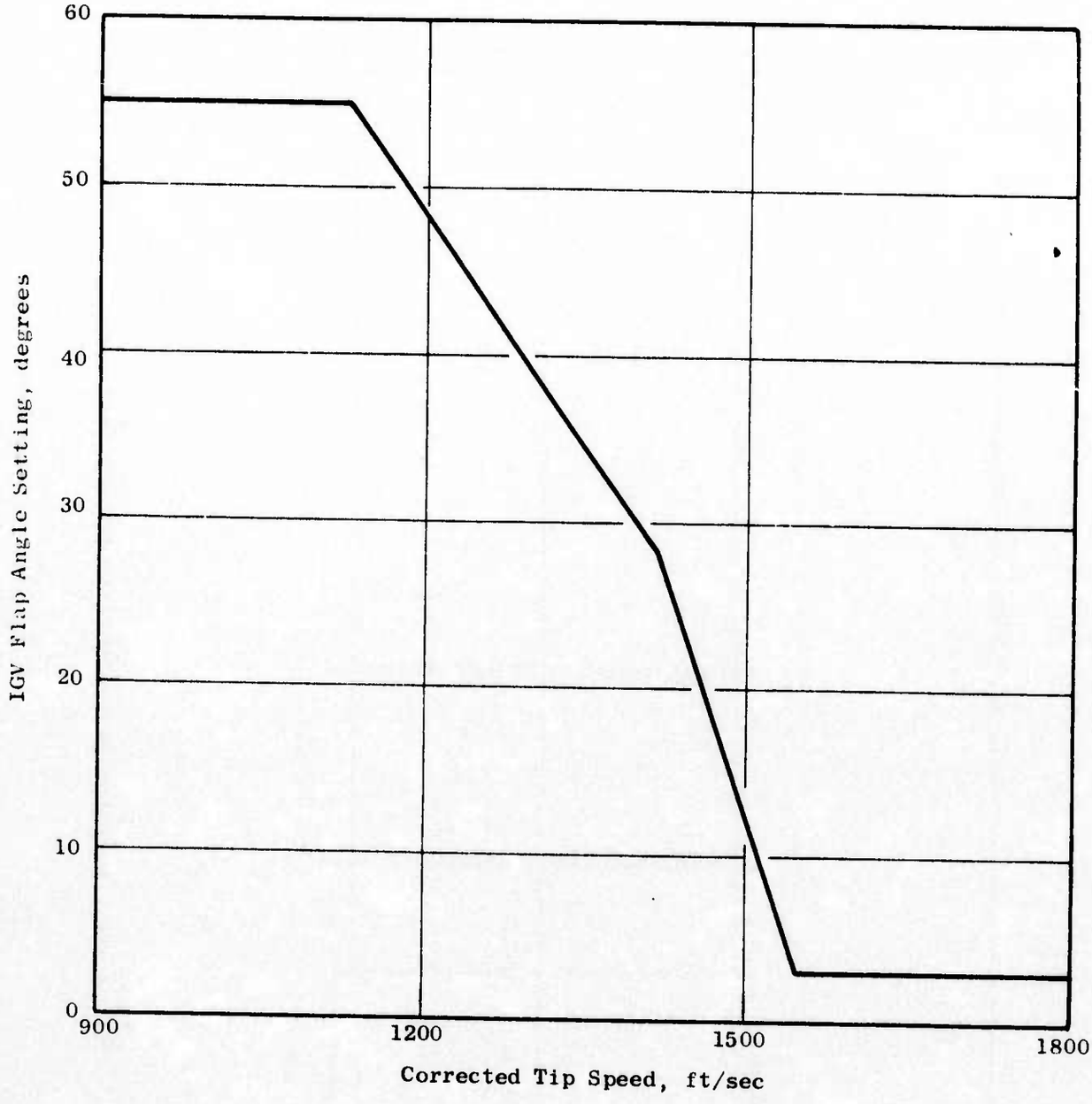

Figure 408. IGV Schedule.

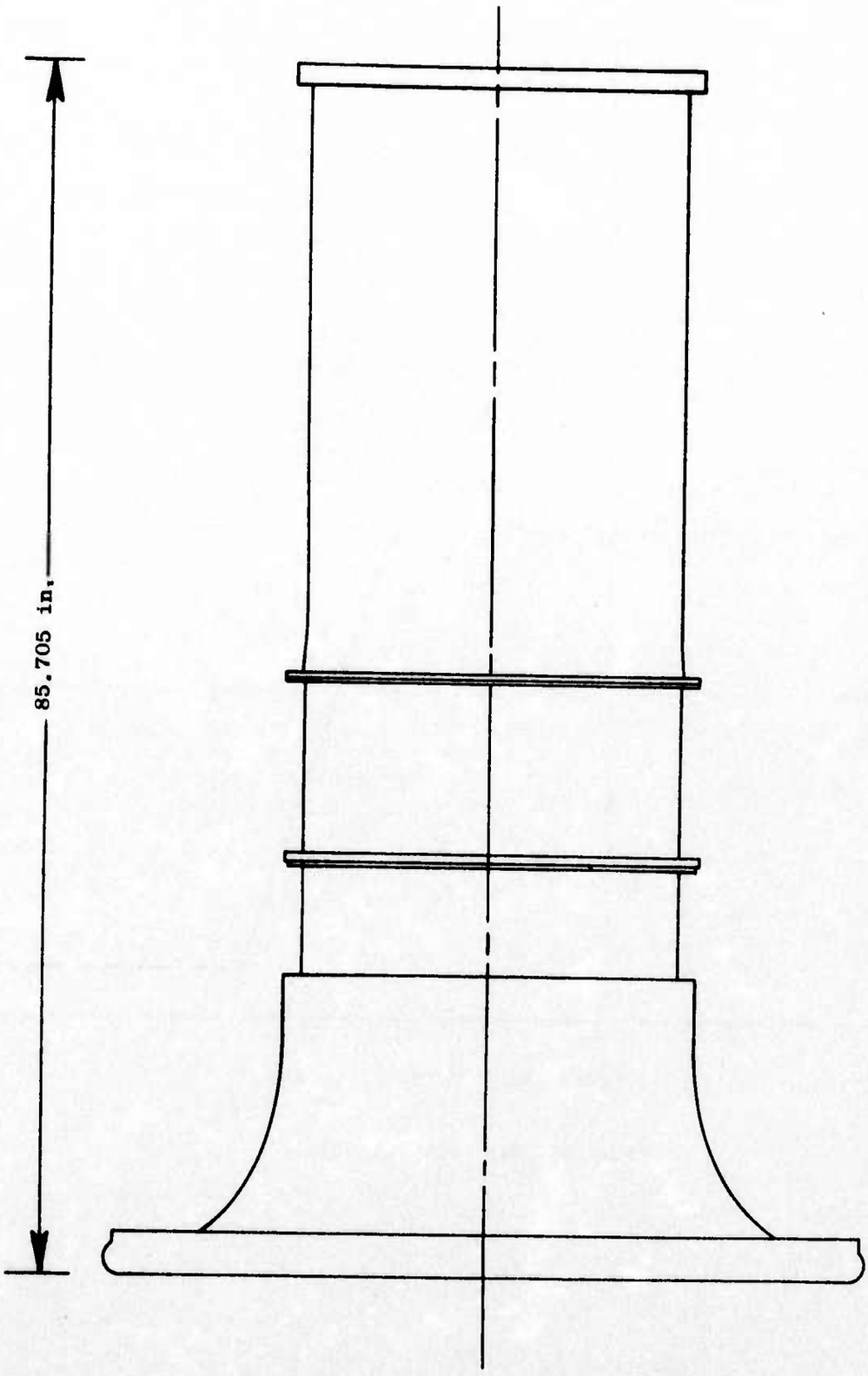

Figure 409. Baseline Bellmouth Cylindrical Inlet.

The design of the hybrid inlet was based on the following ground rules:

- Design for cruise Mach number of 2.50 using a mixed compression, translating centerbody type of inlet.
- Incorporate auxiliary inlets featuring internal and external cowl doors/flaps positionable to more than one discrete setting.
- Include six support struts in the inlet having a chord of 10-12".
- Allow the inlet length to reflect only the foregoing requirements plus the desire for unseparated operation in both approach and take-off configurations. Provide a separate cylindrical section between the inlet, as such, and the LPC for additional acoustic treatment. The acoustic treatment design is discussed in Section 4.4.1.2.3.

While the Boeing SST N5 inlet design provided an obvious reference design, several factors acted to preclude directly scaling it for the present application, among them:

- Difference in design cruise Mach number, 2.50 versus 2.70
- Difference in design point specific flow and hub-to-tip ratio between the advanced LP compressor and the GE4 compressor
- Decision to size the take-off inlet position at 95% corrected speed to provide design point margin and allow above-the-design throat Mach number testing.
- Necessity to recontour the Boeing inlet to prevent observed flow separation that was reattached prior to reaching the compressor due to flow area reduction through the frame struts. This situation was compounded for the present design, because its required support struts had relatively greater blockage than the Boeing design. Therefore, the struts had to be located further aft in the inlet, to preclude local flow choking.

Consequently, although the Boeing N5 inlet design was a good starting point, several modifications were necessary to conform to the particular requirements of the present application. The following discussion will illustrate the design approach employed.

The inlet was sized for operation at a supersonic cruise design point of Mach 2.5, 60K feet of altitude, with the following assumptions (based mainly upon data from References 45 and 46):

- Operation at 100% physical speed, which corresponded to 77.0% corrected speed and 71.4 lb/sec corrected compressor inlet flow, for the cruise condition; compressor map from Build No. 1; and, estimated operating line.

- Shock-on-lip operation (mass flow ratio of one)
- Boeing SST wing flow field characteristics
- Total inlet capture flow equal to 112.5% of engine demand
- Subsonic diffuser boundary layer bleed equal to 3% of engine demand
- Total pressure recoveries of 0.91 overall and 0.96 in the subsonic diffuser
- Terminal shock Mach number of 1.26
- Throat flow coefficient of 0.978

These specifications defined the inlet capture area (and cowl lip radius) and the cruise throat area. The cowl throat radius was scaled from the Boeing N5 model value by cowl lip radius; this defined the centerbody throat radius.

The supersonic diffuser length was established by scaling, with respect to cowl lip radius, that portion of the N5 model that accomplished the amount of diffusion applicable to the reduced (2.50) cruise Mach number. Then the N5 internal cowl contour was "stretched," scaling the axial coordinate by supersonic diffuser length and the difference in cowl lip and local radius by the radial increment between cowl lip and throat radii. This step, or the equivalent, was found necessary to yield reasonable internal cowl surface slopes and curvatures. The final contour was defined by passing a cubic segment through several of these calculated points (selected from a full-scale plot). This determined the internal cowl contour from the flight lip to the minimum radius, which is actually located aft of the annular throat station.

The remainder of the cowl contour was generated from the N5 model by scaling on cowl lip radius and smoothing as above, concurrently adding a downstream fairing to achieve the terminal radius required by the compressor IGV leading edge. Thus the internal cowl surface possessed a diffusion rate consistent with that of the Boeing design, while reflecting the differences in design freestream Mach number and compressor geometric and flow characteristics.

The forward portion of the centerbody, from tip to maximum radius (which is actually forward of the annular throat station), incorporated the following considerations:

- Cone tip angle and axial position relative to cowl lip were constrained by desired cruise shock structure.
- Specific cruise flow areas were desired at the throat and cowl lip stations.
- Centerbody contour had to be suitable for achieving the required take-off and approach throat areas with reasonable translations.

Sizing input employed for these conditions is listed in Table 17, together with the cruise values previously given.

- A smooth flowpath was desired.

The forward centerbody portion was eventually formed, together with the aft contour, from a conical tip and a cubic segment. Finalization of the aft contour required considerable iteration, in which the axial location of the six support struts was varied. Eventually, a combination of centerbody contour and strut location was evolved which was acceptable in terms of overall inlet length and predicted flow instability, as determined by flow and boundary layer analysis. The struts were NACA 64 series airfoils and had a 12-inch chord with 10% maximum thickness. They were positioned with the trailing edge near the end of the internal cowl diffusion and the leading edge near the end of the (approach) centerbody diffusion.

Final flowpath coordinates are listed in Table 18. Axial reference was established as the flight cowl lip station, since the flowpath segment between the struts and the compressor was initially undefined. The aeroacoustic lip bellmouth employed for static testing to simulate low-speed flight conditions is included in this tabulation. A flowpath sketch of the entire test configuration is shown in Figure 410. The primary inlet length was 2.29 fan (IGV) diameters from the location of the flight lip leading edge to the diffuser exit. Length of the entire hybrid inlet, from aeroacoustic lip leading edge to the IGV frame was 3.20 fan diameters.

Evaluation of candidate design contours was accomplished by the use of Streamtube Curvature (STC) flow analysis (Reference 47) plus AERO (Reference 48) and Stratford and Beavers (SABBL) boundary layer analysis. Iterations were conducted to define boundary-layer-adjusted coordinates upon which to base a final viscous STC analysis. This tool also was used to "tune" the centerbody positions, since the actual throat for this type of design does not form a radial plane. The analytical model also included the axial and radial area blockage distributions of six support struts lumped together on an equivalent axisymmetric basis. The study configuration was terminated approximately 13-1/2 inches downstream of the strut trailing edge station to avoid predetermining the flow characteristics in that locale.

Analytical wall Mach number distributions for the highest throat Mach number studied are shown in Figures 411 and 412 for the approach and take-off configurations, respectively. The near one-dimensionality of the flow for this high throat radius-ratio, annular inlet is evident, even for these near-choking conditions. Also indicated on Figures 411 and 412 are the locations of the acoustic treatment. Note that the wall Mach numbers on the treatment are <0.7, which was the design intent.

SABBL boundary layer stability assessment corresponding to the conditions of Figures 411 and 412 is presented in Figures 413 and 414, respectively. Stable operation is predicted in both cases, except in the deceleration zone near the strut trailing edge which is moderately steep and occurs where the boundary layer is relatively thick due to prior diffusion. Little significance was assigned to this predicted separation because:

Table 17. Primary Inlet Sizing Parameters.

	Cruise	Approach	Takeoff
Freestream Mach No., M_o	2.50	0.22	0.30
Altitude, h ~ kft	60	---	---
% Corrected Compressor Speed, $N/\sqrt{\theta_2}$	77.0*	80.0	95.0
Corrected Compressor Inlet Flow, $W\sqrt{\theta}/\delta_2$ ~ lb/sec	71.4	77.0	111.0†
Subsonic Diffuser Bleed, % $W\sqrt{\theta}/\delta_2$	3.0	0	0
Subsonic Diffuser Pressure Recovery, η_{R_D}	0.960	0.978	0.973
Throat Discharge Coefficient, $C_{D_{th}}$	0.978	0.9913	0.9913
Average Throat Mach No., M_{th}	1.26‡	0.750	0.750
Physical Throat Area, A_{th} ~ in.^{2}	218.03	235.20	286.73
Diffuser Area Ratio, A_{ex}/A_{th}	2.373	2.199	1.804

* Assumes operation at 100% physical compressor speed

† 85% of this total corrected flow is assumed to enter through the primary inlet

‡ Terminal shock Mach number

Table 18. Primary Inlet Flowpath Definition.

Centerbody†			Internal Cowl		
Z‡	R		Z‡		
-29.497	0	Conical	- 7.281	18.639	Aeroacoustic lip; selected points for ¼ ellipse with a/b = 1.382. Closed out with 90° of 3.812" R + 2" diameter tangent cylinder.
-19.788*	1.915294		- 7.238	18.069	
-17.288	2.449		- 7.111	17.507	
-11.288*	3.950		- 6.90	16.957	
- 7.288	4.997		- 6.608	16.427	
- 3.288*	5.950		- 6.026	15.683	
- 0.288	6.543		- 5.±86	15.016	
2.300*	6.976		- 4.406	14.445	
4.712	7.317		- 3.411	13.985	
7.040*	7.543		- 2.325	13.647	
8.712	7.623		- 1.565	13.494	
10.594*	7.669		- 0.787	13.402	
12.712	7.709		0.000	13.371	Cylinder
14.150*	7.714		3.247*	13.371	
15.000	7.700		4.000	13.369	
16.00	7.666		5.000	13.356	
17.000	7.612		6.000	13.328	
18.000	7.538		6.772*	13.292	
19.000	7.442		7.000	13.279	
20.000	7.324		8.000	13.207	
21.000	7.183		9.000	13.111	
22.142*	6.994		9.142*	13.095	
23.000	6.832		10.000	12.991	
24.000	6.624		11.512*	12.768	
25.000	6.402		13.000	12.505	
26.000	6.170		15.000	12.119	
27.000	5.932		17.438*	11.679	
28.000	5.695		19.000	11.454	
29.000	5.463		20.992*	11.232	
30.000	5.241		21.992	11.146	
31.000	5.034		22.992	11.076	
31.650*	4.910		23.992	11.020	
32.000	4.847		24.992	10.977	
33.000	4.683		25.992	10.947	
34.000	4.539		26.992	10.928	
35.000	4.414		27.992	10.919	
36.000	4.307		28.318*	10.918	
37.000	4.216		28.992	10.919	
38.000	4.138		29.992	10.928	
39.000	4.072		30.792*	10.942	
40.000	4.016		30.992	10.946	
41.000	3.969		32.992	11.009	
41.450*	3.950		34.890*	11.101	
42.000	3.928		36.992	11.235	
43.000	3.894		38.988*	11.383	
44.000	3.865		40.992	11.544	
45.000	3.841		42.992	11.721	
46.000	3.823		44.453*	11.866	
47.000	3.810		46.992	12.152	
48.000	3.803		48.992	12.394	
49.000	3.800		50.992	12.636	
Cylinder + Hub Firing			52.623*	12.823	
			55.992	13.148	
			60.992	13.381	
			61.400*	13.383	
			Cylinder to IGV L.E.		

† Centerbody approach position is tabulated. Translate 6.5" forward for takeoff.

* Control points for splined curve fit. All other radii rounded to nearest 0.001".

‡ Z = 0.0 corresponds to flight cowl leading edge and vehicle station -85.54. Vehicle station 0.0 represents rotor 1 leading edge.

- - - -All dimensions in inches- - - -

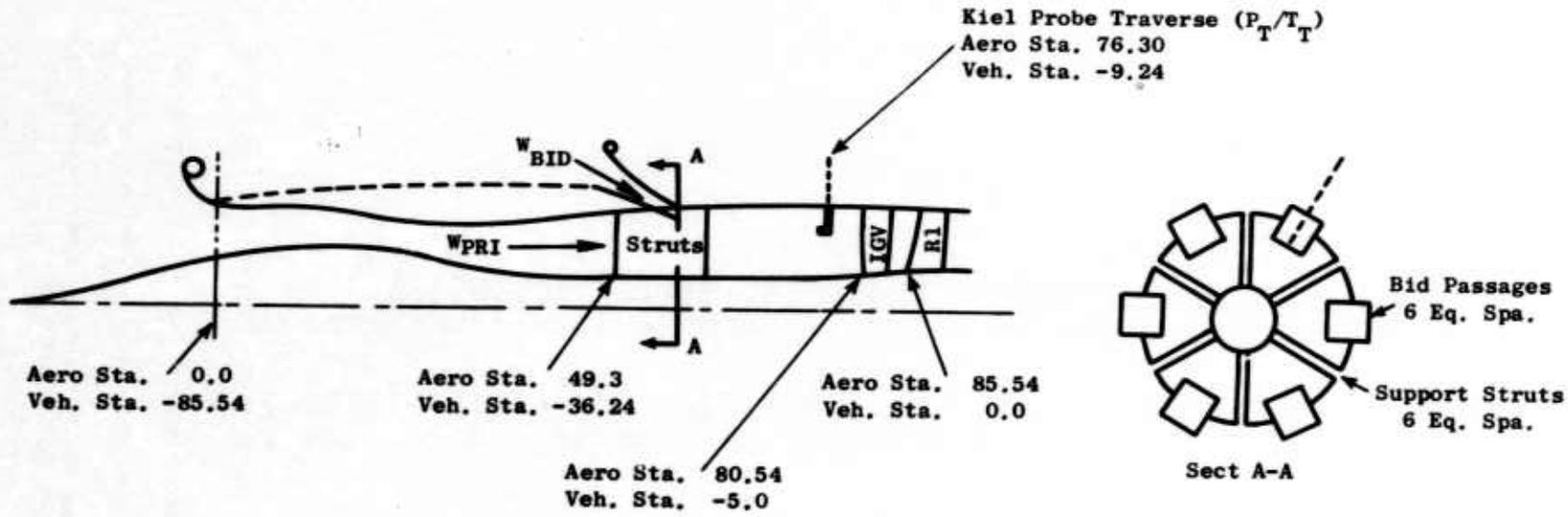

Figure 410. Flowpath of LPC Supersonic Inlet Test Configuration Showing Key Station Designations.

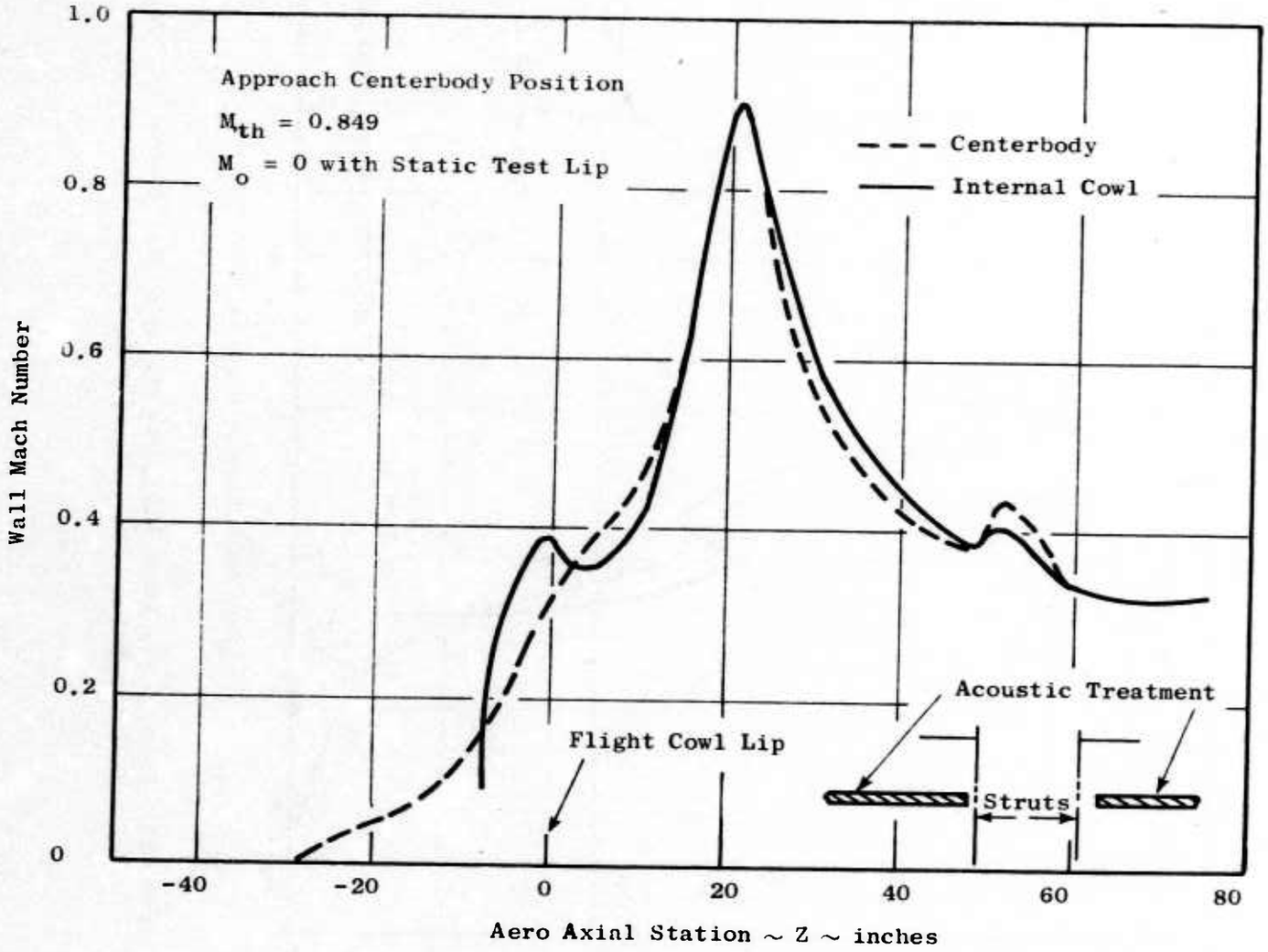

Figure 411. Viscous STC Inlet Wall Mach Number Distributions for the Approach Mode.

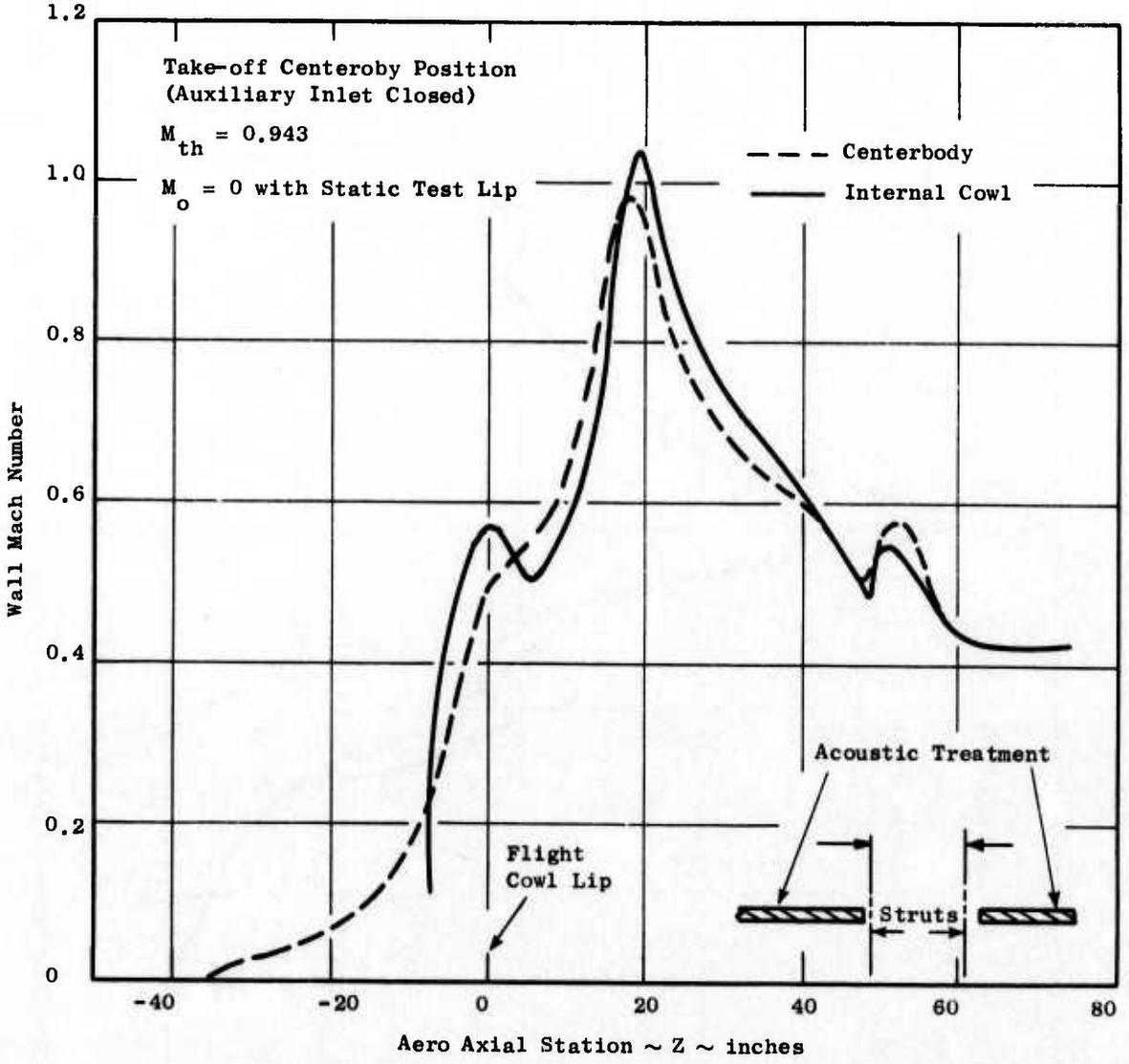

Figure 412. Viscous STC Inlet Wall Mach Number Distributions for the Take-off Mode.

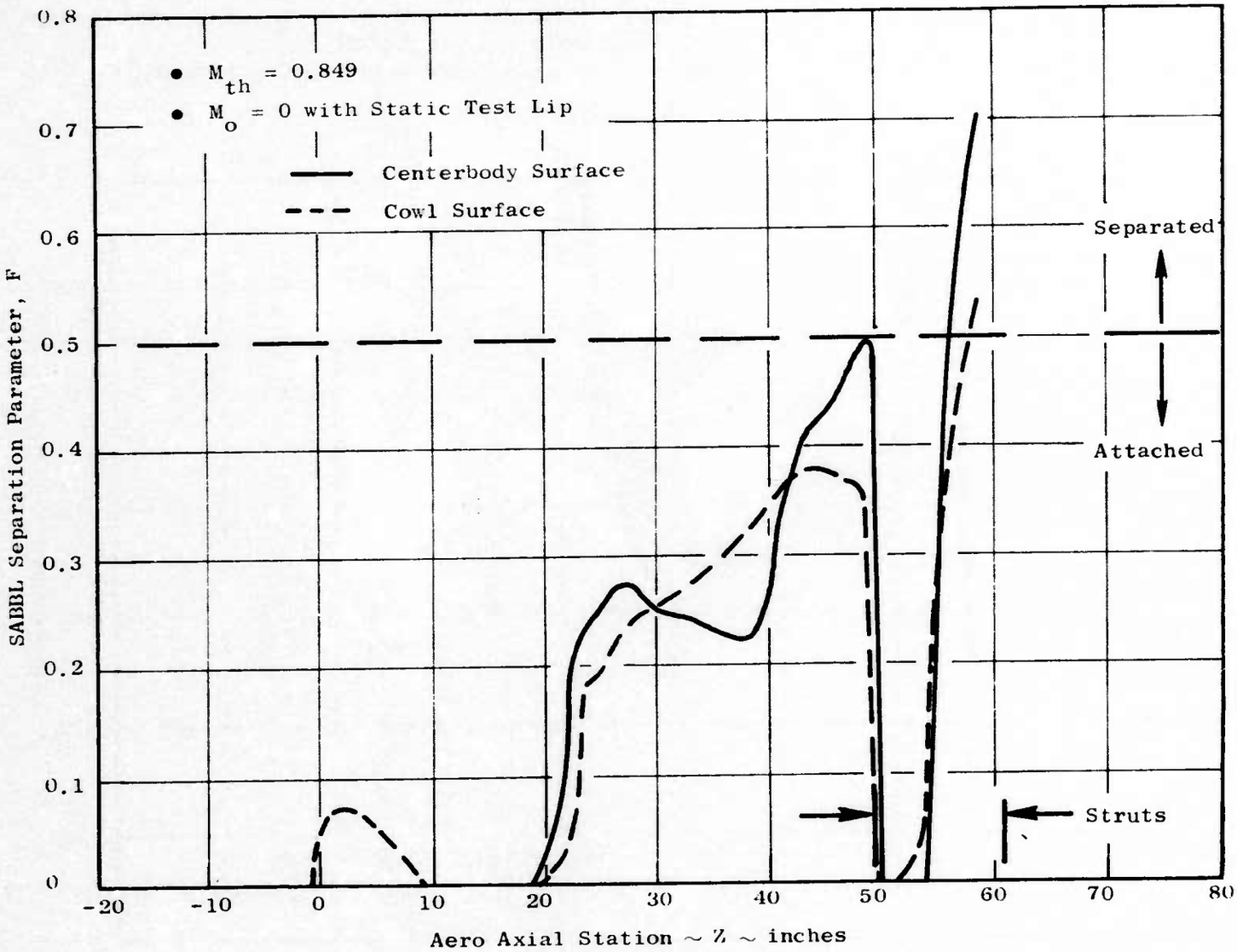

Figure 413. Boundary Layer Stability Characteristics Predicted by Viscous STC/SABBL Analysis for the Approach Mode.

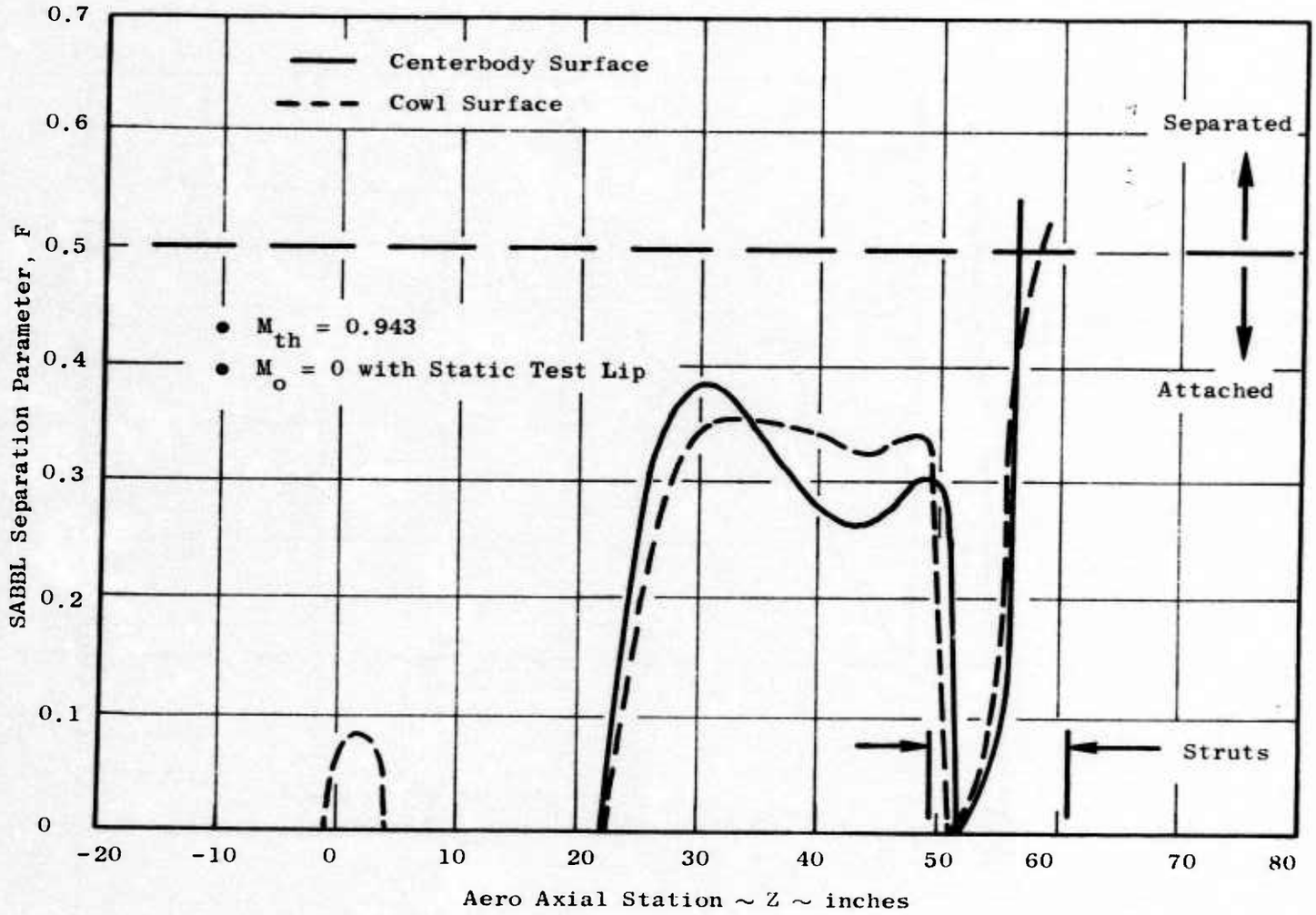

Figure 414. Boundary Layer Stability Characteristics Predicted by Viscous STC/SABBL Analysis for the Take-off Mode.

- The exact, three-dimensional flow pattern due to the annular inlet and contoured struts plus viscous effects cannot be simulated by STC; consequently, the predicted separation may either not occur at all or, alternatively, it may be confined to the immediate vicinity of the struts.

- Flow separation in the relatively low Mach number region of the strut trailing edge would not adversely affect the bulk of the primary inlet upstream of the struts, would likely be reattached prior to entering the compressor by the hub flowpath convergence, and would be a relatively low-loss producer.

The main objective of the blow-in-door auxiliary inlet design was to provide a controlled diffusion process that allowed discretely variable flow rates and BID throat Mach numbers, in order to facilitate investigation of the acoustic effect of auxiliary inlet design independently of primary inlet operational characteristics. The desire was for three internal door settings that would approximate the flow splits indicated below:

BID Area	$M_{th_{pri}}$	$M_{th_{BID}}$	$\omega_{BID}/\omega_{TOTAL}$
Small	1.0	0.6	*
Nominal	0.75	0.75	0.15
Large	0.6	1.0	*

The quantity ($\omega_{BID}/\omega_{TOTAL}$) had to be determined for the small and large BID setting to obtain the required flow splits.

Preliminary sizing calculations were made, with these objectives in mind. The results of these sizing calculations indicated that this concept was feasible from a combined aeromechanical standpoint. This investigation presupposed the BID system to be placed in its "natural" location between the six support struts. Such a design was desirable since it facilitated a minimum length inlet, for the constraints already cited, as it did not intrude on either the forward or aft acoustic treatment zones.

Pertinent features of the BID system that evolved include:

- Six identical discrete modular passages, one between each pair of support struts, were each exposed by rotation of a pair of doors/panels situated on the internal (inward rotation) and external (outward rotation) cowl surfaces. The actual test configuration had a fixed outer door and a manually positionable inner door.

- The passages were essentially two-dimensional, with side-plates to preclude lateral flow spillage. Only the fixed outer flowpath of the BID passage was axisymmetric, since it led directly to

the internal cowl flowpath. Each passage was roughly 20° in circumferential extent, allowing sufficient strut clearance for the primary tip flow.

- The external surface of the inner door was made conical, after initial evaluation of a contoured design exhibited too peaky a wall Mach number distribution that required excessive diffusion.

STC/SABBL analysis was again used to guide the detail design. In this case, however, the procedure was not straightforward, for two reasons:

- The primary inlet passage was axisymmetric, except for the support struts, while the BID inlet system was asymmetric, being composed of circumferentially discrete, two-dimensional openings. While the STC program could solve either axisymmetric or planar flow problems, it was not designed for a mixed geometry like the complete supersonic inlet.

- Both passage flow rates could not be specified independently, since only unique pairs of primary and BID flow rates would satisfy the Kutta condition, i.e., matched static pressures at the inner door trailing edge.

To circumvent the above, a scheme was devised whereby the BID passage was modeled as a continuous 360° slot, coannular with the primary inlet. A section of the inlet extending axially from upstream of the struts and BID entrance to beyond the strut trailing edge was included, with the primary duct wall coordinates adjusted for estimated boundary layer growth. The door trailing edge was approximated by a section gradually tapering to zero thickness, with about a 21-22° included angle, as opposed to the actual 0.08 inch trailing edge radius, to facilitate the STC analysis.

An existing STC feature was then utilized whereby the BID passage flow rate was input and fixed at the desired value while the primary passage flow rate was iterated from the initial input value until the Kutta condition was satisfied at the internal door trailing edge. The resulting primary and predetermined BID flow rates were then adjusted to estimated actual test configuration values by the ratio of actual-to-STC (axisymmetric) passage discharge area, with the actual discharge area calculated to reflect the effects of local strut blockage, boundary layer, and BID blockage as applicable.

Internal door settings were varied until three positions were identified that produced the approximate primary/BID flow relationship desired. Pertinent BID sizing and design parameters resulting from the analysis are summarized in Table 19. Note that the various door settings possess different diffuser area ratios as well as different absolute flow areas. The BID system flowpath is shown in isolation in Figure 415 and in relation to the overall inlet in Figure 410. Figure 416 shows some approximate dimensions of the internal door in its three open settings. The flowpath coordinates for the remaining (fixed) portions of the BID system are listed in Table 20. Figure 417 is a trimetric representation of the BID module. A sufficient amount of the inlet external

Table 19. Summary of Blow-In Door Design Characteristics.

	Configuration - Relative Throat Area Setting		
	81%	100% (Nominal)	114%
* Primary Flow Rate, $W\sqrt{\theta/\delta})_{pri}$ ~ lb/sec	101.12	92.78	83.62
* Total BID Flow Rate, $W\sqrt{\theta/\delta})_{BID}$ ~ lb/sec	10.65	14.82	17.79
* Total Inlet Flow Rate, $W\sqrt{\theta/\delta})_{total}$ ~ lb/sec	111.77	107.60	101.41
BID-to-Total Flow Ratio, W_{BID}/W_{total}	0.0953	0.1377	0.1754
Total BID Throat Area, $A_{th_{BID}}$ ~ in.^{2}	37.59	46.22	52.63
Primary Total-Pressure Recovery, $\eta_{R_{pri}}$	0.973	0.973	0.973
BID Total-Pressure Recovery, $\eta_{R_{BID}}$	0.980	0.980	0.980
Primary Throat Discharge Coefficient, $C_{d_{pri\ th}}$	0.987	0.987	0.087
BID Throat Discharge Coefficient, $C_{d_{BID\ th}}$	0.965	0.965	0.965
* Primary Throat Mach Number, $M_{th_{pri}}$	> 1 (Super-critical)	0.728	0.596
* BID Throat Mach Number, $M_{th_{BID}}$	0.597	0.766	~ 1.0
BID Diffuser Area Ratio, $(A_{ex}/A_{th})_{BID}$	1.015	1.099	1.180
BID Equivalent Diffusion Angle, θ_{eq} ~ deg.	2.23	2.95	4.12
BID Trailing Edge Location:			
(Radial Distance from $\mathcal{C}$), R_{te} ~ in.	12.05	11.62	11.25
(Axial Station), Z_{te} ~ in.	57.25	25.125	56.97
BID Entrance Area Ratio (Entrance Area on First Orthogonal Entirely Within BID Duct), A_{en}/A_{th}	2.022	1.645	1.444
Door Angle† (Outer Surface), θ_{BID} ~ deg.	-15.14	-21.18	-26.14
BID Passage Width (Constant), W_{BID} ~ in.	4.461	4.461	4.461
Number of BID Passages, η_{BID}	6	6	6

* Actual configuration values estimated from STC analysis of continuous BID slot.

† Relative to inlet centerline.

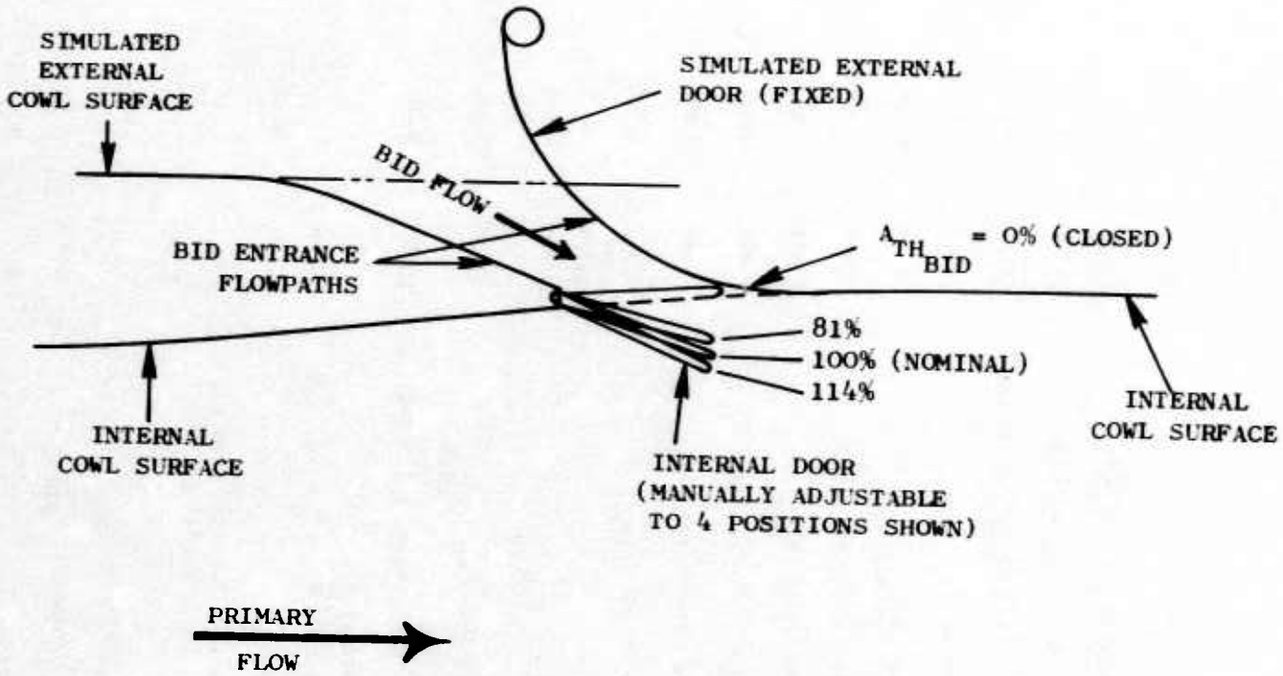

Figure 415. Blow-In Door Inlet Flowpath.

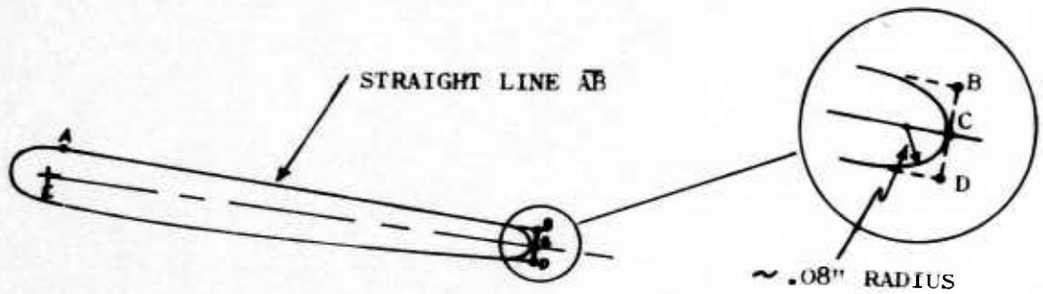

		BID Setting: 81% A_{th}		100% A_{th}		114% A_{th}	
	Point	Z	R	Z	R	Z*	R**
	A	53.13	13.26	53.13	13.26	53.12	13.235
	B	57.27	12.14	57.155	11.70	56.99	11.34
(Trailing Edge)	C	57.25	12.05	57.125	11.62	56.97	11.25
	D	57.23	11.98	57.10	11.55	56.94	11.19
(Door Hinge Point)	E	52.98	13.10	52.98	13.10	52.98	13.10
Angle	$\overline{AB}$	-15.138°		-21.184°		-26.143°	

* Z = 0.0 Corresponds to Flight Cowl Leading Edge

** R = 0.0 Corresponds to Hybrid Inlet Centerline

Figure 416. Selected Dimensions of Variable Blow-In Door.

Table 20. Blow-In-Door Passage Fixed Flowpath Definition.

	Inner Surface of BID Passage		Outer Surface of BID Passage		
	Z	R_1	Z	R_2	
Cylindrical	40.000	16.210	51.270	20.440	
	44.159	16.210	51.332	19.572	Circular Arc Aero-Acoustic Lip Extension Plus External Door
Circular Arc	44.555	16.201	51.517	18.717	
	44.951	16.173	51.887	17.757	
	45.348	16.127	52.380	16.917	
	45.744	16.062	52.750	16.440	Fixed Surface of BID Passage
	46.140	15.977	54.000	15.188	
	46.536	15.873	55.150	14.370	
	46.933	15.747	56.500	13.755	
	47.329	15.600	57.960	13.410	
Conical	47.725	15.430	59.000	13.312	
	52.970	13 320			

Refer to Figure 416 for door surface detail, which forms the remainder of this surface.

Interfaces with internal cowl surface of primary inlet here.

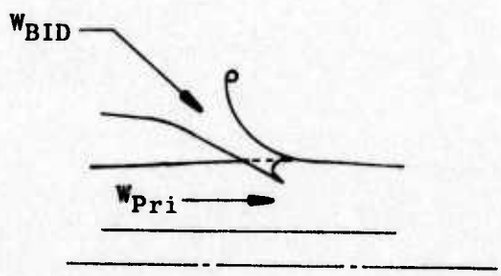

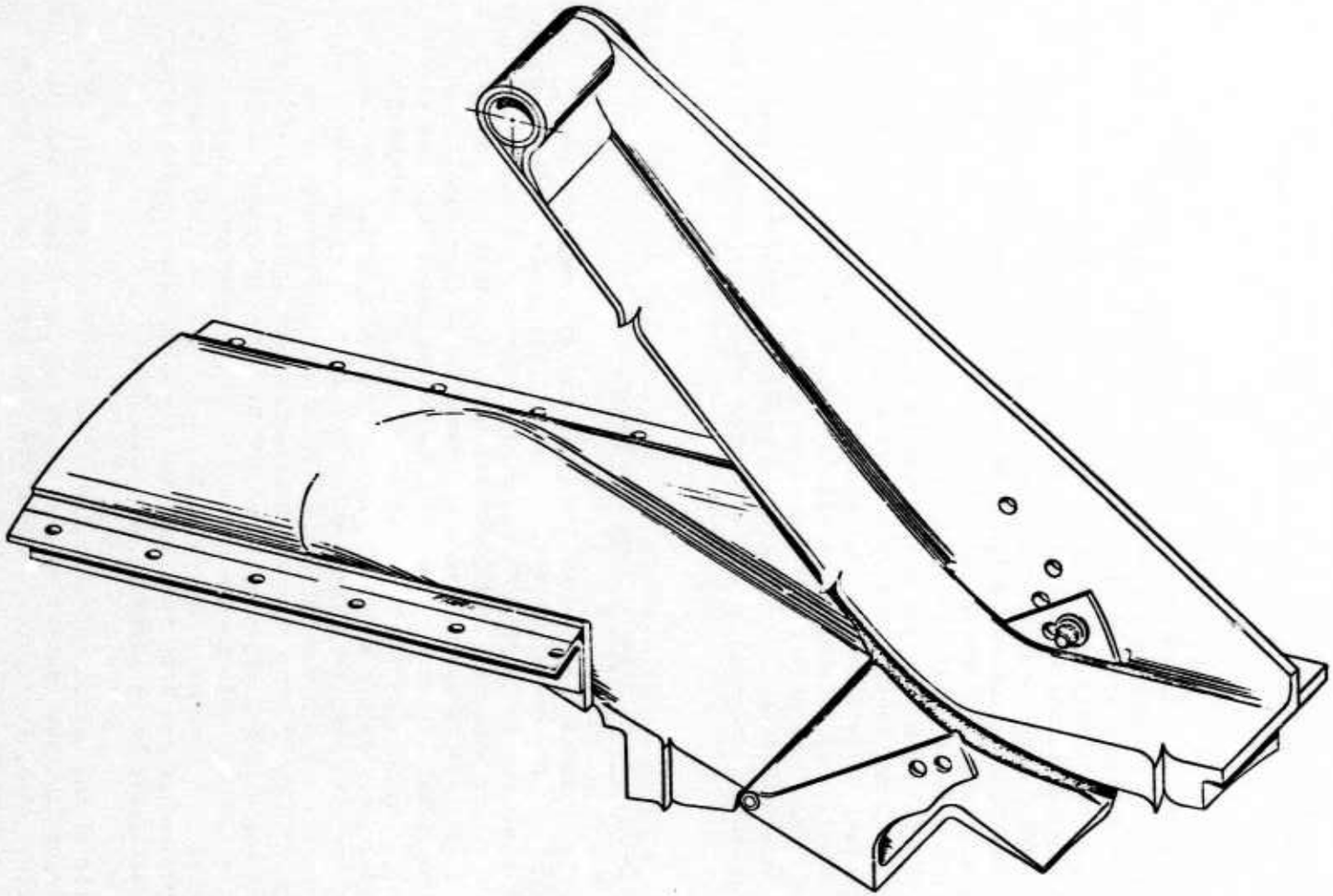

Figure 417. Trimetric View of a Blow-In Door.

cowl surface was simulated to reduce the local wall velocity to relatively low levels - less than 25 ft/sec. The simulated external door had a well-rounded lip extension to be more representative of flight speed operation. However, a structural design of the BID entrance side edges precluded a significant amount of rounding and limited it to radiusing the stock thickness.

The analytical flow characteristics of the BID passage are shown in Figures 418, 419, and 420 for reference, notwithstanding the previously described difference between the STC model and the actual test configuration. Downstream of the entrance section, the flow is seen to be nearly one-dimensional. The primary side surface of the internal door is also shown to point up the manner in which flow along it accelerates, while the BID side decelerates, to match static pressure at the juncture of the door trailing edge. SABBL separation parameters calculated for these predicted BID passage flow characteristics are included in Figures 421, 422, and 423. The three designs are free of predicted flow separation, except for a small region within 0.2-0.3 inch from the door trailing edge for the nominal (100%) and large (114%) BID settings. This is a consequence of the relatively high local diffusion rate imposed on the door surface by the Kutta condition. Its resolution is not directly amendable to simple flowpath modifications of the basic design adopted. The design (as shown) was selected for fabrication in spite of this undesirable feature because the predicted separation zone was quite small and was not expected to significantly affect the design diffuser area ratio.

4.4.1.2.3 Hybrid Inlet - Acoustic Design

The acoustic treatment for the hybrid inlet was designed for noise suppression across a wide range of frequencies. In particular, the treatment was designed for suppression at the blade passing frequency of all three rotors, the first rotor second harmonic, and lower frequency multiple pure tones as shown in Figure 424. The acoustic treatment consists of four Single Degree Of Freedom (SDOF) liner segments. The liner resonator parameters and the respective tuning frequencies are given in Table 21. The liner segment lengths and axial location are shown in Figure 425. The specific reactances of the four liners are shown as a function of frequency in Figure 426. Treatment is applied between the BID's and the fan face to provide noise suppression prior to the BID's. The thick treatment was applied in this area to suppress the higher order modes up to 10,000 Hz. The treatment panels were replaceable with hardwall panels so that acoustic treatment suppression could be isolated. A treatment length of L/D = 1.0 was selected because it fit well and because it was felt that this was the maximum treatment length which could practically be included in an actual SST.

A schematic of the hybrid inlet configuration is shown in Figure 425. A sketch of a flight lip (not tested) is also shown for comparison with the aeroacoustic lip. Also, in Figures 427 and 428, photographs of the hybrid inlet with and without the BID's are shown.

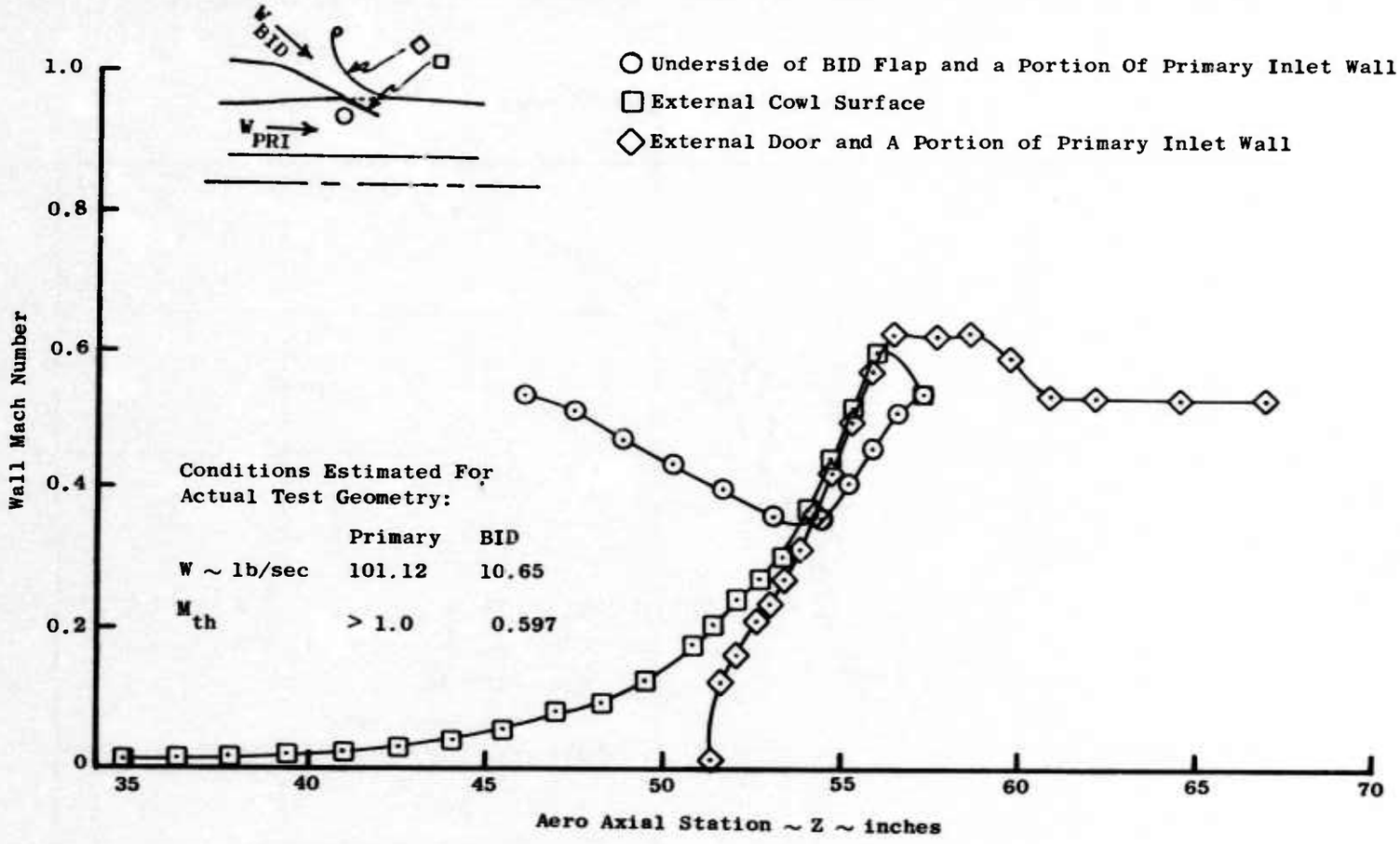

Figure 418. STC-Predicted Flow Characteristics, Using Continuous-Slot Coannular Model for 81% A_{th} BID Setting.

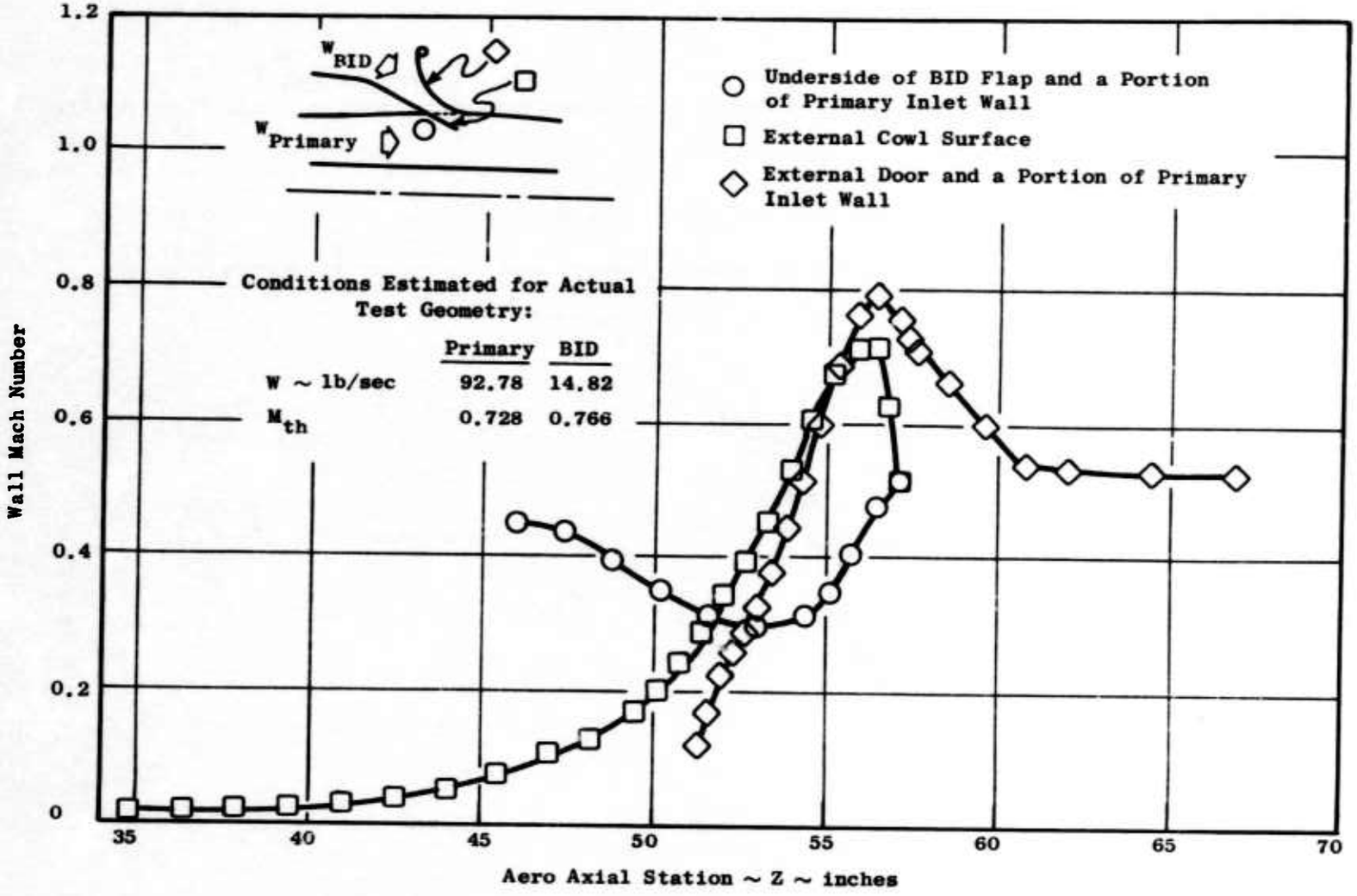

Figure 419. STC-Predicted Flow Characteristics, Using Continuous-Slot Coannular Model for 100% A_{th} BID Setting.

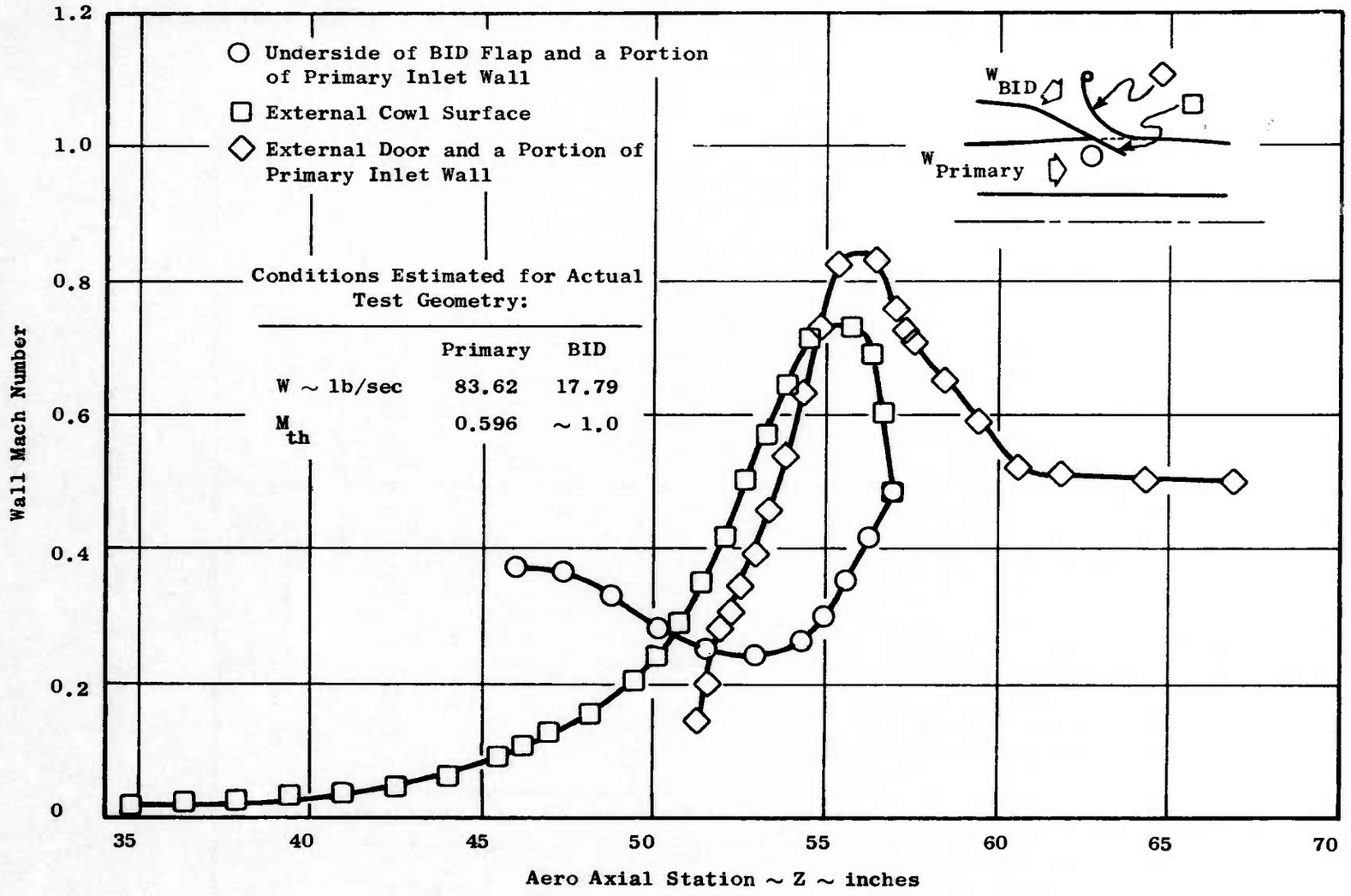

Figure 420. STC-Predicted Flow Characteristics, Using Continuous-Slot Coannular Model for 114% A_{th} BID Setting.

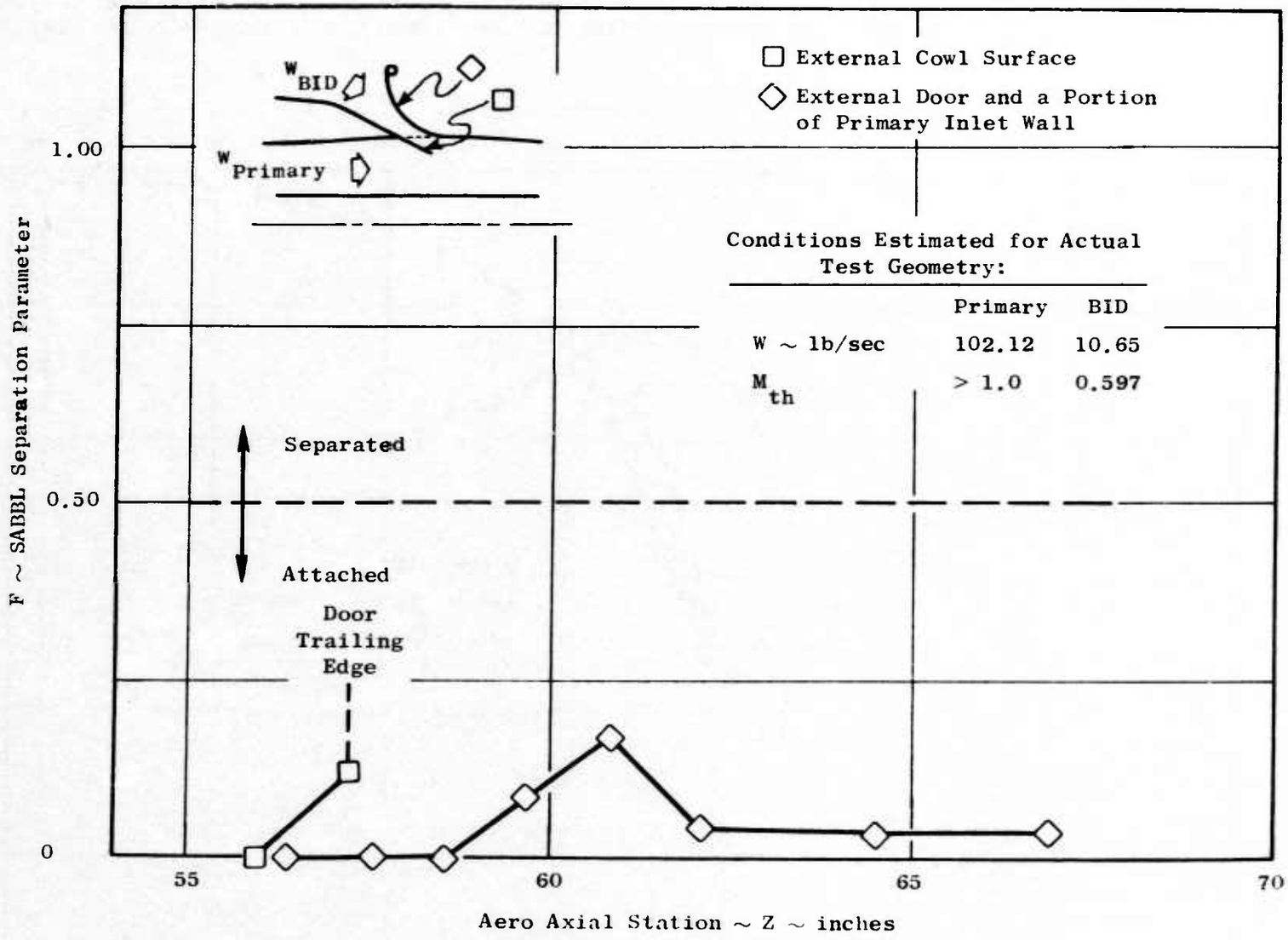

Figure 421. Boundary Layer Stability Characteristics Predicted by STC/SABBL for 81% A_{th} BID Settings, Based on Continuous-Slot Coannular Model.

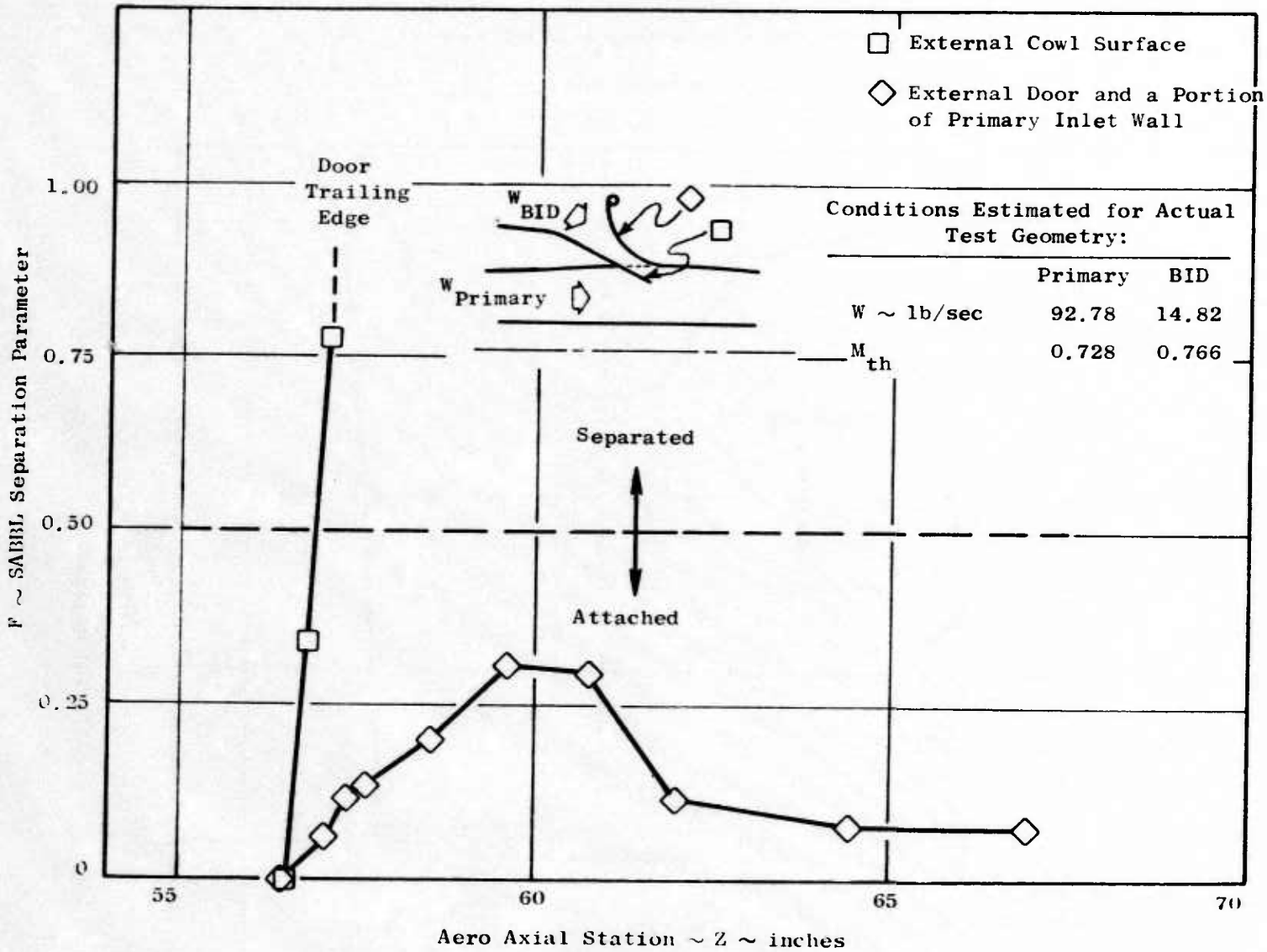

Figure 422. Boundary Layer Stability Characteristics Predicted by STC/SABBL for 100% A_{th} BID, Settings, Based on Continuous-Slot Coannular Model.

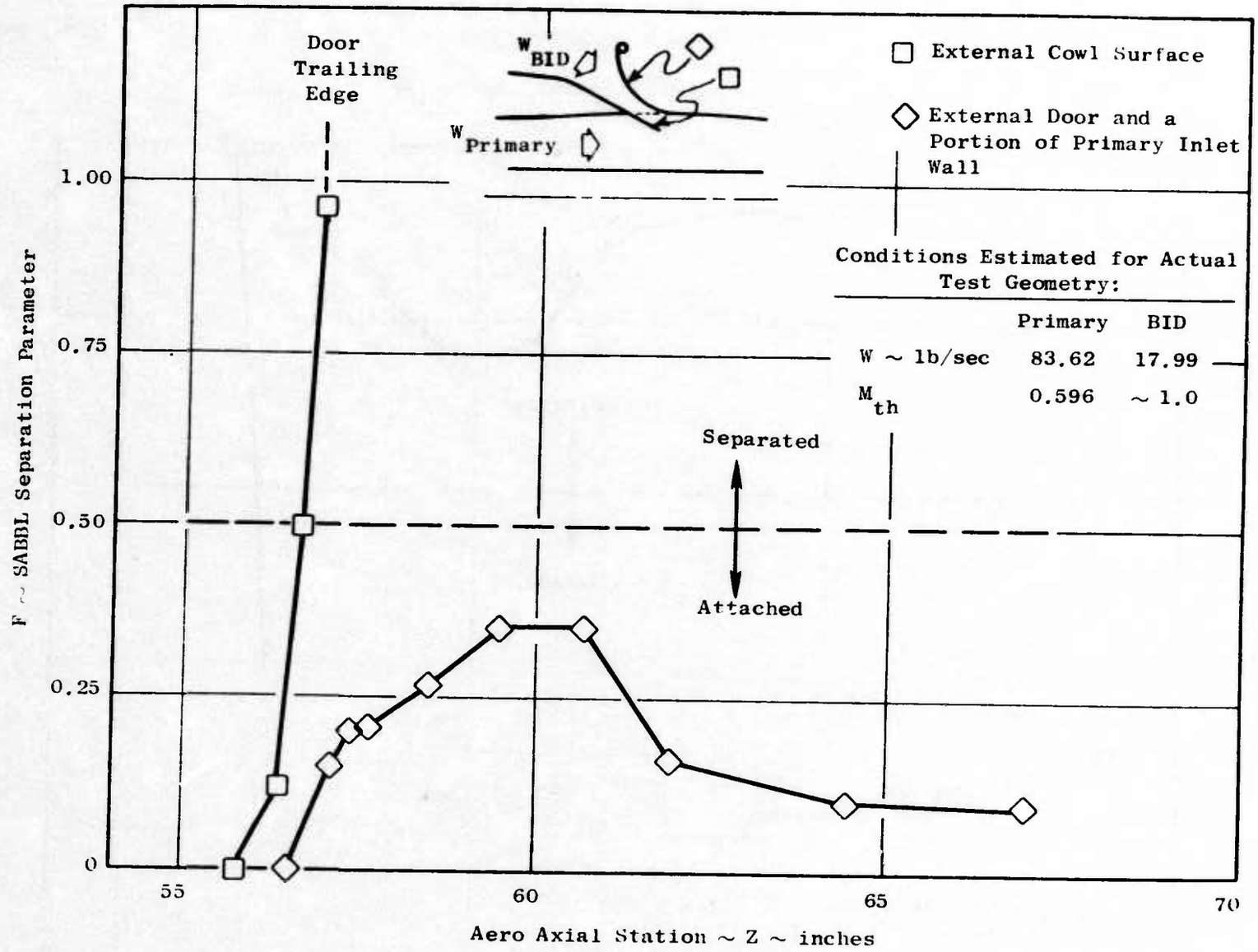

Figure 423. Boundary Layer Stability Characteristics Predicted by STC/SABBL for 114% A_{th} BID, Settings, Based on Continuous-Slot Coannular Model.

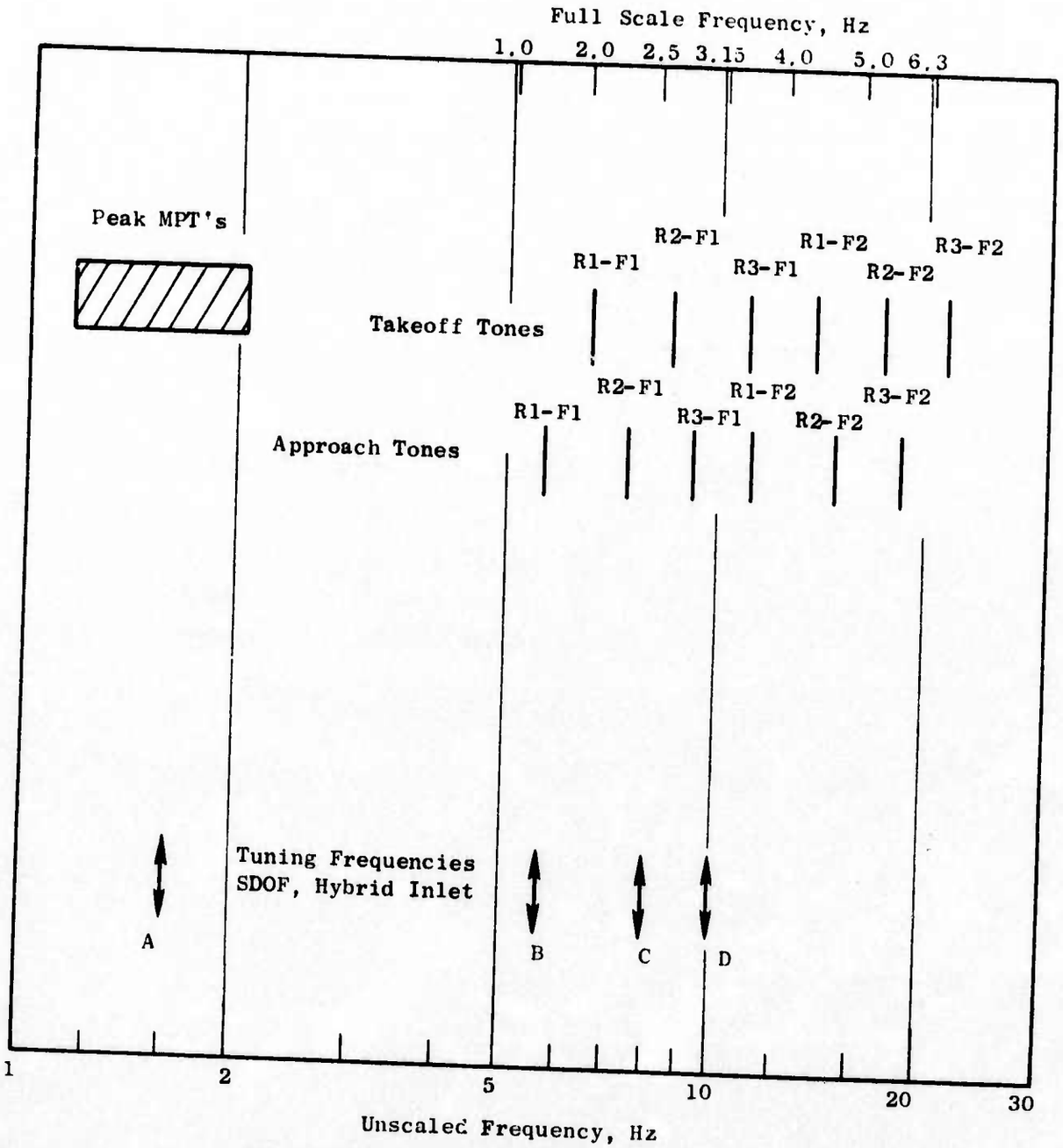

Figure 424. Treatment Tuning Frequencies.

Table 21. Resonator Parameters, Hybrid Inlet Acoustic Treatment.

	Faceplate Liner	
	A	B,C,D
Thickness, inch	0.012 ± 0.002	0.012 ± 0.002
Hole Diameter, inch	0.040 ± 0.002	0.045 ± 0.002
Open Area Ratio, % (After Bonding)	14.0 ± 0.4	9.2 ± 0.3

Core

Liner	Cavity Depth, inch	Tuning f, Hz
A	1.000 ± 0.020	1600
B	0.170 ± 0.005	5600
C	0.120 ± 0.005	8000
D	0.085 ± 0.002	10000

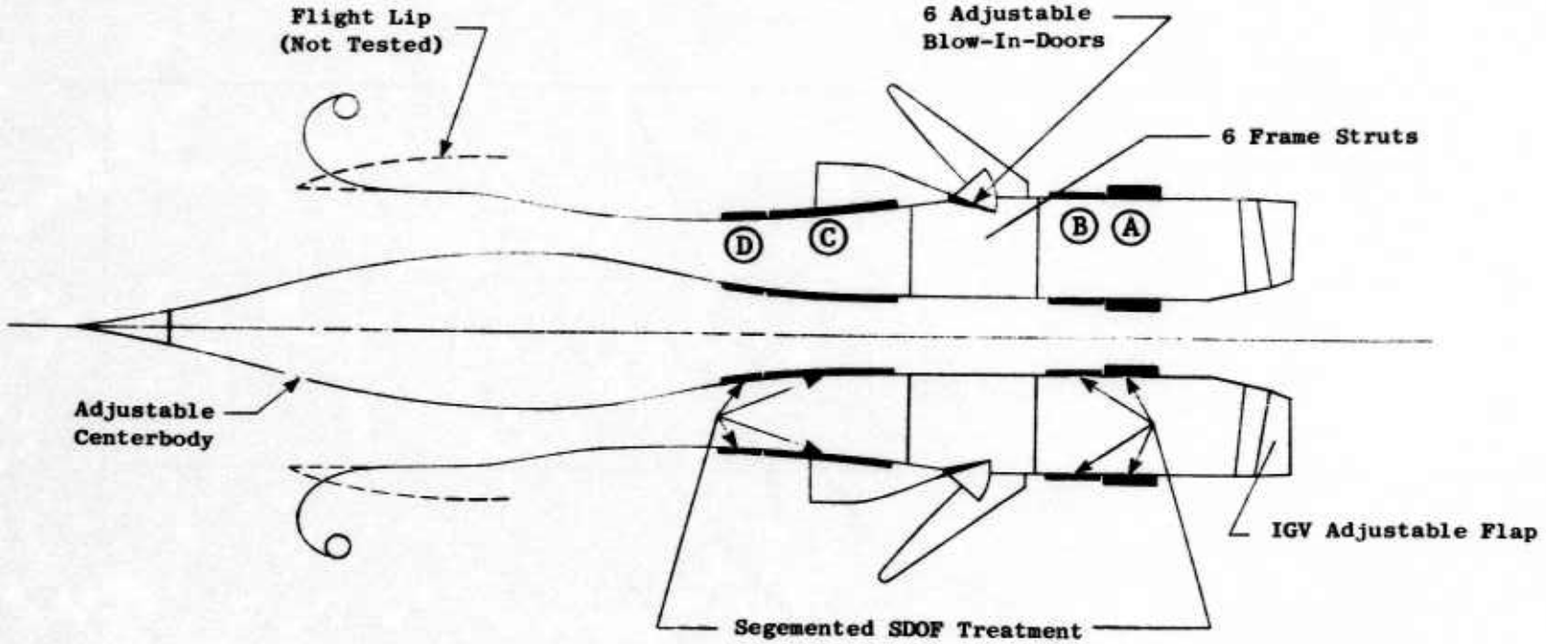

Treatment Panel	Tuning Frequency	Length (ft)
A	1600 Hz	0.42
B	5600 Hz	0.42
C	8000 Hz	1.00
D	10000 Hz	0.33

Figure 425. Hybrid Inlet, Take-off Mode.

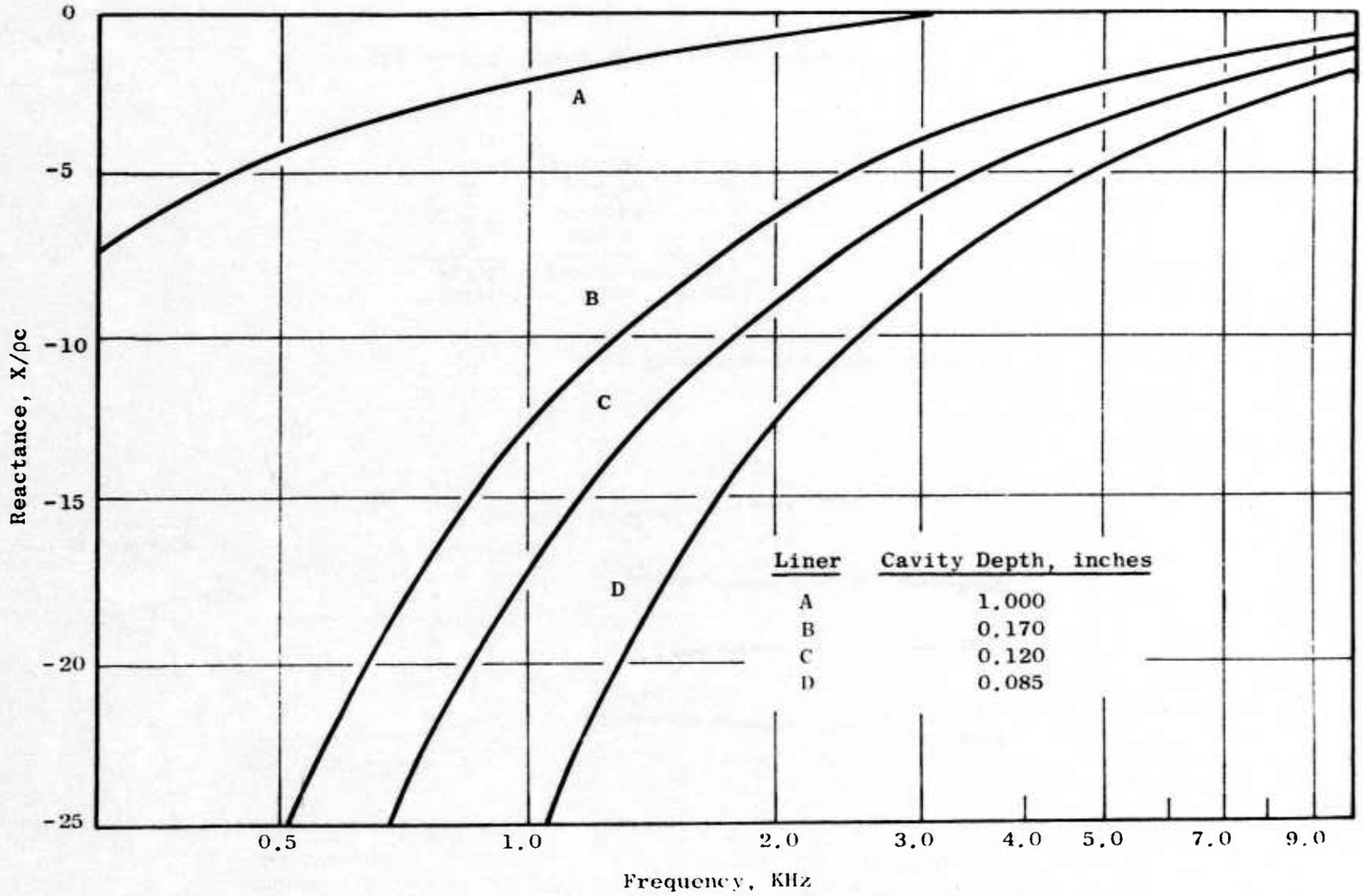

Figure 426. Specific Acoustic Reactances of Hybrid Inlet Treatment.

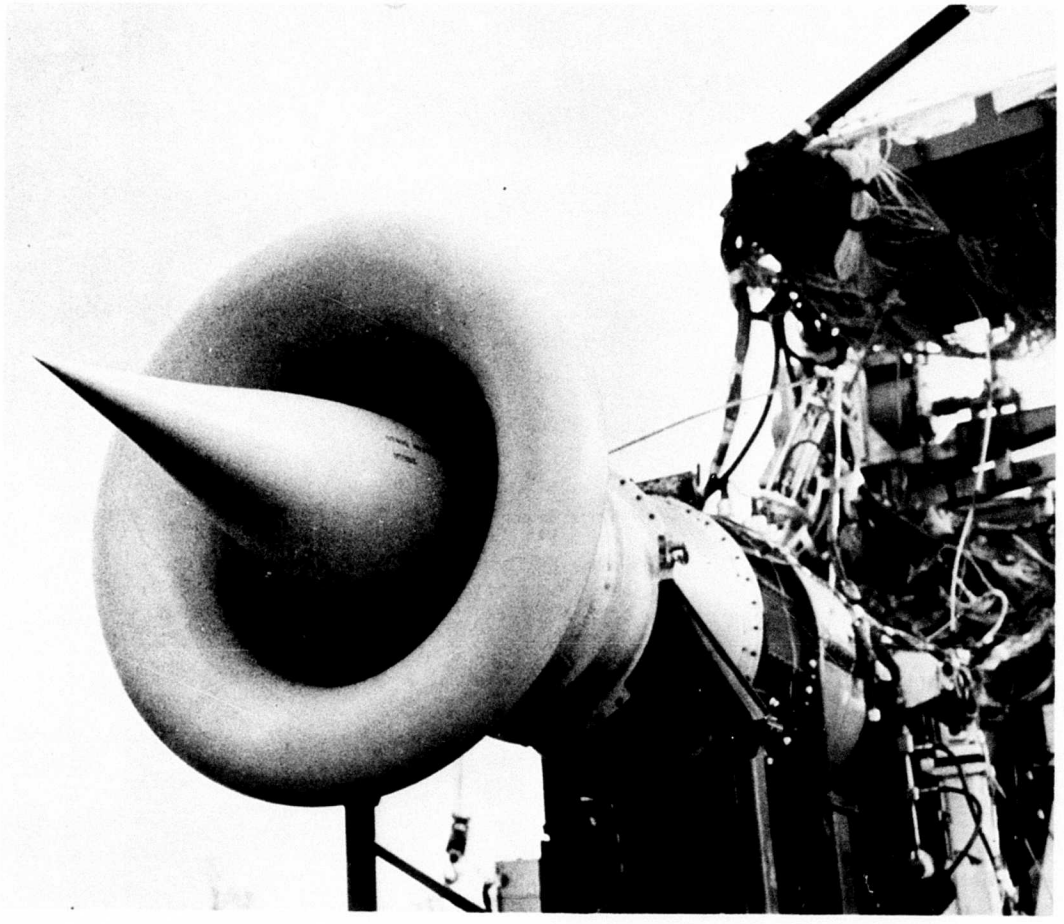

Figure 427. Hybrid Inlet without Blow-In Doors.

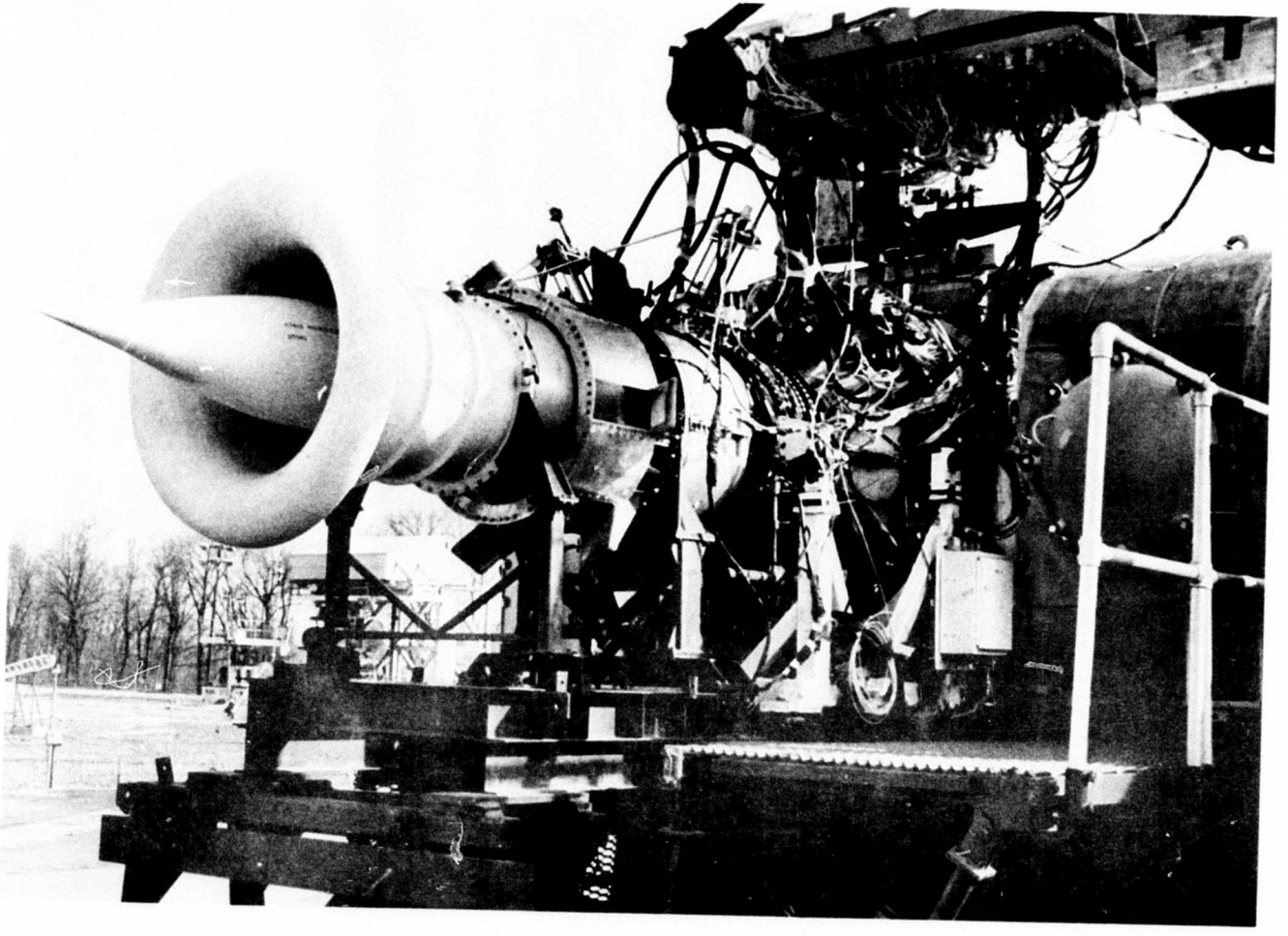

Figure 428. Hybrid Inlet with Blow-In Doors Open.

4.4.1.3 Test Program

Testing of the scale model fan vehicle was performed at the Peebles Test Operation, General Electric's outdoor test site. The facility is described in Appendix A along with a description of the acoustic and aerodynamic instrumentation.

Far-field acoustic measurements for the hybrid and accelerating (no acoustic treatment) inlets were performed for the approach and take-off modes for a range of inlet throat Mach numbers up to the fully choked condition with the blow-in doors closed. Also, for the hybrid inlet in the take-off mode, the noise was measured at each of three blow-in-door positions at a range of primary inlet throat Mach numbers to evaluate the effect of the blow-in doors.

The baseline cylindrical bellmouth inlet was operated over a wide speed range to provide unsuppressed far-field noise levels for comparison with the above hybrid inlet results. Also, for this inlet, an additional test was performed to evaluate the effect of increasing the angle of the IGV's to produce noise acceleration suppression in the IGV passages. The far-field noise was measured as a function of IGV flap angle for two top speeds

For each acoustic measurement point, digital performance data (including inlet wall static pressures) were obtained. For the hybrid and accelerating inlet configurations, aerodynamic traverse data were acquired at six selected speed points corresponding to desired inlet throat Mach numbers. Also, for selected points, near-field acoustic measurements were made with a traversing acoustic probe mounted near the fan IGV face.

4.4.1.4 Data Analysis

In Appendix B, the acoustic data reduction system is described. The scale model one-third octave band data were scaled to the full size SST engine diameter of 75.44 inches and extrapolated to the 200-foot sideline. (This engine was designed under Contract NAS3-16950). The engine has a design airflow of 1045 lbm/sec versus 127 lbm/sec for the scale model vehicle. All data presented in this report are for the SST size unless otherwise noted.

As a result of scaling the test vehicle acoustic data, high frequency noise was shifted into the audible region. The scaling process involved shifting the one-third octave band data five bands. For example, measured data in the 31,500 Hz band were shifted to the 10,000 Hz band in the scaling process. The scaling process was employed to provide more realistic absolute noise levels and to improve the effect of extrapolating the noise data to far distances. The improved extrapolation accuracy results because of the difference in attenuation of various frequency noises in air. That is, with the spectral components of noise in their proper full-size one-third octave bands, the air attenuation is applied in a more realistic manner.

Aerodynamic information consisted of a radial total-pressure survey (which was evaluated in terms of its integrated average recovery and loss coefficient) and wall static pressures (which were used to infer wall Mach number characteristics). In addition, two venturi flow component measurements were summed to provide total inlet/compressor flow and hence, inlet throat Mach number (See appendix A).

4.4.2 Unsuppressed Compressor Noise

4.4.2.1 Introduction

Acoustic tests were performed on an advanced three-stage low pressure (LP) compressor fitted with a cylindrical bellmouth inlet to evaluate the unsuppressed fan noise. By defining the unsuppressed fan noise, the acoustic benefit of a hybrid inlet and high Mach number inlet guide vanes (IGV's) in suppressing the compressor noise was determined. Testing was performed on two fan operating lines and along a constant fan thrust line to determine the effect of changing airflow and pressure ratio on compressor source noise.

4.4.2.2 Nominal Operating Line Results

In Figure 429, the maximum perceived noise level (PNdB) as a function of tip speed is plotted at the 200-foot sideline. From this curve the maximum perceived noise level (PNL) for the approach, take-off, and cutback flight conditions can be determined. The tip speed representing each of these conditions for a 1045 lb/sec SST engine is indicated in Figure 429. The maximum PNL's measured for the baseline inlet are as follows (at the 200-foot sideline):

Approach	120.0 PNdB
Takeoff	116.5 PNdB
Cutback	120.5 PNdB

The above levels then define the baseline levels with which the results of the application of hybrid inlet technology can be compared to determine the noise suppression achieved.

Examining Figure 429 more closely, there are several interesting points. First, in the range of tip speeds between 900 and 1250 ft/sec, the maximum perceived noise level (PNL) is decreasing as the tip speed increases. This trend is attributed to the larger wake generated by the inlet guide vanes at the low tip speeds. The variation of the inlet guide vane angle as a function of tip speed is shown in Figure 430; in the tip speed range of interest, the angle generally is decreasing. At large angles the wake generated off the trailing edge of the IGV is much more extensive as illustrated in Figure 431. This large wake increases the noise intensity at the blade passing tones. This is evident in Figure 432 where the blade passing tone at the low tip speed (1600 Hz) is much larger than that at the higher tip speed (2000 Hz).

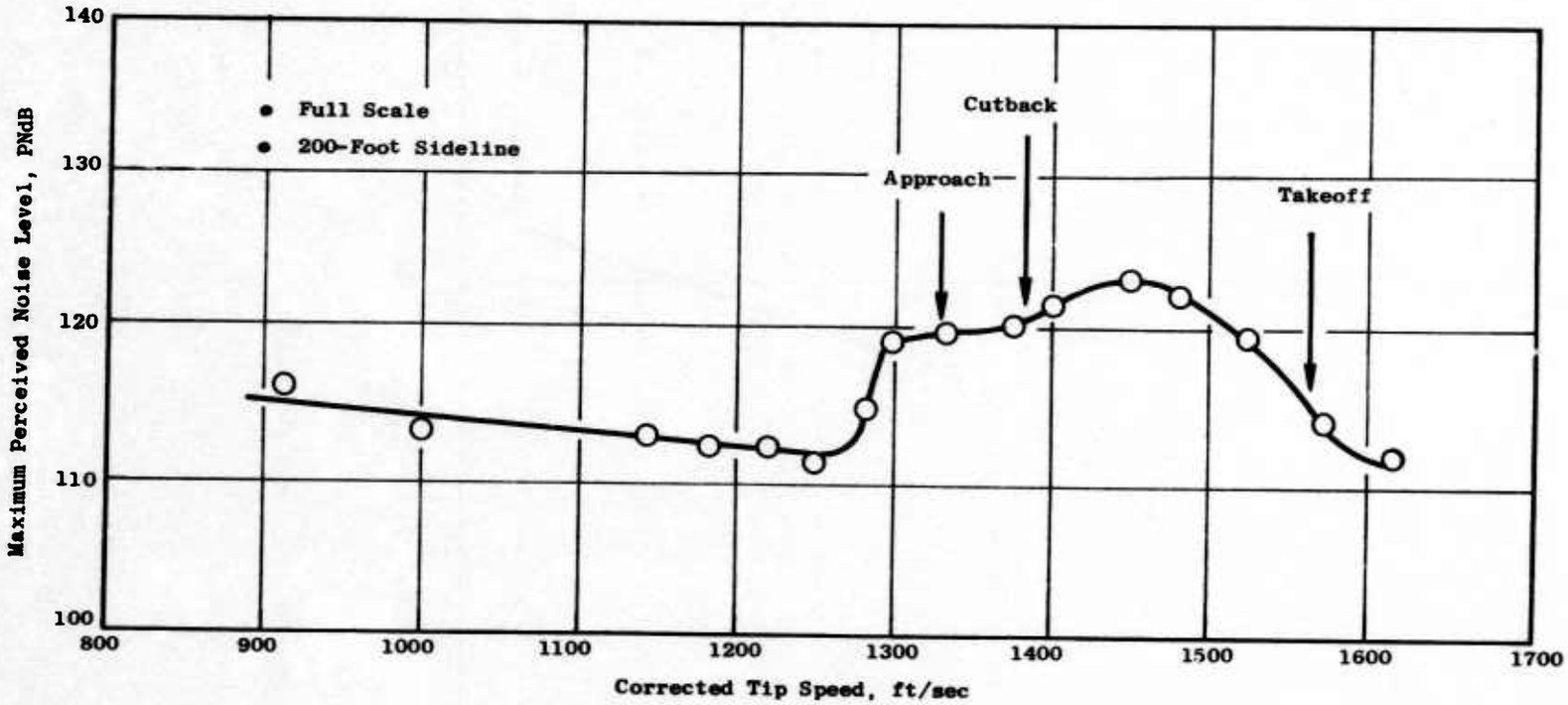

Figure 429. Maximum PNL as a Function of Corrected Tip Speed Along the Normal Operating Line.

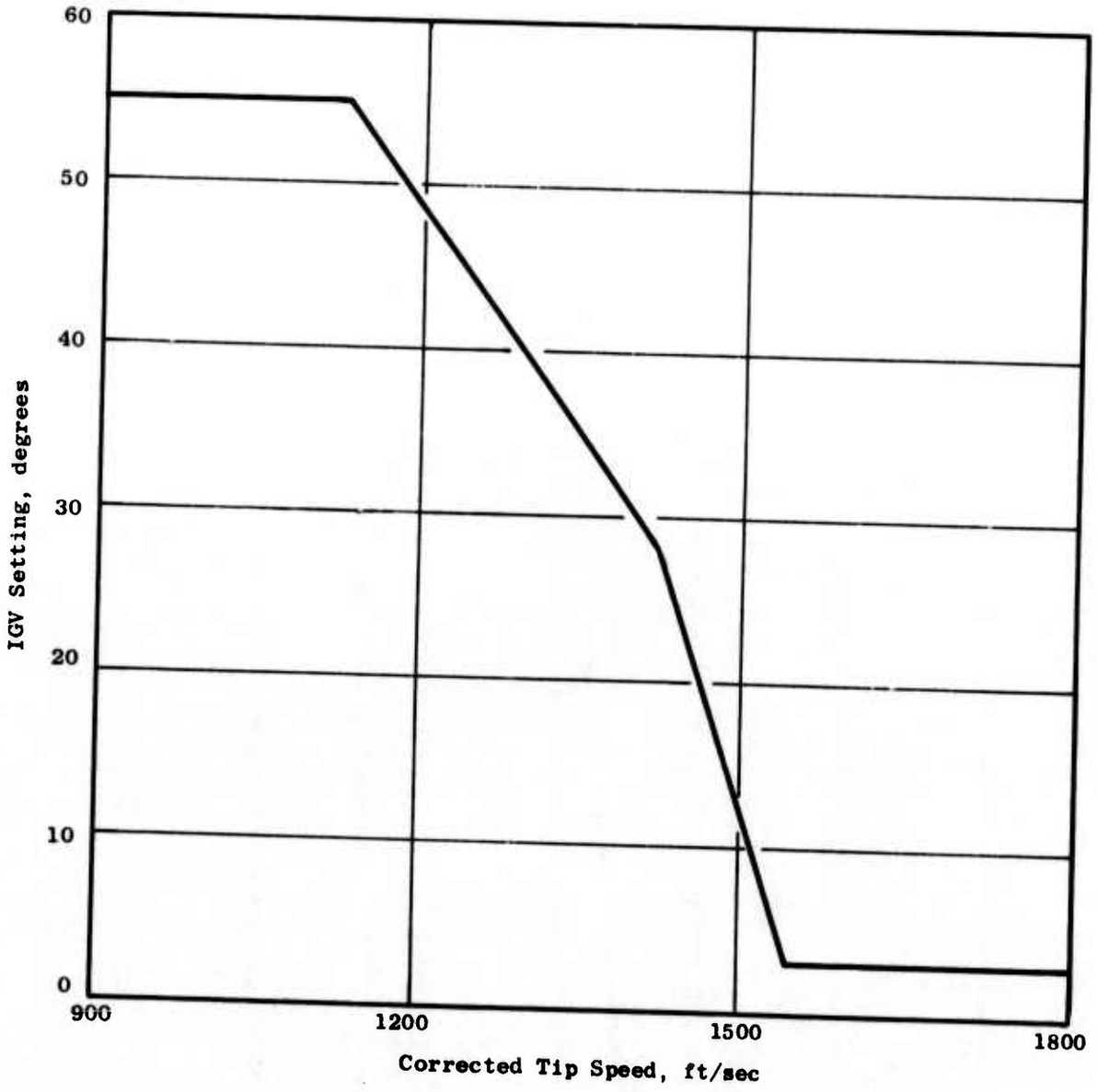

Figure 430. IGV Schedule.

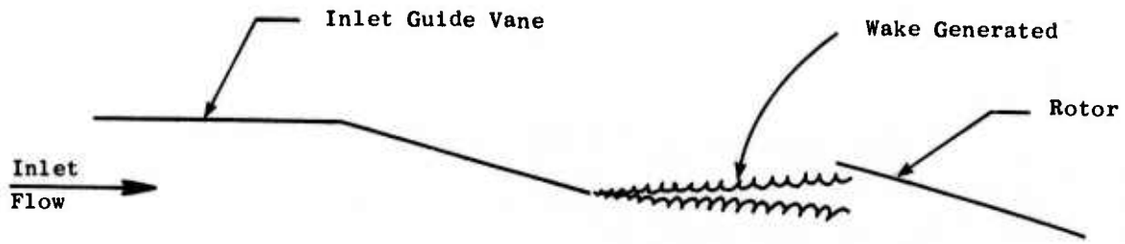

Small IGV Angle

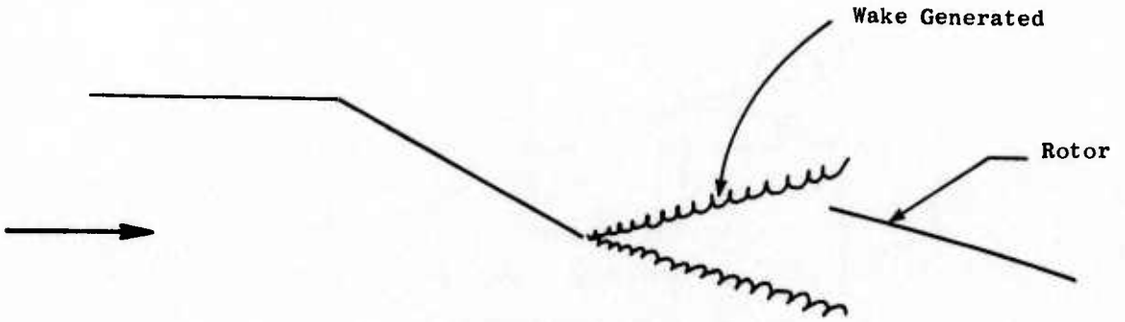

Large IGV Angle

Figure 431. Wake Generated Off the IGV Trailing Edge.

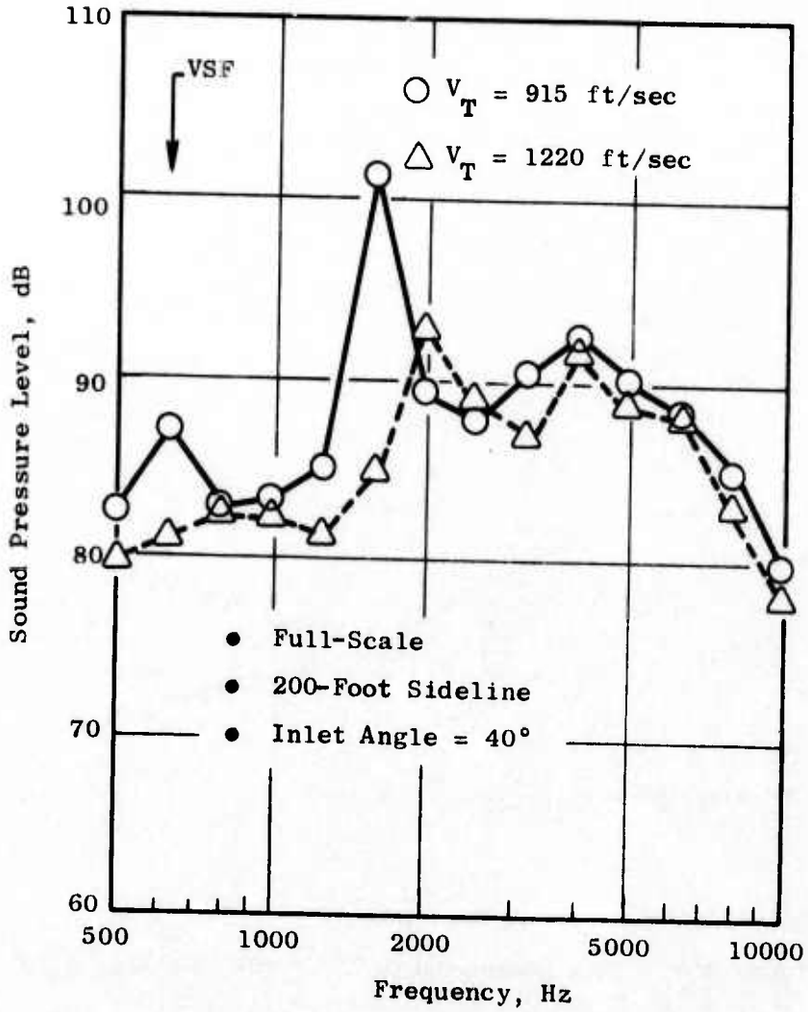

Figure 432. 1/3-Octave Band Comparison of V_T = 915 and 1220 ft/sec Corrected Tip Speeds.

This explanation is further verified by the presence of the tone at 630 Hz in the 1/3-octave band spectra for the 915 ft/sec tip speed (Figure 432). This tone corresponds to the vortex-shedding frequency of the inlet guide vanes. The tone is not present at the 1220 ft/sec tip speed. Calculation of the vortex-shedding frequency (VSF) is shown below:

$$VSF = \frac{.2U}{t_{max.}}$$ (See Reference 50)

where U = flow velocity at the obstruction
$t_{max.}$ = maximum obstruction thickness

For the tip speed of interest, U = 275 ft/sec and the maximum thickness of the IGV ($t_{max.}$) is 0.38 inch. Therefore, the VSF equals 1740 Hz, which places it in the 1600-Hz, 1/3-octave band. Shifting this five bands in scaling to full size, it corresponds to the 630 Hz tone in the spectra. The vortices, shed off each of the 18 IGV's, increase the strength of the wakes and, therefore, will also increase the tone generated at the blade passing frequency. Because the PNL is dominated by the blade passing tone, the decrease in PNL with increasing tip speed is expected in the above range of tip speeds.

At a tip speed of 1250 ft/sec, there is a sharp discontinuity in the $PNL_{max.}$ trend of Figure 429. This also corresponds to a large increase in the blade passing tone at this tip speed. In Figure 433, the 1/3-octave band spectra are compared at the 1250 and 1295 ft/sec corrected tip speeds. The large increase in both the rotor 1 blade passing tone and its harmonic is noted along with the increase in the SPL in the 630 Hz and 800 Hz bands. This corresponds to the band where the vortex-shedding frequency off the IGV's would be expected. It, therefore, is speculated that the large increase in the rotor 1 blade passing tone and its harmonic may be caused by large vortices shed off the IGV's at the higher tip speed. This indicates a particular sensitivity at this higher speed to the IGV wake which is not understood. The increase in PNL at a corrected tip speed of 1400 ft/sec is caused by a shift in the location of the blade passing to a higher noy-weighted 1/3-octave band (2000 to 2500 Hz).

At tip speeds above 1450 ft/sec, the maximum PNL in Figure 429 begins to decrease with increasing tip speed. This is attributed to stronger and more extensive detached shocks which limit the propagation of noise forward. Comparison of the 1/3-octave band spectra at tip speeds of 1450 and 1524 ft/sec (Figure 434) shows that, under this condition, both the rotor 1 blade passing tone and its harmonic are attenuated along with the noise above 4000 Hz.

From Figure 434 it also is noted that a large tone is present in the 800 Hz band. On a scale model basis, this corresponds to the 2000 Hz band. From the narrowband at the 40° angle shown in Figure 435, this corresponds to a peak in the multiple pure tone (MPT) structure. This peak is attributed to a ground reflection reinforcement which occurs at 2170 Hz.

In the range of tip speeds between 1524 and 1570 ft/sec, the shock is swallowed in the rotor/blade passage. This causes a reduction in the MPT's

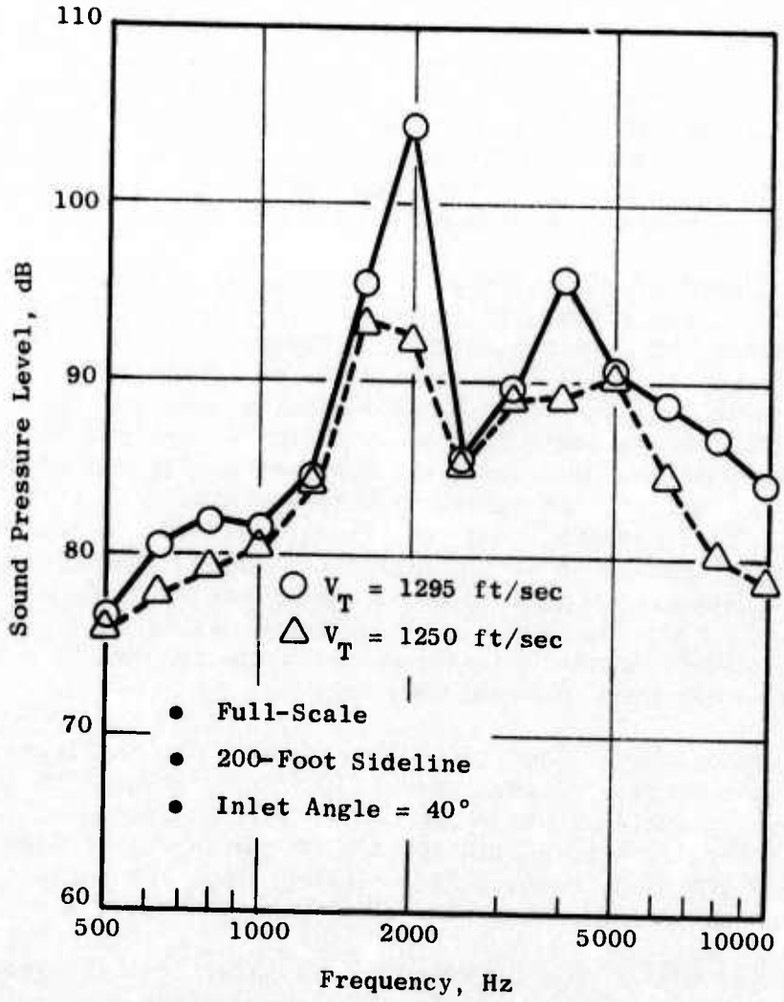

Figure 433. 1/3-Octave Band Comparison at 1250 and 1295 ft/sec Corrected Tip Speeds.

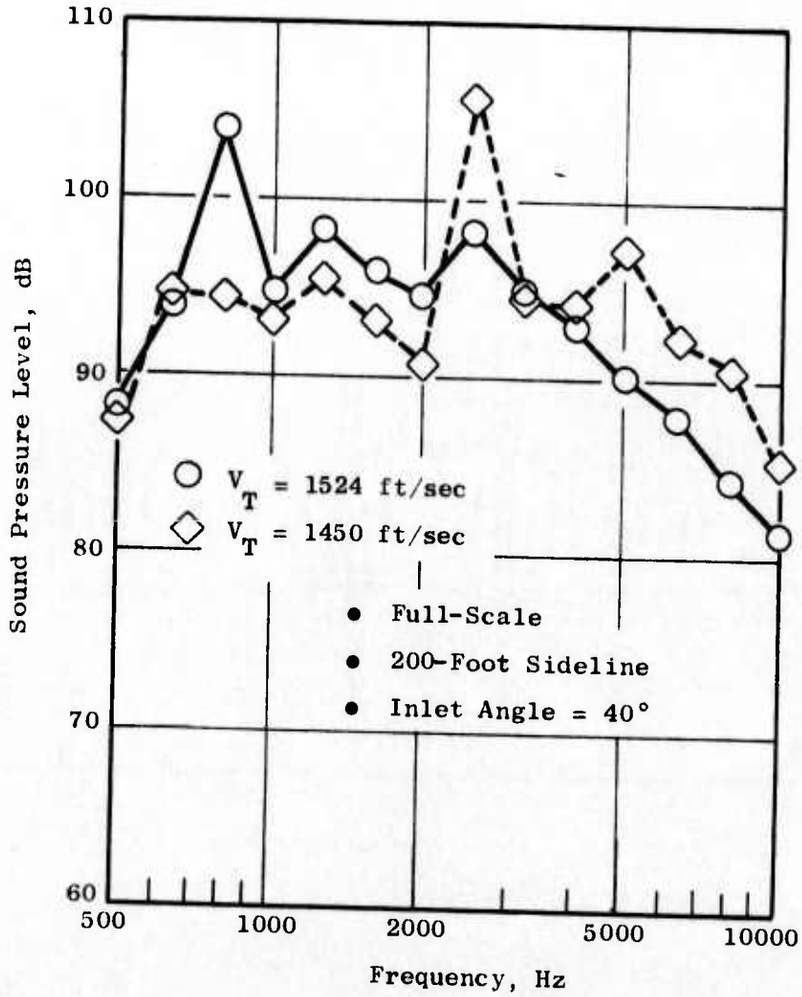

Figure 434. 1/3-Octave Band Comparison at 1450 and 1524 ft/sec Corrected Tip Speeds.

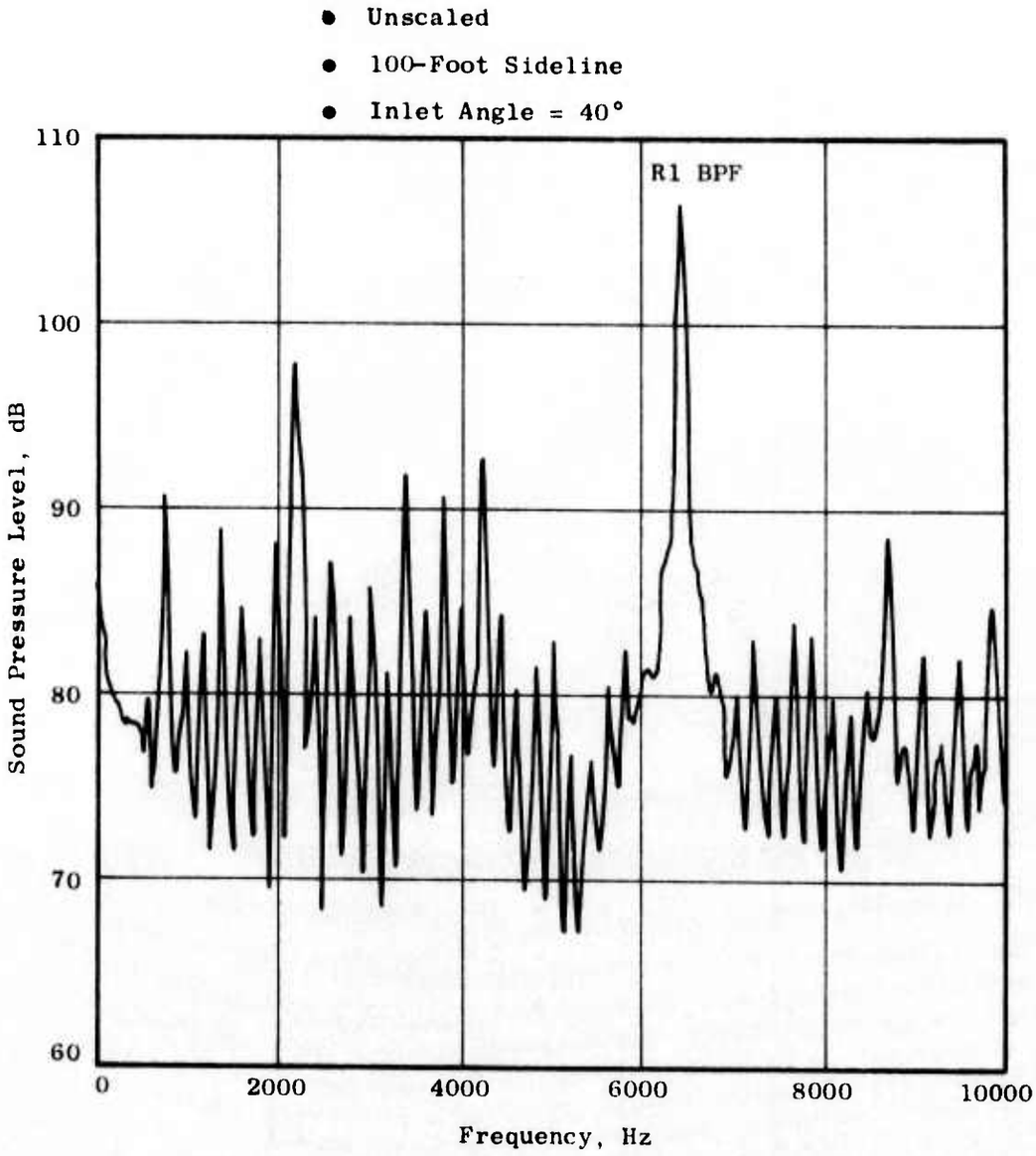

Figure 435. Narrowband of V_T = 1524 ft/sec.

and the rotor 1 BPF (2500 Hz) which can be seen in the 1/3-octave band comparison in Figure 436 and the narrowband comparison in Figure 437.

In Figure 438 the 1/3-octave band spectra for three supersonic tip speeds ranging from 1295 to 1448 ft/sec are compared. It is interesting to note that for all tip speeds the rotor 1 blade passing tone dominates the spectra. This is unusual since, at high supersonic tip speeds, the MPT's generally dominate the spectra. The dominance of the blade passing tone over the MPT's is shown clearly in the Figure 439 narrowband. The explanation for this phenomenon lies in the presence of the IGV's. The variation of the IGV angle as a function of tip speed is shown in Figure 430. For an inlet without IGV's, MPT generation is initiated at a tip speed of approximately 1080 ft/sec as seen in Figure 440. Figure 440 shows the fan relative tip Mach number as a function of fan speed for a configuration with no IGV's and with the test vehicle IGV schedule along with a sketch illustrating the effect. It can be seen that by turning the flow using IGV's, the initiation of MPT's is delayed until approximately 1280 ft/sec.

From the sketch in Figure 440 this is due to the velocity component ($M_i \sin \theta$) generated by turning the flow. This velocity component is in a direction counter to that for the fan. The fan relative tip speed is ($M_{TipRel} = M_{Tip} - M_i \sin \theta$). Therefore, increasing the IGV flap angle (θ) reduces the fan relative tip Mach number. In conclusion, the blade passing tone dominates the one-third-octave spectra for two reasons. The MPT's are delayed and weakened by the reduced relative tip Mach number of the fan at speed due to the presence of the IGV's. Secondly, the IGV's, which shed a strong wake and are closely spaced to the first rotor (which, in turn, has relatively close spacing to the first stator), generate a strong blade passing tone.

In Figure 441 the 1/3-octave band rotor 1 blade passing tone is plotted as a function of corrected tip speed. Comparing this to Figure 429, it is noted that the blade passing tone variation closely follows the variation in PNL with tip speed. This is expected, since (as shown previously) the rotor 1 blade passing tone dominates the spectra even at high tip speeds.

4.4.2.3 Directivity

In Figure 442, the directivity of the rotor 1 blade passing tone as a function of angle from the inlet is compared for four tip speeds - 1000 ft/sec and 1230 ft/sec corresponding to tip speeds below that where the fan relative fan tip Mach number is unity, 1300 ft/sec where the tip Mach number is supersonic, and 1524 ft/sec where the detached shocks limit the propagation of noise forward. Obviously, the directivity varies markedly with tip speed. Also, the blade passing SPL's vary considerably. The reason for these changes in the blade passing SPL's were discussed previously.

Comparing the two lowest tip speeds, it is seen that, at 1230 ft/sec, the directivity is much less "peaky" and the maximum angle moves from 40° to 50°. At the 1300 ft/sec tip speed, the directivity of the blade passing

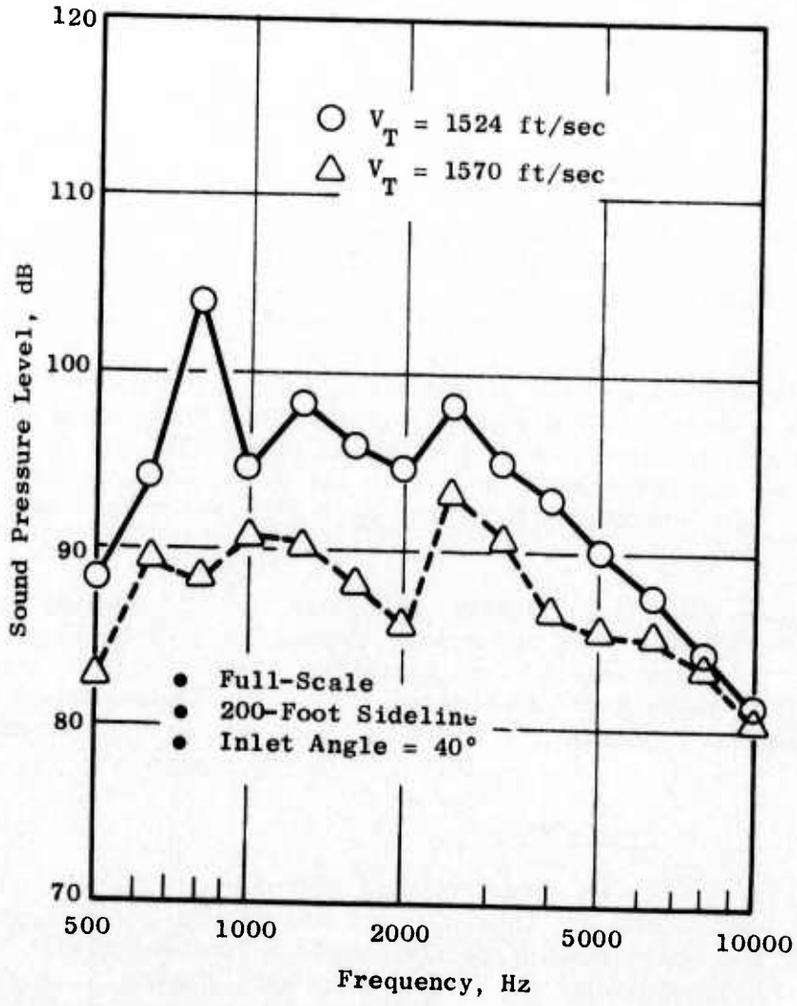

Figure 436. 1/3-Octave Band Comparison at the 1524 and 1570 ft/sec Tip Speeds.

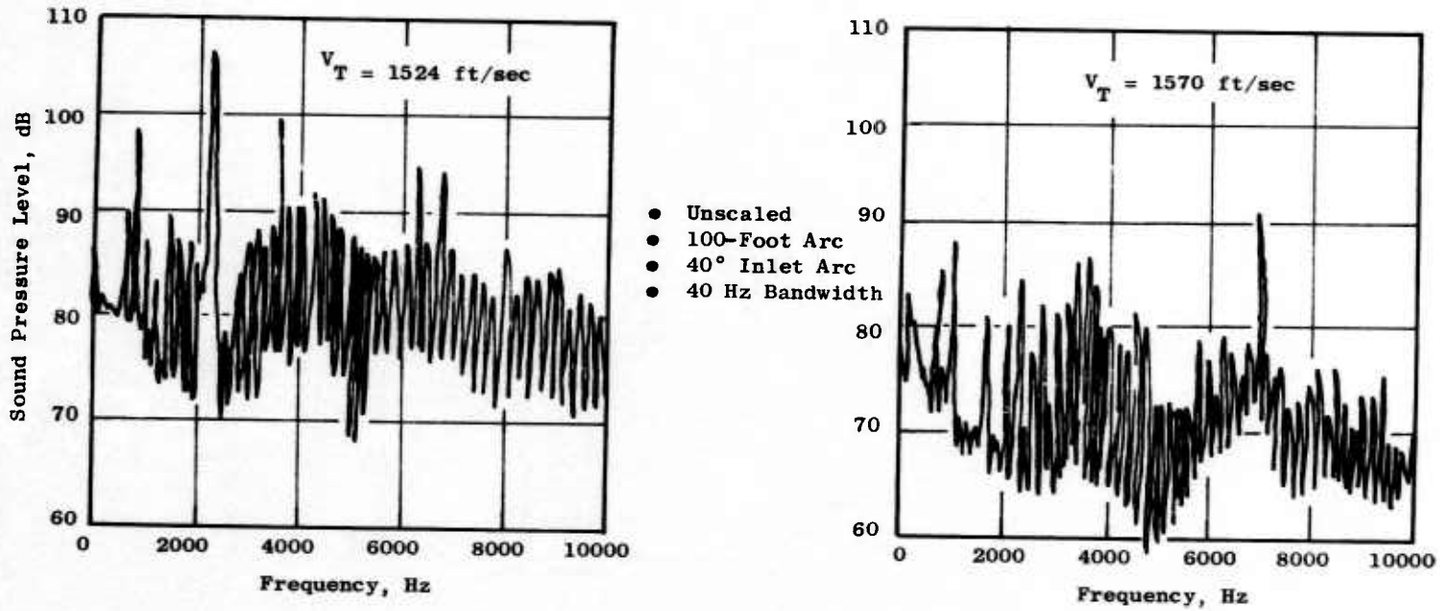

Figure 437. Narrowband Comparison.

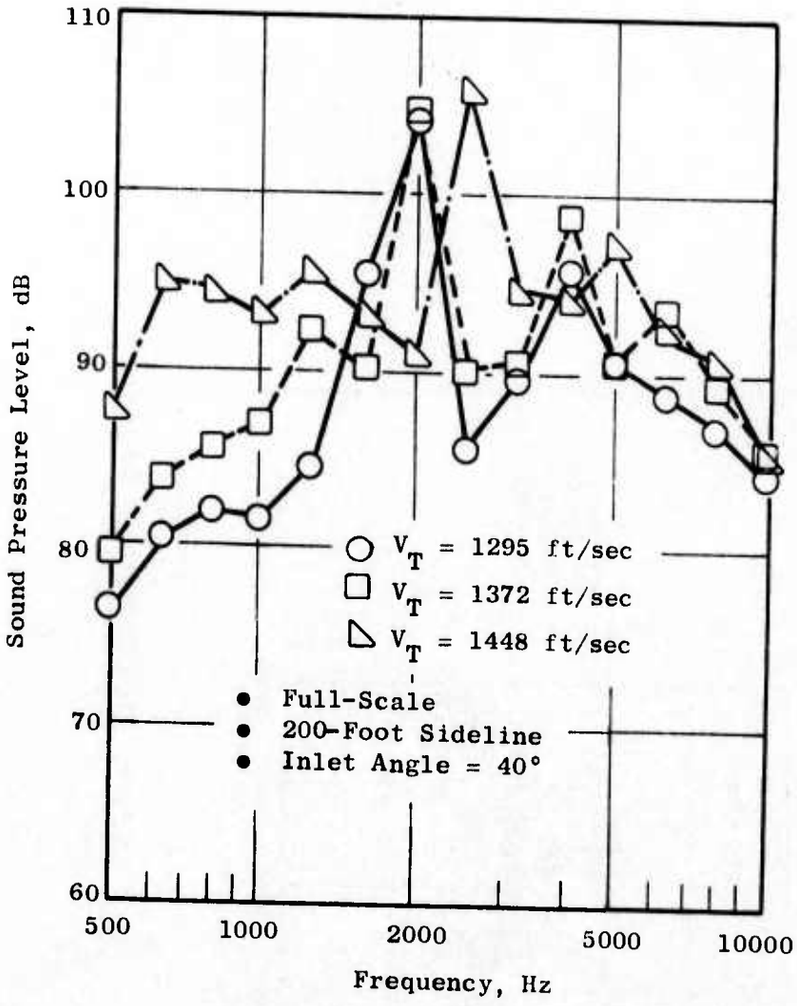

Figure 438. 1/3-Octave Band Comparison at Three Tip Speeds.

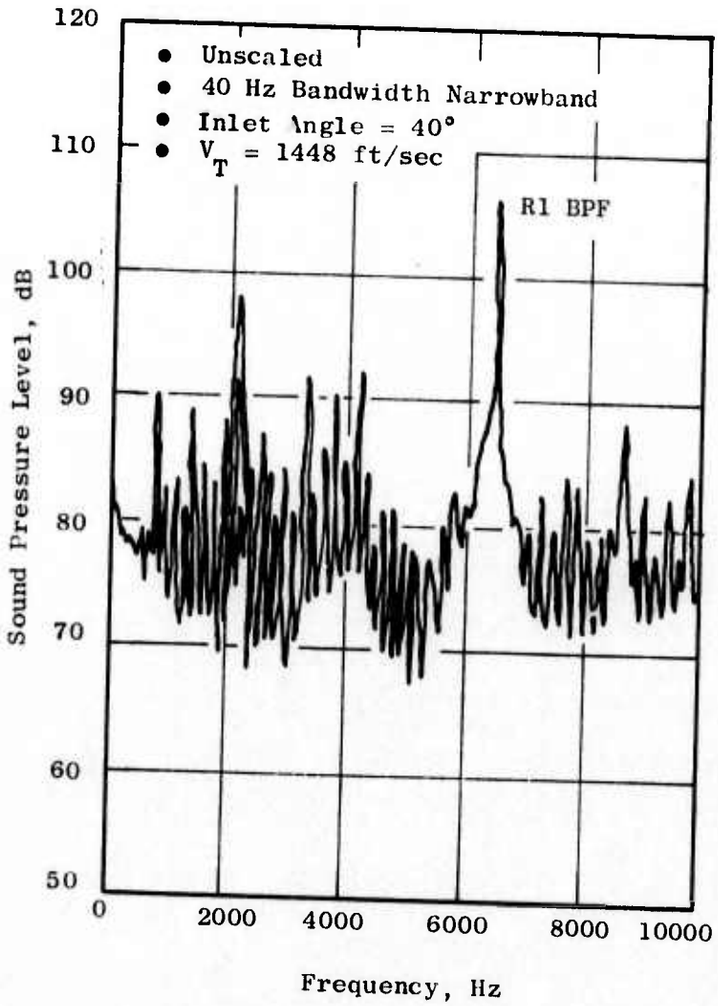

Figure 439. 40-Hz Bandwidth Narrowband at V_T = 1448 ft/sec.

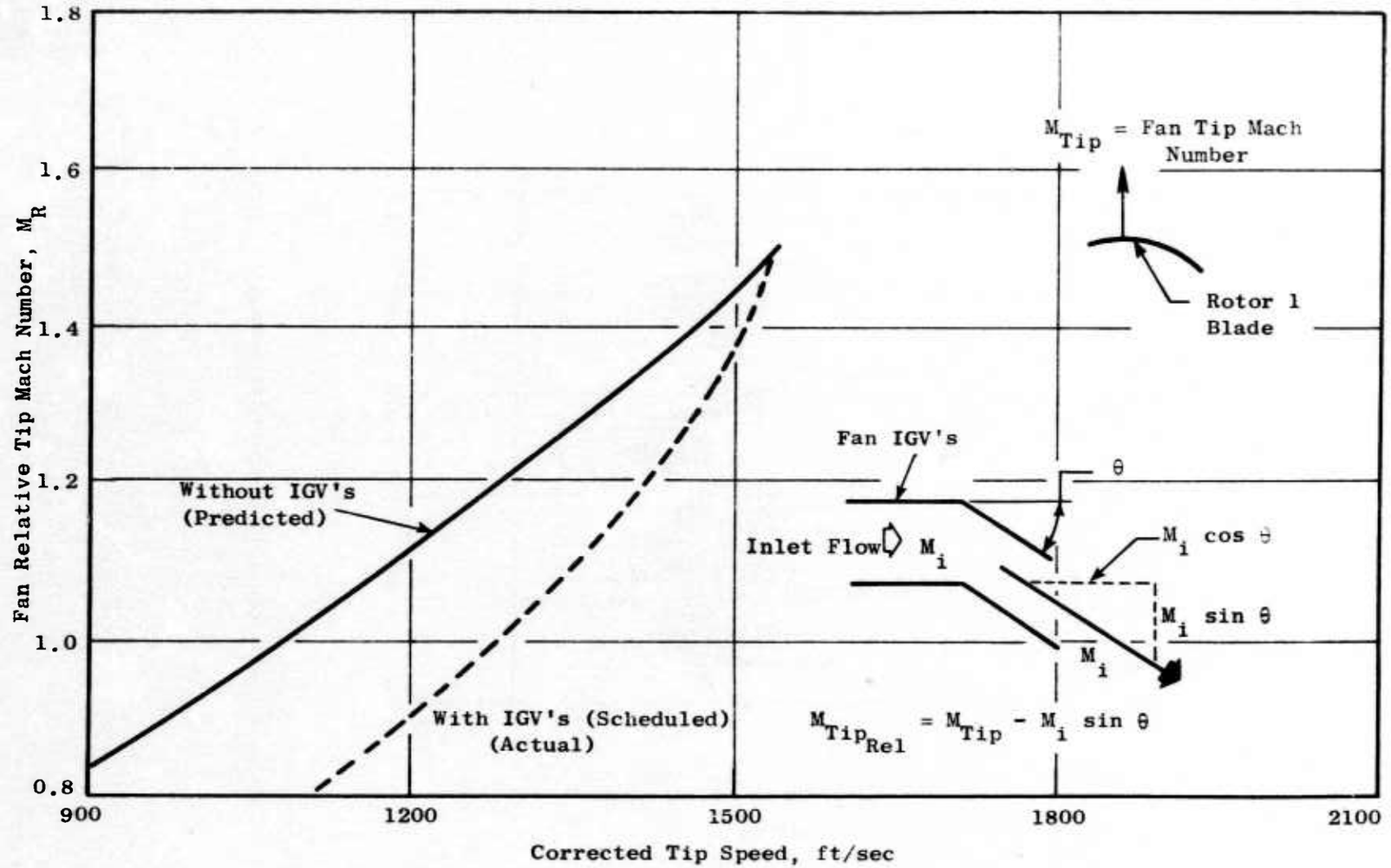

Figure 440. Fan Relative Tip Mach Number as a Function of Tip Speed (with and without IGV's).

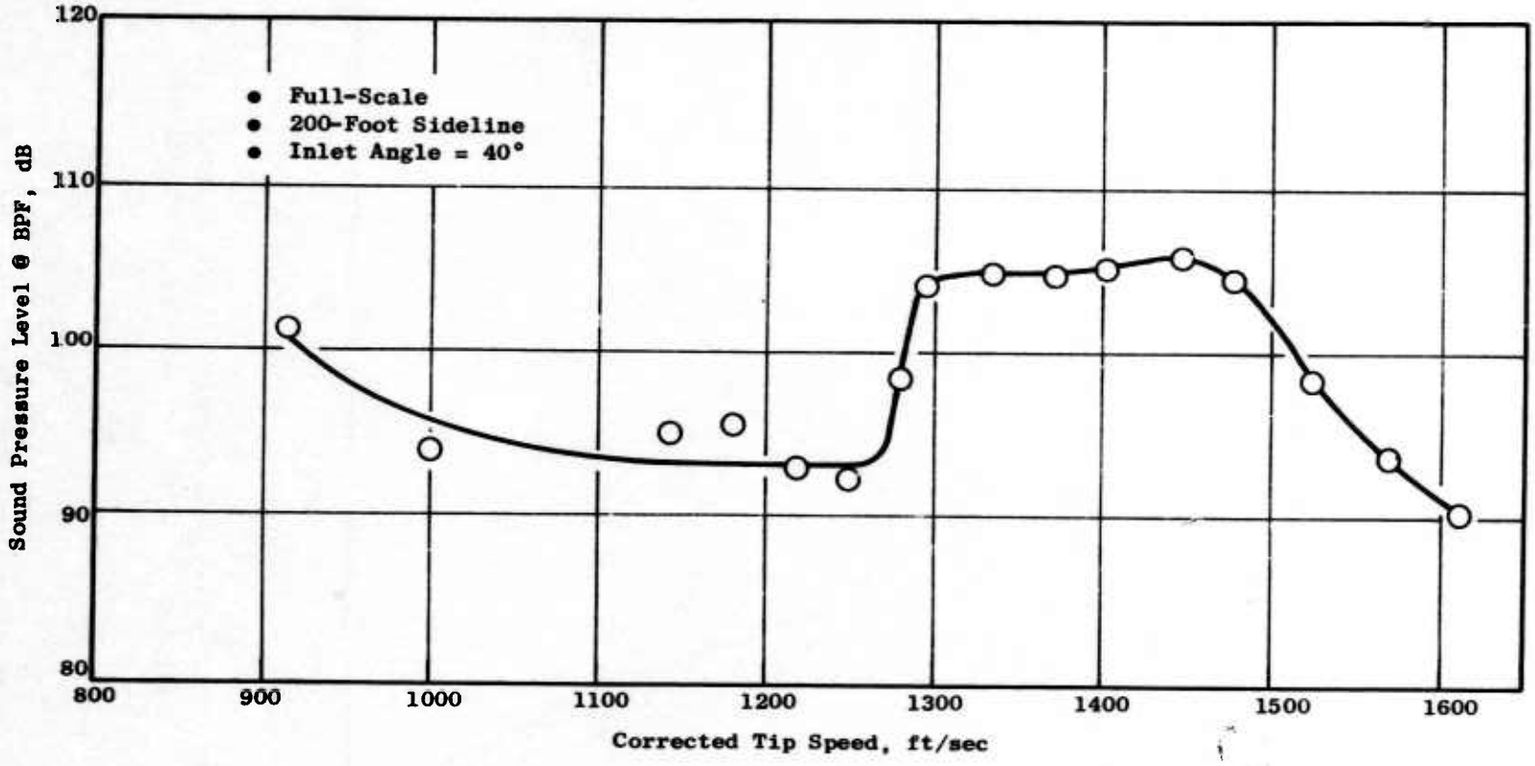

Figure 441. 1/3-Octave Band SPL at Blade Passing Frequency (BPF) as a Function of Corrected Tip Speed.

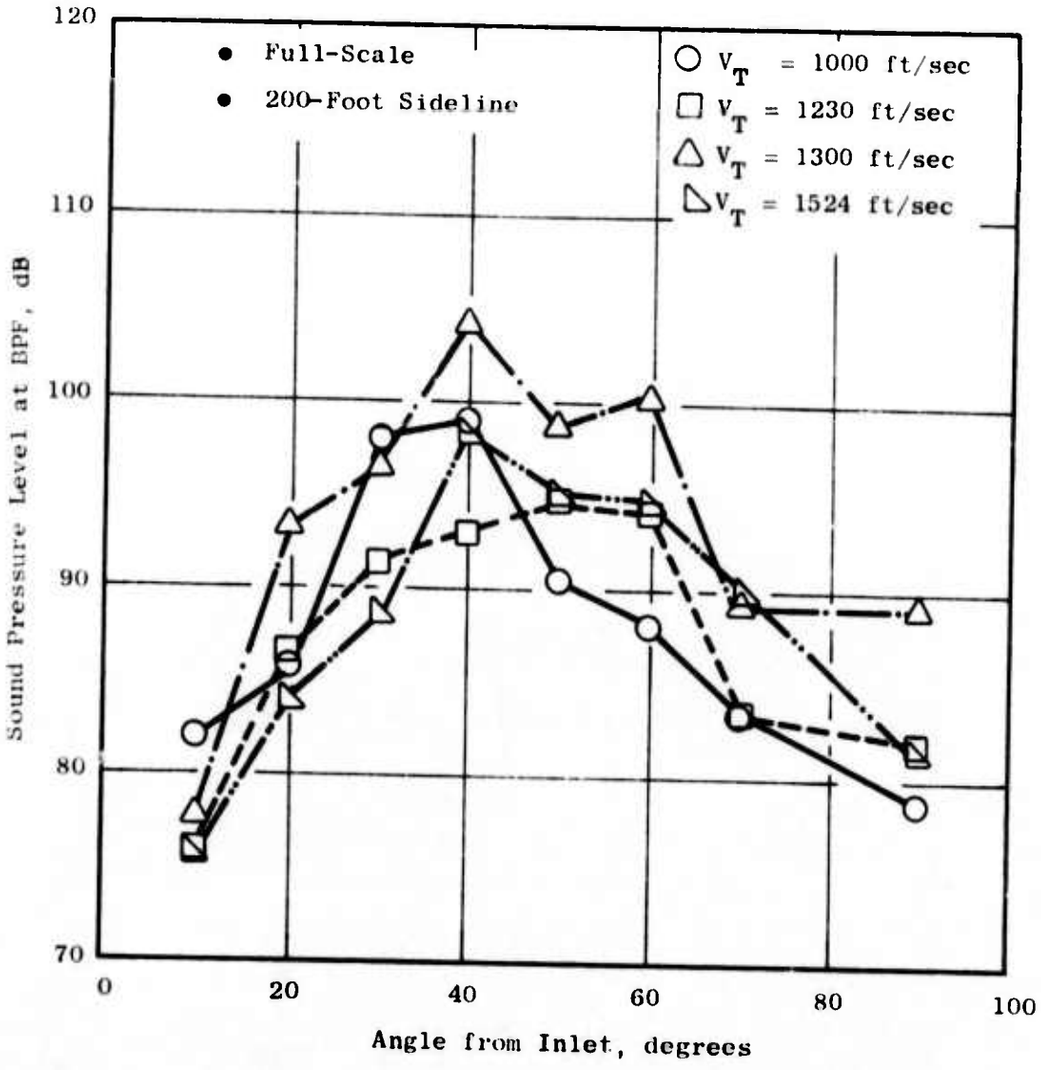

Figure 442. Directivity Comparison of SPL at Blade Passing Frequency (BPF) for a Range of Tip Speeds.

tone again has a sharp peak and the maximum angle moves to 40°. At the 1524 ft/sec tip speed, the directivity is very similar to that at 1300 ft/sec. The blade passing SPL's are reduced, however, due to the strong detached shock at this tip speed.

4.4.2.4 Effect of Operating Line

As noted previously, acoustic measurements were made on two operating lines. A comparison of the PNL as a function of tip speed for the two operating lines is shown in Figure 443. As expected, the PNL's are somewhat lower (1-2 PNdB) for the lower operating line due to the reduction in loading on the fan blades. A one-third-octave band comparison (Figure 444) at the 1372 ft/sec corrected tip speed for the two operating lines shows that, for this reduced loading, the fan noise is somewhat lower in nearly all 1/3-octave bands. However, because the fan thrust is less on the low operating line for an equivalent tip speed on the nominal operating line, this comparison does not answer the question as to whether an operating line selection can be made to get equivalent thrust with less noise.

The maximum PNL on the 200' sideline for three operating points on a constant thrust line are shown below:

Discharge Valve Setting	Tip Speed	PNL
DV = 26	V_T = 1402 ft/sec	121.9 PNdB
DV = 32	V_T = 1448 ft/sec	120.9 PNdB
DV = 40	V_T = 1463 ft/sec	121.3 PNdB

From the above results, it is seen that there are only small differences in the maximum PNL along the constant/thrust operating line. Comparison of the 1/3-octave band spectra for these three tip speeds, each having the same fan thrust, is shown in Figure 445. The spectra for the two high tip speeds are nearly the same, while at the lower tip speed, the rotor 1 blade passing tone and its harmonic are higher and the low frequency MPT noise is less. Comparing the Figure 445 spectra with that in Figure 434, which defines the effect on the 1/3-octave band spectra caused by a strong shock, it can be seen that, at the high tip speeds, a strong and extensive shock is causing the change in spectral characteristics.

4.4.2.5 Summary of Baseline Results

1. The maximum perceived noise levels at the 200' sideline for a 1045 lb/sec flow, three-stage LP compressor are:

Approach	120.0 PNdB
Takeoff	116.5 PNdB
Cutback	120.5 PNdB

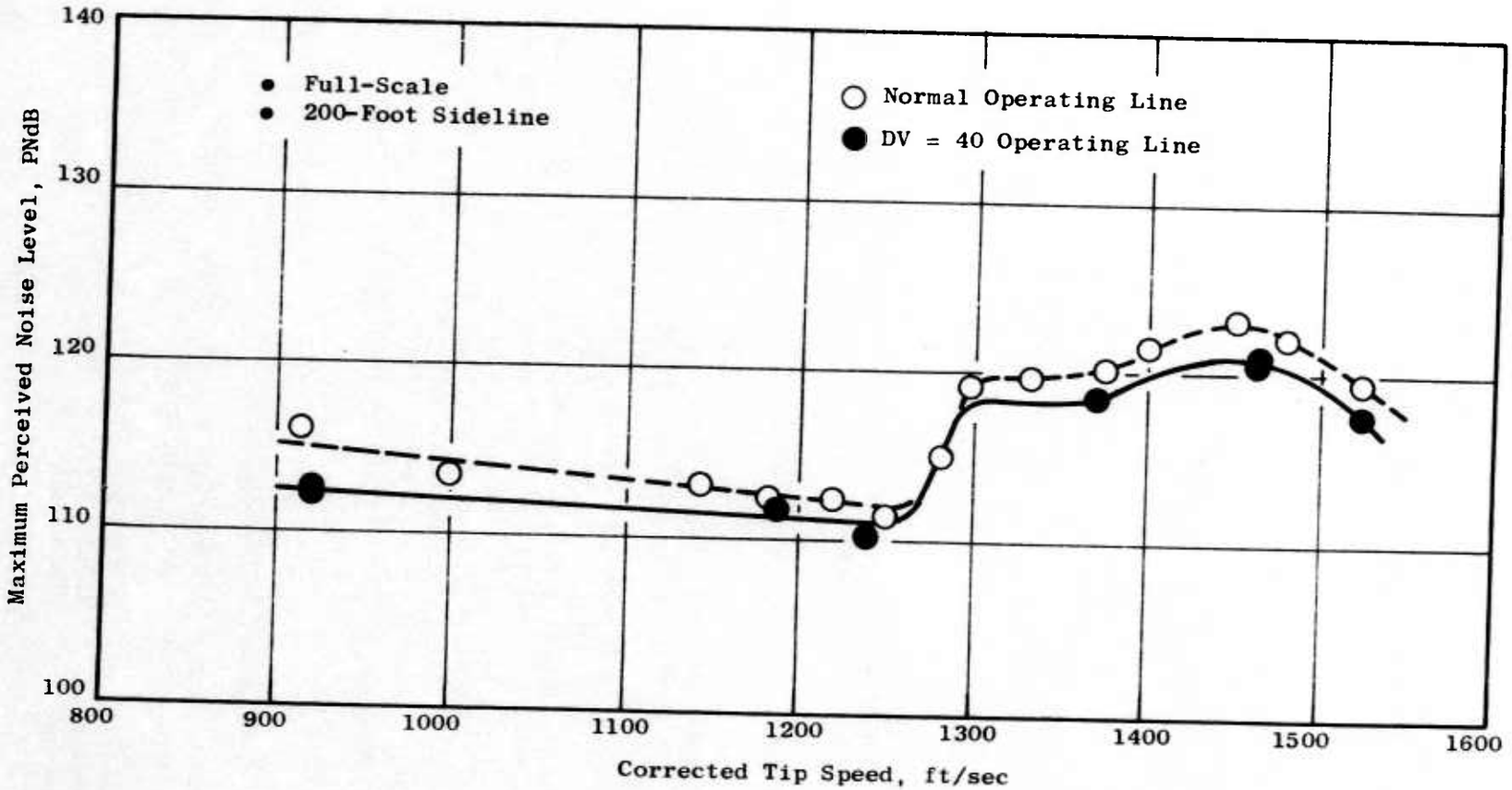

Figure 443. Comparison of the Maximum PNL as a Function of Corrected Tip Speed Along Two Operating Lines.

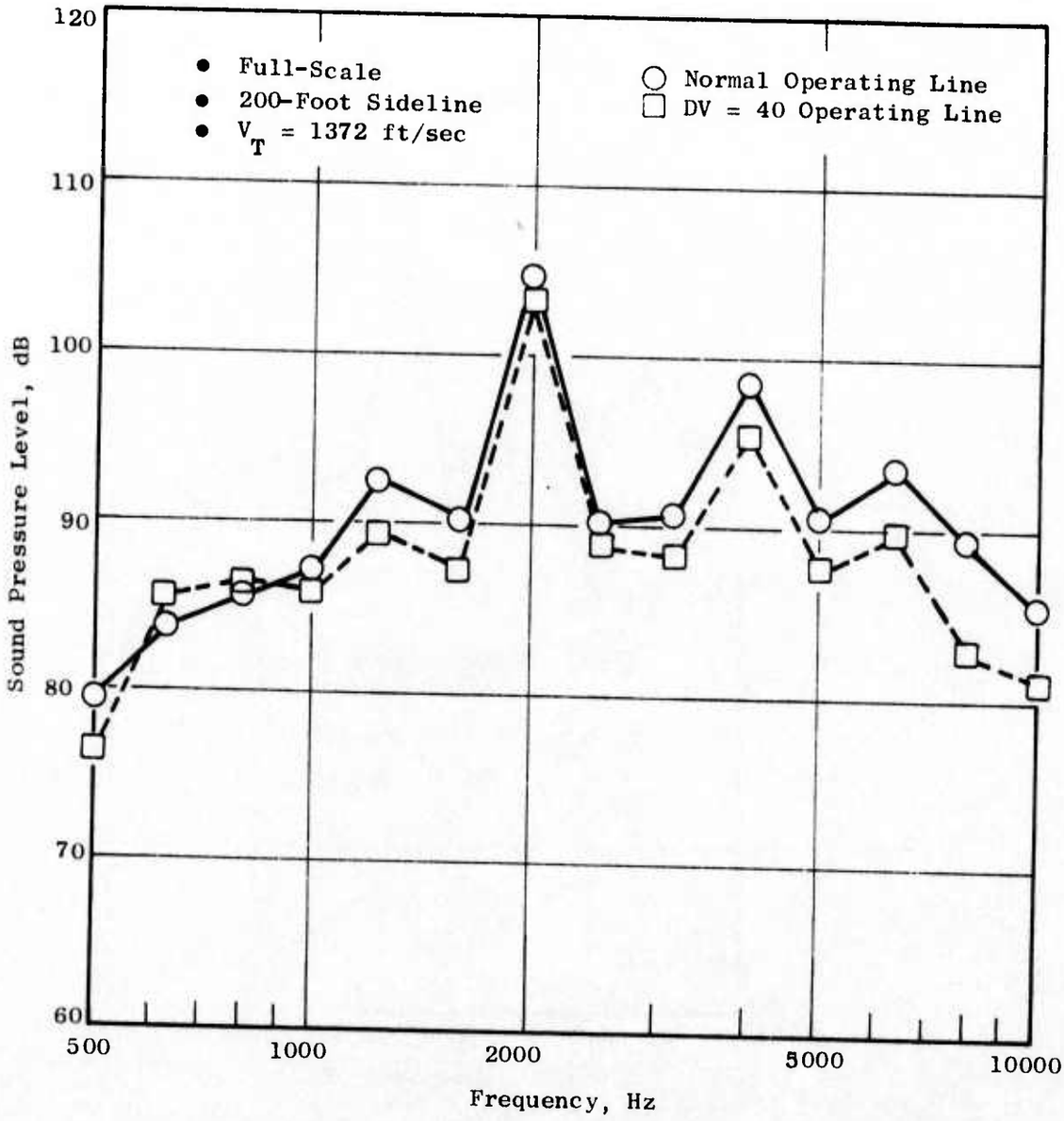

Figure 444. One-Third-Octave Band Comparison Along Different Operating Lines.

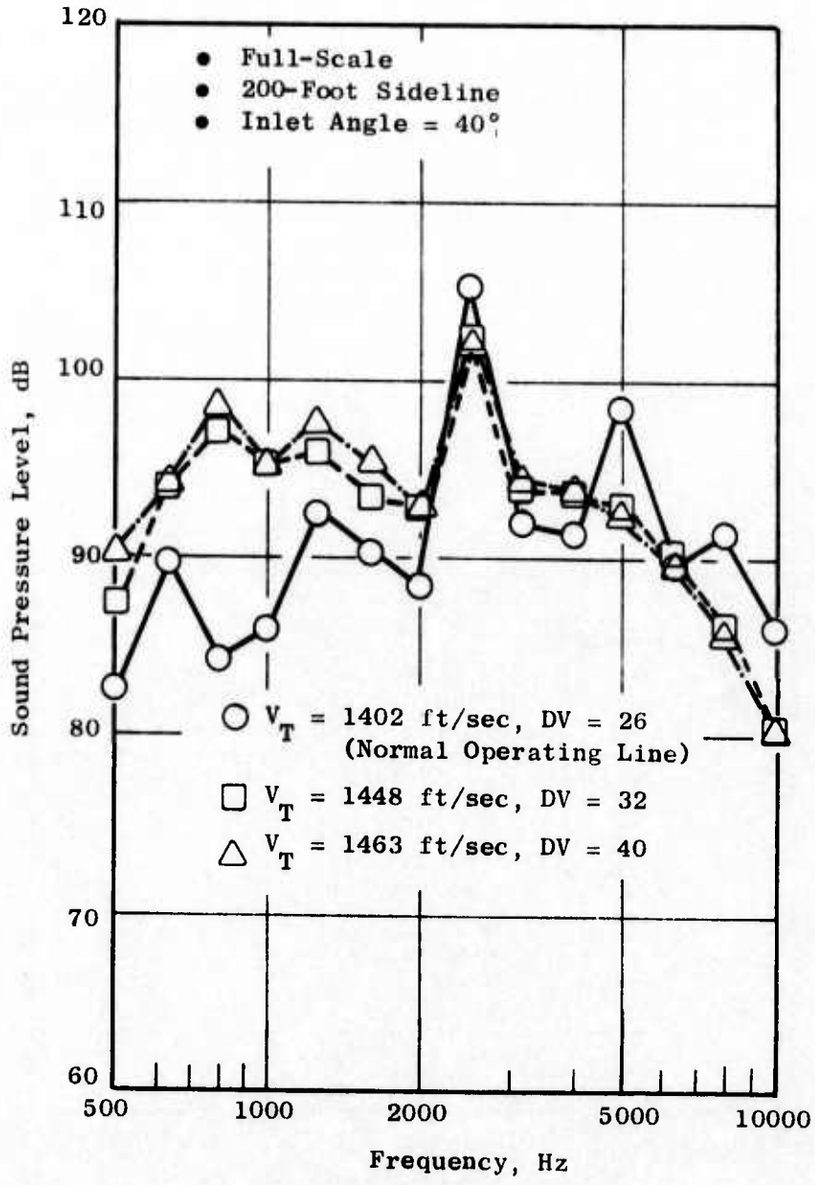

Figure 445. 1/3-Octave Band Spectra Comparison Along a Constant Fan Thrust Operating Line, 40° Angle.

2. The inlet guide vanes delayed the initiation of the MPT's to a tip speed of 1280 ft/sec and reduced their strength at higher speeds. This was due to the IGV's effect on the fan relative tip Mach number.

3. The perceived noise levels did not change significantly along a constant fan thrust line.

4. Presence of the IGV's and tight spacing caused the PNL to be dominated by rotor 1 blade passing tones throughout the entire speed range.

4.4.3 Hybrid Inlet Results, Approach Mode

4.4.3.1 Introduction

Acoustic tests were performed on an advanced three-stage low pressure compressor fitted with a hybrid inlet (see Figure 425) to determine the noise suppression relative to a cylindrical hardwall baseline at the approach condition. Acoustic testing was performed over a range of inlet throat Mach numbers up to the fully choked condition with and without acoustic treatment. The aerodynamic performance of the hybrid inlet was also measured.

4.4.3.2 Hybrid and Accelerating Inlet PNL Suppression

In Figure 446, the PNL at the 40° angle as a function of tip speed is compared for the baseline cylindrical bellmouth inlet, the accelerating inlet, and the hybrid inlet. At the 40° angle, the PNL is a maximum on the 200' sideline for all tip speeds of the baseline configuration. The inlet throat Mach number of the hybrid and accelerating inlet is also indicated on Figure 446. At low tip speeds, the accelerating inlet is 3 to 4 PNdB quieter than the baseline inlet. This is attributed to the differences in inlet configuration, i.e., the inlet contouring and large centerbody, (this is discussed further in Section 4.4.3.5). Significant noise suppression due to airflow acceleration results above throat Mach numbers (M_{th}) of 0.72. This is shown more clearly in Figure 447 which defines the PNL suppression relative to the baseline as a function of inlet throat Mach number for the accelerating and hybrid inlet at the 40° angle. At M_{th} = 0.78, which was selected as the operating point based on the aerodynamic performance (see Section 4.4.3.5), the hybrid inlet provides 11.5 ΔPNdB noise suppression relative to the baseline configuration for the approach mode.

As noted previously, testing was performed at inlet throat Mach numbers beyond the selected operations point (M_{th} = 0.78) to determine the noise suppression at and near choked. In Figure 448, the 1/3-octave band spectra for the hybrid inlet at the 40° angle is compared for the operating point, the 0.84 inlet throat Mach number, and the fully choked condition. When the inlet is fully choked, the fan noise is theoretically completely suppressed.

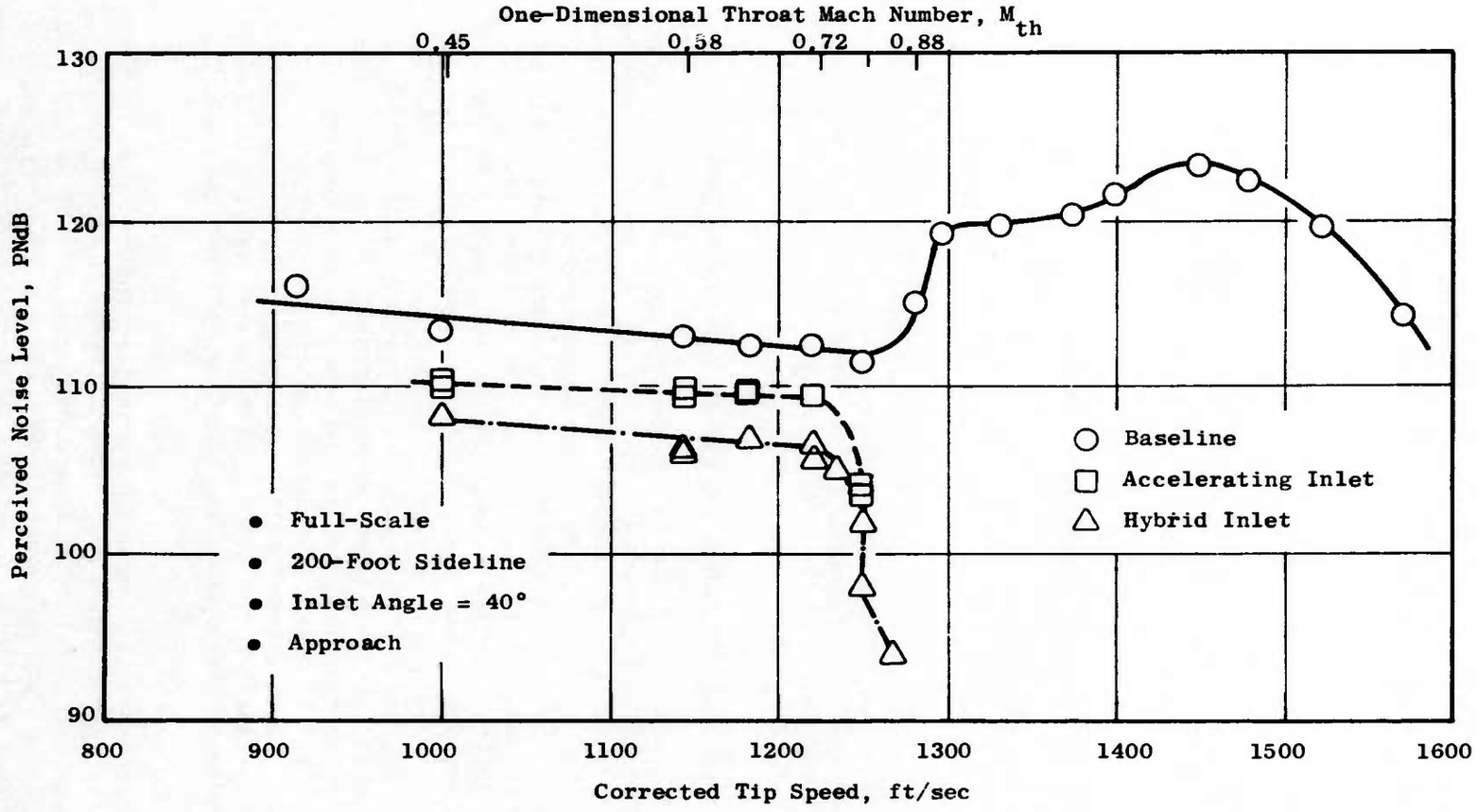

Figure 446. PNL as a Function of Corrected Tip Speed for the Baseline, Accelerating, and Hybrid Inlets.

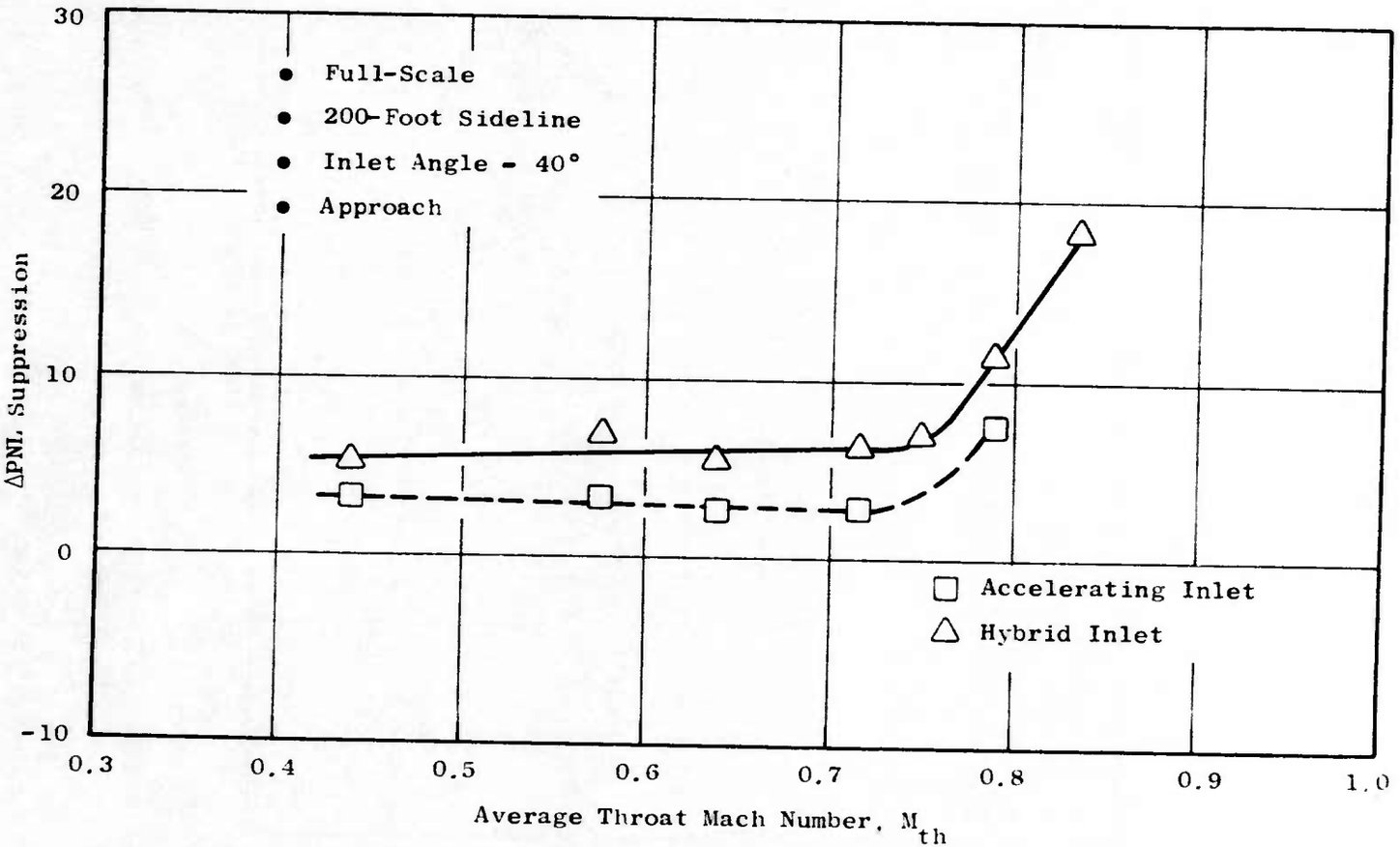

Figure 447. ΔPNL Noise Suppression (Reference Baseline) as a Function of M_{th} for the Hybrid and Accelerating Inlets at the 40° Angle.

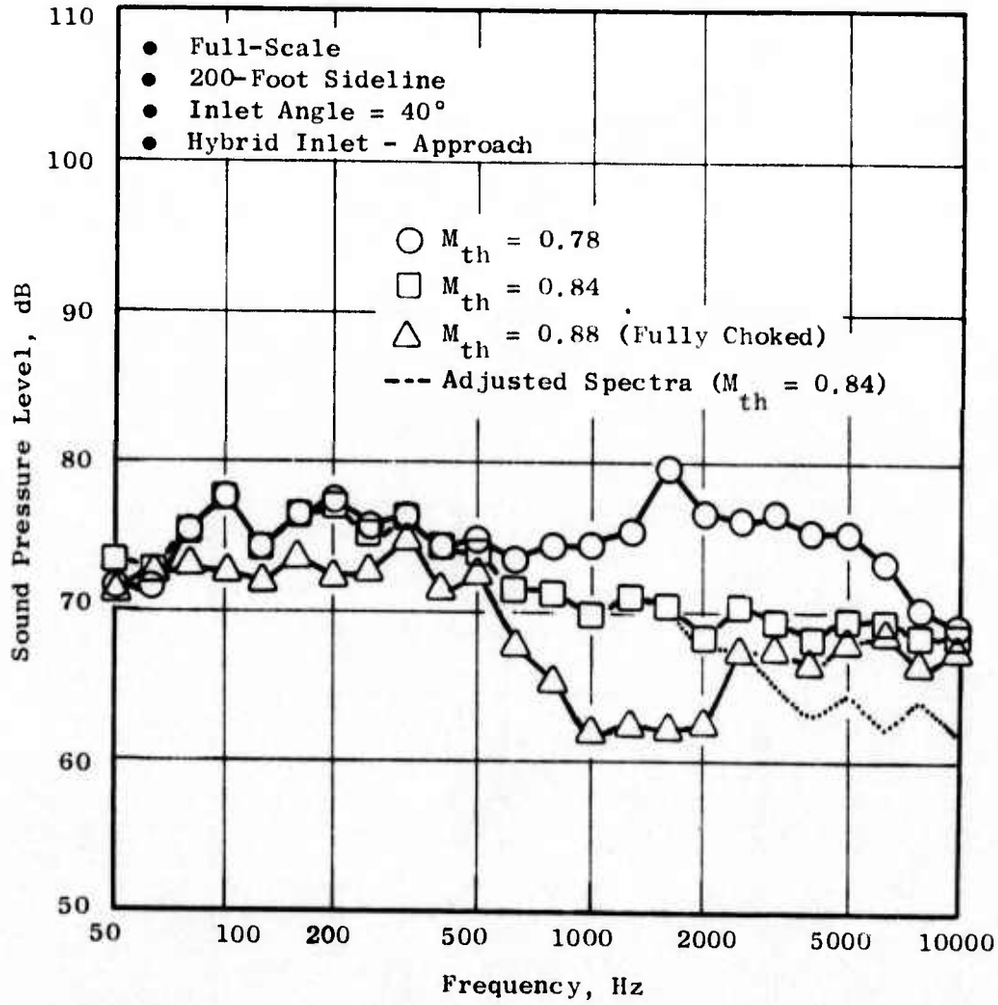

Figure 448. 1/3-Octave Band Comparison for Three Inlet Throat Mach Numbers.

Only the fan noise which leaks through the boundary layer and that which is radiated through the engine casing should remain. Therefore, when the inlet is fully choked, a large reduction in the noise levels at all frequencies is expected. Referring to Figure 448, this did not occur in the subject test. From this result it is concluded that the measured noise level (when the inlet was fully choked) is the facility noise floor and not the noise from the fan. For a large portion of the 1/3-octave-band spectra, the measured noise levels at a throat Mach number of 0.84 also are near or at the estimated "facility noise" floor. This M_{th} = 0.84 PNL was calculated from the approximate spectra shown in Figure 448. These spectra were calculated based on the difference between the measured data and the estimated facility noise level at all high noy weighted frequencies. For the selected operating point, the data in the 6300 Hz band and above and those below 630 Hz are being held up by the estimated facility noise. The low frequency contamination does not affect the PNL calculation significantly. At the high frequencies the spectra were adjusted to eliminate the effect of the facility noise on the measured data. The effect on the PNL of adjusting the spectra is shown below:

M_{th}	PNL	Adjusted PNL
0.78	98.1	97.7
0.84	95.3	94.3
Choked	92.8	-

In Figure 449, the acceleration suppression at the 40° angle as a function of frequency is shown for the selected operating point. It is seen that, in general, the acceleration suppression improves with increasing frequency. The acceleration suppression was determined by comparing the 1/3-octave-band spectra at M_{th} = 0.72, where there is no significant acceleration suppression, with that at the selected operating point. Also shown in Figure 449 is the accelerating inlet suppression relative to the baseline inlet. This suppression includes the effect of differences in inlet configuration plus the acceleration suppression. It is seen that the inlet configuration has a marked effect on the "accelerating inlet" suppression.

The acoustic treatment provides an additional 3 to 4 PNdB suppression at all throat Mach numbers above M_{th} = 0.50. At lower throat Mach numbers, the suppression falls to 2 PNdB. It is interesting to note that (in general) for other hybrid inlets, treatment effectiveness has decreased with increasing throat Mach number.

In Figure 450, a comparison of the one-third-octave-band spectra at the operating point for the hybrid and accelerating inlets is shown at the 40° angle. Two to four dB suppression generally is realized through the addition of treatment up to the 2500 Hz one-third-octave band. No noise suppression is realized above this band, nor was it expected, since no treatment was tuned to the higher frequencies. Six dB suppression is obtained at the Rotor 1 BPF (2000 Hz).

Figure 451 shows a similar comparison of the one-third-octave band spectra at a 40° angle for a low inlet throat Mach number. The treatment does not

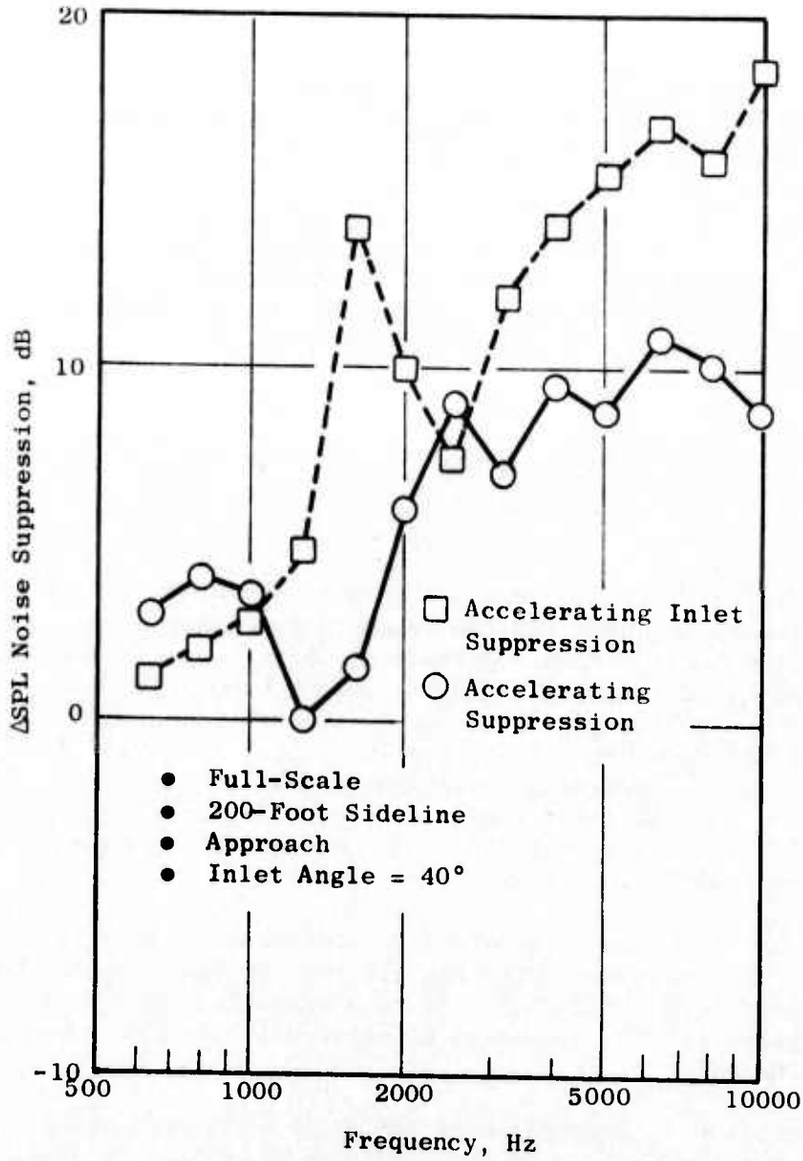

Figure 449. Acceleration Suppression (ΔSPL) and "Accelerating Inlet" Suppression as a Function of 1/3-Octave Band at M_{th} = 0.78.

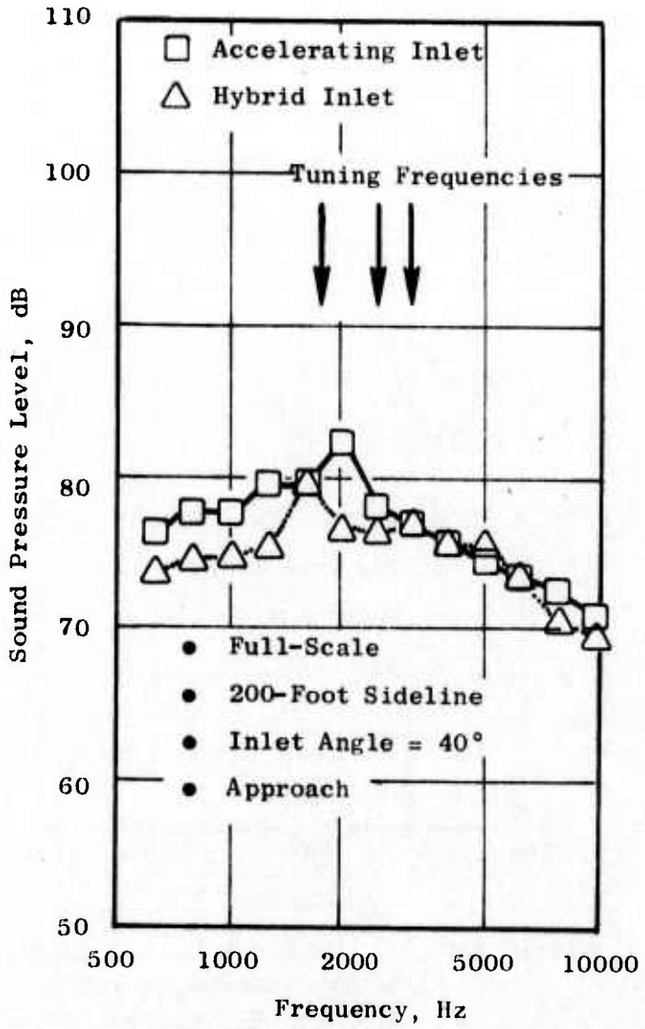

Figure 450. 1/3-Octave Band Comparison of Accelerating and Hybrid Inlets at $M_{th} = 0.78$.

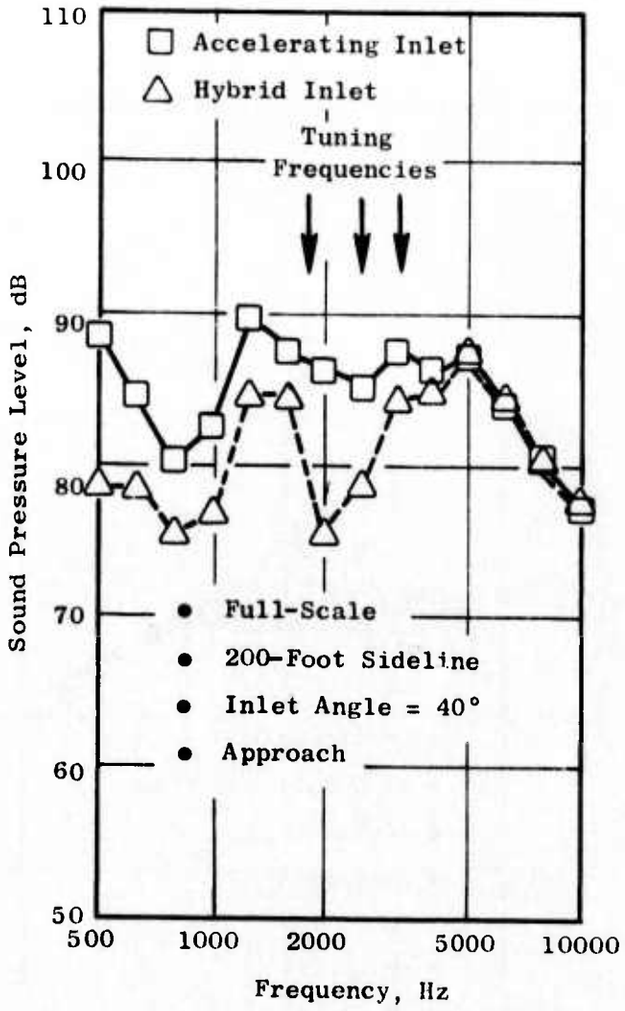

Figure 451. 1/3-Octave Band Comparison of Accelerating and Hybrid Inlet at M_{th} = 0.45.

reduce the noise levels above the 4000 Hz band (full scale) which is consistent with the tuning frequencies for which the treatment was designed (see Figure 424).

In Figure 452, the noise suppression in terms of ΔSPL (Hybrid - Accelerating) due to the acoustic treatment is compared on a one-third-octave band basis for the low and high throat Mach numbers. It is seen that on this basis the treatment is less effective at the high throat Mach number which is consistent with past results for the hybrid inlet. The ΔPNdB treatment suppression does not reflect this because, for the low throat Mach number condition, the noise in the 4000 Hz band and above dominates the PNL calculation. At these high frequencies, the treatment suppression is low and, therefore, the treatment effectiveness at the lower frequencies is not fully reflected in the ΔPNL values. At high throat Mach numbers, it was shown previously that the acceleration suppression reduces high frequency noise more effectively. Therefore, for high throat Mach numbers, the PNL is no longer dominated by the high frequency noise, and larger ΔPNdB reductions are obtained for the treatment.

Therefore, by designing the treatment for maximum suppression at low frequencies (on a full-scale basis) where the effectiveness of acceleration suppression is lower, good treatment effectiveness for the hybrid inlet in the approach mode was achieved at high inlet throat Mach numbers relative to historical experience.

4.4.3.3 Effect of the Accelerating Inlet on Source Noise

In Figure 453, the narrowband spectra measured with the traversing acoustic probe at the fan face for the accelerating inlet and baseline inlet are compared for a 1000 ft/sec corrected tip speed (M_{th} = 0.45 for accelerating inlet). There are several differences in the spectra. First, the broadband levels measured by the inlet acoustic probe are higher for the accelerating inlet. This may be due to higher flow turbulence over the probe for the accelerating inlet and, therefore, the increase in the broadband levels cannot necesarily be attributed to an increase in the fan broadband noise levels. From Figure 453, it is also noted that the Rotor 3 blade passing tone is not present for the accelerating inlet. There is also "haystacking" around the Rotor 1 and 2 blade passing tones for the accelerating inlet. Per Reference 51, thick boundary layers in the inlet may cause this phenomenon. For the accelerating inlet, it would be expected that the boundary layers would be thicker than for the equivalent length baseline inlet. This is due to the flow diffusion from the inlet throat to the fan face, which thickens the boundary layer.

Based on the increased haystacking, around the blade passing tones, it might be expected that the accelerating inlet perceived noise levels measured in the far field would be higher than those for the baseline inlet. It is noted from Figure 446, however, that the PNL at the maximum angle for the accelerating inlet is 3 to 4 PNdB lower than the equivalent baseline results. A comparison of the narrowband spectra for the accelerating and baseline inlets at 1000 ft/sec corrected tip speed (M_{th} = 0.45) is shown in Figure 454 for the

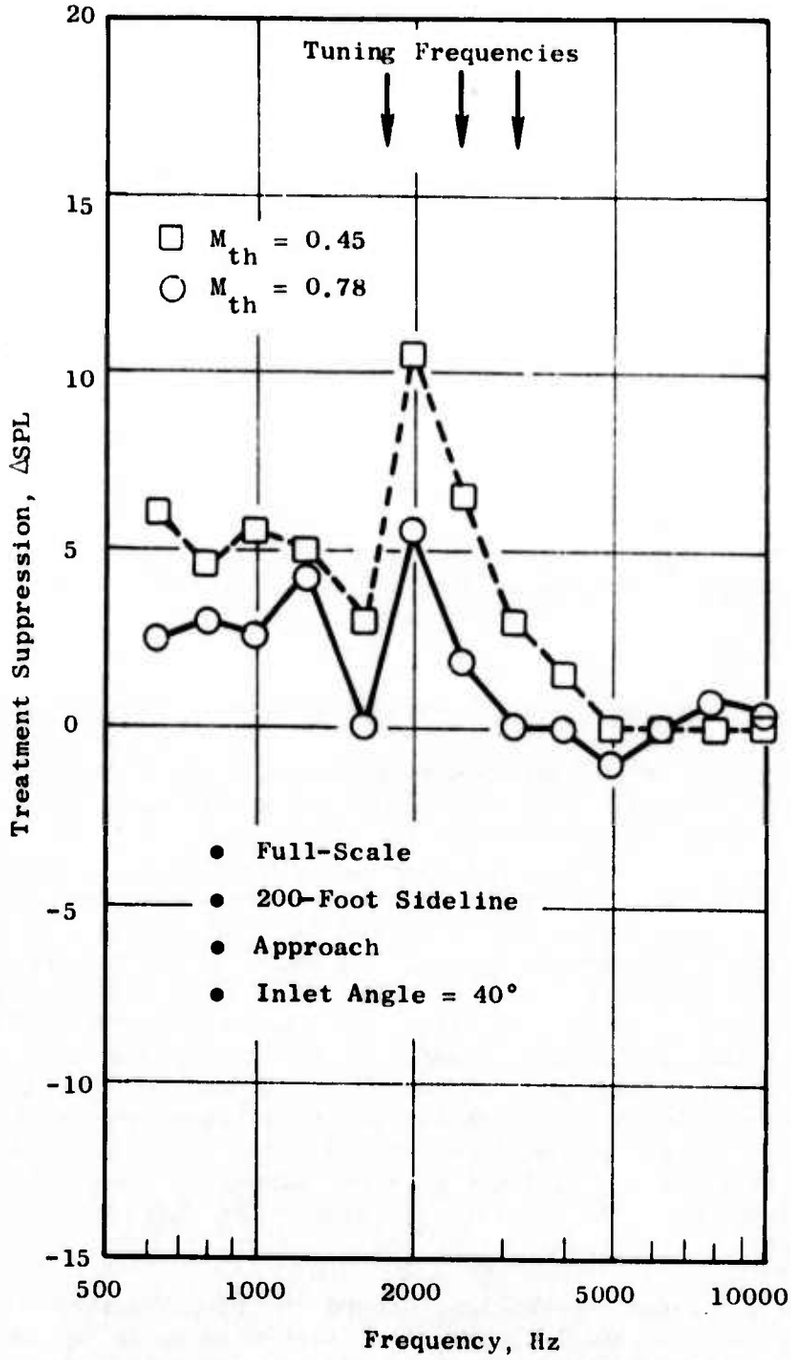

Figure 452. Comparison of Treatment Effectiveness at a High and Low Inlet Throat Mach Number.

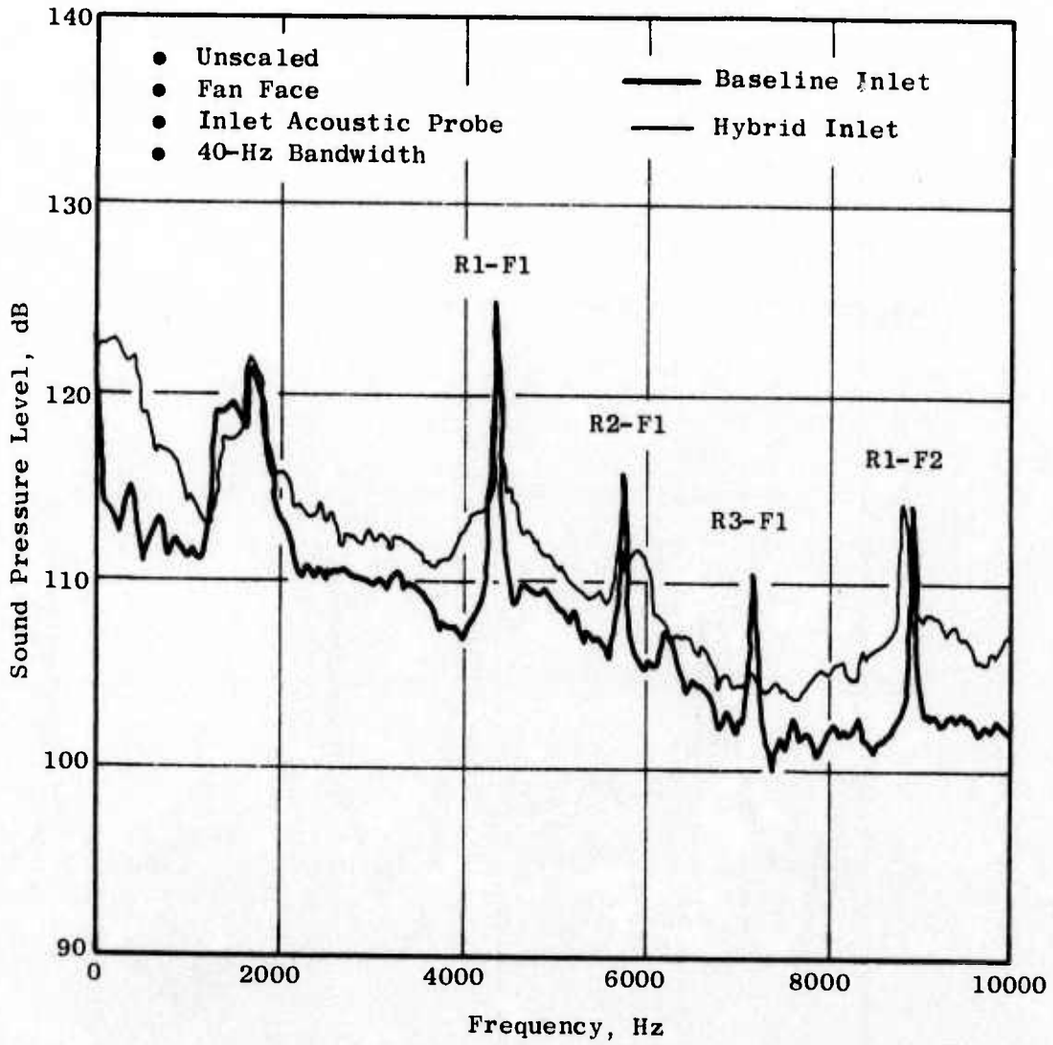

Figure 453. Narrowband Comparison of the Source Noise for the Baseline and Hybrid Inlets, V_T = 1000 ft/sec.

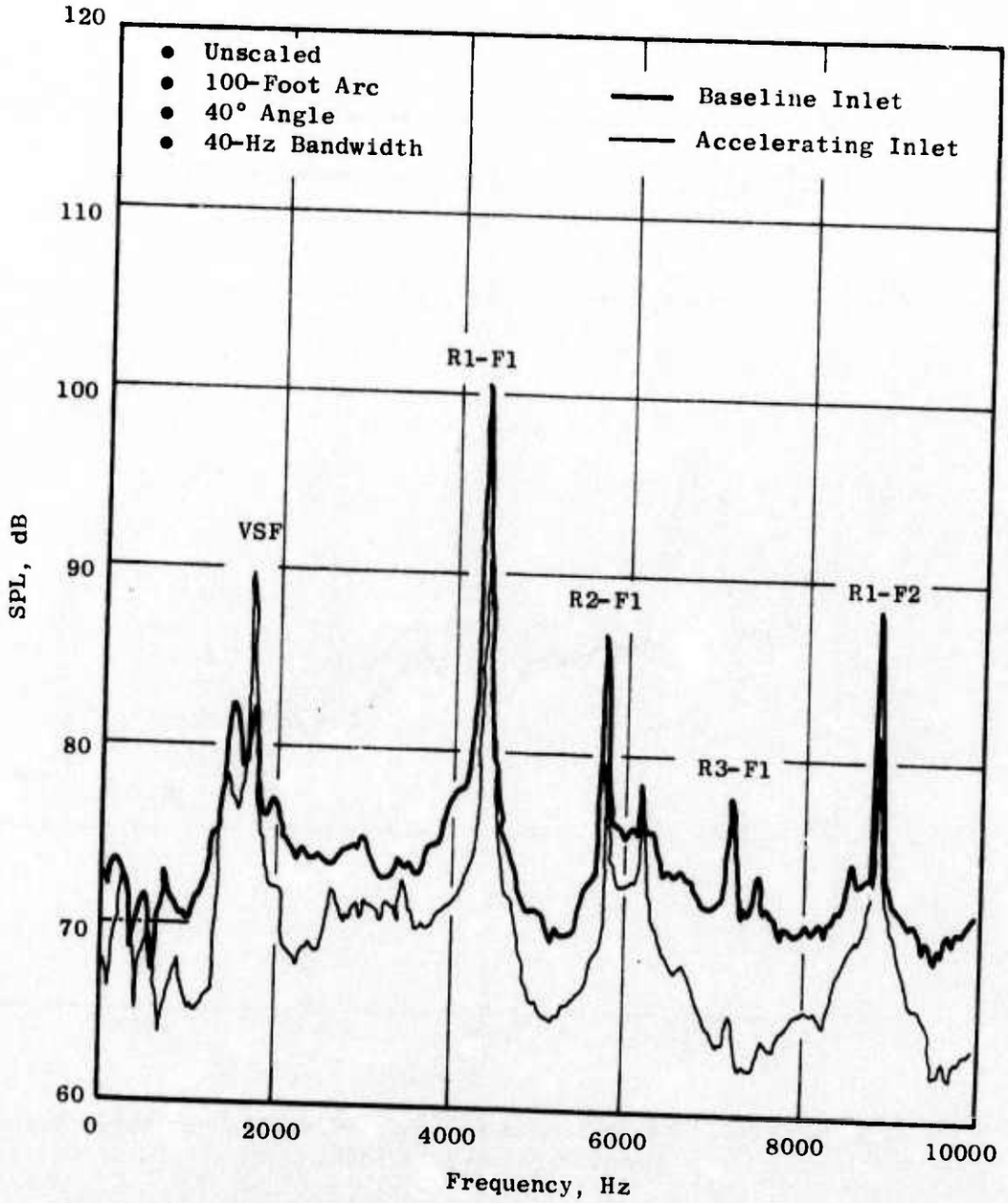

Figure 454. Narrowband Comparison for Accelerating and Baseline Inlets at V_T = 1000 ft/sec.

40° angle on the 100-foot arc. It is seen that, in the far field, the blade passing tones and the broadband noise are higher for the baseline inlet. This is attributed to the presence of the centerbody and the inlet contouring for the accelerating inlet. The centerbody increases the effective L/D ratio of the inlet, and the inlet contouring provides some "line of sight" acoustic blockage.

In Figure 455, the narrowband spectra at the fan face for the accelerating and baseline inlets are compared for a 1220 ft/sec tip speed. At this tip speed, the accelerating inlet has a throat Mach number of 0.72. At this speed, the "haystacking" around the Rotor 1 blade passing tone for the accelerating inlet is very pronounced. This is again attributed to the increased boundary layer thickness. It is also noted that the Rotor 2 and 3 blade passing tones are not present in the accelerating inlet results. The narrowband comparison for the 40° angle on the 100' arc (Figure 456) again shows the noise attenuation through the accelerating inlet.

4.4.3.4 Directivity

In Figure 457, the noise suppression, in terms of ΔSPL as a function of angle from the inlet in the blade passing 1/3-octave band, is compared for the accelerating and hybrid inlets. The comparison is for the selected operating point (M_{th} = 0.78). The baseline levels of the blade passing tone are also shown as a function of angle from the inlet. It is seen that the largest SPL reductions generally occur at angles where the baseline levels are highest. From Figure 457, it is also noted that the acoustic treatment is more effective in reducing the blade passing tone at large angles from the inlet.

4.4.3.5 Aerodynamic Performance

A radial total-pressure traverse typical of those used to determine inlet recovery, is shown in Figure 458. Integration was performed along a line faired through the data to approximate the average pressure that appeared to prevail. The results of all traverses taken for the approach inlet operating position are shown in Figure 459 in the form of area-weighted average total-pressure recovery versus throat Mach number based on design physical throat area. Relatively high recoveries are apparent, out to the vicinity of the choking point (M_{th} = 0.875), especially in view of the amount of diffusion (and, hence, length) involved and the absence of any form of boundary layer control (e.g., vortex generators or bleed). At the 0.75 M_{th} design point, the recovery is about 0.3 points above the empirical value used to size the inlet. There is no significant difference in the measured total-pressure recovery for the hybrid and accelerating inlet. This is important, since it indicates that there is no significant performance penalty due to the addition of treatment. In the past, a significant penalty due to frictional losses had been assumed. From Figure 459, the operating point of M_{th} = 0.78 was selected. At this throat Mach number the recovery is very good (0.98), and there is adequate design margin such that the steep drop in recovery will not be encountered in normal operation.

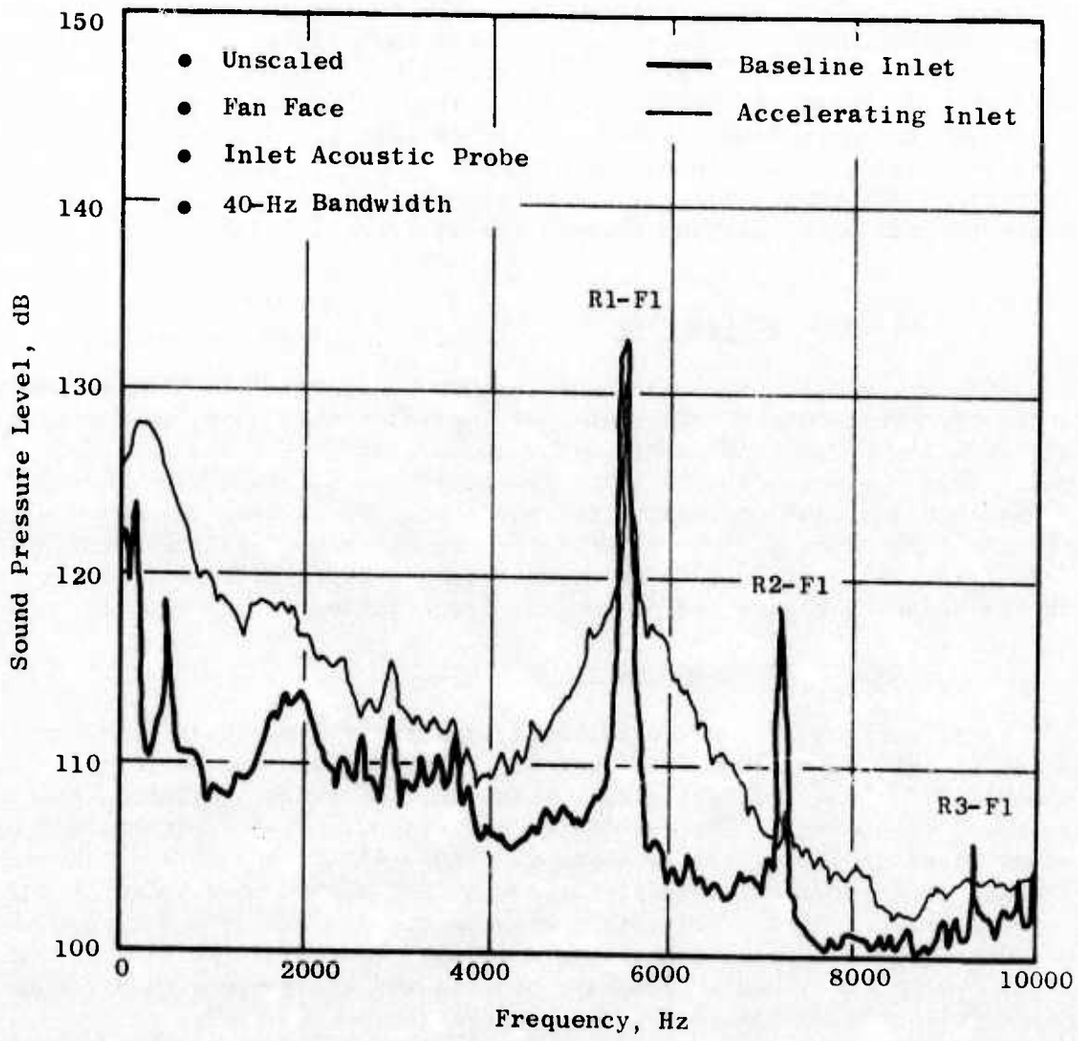

Figure 455. Narrowband Comparison of the Source Noise for the Baseline and Accelerating Inlets, V_T = 1220 ft/sec.

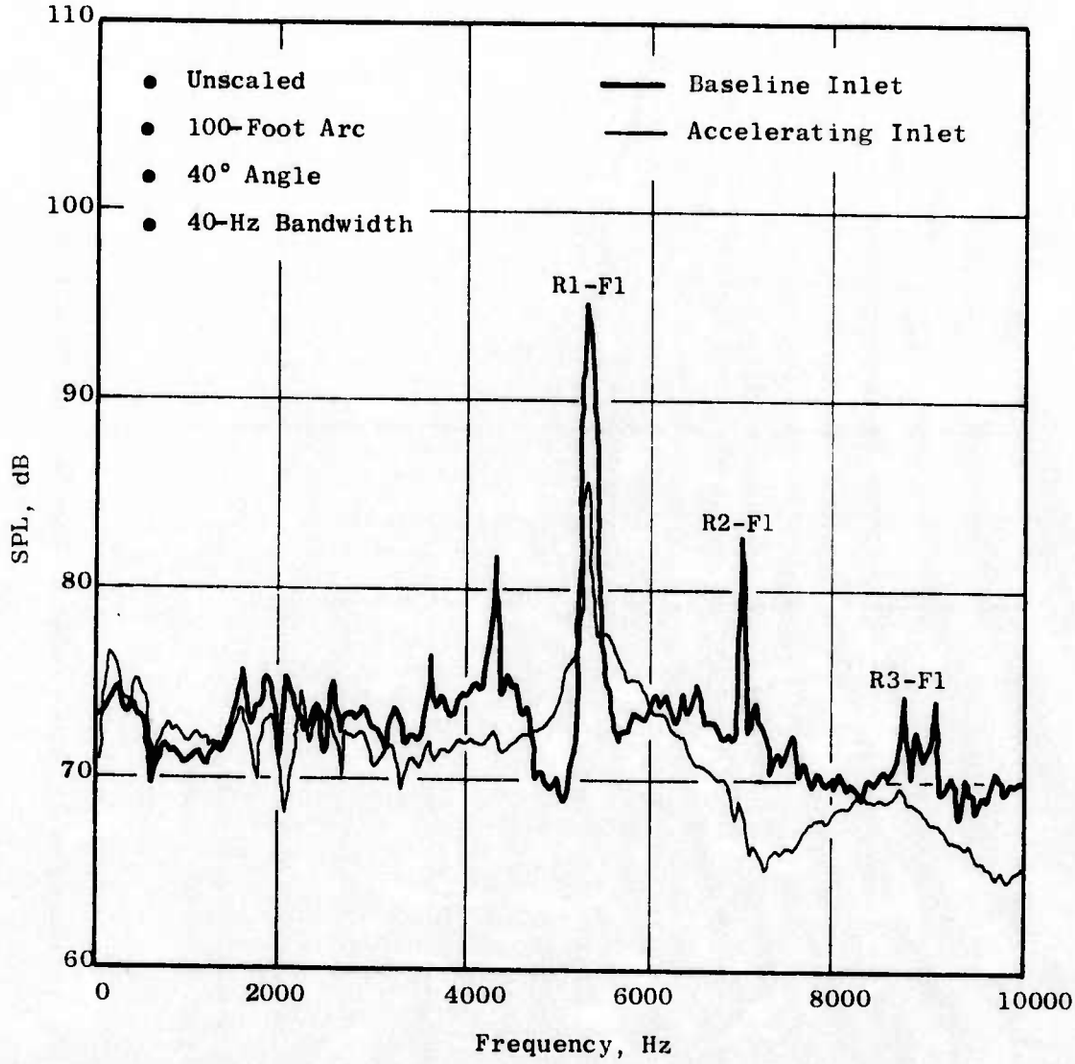

Figure 456. Narrowband Comparison for Accelerating and Baseline Inlets at V_T = 1220 ft/sec.

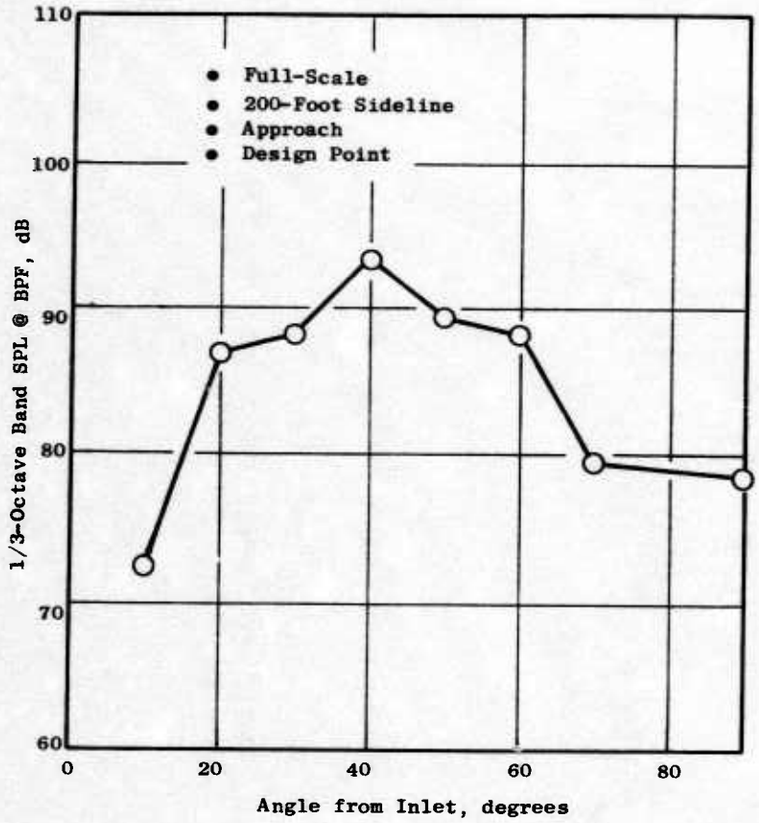

(a) Directivity of SPL at BPF for Baseline Inlet

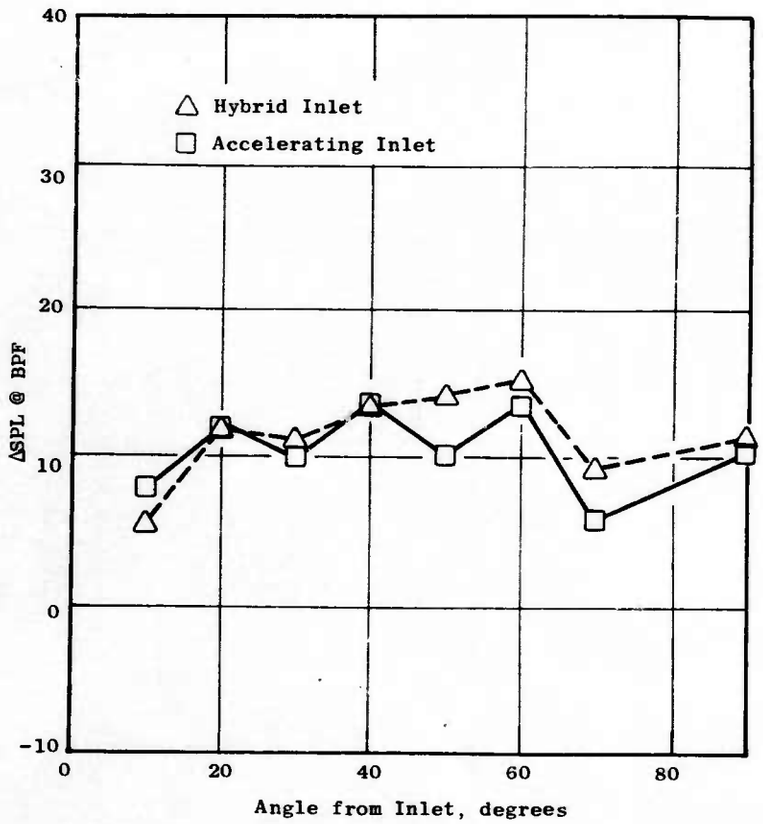

(b) ΔSPL at BPF as a Function of Angle from Inlet

Figure 457. Comparison of Noise Suppression for the Accelerating and Hybrid Inlets.

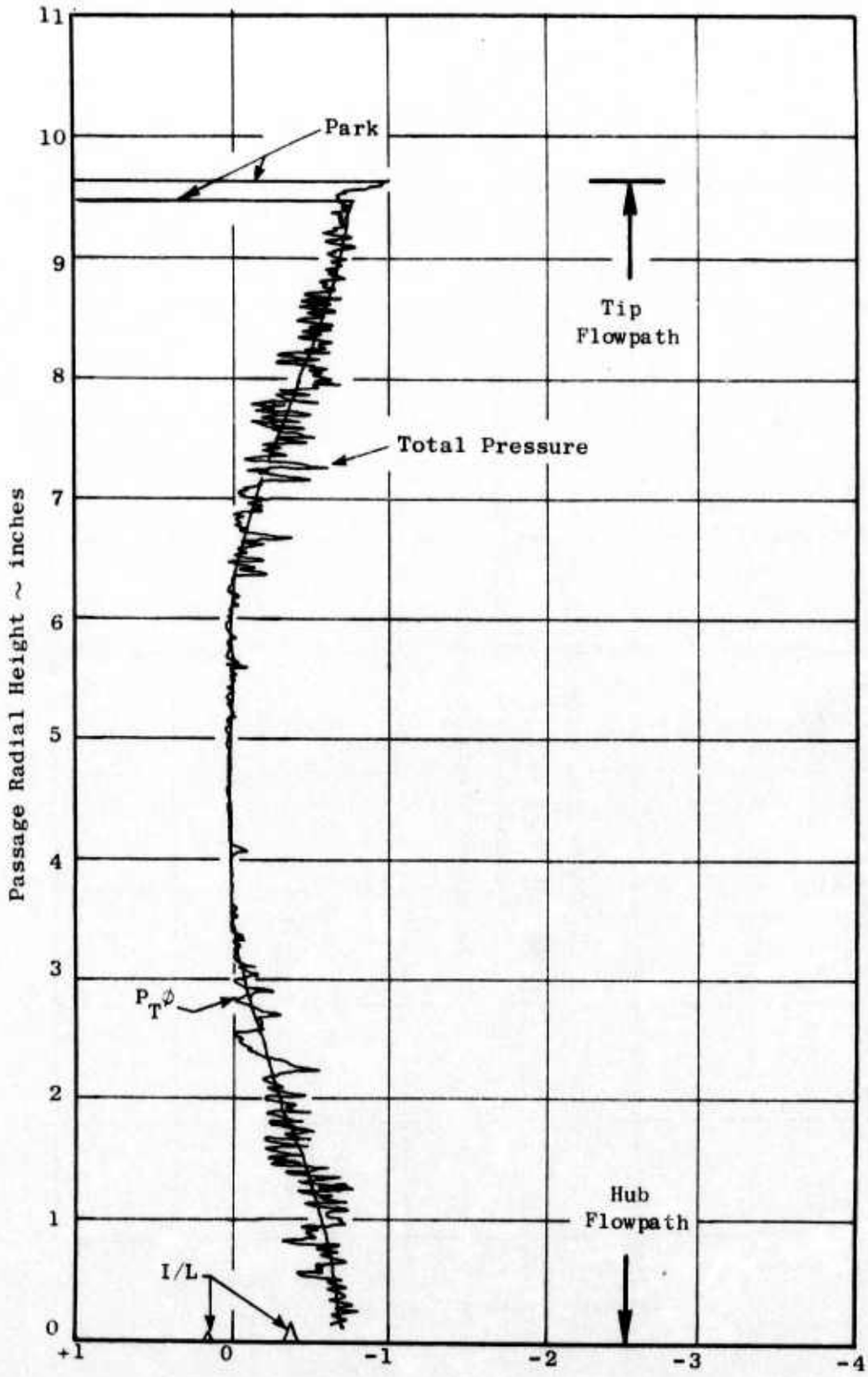

Figure 458. Typical Total Pressure Traverse Acquired after Elimination of Probe Leak; Approach Centerbody Position, M_{th} = 0.781.

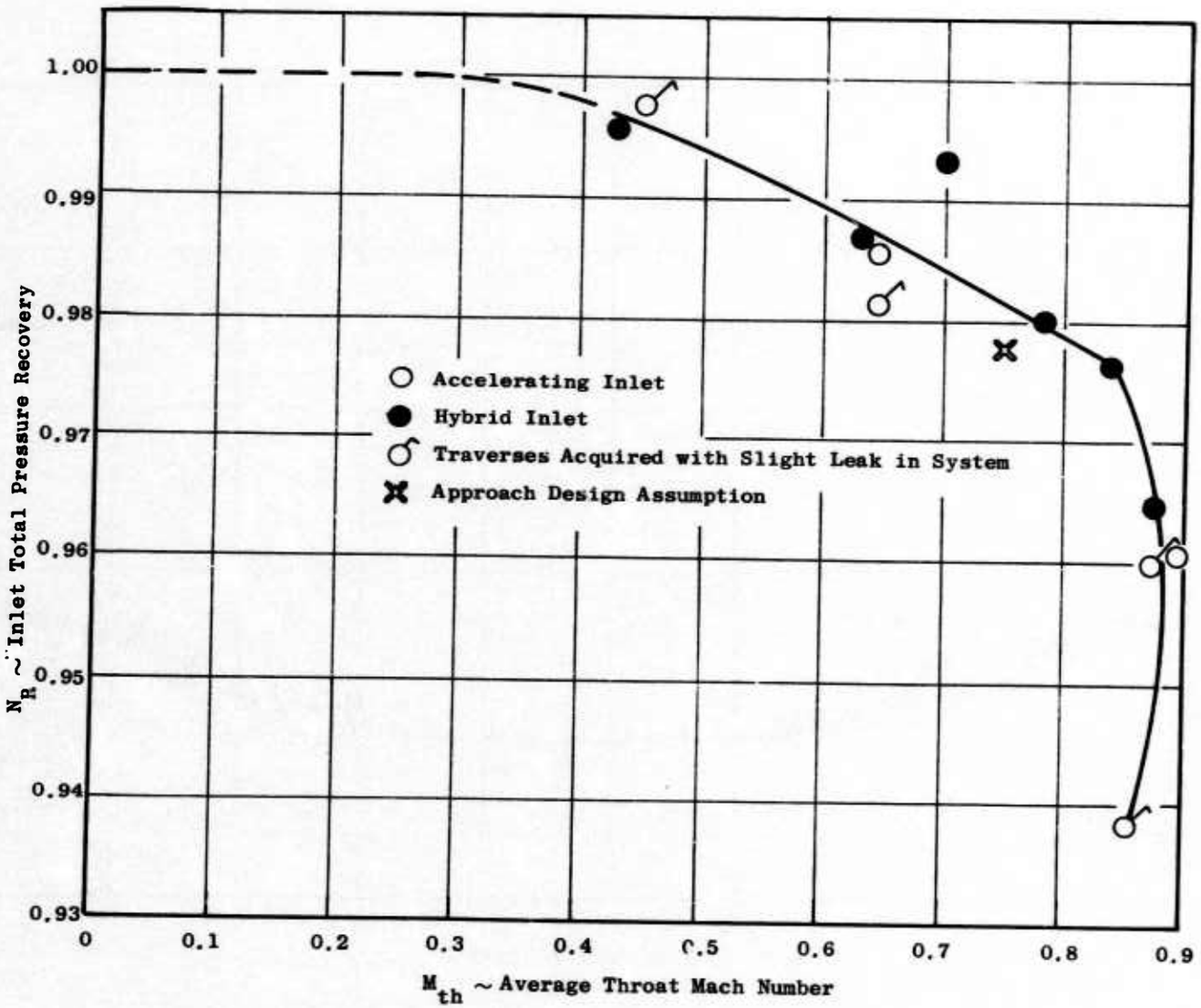

Figure 459. Inlet Total-Pressure Recovery Characteristics for Approach Operating Mode.

Figure 460 contains the same data expressed in terms of total-pressure loss coefficient $(P_{TO} - P_{T2})/q_{cth}$, where the denominator is the difference between throat average total and static pressure or the "compressible" dynamic head. The loss coefficient, while somewhat scattered, is seen to increase gradually with throat Mach number until the choking point is reached.

As noted previously, the foregoing data were obtained with a single traverse, located midway between support struts, and, hence, do not reflect the effects of these flowpath obstructions. The actual performance, therefore, might be expected to be slightly below that presented here.

With 10% of the flow area excluded for normal boundary layer growth along the hub and tip surfaces, (radial) distortion from the traverse is about 4-1/2% $(P_{T_{max.}} - P_{T_{min.}})/P_{T_{AV}}$ at the 0.78 throat Mach number. This distortion is acceptable from an aerodynamic performance standpoint.

Typical measured wall Mach number characteristics are compared with various STC predictions for a throat Mach number slightly above design in Figures 461 and 462. Good agreement is seen, with the predicted peak Mach number slightly below that of the data, even allowing for the slight mismatch in throat Mach number. The remainder of the difference between the measured and predicted characteristics, especially in the aft portion of the inlet, may be ascribed to use of ambient total pressure to infer measured wall Mach number, whereas the actual local total pressure decreases below that value due to inlet losses. Incorporating this effect would tend to lower measured wall Mach numbers and bring them into even better agreement with the STC results.

4.4.3.6 Summary

1. At the selected operating point (throat Mach number = 0.78), the hybrid inlet provides 11.5 ΔPNdB noise suppression relative to the baseline configuration for the approach mode.

2. The acoustic treatment provides four ΔPNdB noise suppression at the selected operating point.

3. Acceleration suppression for the inlet attenuates the high frequency noise more effectively than low frequency noise.

4. The presence of the centerbody and the inlet contouring in the accelerating inlet results in noise attenuation in the inlet duct relative to the baseline inlet. This reduces the PNL of the accelerating inlet relative to baseline by 3 to 4 PNdB at inlet throat Mach numbers where there is no apparent acceleration suppression.

5. In the 1/3-octave band containing the Rotor 1 blade passing tone, the ΔSPL suppression for the hybrid inlet relative to the baseline is greatest at angles where the baseline levels are a maximum.

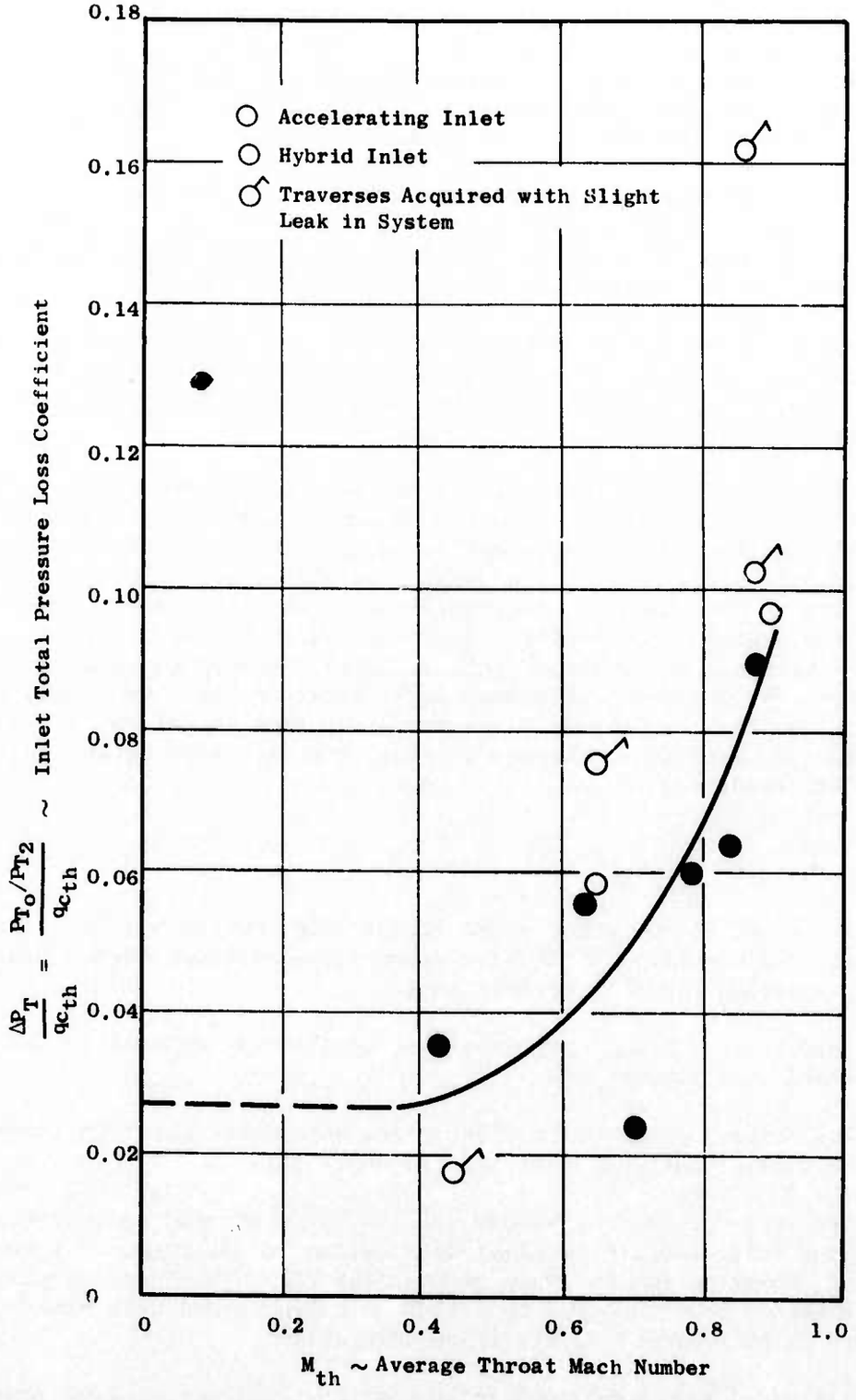

Figure 460. Inlet Total-Pressure Loss Coefficient Trend for Approach Operating Mode.

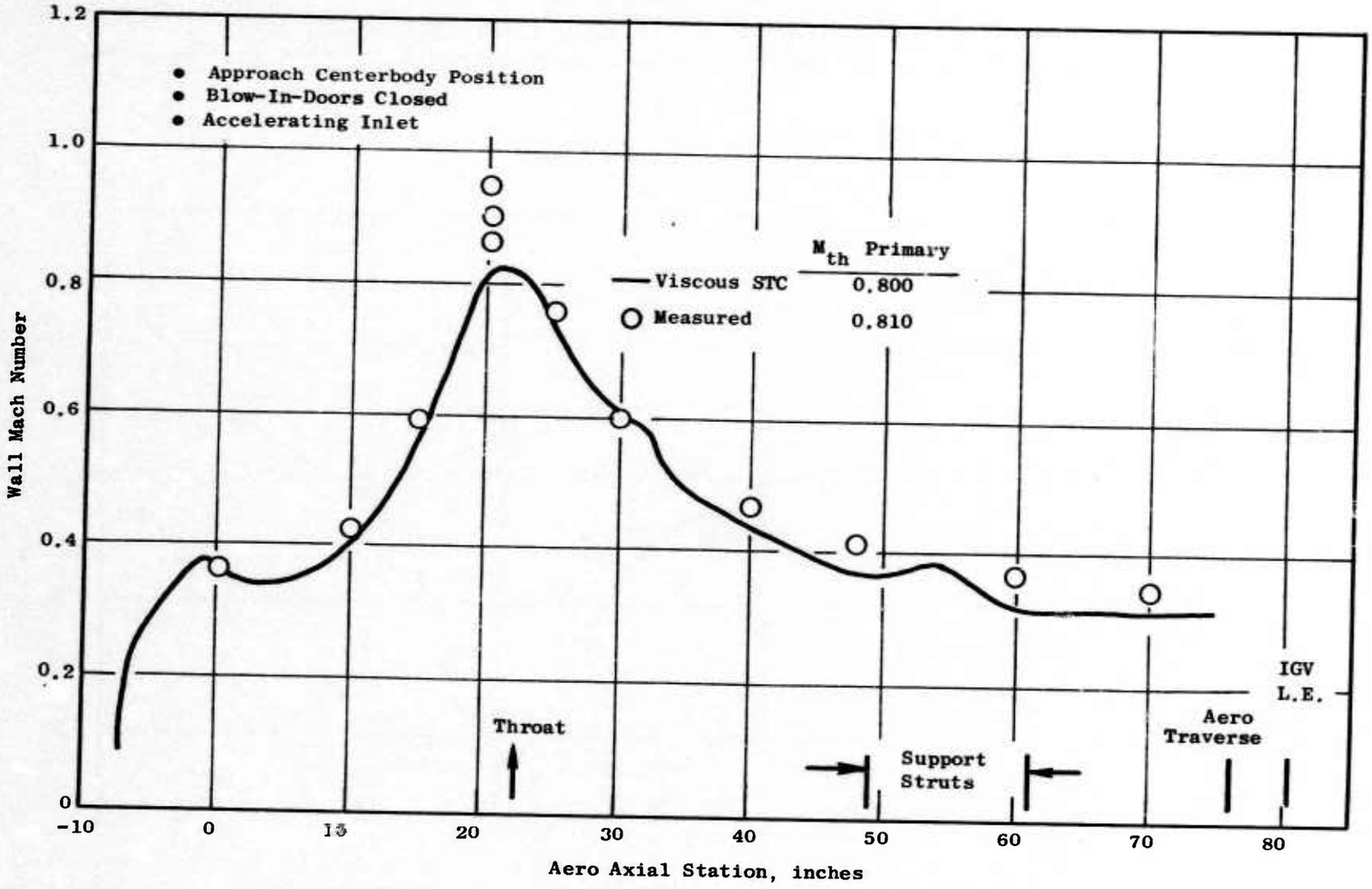

Figure 461. Comparison of Measured and Predicted Cowl Surface Mach Number Distributions for the Approach Operating Mode.

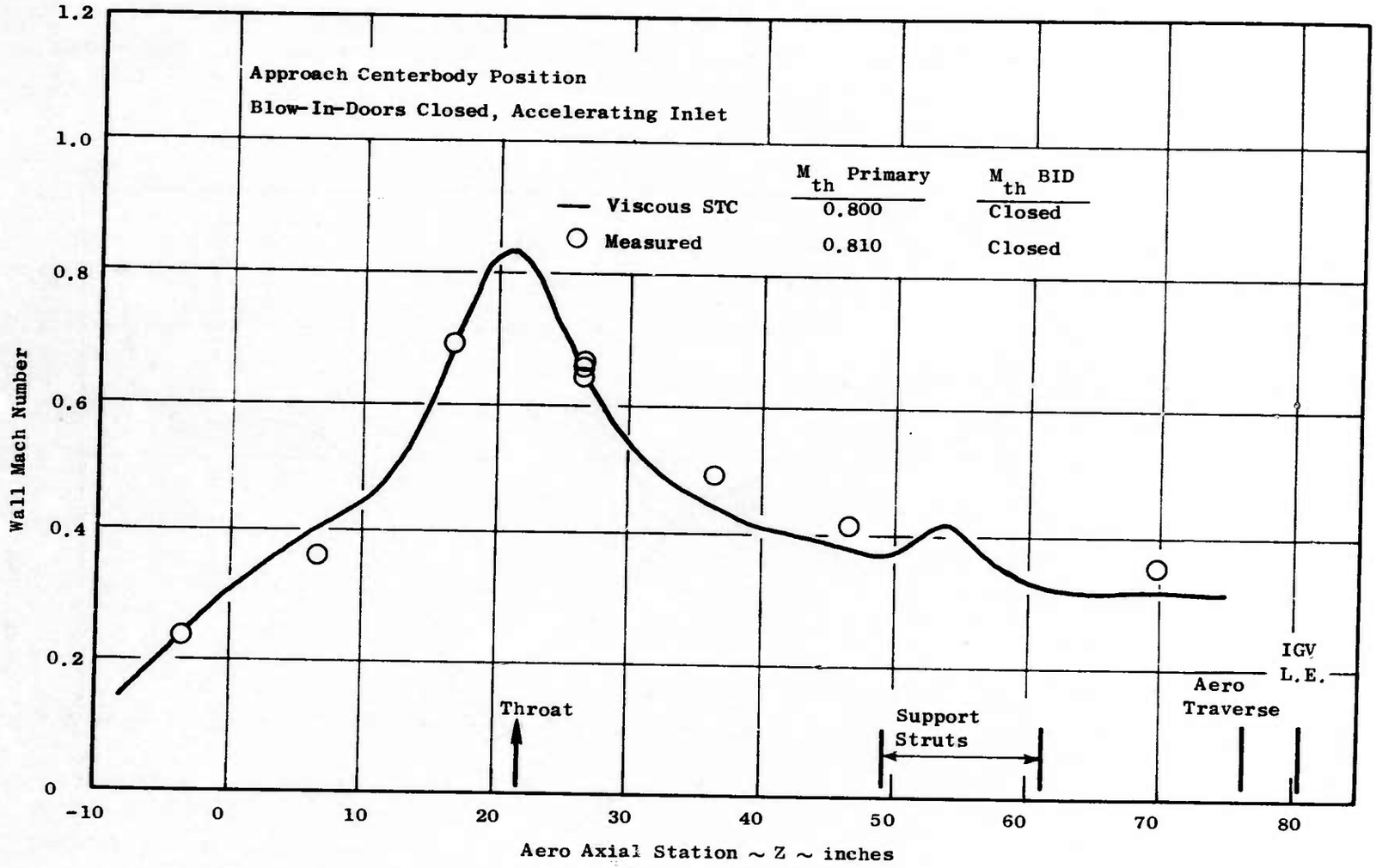

Figure 462. Comparison of Measured and Predicted Centerbody Surface Mach Number Distributions for Approach Operating Mode.

6. At the hybrid inlet selected operating point, the acoustic treatment is more effective at high inlet angles in reducing the blade passing tone.

7. At the selected operating point, the total-pressure recovery for the hybrid inlet is very good (0.98) with no apparent penalty in performance due to the wall treatment.

8. The measured wall Mach number characteristics agree well with the predicted levels.

4.4.4 Hybrid Inlet Results - Take-off Mode, Blow-In Doors Closed

4.4.4.1 Introduction

The only difference between the hybrid inlet for the take-off mode (blow-in doors closed) and that for the approach mode is that the centerbody is 6.54 inches longer. This increases the inlet throat area such that high inlet throat Mach numbers are reached at an engine speed characteristic of takeoff. Since, for an SST engine, the blow-in doors are required to be open during takeoff, these results only provide a baseline level for evaluating the effect of the blow-in doors.

4.4.4.2 Hybrid and Accelerating Inlet PNL Suppression

In Figure 463 the PNL at the 40° angle as a function of tip speed is compared for the baseline cylindrical inlet, the accelerating inlet, and the hybrid inlet in the take-off mode with the auxiliary inlets closed. At the 40° angle the PNL is a maximum on the 200-foot sideline for all tip speeds of the baseline configuration. The inlet throat Mach number of the hybrid and accelerating inlet is also indicated on Figure 463.

At tip speeds up to 1250 ft/sec, the PNL for the accelerating inlet is nearly equal to that for the baseline inlet. In Figure 464, the one-third octave band spectra at the 40° angle are compared for the baseline and accelerating inlet in the take-off mode at V_T = 1000 ft/sec. The rotor 1 blade passing tone (1600 Hz band) is lower for the accelerating inlet; however, the second harmonic in the 3150 Hz band, which dominates the PNL, is equal for the baseline and accelerating inlets. In Section 4.4.3.2 it was shown that, in the approach mode, the accelerating inlet was 3-4 PNdB quieter than the baseline inlet at tip speeds up to 1250 ft/sec. The one-third octave spectra for the approach mode are also shown in Figure 464. The one-third-octave band spectra for the approach mode are, in general, lower across the entire noise spectrum. A comparison of the inlet probe source noise measurement nearest the wall for the approach and take-off modes (Figure 465) shows that the rotor 1 second harmonic is significantly lower at the fan face for the accelerating inlet in the approach mode. Therefore, the reduced 1/3-octave band level at 3150 Hz is attributed primarily to lower fan source noise.

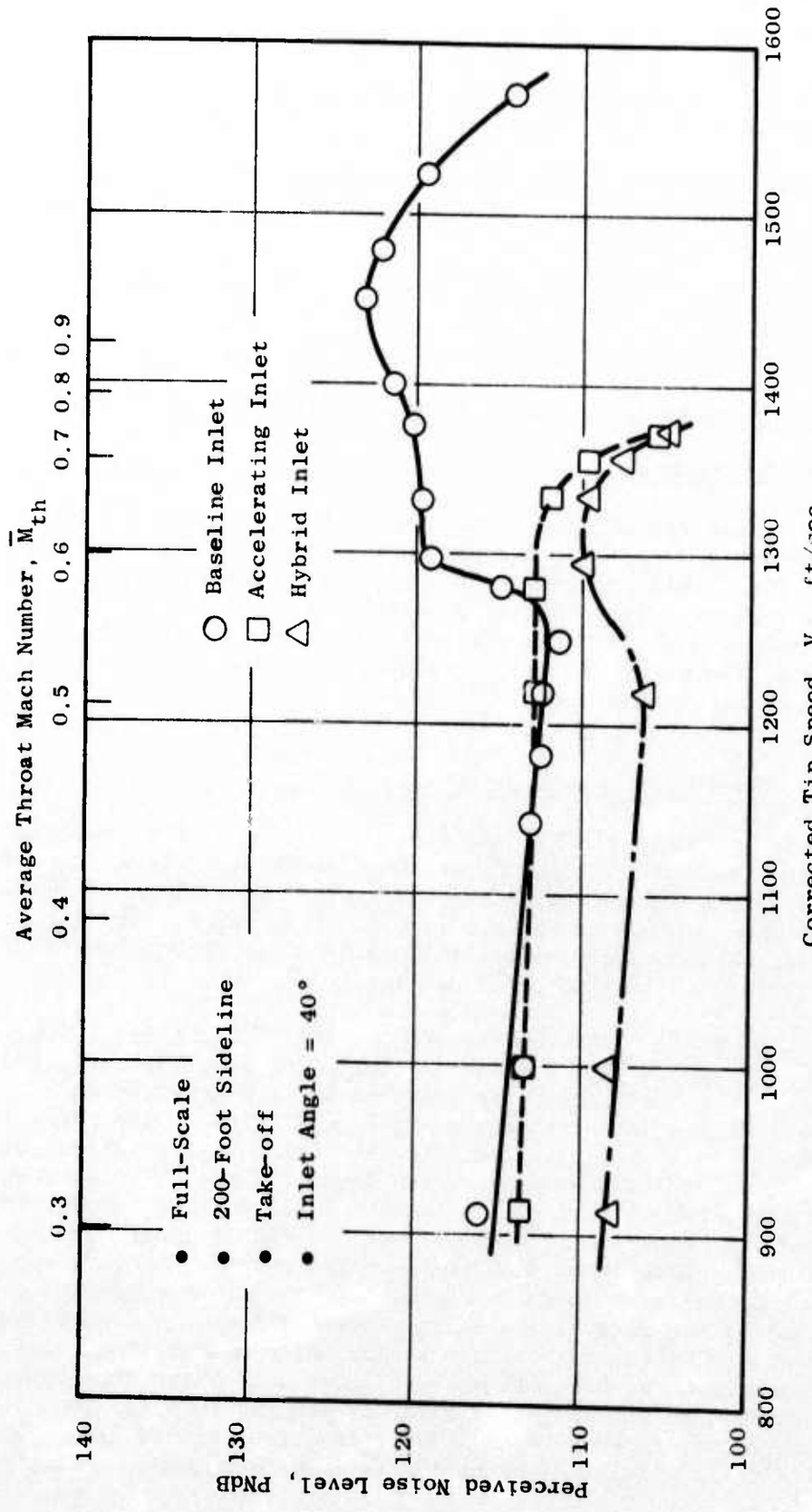

Figure 463. PNL as a Function of Tip Speed.

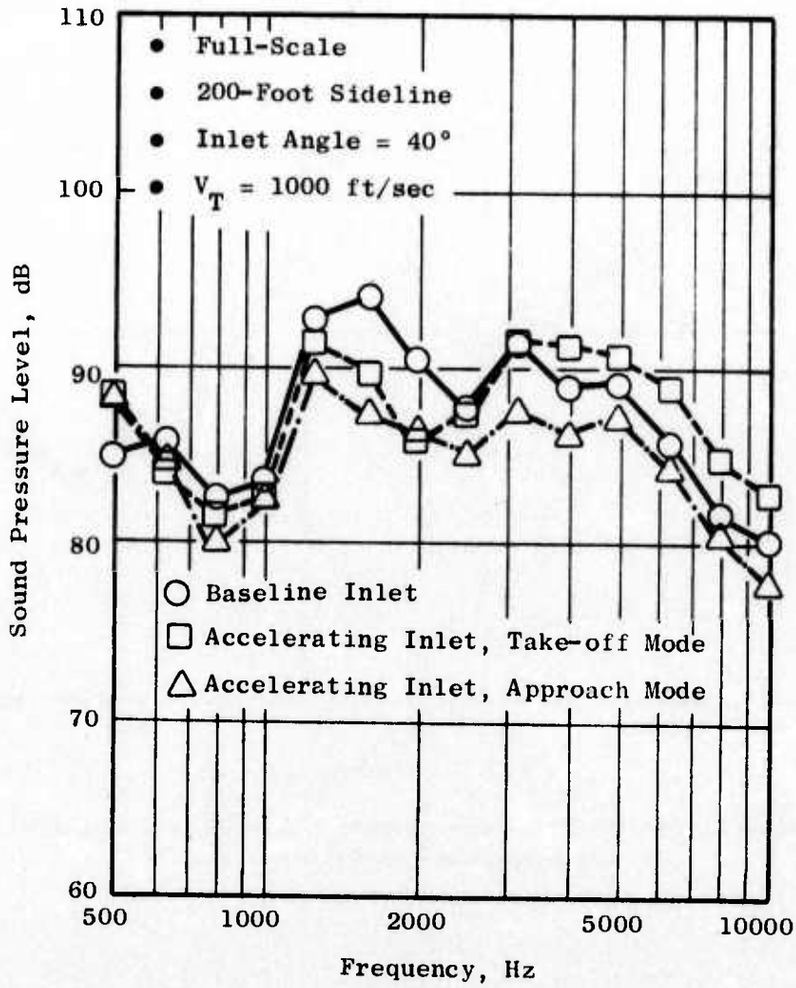

Figure 464. One-Third-Octave Band Comparison for the Baseline Inlet and the Accelerating Inlet in Both the Approach and Take-off Mode.

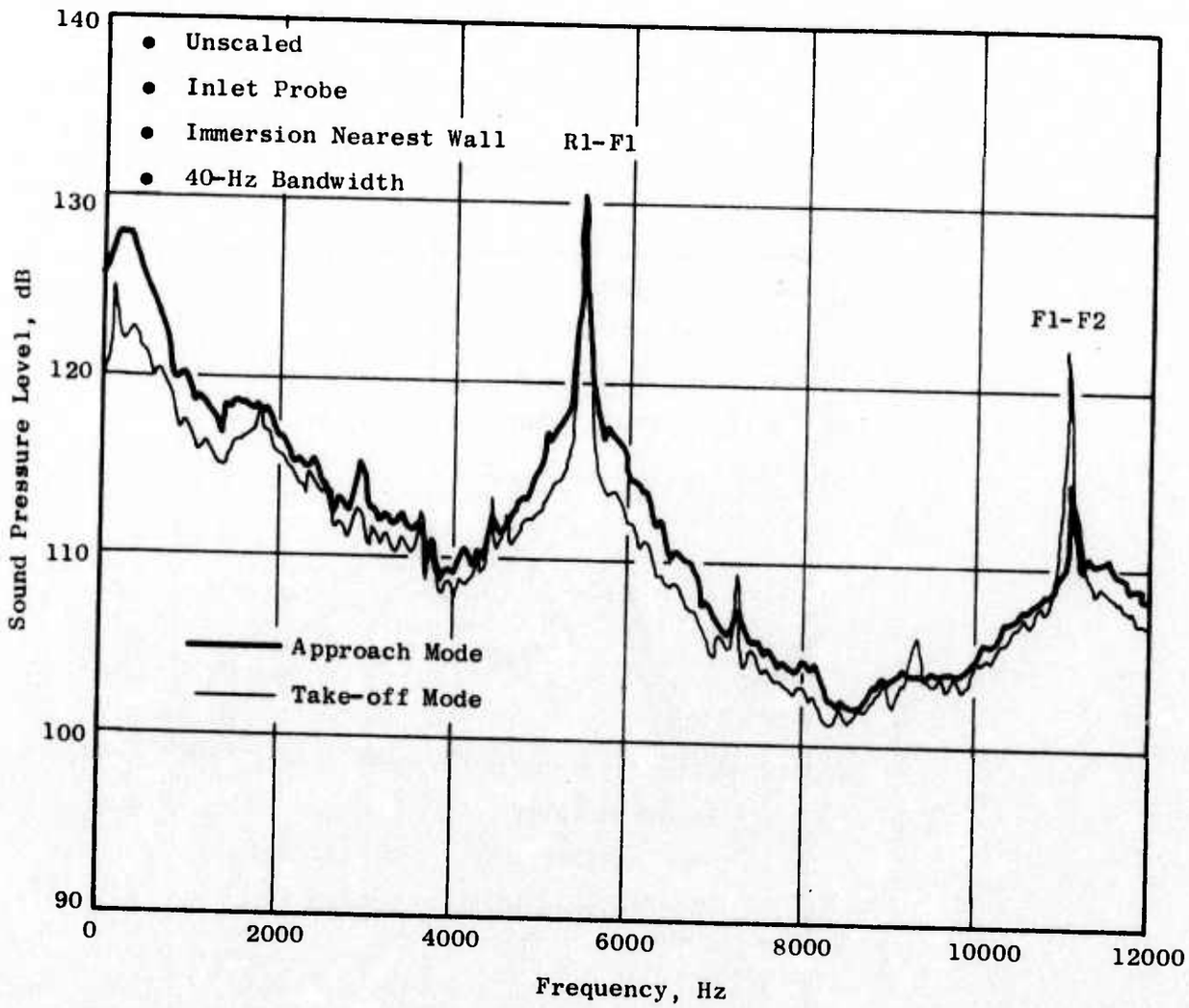

Figure 465. Inlet Probe Narrowband Comparison for the Accelerating Inlet in the Approach and Take-off Modes.

At a tip speed of 1250 feet/second the PNL for the baseline inlet increases sharply, while for the accelerating inlet the PNL remains nearly constant as a function of tip speed. The throat Mach number is only about 0.60 and, therefore, this cannot be attributed to acceleration suppression. In Figure 466 the SPL at the rotor 1 second harmonic blade passing frequency measured at the five equal area immersion depths at the fan face are shown for the baseline inlet and accelerating inlet in the take-off mode. The comparison is made between V_T = 1220 and 1372 ft/sec, the speeds before and after the abrupt increase in the PNL for the baseline inlet. It is seen that for the baseline inlet, there is a large increase in the source tone level; however, this did not occur for the accelerating inlet in the take-off mode. Thus, it appears that, due to the different inlet configuration for the accelerating inlet, this abrupt change in the source noise did not occur.

In Figure 467 the one-third-octave band spectra at 40° are shown for the accelerating and baseline inlets at a corrected tip speed of 1340 ft/sec. At this tip speed, the inlet throat Mach number is 0.68 for the accelerating inlet. The acceleration suppression is not significant at this throat Mach number. The comparison shows that the noise levels, especially at the rotor 1 blade passing tone and its harmonics, are much higher for the baseline configuration. This is attributed to the higher fan source noise for the baseline inlet as shown above. It is also noted that the vortex-shedding tone at 630 Hz is less for the accelerating inlet. In Section 4.4.2.2, this tone was linked with an increase in the blade passing tones for the baseline inlet. Therefore, it is speculated that perhaps the lower fan source noise for the accelerating inlet is due to smaller vortices being shed off the IGV's.

Because of the difference in source noise between the baseline inlet and the accelerating inlet in the take-off mode, it was necessary to isolate the acceleration suppression by referencing to the accelerating inlet results at V_T = 1340 ft/sec where M_{th} = 0.68. At this throat Mach number, there is no significant acceleration suppression. This can be seen in Figure 468 which compares the one-third-octave band spectra at V_T = 1280 and 1340 ft/sec. There is no significant reduction in the 1/3-octave band levels. From Figure 463 the acceleration suppression at the selected operating point (M_{th} = 0.77, see Section 4.4.4.4) is, therefore, 6.5 PNdB. The inlet configuration provides an additional 8.5 PNdB noise suppression relative to the baseline and the total suppression, therefore, is 15 PNdB at the selected operating point relative to the baseline cylindrical hardwall inlet.

The acceleration suppression in terms of ΔSPL as a function of frequency is shown in Figure 469 at 40° for M_{th} = 0.77. The acceleration suppression increases with frequency and also peaks at the rotor 1 BPF (2000 Hz). These results are consistent with those presented earlier for the accelerating inlet in the approach mode.

From Figure 463 it is seen that the treatment effectiveness varies markedly as a function of tip speed. Up to a tip speed of approximately 1230 ft/sec, the treatment provides between 5 to 6.5 ΔPNdB suppression. The one-third-octave band comparisons for the accelerating and hybrid inlets at V_T = 1000 and 1219 ft/sec are shown in Figures 470 and 471, respectively. The treatment

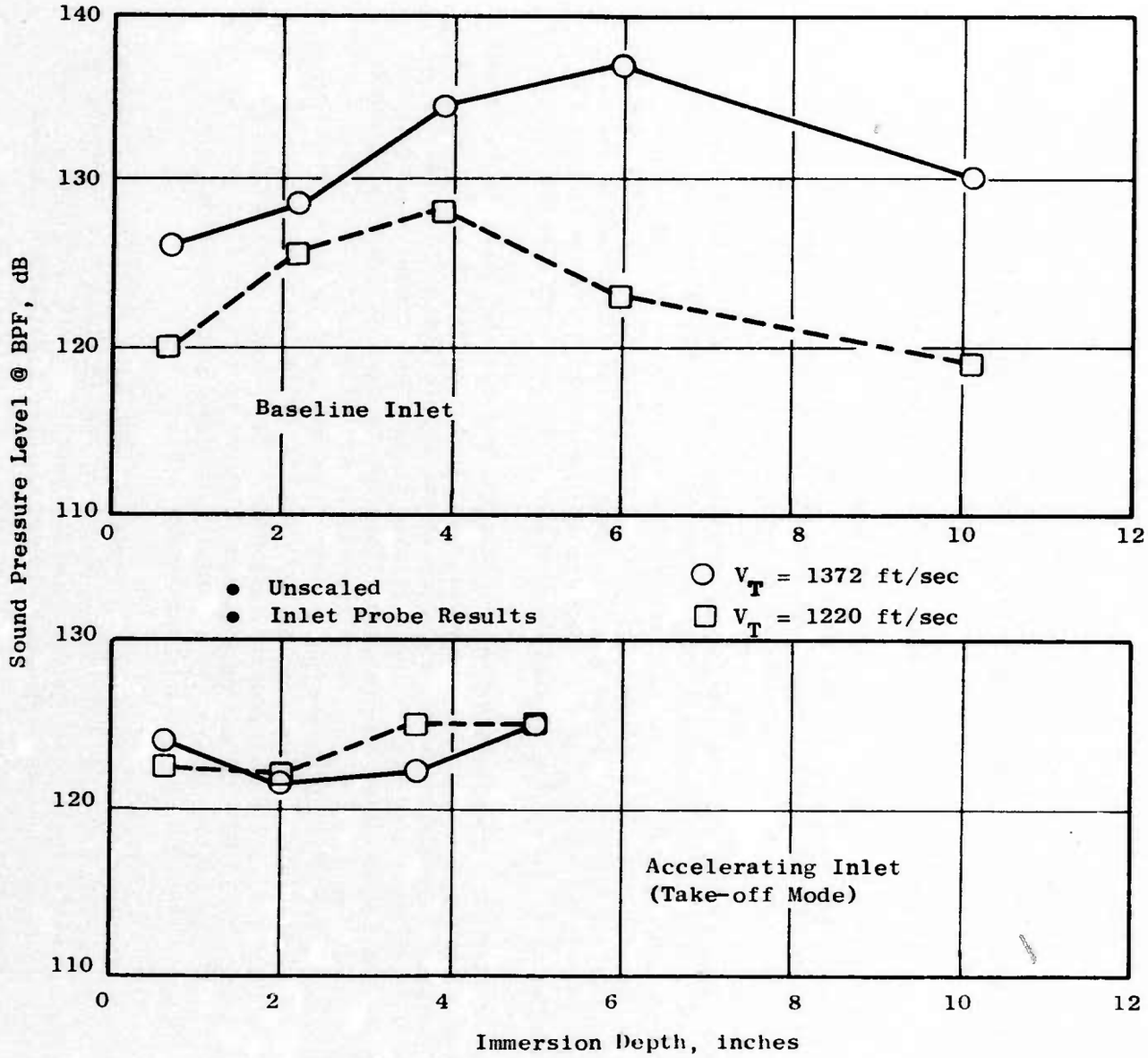

Figure 466. Rotor 1 Second Harmonic Tone as a Function of Immersion Depth at the Fan Face.

- Full-Scale
- 200-Foot Sideline
- Inlet Angle = 40°
- V_T = 1340 ft/sec

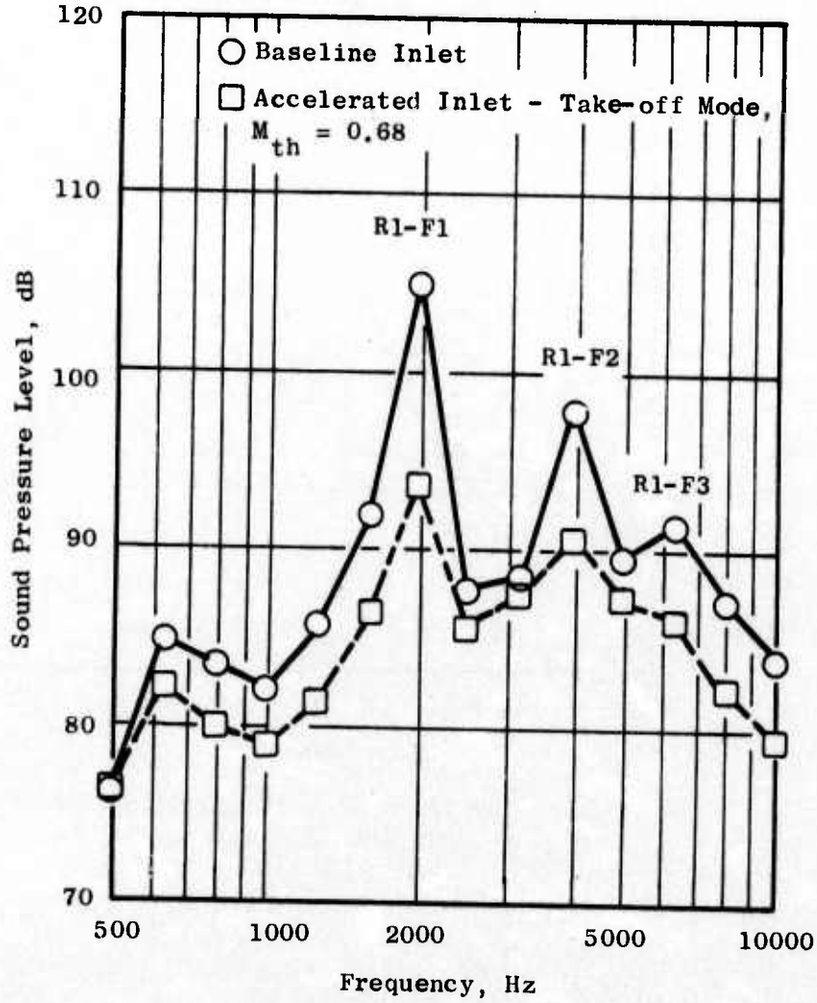

Figure 467. One-Third-Octave Band Comparison for the Baseline Inlet and the Accelerating Inlet in the Take-off Mode.

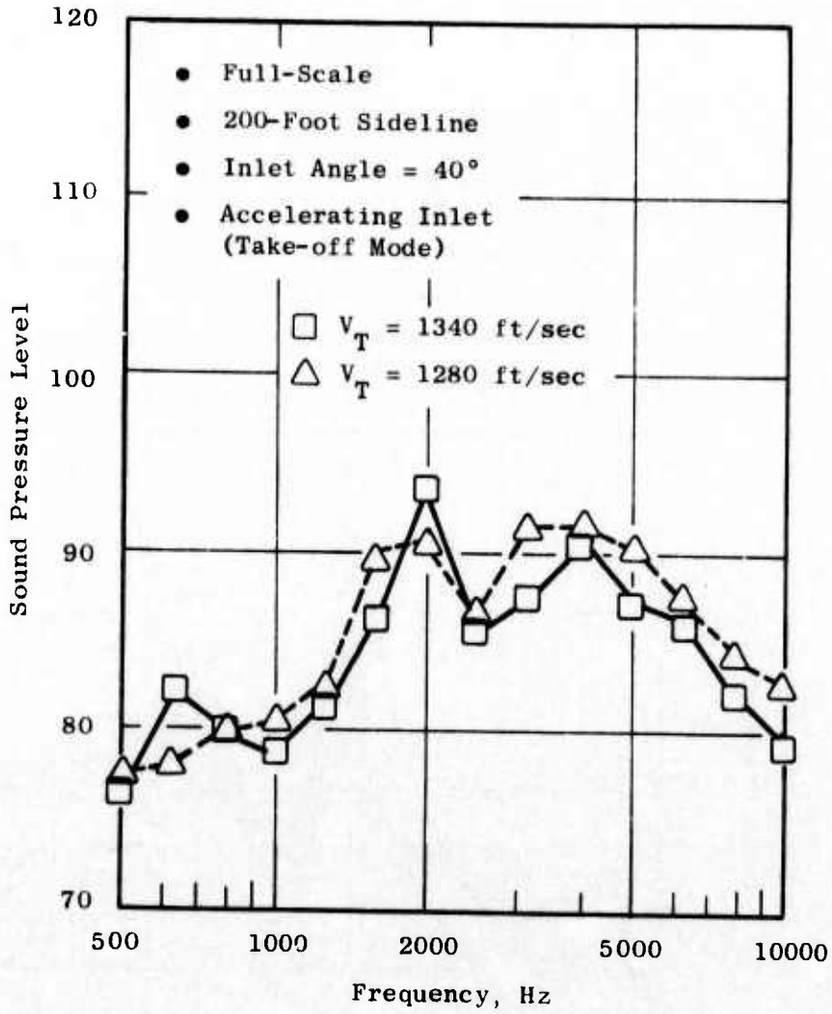

Figure 468. One-Third-Octave Band Spectra Comparison at 1340 and 1280 ft/sec.

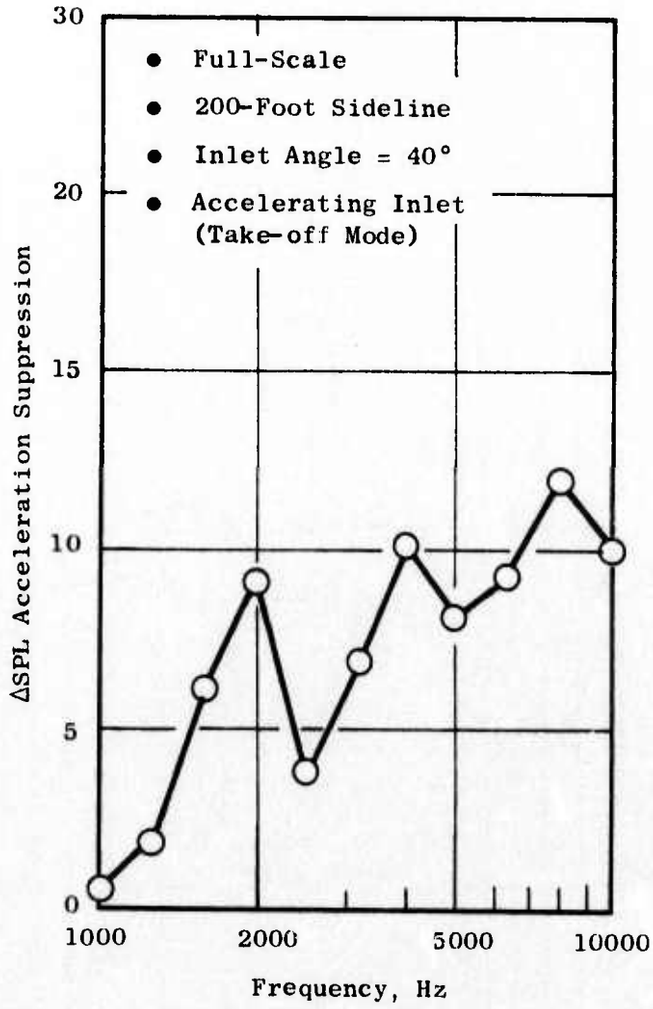

Figure 469. One-Third-Octave Band ΔSPL Acceleration Suppression at M_{th} = 0.77.

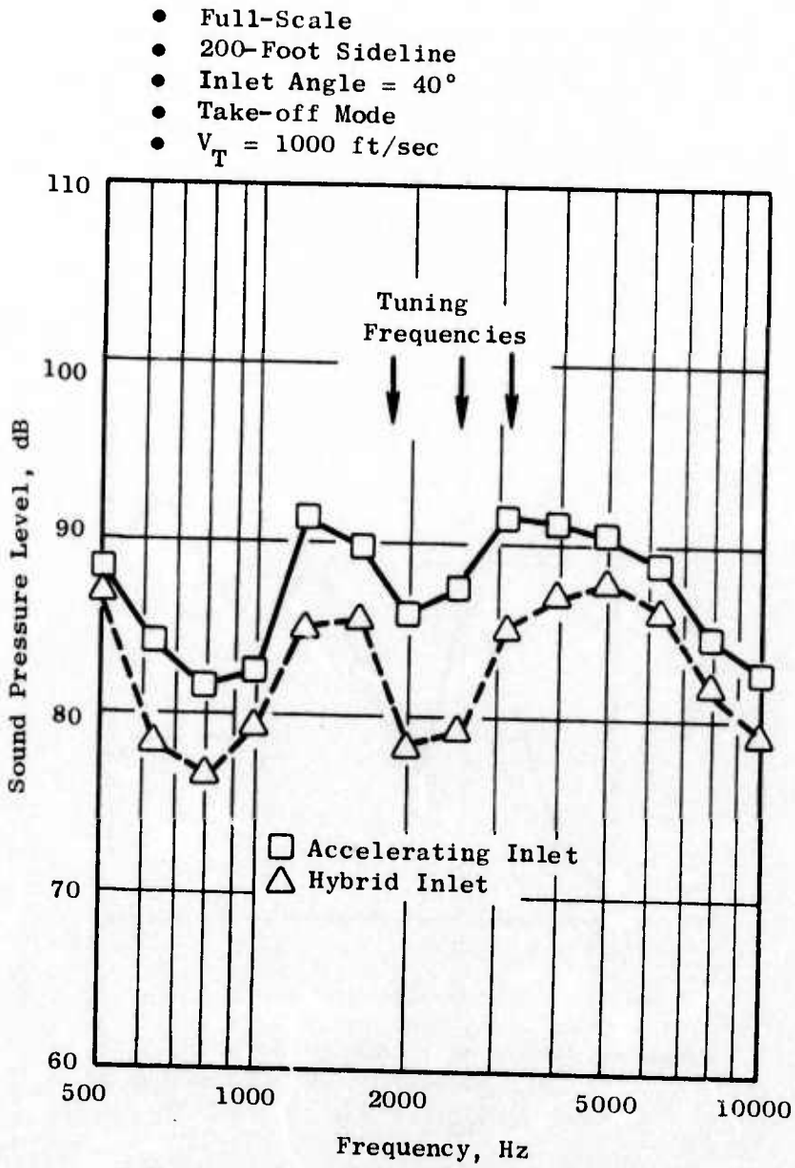

Figure 470. One-Third-Octave Band Comparison Between Accelerating and Hybrid Inlets, V_T = 1000 ft/sec.

- Full-Scale
- 200-Foot Sideline
- Inlet Angle = 40°
- Take-off Mode
- V_T - 1219 ft/sec

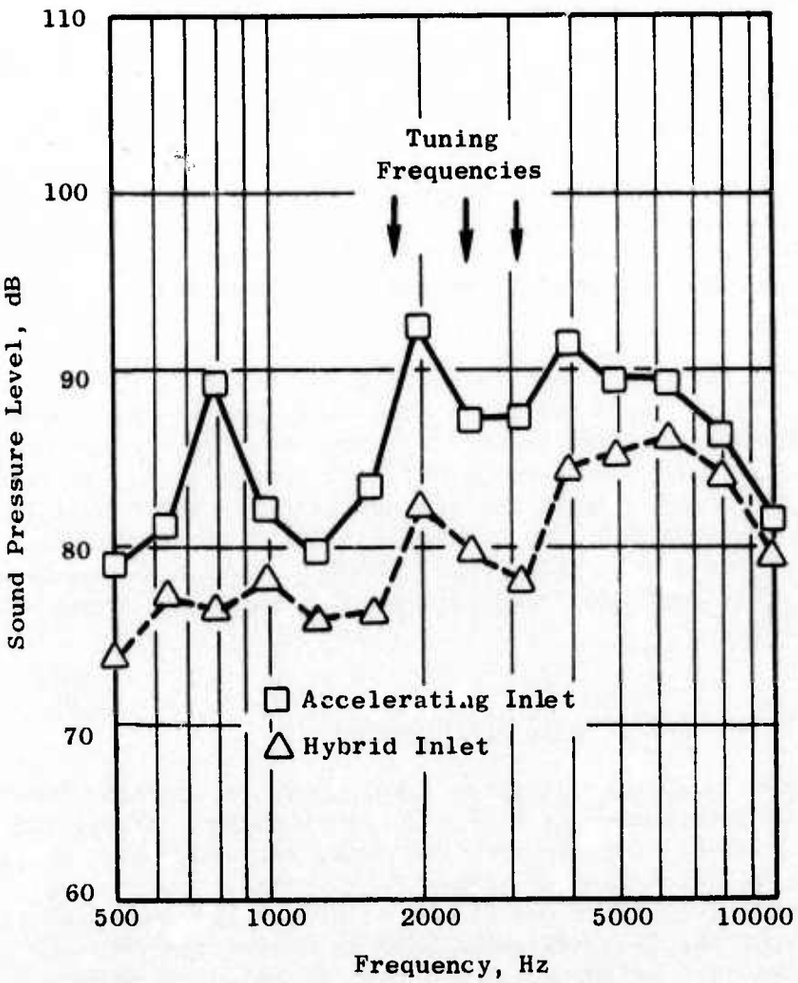

Figure 471. One-Third-Octave Band Comparison Between Accelerating and Hybrid Inlets, V_T = 1219 ft/sec.

tuning frequencies are indicated on both plots. At both speeds, the treatment is providing suppression across the frequency bandwidth over which the treatment is designed.

Above the 1230 ft/sec tip speed there is a significant reduction in treatment effectiveness. A comparison of the one-third-octave band spectra at V_T = 1334 ft/sec for the accelerating and hybrid inlets is shown in Figure 472. It is seen that in the rotor 1 blade passing 1/3 octave band (2000 Hz), the treatment effectiveness is near zero. In Figure 473 the treatment effectiveness in terms of ΔSPL is compared as a function of one-third-octave band for this tip speed and 1219 ft/sec. There is a significant reduction in treatment effectiveness in most one-third-octave bands.

In Figure 474 the ΔSPL due to treatment at the rotor 1 BPF is compared for these same tip speeds as a function of angle from the inlet. At all angles, the treatment effectiveness is lower for the higher tip speed. It is interesting to note that at the 10° angle there was an increase in the blade passing tone when treatment was added for both speeds. Also, for both tip speeds, the treatment is more effective at large angles from the inlet centerline which is expected, since the treatment is more effective in attenuating higher-order modes. These higher-order modes are dominant at high angles from the inlet.

At inlet throat Mach numbers above 0.68, there is significant acceleration suppression. From Figure 463 it is seen that the treatment effectiveness is reduced at these high inlet throat Mach numbers. At the selected operating point, the treatment provides only 0.5 PNdB suppression. In Figure 475 the one-third-octave band spectra for the accelerating and hybrid inlets at M_{th} = 0.77 are compared at the 40° angle. There is no treatment suppression in the blade passing 1/3 octave band (2000 Hz) which is consistent with results for other high tip speed points which have low throat Mach numbers (see Figure 473).

4.4.4.3 Aerodynamic Performance

Figure 476 is a representative total-pressure traverse taken at an average throat Mach number of 0.77. Total-pressure recovery and loss coefficient, derived from the traverse data, are shown in Figures 477 and 478, respectively, as a function of throat Mach number. The recovery data exhibit relatively good performance out to the choking point indicated at about 0.85 - 0.86 M_{th}; the recovery value used in sizing the take-off position at 0.75 M_{th} is exceeded by about 0.8 points. Based on these recovery data, an operating point of M_{th} = 0.77 was selected; the recovery is 0.98 at this throat Mach number, and there is adequate design margin before the steep drop in the recovery curve. There is no significant difference in the measured total-pressure recovery for the hybrid and accelerating inlets. Therefore, there is no performance penalty due to the addition of the acoustic treatment. This result is consistent with that for the approach mode. Radial distortion of about 6.2% $(P_{T_{max.}} - P_{T_{min.}})/P_{T_{av}}$ is indicated by the Figure 476 traverse, based on the standard 10% area exclusions. This is acceptable from an aero-

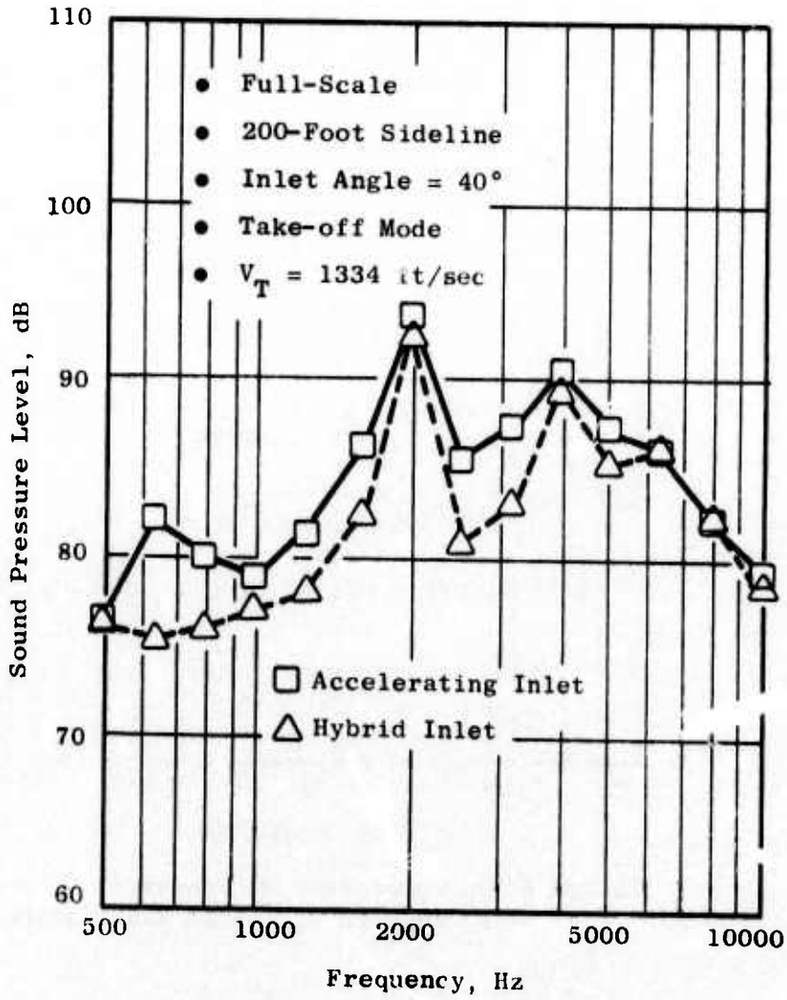

Figure 472. One-Third-Octave Band Comparison Between Accelerating and Hybrid Inlets, V_T = 1334 ft/sec.

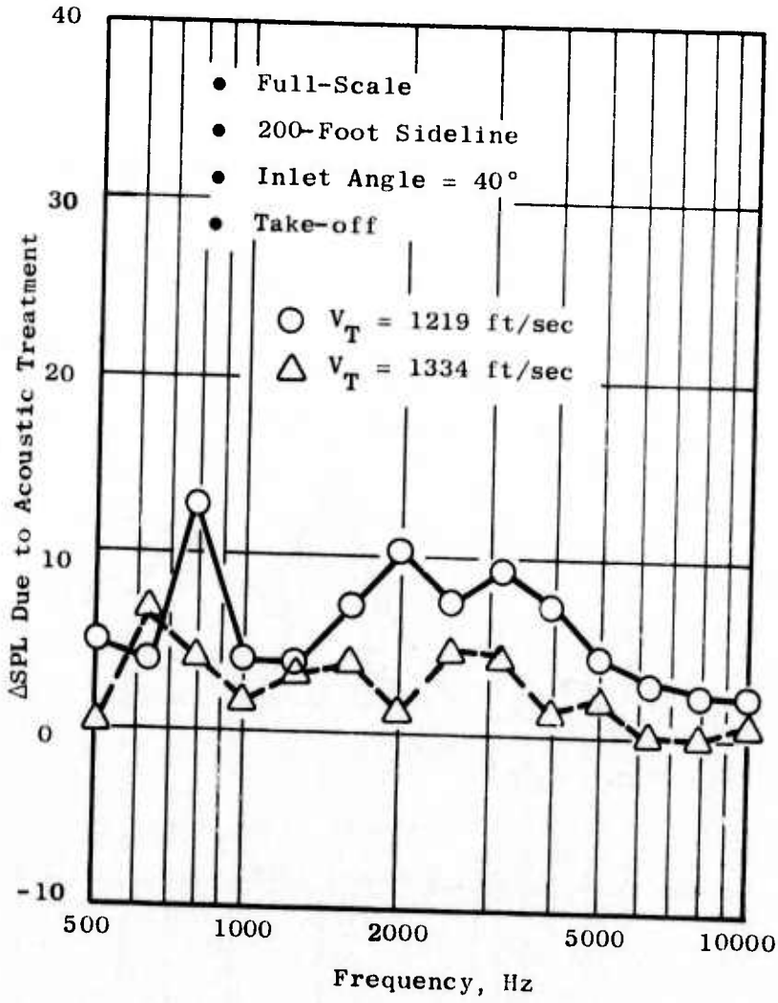

Figure 473. Comparison of Treatment Effectiveness at V_T = 1219 and 1334 ft/sec.

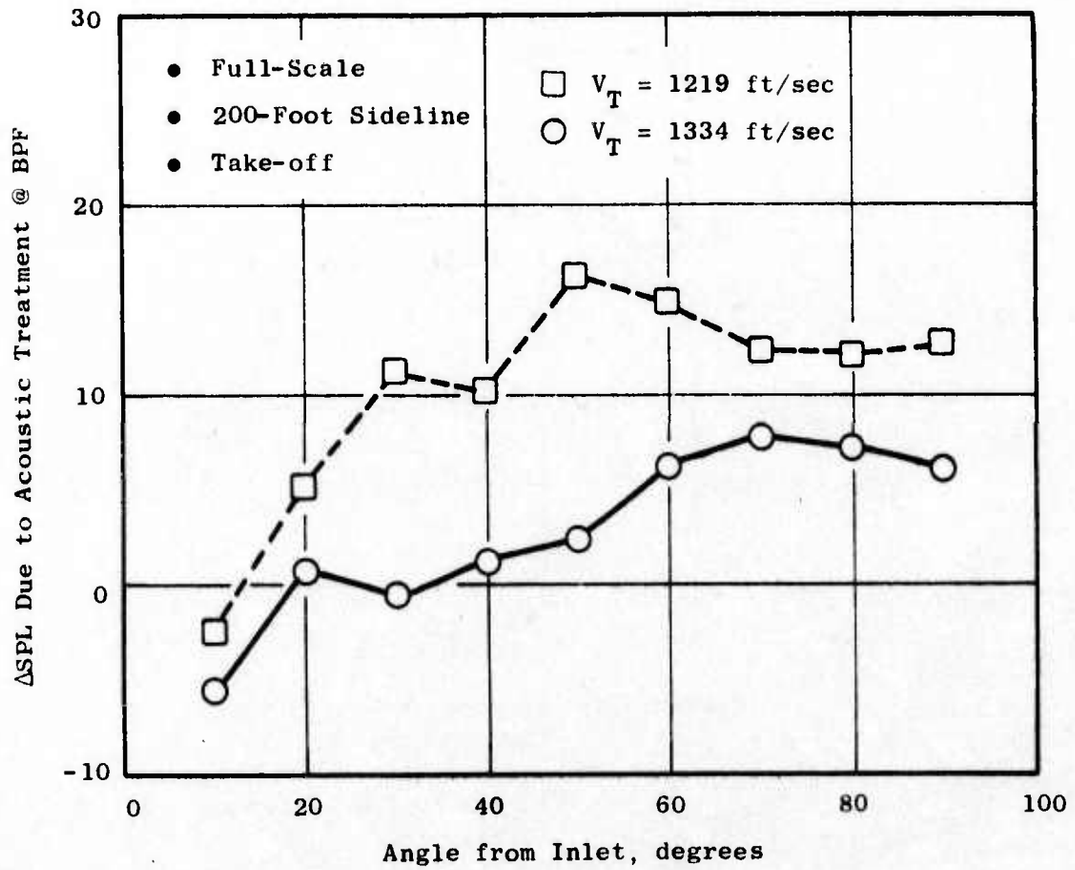

Figure 474. Treatment Effectiveness Comparison as a Function of Angle at Rotor 1 Blade Passing 1/3-Octave Band.

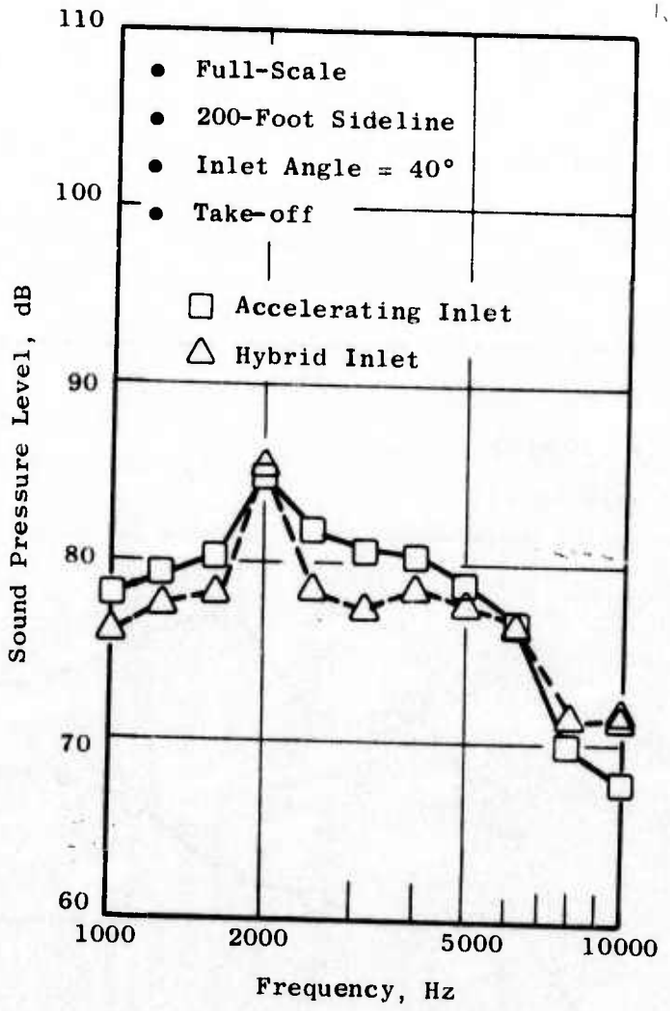

Figure 475. Comparison of 1/3-Octave Band Spectra for the Accelerating and Hybrid Inlets at the Operating Point.

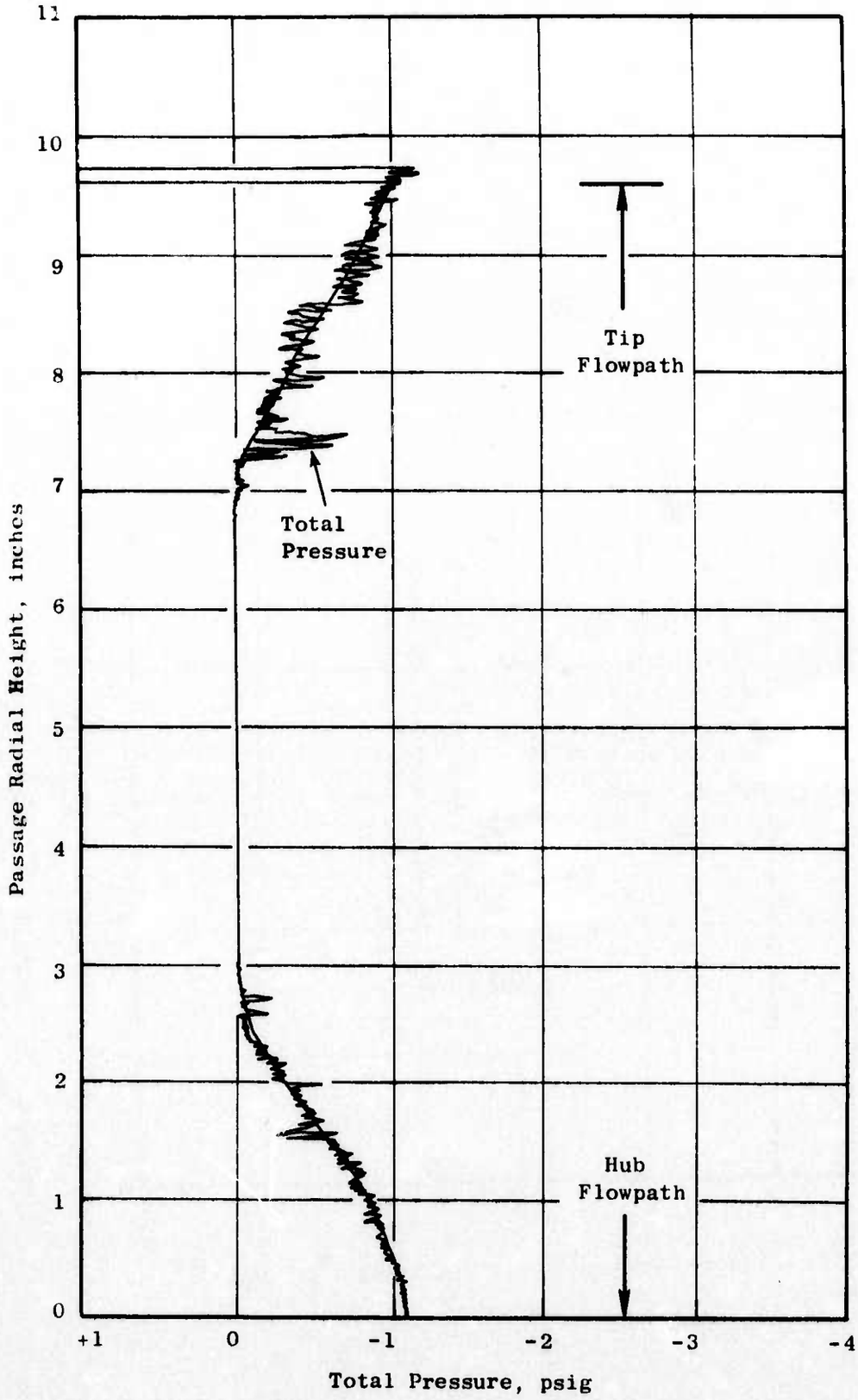

Figure 476. Typical Total-Pressure Traverse for the Takeoff Centerbody Position, BID's Closed, M_{th} = 0.771.

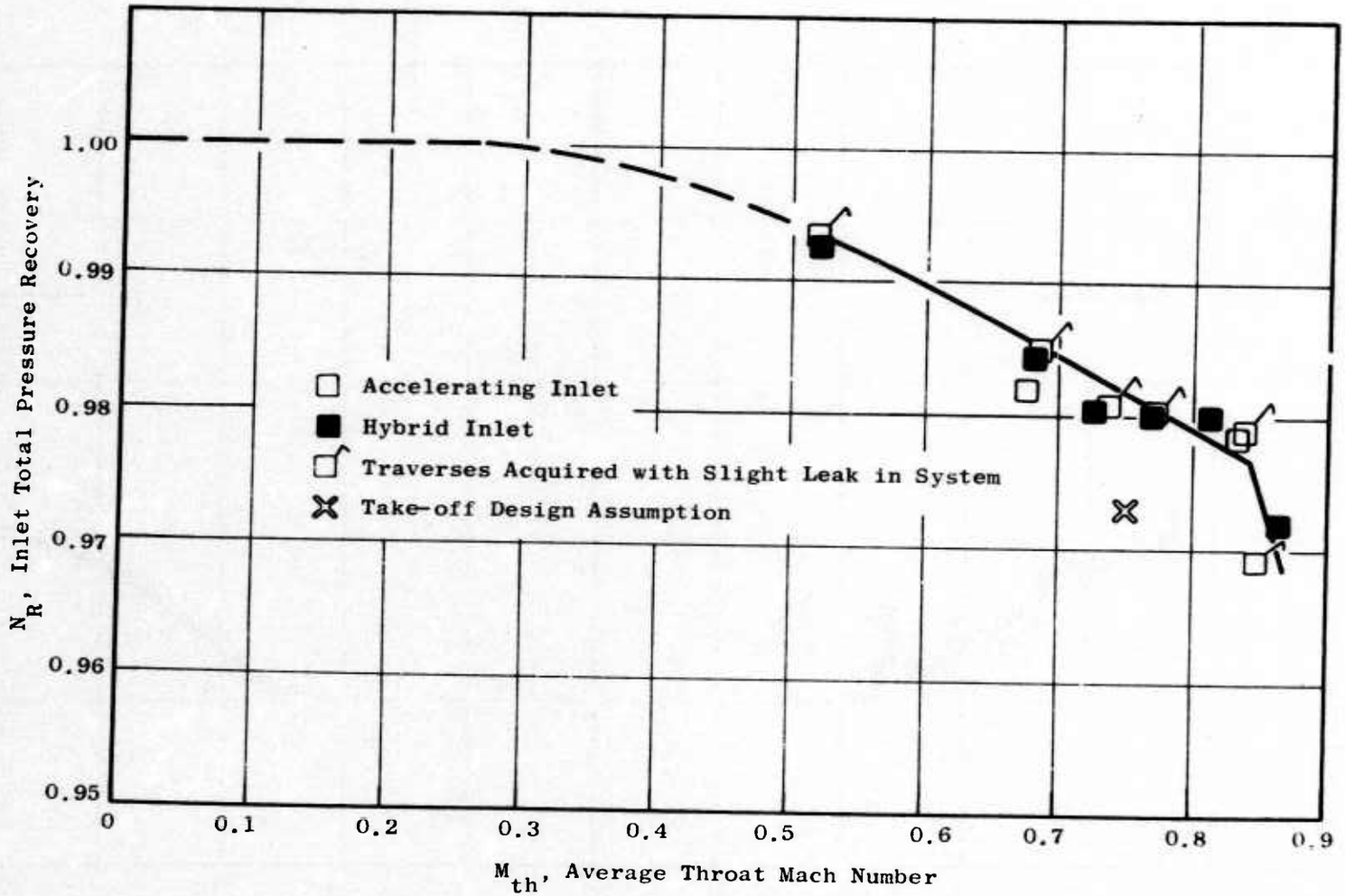

Figure 477. Inlet Total-Pressure Recovery Characteristic for the Take-off Operating Mode with BID Inlets Closed.

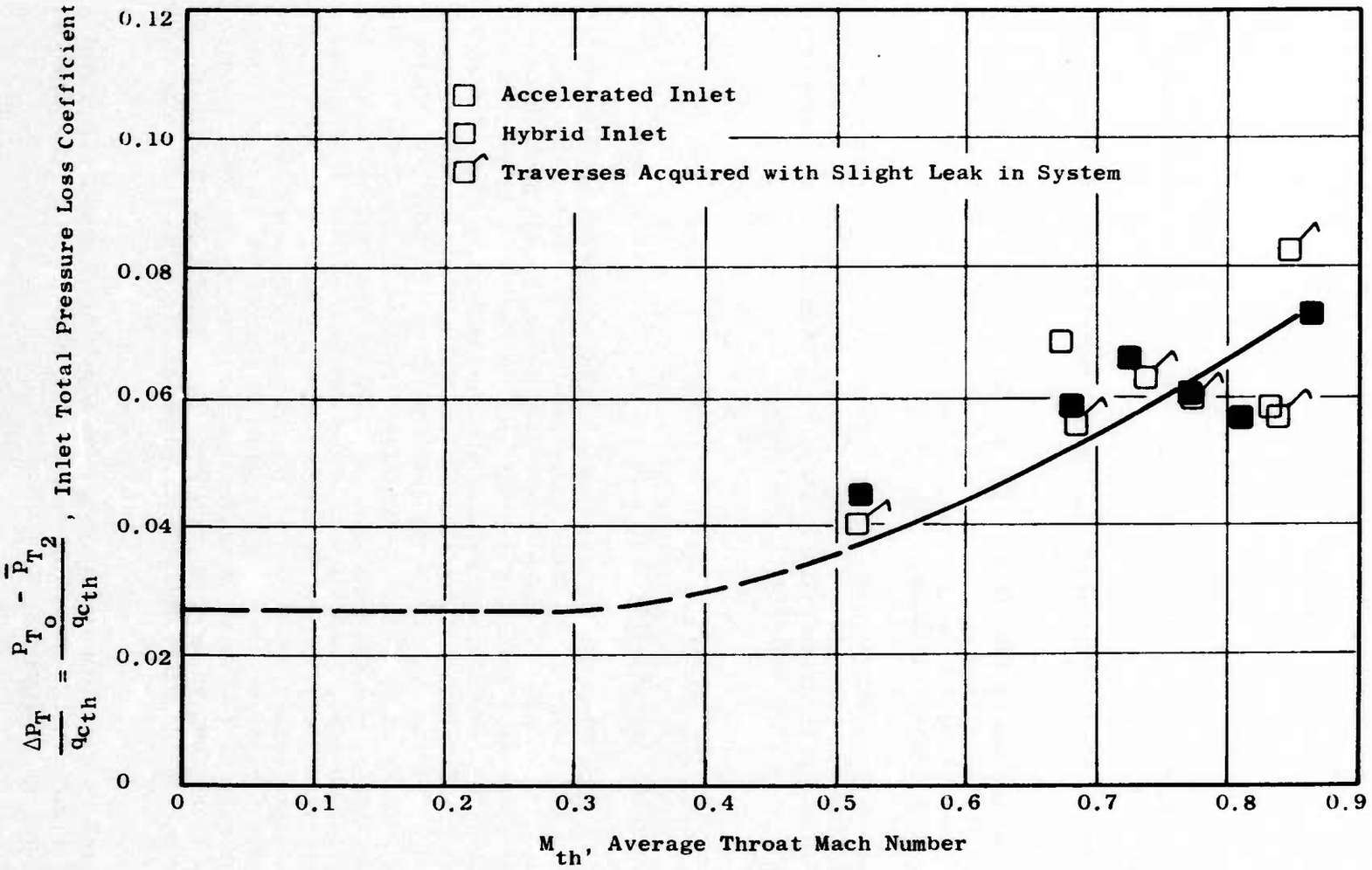

Figure 478. Inlet Total-Pressure Loss Coefficient Trend for the Take-off Operating Mode with BID Inlets Closed.

dynamic standpoint. In Figures 479 and 480, the predicted and measured wall Mach number distributions are shown. Good agreement between the measured and predicted distribution is demonstrated.

4.4.4.4 Summary

1. At the selected operating point (M_{th} = 0.77) the hybrid inlet in the take-off mode (BID closed) provides 15.5 ΔPNdB noise suppression relative to the baseline inlet.

2. Acceleration suppression was initiated at an inlet throat Mach number of M_{th} = 0.7.

3. At tip speeds up to 1230 ft/sec, the acoustic treatment provides from 5 - 6.5 PNdB suppression. Above this speed, however, there is a significant reduction in treatment effectiveness even for low inlet throat Mach number conditions (M_{th} = 0.60).

4. For the design point with the BID's closed, the total-pressure recovery is 0.98 for the take-off mode. There is no significant difference in the hybrid and accelerating inlets. Therefore, there is no performance penalty due to the addition of treatment.

4.4.5 Effect of Blow-In Doors

4.4.5.1 Introduction

Most airplanes designed for supersonic flight require some form of auxiliary air inlet as part of their induction system. This is because, in general, the capture area of the primary inlet is set by the supersonic flight condition. As a result, the inlet area is too small to provide good recovery and distortion performance with the characteristic sharp-lipped inlets for the high airflow take-off condition. Auxiliary inlets or "blow-in doors" are provided to reduce the flow drawn over the sharp lip into the primary inlet. The primary inlet generally operates separated at low forward speed take-off conditions, and the blow-in doors thus improve take-off thrust performance. In some systems, these blow-in doors may be designed to double as a bypass flow system for inlet/engine airflow matching at certain off-design supersonic flight conditions. At any rate, the blow-in doors provide another potential path for compressor noise propagation during the take-off condition. That is, not only must an attempt be made to suppress the compressor noise in the primary inlet, but it must be prevented from leaking out through the blow-in doors so as not to negate the effectiveness of the inlet noise suppression system.

This problem was addressed by providing six blow-in doors (described in Section 4.4.1.2.2) in the inlet frame area. The objectives of the blow-in door tests were as follows:

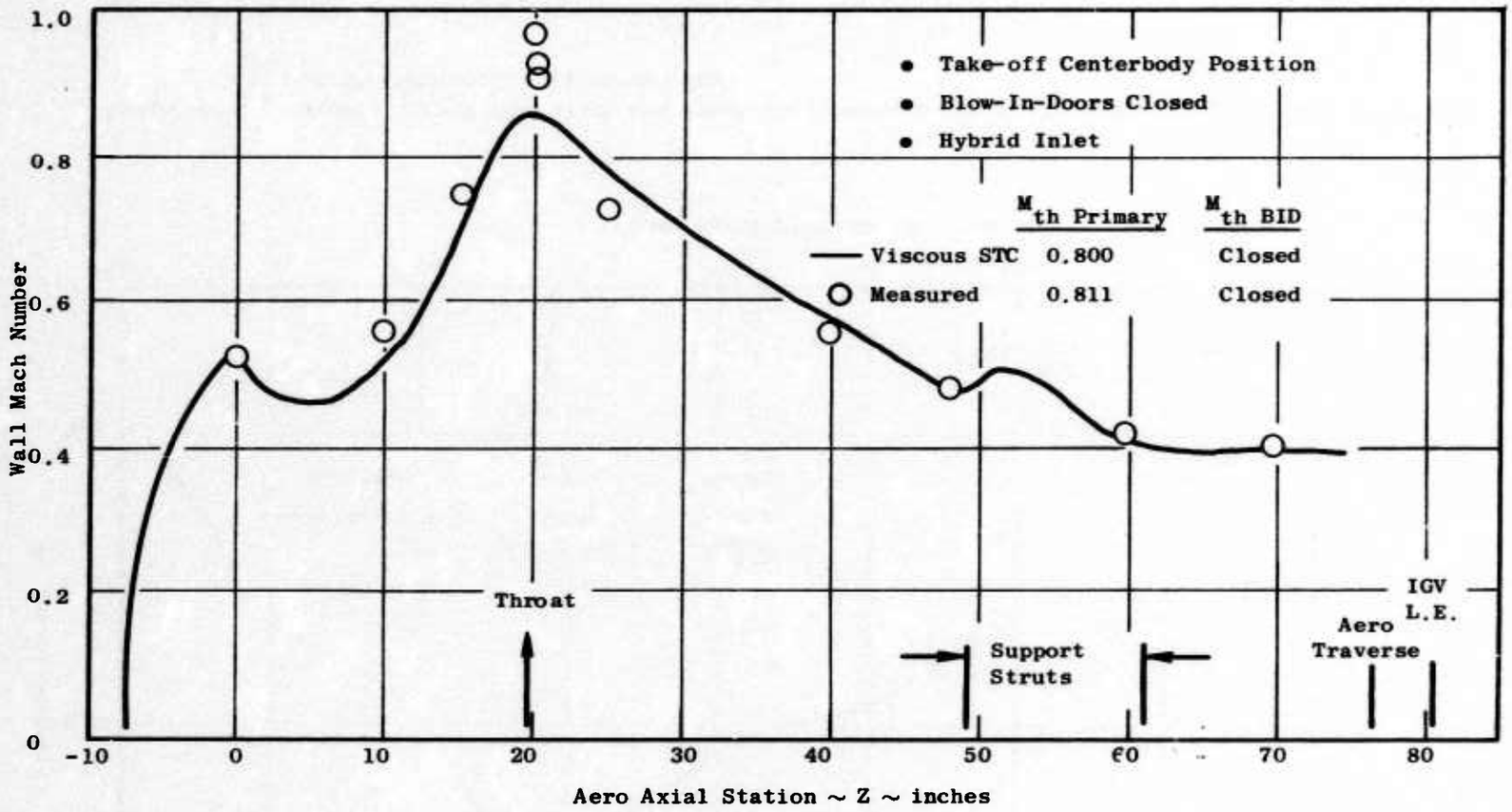

Figure 479. Comparison of Measured and Predicted Cowl Surface Mach Number Distributions for the Take-off Operating Mode.

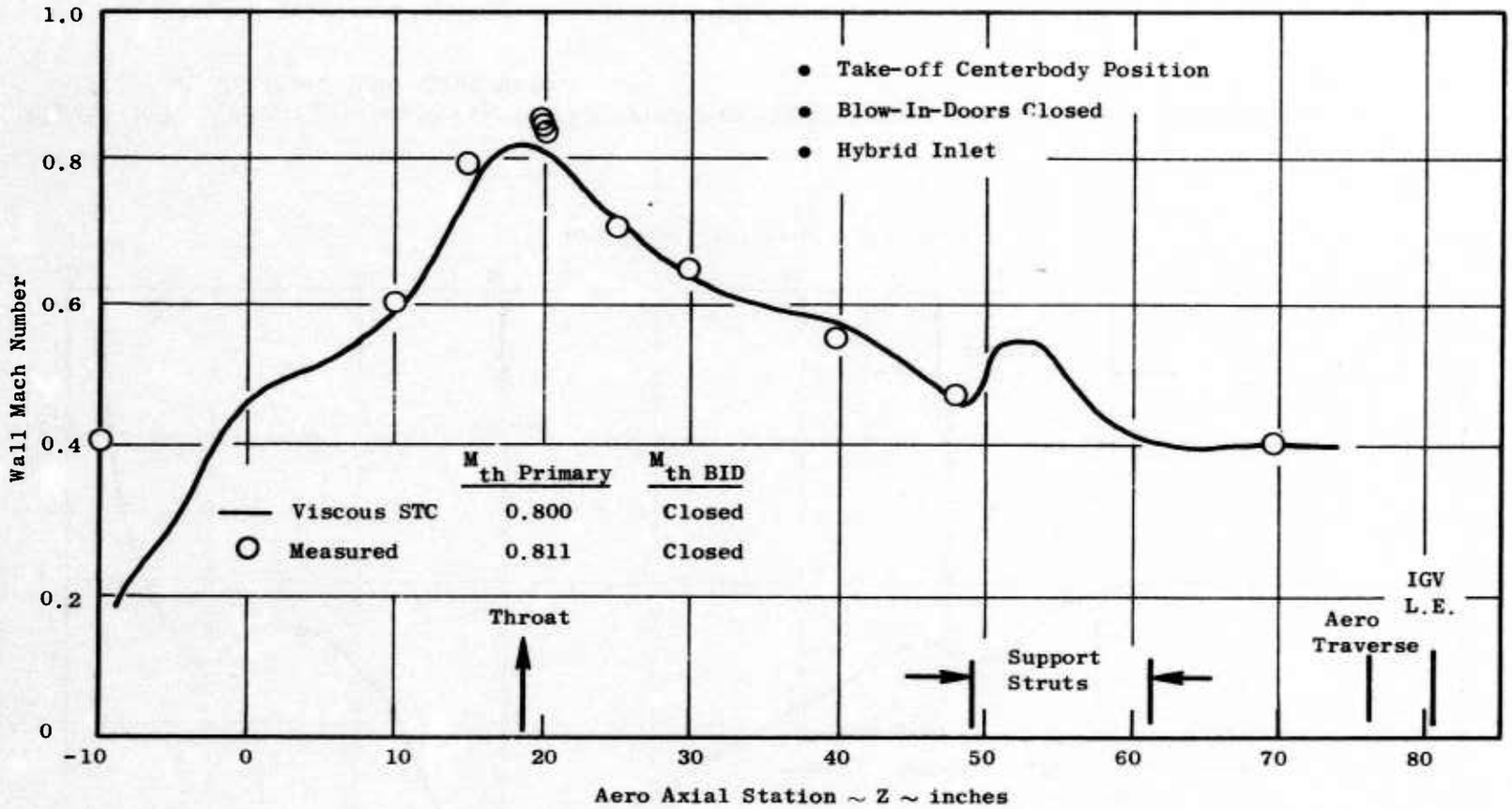

Figure 480. Comparison of Measured and Predicted Centerbody Surface Mach Number Distributions for the Take-off Operating Mode.

1. To evaluate the noise leakage through the doors

2. To partially suppress the noise leakage through the doors with acoustic treatment

3. To suppress the noise leakage through the doors with airflow acceleration (high Mach numbers) in the blow-in-door passage

The approach to meeting the second objective was simply to locate some acoustic treatment in the primary inlet between the compressor IGV's and the doors (see Figure 475). In order to meet the third objective, the doors were designed to be mechanically adjustable to three separate positions, referred to herein as nominal, 114% nominal, and 81% nominal. This was predicted to result in Mach numbers in the blow-in-door passage, relative to the primary inlet which were, respectively, equal to, higher than, and lower than the primary inlet. Thus, the amount of leakage and the effect of acceleration suppression on the leaked noise could be defined. Also, the effect of noise leakage through the blow-in doors could be isolated by comparison with the hybrid inlet results for the take-off mode with no BID's (i.e., BID's closed), described in Section 4.4.4.

4.4.5.2 Aerodynamic Performance

The test facility employed a flow collector with two venturis downstream of the low-pressure compressor to measure total inlet/compressor flow rate; no direct means of measuring the separate primary and auxiliary inlet flow rates was available. The scheme used for this flow-split determination was to correlate primary inlet flow, from the results with the BID's closed, with a wall static pressure measurement; infer primary inlet flow for the open BID configurations in this manner; and, deduct this primary inlet flow rate from the measured total flow to arrive at the residual, BID (total of all six passages) inlet flow. Streamtube curvature program results were used to facilitate and lend consistency to this procedure as follows. The primary inlet was analyzed over a wide range of flow rates in the take-off mode. Indicated wall Mach-number flow relationships were then plotted for several selected static taps, located on either surface somewhat forward of the physical throat (to preclude possible shock/boundary layer effects near the tested inlet choke point). These characteristics are shown in Figure 481; they were used to infer inlet flow rate for various test points. The difference between this inferred flow and the actual measured flow was then determined and is presented, as a percent of measured flow, versus measured flow in Figure 482. Based on these results, the centerbody pressure tap at aero station 10.0 correlated best with the measurements. A line was faired through the corresponding data of Figure 482 as shown, and this characteristic was then used, in conjunction with the appropriate curve of Figure 481, to determine primary inlet flow with BID's open, from a single static pressure measurement. The assumption implicit in this procedure is that the primary inlet aerodynamic characteristics are a function only of primary passage corrected flow and do not depend on auxiliary inlet setting or total inlet flow.

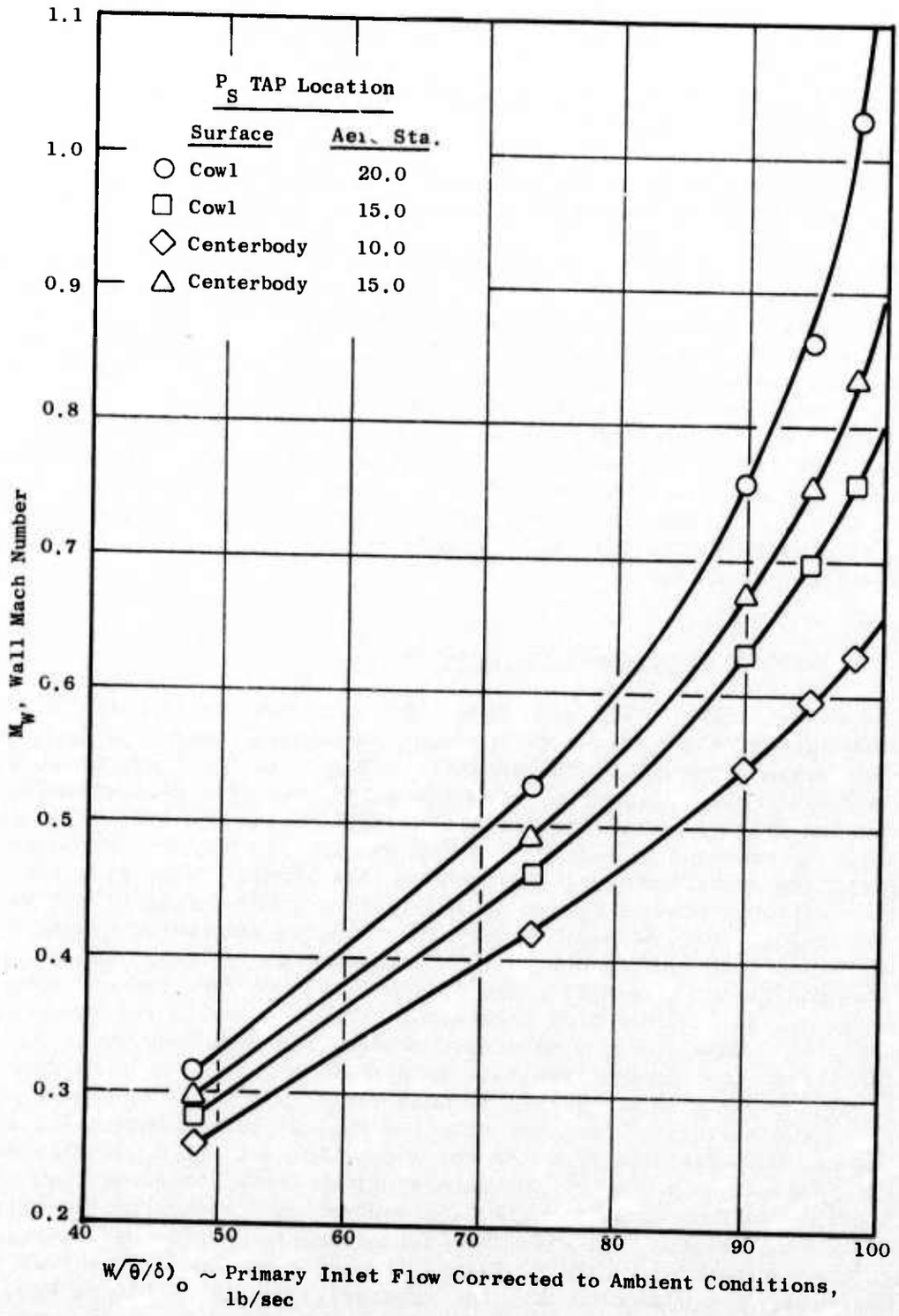

Figure 481. Analytical Correlation of Wall Mach Number and Flow for Primary Inlet in Take-off Mode.

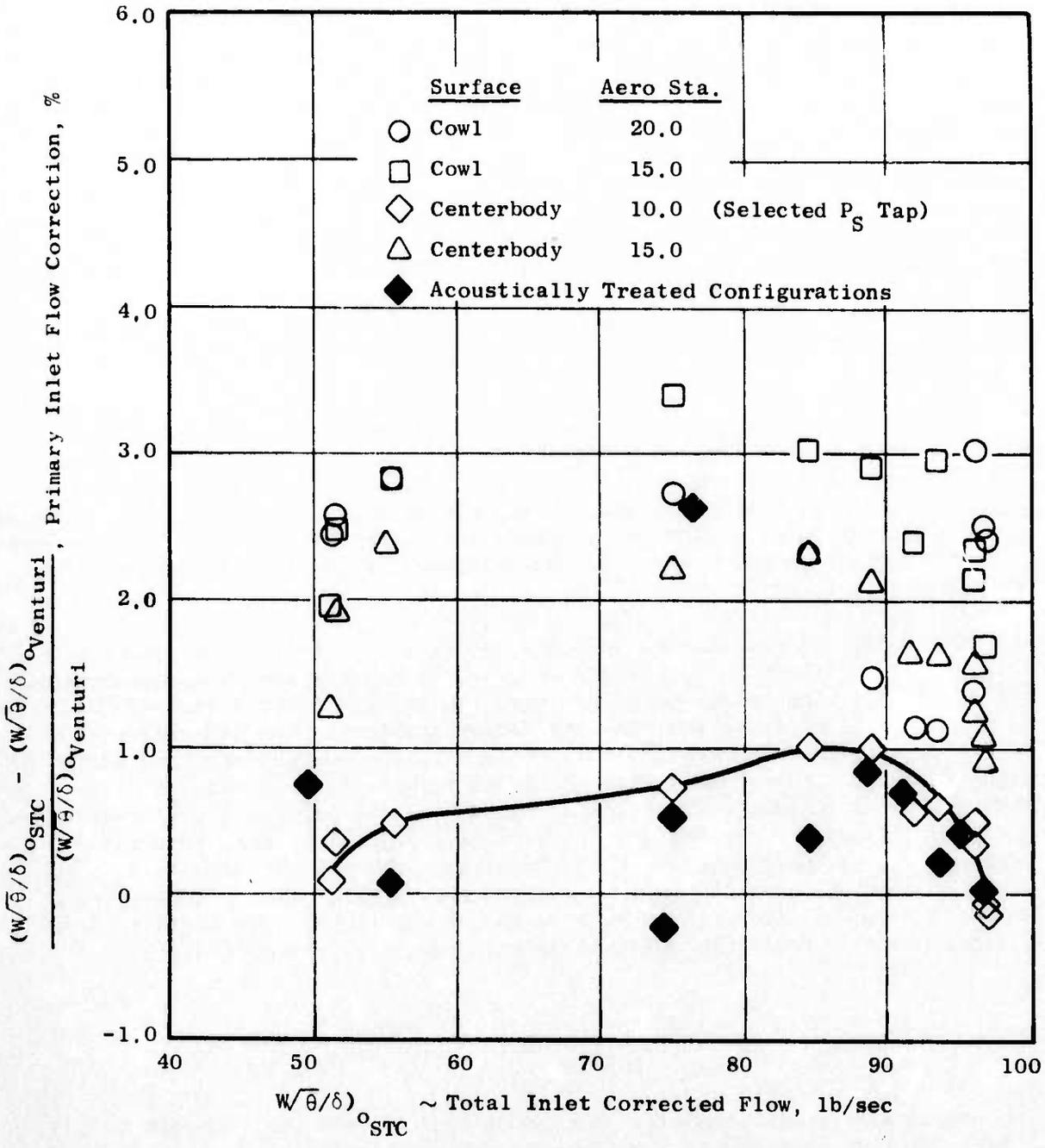

Figure 482. Analytical-to-Actual Primary Inlet Flow Correction Factor.

With this methodology, the individual passage flow rates and throat Mach numbers may be determined and compared to objective values. This has been done in Figures 483 through 486. Figure 483 shows (total) BID corrected flow as a function of total inlet corrected flow for the three BID configurations. A linear relationship prevails over the range of test conditions of interest. The design values estimated from the STC design analysis are noted for comparison. It is apparent that, while the smallest (81% of nominal) BID throat area design performed about as intended, the nominal and largest (114%) BID settings appear to be roughly 14% and 21% deficient in design flow, respectively. While some deviation is inherent in the nature of the scheme employed to determine BID flow, i.e. taking the difference of two numbers of comparable magnitude, these values exceed a reasonable allowance for that factor. Figures 484, 485, and 486 express this same trend in different formats: BID M_{th} versus primary M_{th}, primary M_{th} versus total inlet corrected flow, and BID M_{th} versus total inlet corrected flow, respectively.

These data all suggest that, for a given total inlet/compressor flow rate, relatively more flow passed through the primary inlet and less through the BID inlet than desired, excluding the 81% BID throat area setting which performed about as designed. This result may be due to a larger total-pressure loss in the BID inlet than in the primary inlet, relative to the design values of 0.973 primary recovery and 0.980 BID recovery, upon which the design flow estimates were based.

The foregoing explanation is borne out by the primary inlet recovery data previously shown in Figure 477 and the BID inlet recovery characteristics of Figure 487. The former data indicated the primary inlet's recovery to be about 0.8 point above the take-off design estimate. The BID recovery levels were determined from the measured overall recovery levels and the assumption that the primary inlet continues to perform as it did with the BID closed. This implicitly assumes that all losses occurring aft of the door trailing edge, i.e., mixing and flow redistribution, are arbitrarily "caused" by, or assignable to, the BID system. The BID recovery is calculated as that value which, when it and the appropriate primary recovery are weighted by their respective effective flow areas at the door trailing edge (mixing plane), yields the measured overall recovery. Symbolically:

$$\eta_{R_{overall}} \equiv \frac{(A_{pri})_{TE}}{(A_{pri} + A_{BID})_{TE}} \eta_{R_{pri}} + \frac{(A_{BID})_{TE}}{(A_{pri} + A_{BID})_{TE}} \eta_{R_{BID}}$$

The BID total-pressure recovery characteristics (Figure 487) exhibit relatively poor performance - well below the design recovery value. The loss coefficient data, shown in Figure 488, indicate that the increased loss experienced with the BID's open generally exceeds a dump loss from the throat flow conditions.

For reasons to be discussed, entrance losses are not felt to be a significant factor in this situation. Indeed, the total-pressure traverses of Figures 489 through 491 suggest that flow mixing is inefficient, since the

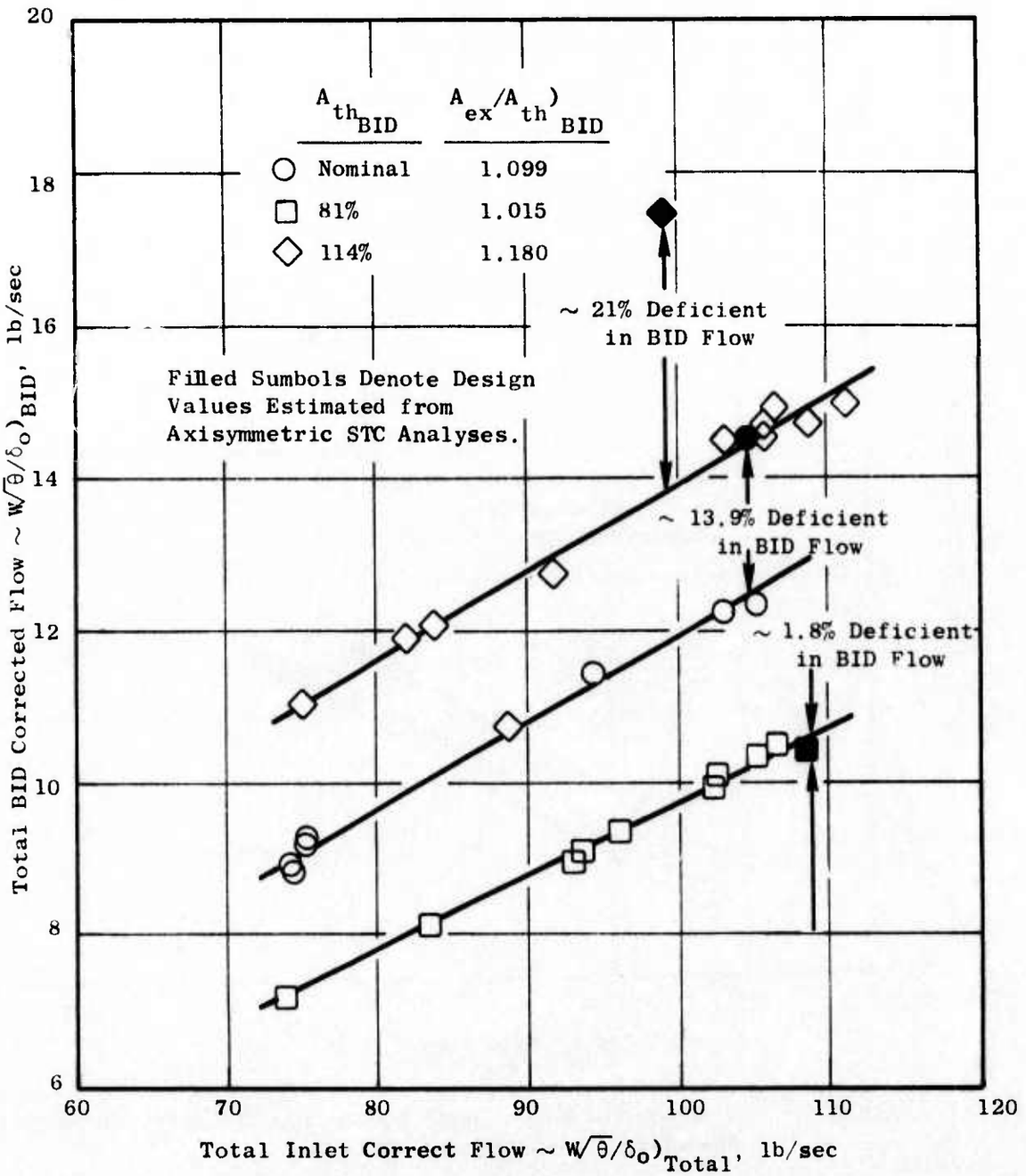

Figure 483. Comparison of Measured and Predicted BID Passage Flow Characteristics.

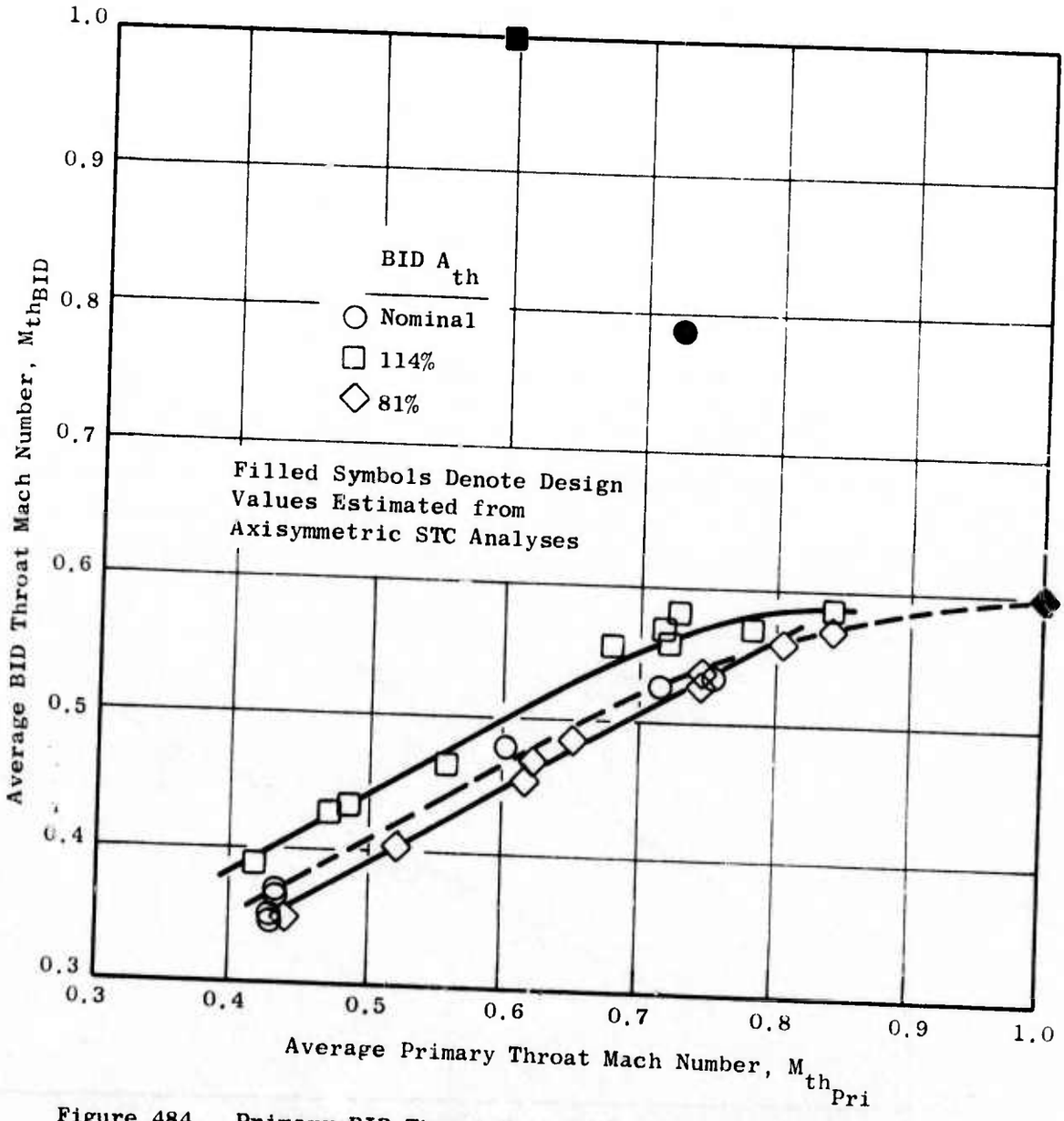

Figure 484. Primary-BID Throat Mach Number Relationship, Comparison of Measurements and Design Predictions.

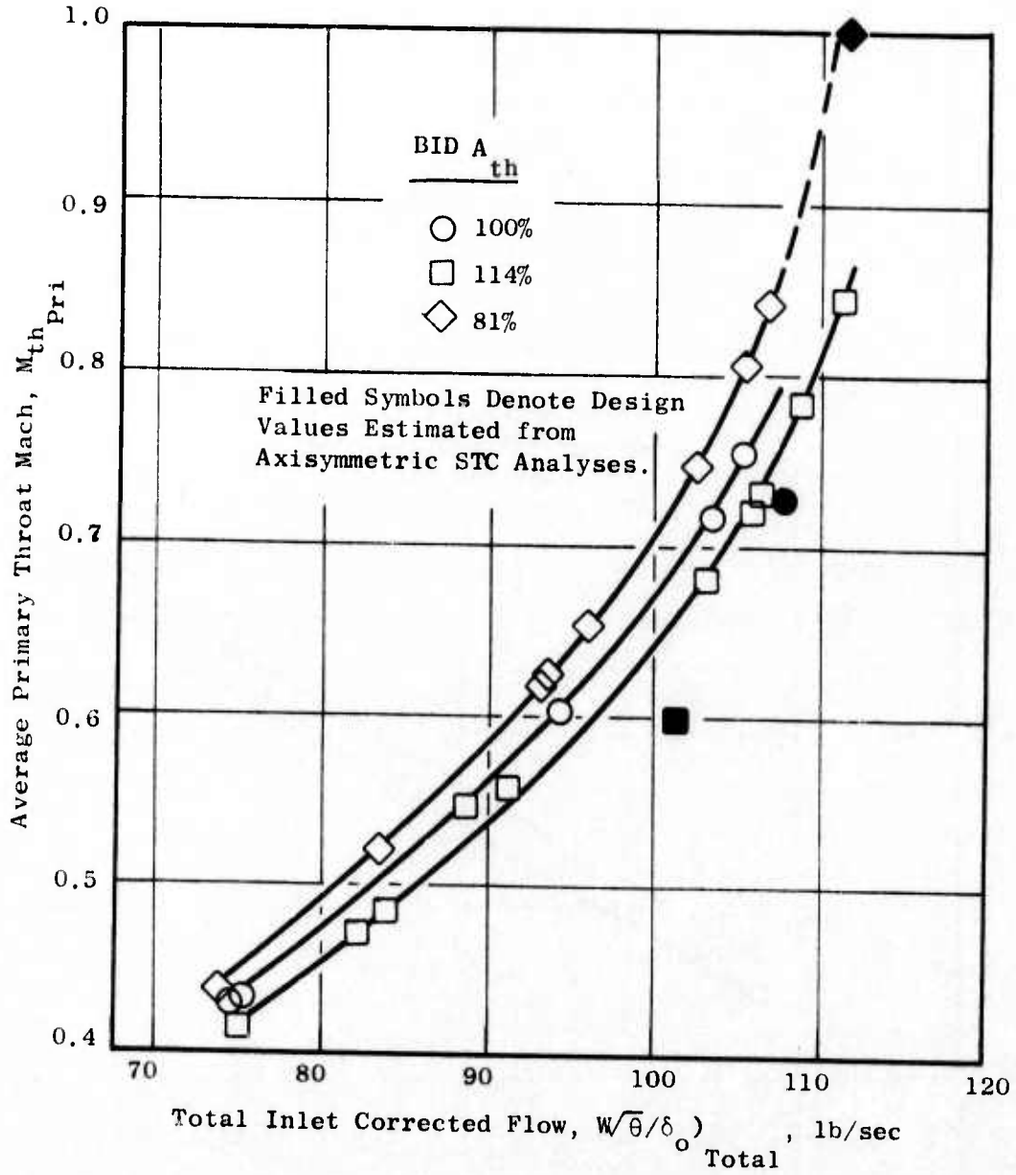

Figure 485. Primary Throat Mach Number, Flow Characteristic.

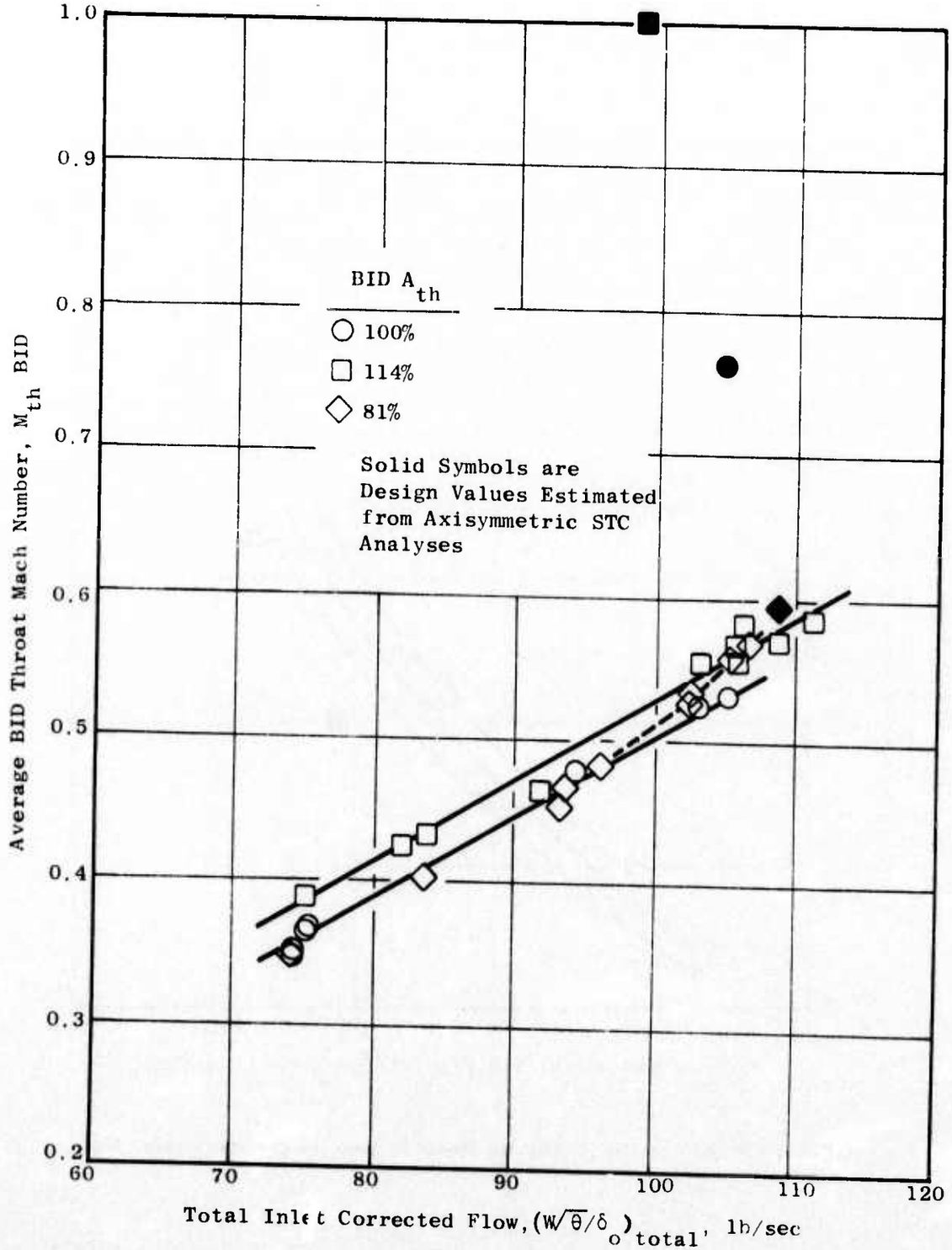

Figure 486. BID Throat Mach Number, Flow Characteristic.

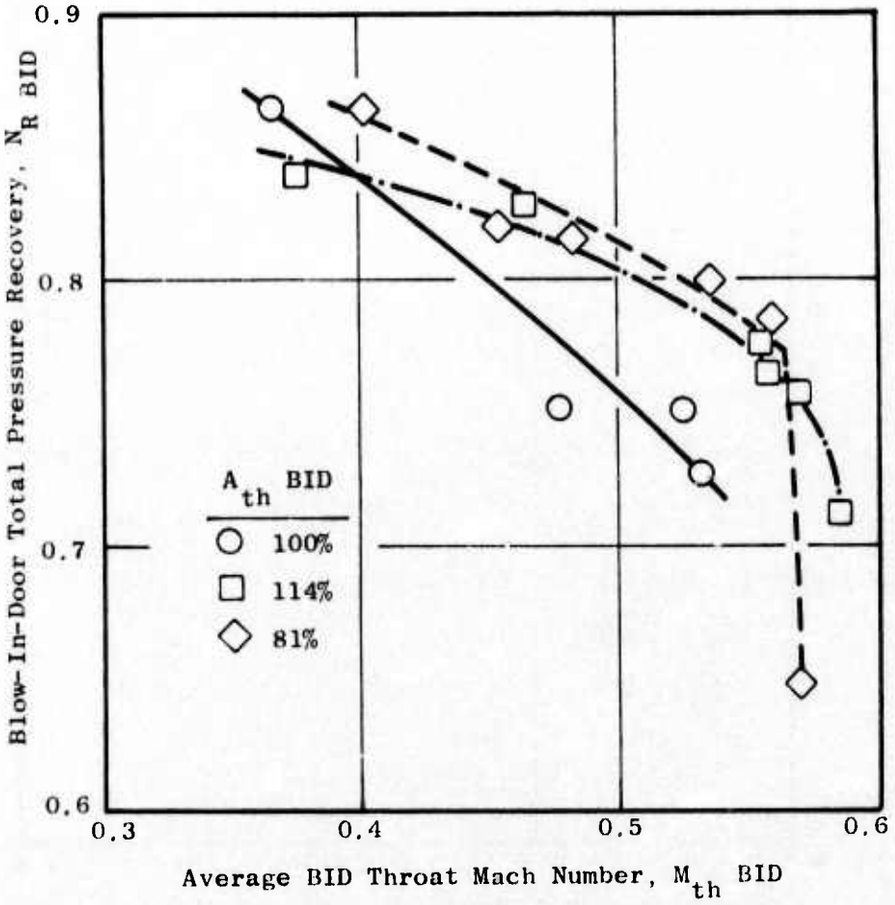

Figure 487. Blow-In Door Total-Pressure Recovery Characteristics.

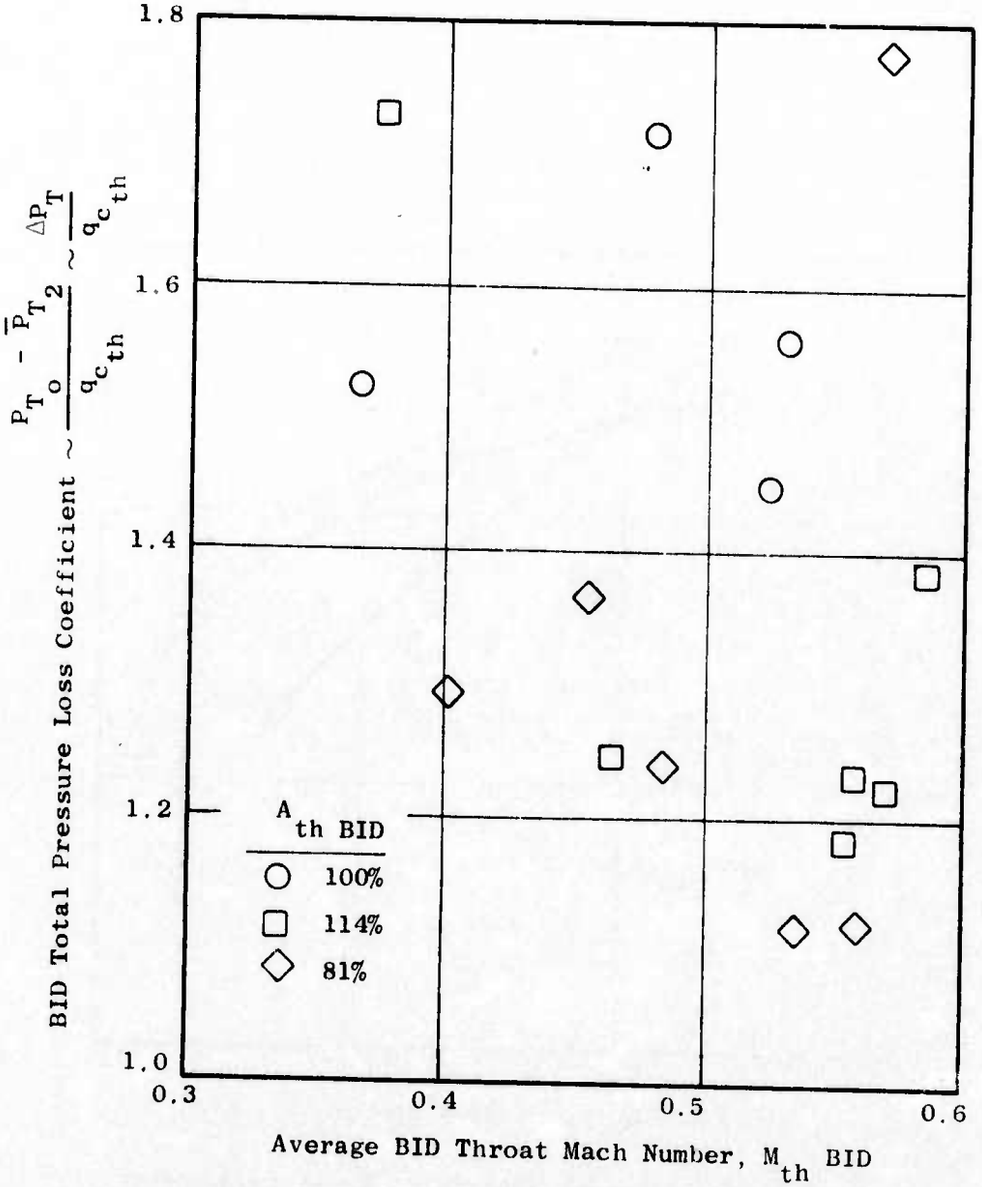

Figure 488. BID Total-Pressure Loss Coefficient Trends.

total pressure deficit is still present radially inward of the predicted door trailing edge streamline location, i.e., in the primary flow zone which is relatively "clean" when the BID's are closed (see Figure 476).

It is felt that this performance degradation may be due to a combination of: 1) the BID side plates, which are uncontoured; 2) the fact that the primary flow boundary layer is relatively thick and "tired" as it approaches the support strut (due to the diffusion already accomplished and the lack of any boundary layer control feature) and 3) to the irregularly shaped primary flow passage formed by the struts and depressed BID "chutes". It may also be noted that the two larger BID configurations (Figures 489 and 490) exhibit a flat (separated) total pressure for several inches inward from the tip flowpath, while the smallest BID (Figure 491) has a gradually increasing total-pressure characteristic of a boundary layer and consistent with its performance advantage (Figure 487).

Wall Mach number characteristics, calculated from measured static pressures, do not exhibit any flow separation in either the primary or BID passages. Primary inlet data are shown in Figures 492 through 497 for each of the three BID configurations. Agreement with the STC predictions is good, allowing for the slight difference in throat Mach numbers and the absence of the BID system in the STC analysis. Corresponding data for the BID passage and internal door surface are presented in Figures 498 through 500. No comparisons with analytical predictions are given, due to the aforementioned BID geometry difference between the STC model and the actual test article. However, the following observations of these data may be made:

- Indicated peak wall Mach numbers are consistent with the average BID throat Mach numbers determined as previously outlined: i.e., the average throat Mach numbers are somewhat less than the maximum local wall values, as would be expected, due to wall curvature effects. It should be noted that, if anything, the wall Mach numbers are overstated since they do not reflect entrance total-pressure losses.

- No flow separation or anything that would suggest the relatively poor performance measured by the downstream total-pressure traverse is indicated. A smooth acceleration and deceleration is seen (except for the 81% nominal configuration, where no significant diffusion is expected due to the design throat being located within ~0.3 inch of the trailing edge). Taps on either side of the door near the trailing edge indicate essentially equal static pressures; exact agreement is not expected, since the nearest taps are 0.22 - 0.2 inch from the trailing edge and different doors were instrumented for each surface - relatively thin door section thickness necessitated this.

As a further check on the BID passage wall pressure data, they were compared with one-dimensional values based on physical orthogonal flow areas and ambient pressure (consistent with the test data reduction procedure). The results are presented in Figures 501 through 503, corresponding

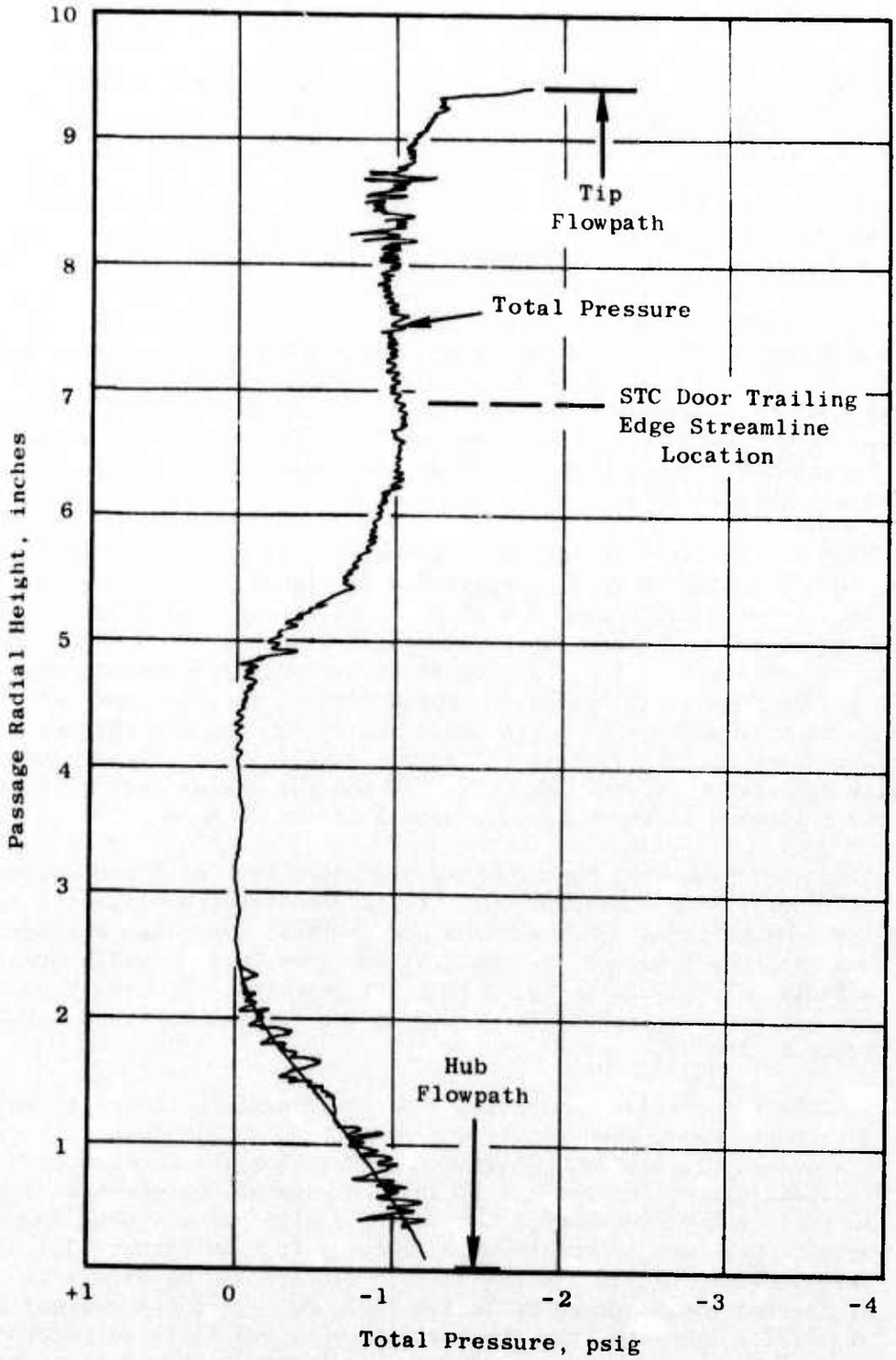

Figure 489. Total-Pressure Traverse for Nominal Blow-In-Door Configuration, $M_{th_{Pri}} = 0.755$, $M_{th_{BID}} = 0.532$.

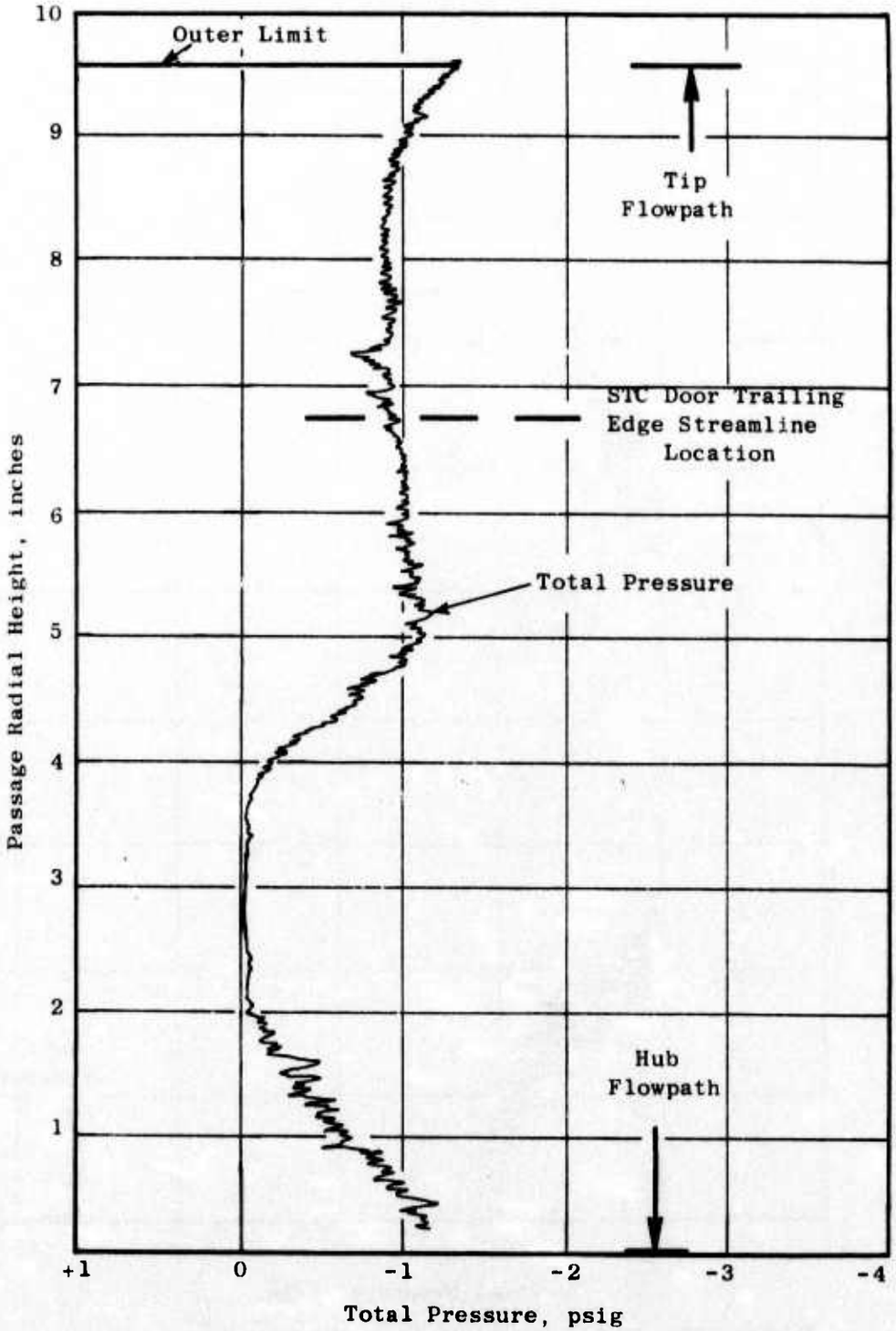

Figure 490. Total-Pressure Traverse for 114% A_{th} Blow-In-Door Configuration, $M_{th_{Pri}} = 0.783$; $M_{th_{BID}} = 0.570$.

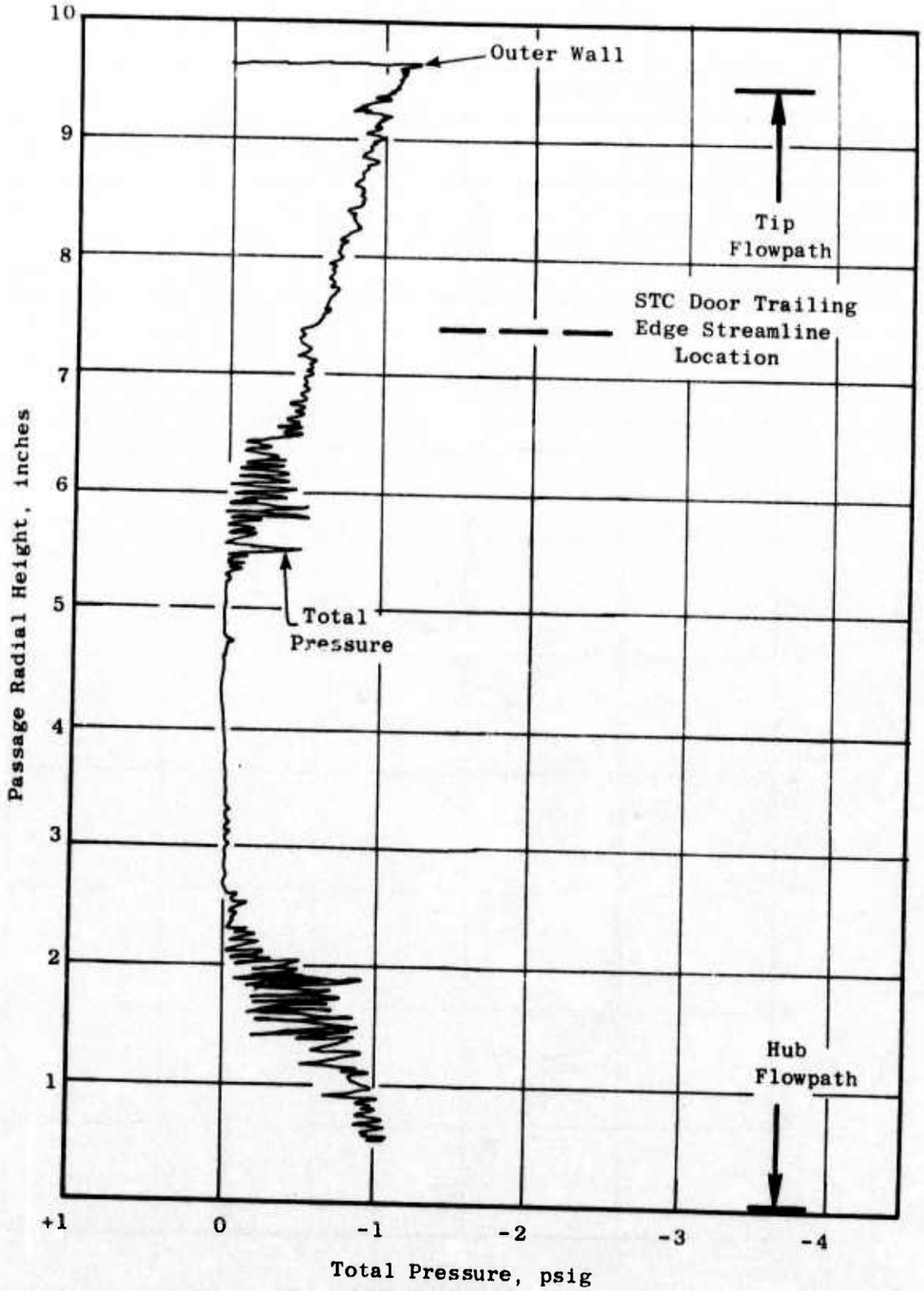

Figure 491. Total-Pressure Traverse for 81% A_{th} Blow-In-Door Configuration, $M_{th_{Pri}} = 0.746$, $M_{th_{BID}} = 0.536$.

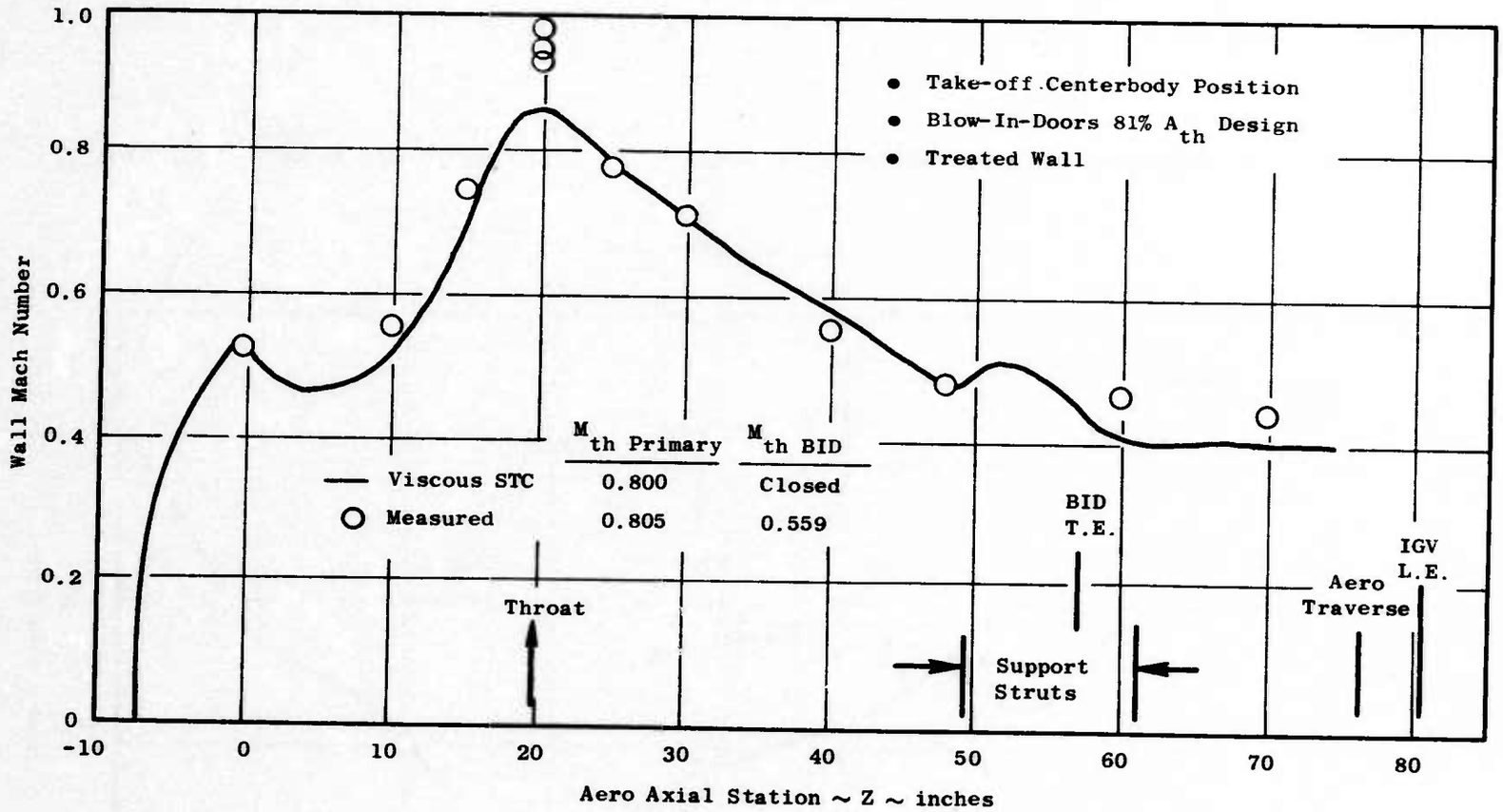

Figure 492. Comparison of Measured and Predicted Cowl Surface Mach Number Distributions for 81% A_{th} BID Configuration.

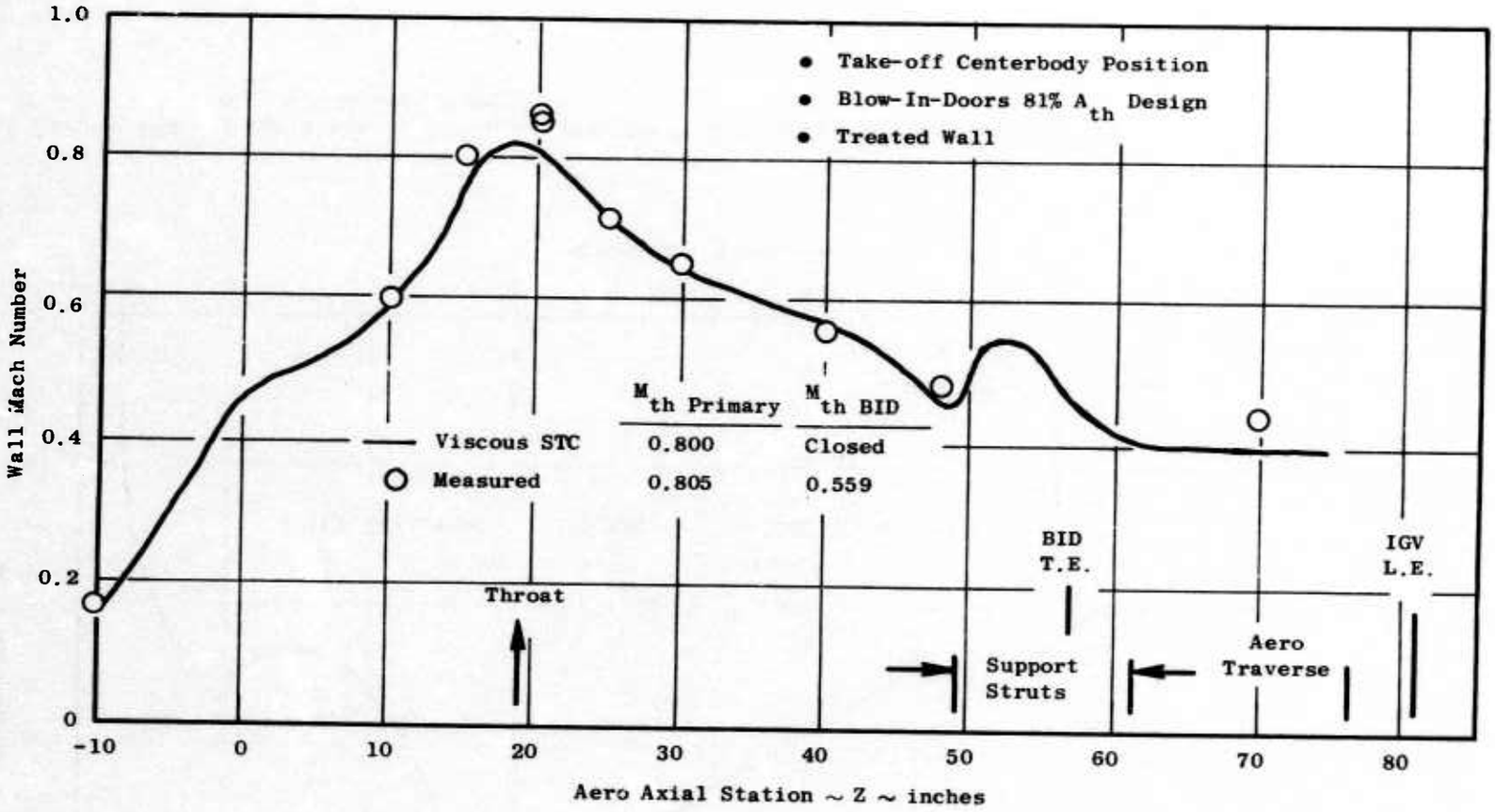

Figure 493. Comparison of Measured and Predicted Centerbody Surface Mach Number Distribution for 81% A_{th} BID Configuration.

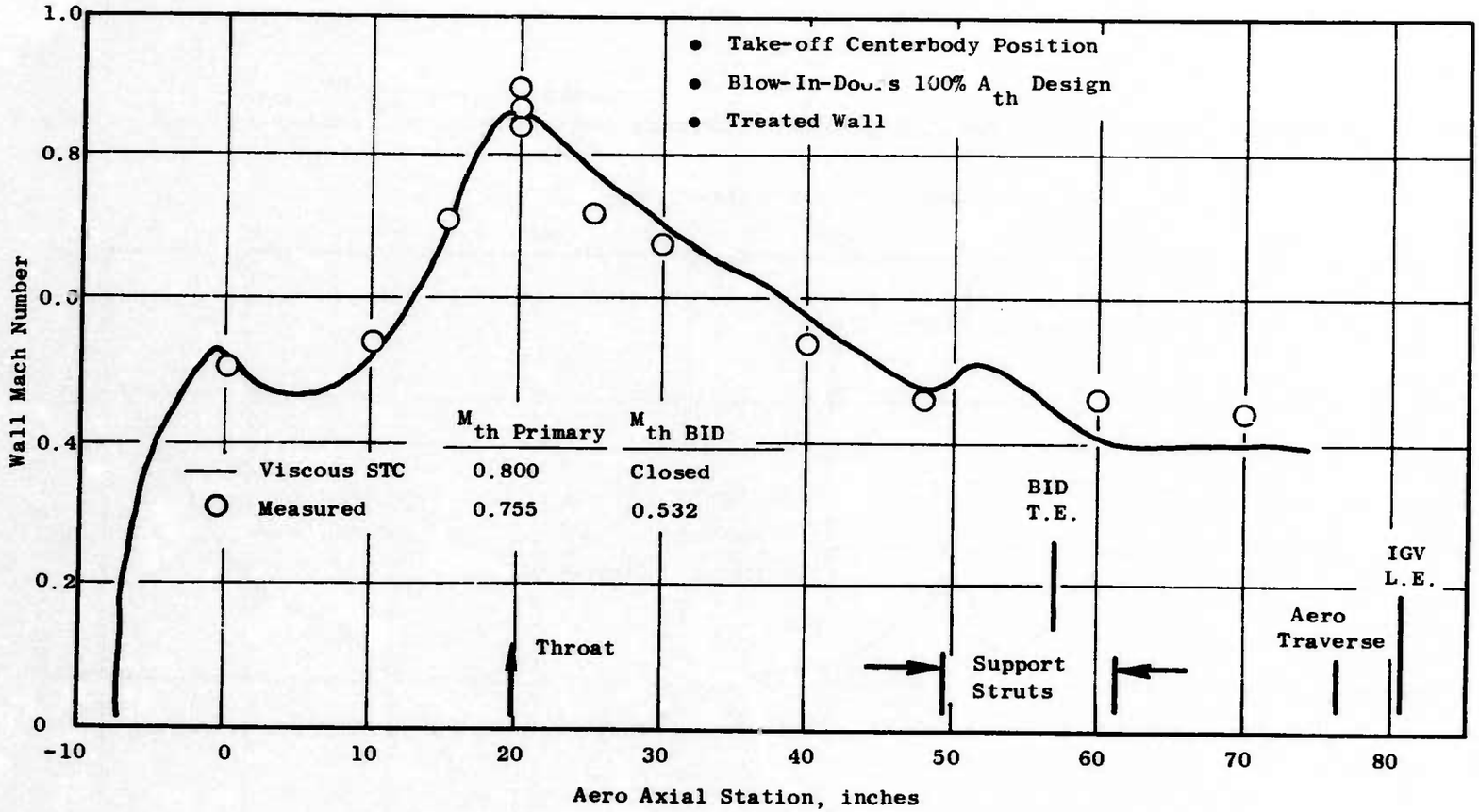

Figure 494. Comparison of Measured and Predicted Cowl Surface Mach Number Distributions for 100% A_{th} BID Configuration.

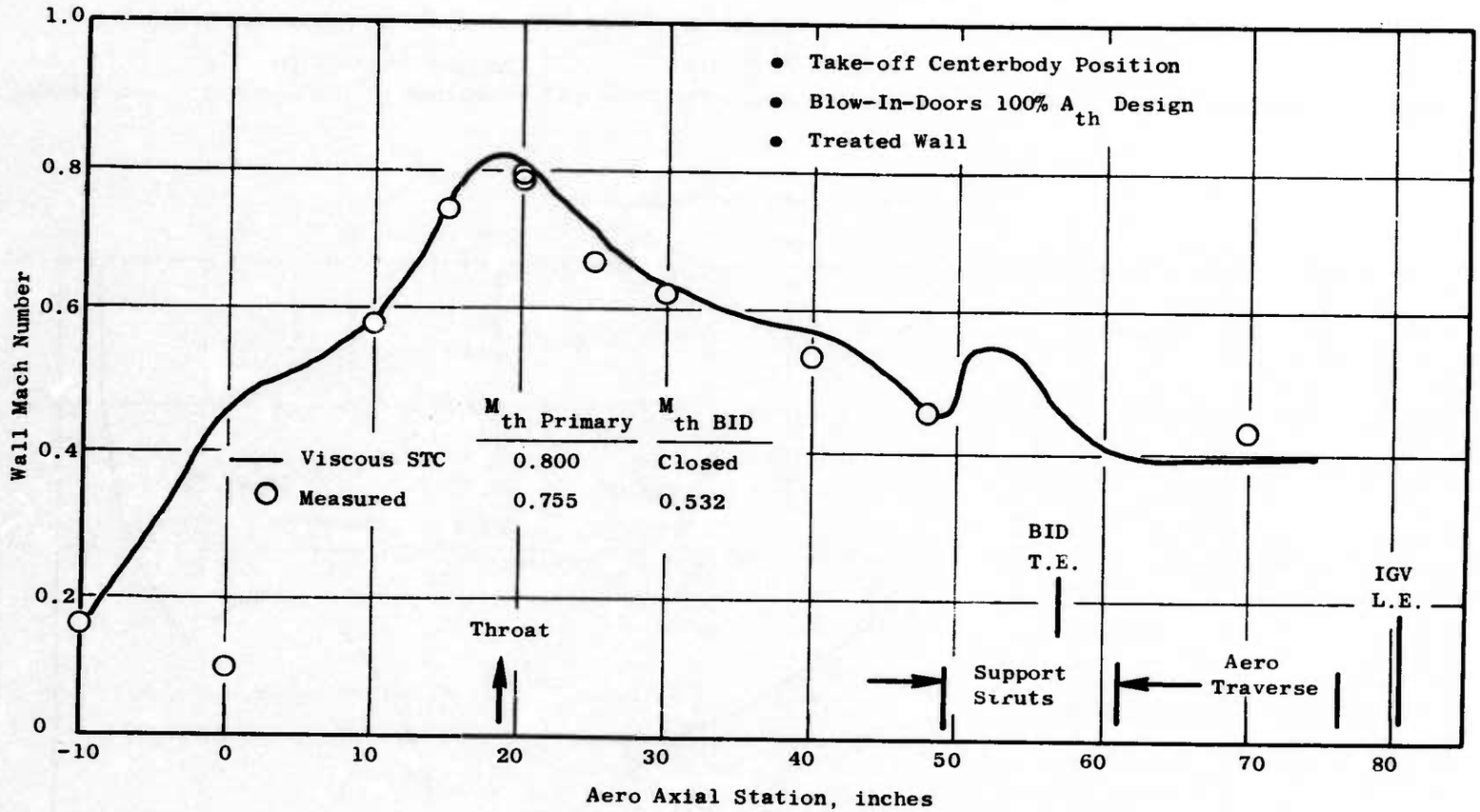

Figure 495. Comparison of Measured and Predicted Centerbody Support Mach Number Distributions for 100% A_{th} BID Configuration.

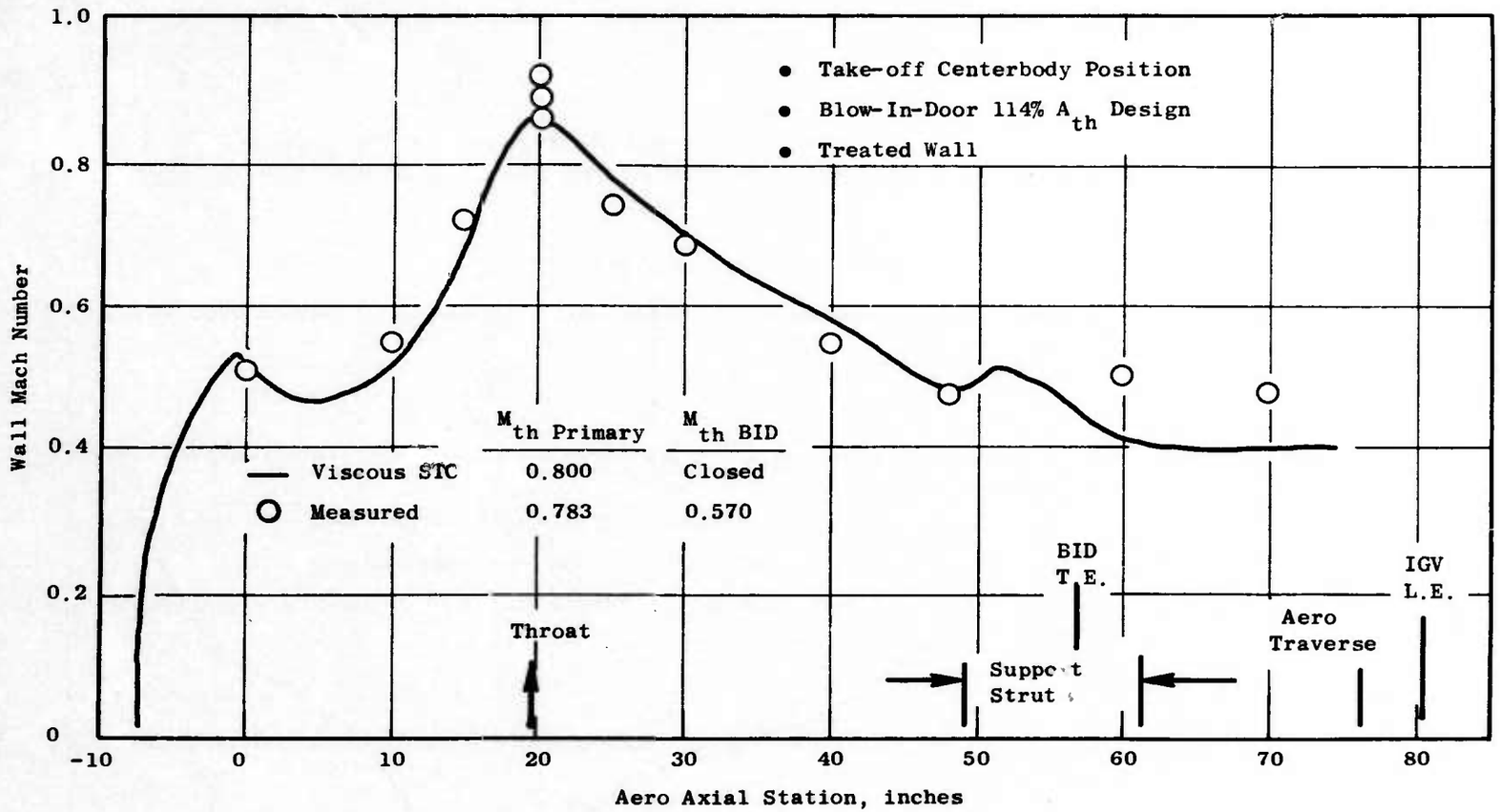

Figure 496. Comparison of Measured and Predicted Cowl Surface Mach Number Distributions for 114% A_{th} BID Configuration.

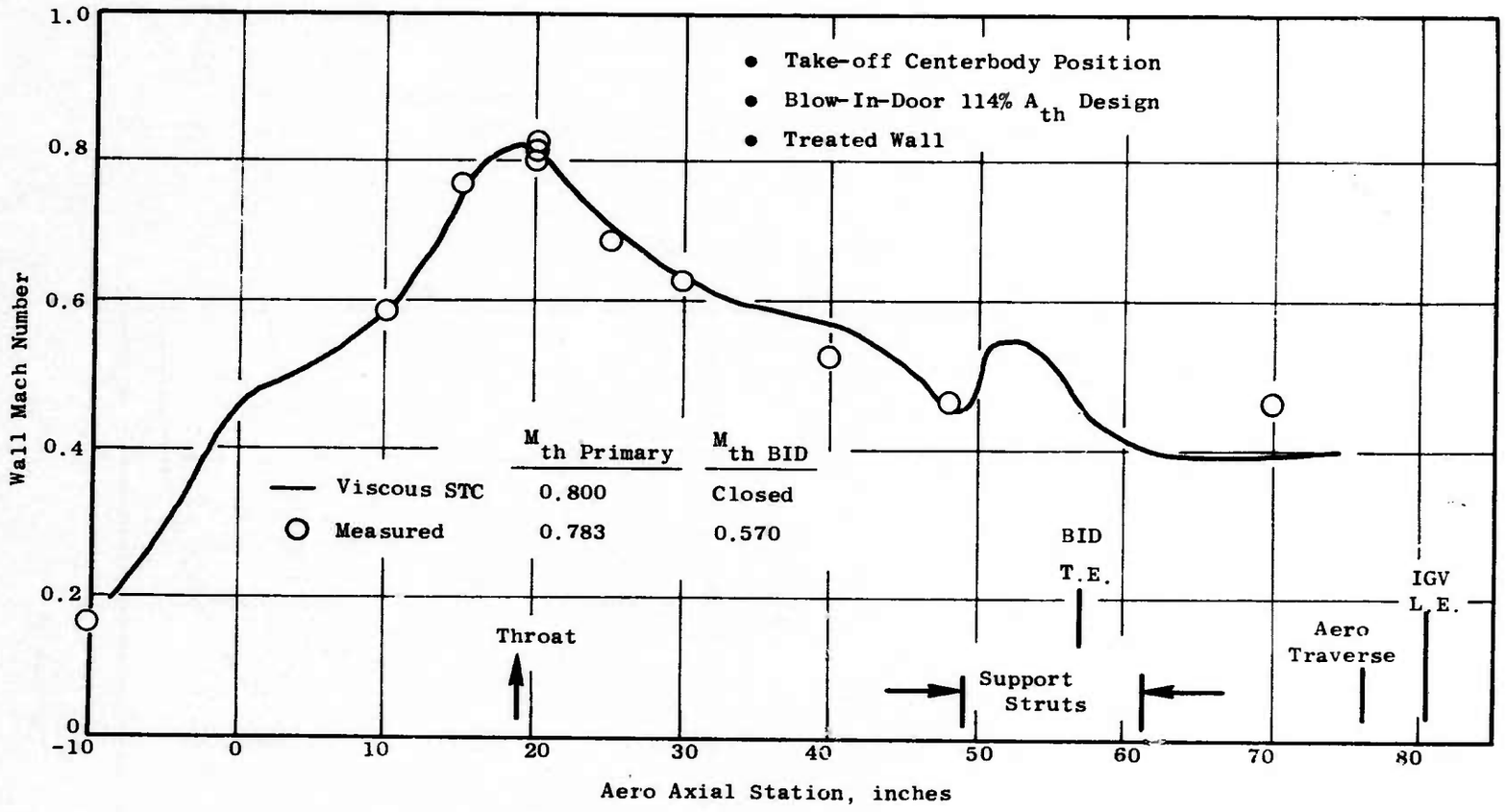

Figure 497. Comparison of Measured and Predicted Centerbody Surface Mach Number Distributions for 114% A_{th} BID Configuration.

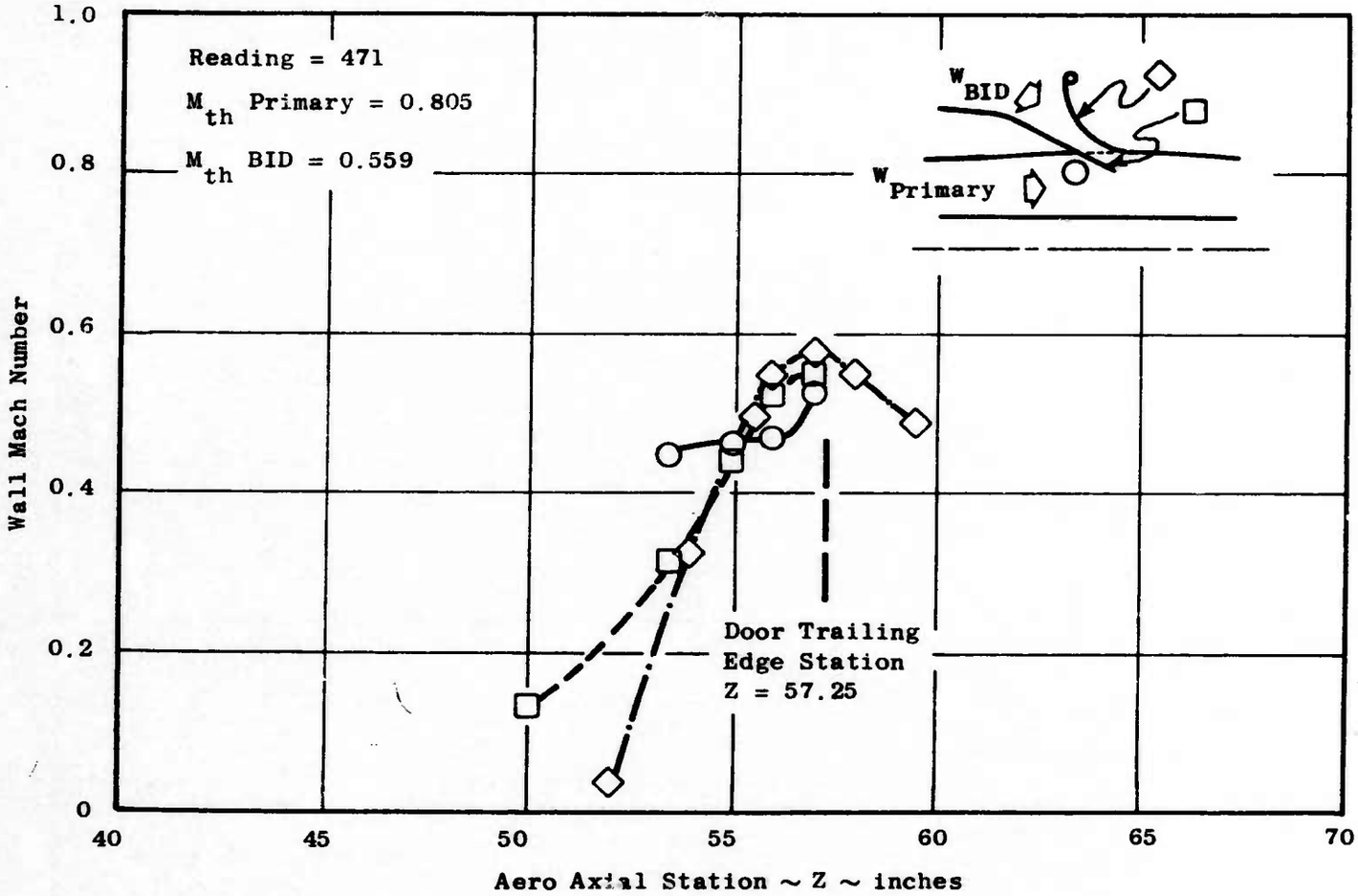

Figure 498. Measured Blow-In-Door Wall Mach Number Distributions for the 81% A_{th} BID Setting.

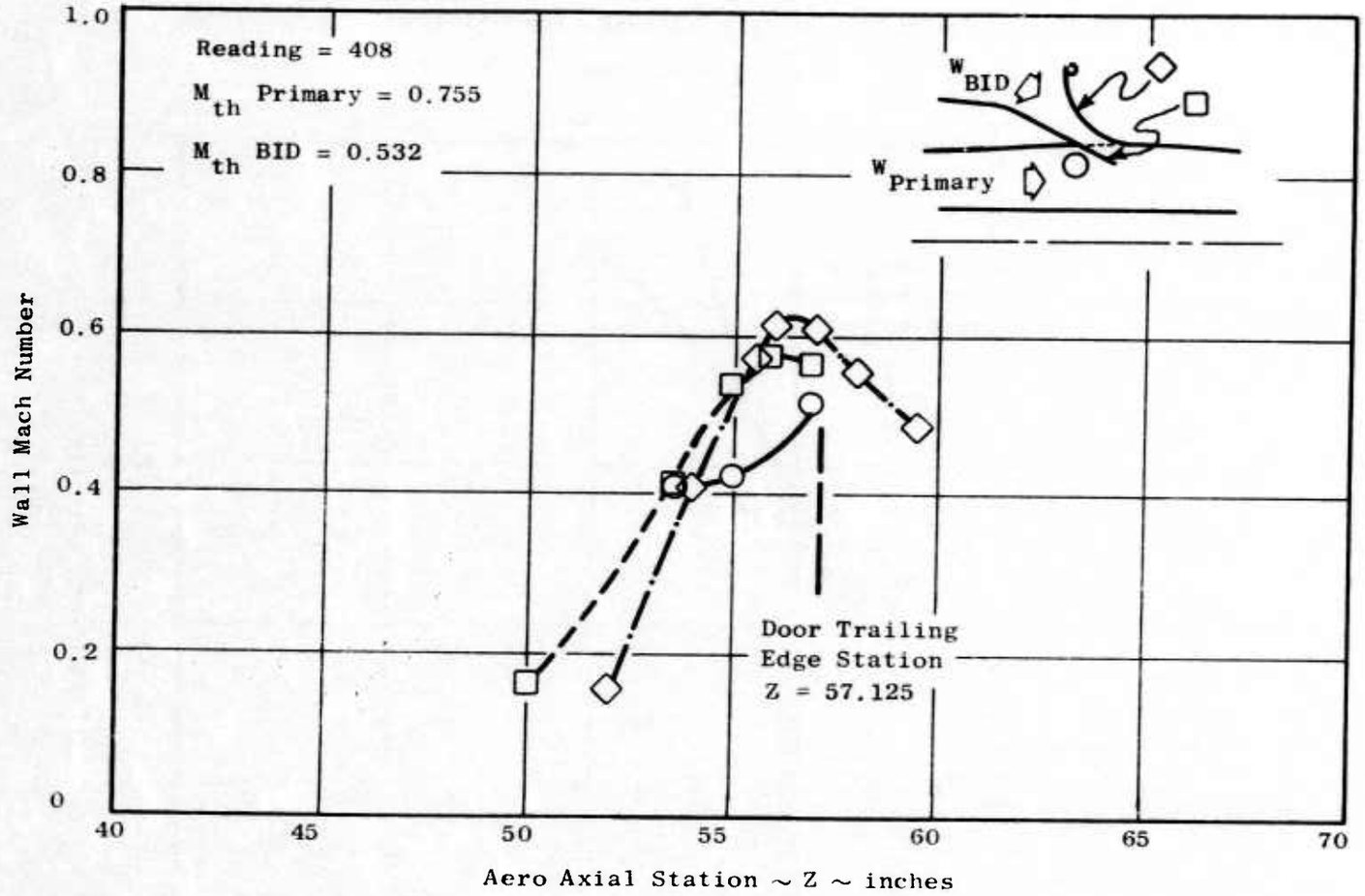

Figure 499. Measured Blow-In-Door Wall Mach Number Distributions for the 100% A_{th} BID Setting.

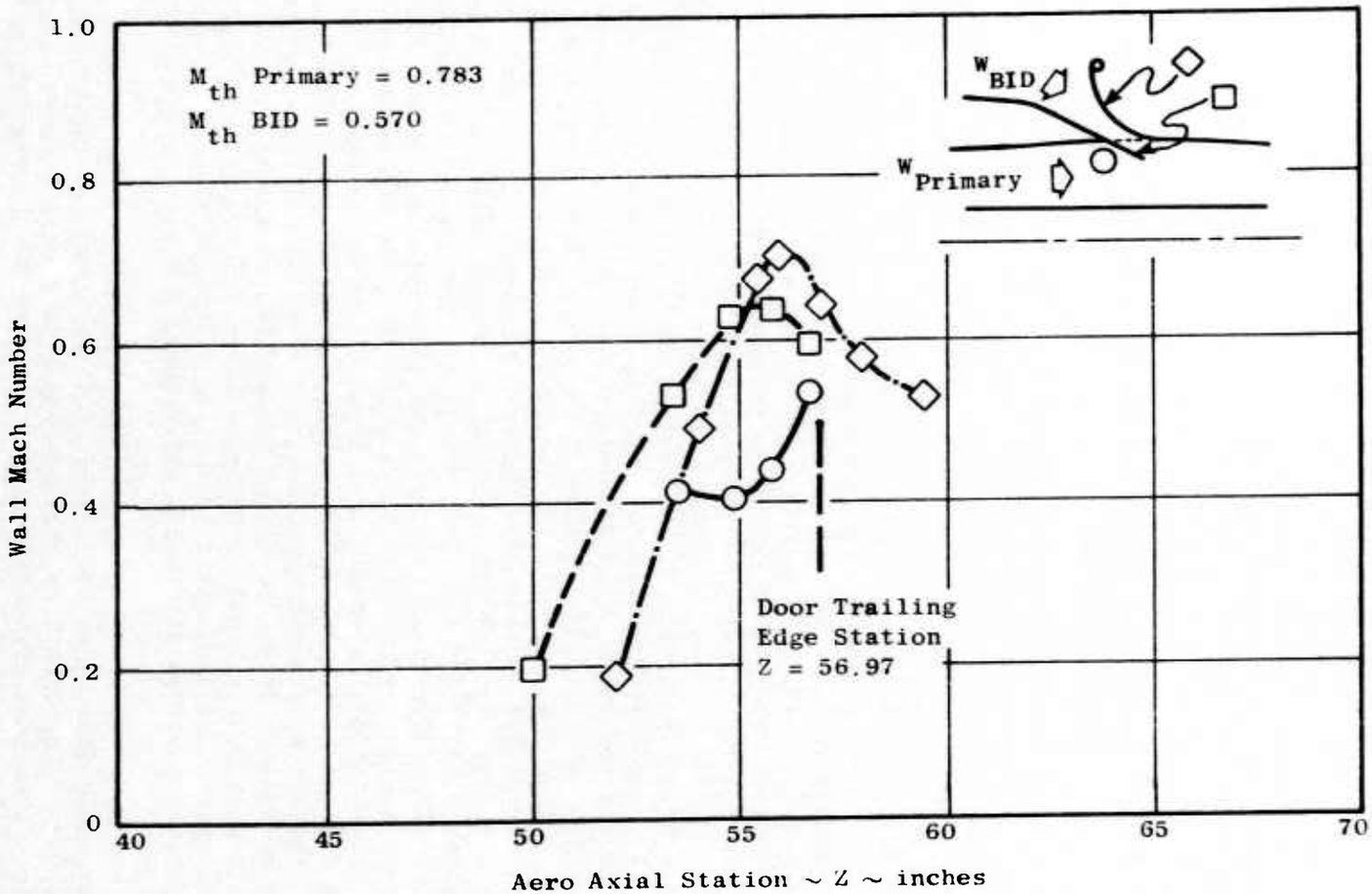

Figure 500. Measured Blow-In-Door Wall Mach Number Distributions for the 114% A_{th} BID Setting.

to the data of Figures 498 through 500, respectively. Except in the vicinity of the entrance region, where the effective flow area is understated due to the fact that flow can enter via the sides near the outer door, the data are greater than or equal to these simple one-dimensional calculations. This indicates that the BID passages do not have any significant dead regions (e.g., in the corners) and are "flowing full." However, the foregoing information suggests that performance degradation occurs in the mixing region, rather than in the BID passages themselves.

4.4.5.3 Aerodynamic Performance Comparison for Various Inlet Operating Modes

To place the preceding discussion in perspective and integrate the performance results from the various test configurations, Figures 504 and 505 show overall inlet recovery as a function of primary inlet throat Mach number and compressor inlet corrected flow, respectively. Figure 504 shows that the approach and takeoff-with-BID-closed configurations perform quite similarly in terms of throat Mach number despite the difference in required diffusion. The three BID configurations exhibit performance decrements, relative to these primary-only data, of about 1.7 points (114% nominal), 1.9 points (81% nominal), and 3.2 points (100% nominal) at the respective design points. When these same recovery data are expressed in terms of compressor corrected flow in Figure 505, the significance of the auxiliary (BID) inlet system is obvious. In the take-off mode with BID's closed, the inlet chokes well before the 111 lb/sec design point, as intended. Without an auxiliary system, required additional flow would necessitate extreme centerbody translation and/or inlet oversizing, either of which would severely compromise system performance by increasing weight and/or drag. Inclusion of an auxiliary inlet system, as indicated in Figure 505, produces the required airflow without otherwise modifying the primary inlet, albeit at a recovery penalty in this case. However, even with the relatively poor BID performance already noted, overall recovery levels of about 0.952 (100% and 114% nominal BID settings) to 0.962 (81% nominal BID setting with minor resizing) are achievable at the 111 lb/sec design corrected flow. (It should be recalled that the BID entrances in the test were not optimized for static operation, while the primary entrance was. Performance decrements for the 3 BID designs, relative to the BID-closed configuration, therefore, are not representative of an actual installation operating either statically or at low flight speed. For an actual, sharp-lipped inlet, performance levels would probably be lower statically, and higher at take-off and approach flight speeds, than the values of Figure 505, due to increased primary lip loss statically and reduced BID lip loss in flight due to ram effects.)

Corresponding distortion characteristics are shown in Figures 506 and 507, with the qualification that they are based on a single radial traverse and therefore do not reflect circumferential variations due to the BIDs and struts. Main points to be drawn from these plots plus the various total pressure traverses presented earlier, are as follows:

- Radial distortion levels are moderate, with design point values of about 4+% (approach), 6% (take-off-with-BIDS-closed), and 7-8%

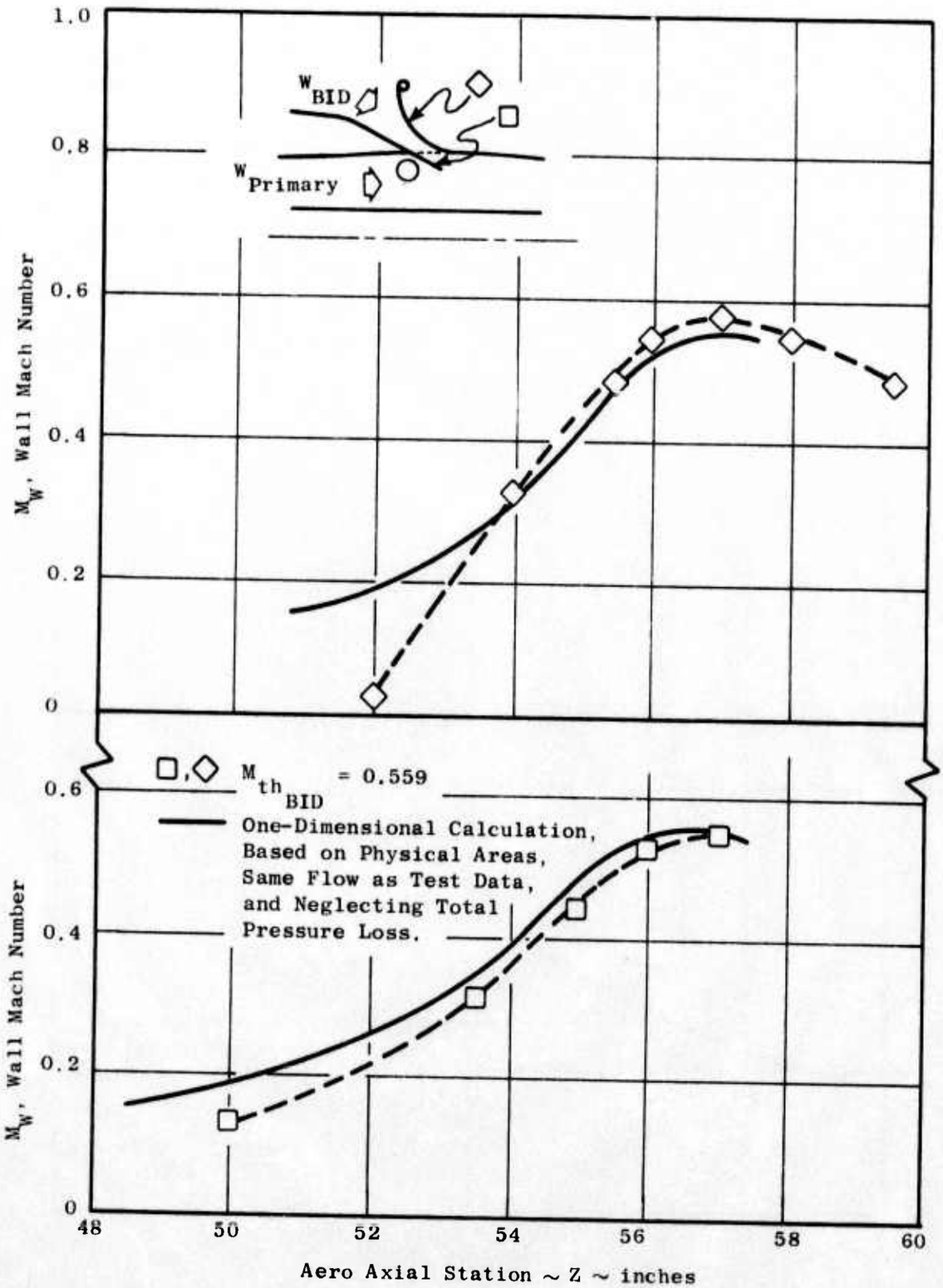

Figure 501. Comparison of Measured BID Wall Mach Distributions with One-Dimensional Calculations for the 81% A_{th} BID Setting.

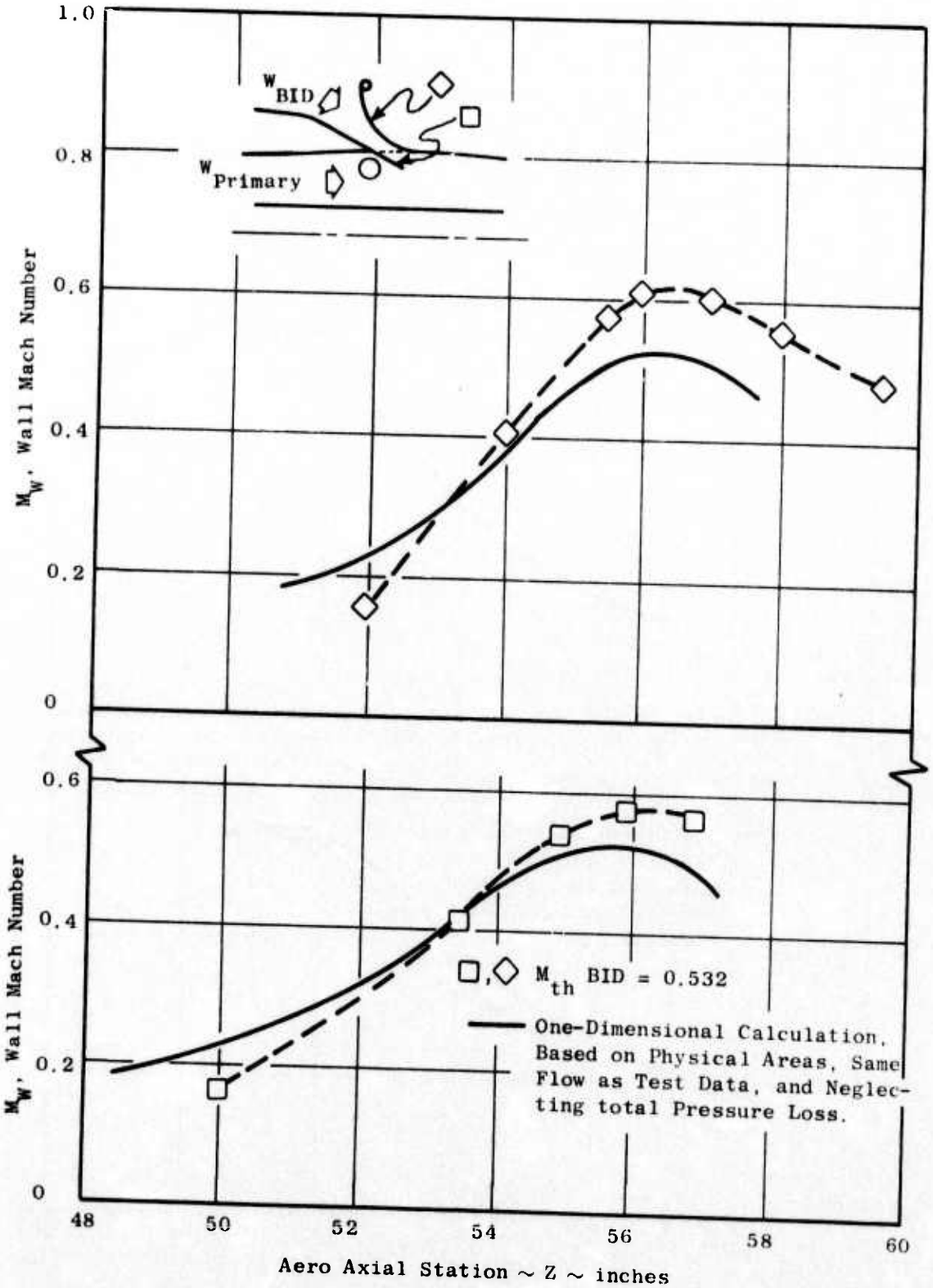

Figure 502. Comparison of Measured BID Wall Mach Distributions with One-Dimensional Calculations for the 100% A_{th} BID Setting.

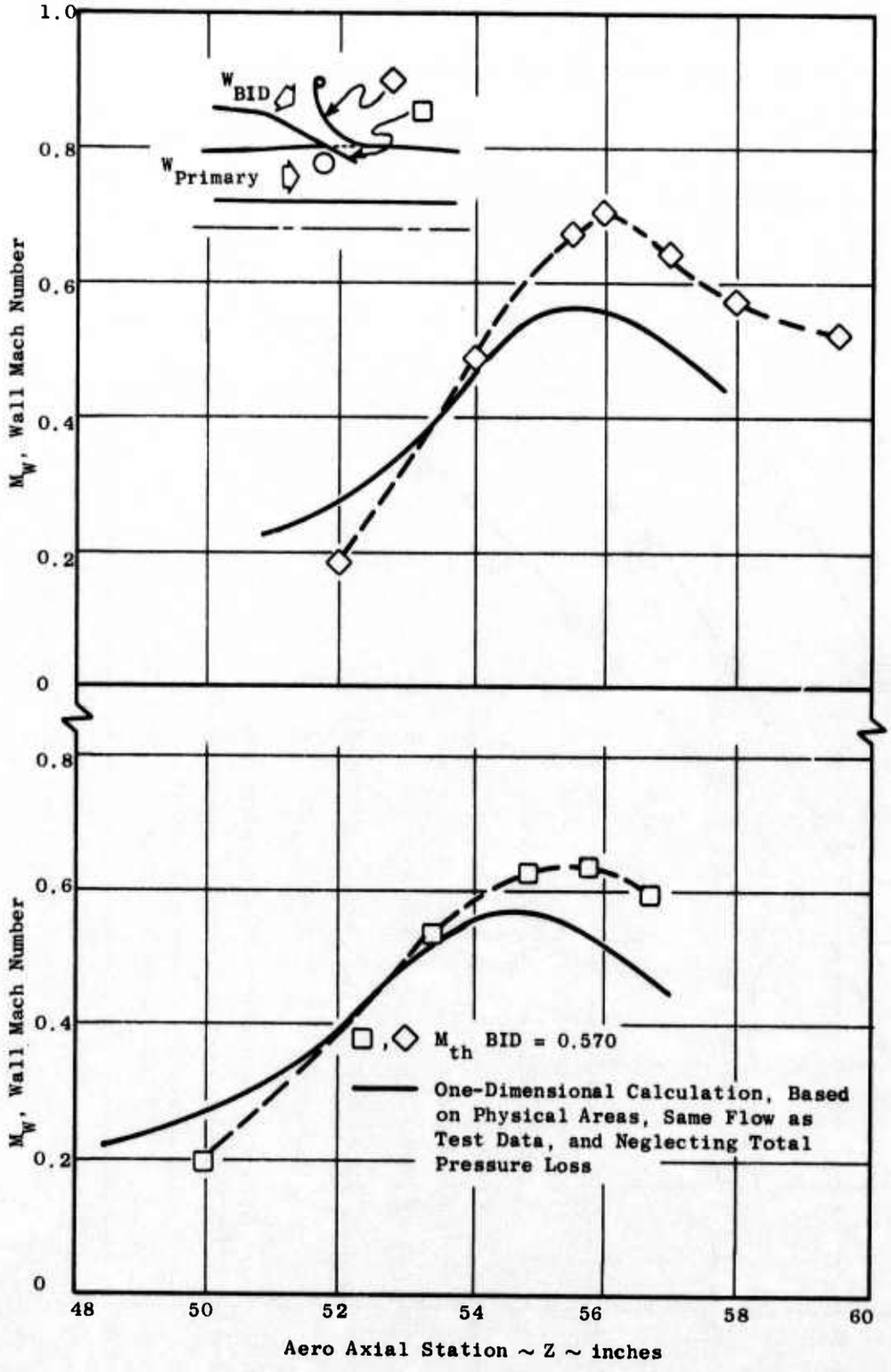

Figure 503. Comparison of Measured BID Wall Mach Distributions with One-Dimensional Calculations for the 114% A_{th} BID Setting.

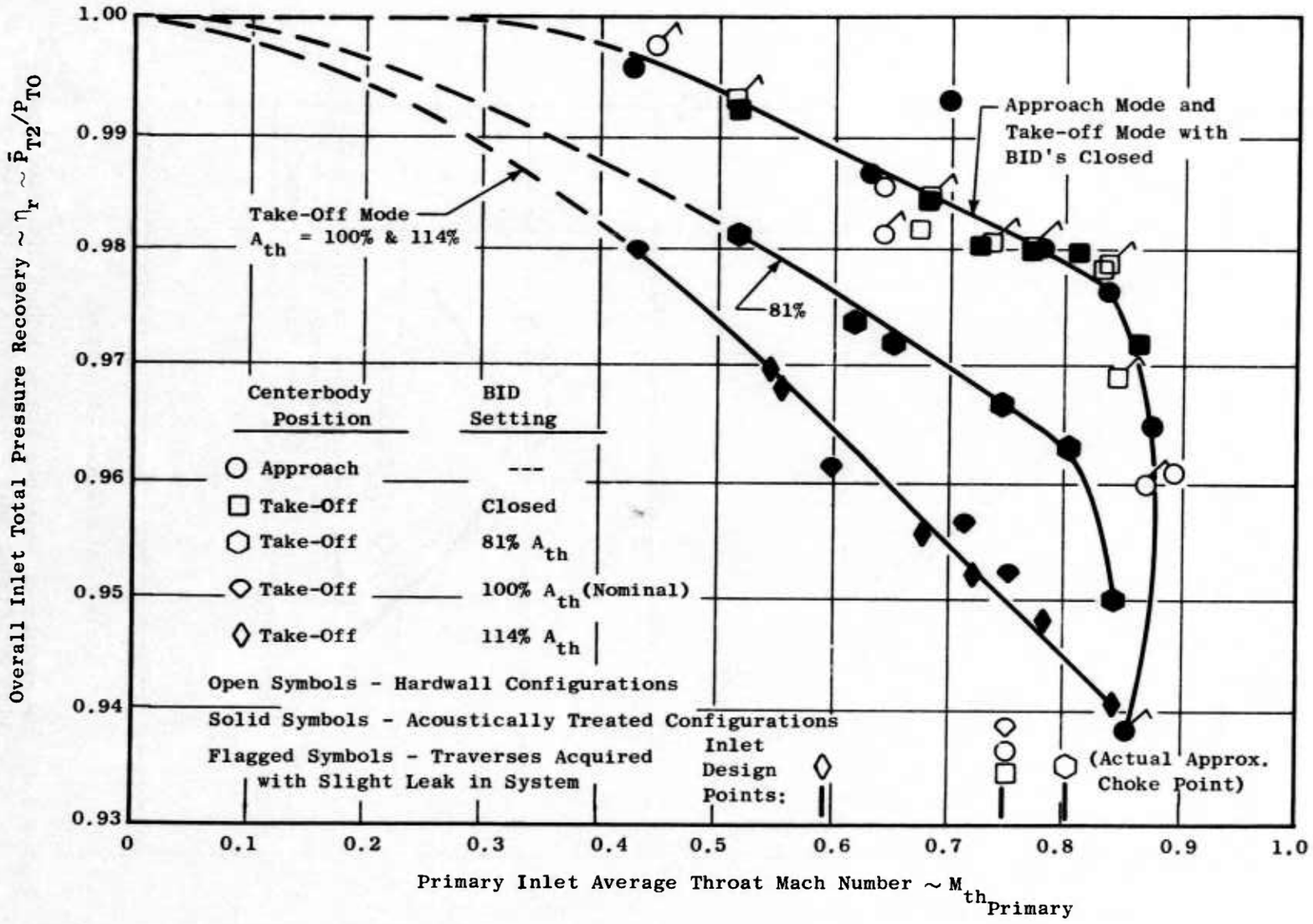

Figure 504. Overall Inlet Recovery for All Test Configurations as a Function of Primary Inlet Throat Mach Number.

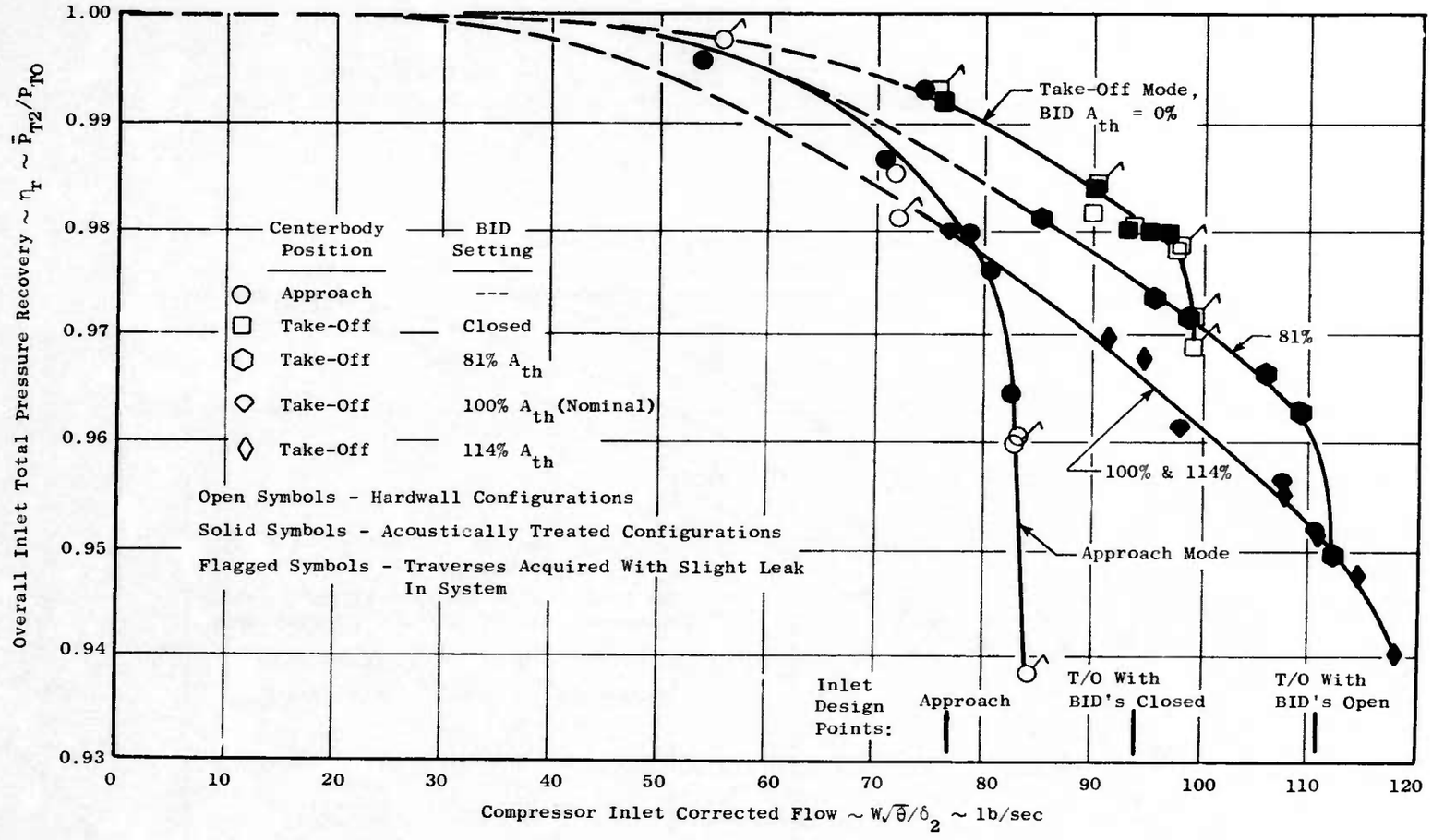

Figure 505. Overall Inlet Recovery for All Test Configurations as a Function of Compressor Corrected Flow Demand.

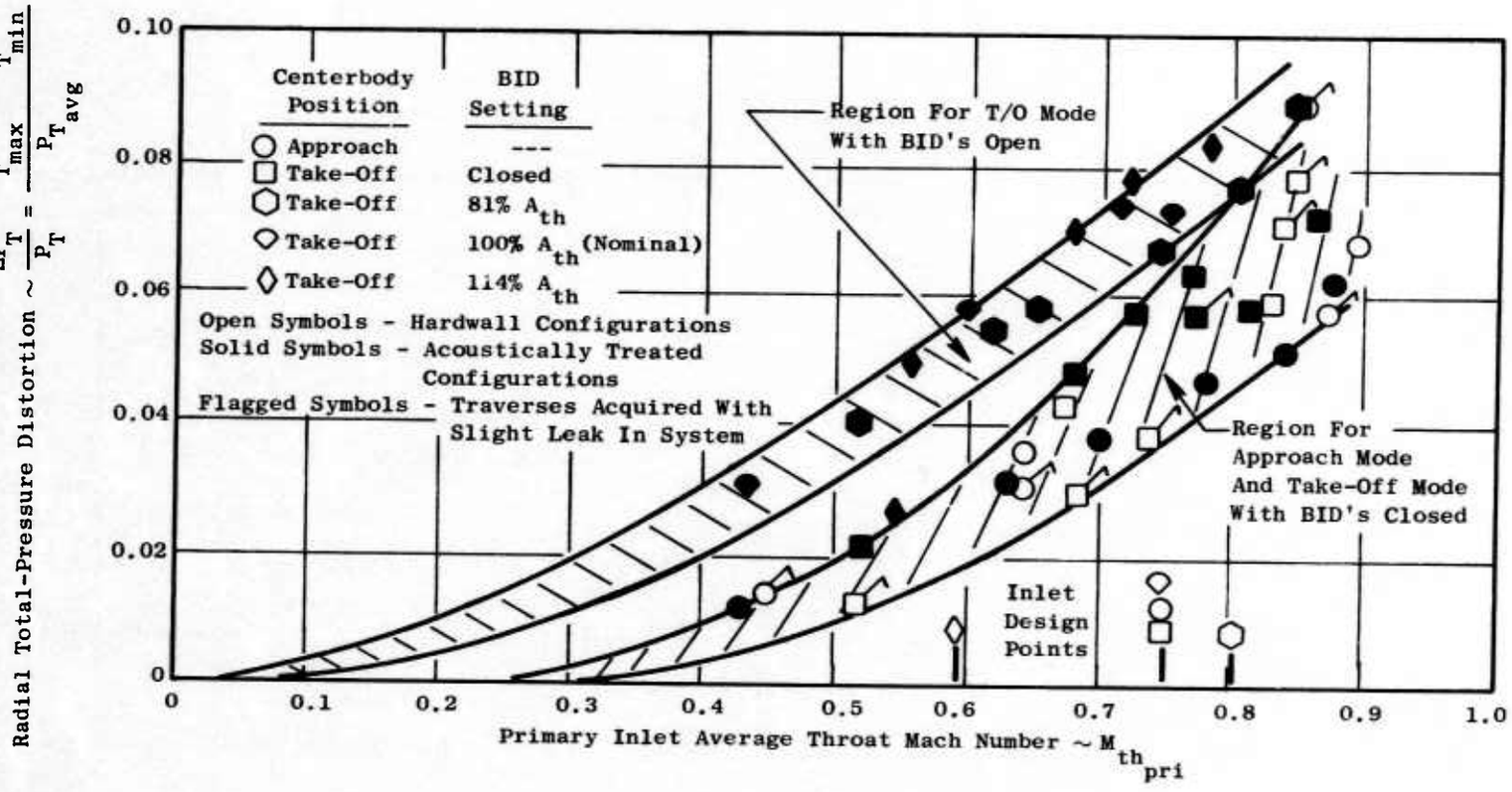

Figure 506. Radial Total-Pressure Distortion for All Test Configurations as a Function of Primary Inlet Throat Mach Number.

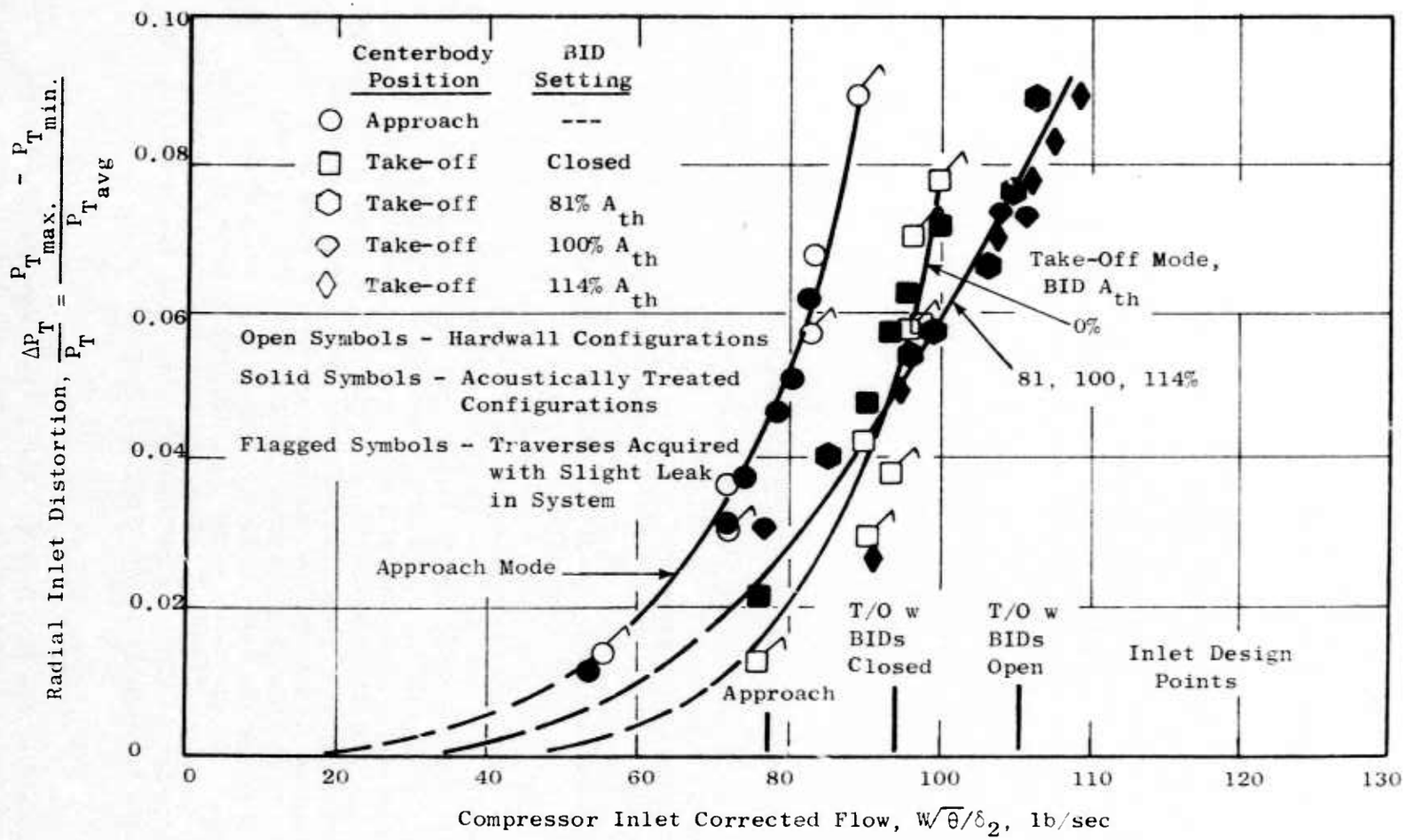

Figure 507. Radial Total-Pressure Distortion for All Test Configurations as a Function of Compressor Corrected Flow Demand.

(take-off-with-BIDS-open). (These levels are based on corrected flow, Figure 506, since the BID-open configurations do not all yield design flow at the design primary throat Mach number, as already discussed).

- For the approach, take-off-with-BIDs-closed, and take-off-with-81%-BID A_{th} configurations, total pressure gradually recovers from the wall to the free-stream values. However, with the 100% and 114% A_{th} designs, separated flow (characterized by a flat radial total-pressure profile) persists to a point 1-2 inches inward of the predicted door trailing edge streamline location. These last 2 configurations thus possess a much greater distortion extent than the first 3 mentioned.

Salient data extracted from Figures 504 thru 507 and the total-pressure traverses are summarized in Table 22. They are interpreted to suggest that, while room for improvement exists in the BID area, overall aerodynamic performance is considered acceptable for applications currently under consideration.

4.4.5.4 Description of Acoustic Results

In Figure 508, the PNL at the 40° angle as a function of tip speed is compared for the hybrid inlet at the three open-BID positions. The PNL for the nominal and 114% BID positions are nearly equal, while the results for the 81% position, in general, are somewhat lower. In Figure 509, it is seen that the primary inlet throat Mach number at high tip speeds is significantly different for the three BID positions. For example, at a corrected tip speed of 1450 ft/sec, the respective primary throat Mach numbers for the 81% nominal, nominal, and 114% nominal positions are 0.72, 0.755, and 0.805. With this difference in primary inlet throat Mach numbers, the measured PNL levels would show a significant spread between the low and high Mach numbers if the BID's were closed. This is based on the results presented earlier on acceleration suppression with the BID's closed (see Figure 463). However, at this tip speed (1450 ft/sec), the perceived noise levels are nearly equal for the three BID positions. From this result it is concluded that there is no significant net noise acceleration suppression with the BID's open. This lack of acceleration suppression indicates that the dominant path of noise at these high tip speeds must not be through the primary inlet. The other path which the noise can take is through the blow-in doors. The throat Mach number in the BID's as shown in Figure 510 was never above 0.6, although they were designed to reach higher Mach numbers. The measured aerodynamic performance with the BID's open was discussed in the previous section. At these BID passage throat Mach numbers, there is probably no acceleration suppression.

In Figure 511, the SPL in the rotor 1 blade passing 1/3-octave band as a function of angle is compared for the three open BID positions at the 1448 ft/sec tip speed. There is no significant difference in the directivity over the range of BID positions investigated.

Table 22. Summary of Selected Inlet Performance Characteristics.

	Centerbody Position BID A_{th} Setting				
	Approach	Take-off 0 (Closed)	Take-off 81%	Take-off 100%	Take-off 114%
Reading No.	333	366	467	408	436
Primary M_{th}	0.781	0.771	0.805	0.755	0.723
Compressor Corrected Flow, $W\sqrt{\theta}/\delta_2$ (lb/sec)	78.66	95.46	109.38	110.51	111.11
Inlet Recovery, η_R	0.9802	0.9803	0.9630	0.9522	0.9520
Inlet Distortion, $\Delta P_T/P_T)_{Max.}$*	0.0467	0.0631	0.0768	0.0732	0.0780
Distortion Extent - % Area†	31.5	28.6	41.5	52.9	65.5

Note: Recovery and distortion are based on 1 Kiel probe traverse positioned mid-way between support strut locations and in line with the middle of a blow-in-door passage where applicable.

* $\Delta P_T/P_T)_{Max.} = \dfrac{P_{T_{Max.}} - P_{T_{Min.}}}{P_{T_{Av}}}$ with 10% Area Exclusion Adjacent to Hub and Tip Flowpaths

† Distortion extent is here defined as the percentage of the flow area in which the total pressure is below average, considering only the larger of the Hub and Tip flowpath-associated deficits. It includes the 10% area excluded in computing the distortion level.

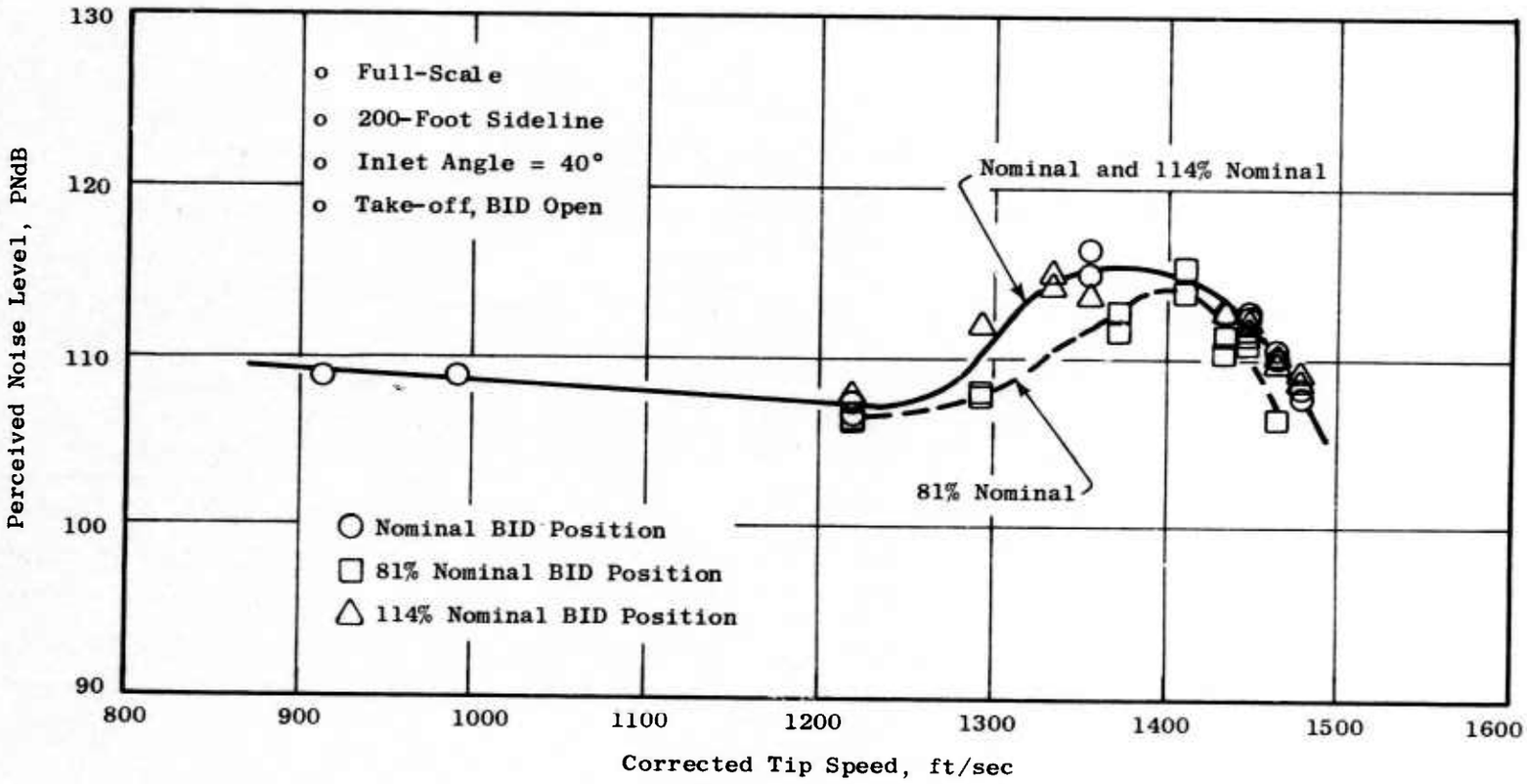

Figure 508. PNL as a Function of Tip Speed for the Three BID Positions.

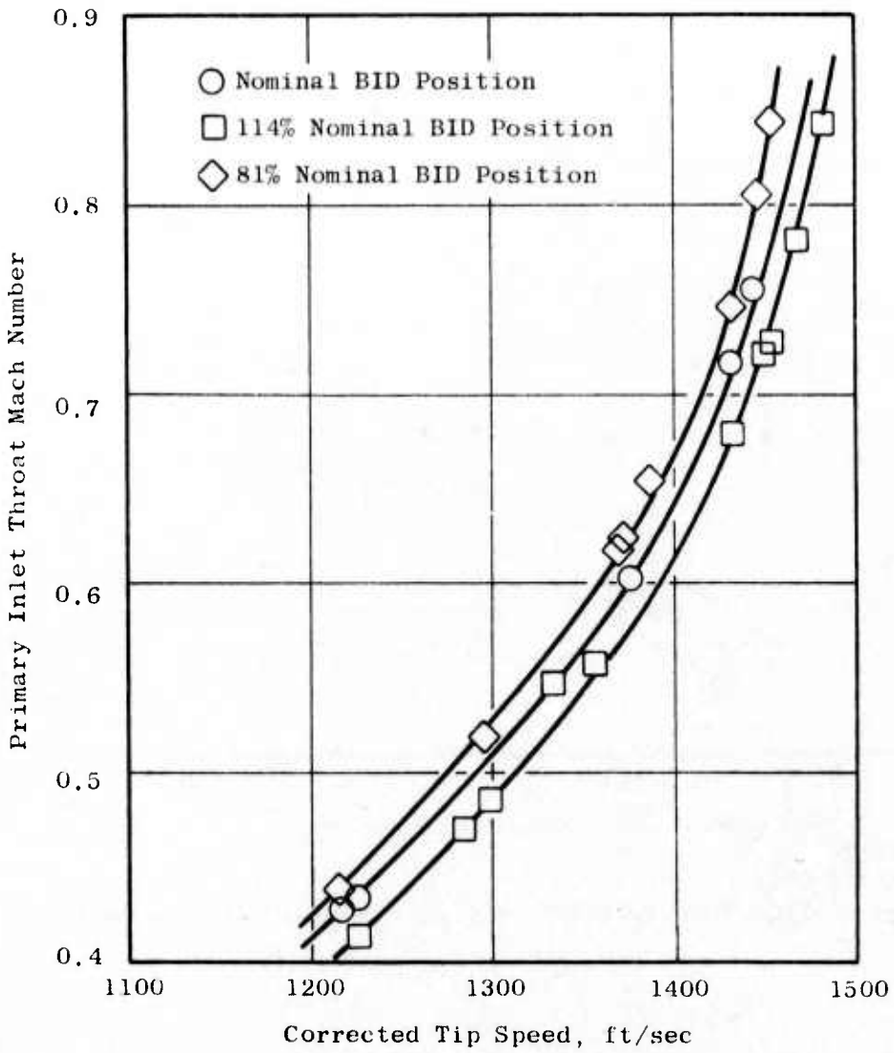

Figure 509. Primary Inlet Throat Mach Number as a Function of Tip Speed for the Three BID Positions.

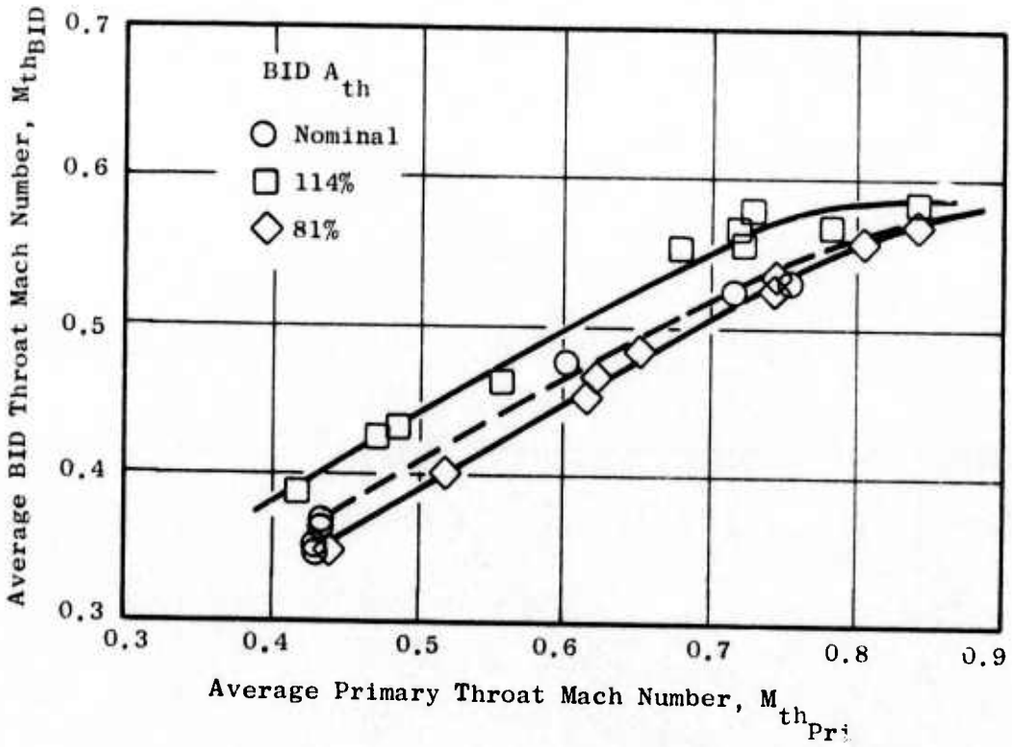

Figure 510. Primary-BID Throat Mach Number Relationship.

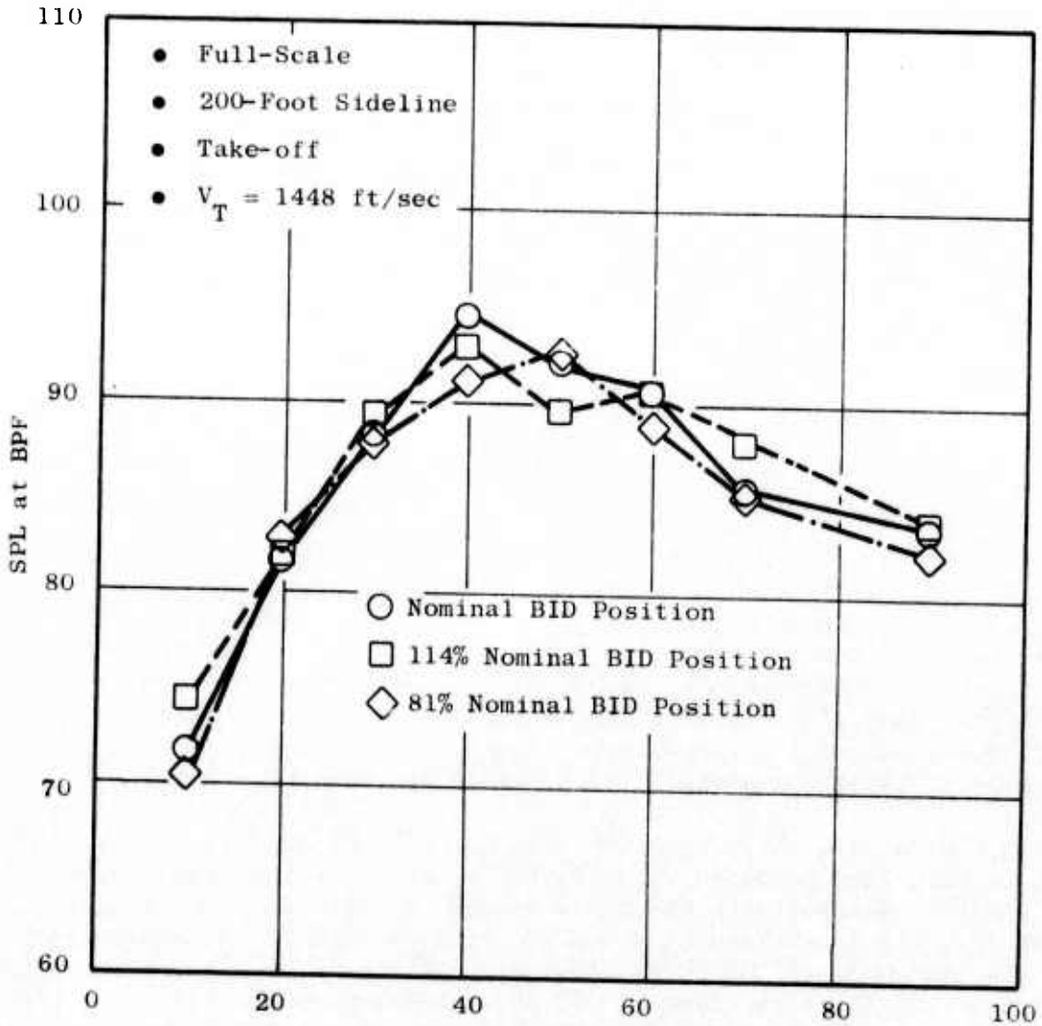

Figure 511. Directivity Comparison of Rotor 1 BPF for the Three BID Positions.

In Figure 512 the rotor 1 blade passing tone measured at the fan face is plotted as a function of immersion depth for the three BID positions at the same speed. For a given immersion depth, the values vary somewhat for the various BID positions. This is attributed to differences in the flow characteristics for the three BID positions. However, as noted on Figure 512, the power levels do not vary significantly.

It was noted that the PNL values are somewhat lower for the 81% nominal position. In Figure 513, the 1/3-octave band spectra for 1372 ft/sec tip speed are compared for the nominal and 81% nominal BID position. It is seen that the rotor 1 blade passing tone and its harmonics are lower for the 81% nominal position. The power levels measured in the rotor 1 blade passing 1/3-octave band and its harmonics are compared below for the three BID positions:

	114% Nominal	Nominal	81% Nominal
R1-F1	144.2	146.0 dB	142.9 dB
R1-F2	138.7	139.2 dB	134.0 dB
R1-F3	136.7	136.7 dB	132.4 dB

Therefore, less power is radiated with the doors in the 81% nominal position. This lower level might be due either to the smaller BID passage area in this 81% nominal position (higher acoustic impedance) or to the source noise. Insufficient acoustic probe data were available, however, at this tip speed to determine if there was a significant change in the source noise.

In Figure 514, the PNL at 40° with the BID's closed (i.e., no BID's) is compared with that measured with the BID's open. At tip speeds up to 1300 ft/sec, the PNL measured with the BID's closed and open are nearly equal. In Figure 515, the 1/3-octave band spectra at V_T = 1000 ft/sec are compared with the BID's closed and in the nominal position. The spectra are nearly identical except for the tone at 500 Hz, present when the BID's are closed. This tone is probably the vortex shedding tone of the IGV's which was discussed in Section 4.4.2.2. Based on the fact that the spectra are nearly identical with the BID's opened and closed, it is concluded that the noise passing through the BID's is less than that passing through the primary inlet entrance area at this low tip speed for the 40° angle. In Figure 516, the SPL in the blade passing 1/3-octave band as a function of angle from the inlet is compared for the same conditions. From this curve it is seen that, at high angles from the inlet, the noise passing through the BID's becomes an increasingly large part of the measured noise level. In fact, at high angles it dominates the measured noise level. At angles below 40°, however, the presence of the BID's does not change the measured blade passing SPL.

In Figure 517, the 1/3-octave band spectra at 40° are compared for the 1340 ft/sec tip speed with the BID's closed and the 1356 ft/sec tip speed with the BID's in the nominal position; for this small difference in

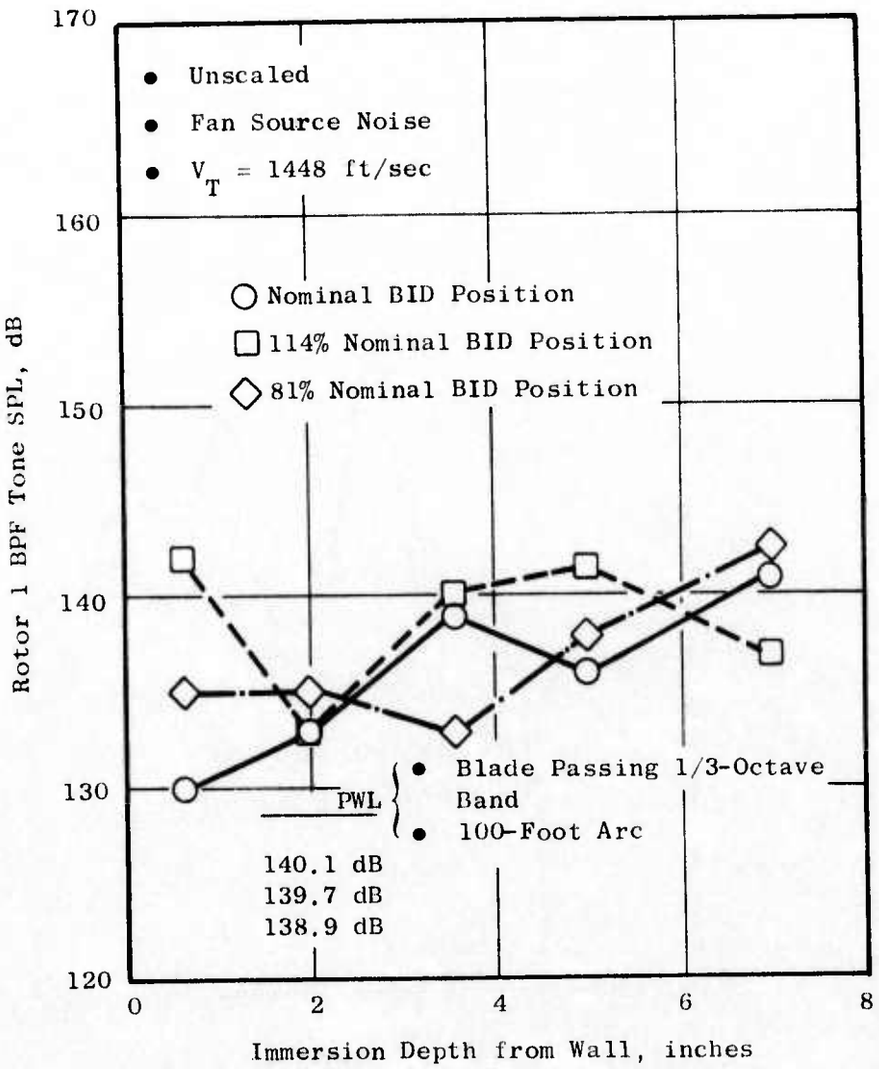

Figure 512. Rotor 1 BPF Tone Measured at the Fan Face for Three BID Positions and the PWL Measured in the Far Field.

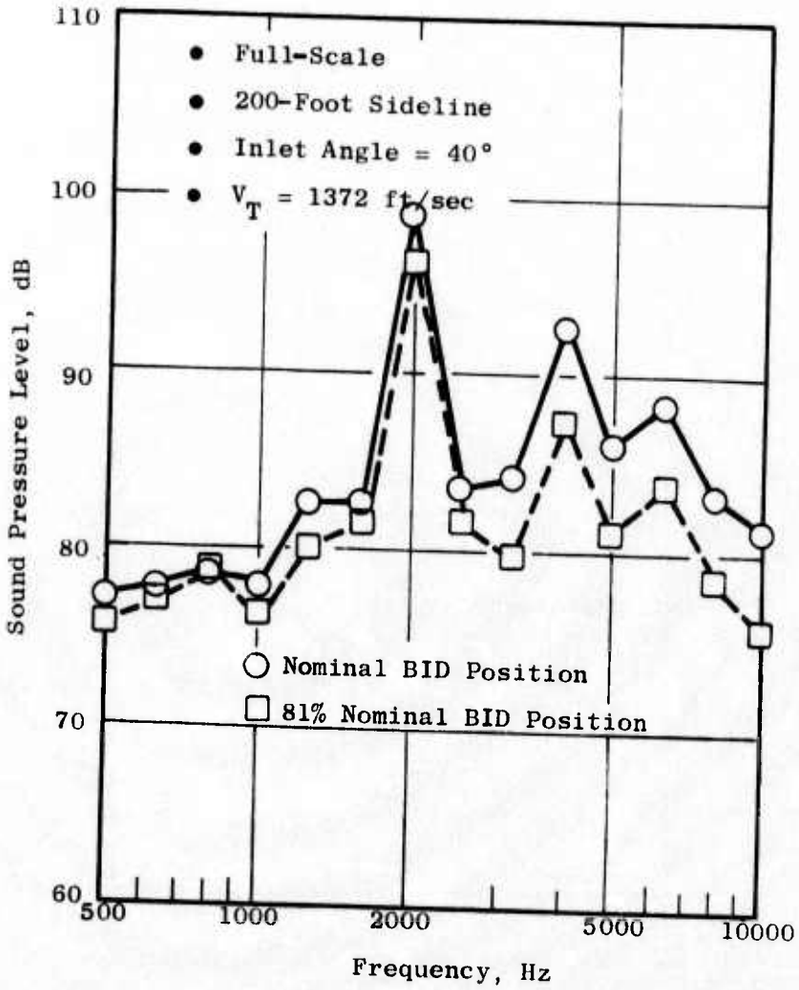

Figure 513. 1/3-Octave Band Comparison at Two BID Positions.

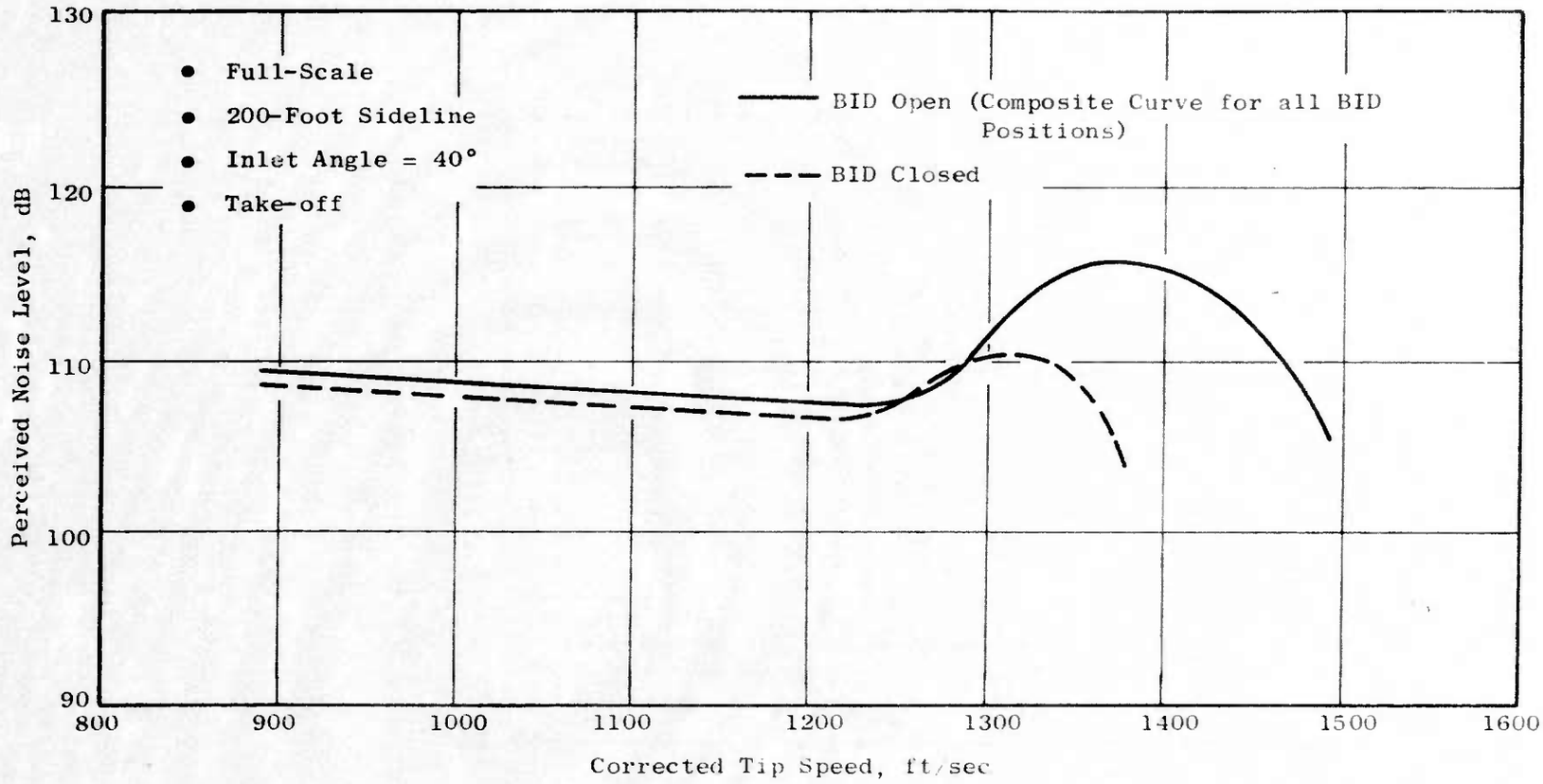

Figure 514. Comparison of PNL as a Function of Tip Speed with the BIDs Open and Closed.

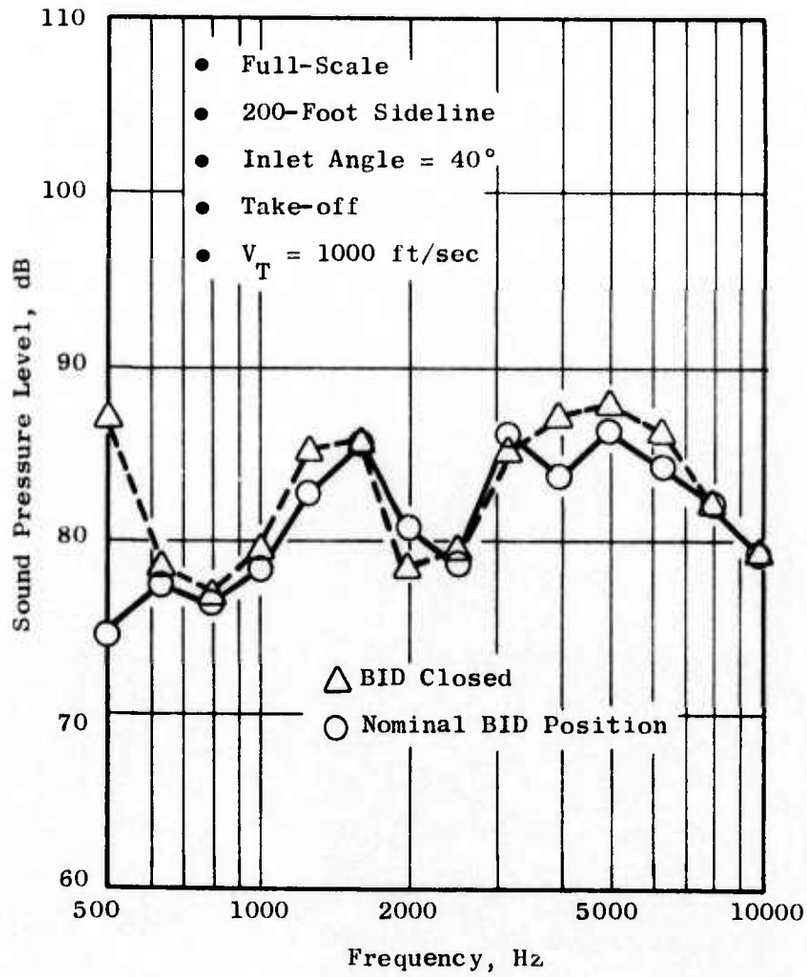

Figure 515. One-Third-Octave Band Comparisons.

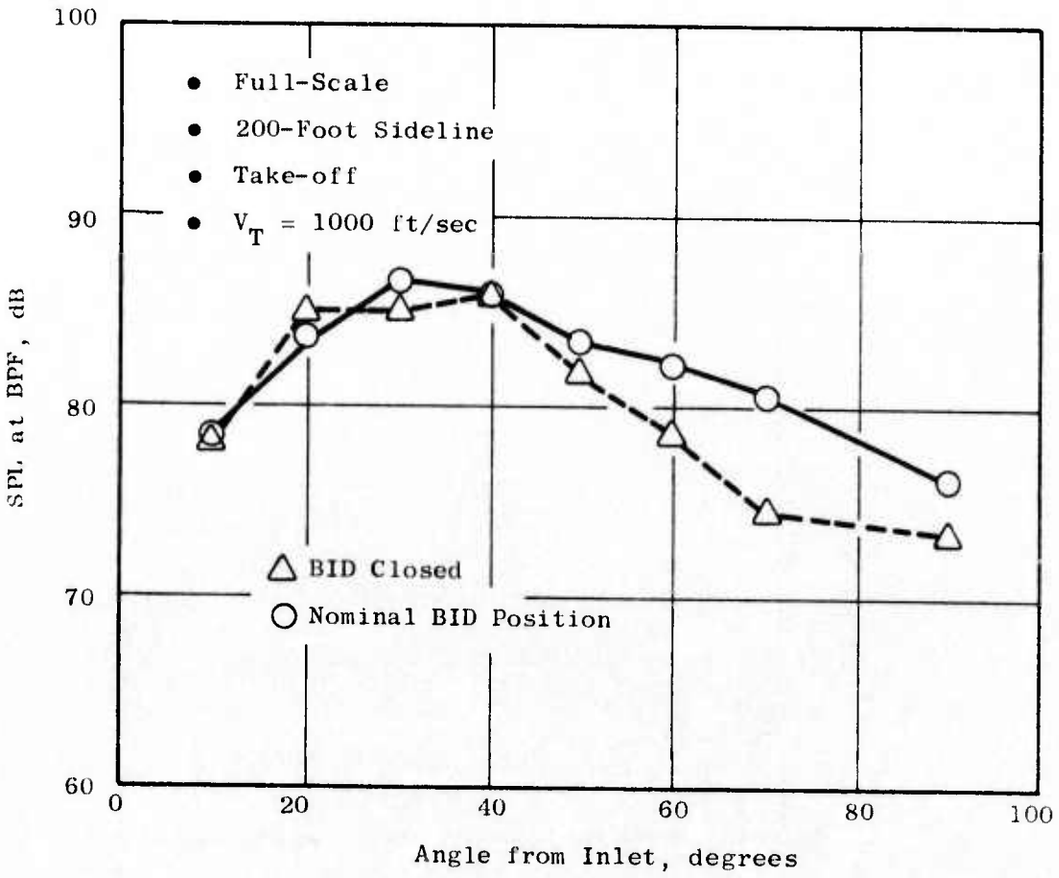

Figure 516. Directivity Comparison of SPL at BPF.

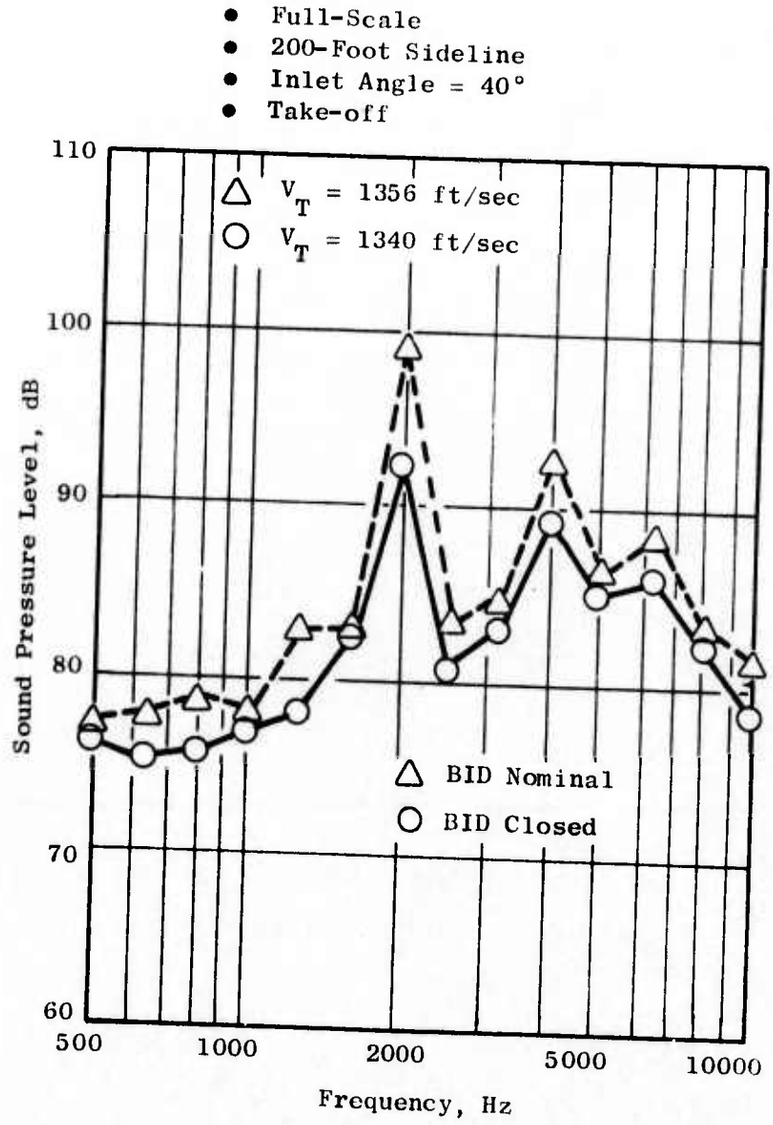

Figure 517. One-Third-Octave Band Comparison.

tip speed, it is seen in Figure 514 that the noise levels for each specific configuration did not change significantly. At these tip speeds the inlet throat Mach numbers are low and there is no significant acceleration suppression. However, from Figure 514, the PNL with the BID's open is 5 PNdB higher. Figure 517 shows that this is due primarily to a marked increase in the rotor 1 blade passing tone with the BID's open although the levels have increased in all bands. In Figure 518, the SPL in the blade passing 1/3-octave band as a function of angle from the inlet is compared for the same conditions. The increase in the blade passing tone with the BID's open indicates that the noise passing through the BID passages is greater than that emanating from the primary inlet entrance area at this speed for most angles (there is no primary acceleration in either case). This result may indicate a large increase in the fan source noise with the BID's open. However, a comparison of the measured blade passing tone as a function of immersion depth at the fan face for a slightly higher tip speed (Figure 519) shows that the blade passing tone is actually lower with the BID's open. Since the noise passing through the BID's dominates the spectra at the maximum angle (40°), as the inlet throat Mach numbers are increased to values above 0.7 where acceleration suppression is achieved in the primary inlet, there was no significant effect on the noise levels.

In Figure 520, the results for the hybrid inlet with the BID's open, the hybrid inlet with BID's closed, and the baseline cylindrical bellmouth inlet are compared. For the hybrid inlet with the BID's open, the compressor operated to higher tip speeds than with the BID's closed. This is, of course, the purpose of the doors, which provided a much more realistic compressor speed/flow operating condition for takeoff than did the BID-closed configuration.

Also, in Figure 520 it is seen that significant noise suppression (up to 15 ΔPNdB) was achieved for the hybrid inlet with the BID's open relative to the baseline cylindrical bellmouth inlet results. With the BID's closed, the hybrid inlet provided 15.5 ΔPNdB. At the low tip speeds, the 4-5 PNdB reduction (with the BID's open) is attributed to the acoustic treatment in the hybrid inlet. In Figure 521, the 1/3-octave band spectra are compared for these two inlets at the 40° angle for the 1448 ft/sec tip speed. A similar far-field narrowband comparison is shown in Figure 522. These comparisons show that, with the BID's open, the SPL's are significantly reduced in all bands. From the narrowband comparison, it is seem that the MPT's are reduced along with the blade passing tones. A protion of this noise reduction is attributed to the acoustic treatment between the compressor IGV's and the BID's. However, based on the magnitude of the PNL reduction and the fact that is occurred in all 1/3-octave bands, it follows that an additional suppression mechanism exists. As seen in Figure 523, there was no major change in the fan source noise characteristics at the rotor 1 BPF and, therefore, a change in the fan source noise is not producing this additional noise suppression. This attentuation might be attributed to the rapid area change seen by the fan noise when it encounters the BID's. This rapid area increase produces a large acoustic impedance, and a large portion of the

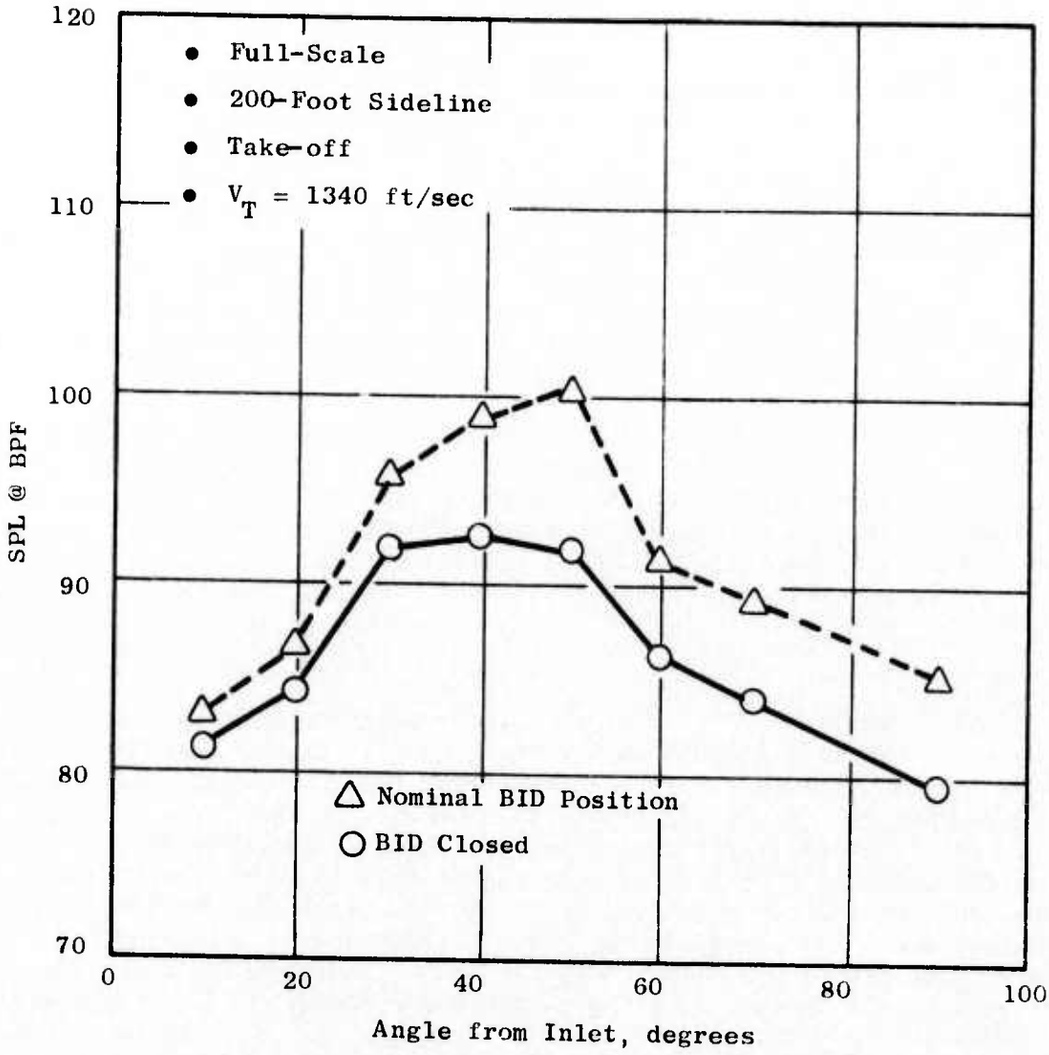

Figure 518. Directivity Comparison of SPL at BPF.

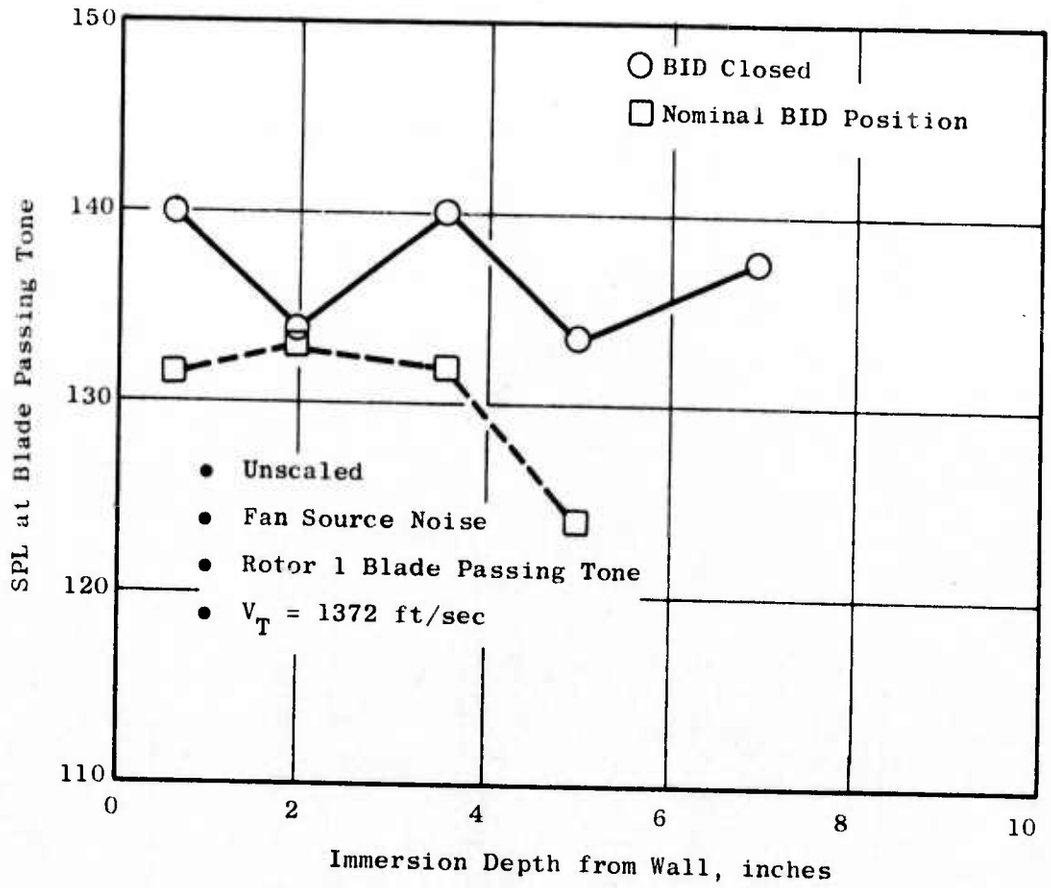

Figure 519. Rotor 1 Blade Passing Tone Measured at the Fan Face.

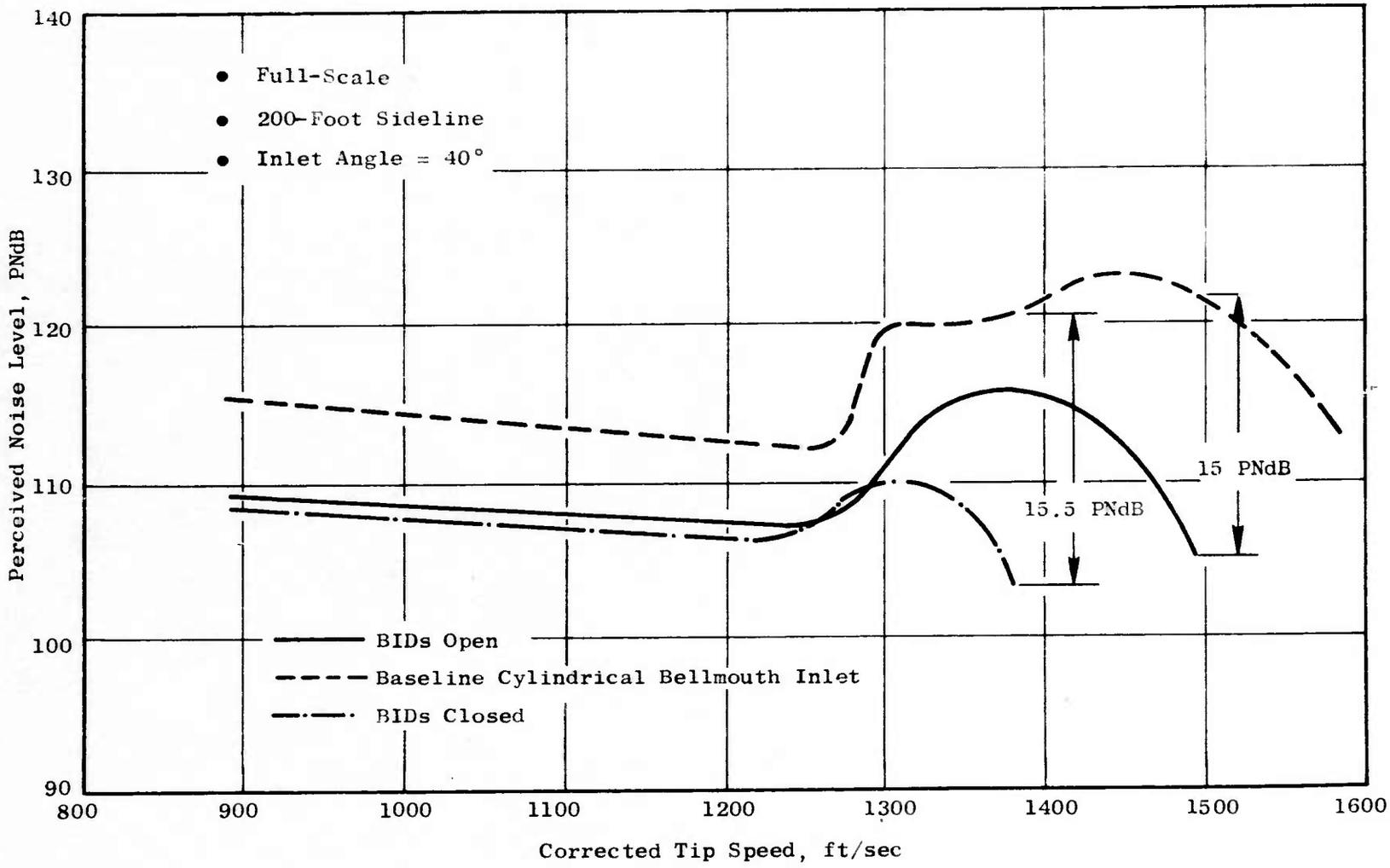

Figure 520. Comparison of PNL as a Function of Tip Speed for the Baseline Inlet and the Hybrid Inlet with the BIDs Open and the BIDs Closed.

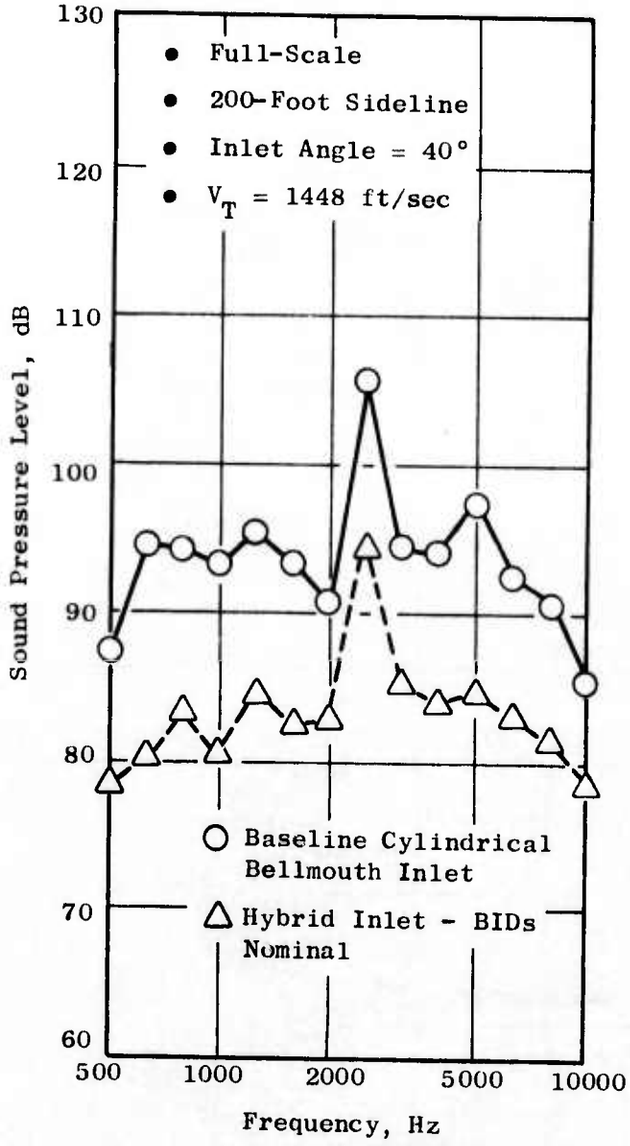

Figure 521. One-Third-Octave Band Comparison.

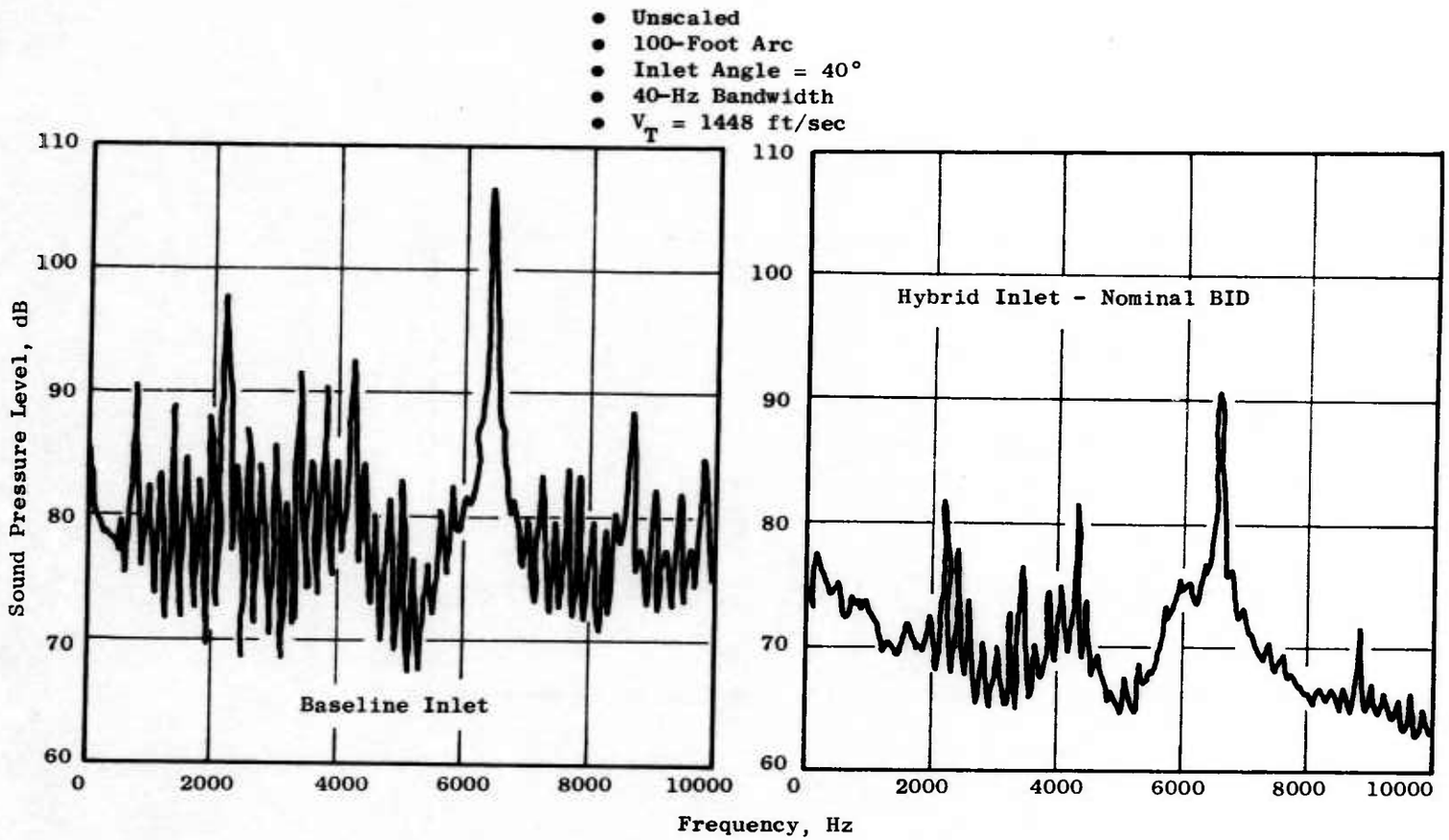

Figure 522. Narrowband Comparison Between Baseline Inlet and Hybrid Inlet with BIDs in Nominal Position.

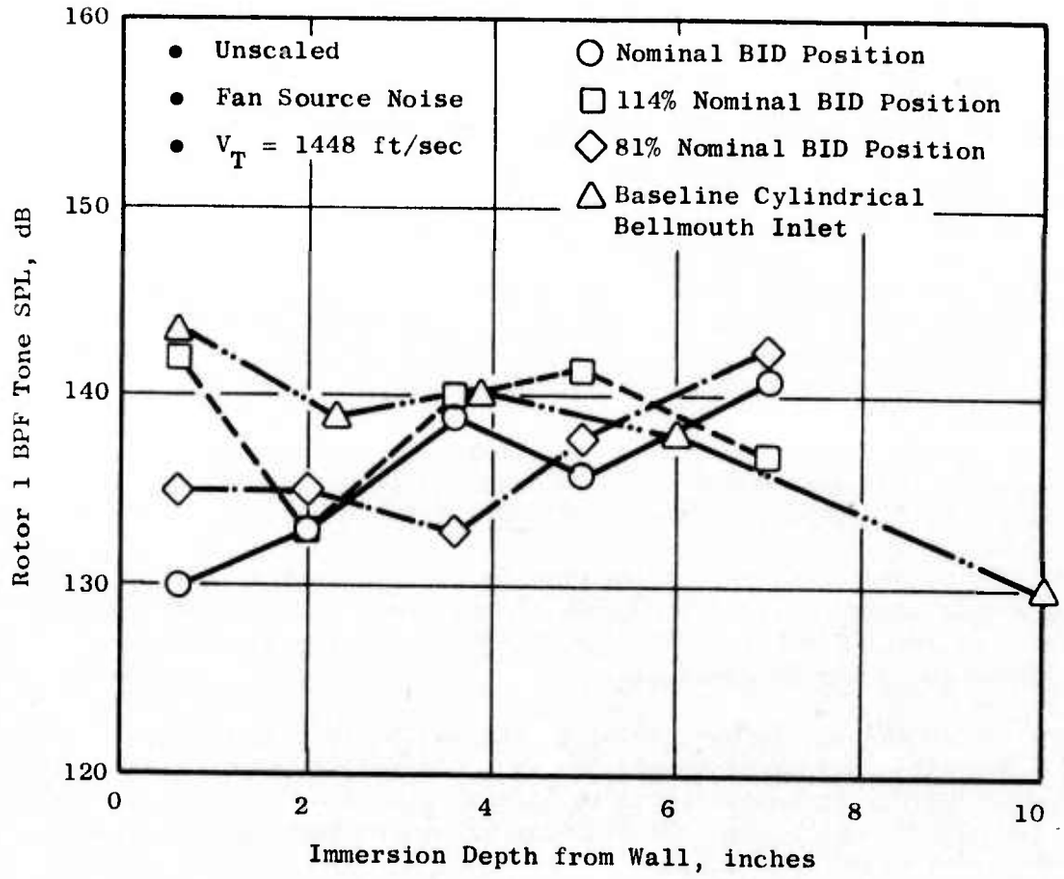

Figure 523. Rotor 1 BPF Tone Measured at the Fan Face for the Three Open BID Positions and the Baseline Cylindrical Bellmouth Inlet.

acoustic energy is reflected back toward the fan rather than being transmitted through the BID passages or the primary inlet duct.

In order to obtain additional noise suppression for the hybrid inlet with the BID's open, the flow in the BID's also must be accelerated to higher throat Mach numbers. This was the original design intent for these BID's; however, the flow in the BID passages never reached high throat Mach numbers. A full discussion of the BID aerodynamic performance is provided in Section 4.4.5.2.

4.4.5.5 Summary

1. For the low tip speeds (below 1300 ft/sec), the blow-in doors do not change the PNL at the maximum angle. At high angles from the inlet, the measured blade passing tone is significantly higher with the BID's open, relative to closed in the hybrid inlet.

2. At tip speeds above 1300 ft/sec, the noise passing through the BID's is greater than that which emanates from the primary inlet entrance area for most angles from the inlet centerline.

3. When the inlet throat Mach number was at or near choked for the high tip speeds, no acceleration suppression was realized because the Mach number in the BID's never was high enough to provide acceleration suppression in the BID passage.

4. At high tip speeds the hybrid inlet with the BID's open provided up to 15 ΔPNdB noise suppression relative to the baseline inlet. This large suppression was probably due to the large acoustic impedance produced by the blow-in-doors, and the acoustic treatment between the blow-in doors and the IGV fan face.

4.4.6 High Mach IGV Test

4.4.6.1 Introduction

This section describes the results of turning the inlet guide vane flaps of the compressor to reduce passage area and increase the Mach numbers in the IGV passages to provide acceleration suppression. The testing was performed on the cylindrical bellmouth inlet for two corrected tip speeds - 1410 and 1524 ft/sec. These speeds were selected because of the associated higher airflow which was required to generate the high Mach numbers. The basid test procedure was to set the desired tip speed and then, maintaining this speed, the IGV angle was increased and the noise levels were recorded. The investigation covered the entire range of practical flap angles for the three-stage LPC IGV's.

4.4.6.2 Aerodynamic Performance

When the IGV angle is increased, it has the effect of decreasing the flow area. In Figure 524 the calculated throat passage area as a function of IGV angle is shown. To arrive at this, three sections (tip, pitch, and hub) were analyzed and a throat area calculated at each section for a 10% flow streamtube. The total area represents a summation of ten 10% streamtubes from tip to hub. Based on Figure 524, the IGV passage throat Mach number as a function of total corrected airflow was calculated for various IGV angles. These are shown in Figure 525. Increasing the IGV flap angle from the nominal design value had the effect of reducing both fan airflow and pressure ratio at speed.

The reduction in fan airflow can be seen in Figure 525 which shows, for both tip speeds, the airflow decreasing with IGV angle. Also shown in Figure 525 is the average throat Mach number as a function of IGV angle. For both tip speeds, at the largest IGV angle, high throat Mach numbers were achieved.

In Figure 526 the nominal fan performance map is shown. The effect of varying the IGV angle is also indicated. It is seen that, as the IGV angle is increased, the points move down the normal operating line. For example, when the IGV's are at the maximum angle at the 1524 ft/sec tip speed, the weight flow is 84.3 lbm/sec and the pressure ratio is 2.85. At the nominal IGV position, the weight flow is 127 lbm/sec and the pressure ratio is 4.1. Therefore, turning the IGV's causes a significant loss in fan performance. This loss in performance must be considered intolerable from a practical applications standpoint, if low noise and high thrust are required simultaneously. Also, since fan efficiency is reduced, the turbine could not extract enough energy from this reduced flow to maintain the required tip speed.

4.4.6.3 Noise Suppression Achieved

In Figure 527 the maximum PNL on the 200' sideline is shown for the two tip speeds as a function of IGV angle. The maximum ΔPNL suppression at the 1410 ft/sec tip speed is approximately 9 PNdB, and at the 1524 ft/sec tip speed it is 5.5 PNdB. As expected, the greatest suppression occurred at the largest IGV angle which also has the highest average IGV passage throat Mach number. It is interesting to note in Figure 527 that there is also noise suppression at IGV angles other than 54° where the IGV passage throat Mach numbers are below 0.7.

In Figure 528, the PNL suppression is shown as a function of percent loss in ideal fan thrust. For both tip speeds it is seen that there is a large decrease in fan performance associated with the noise reduction.

In Figure 529 the 1/3-octave band spectra are compared at 1410 ft/sec for the nominal IGV angle and the maximum IGV angle. At this maximum angle, the average throat Mach number is 0.86. The comparison shows there was a 13 dB

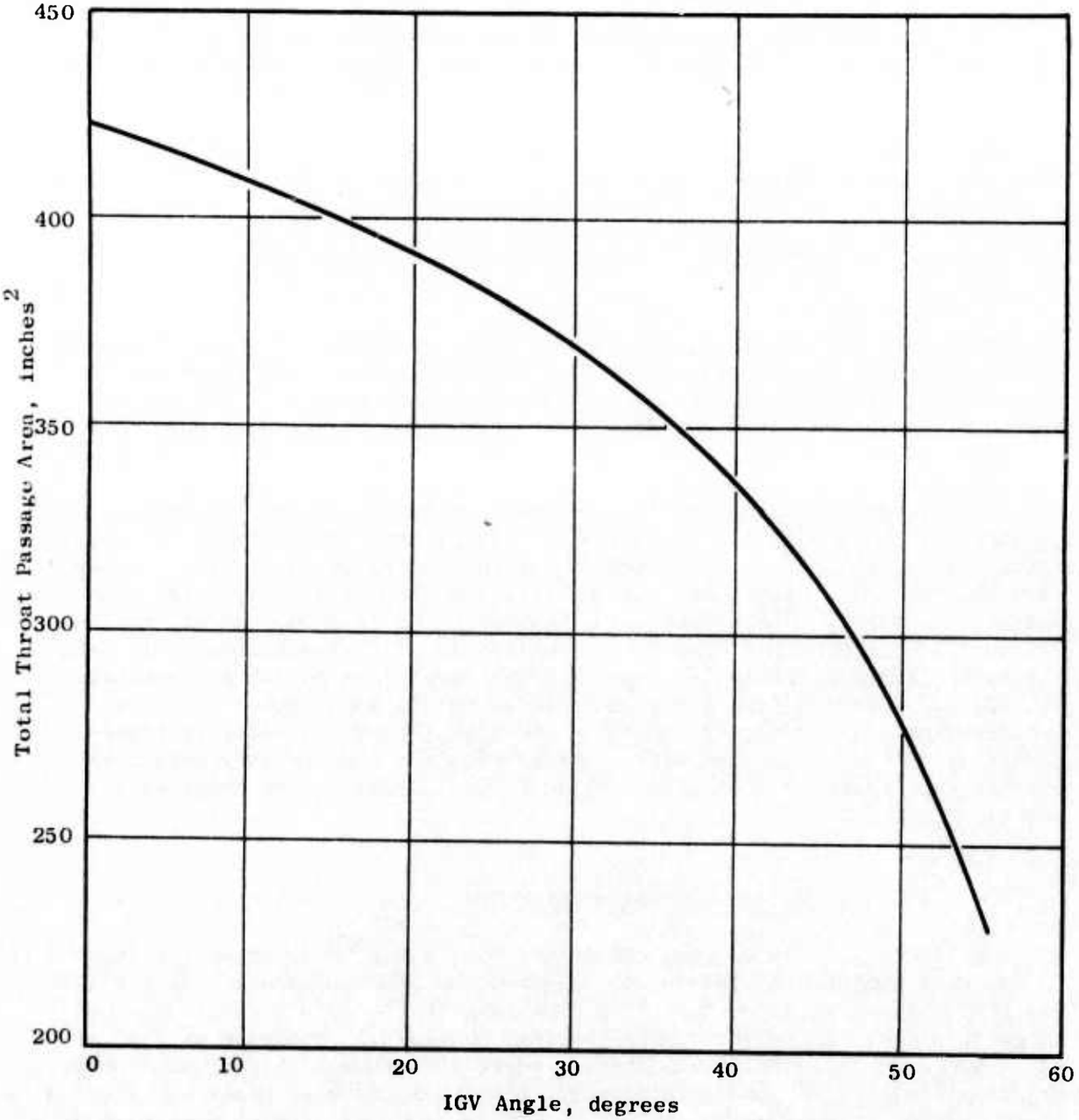

Figure 524. IGV Throat Area Versus Angle.

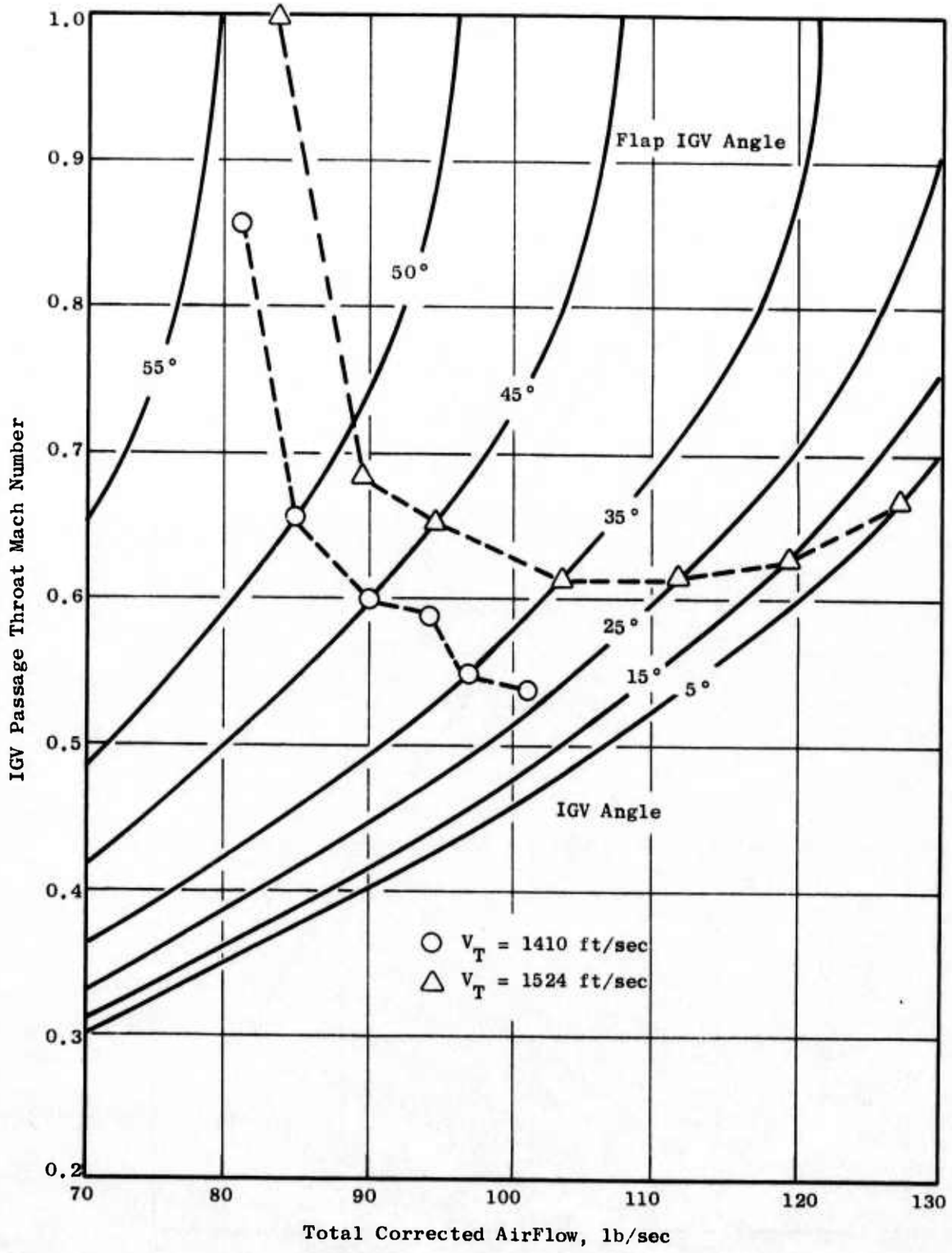

Figure 525. IGV Mach Number Versus Flow Rate for Various IGV Flap Angles.

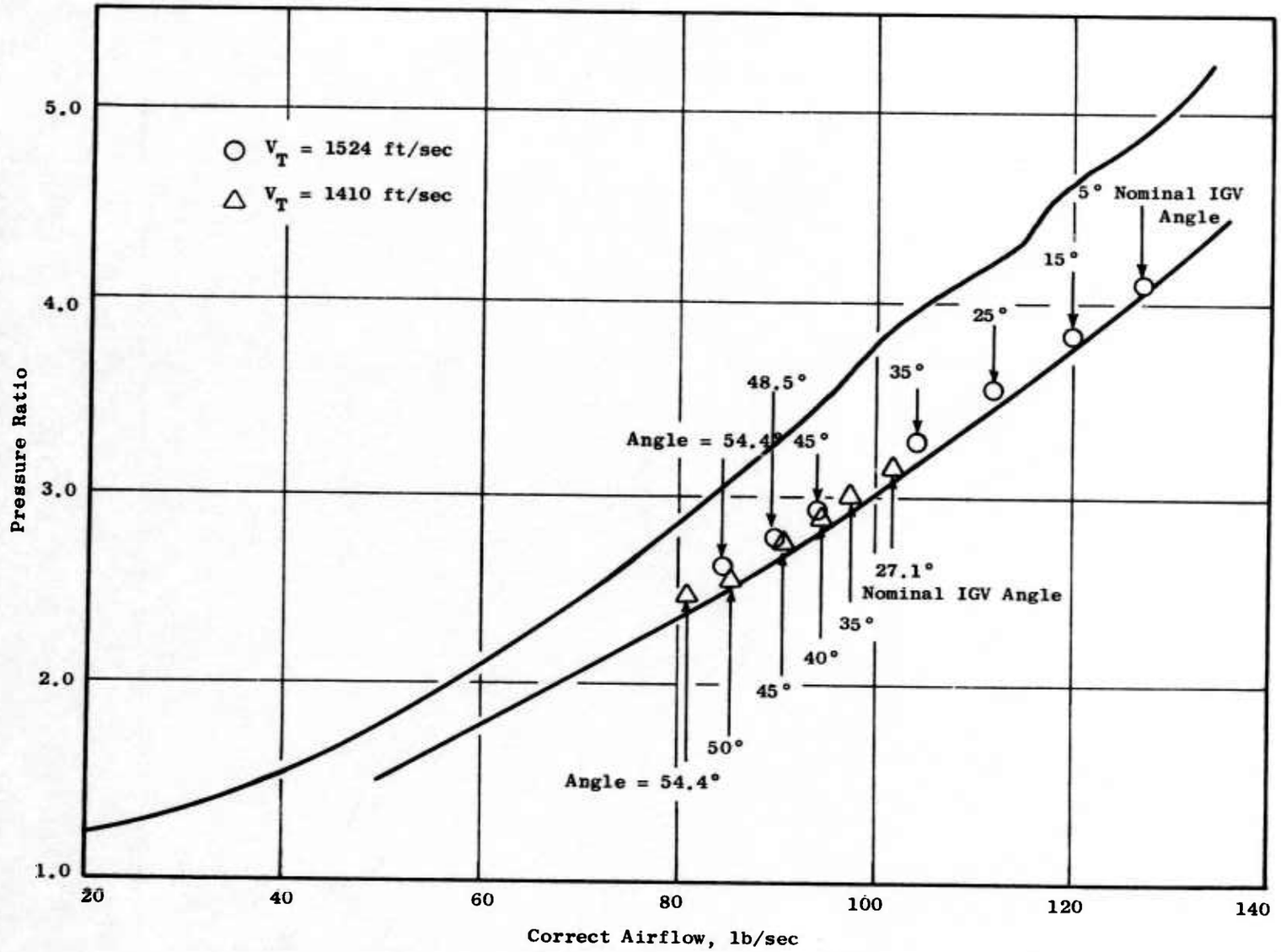

Figure 526. Fan Performance as a Function of IGV Angle.

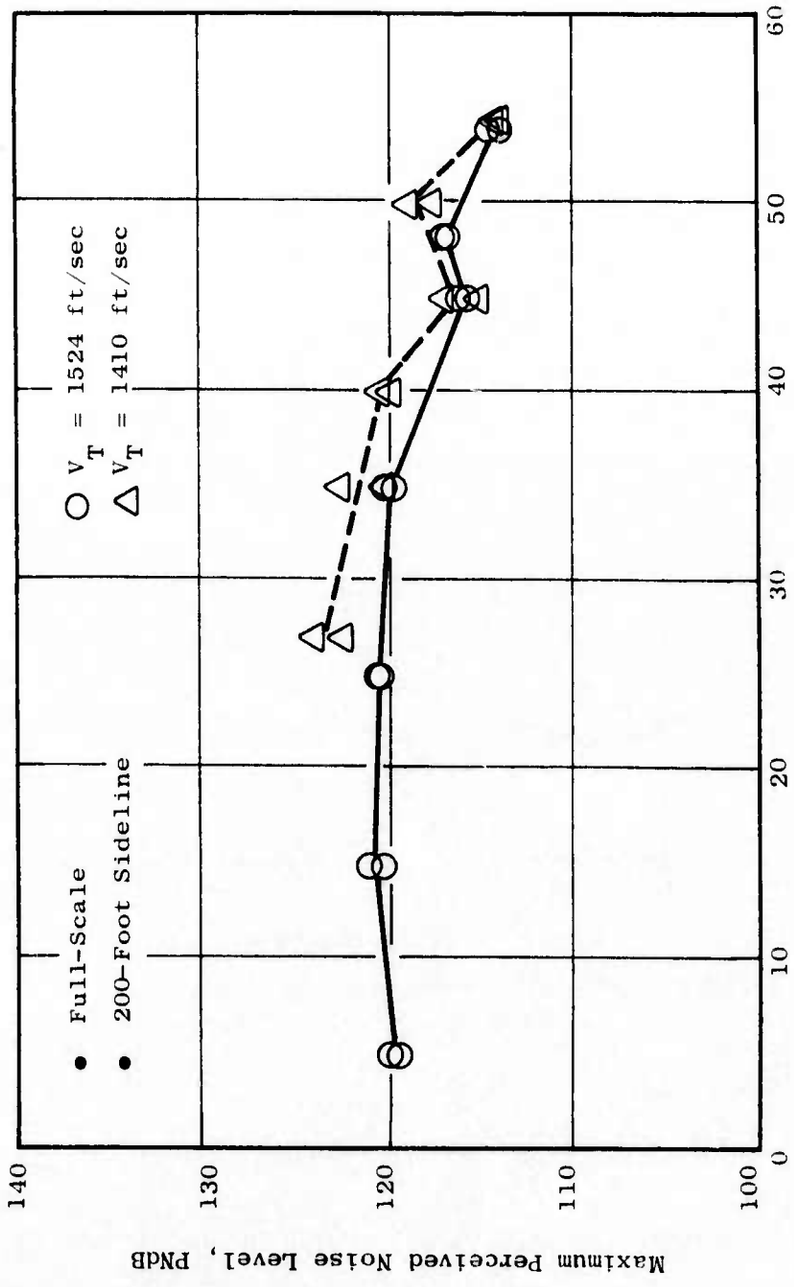

Figure 527. Maximum PNL as a Function of IGV Angle.

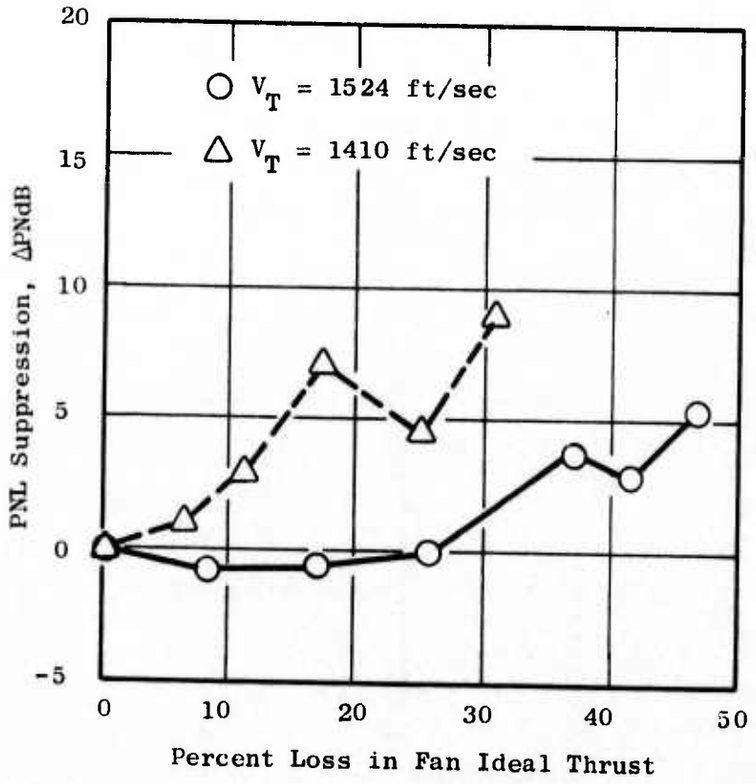

Figure 528. PNL Suppression as a Function of Loss in Ideal Fan Thrust.

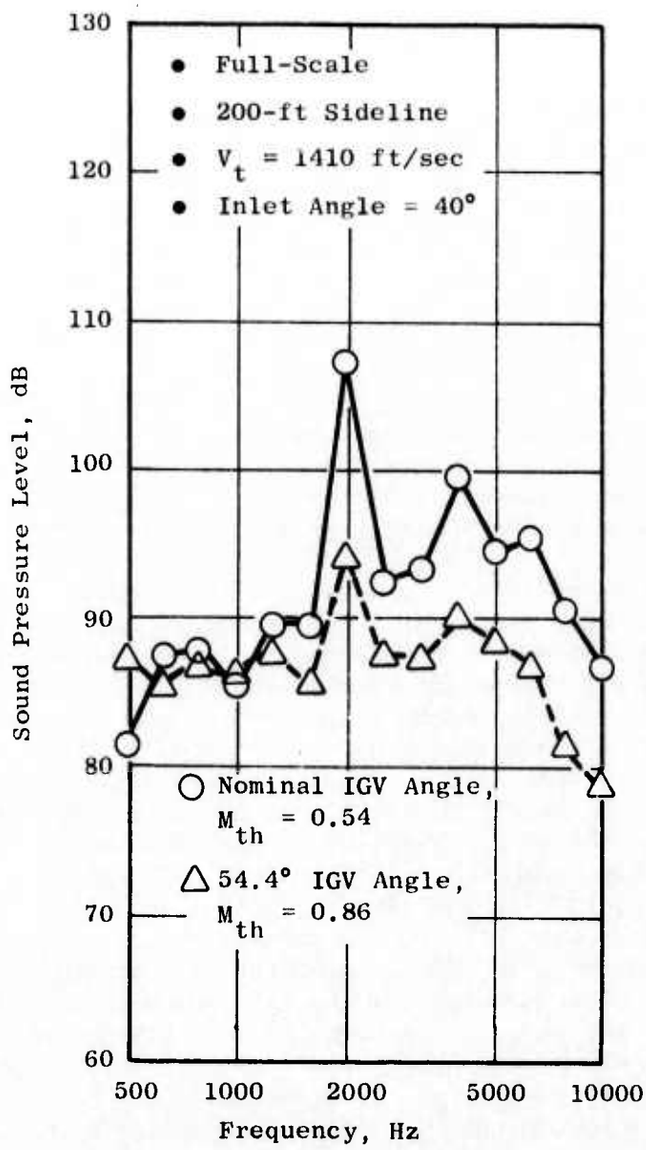

Figure 529. One-Third-Octave Band Comparison at Two IGV Angles.

reduction in the rotor 1 blade passing tone. The narrowband comparison in Figure 530 shows that the rotor 1 BPF and its harmonics are suppressed along with the MPT's. The MPT suppression is due to the fact that when the IGV angle increases, the fan relative tip Mach number decreases, and, therefore, the MPT's generated are less. It is also noted that the MPT reduction below BPF does not show up on the 1/3-octave band comparison because of the broadband noise increase associated with the high flap angles. It is speculated that this broadband noise increase is caused by the nonuniform flow characteristics over the IGV's into the fan at the high IGV angles.

At the 45° IGV angle, the throat Mach number is only 0.60 and, therefore, no significant acceleration suppression would be expected based on historical results. However, a 7 PNdB reduction was realized. In order to explain this difference, the 1/3-octave spectra at the 1410 ft/sec tip speed is compared for the nominal position and at a 45° angle in Figure 531. A similar far-field narrowband comparison is in Figure 532. It is seen that the PNL reduction is due to both a reduction in the MPT's and a reduction in the rotor 1 blade passing tone and its harmonics. The reduction in MPT's is due to the lower fan relative tip Mach number for this higher angle. For the 45° IGV flap angle, there was only a slight increase in broadband noise which did not negate the MPT reduction on a 1/3-octave-band basis. The reduction in the blade passing tones is attributed to the reduction in fan blade loading due to the drop in fan weight flow and pressure ratio when the IGV angles are increased, and, also, increased "line of sight" blockage through the IGV's.

At the 1524 ft/sec tip speed, only a 5.5 PNdB noise reduction was achieved at the maximum IGV angle where the inlet throat is choked ($M_{th} = 1.0$). Theoretically, if this area were fully choked, only the noise which leaks through the boundary layer and that which is radiated through the engine casing would remain. Therefore, a large reduction in noise level would be expected. Since this did not occur, the flow was obviously not fully choked. It is suspected that the calculated passage areas, which are approximate as discussed previously, may be underestimated, or that local subsonic flow regions exist in the passage which allow the noise to escape. Comparison of the 1/3-octave-band spectra and narrowband spectra for the nominal and maximum IGV settings are shown in Figures 533 and 534. Excellent MPT suppression is achieved; however, there is only 4 dB (Figure 533) of suppression at the rotor 1 blade passing tone which explains the lower PNL suppression at this tip speed. This lower suppression at the blade passing tone is attributed to the fact that, at this tip speed, the fan source noise is significantly attenuated by a strong and extensive detached shock as explained in Section 4.4.2.2. The blade passing tone which reaches the IGV passage is lower; and, therefore, the ΔSPL reduction due to the acceleration suppression would be expected to be less.

4.4.6.4 Directivity

In Figure 535, the SPL in the rotor 1 BPF 1/3-octave band, as a function of angle from the inlet, is compared for various IGV angles at a tip speed of 1410 ft/sec. The nominal IGV angle has a sharp peak at the 40° angle from the inlet. As the IGV angle is increased up to 45°, the curve becomes flatter

- Unscaled
- 40 Hz Bandwidth
- 100-ft Arc
- Inlet Angle = 40°
- V_t = 1410 ft/sec

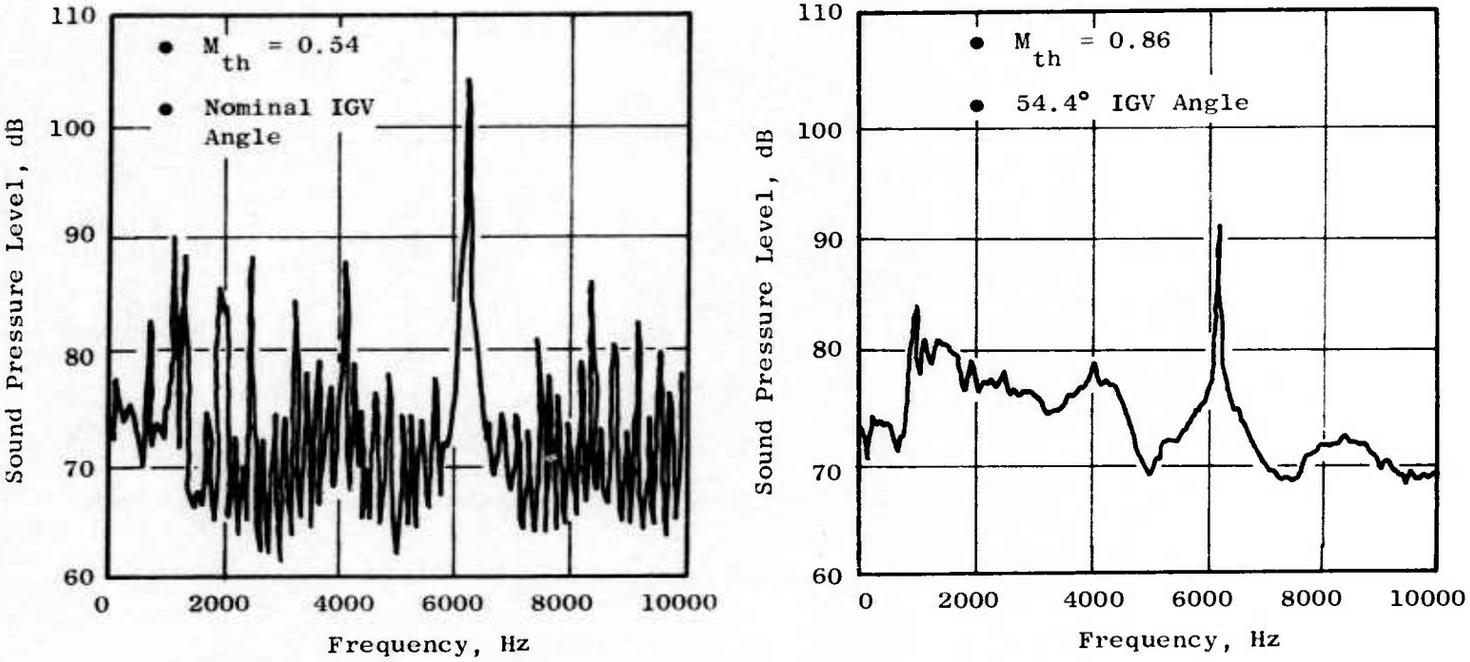

Figure 530. Narrowband Comparison at Two IGV Angles.

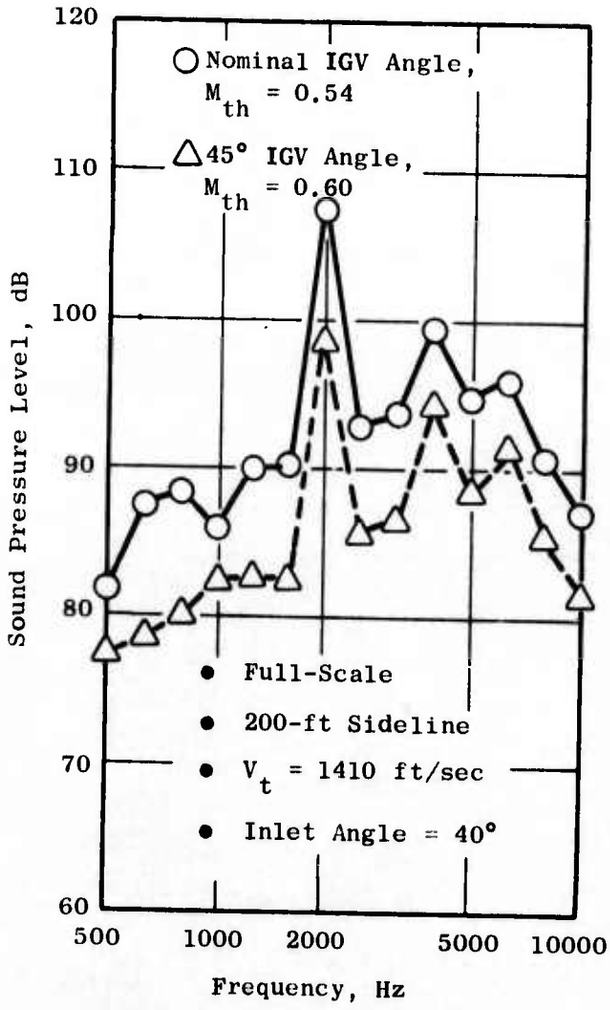

Figure 531. One-Third-Octave Band Comparison at Two IGV Angles.

- Unscaled
- 40 Hz Bandwidth
- 100-ft Arc
- Inlet Angle = 40°
- V_t = 1410 ft/sec

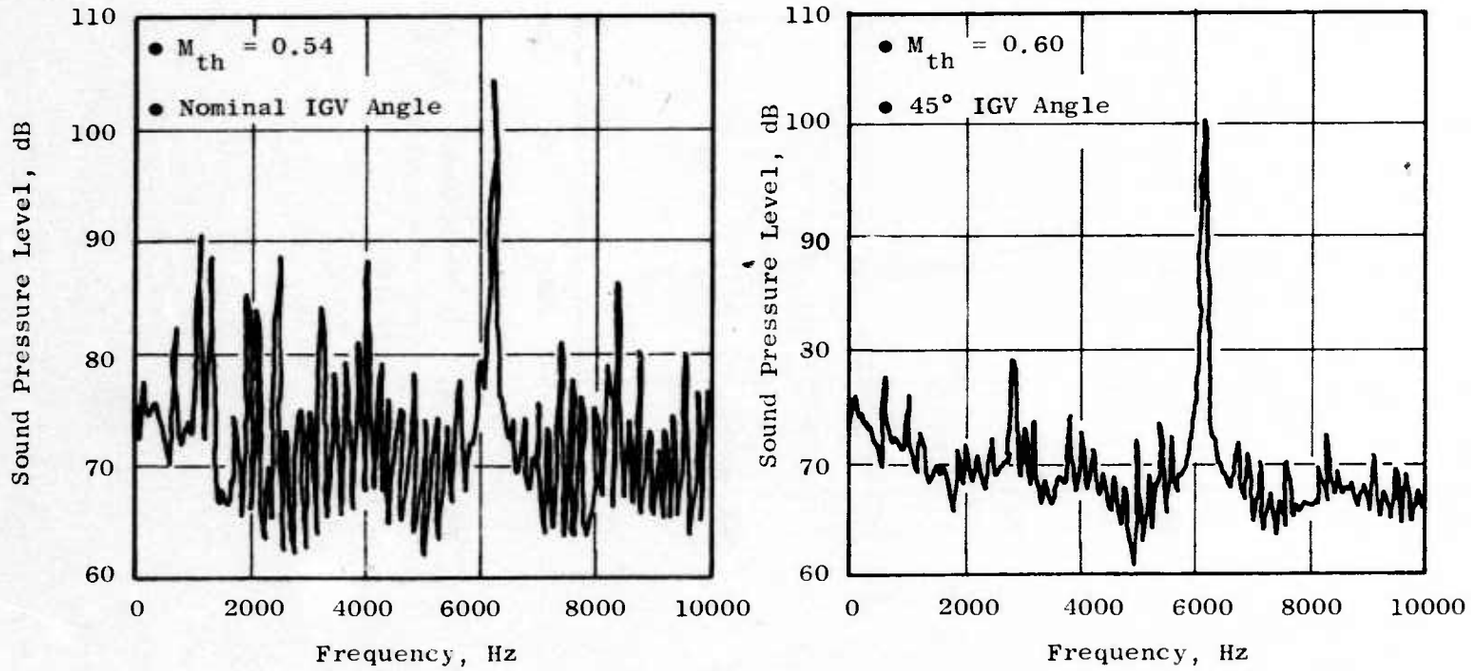

Figure 532. Narrowband Comparison at Two IGV Angles.

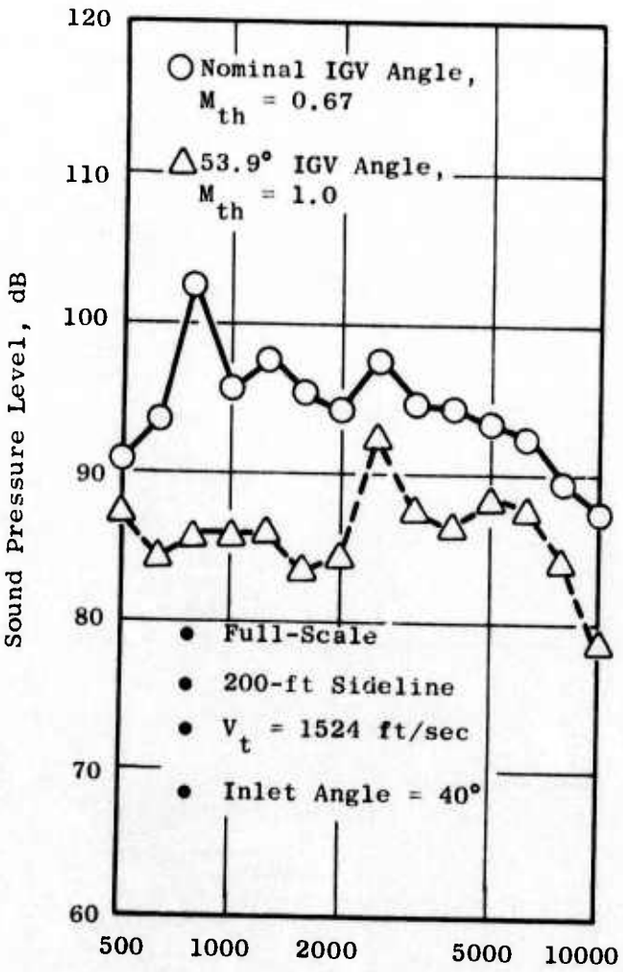

Figure 533. One-Third-Octave Band Comparison at Two IGV Angles.

- Unscaled
- 40 Hz Bandwidth
- 100-ft Arc
- Inlet Angle = 40°
- V_t = 1524 ft/sec

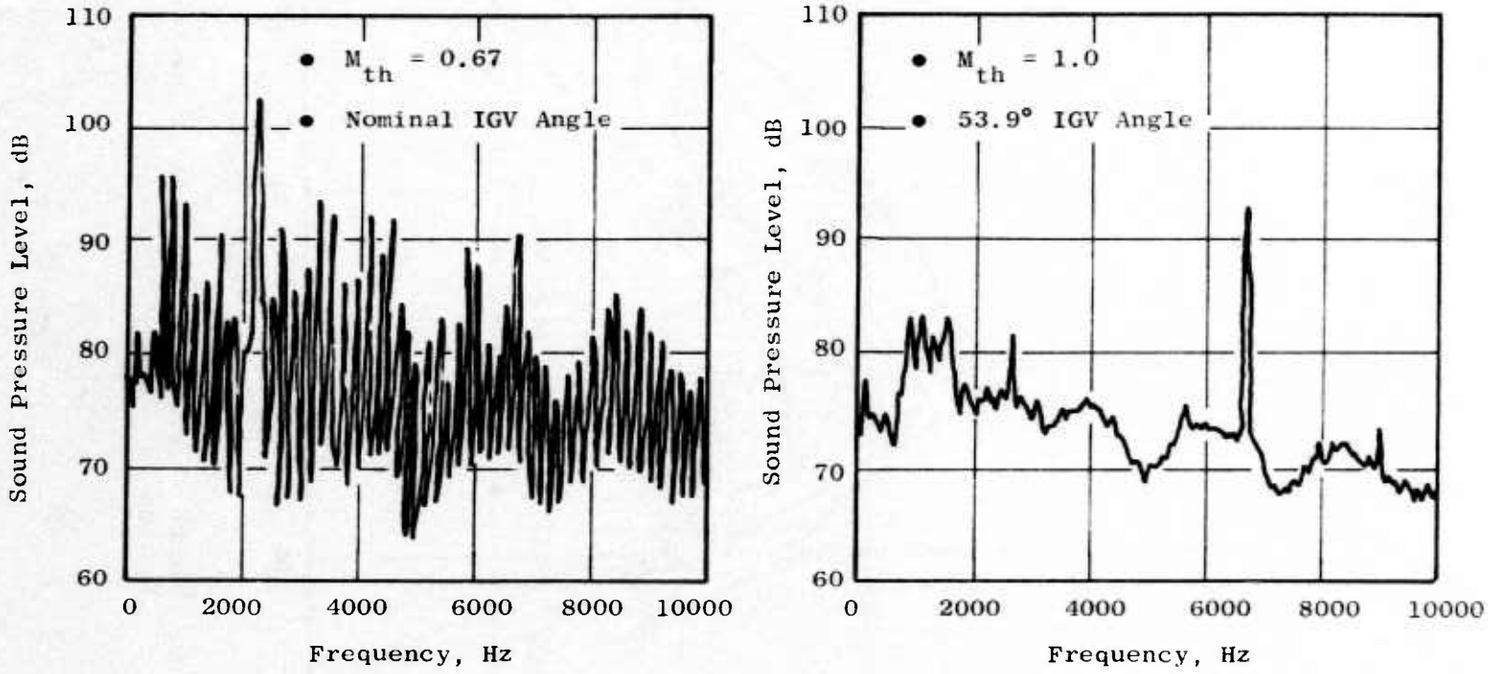

Figure 534. Narrowband Comparison at Two IGV Angles.

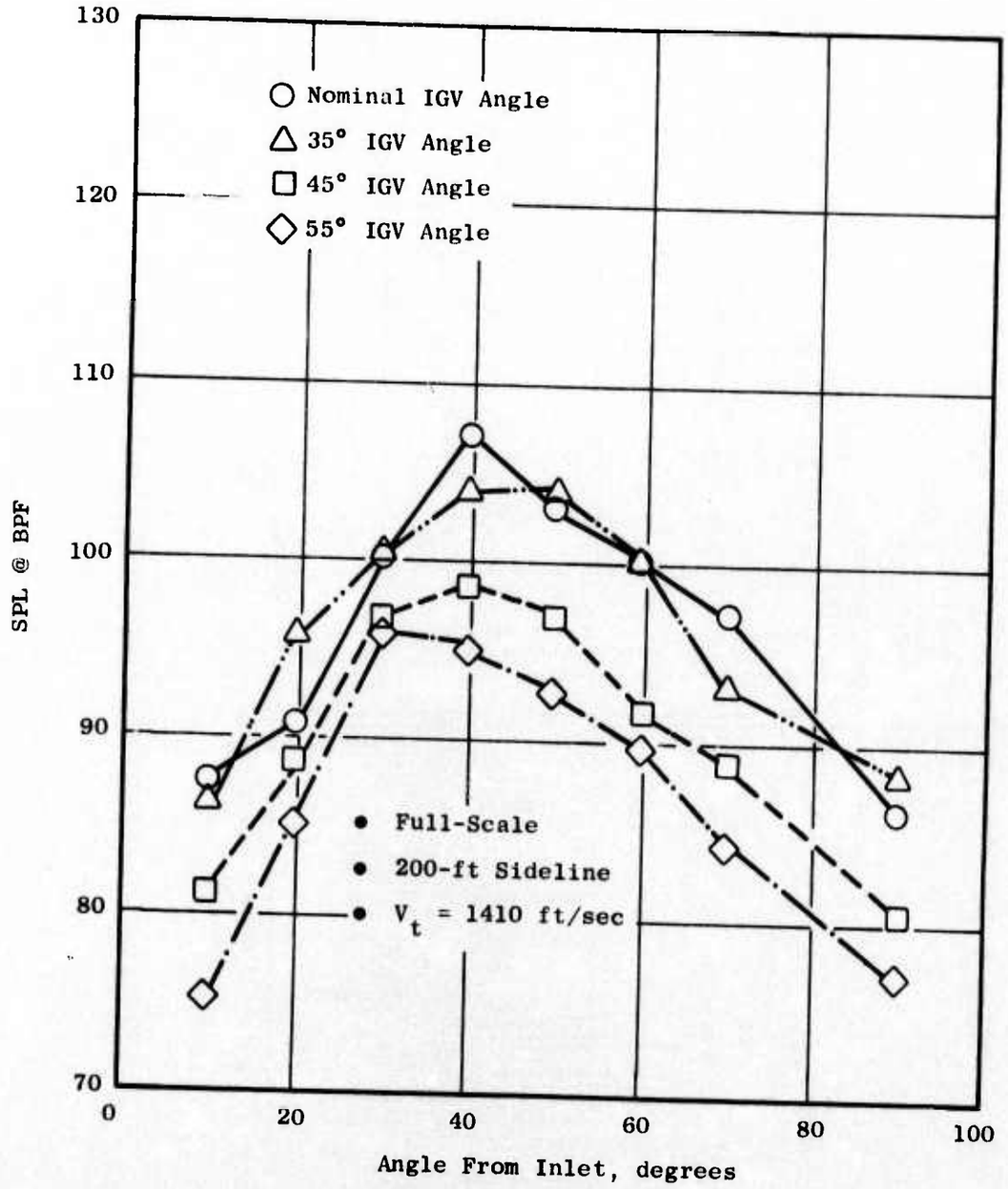

Figure 535. Directivity Comparison of SPL at the Rotor 1 BPF for Various IGV Angles.

near the maximum. Also, it is seen that there is increased suppression at the blade passing tone relative to the nominal at higher angles from the inlet centerline. At the 55° IGV flap angle, the maximum BPF level moved to the 30° inlet angle.

4.4.6.5 Conclusions

From the above results it is seen that significant PNL suppression may be achieved by increasing the IGV angle. However, as the IGV angle was increased beyond the nominal value, fan performance was severely degraded.

For the cylindrical baseline inlet tested in this program, the noise level at approach on the 200' sideline is 120 PNdB. By operating the fan at the 1524 ft/sec tip speed with the IGV angle at 55°, the noise level would be approximately 114 PNdB. This technique would then provide a noise reduction of 6 ΔPNdB at approach. The fan performance at this IGV angle is sufficient for approach. Of course, by operating the fan at these conditions, there would be a significant reduction in engine efficiency which would increase the total fuel consumption for a given mission. In addition, a noise suppression technique for the take-off condition would still be required. Considering this and the compromises required for the limited suppression obtained, the high Mach IGV technique for SST compressor noise suppression does not seem practical, particularly in view of the higher suppressions with practically no penalty associated with the hybrid inlet.

4.4.6.6 Summary

1. Significant PNL suppression was obtained (9 PNdB maximum) by increasing the angle of the IGV's and holding the fan speed constant.

2. As the IGV angle increases, the fan performance decreases.

3. This technique of compressor noise suppression appears to have little practical value for an SST engine.

SECTION 5.0

AIRCRAFT SYSTEM INTEGRATION

5.1 INTRODUCTION AND BACKGROUND

The aircraft systems integration studies were conducted to investigate the combined effects of the individual component noise sources in a typical supersonic transport aircraft engine system. The systems integration effort was coordinated with the preliminary design engineering work conducted under the NASA-Lewis Advanced Supersonic Technology Propulsion System Study (Contract No. NAS3-16950). Several types of engine cycles were investigated under the NASA-Lewis program including dry and augmented bypass turbojets, duct-burning turbofans, mixed-flow augmented turbofans, and variable cycle engines.

The system integration studies presented herein utilize the low bypass, mixed-flow turbojet cycle which, along with the duct-burning turbofan engine, appeared to be the most acceptable from the conventional engine category.

A discussion of the mechanical considerations for the design and implementation of a "typical" multichute/annular plug nozzle exhaust suppressor system is presented also, along with a brief comparison of the advantages and disadvantages of a treated conical ejector system. Some practical aspects of incorporating turbomachinery suppression also are addressed.

The procedure employed to estimate the EPNL used static SPL spectra obtained from the individual noise component tests (jet, turbine, and compressor). Results of the system evaluation represent current acoustic technology combined with the most favorable trades from an aerodynamic and mechanical viewpoint. The in-flight noise evaluation of unsuppressed and suppressed aircraft engine systems is presented in terms of EPNL at the FAR-part 36 monitoring points and in terms of the area of noise footprints.

5.2 AIRCRAFT/ENGINE SYSTEM SELECTION

The aircraft and engine system utilized in the integration study was drawn from the aforementioned preliminary design engineering work conducted under the NASA-Lewis AST Study. The baseline airplane is of arrow wing planform with a tail. It has four engines in axisymmetric nacelles mounted under the wing at the trailing edge. The wing has leading and trailing edge flaps. The payload is 292 passengers totaling 61,030 pounds. The cruise speed of the airplane is a Mach number of 2.4 at altitudes greater than 53,400 feet. The airframe is constructed from titanium and its take-off gross weight (TOGW) is about 900,000 pounds.

In reality, many detailed and involved considerations are necessary in selecting an engine cycle for a supersonic aircraft system. The objective

is to strike the right balance between the two driving forces of economics and environmental impact. For the purposes of the systems integration study, a low-bypass, mixed-flow turbojet was selected. This engine served as the baseline for comparison of other engines studies in the NASA-Lewis study. It was selected because it, along with the duct-burning turbofan engine, appeared to be the most acceptable from the conventional engine category. The engine cycle was based on a design low pressure compressor pressure ratio of 4 to 1, a bypass ratio of 0.43, and an overall pressure ratio of 22.5. It had a mixed-flow exhaust system where all the airflow could be mixed and reheated up to 1900° F average temperature. At these design point conditions the ideal jet velocity was 2500 ft/sec. This basic engine had a design corrected flow of 1045 lb/sec. The engine/airframe combination results in an all-supersonic range of just over 3400 nautical miles with a full payload of 292 passengers and enough fuel reserve to meet the divert and hold requirements. This range is quite adequate for flights between the eastern seaboard of the United States and Western Europe. One of the primary purposes of the systems integration effort was to add a practical aspect to the technology developed in the current program by assessing the practicality of applying the technology and assessing the current state-of-the-art noise levels for the realistic and economically feasible SST system.

5.3 SYSTEM INTEGRATION OF NOISE TECHNOLOGY

5.3.1 Jet Noise Technology

5.3.1.1 Mechanical Feasibility of the Jet Suppressor

Annular/Plug Suppressor Nozzle Description

The translating shroud annular nozzle is particularly attractive for SST engines requiring jet sound suppressors and reversers. In addition to having high supersonic and subsonic performance, it has many desirable mechanical features. The plug assembly provides a convenient space for housing a retractable jet noise suppressor. The translating shroud can withstand the high internal pressures imposed by the subsonic flow to the chutes during the sound suppression mode. A cascade-type thrust reverser may be incorporated with minor increase in nozzle diameter. The nozzle is adaptable to single-flow, mixed-bypass-flow, and double-bypass-flow engine configurations.

A translating shroud annular nozzle with chute suppressors is shown in Figure 536. A significant feature of this nozzle is the fixed diameter, translating A9 shroud. With no flaps and seals required for shroud diameter modulation there will be little overboard leakage. Translation of the shroud establishes the internal A9/A8 ratio for best performance at any particular operational Mach number, altitude and power setting. During suppressed operation the shroud is extended aft to engage with the suppressor chutes forming the duct for the exhaust airflow to the throat which is at the chute trailing edges. In this mode the high internal pressures cause only hoop stresses in the cylindrical shroud which results in a light design in comparison to a flap and seal type of A9 control. The throat area (A8) is

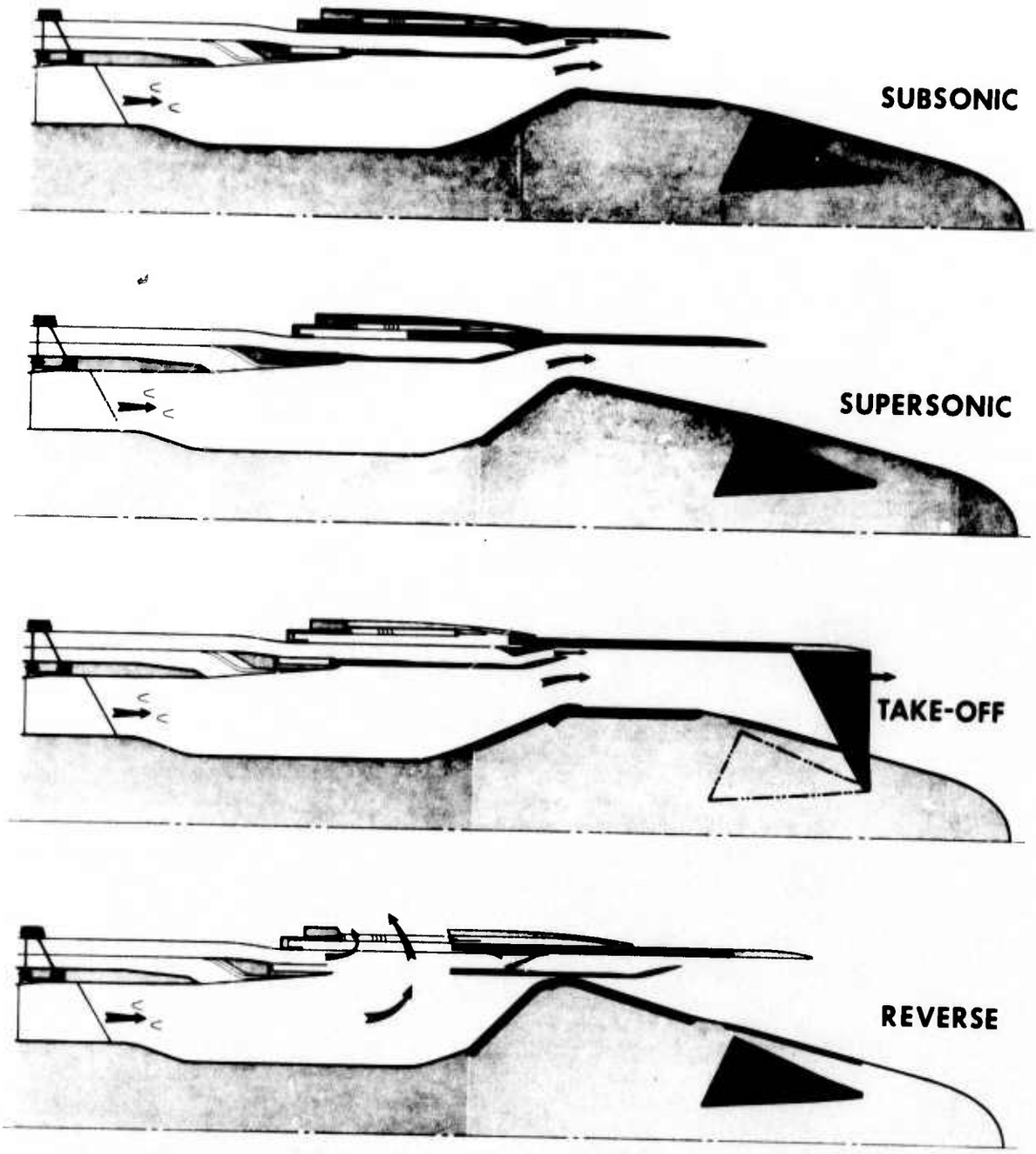

Figure 536. Schematic of Jet Suppressor Operational Modes.

varied by modulating the plug diameter through the operation of flaps and seals. During suppressed operation the flaps are positioned for maximum flow area to effect about Mach 0.5 flow. This minimizes diffusion losses to the chutes.

The thrust reverser is of the cascade type sized for 180 degrees discharge. This arrangement allows the required flexibility in discharge pattern to meet aircraft installation requirements and prevent inlet reingestion problems. For reverser operation, the annular shroud, reverser inner cover, and reverser outer cover are translated aft to expose the fixed-position cascades. No separate blocker doors are required. The A8 flaps close against the translated reverser inner cover to form the blocker. Since the annular shroud is already in the aft position during suppressed operation, transition to reverse can be made during the suppressed mode (as well as the unsuppressed mode) without sequencing the movement of the suppressor chutes or cover door. This reduces the time to go to reverse operation.

The jet noise suppressor shown on this nozzle consists of 32 vee-section chutes which, when deployed, are positioned radially between the plug surface and the aft edge of the extended shroud. The aft edge of the shroud is serrated to conform to the vee-section shape of the outer edges of the chute. This permits ambient air ventilation of the chutes while containing the internal gas flow between chutes to the throat at the aft end of the chutes. To stow the chutes, the plug cover flaps and seals are moved forward, then the chutes are rotated forward into the plug cavity. The chutes rotate forward so that the widest part of the chute is stowed inside the largest available plug diameter. When the chutes are in the stowed position, the plug cover flaps and seals are moved aft, again, to provide a smooth plug profile. A feature of the chute design is that the chute pivot is located radially inward from the chute outer aft edge so that either the chute or the annular shroud can be moved to and from the suppressed position independently. The weight of each suppressor is approximately 1500 lbs for the 1045 lbs/sec weight flow engine employed in this study, making a total of 6000 lbs for the four-engine aircraft.

Ejector Shrouds

Use of an ejector similar to that tested on the J79 suppressor demonstrator (Section 3.4.3) would add considerable weight to the exhaust system (about 800 lbs), add complexity, and cause a maximum diameter increase. The diameter increase for the stowed ejector shroud would cause additional drag throughout the unsuppressed mission. The complexity results from the shroud having to be translated about 9 feet from the stowed position to the deployed position and from the shroud having to increase in diameter and change slope in the stowed position. To do this, the shroud would have to be a set of flaps and seals. Therefore, since large suppression gains were not made during the demonstrator tests, the ejector shroud was not recommended for use with the integrated system.

5.3.1.2 Aeroacoustic Performance Trades

The jet suppressor system selected for incorporation into the aircraft/engine systems phase of this program exhibited a good trade between PNL suppression and thrust loss (Figure 537) resulting in a design point $\Delta PNL/\Delta C_{f_g}$ of greater than 2.1. The peak PNL suppression relative to an unsuppressed conical nozzle is based on static test conditions of $V_j \sim 2500$ ft/sec and $P_{T8}/P_o \sim 3.0$ at the 2128-ft sideline and assumes no change in suppression due to flight effects. The thrust loss relative to an unsuppressed annular plug nozzle ($C_{f_g} = 0.981$) is based on wind tunnel data at a freestream Mach number of 0.36 and nozzle pressure ratio of $P_{T8}/P_o \sim 3.0$. (Flight effects on PNL suppression are not as yet well determined, but an indication of the relative velocity influence is found in Section 5.4.2).

This attractive trade combines a reasonable level of suppression (12 PNdB at $M_o = 0$) with good aerodynamic wind-on performance (0.924 at $M_o = 0.36$) and mechanical feasibility in a jet exhaust suppression system for application to advanced technology engines.

5.3.2 Turbomachinery Noise Technology

5.3.2.1 Turbine Noise Reduction

Turbine noise reduction was investigated in this program using a YJ85 engine. Both turbine second-stage spacing (blade-vane) and exhaust duct treatment were determined to be useful ways of reducing turbine noise in the far field. In applying this technology to an SST engine system, consideration was given to how much turbine noise suppression would be required to be compatible with current FAR-part 36 noise regulations for turbojet engines. Considering that turbine noise would likely be a factor only at approach conditions and large suppressions would probably not be required, it followed that spacing the turbine should be sufficient. That is, there was no benefit to be gained in trying to reduce turbine noise below the noise floor defined by other engine components. Turbine spacing by itself has associated with it a rather minor penalty. Thus, the suppression due to spacing only was used in the system noise evaluation.

5.3.2.2 Compressor Noise Reduction

The hybrid inlet approach to compressor noise reduction is particularly suited to a supersonic transport system. (Section 4.2.3). The hybrid inlet uses both airflow acceleration and wall acoustic treatment to achieve suppression. The airflow acceleration is limited in terms of inlet throat Mach number to avoid the performance problems (such as poor total-pressure recovery and high-pressure distortion) normally associated with hard choking the inlet to obtain suppression. Figure 538 shows the trend of pressure recovery with throat Mach number obtained during the hybrid inlet test with the inlet in the take-off position. The rapid degradation in performance

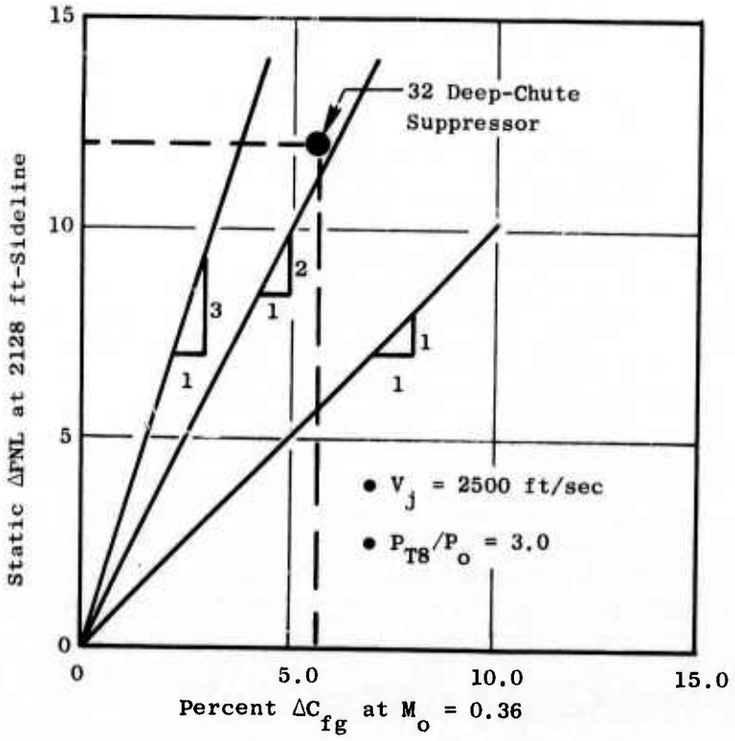

Figure 537. Aeroacoustic Trade for Jet Suppressor.

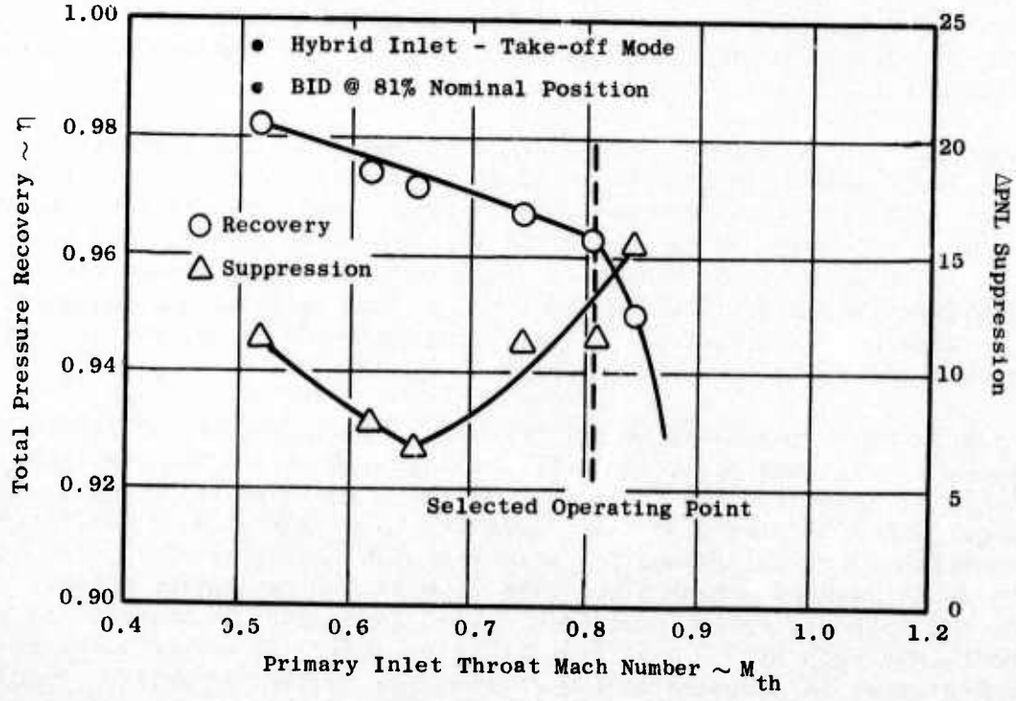

Figure 538. Aeroacoustic Trade for Hybrid Inlet.

beyond the selected operating throat Mach number is obvious. Since high throat Mach numbers ($0.72 \leq M_{th} \leq 0.80$) do not provide as much suppression as choking ($M_{th} = 1.0$), wall treatment is provided for additional suppression. The airplane chosen for the system integration study had a translating centerbody, axisymmetric mixed-compression inlet, quite similar to the hybrid inlet tested for compressor noise reduction (Section 4.4). In addition, the airplane would require a variable area nozzle and an inlet airflow control system. With these features, it would be possible and practical to set the desired throat Mach number at any noise measurement point without any added penalty due to mechanical system complexity. Thus, the only significant penalty associated with the hybrid inlet is the added weight and cost of the wall acoustic treatment, which could be reduced by using the treatment as a load-carrying structure.

Thus it is seen that the hybrid inlet suppression device is a very practical approach to SST engine compressor noise control. The compressor and inlet system studied in the technology portion of the program are essentially identical to those selected for the systems integration study; and, thus, the test data have been applied directly in the system noise evaluation, after making certain necessary adjustments which are discussed.

5.4 DESCRIPTION OF FLYOVER NOISE ESTIMATION METHODS

5.4.1 Ground Rules

In order to make the system noise evaluation as realistic as possible, certain ground rules were followed in determining the flyover noise. These ground rules were set by predicted operation of the airframe/engine system with standard FAA operating procedures used as the basis.

Specifically, the engine operating conditions (or thrust) are set to meet a balanced field length (BFL). A "balance" is obtained between the critical distance for engine failure for two cases. First, when the pilot elects to proceed down the runway and can clear the obstacle and, second, when he elects to abort and can stop at the obstacle. Thus, the thrust is a function of the in-ground-effect aerodynamic characteristics of the airplane and the geographical facts of the airport. The resulting take-off thrust for the system considered was 61,400 pounds per engine.

The three noise measuring points for the current FAR-Part 36 regulation on subsonic aircraft are depicted in Figure 539. There are two regulatory noise levels at takeoff. The first is sideline noise measured along a line parallel to, but displaced 0.35 n mi (2128 ft) to either side of the flight path projection along the ground for a four-engine aircraft. The point at which the noise reaches a peak along this line is the regulation point. Secondly, the take-off noise (sometimes called community) is measured directly under the flight path at 3.5 n mi from brake release. At approach the regulatory noise level is measured at 1 n mi from the runway threshold. Regulation noise limits are a function of TOGW and, for the airplane used in the study, are currently 108 EPNdB at all three measuring points. Noise footprint

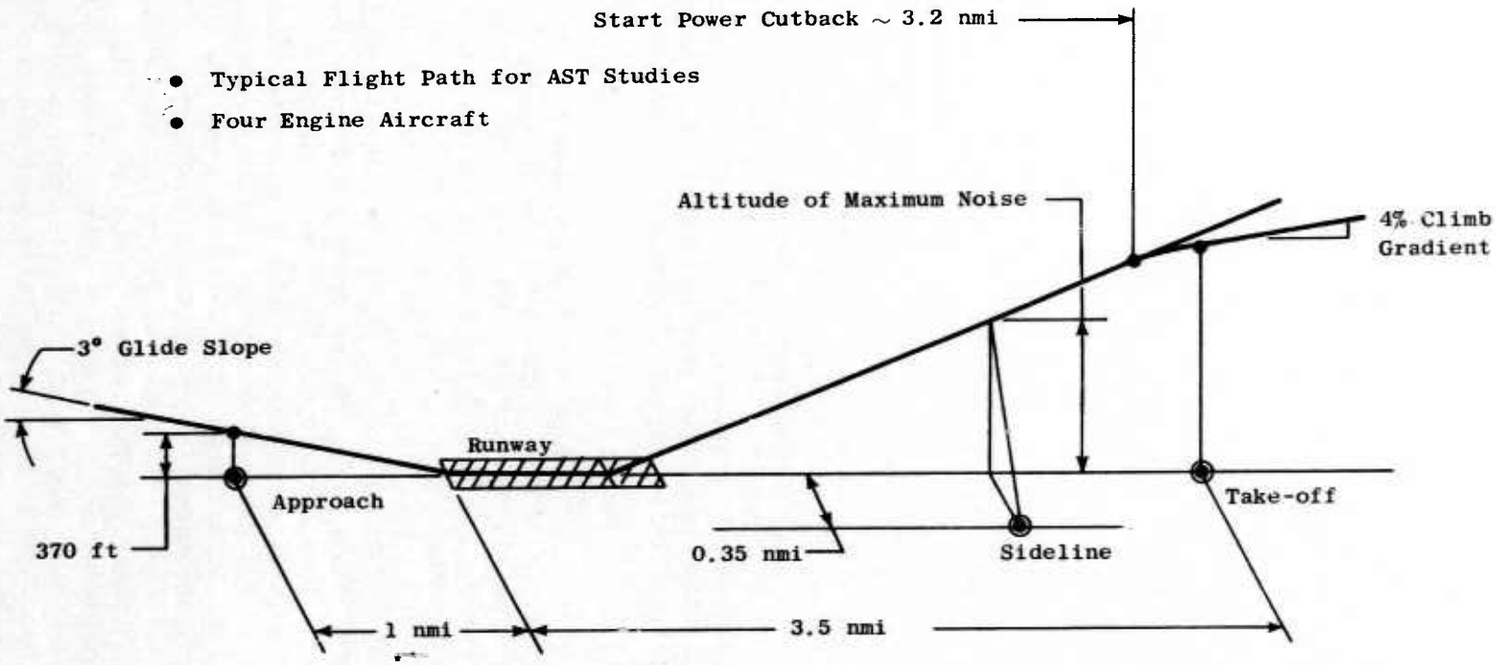

Figure 539. FAR-Part 36 Aircraft Noise Monitoring Points.

area, which is the area enclosed by a contour of equivalent perceived noise (90 EPNdB was used for this study), is currently not regulated.

Take-off noise at 3.5 n mi depends upon the flight path at this point. One path continues the climbout at the take-off power setting, while the second path involves a power cutback before the measuring station to put the airplane into a minimum climb gradient of 4% for a four-engine airplane. The second path usually has the lowest noise levels. It has been determined that, in order to take full advantage of the reduced noise levels at cutback power, it should be performed at about 3.2 n mi from brake release. This assures that the complete noise-time history at the measuring point is associated with the reduced-power condition. Before power cutback, a constant climb gradient at constant flap and power setting is maintained starting at about 0.35 Mach number after the undercarriage has been retracted.

The quietest SST airplane at takeoff is that one which has reached the highest altitude (acoustic range effect) at the measuring station and needs the least thrust (highest lift-to-drag ratio) for the minimum climb gradient. This altitude depends upon the climb gradient multiplied by the difference between 3.5 n mi and the distance required to set up the climb gradient. This distance depends upon the ground roll to lift-off plus the distance to bring the airplane to the climb gradient at initial climb speed. Ground roll distance depends mainly upon airplane lift coefficient, wing loading, and minimum thrust for the assigned balanced field length. The climb gradient depends upon thrust minus drag. The airplane with the highest climb-out lift-to-drag ratio will have the steepest gradient. Flight speed enters into both thrust and drag calculations and into noise by way of relative velocity effects and the conversion from perceived to effective perceived noise.

Sideline noise is reduced by EGA and engine shielding at low altitude and by increases in acoustic range. A maximum noise level is obtained where the reduction in noise by EGA and shielding reaches a minimum. The thrust level is practically equal to that at liftoff, which must be at least that required for the balanced field length.

The thrust at approach is about one quarter of the thrust for takeoff, since the airplane weight is down to the order of its empty weight and the airplane is sinking rather than climbing. At approach, the nozzle area is normally kept wide open. This is done to maintain high engine rpm in order to minimize spool-up time in the event that a go-around is required. Aerodynamically practical jet noise suppressors thus far have been fixed nozzle area devices and, as such, are inconsistent with the need for high rpm at approach. In addition, the off-design jet noise suppressor is normally ineffective at approach jet velocities. In the integration studies, the jet suppressor has been stowed at approach; the jet nozzle has been opened to get the lowest jet velocity for the required thrust and to be consistent with the need for short engine spool-up time. This low jet velocity also reduces jet noise to near or below the turbomachinery noise floor.

The monitoring point geometry, using the criteria discussed above, is summarized in Figure 539 for the airplane/engine system selected for the systems noise evaluation. The resulting altitude at the sideline point is 1110 feet, which gives an acoustic range of 2400 feet. Power cutback at 3.2 n mi (out) results in an altitude of 1860 feet at the overhead community measuring point (3.5 n mi). Table 23 summarizes the aircraft/engine operating conditions used in the system integration study.

5.4.2 EPNL Calculation Method

The method used for predicting noise of the selected SST system utilized component test data (SPL versus frequency) obtained in the current program. The data were selected at, or adjusted to, the proper operating conditions, scaled to the selected engine size and frequency range, and flown using a flyover noise computer program. Within this program, suitable corrections were made for such acoustic effects as extra ground attenuation (EGA), Doppler frequency shift, relative velocity effects (V_R), and dynamic effect.

A flow chart of the method is provided in Figure 540. Scale model jet noise data at the appropriate jet velocity were selected for the unsuppressed conical nozzle (baseline) and 32-chute suppressor for each of the three measuring point conditions, except at approach, where a suppressed jet was not considered for reasons mentioned in Section 5.4.1.

Suppressed low pressure compressor data were flown at the three monitoring points. Unsuppressed data were also flown at approach (where it might be the dominant source) so the effect of suppressing the compressor could be examined.

SPL suppressions due to the hybrid inlet were obtained at the 0.78 and 0.81 throat Mach number condition for the inlet in the approach and take-off (blow-in-door 81% nominal setting) configurations, respectively. The suppressions then were applied to the measured unsuppressed baseline levels at the appropriate Rotor 1 tip speeds for each condition, as determined by the engine cycle selected for the systems integration study. The 81% nominal blow-in-door configuration was selected because it was the only setting which operated as designed aerodynamically and because it resulted in somewhat lower noise levels than the other two positions tested. The blow-in-doors were assumed to be open for the community cutback operating point as well as for sideline. The low pressure turbine for the low-bypass ratio turbojet turbine selected for the study was considerably different in terms of loading and geometry relative to the J85 high pressure turbine tested in this program. For this reason, an empirical turbine noise prediction developed in the Core Engine Noise Control Program (Reference 29) was used to estimate the unsuppressed turbine noise. This method utilizes the stage pressure ratio, the blade relative velocities into the turbine blades, the blade tip speeds, the turbine stage exit area, and the spacing between blade rows. The noise levels for each stage are computed separately and then summed to give the turbine noise spectra. Suppressed turbine spectra were obtained by applying the ΔSPL's measured due to spacing from the J85 tests to the predicted unsuppressed

Table 23. Monitoring Point Definition and Conditions.

Conditions	Takeoff (Sideline)	Community (Cutback)	Approach
Aircraft			
• Altitude - ft	1110	1860	370
• Sideline Distance - ft	2128	0	0
• Acoustic Range - ft	2400	1860	370
• Approximate Flight Speed Mach Number	.328	.328	.221
• Flight Path Angle - degrees	9.0	2.5	-3
• Angle of Attack - degrees	6.5	6.7	12
Engine			
• Nozzle Pressure Ratio	3.33	2.47	1.24
• Nozzle Exit Temperature - ° R	1630	1330	1040
• Jet Velocity - ft/sec	2400	1900	970
• Turbine Tip Speed† - ft/sec	1310	1162	1110
• Turbine Pressure Ratio (overall)	6.03	5.83	7.10
• Compressor Tip Speed‡	1560	1435	1369
• Compressor Pressure Ratio	3.54	2.79	2.20
• Engine Airflow	1045	870	795
• Engine Thrust	61,400	35,000	15,000
• Bypass Ratio	.709	.823	1.122

† Second-stage low pressure turbine blade

‡ Rotor 1

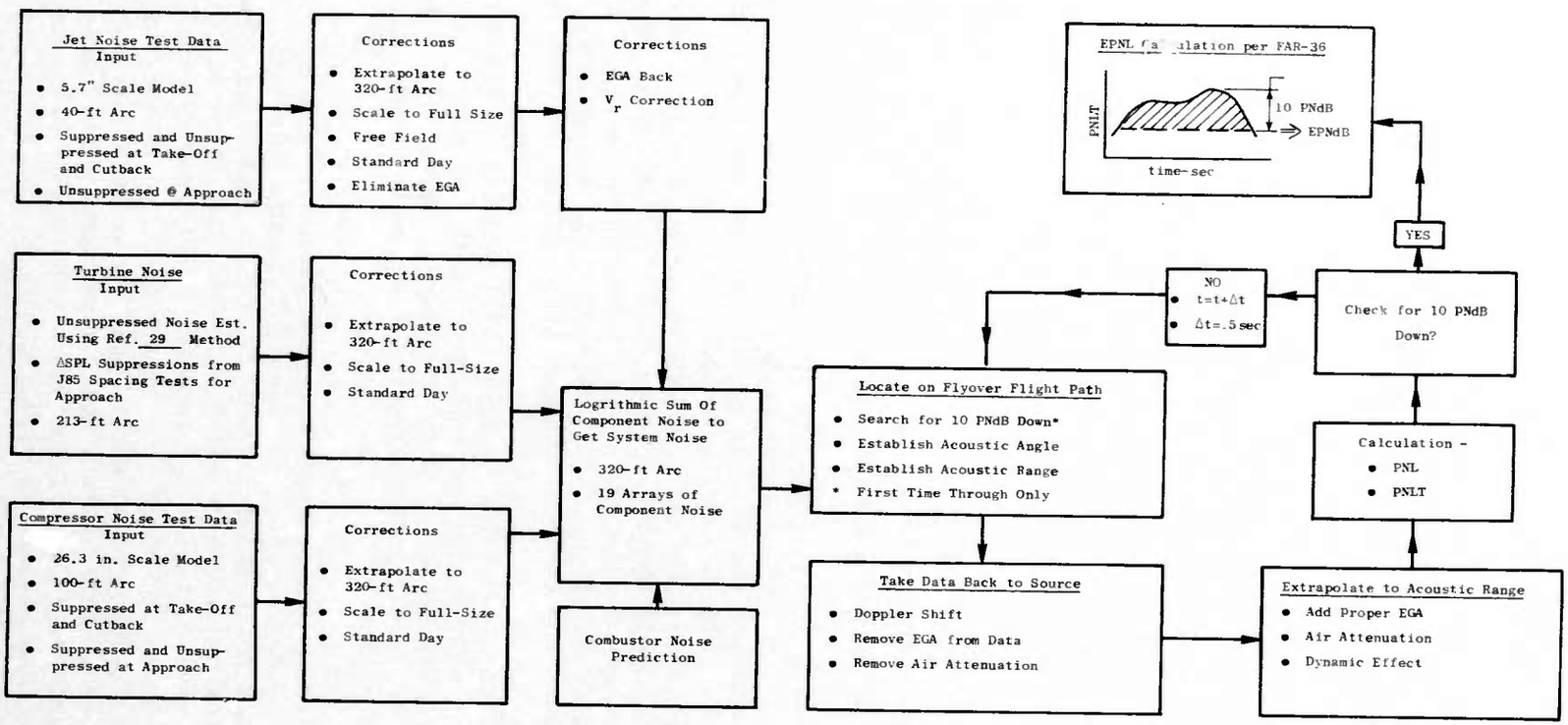

Figure 540. Description of System Noise Evaluation Procedure.

spectra. The turbine noise was flown unsuppressed at approach also, in order to determine its effect on system EPNL at that condition.

Although combustor noise was not studied as part of the technology portion of this program, it was included in the Systems Integration Study for completeness. The method of Reference 29 was used to predict the combustor noise; the overall power level of the combustor as defined therein is:

$$OAPWL = 20 \log_{10} \left[\sqrt{\dot{w}} \, (T_4 - T_3) \, (\rho_3/\rho_o) \right] + K$$

where, $\dot{w}$ = air weight flow through combustor

T_4 = combustor exit temperature

T_3 = combustor inlet temperature

ρ_3 = combustor inlet density

ρ_o = reference density (ambient)

and where,

K = 64 for turbojet engines

K = 56 for turboshaft engines

K = 48 for high bypass turbofan engines

The difference in the K value is attributed to the difference in the turbine attenuation of combustor noise for the three engine types. That is, there is more combustor noise attenuation through the turbine as you increase turbine stages, and the number of turbine stages increases going from turbojets to turboshafts to turbofan engines. For the low bypass turbofan engine selected as the Systems Integration Study engine, a value of K = 54 was used. That is, the lower bypass ratio was assumed to result in a power level increase of 6 dB relative to high bypass turbofans. This type of a difference was witnessed in the low bypass JT8D engine combustor noise data, for example.

The component test data were scaled in terms of frequency to match the full-scale blade passing frequency for the turbomachinery components (compressor and turbine) and on nozzle diameter ratio for the jet noise data. Absolute noise levels were scaled by 10 $\log_{10}$ of the weight flow ratio between the scale model and full size engine.

The data (unsuppressed and suppressed) obtained from static model component tests and previously corrected to free-field conditions (see Section 3.4) were corrected to standard day (77° F, 70% relative humidity) conditions prior to scaling by frequency and size. Extrapolations for distances were made using inverse square law, air attenuation (SAE ARP 866), and extra ground attenuation (EGA, SAE AIR 923). These corrected full-scale data were further adjusted for flight effects which included dynamic effects and the Doppler shift. For the purpose of this study, soft ground reflections and engine shielding effects were incorporated into the results based on assumed average values at peak angles. A +1.0 dB adjustment was applied to the free-field component data at takeoff, while +1.5 dB were similarly

applied to both cutback and approach conditions to simulate the in-flight influence of these factors. The amount of adjustment for the soft ground reflection and engine shielding corrections was assumed to be applied equally to both the PNL and EPNL values.

Jet relative velocity effects were applied using the results of the latest General Electric studies which provide correlations of existing data on suppressed and unsuppressed nozzles. Comparisons of results with similar correlations (References 52 - 55) show similar trends. In the case of the suppressor nozzles, there was limited flight data available (none at takeoff) at the conditions of interest in this study to give a complete understanding of the relative velocity influence on suppression. There was sufficient information available, however, to indicate the dynamic effect on the static data. The method used to adjust the static data to flight included applying the full dynamic effect at all jet velocities with no V_R effect at takeoff, but one-half of the V_R effect for the GE unsuppressed conical nozzle applied to the suppressor at cutback. It should be noted that no correction for inlet flight effect (clean-up) was employed. Shock tones apparent in the unsuppressed conical convergent nozzle SPL spectra at the take-off condition were smoothed to reflect, as near as possible, the normal operation with typical convergent-divergent exhaust nozzles. No corrections for the broadband shock noise contribution were made. Similarly, no corrections for shock noise were made to the suppressed data, since the influence (if any) was primarily broadband.

The EPNL calculation was performed according to the FAR-Part 36 regulation with an integration time interval of $\Delta t = 0.5$ sec. Depending on which flight condition was being evaluated for noise, certain component EPNL's were calculated separately to determine their contribution to overall system noise.

5.4.3 Noise Footprint Calculating Procedure

Aircraft noise contours, or footprints, were determined using an EPNL decay rate with range for the given aircraft at approach and takeoff, and the aircraft flight path. The EPNL attenuation rate with range used in this study was based on actual flyover data from JT8D powered aircraft obtained from published reports. The JT8D was selected due to its similarity in component contribution to system noise as compared to the SST engine selected for study.

In determining the x and y coordinates of the contour, the range associated with the EPNL of interest was determined from the EPNL versus range curve. This distance was then adjusted for EGA and engine shielding effects using the sight angle between the engine and the observer. The sight angle was determined based on aircraft altitude with distance down the runway (from the flight path) and distance to the side. An iterative process was used to determine the actual side (y) coordinate distance for each x chosen. Areas were determined by dividing the contour into segments at intervals of x and, using the average y distance, calculating the area of each segment. These areas were then summed to arrive at the total area.

5.5 OVERALL SYSTEM AND COMPONENT NOISE EVALUATION

5.5.1 Component Noise Results

Each of the major engine noise components was evaluated separately to help determine the contribution to overall engine noise at the FAR-Part 36 monitoring points and flight conditions. Test data obtained from static component tests were used for the basic input. Figures 541, 542, and 543 show the full-scale static PNLT (tone corrected) distributions of the component noise sources for the four-engine aircraft at the take-off, community, and approach conditions, respectively. These data include adjustments for soft ground and contain no EGA correction. The data were processed through the flyover noise prediction procedure to obtain estimated EPNL values.

For the sideline and community points, the jet noise was estimated both unsuppressed and suppressed, while the turbomachinery noise was calculated for the suppressed case only. At the approach condition, the turbine and compressor noise was determined both suppressed and unsuppressed, while jet noise was calculated only for the unsuppressed case (jet suppressor stowed at approach). A comparison was done to determine each component's contribution to the system noise at each condition.

A comparison of EPNL components contribution to the system noise was done at each condition. A summary of the results is presented in Table 24 in terms of maximum PNLT at the forward and aft angles and component EPNL. It is seen that, as expected, the jet is by far the dominant noise component at the sideline and community conditions. The difference between the jet and turbomachinery noise at the take-off/sideline condition is so great that the turbomachinery components make no contribution to system noise at all. The combustor also has little or no effect on the overall system noise at this condition. Similarly, at the cutback community condition, the turbomachinery noise influence is negligible except for the compressor at the forward angles which adds a small amount to the system noise as does the combustor in the forward and aft angles. The jet suppressor is seen to result in about 9.2 PNdB suppression in the maximum forward angle and 10.5 PNdB at the maximum aft angles, resulting in approximately 8.2 EPNdB suppression for the sideline point. At community, the forward angle suppression for the jet is 5.4 PNdB and 5.9 PNdB at the maximum aft angles, giving about 6.2 EPNdB suppression at this condition. The peak angle for both take-off and cutback conditions (jet noise dominated) is 120°.

For the approach condition, the unsuppressed noise is dominated by the compressor in the forward angles (~40°). With turbomachinery suppression the total system noise in the maximum aft angles is influenced by the combined effects of the unsuppressed jet and combustor noise in addition to the noise of the suppressed turbine. The suppressed compressor remains as the dominant source in the maximum forward angles.

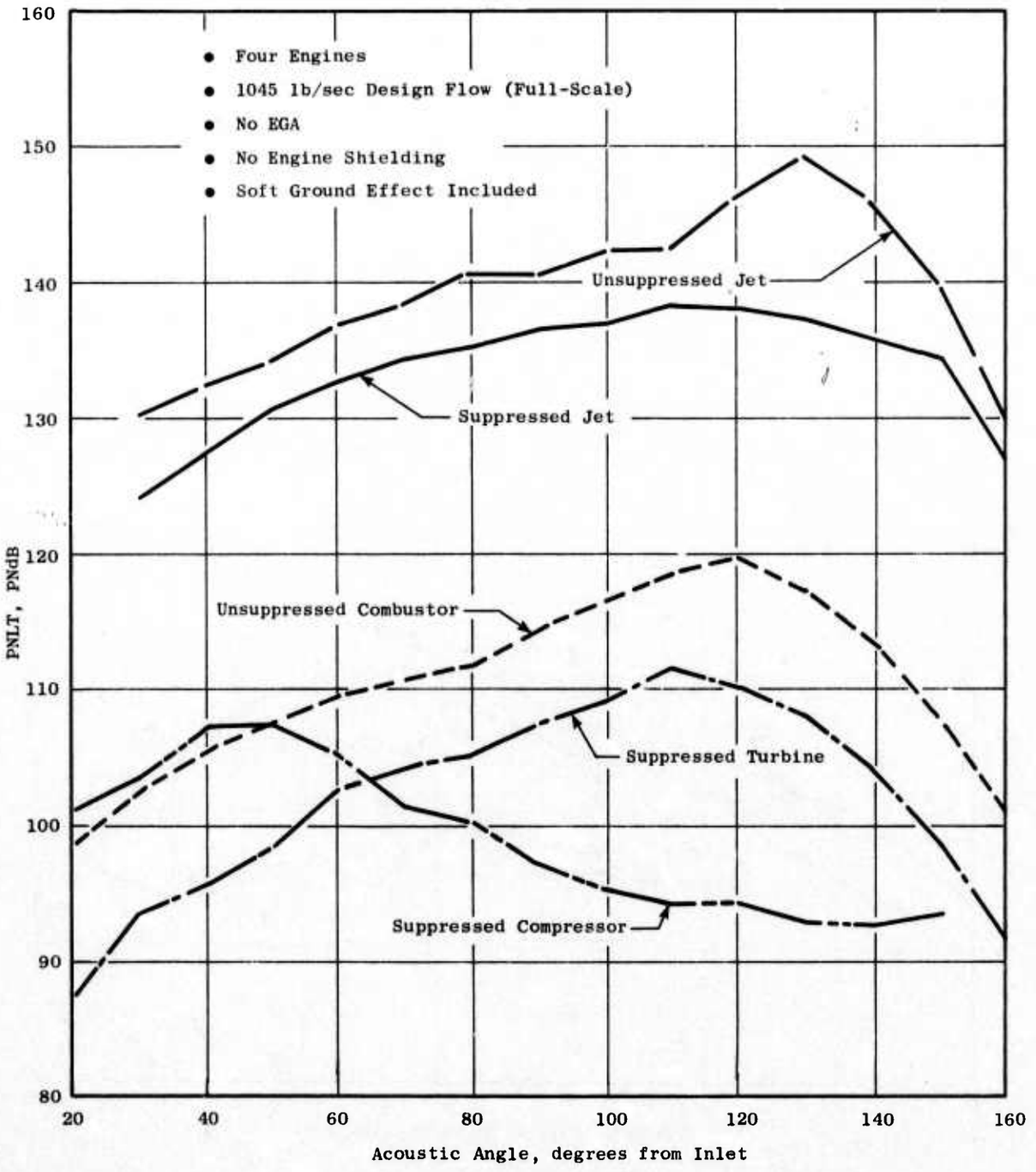

Figure 541. 300-foot Sideline Static PNLT Directivity for Component Noise Sources at Takeoff.

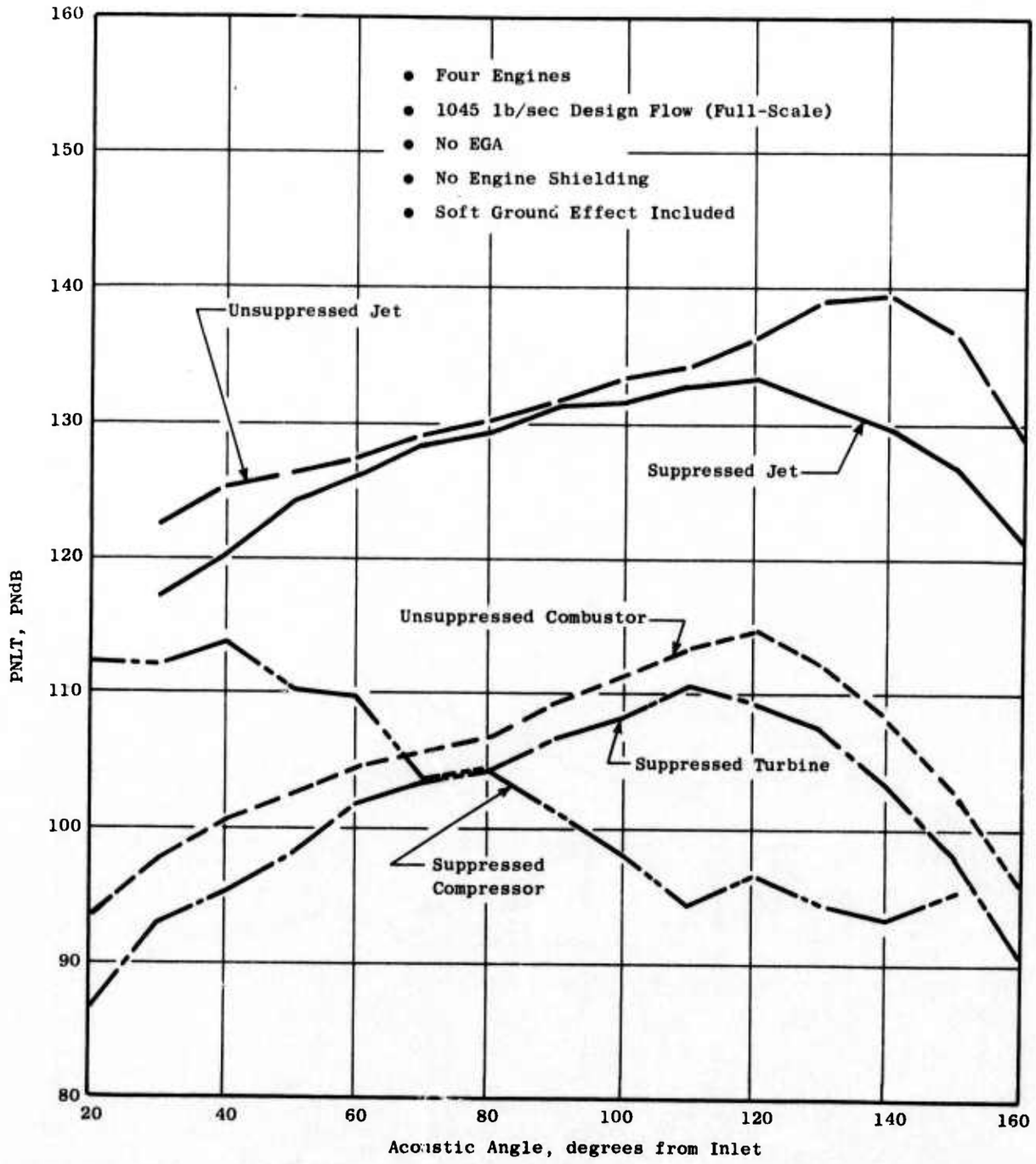

Figure 542. 300-foot Sideline Static PNLT Directivity for Component Noise Sources at Cutback.

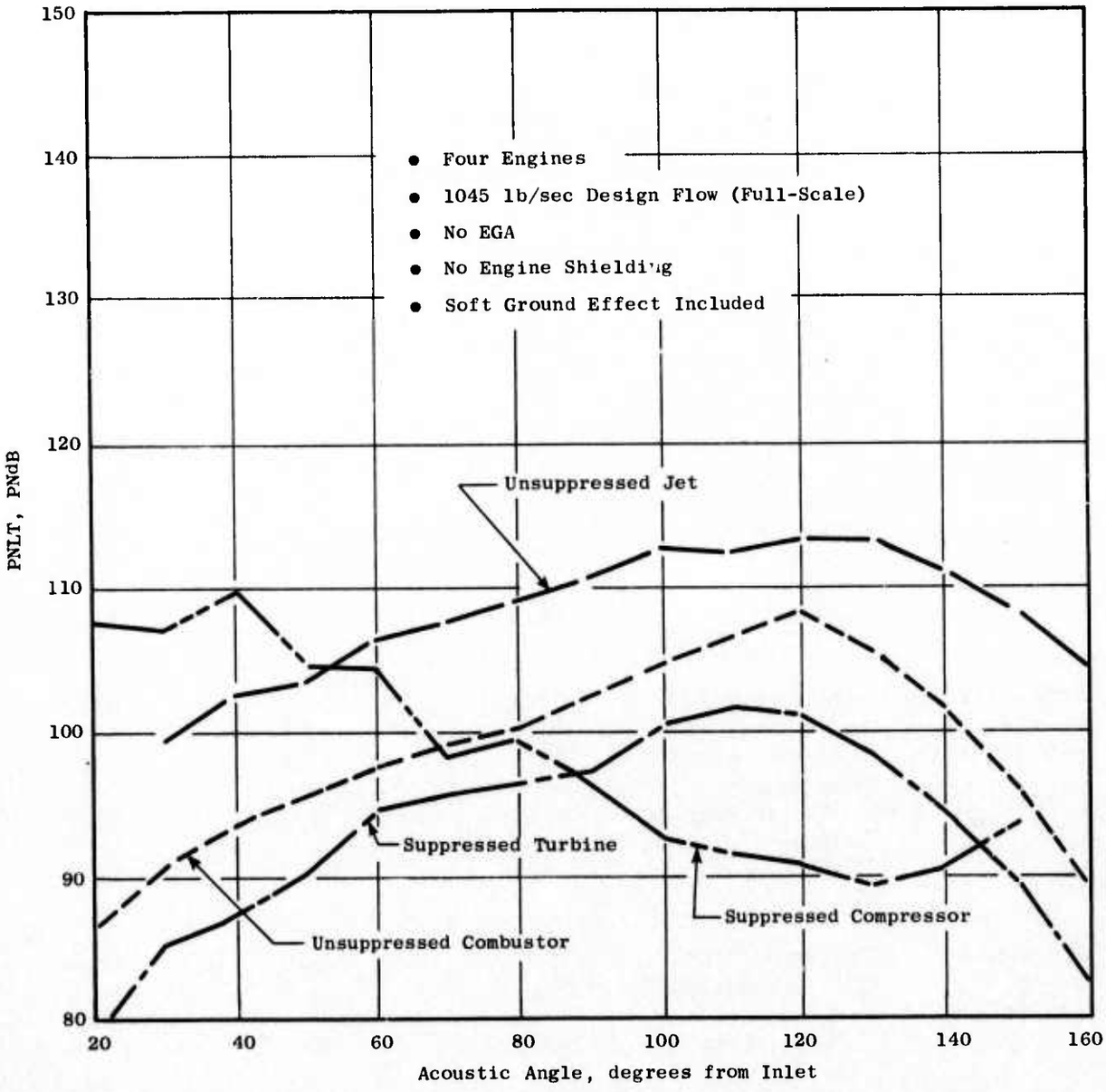

Figure 543. 300-foot Sideline Static PNLT Directivity for Component Noise Sources at Approach.

Table 24. Component Noise Summary.

- 4-Engine Aircraft (TOGW=900,000 lbs)
- Take-off Thrust = 61,400 lbs/engine
- Altitude at Community = 1860 ft
- Approach Thrust ∿ 15,000 lbs/engine
- Includes Adjustments for Soft Ground and Engine Shielding

Monitoring Point	Engine Noise Component	PNLT at Max. Fwd Angle∿40°	PNLT at Max. Aft Angle∿120°	EPNL
Sideline (Take-off) 0.35 n mi SL	Jet-Suppressed	104.1	110.0	110.9
	Jet-Unsuppressed	113.3	120.5	119.1
	Core-Unsuppressed	89.1	96.2	94.9
	Compressor-Suppressed	80.2	67.3	77.0
	Turbine-Suppressed	66.2	79.1	77.0
Community (Cutback) 1860 ft Alt	Jet-Suppressed	103.3	109.1	107.5
	Jet-Unsuppressed	108.7	115.0	113.7
	Core-Unsuppressed	88.3	95.6	92.7
	Compressor-Suppressed	91.2	72.2	87.8
	Turbine-Suppressed	73.3	85.2	81.8
Approach 1 n mi 370 ft Alt	Jet-Unsuppressed	94.0	104.0	98.2
	Core-Unsuppressed	92.4	106.0	97.4
	Compressor-Suppressed	107.8	89.0	101.8
	Compressor-Unsuppressed	126.5	108.0	119.8
	Turbine-Suppressed	82.7	100.3	92.2
	Turbine-Unsuppressed	85.1	104.4	95.6

The engine component contributions to the overall system EPNL at the three flight conditions of takeoff, cutback and approach are illustrated in Figures 544, 545, and 546. Shown in each figure are the PNLT directivities for the total system and similarly, for each engine noise source consisting of the jet, turbine, combustor, and compressor.

The total system noise for takeoff and cutback is dominated by the jet in both unsuppressed and suppressed versions of the system as shown in Figures 544 and 545, respectively. At takeoff, the suppressed turbomachinery is 24 to 30 dB below the suppressed jet. The unsuppressed combustor noise is also greater than 10 dB below the jet, and hence does not influence the overall noise level. A similar situation exists at cutback for all components except that, at the forward angles (<60°), both the unsuppressed combustor and suppressed compressor influence the system noise, while in the aft quadrant (120 - 130°) the combustor noise has a slight effect on the total system. The difference between the total suppressed system EPNL and the suppressed jet alone is only 0.3 EPNdB.

For the approach condition (Figure 546), the unsuppressed jet and combustor noise appear to combine with the suppressed compressor noise to achieve the suppressed system noise level of 106.5 EPNdB. The suppressed turbine also contributes to the overall noise, but to a lesser extent. The unsuppressed system (which includes all components unsuppressed) is 13.7 EPNdB higher than the suppressed system.

In order to examine the contributions to system noise in greater detail, component spectral comparisons at maximum forward and aft angles are presented for takeoff (sideline) and approach in Figures 547 and 548, respectively. Again it is seen that the suppressed jet is the only significant contributor to the system noise at takeoff for both forward and aft angles. In the mid-frequency range, the compressor contribution is minimal at the forward angle, as is the combustor at the aft angles. At the approach condition (Figure 548), the situation is somewhat more complex. At the maximum forward angle, the unsuppressed jet dominates the low frequency noise, the unsuppressed combustor controls the mid-frequency noise from about 300 to 1250 Hz, and the suppressed compressor controls the high frequency noise from 1250 Hz to 10 kHz. Thus, the compressor is the prime contributor to system noise at the forward angles for the approach condition. At the aft angles, the situation is somewhat similar, but in this case the suppressed turbine dominates the high frequency noise (from 2500 Hz to 10 kHz). Also, the unsuppressed combustor makes the most significant contribution to the system noise at the aft angles. Thus, it is seen that all of the components are important as regards noise at the approach condition (in particular, the compressor and the combustor).

Figure 549 illustrates the effect of turbomachinery suppression at approach for both maximum forward (compressor) and aft angles (turbine). With compressor (hybrid inlet) suppression, the spectra in the forward angles are lower by 10-15 dB across the frequency range, with the high frequency BPF tone (2500 Hz) and 2nd harmonic reduced by about 20 dB. The turbine suppression at the aft angles is not as significant, because only second-stage (blade-vane)

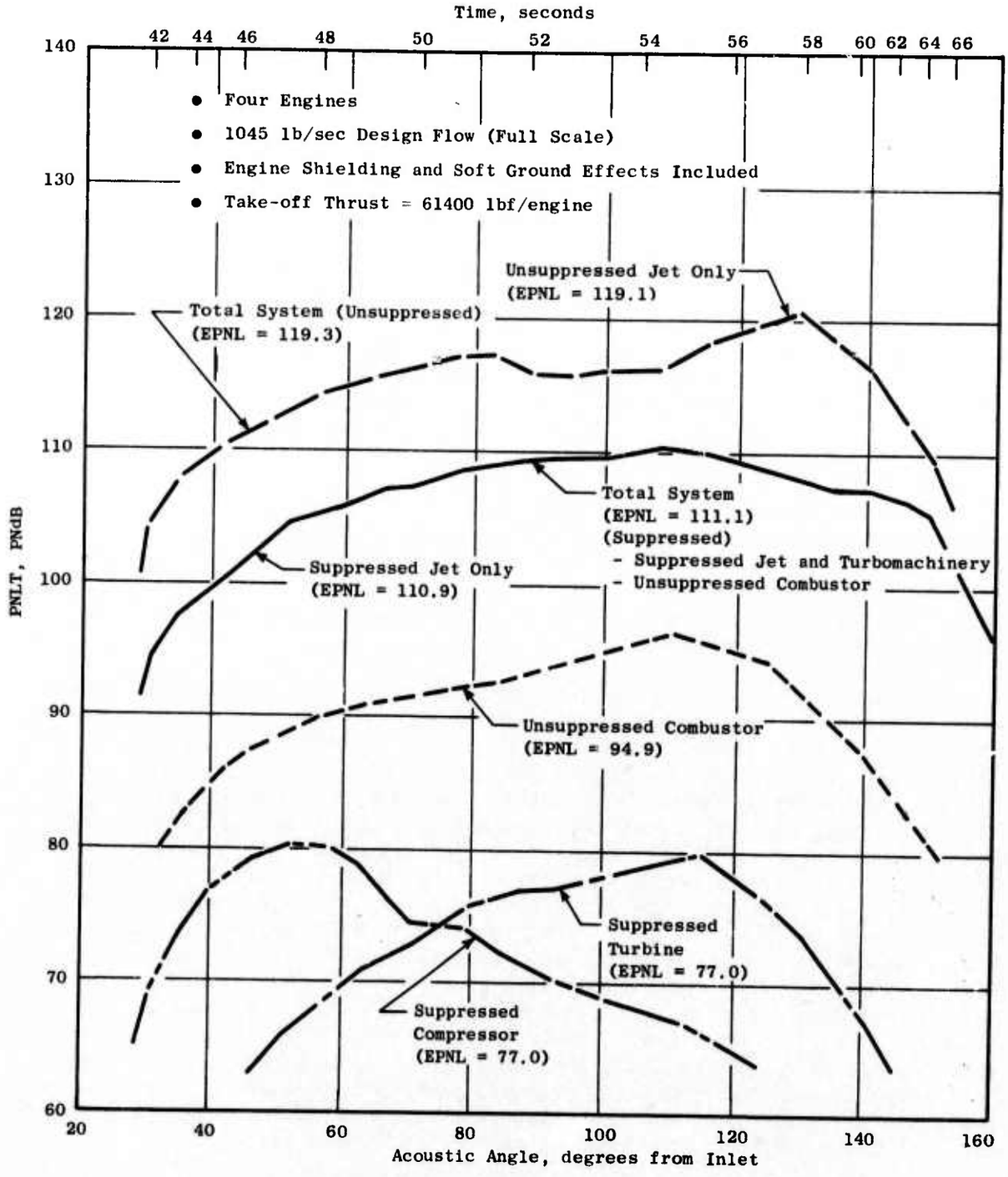

Figure 544. Component Contribution to EPNL at Takeoff.

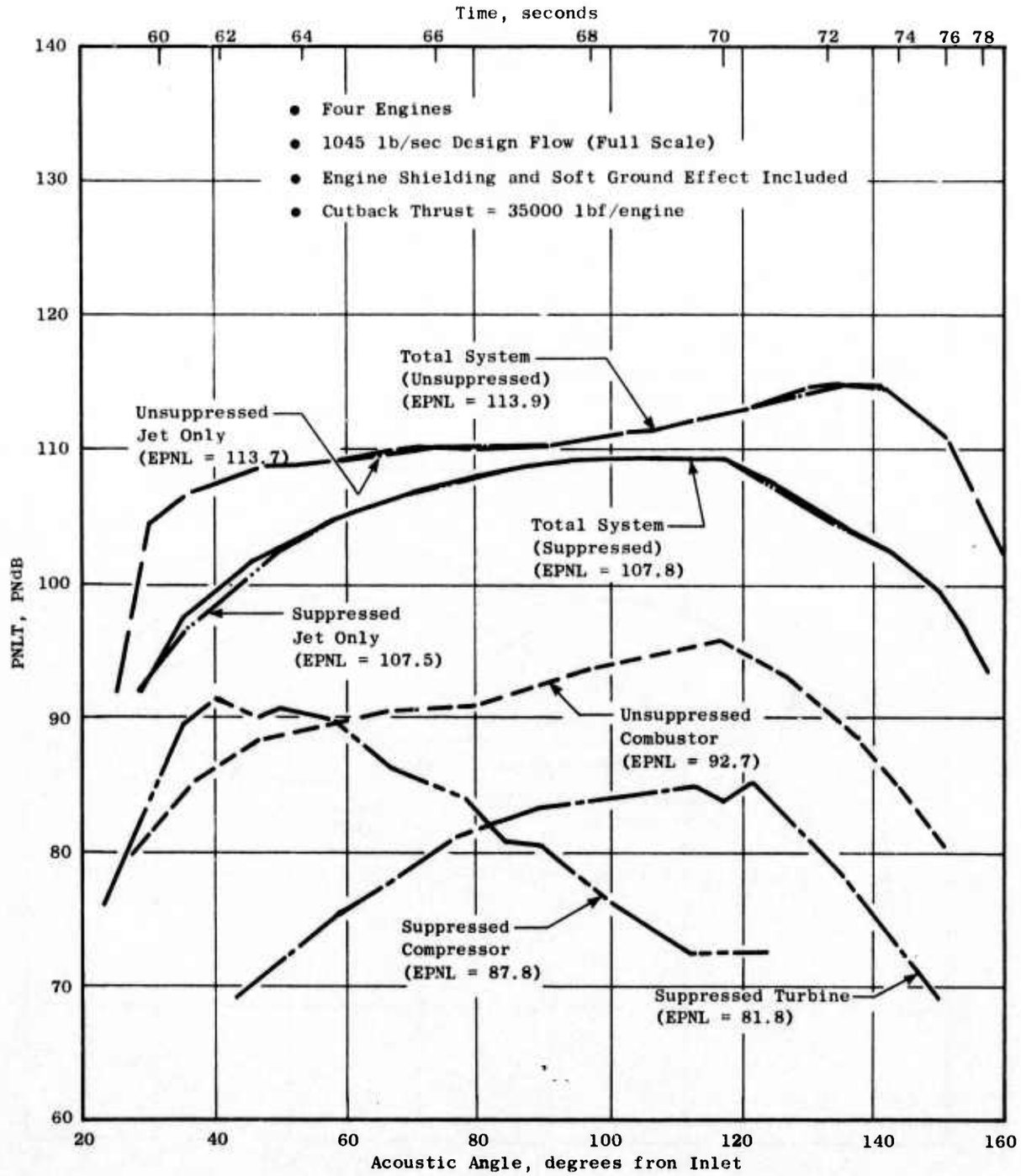

Figure 545. Component Contributions to EPNL at Cutback.

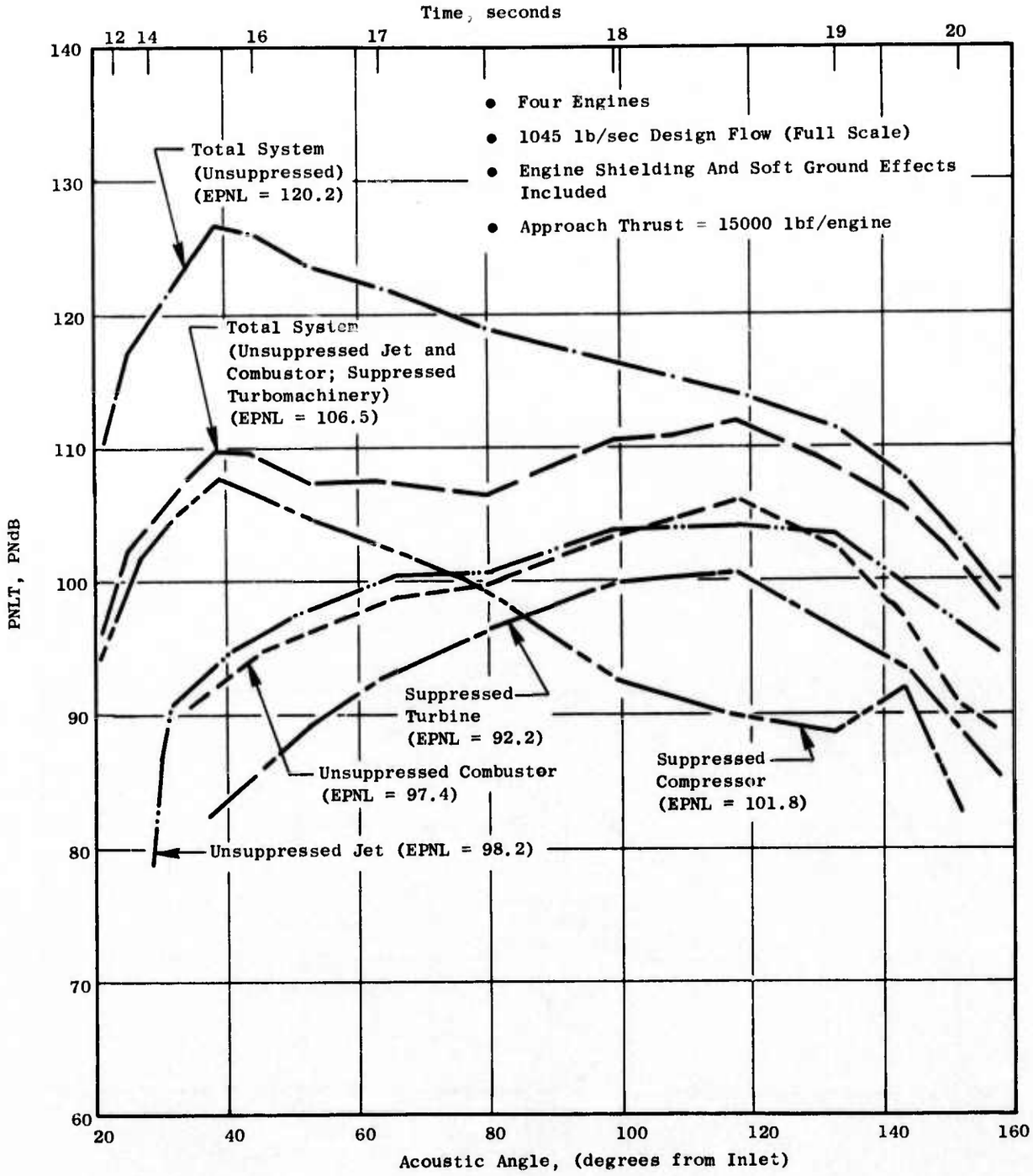

Figure 546. Component Contributions to EPNL at Approach.

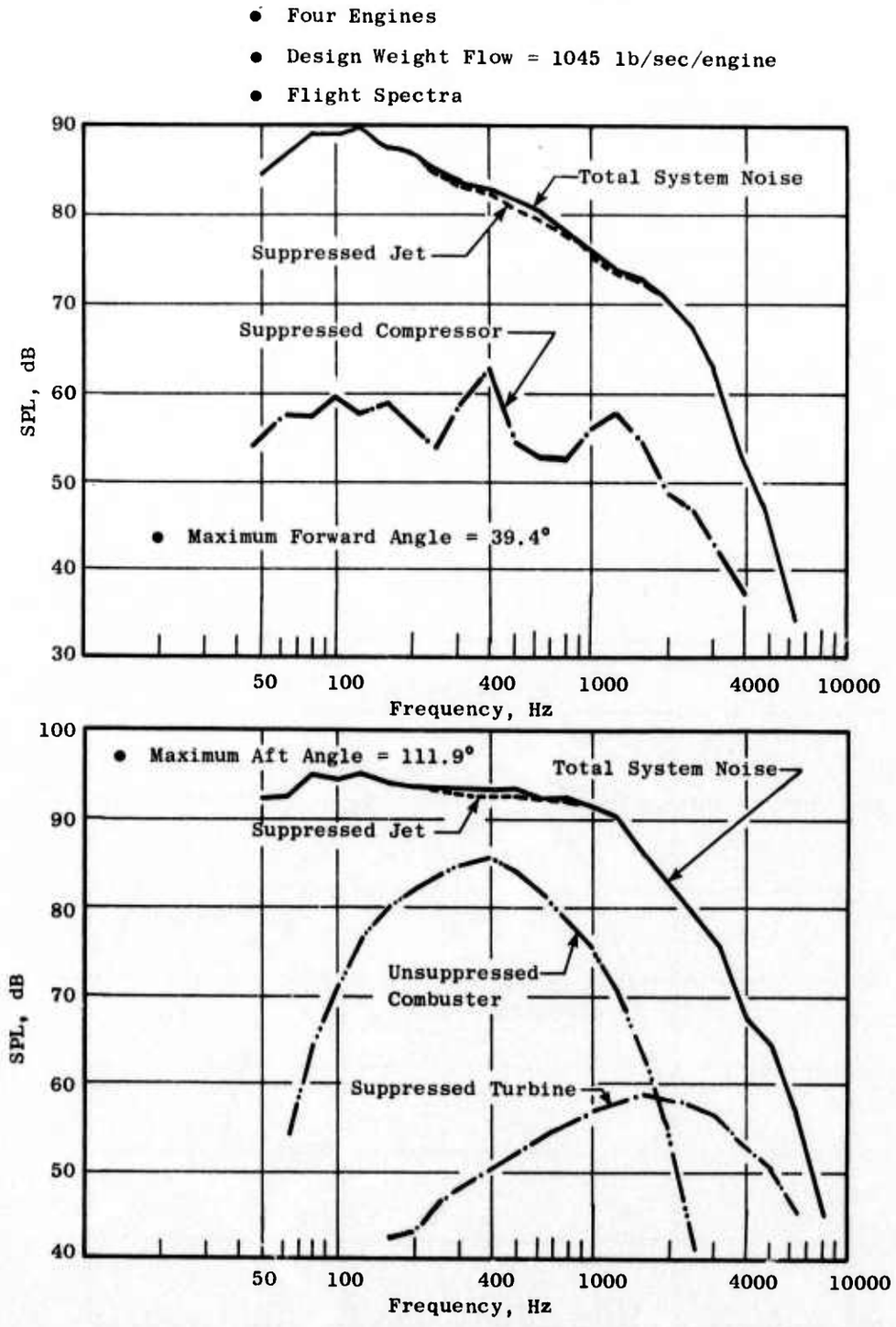

Figure 547. Component Spectral Comparisons, Takeoff (Sideline).

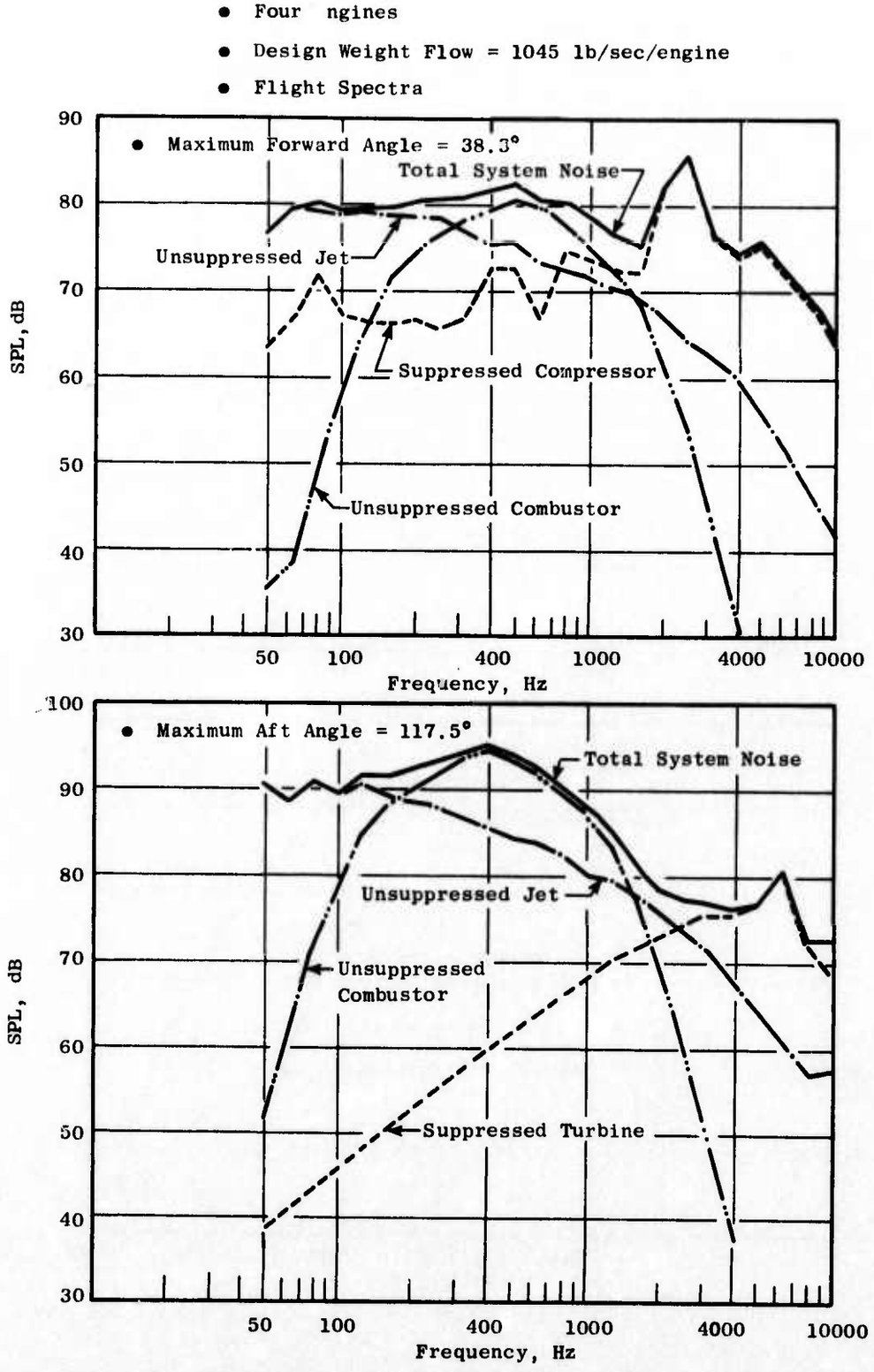

Figure 548. Component Spectral Comparisons, Approach.

- Four Engines
- Design Weight Flow = 1045 lb/sec/Engine
- Flight Spectra

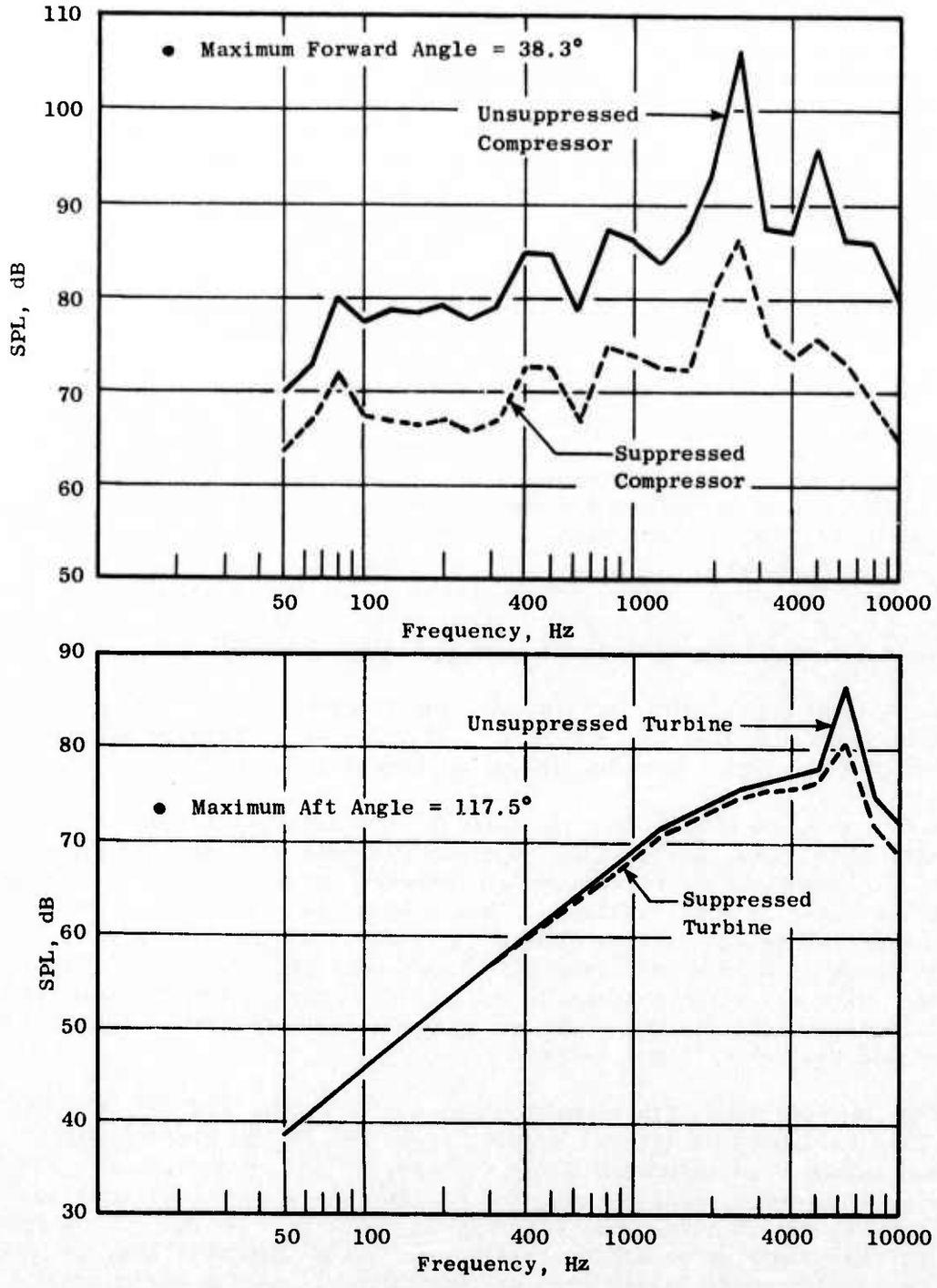

Figure 549. Turbomachinery Suppression at Approach.

spacing was used to obtain blade passing frequency tone suppression, although some higher frequency suppression also resulted.

5.5.2 System Flyover Noise Summary

Table 25 summarizes the overall system predicted EPNL at the FAR-Part 36 monitoring points based on current FAR-Part 36 noise regulations. Table 25 shows a comparison of EPNL values for the FAR-Part 36 monitoring points for the SST configuration model. The operational procedures for aircraft of this type are for the jet suppressor to be deployed during take-off (sideline) and cutback (community) conditions, while, at approach, the jet suppressor is stowed. The engine configuration in the comparison included the jet, compressor, and turbine components which were suppressed while the combustor was unsuppressed. This model was used to estimate the EPNL's at sideline and community points. For the approach point EPNL, the jet and combustor were unsuppressed while the compressor and turbine were suppressed.

As can be seen from the comparison of the results tabulated for these configurations, the sideline noise, dominated by the jet, is the controling factor in the traded FAR-Part 36 EPNL computation. On a traded EPNL basis, the SST configuration with fully suppressed (jet and turbomachinery) low bypass turbojet engines was estimated at FAR-Part 36 +1.1 using the current regulation level for subsonic transport aircraft. It should be noted that no design tolerance has been assumed. This result can be considered a measure of the current state of the art in SST noise reduction technology and indicates that such a system has the potential of meeting the current FAR-Part 36 noise requirements; although some additional work would be required.

It is apparent that, if turbomachinery suppression was not employed at the approach condition, the traded FAR-Part 36 value would be even greater than 109.1. This indicates the significance of suppressing the turbomachinery.

A comparison of 90 EPNL noise contours for the suppressed version of the SST (with 1045 lb/sec design flow engines) was made with similar contours for present day unsuppressed narrow-bodied subsonic transports like the Douglas which does not employ a power cutback. This system was selected for comparison because of the relatively low bypass ratio ($\beta \approx 1$) of the JT3D engine, even though there is a large difference in engine thrust. Figure 550 shows the take-off (with and without cutback) and approach footprints for the suppressed SST model, while the unsuppressed subsonic transport footprints consist of approach and takeoff without cutback.

For the take-off condition without cutback, the suppressed SST 90 EPNL footprint area is approximately 36% greater than that of the present day unsuppressed subsonic narrowbodied aircraft. The region of influence along the sideline is somewhat large for the SST in the take-off mode without cutback. But with cutback, the sideline area affected is reduced to be more compatible with that of the unsuppressed subsonic aircraft. This indicates that the SST would not be significantly louder than current aircraft in the vicinity of

Table 25. Comparison of Overall Predicted EPNL with Current FAR-Part 36 Noise Regulations.

- 4-engine aircraft (TOGW = 900,000 lb)
- Take-off thrust = 61,400 lb/engine
- Altitude at cutback = 1,860 ft
- Approach thrust = 15,000 lb/engine

Monitoring Point	Current FAR-Part 36 Regulation	Suppressed SST Configuration
• Sideline	108	111.1
• Community	108	107.8
• Approach	108	106.5
• Traded FAR-Part 36	108	109.1
• Traded ΔEPNL	---	+1.1

90 - EPNL Footprint Areas

	Suppressed SST	Unsuppressed Narrow-Bodied Subsonic Transport
Takeoff	67.6 sq n mi	49.8 sq n mi
Cutback	80.8 sq n mi	----
Approach	5.5 sq n mi	11.3 sq n mi

- 4 Engine Aircraft

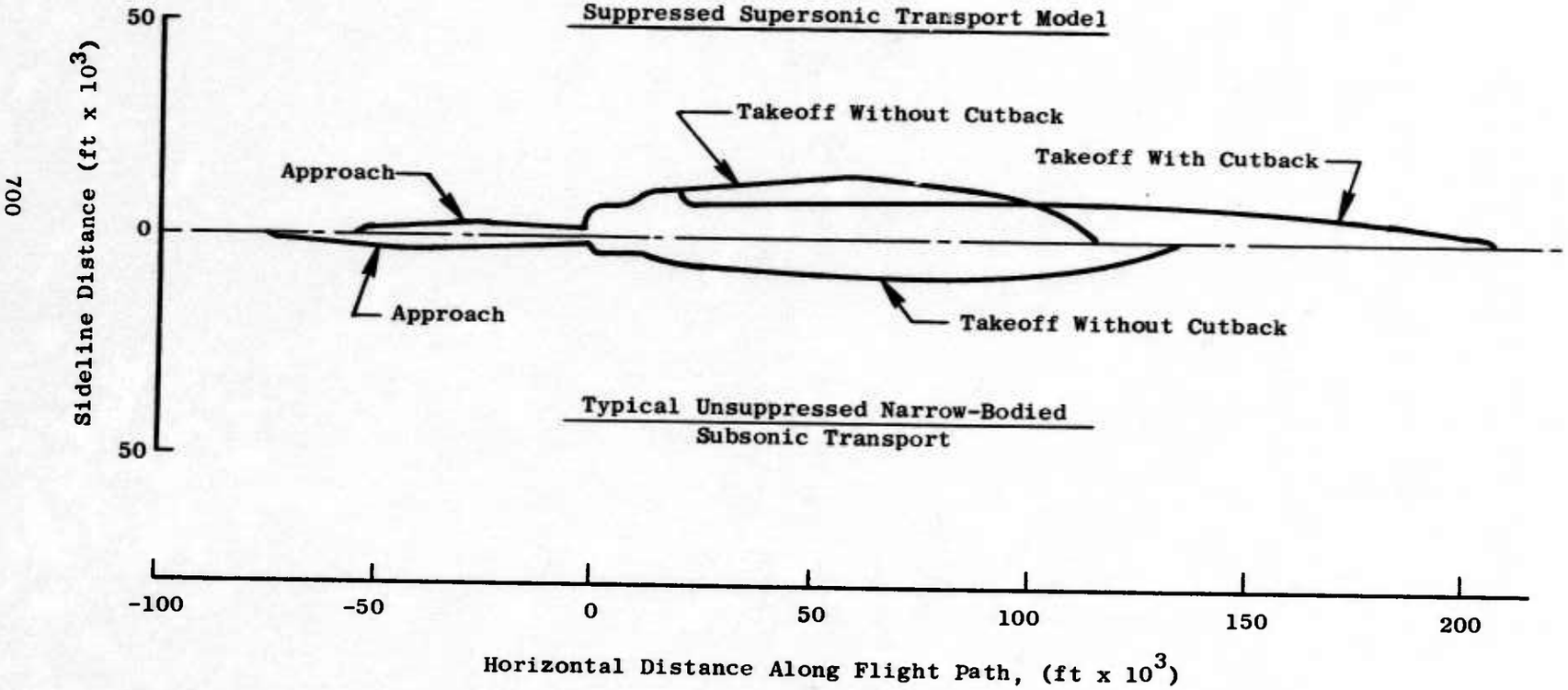

Figure 550. Comparisons of 90 EPNL Noise Contours.

the airport. Although the SST contour (with cutback) extends some 75,000 ft further down the flight path than the unsuppressed subsonic transport, this might not be of major significance if takeoff was performed over water.

At the approach condition, the SST model contour was approximately one-half of that of the unsuppressed narrow-bodied subsonic transport.

In summary, an overall system noise evaluation was performed on a representative suppressed SST aircraft using low-bypass, mixed-flow turbojet engines. Component noise technology developed in this program was evaluated on a flyover basis. Comparisons of component results and overall system results were made between suppressed and unsuppressed versions of the engines. Significant gains in jet and turbomachinery component suppression technology have been made as evidenced by the results of this study. The traded EPNL for the integrated aircraft system was 1.1 EPNdB above the current FAR-Part 36 noise regulation levels for subsonic transports. This result is primarily due to the dominance of the jet noise at takeoff and cutback, even with jet suppression. In addition, the influence of combustor noise (along with the unsuppressed jet) is also apparent at approach. The potential for meeting the current FAR-Part 36 noise regulation with this type of suppressed SST system has been demonstrated, although additional work would be necessary.

SECTION 6.0

CONCLUSIONS

The results of the individual Noise Suppression Technology Task efforts described in the preceeding sections provide a number of conclusions along with some observations of needed technology that would enhance the information already at hand.

6.1 JET NOISE REDUCTION

The jet noise reduction technology on mid-to-high velocity jets has led to the following observations and conclusions:

- The program has provided an acoustic and aerodynamic data bank on a number of advanced technology suppressor configurations, complementing the jet suppression data bank acquired during the SST program.

- A number of unique suppression schemes was identified as having potentially high suppression benefit. Among these, are the over-the-wing asymmetric 2-D suppressed nozzle systems which appeared attractive from an aeroacoustic standpoint, but required a more comprehensive systems integration effort for implementation to advanced technology aircraft.

- The multichute annular plug suppressor concept was developed into a viable system for advanced technology application as an outgrowth of the test results from the model and engine 32-deep-chute suppressor configurations.

- Acceptable model-to-engine acoustic scaling was demonstrated from the results of model and engine tests.

- Although some of the suppressor systems evaluated in this program show promise of higher levels of suppression with acceptable aerodynamic performance, considerably more development work complemented by better definition of the jet noise generation mechanisms is required if current subsonic Federal Noise Regulations are to be met by advanced supersonic aircraft.

- To more clearly understand in-flight effects on suppression and their relationship with static model and large-scale suppressor test results, the J79 engine suppressor configuration should undergo wind-on acoustic testing.

6.2 TURBOMACHINERY NOISE REDUCTION

The turbomachinery noise reduction technology work on a three-stage low pressure compressor and a two-stage high pressure turbine has led to the following observations and conclusions:

- The program has provided valuable information on the character of turbine and compressor noise for studying possible future SST engine cycles.

- Turbine noise in the far field is characterized by modulated tones. Two viable means of controlling turbine noise are: 1) increased vane-blade spacing, and 2) acoustic treatment.

- Further investigation of turbine noise is warranted, in view of the progress made in the technology for reducing other SST engine component noise.

- The presence of inlet guide vanes and close spacing of the compressor components causes compressor noise to be tone dominant. This type of noise is particularly annoying and, thus, the compressor can play an important role in overall SST engine noise, especially at part-power conditions.

- The hybrid inlet is seen as a very practical and effective way of limiting compressor noise propagation. It utilizes the variable geometry inlet and nozzle plus the airflow control system already present in an SST engine. Thus, the penalty associated with its use is greatly minimized. It avoids the performance and operational problems associated with hard choking the inlet to obtain suppression.

- While the hybrid inlet with auxiliary inlets (blow-in-doors) open resulted in far-field compressor noise levels significantly lower than with a hardwall cylindrical inlet, the doors did not operate as designed. Since auxiliary inlets are a necessary part of any SST inlet system and have been shown to provide a noise leakage path, further investigation is warranted. This investigation would be aimed at obtaining in-flight flow conditions during static testing and better defining a suppression technique for limiting noise leakage through doors.

- Generating high Mach numbers in the compressor IGV passage does not appear to be a viable means of suppressing compressor noise, because of the large fan performance penalties associated with "off-design" operation.

6.3 AIRCRAFT SYSTEMS INTEGRATION

The results of the Aircraft System Integration study using the component noise suppression systems with low-bypass mixed-flow turbojet cycle engines lead to the following observations and conclusions:

- Significant gains in jet and turbomachinery component suppression technology have been made as a result of this program as demonstrated in the systems integration work.

- Current acoustic technology indicates that this type of suppressed Aircraft Engine System has the potential for viable application since, on a traded EPNL basis, it was only 1.1 EPNdB above current FAR-Part 36 noise regulation levels for subsonic aircraft.

- Observations from the 90-EPNL noise footprints in Figure 550 show that the SST (suppressed) has a larger area influencing the sideline during takeoff without cutback than the unsuppressed narrowbodied subsonic transport. But with cutback, the sideline area is reduced to be more compatible with the unsuppressed aircraft, indicating that the SST would not be significantly louder than current aircraft in the vicinity of the airport.

APPENDIX A

TEST FACILITIES

A.1 AEROACOUSTIC TEST FACILITIES

The scale model tests and engine demonstrations performed during the DOT/FAA Phase II Program for the investigation of jet suppression and turbomachinery noise reduction were conducted on several different facilities, located both in General Electric Aircraft Engine Group plants and at outside vendor locations.

Acoustic suppression tests of scale model jet suppressor exhaust nozzles were conducted on the JENOTS hot-jet facility at the General Electric plant in Evendale, Ohio (discussed in Section A.2). In-jet correlation measurements work performed at General Electric's Corporate Research and Development Centers Hot Jet Facility (Section A.3) in Schenectady, N.Y. Turbomachinery noise reduction investigations were conducted in model engine size at General Electric's Peebles Proving Ground, Peebles, Ohio, on the acoustic facility site (discussed in Section A.4). Moderate and large size engine test demonstrations of turbomachinery noise reduction and jet noise suppression were conducted at General Electric's Edwards Flight Test Center, Edwards, California, on the static acoustic facility, North Site (discussed in Section A.5).

Aerodynamic static and installed gross thrust measurements obtained for the jet suppressor systems were made on model scale nozzles tested at both the FluiDyne Engineering Corporation's Medicine Lake Laboratories (Section A.6), located at Medicine Lake, Wisconsin, and at the NASA-Lewis Research Center's wind tunnel facilities in Cleveland, Ohio (Section A.7).

The above facilities are discussed individually and in greater detail in the following sections of this appendix. A description of the test facility with the capabilities and limitations is included in each section.

A.2 GENERAL ELECTRIC JENOTS SCALE MODEL ACOUSTIC TEST FACILITY

The JENOTS (Jet Engine Noise Outdoor Test Stand) has been under continuous development since its establishment in the late 1950's for early turbojet noise and suppressor studies. It is located at the north end of the Evendale, Ohio, General Electric plant remote from the main factory area or engine test cells.

A.2.1 The Acoustic Arena

A planform of the sound field is shown in Figure 551. It consists of 15 microphones arranged at 10° intervals around a 40-foot arc from 20° to 160°

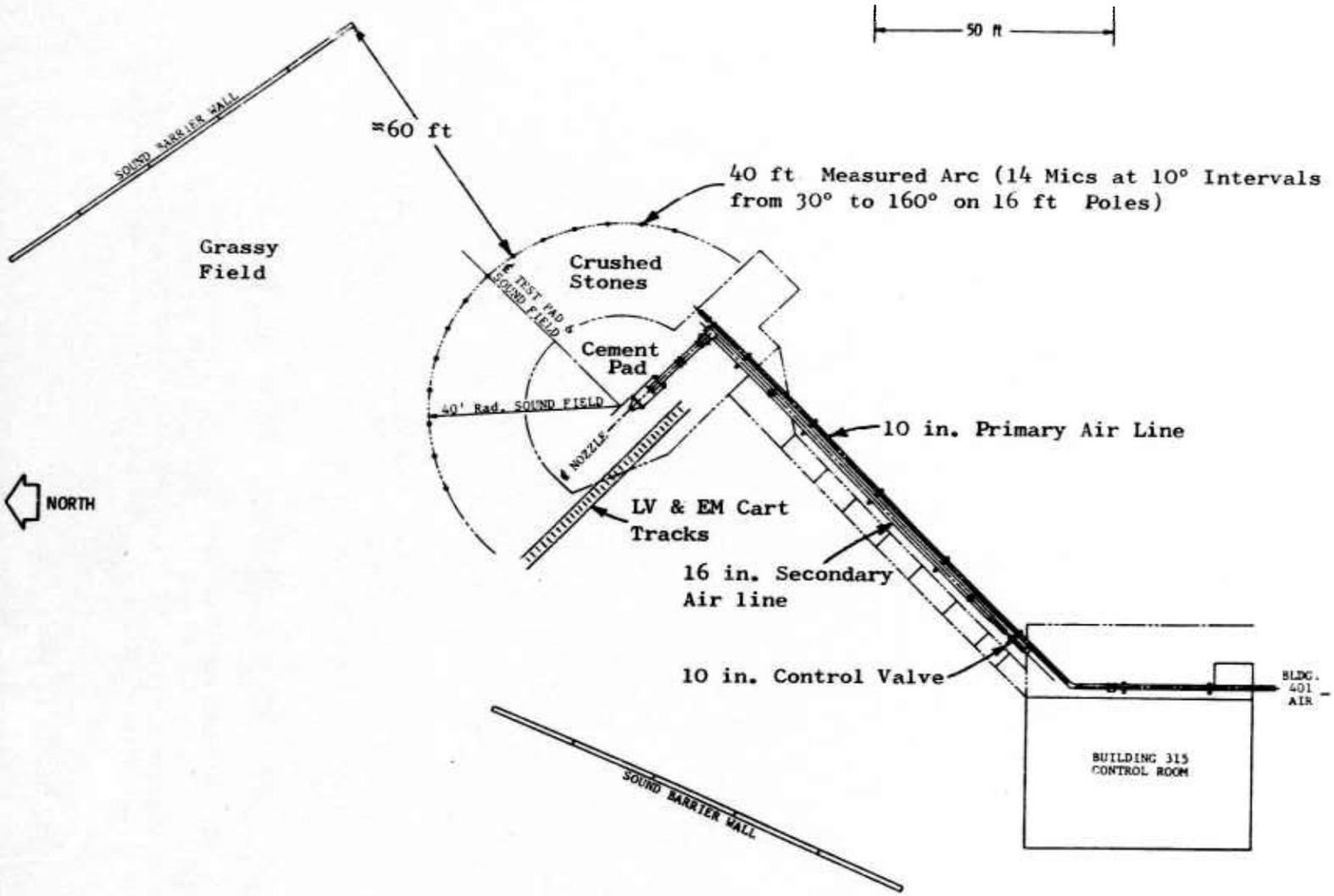

Figure 551. Schematic of JENOTS Facility.

centered at the nozzle discharge plane centerline. The microphones are elevated 16 feet above the ground on specially designed "gooseneck" mounts to minimize the influence of reflections.

The ground plane is composed of concrete to approximately a 20-foot radius from the nozzle exit, then crushed rock to a 40-foot radius. A grassy field exists beyond the acoustic arena. Specially designed acoustic barriers are located approximately 60 foot from the sound field to protect the neighboring community from the high sound levels. These barriers are designed to prevent any measurable reflections back into the sound field. On both the single-flow and dual-flow configurations, the nozzle centerline is 55 inches above the ground.

Special microphone setups can also be employed. One such special microphone setup is shown in Figure 552. The arrangement of microphones consisted of an array of (15) microphones positioned at the 40-foot radius, 55-inch-high microphone stands in addition to the standard array of microphones on the DOT Phase II Program (40-spoke/40-chute suppressors, Section 3.2.2) to maintain continuity with previous data taken with the 55-inch-high microphones during the SST program.

A.2.2 Jet Facility

The JENOTS facility is capable of operation either as a single or coannular flow system, through interchangeable burner and acoustically treated plenum sections. In the single-flow mode, for clean operation from low through highly supersonic jet velocities, the system consists of a preburner and afterburner capable of operating up to 6-inch-diameter nozzles to pressure ratios of 4:1 and temperatures of 3000° R. In the coannular flow mode, the afterburner is replaced by an acoustically treated core/fan plenum chamber. The core flow is fed by the same pipe/preburner system that supplied the single jet facility and is capable of operating to 1600° R. The fan flow is supplied from a separate cold flow system and is independently controlled from the core stream.

A.2.3 Coannular Flow JENOTS Facility

The JENOTS facility as a coannular rig is shown in Figure 553. Air for the primary and secondary streams is supplied from the Evendale central air supply system through 10-inch and 16-inch air lines respectively. The plenum chamber, to which the test models are attached, is shown in Figure 554. It serves a two-fold purpose: 1) gives the flow a uniform velocity profile, and 2) eliminates any high frequency system noise through the use of acoustically treated baffles located in the secondary and primary streams.

Flow conditions for the primary and secondary streams are controlled separately with the airflow being measured using an orifice plate system coupled with pressure and thermocouple rakes.

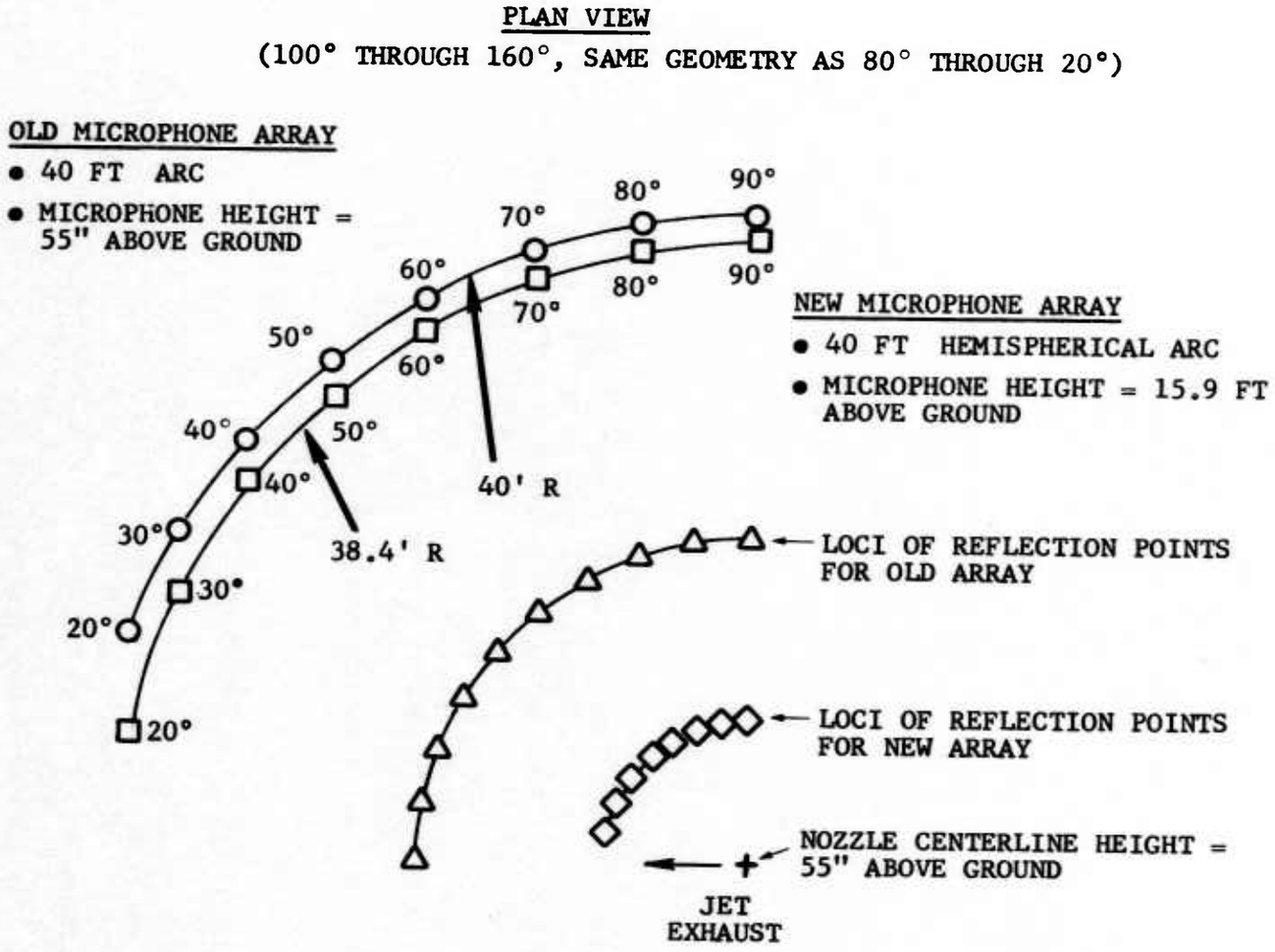

Figure 552. Comparison of JENOTS Old and New Ground-Reflection-Free Microphone Array.

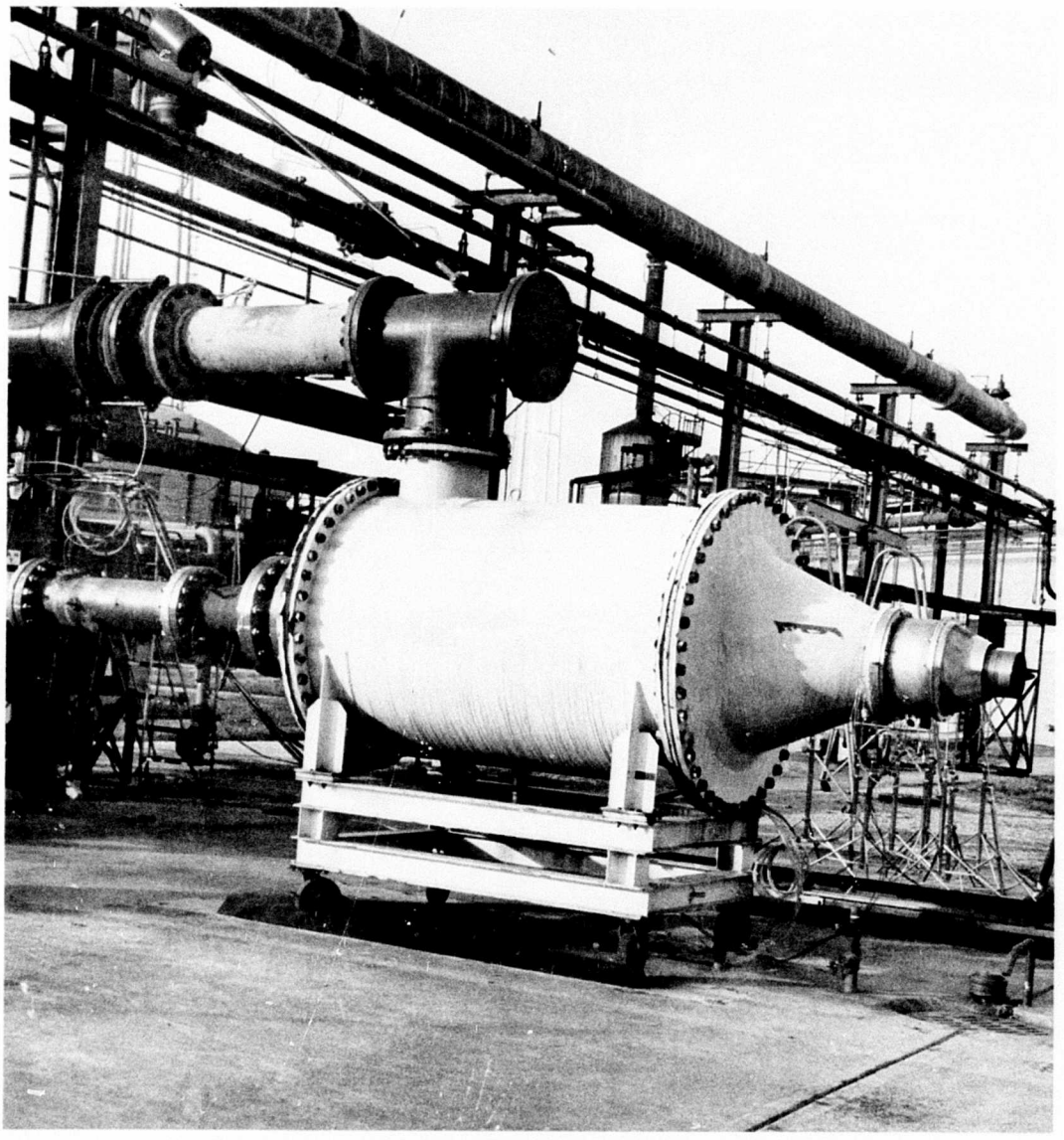

Figure 553. JENOTS Coannular Facility in Evendale, Ohio.

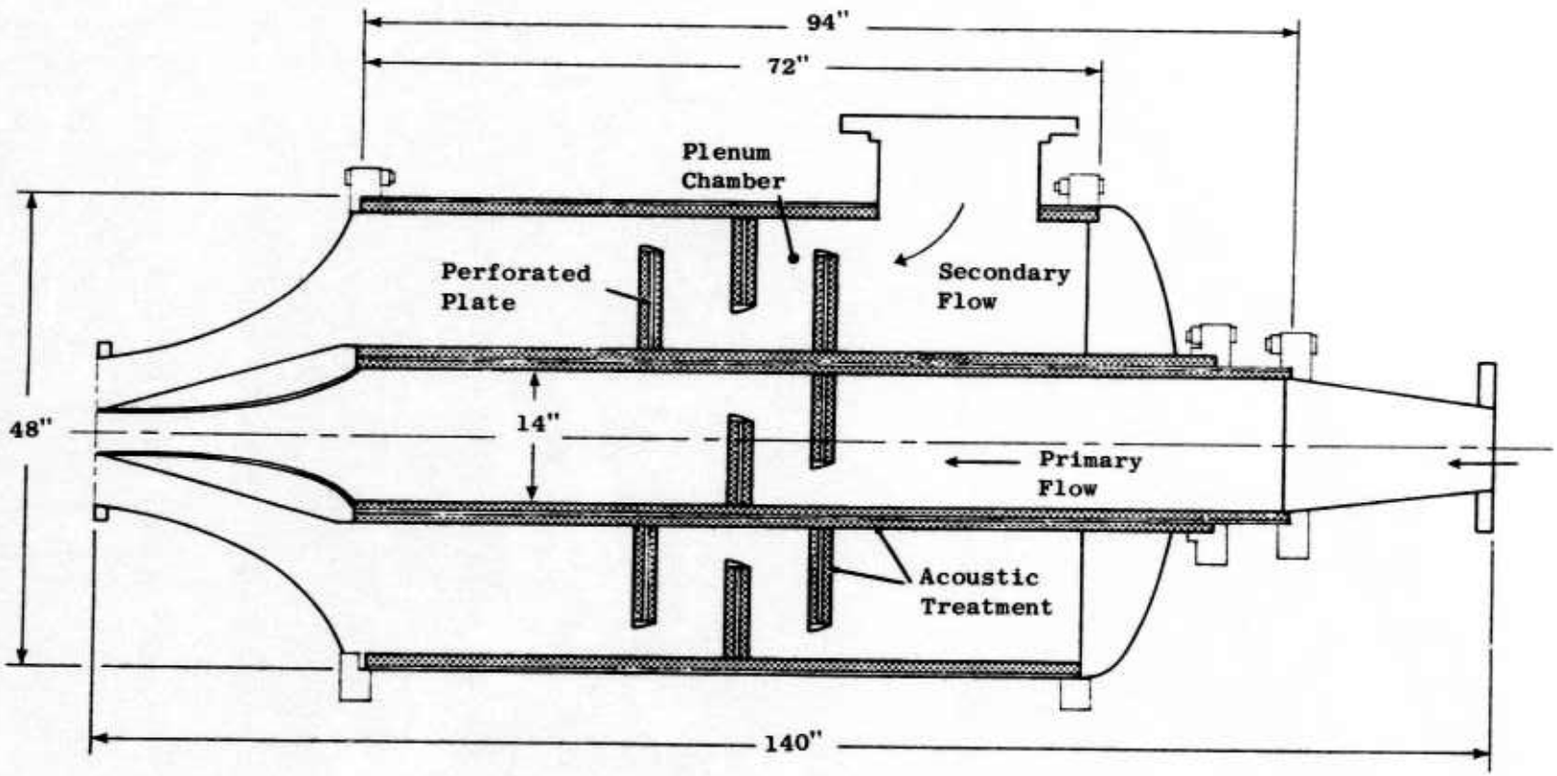

Figure 554. JENOTS Coannular Plenum Chamber.

Flow conditions at the nozzle exit plane of the models are set through the use of total-pressure and total-temperature rakes located on the model. An alternate method, using static pressure taps at the nozzle exit plane and preburner exit temperature, is also available.

The capability of the coannular facility is limited only by the baffle system inside the plenum and the air supply available. The secondary stream will exhaust at ambient temperature while the primary stream may be heated to 1600° R using the existing preburner system located in the primary air supply line ahead of the plenum chamber. The range of conditions under which the facility operates is:

Bypass Ratio	0-15
Fan Temperature (° R)	ambient
Core Temperature (° R)	amgient to 1600
Fan Pressure Ratio	1.05 to 3.5
Core Pressure Ratio	1.05 to 4.0
Fan Weight Flow (lb/sec)	0-50
Core Weight Flow (lb/sec)	0-30

Various model configurations may be tested on the coannular facility. Both primary and secondary nozzle positions may be varied axially with the maximum displacement between exit planes being controlled by model size.

A.2.4 Facility Data and Instrumentation

Airflow

For each test run, facility data consist of air flow, tunnel temperatures and pressures, cooling water temperatures and pressures, and meteorological data.

Primary air flow is obtained with a Daniels 316SS, square-edge orifice 5.000 inches in diameter on a pipe diameter of 10.020 inches with an orifice constant, $\beta = 0.499$. Data taken are main air orifice temperatures and upstream pressure P_1, and main air orifice $\Delta P = (P_1 - P_2)$. Airflow data are recorded on digital punched tape to be used for computation with a time-sharing program and a GE-635 computer.

Secondary air flow (when specific tests require it) is measured with a square-edge Meriam 316SS orifice 1.250 inches in diameter on a 4.026-inch pipe with $\beta = 0.310$. Pressures are obtained by 4-inch Daniels orifice flange static taps. Data used to calculate air flow are upstream pressure, ΔP, and secondary air line temperature.

Tunnel Temperature

In addition to the temperature readings taken to calculate primary and secondary air flow, eight Chromel-Alumel T/C probes are used to measure afterburner inlet (Preburner discharge) Plane-5 temperatures. One of these T/C's is used for input to the Plane-5 auto temperature controller that regulates fuel flow to the preburner. Another T/C is used as an input to the automatic pressure indicator (API) undertemperature and one for the overtemperature trip-outs.

Tunnel Pressures

Static pressure measurements are made at the preburner inlet (Plane 3), afterburner inlet (Plane 5) and afterburner discharge (Plane 7). These measurements are made on a Wallace and Tiernan pressure gage in psia for recording on the operator's log sheets, and are also digitally recorded. The Plane 7 static pressure is used to determine the ideal jet velocity for the single-flow systems.

Another set of eight water-cooled Iridium-Rhodium T/C's (or chromel-alumel T/C's) is used to measure flame tunnel (afterburner discharge) temperature at Plane 7. Two of these T/C's are used as inputs for the T_7 auto temperature controller, which is used to maintain a preset temperature by adjusting afterburner local fuel flow. The controller is used on test runs requiring the same T_7 temperature for a number of readings as a means of cutting down time for setting test points. One T/C is used as an input for the T_7 API overtemperature trip-out.

Meteorological Data

Readings are taken of the outside air temperature and pressure and recorded both on the log sheet and digital punch tape. In addition, wet and dry bulb temperatures for relative humidity, wind speed in mph, and wind direction are recorded on the log sheets. This information is used in correlating sound data.

A.2.5 JENOTS Sound Field and Facility Acoustic Characteristics

The 16-foot high microphone array on the 40-foot hemispherical arc was designed and implemented to minimize the effect of ground reflections on scale model data. By adjusting the path length from source (jet) to receiver (microphone location at 16-foot height), the ground reflection pattern was shifted to the very low frequency range. Thus, when the model data are scaled to full size, the nulls and peaks produced by the ground interference are scaled out of the frequency range of interest.

The previous microphone array (used prior to the start of this program) on a 40-foot arc at nozzle centerline height produced the ground reflection indices of Figure 555 as shown in the spectra of Figure 556. The reflection interference pattern is quite severe in the 500 Hz region, both predicted and measured. Figure 557 shows a typical far-field 1/3-octave acoustic spectrum employing the new microphone array. The ground interference has been shifted to the very low frequency range. Consequently, when the model data are scaled to engine size, the ground interference pattern will not be present.

Several precautions have been taken to eliminate all extraneous noise (piping noise, etc.) emanating from the facility itself. Where possible, all air supply lines are wrapped with acoustically absorbing material to prevent pipe noise from escaping through the walls of the air supply lines. All elbows in the air supply lines are packed with acoustically absorbing material to minimize the generation of turning noise.

Another concern was a possible noise floor created by ambient noise levels. Figure 558 shows a typical set of spectra for a conical nozzle operating over the velocity range of 400 to 1600 ft/sec. For a jet velocity of 372 ft/sec, the spectra at the peak polar OASPL angle is very nearly ambient. The spectrum corresponding to V_j = 582 ft/sec, is however, clearly above the ambient range. For the ideal jet velocity range of interest in this program (V_j's > 1000 ft/sec), the ambient noise was not a factor.

A.3 GENERAL ELECTRIC/CR&DC HOT JET NOISE FACILITY

The General Electric Company constructed a new outdoor test facility at the Company Corporate Research and Development Center (CR&DC) outside of Schenectady, New York.

The unique combination of capabilities that this outdoor facility offers includes hemispherical microphone coverage, permanently installed weatherproof microphones, and acoustically treated ground plane and real-time data processing. This facility is primarily intended for high temperature jet noise research and, as such, has a silenced burner capable of operation to 2200° R.

A.3.1 The Acoustic Arena

Acoustic suppression between combinations of elemental jet flows is quite small on a total-power basis and requires detailed azimuthal far-field measurements to allow the investigator to determine the relative importance between different proposed suppression mechanisms. In the CR&DC facility, a hemispherically swept array of microphones is provided to survey the far-field directivity patterns of nonaxisymmetric nozzles or suppressor configurations. Twelve 1/2" B&K Model 4133 microphones are used and are attached to a traversing boom that pivots about the jet axis. These microphones are positioned every 10° starting at θ = 20° to the jet axis and ending at θ = 130° as shown in Figure 559. In order to not place any

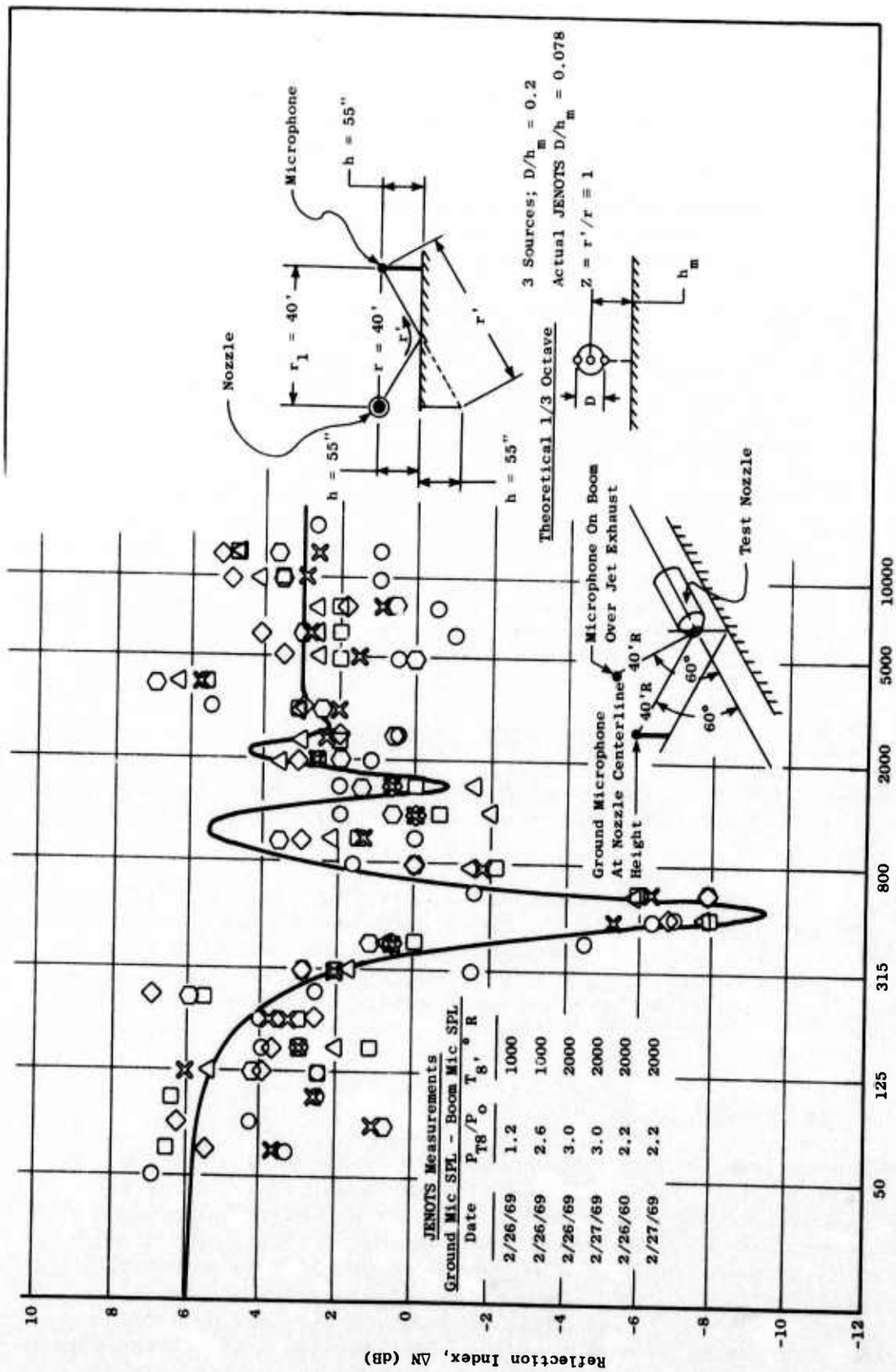

Figure 555. Theoretical Ground Reflection Correction.

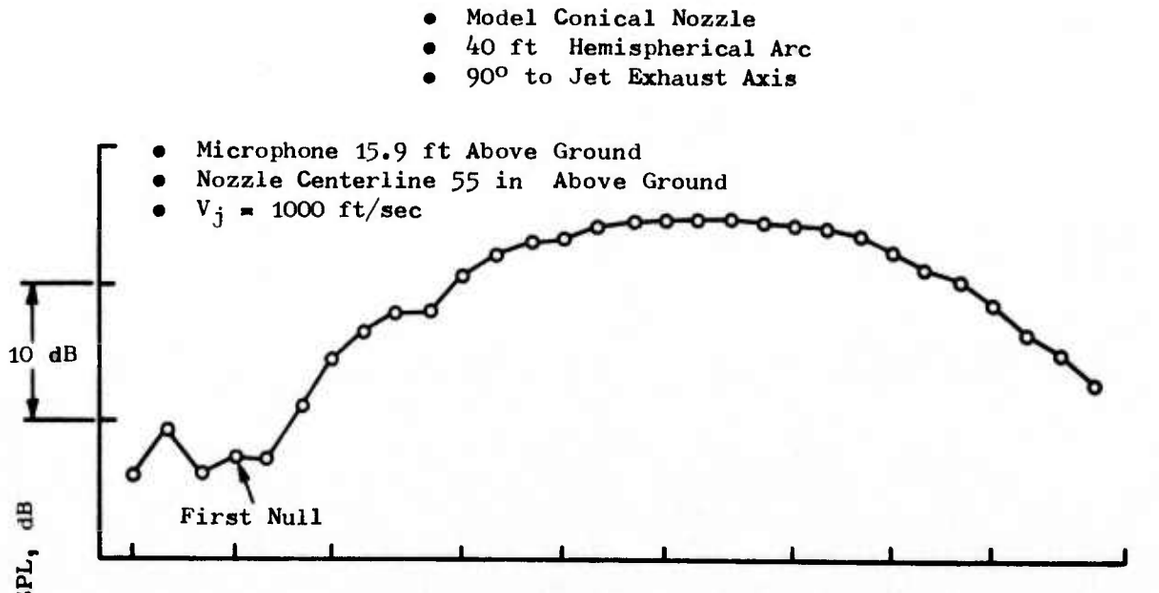

Figure 556. JENOTS Ground Reflection Pattern with Ground-Reflection-Free Microphone Array.

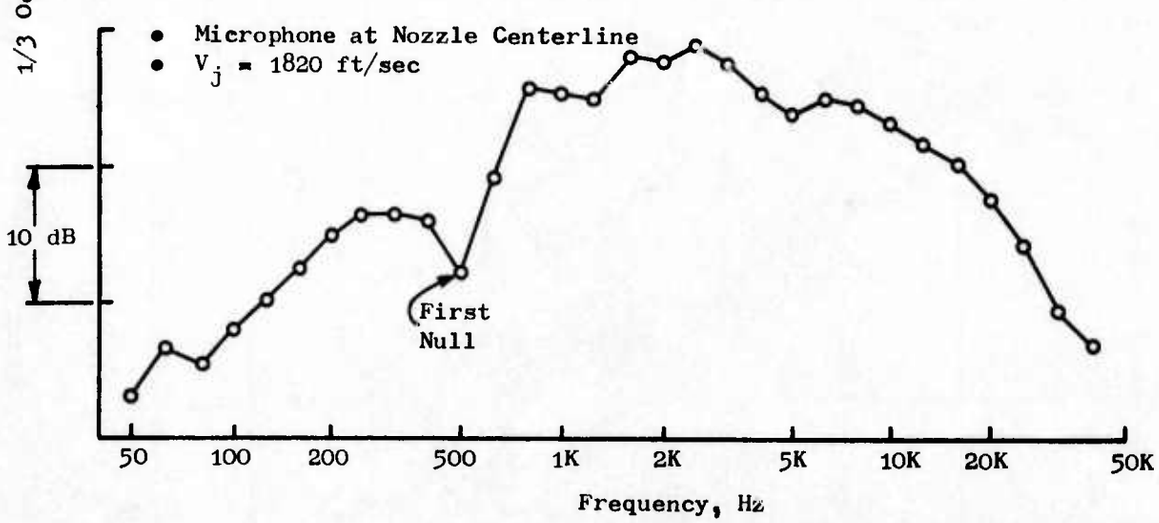

Figure 557. JENOTS Ground Reflection Pattern with Microphone at Nozzle Centerline Height.

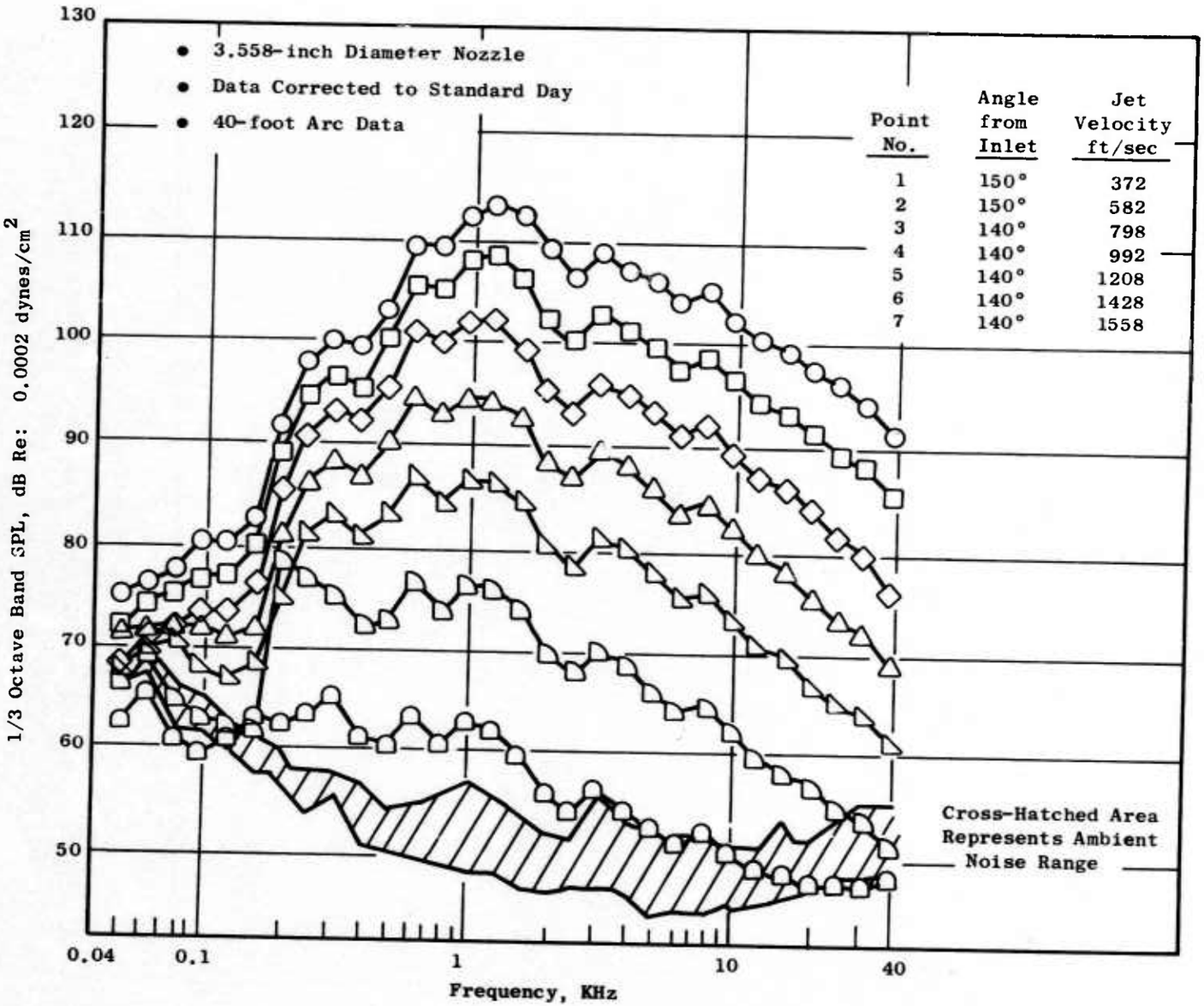

Figure 558. Peak OASPL Spectra for Conic Baseline.

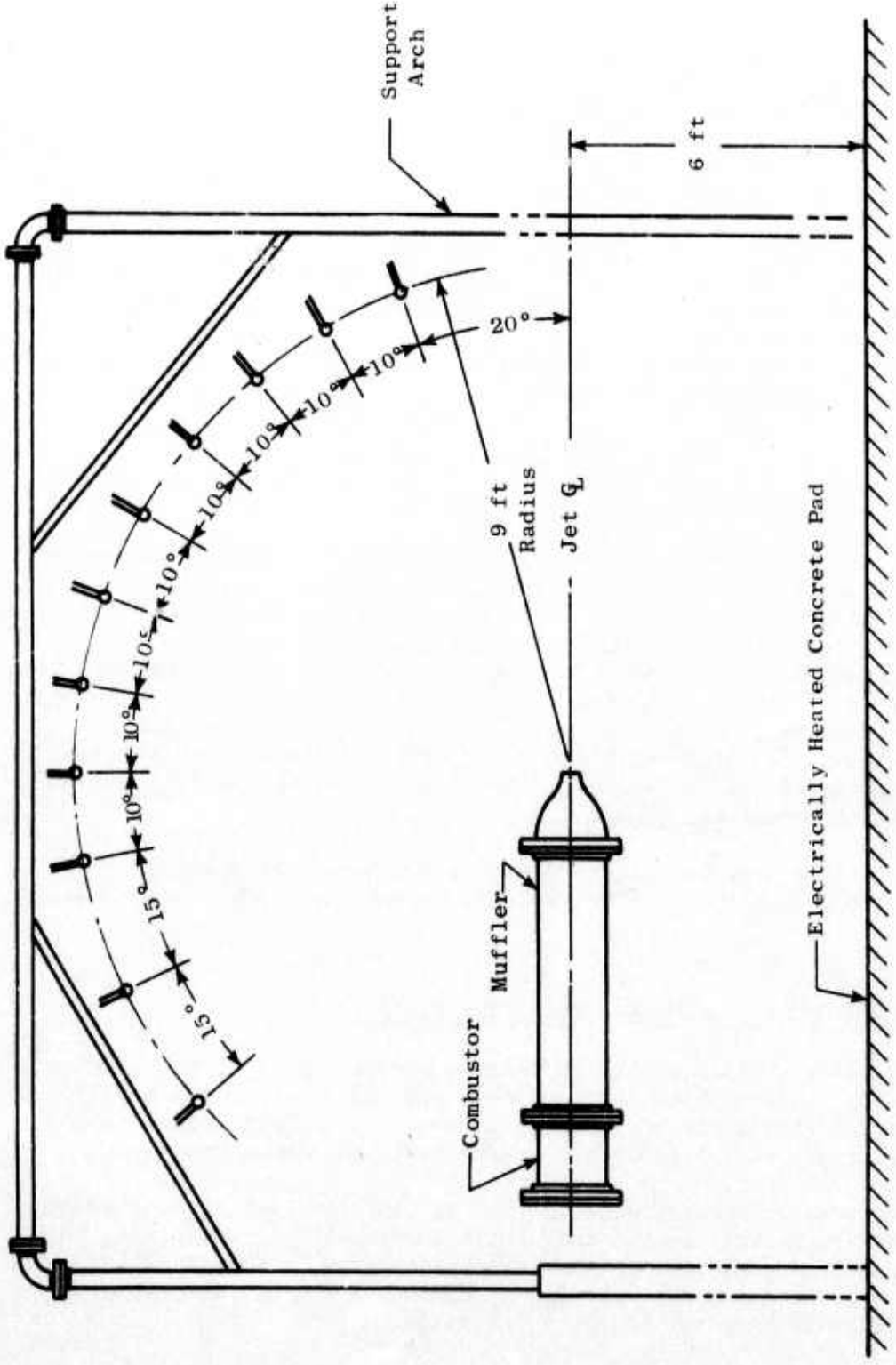

Figure 559. GE CR&DC Hot Jet Facility in Schenectady, New York.

obstruction in the jet plume, a large hoop is used to provide a centerless pivot on the downstream end of the microphone boom. The boom can be moved to any azimuthal angle by the two overhead cables. Since the paths traversed by the microphones are circular arcs centered on the jet axis, any deviation of the radiation patterns from axisymmetry can be easily detected. To avoid long start-up and shut-down times due to intermittent weather, a hermetically sealed microphone holder was designed to allow permanent installation. An additional benefit of this approach is that the electronic noise floor is easily measured when the microphones are covered. An acoustically treated surface is used to minimize the ground reflection effects. By using large sheets of acoustical foam, significant reduction of the ground reflection pattern can be obtained with a minimal time required to lay down and take up the doverings. To allow testing during the winter months, the 30 × 28-foot concrete pad is electrically heated to remove ice and snow.

A.3.2 Jet Facility

To provide the heated air for the high temperature tests, two heaters are used. A large natural gas-fired heat exchanger preheats the air to about 400° F, and this warm air is fed into the burner end of the combustor muffler through a 4" pipe. Two small JP-4 combustors are used to provide the remainder of the heat addition. To prevent combustion noise from contaminating the jet noise downstream of the burners, acoustically treated baffles are used to prevent a see-through path, and the wall of the plenum is lined with two inches of Kaowool and faced with a 1/8"-thick perforated sheet (45% porosity) of Hastelloy X. To date the burner has been operated to 2000° F with no thermal damage.

The jet total temperature and pressure are monitored using wall static taps and a thermocouple in the low velocity plenum upstream of the nozzle contraction.

A.4 PEEBLES SITE IV-B TURBOMACHINERY TEST FACILITY

Testing of the scale model fan vehicle was performed at the Peebles Test Operation, General Electric's outdoor test site, using a General Electric LM1500 stationary gas turbine as the drive system. The gearbox and the LM1500 are contained within acoustically absorbing housings.

The fan vehicle was driven from the rear for the isolation of front noise. With the vehicle in the rear drive configuration, throttling the fan was accomplished with a variable discharge valve located in the fan exhaust duct. The discharge valve in the fan duct (bypass discharge valve) was used to vary the fan pressure ratio.

For the isolation of front end noise, and far more accurate flow measurements, the facility is equipped with a collection system, four standard airflow measuring venturi (two were utilized in the program), and a suppressor

exhaust stack. A schematic of the scale model vehicle facility is shown in Figure 560 for rear drive. Figure 561 shows an aerial view of Peebles Site IVB.

The acoustic data were taken with microphones located on a 100-foot arc positioned at 10° increments from 0° to 150° as measured from the fan inlet axis. The microphones were set at the height of the fan centerline, 15 feet above the sound field surface. Near-field acoustic data were taken with one traversing probe directly ahead of the fan and a stationary probe in the center of the fan discharge duct.

Restrictions were imposed on acoustic testing to assure reliable data. These included steady winds of 5 mph and gusts of no more than 3 mph above the maximum steady wind from any direction. In addition, data were not taken when the field was wet or covered with snow, the relative humidity was less then 30% or in excess of 90%, or temperatures less than 20° F. Also, all instrumentation protruding into the flowpath was removed to far-field acoustic data acquisition.

Quantity and type of aerodynamic instrumentation consisted of:

- Forty steady-state wall static pressures arrayed as follows: 12 each on the internal cowl and centerbody surface, 4 on the inner (primary side) surface of the internal door, 5 on the outer (auxiliary side) surface of the internal door, and 7 on the fixed location and item number for each of these taps.

- A single, radially-traversing, steady-state P_T/T_T Kiel probe, located approximately 4.24 inches forward of the IGV plane and in line with the middle of a blow-in door passage as noted in Table 26.

The following additional parameters were recorded:

- Revolutions per minute (rpm)
- Dry Bulb Ambient Temperature
- Wet Bulb Ambient Temperature
- Wind Velocity and Direction
- Ambient Pressure

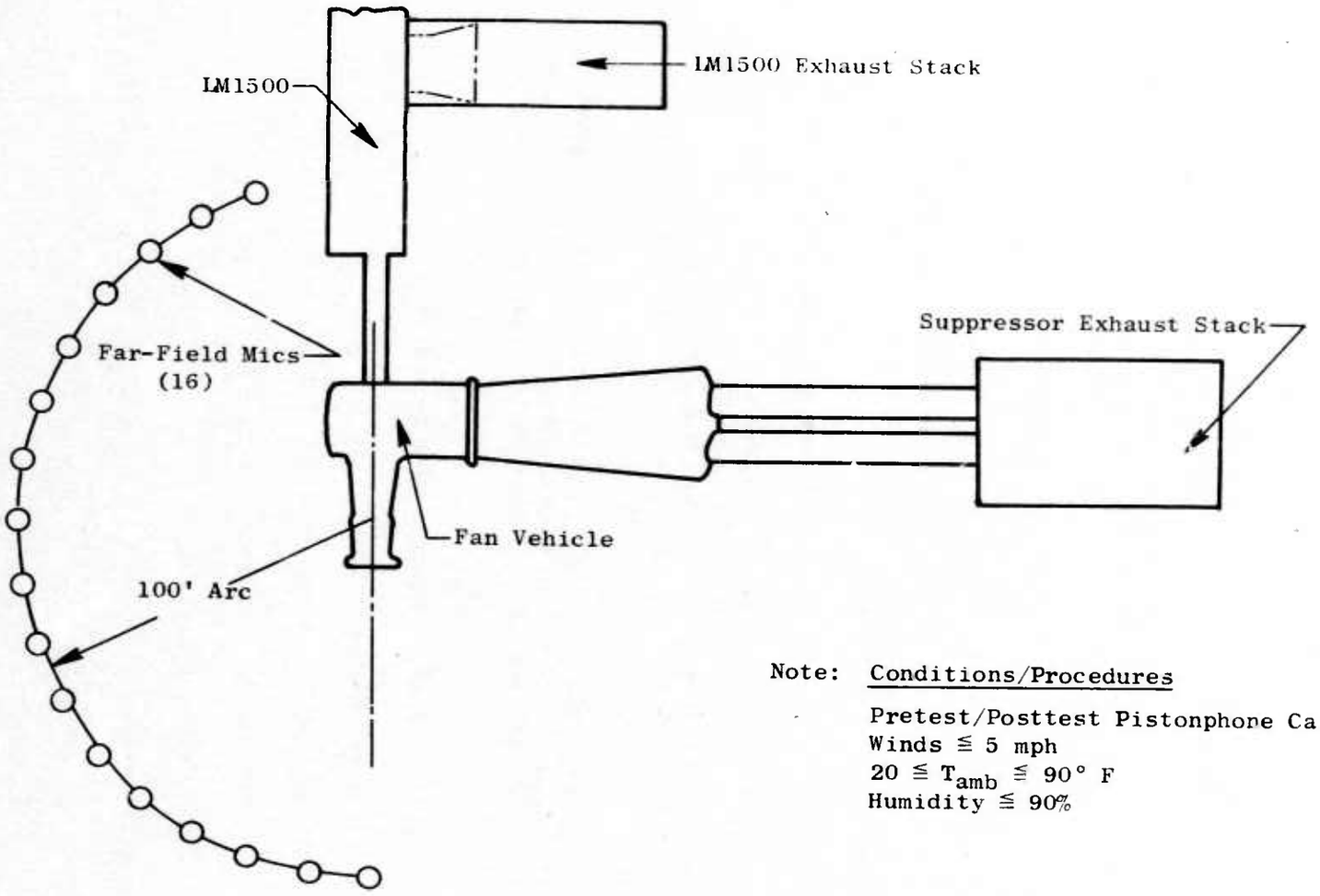

Note: Conditions/Procedures

Pretest/Posttest Pistonphone Calibrations
Winds ≦ 5 mph
$20 \leqq T_{amb} \leqq 90°$ F
Humidity ≦ 90%

Figure 560. GE Peebles Site IV Sound Field in Rear Drive.

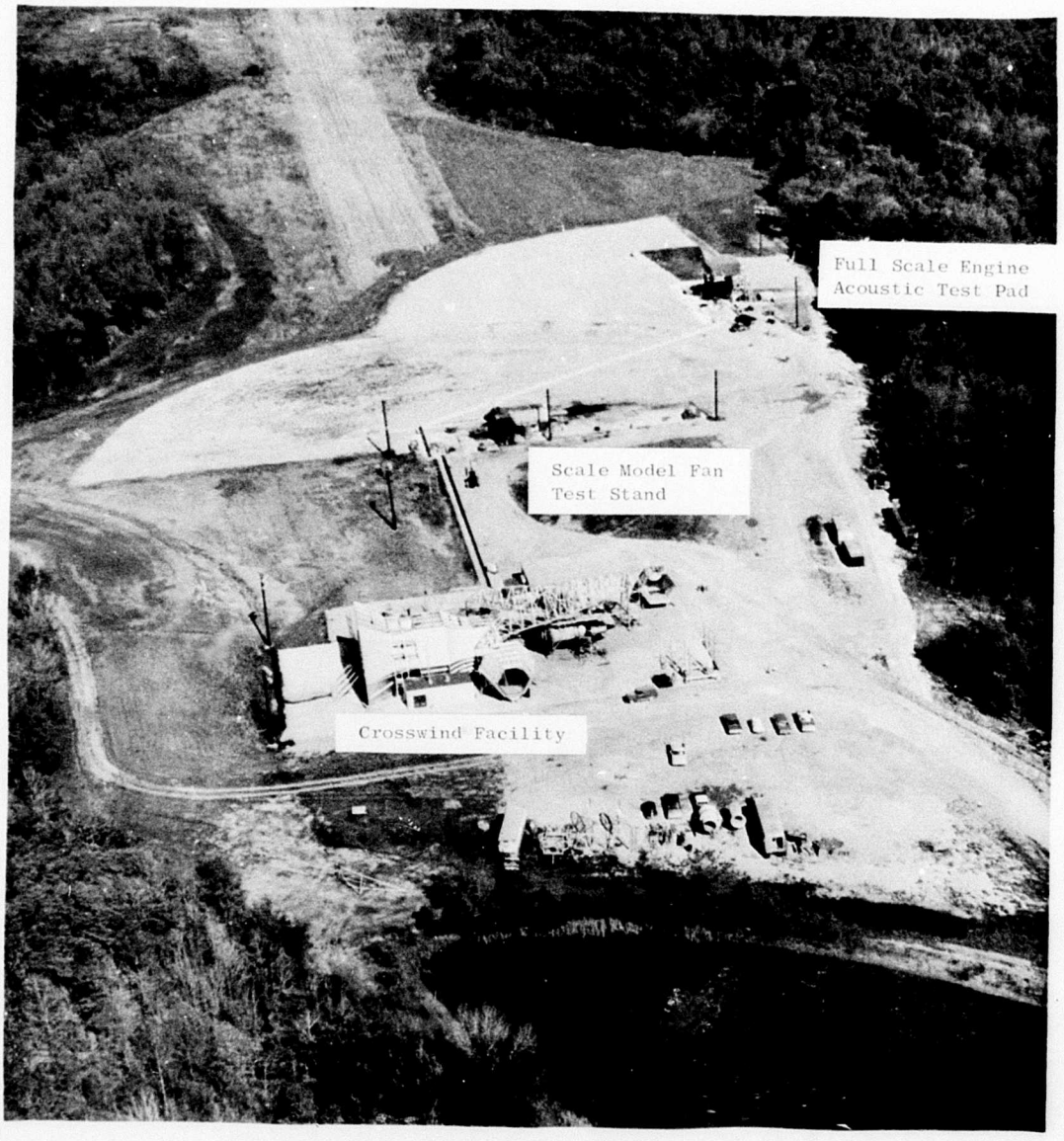

Figure 561. Aerial View of Peebles Site IVB.

Table 26. Inlet Aerodynamic Instrumentation Locations.

I. Steady-State Wall Static Pressure Taps

Surface	Item No.	Circum. Degrees Loc.*	Approach Aero.† Station	Approach Vehicle† Station	Takeoff Aero.* Station	Takeoff Vehicle* Station
Internal Cowl	4000	15	0.0	-85.54	Same as approach	
	4001		10.0	-75.54		
	4002		15.0	-70.54		
	4003		20.0	-65.54		
	4004	135	20.0	-65.54		
	4005	255	20.0	-65.54		
	4006	15	25.0	-60.54		
	4007		30.0	-55.54		
	4008		40.0	-45.54		
	4009		48.12	-37.42		
	4010		60.0	-25.54		
	4011	345	70.0	-15.54		
Centerbody	4012	15	-10.0	-95.54	-3.5	-89.04
	4013		0.0	-85.54	6.5	-79.04
	4014		10.0	-75.54	16.5	-69.04
	4015		15.0	-70.54	21.5	-64.04
	4016		20.0	-65.54	26.5	-59.04
	4017	135	20.0	-65.54	26.5	-59.04
	4018	255	20.0	-65.54	26.5	-59.04
	4019	15	25.0	-60.54	31.5	-54.04
	4020		30.0	-55.54	36.5	-49.04
	4021		40.0	-45.54	46.5	-39.04
	4022		48.0	-37.54	-	-
	4044		70.0	-15.54	70.0	-15.54
Primary Side of Door, 81% A_{th} Setting	4024	90	N/A	N/A	53.48	-32.06
	4025				55.00	-30.54
	4026				56.00	-29.54
	4027				57.00	-28.54
P.S.O.D., 100% A_{th} Setting	4024	90	N/A	N/A	53.49	-32.05
	4025				54.96	-30.58
	4026				55.92	-29.62
	4027				56.89	-28.65
P.S.O.D., 114% A_{th} Setting	4024	90	N/A	N/A	53.49	-32.05
	4025				54.90	-30.64
	4026				55.82	-29.72
	4027				56.75	-28.79
Inner Surfece of BID Passage, 81% A_{th} Setting	4023	90	N/A	N/A	50.00	-35.54
	4035	30			53.51	-32.03
	4036				55.01	-30.53
	4037				56.00	-29.54
	4038				57.01	-28.53
Inner Surface of BID Peesage, 100% A_{th} Setting	4023	90	N/A	N/A	50.00	-35.54
	4035	30			53.47	-32.07
	4036				54.94	-30.60
	4037				55.90	-29.64
	4038				56.88	-28.66
Innar Surface of BID Paeeage, 114% A_{th} Setting	4023	90	N/A	N/A	50.00	-35.54
	4035	30			53.43	-32.11
	4036				54.85	-30.69
	4037				55.79	-29.75
	4038				56.73	-28.81
Outar Surface of BID Passage (Fixed)	4028	30	N/A	N/A	52.0	-33.54
	4029				54.0	-31.54
	4030				55.5	-30.04
	4031				56.0	-29.54
	4032				57.0	-28.54
	4033				58.0	-27.54
	4034				59.5	-26.04

II. Steady-Steady P_T/T_T Radially Traversing Kiel Probe

Located at Aero. Sta. = 76.30†,

Vehicle Sta. = -9.24†,

θ = 3D°*

*Measured clockwise from top, aft looking forward. Blow-in doors are oriented such that 30° and 90° locations are in line with the center of a BID passage, while 15°, 135°, 255°, and 345° lie midway between door center and strut centerline.

†Aero station 0.0 occurs at the (fictitious) flight inlet lip; corresponding vehicle station is -85.54. Vehicle station 0.0 occurs at the 1st stage rotor leading edge.

*Centerbody portion forward of aero. station 49.00 translates 6.5" forward from approach to takeoff position by means of a spool piece.

A.5 EDWARDS TEST FACILITIES

A.5.1 Edwards Test Facility - Jet Acoustic Tests (J79)

The General Electric Flight Test Center facilities, located on Edwards Air Force Base in Southern California's Mojave Desert, were used to perform aeroacoustic jet engine exhaust nozzle tests. Specifically, the existing outdoor test site with its thrust measuring table referred to as "The North Site" was chosen as a prime location for executing acoustic tests due to its absence of tall surrounding buildings. A plan view of the site is shown in Figures 562.

The Acoustic Arena

Before the jet noise acoustic testing was conducted on the North Site, the existing site was graded, leveled, and rolled to provide a smooth surface for the acoustic arena.

The sound field used during exhaust nozzle tests consisted of 13 microphone stations distributed around a 160-foot arc extending from 40° to 160° (engine inlet plane referenced) in 10° increments. At each station two microphones were erected to approximate heights of 2 foot and 12 foot above the ground.

Jet Facility

The noise and air source for the jet exhaust nozzle tests was a J79-15 engine, supplied by the Air Force (Serial Number 439-012). The J79 is an augmented turbojet, single-spool engine as shown in Figure 563.

The engine was modified to obtain, in effect, a gas generator for the jet exhaust nozzle acoustic and related tests. The modifications included a calibrated bellmouth inlet with four 4-element pitot rakes for weight flow determination, and a long treated inlet duct and splitter to reduce forward-radiated noise. A treated housing, separately supported and covering the top, bottom, and sound field side of the engine casing, was used to minimize the casing-radiated noise. The afterburner section and tail pipe assemblies, which are normally connected to the turbine frame, were replaced by an acoustically treated turbine exhaust suppressor to which various exhaust nozzles can be fastened through the use of different adaptor spools, as shown in the engine stack up of Figure 564. Eight wall static taps and two 4-element total-pressure and total-temperature combination rakes were installed in the adaptor spool. The engine was mounted on a stand secured to the thrust pad such that the engine centerline was 12 feet above the thrust pad.

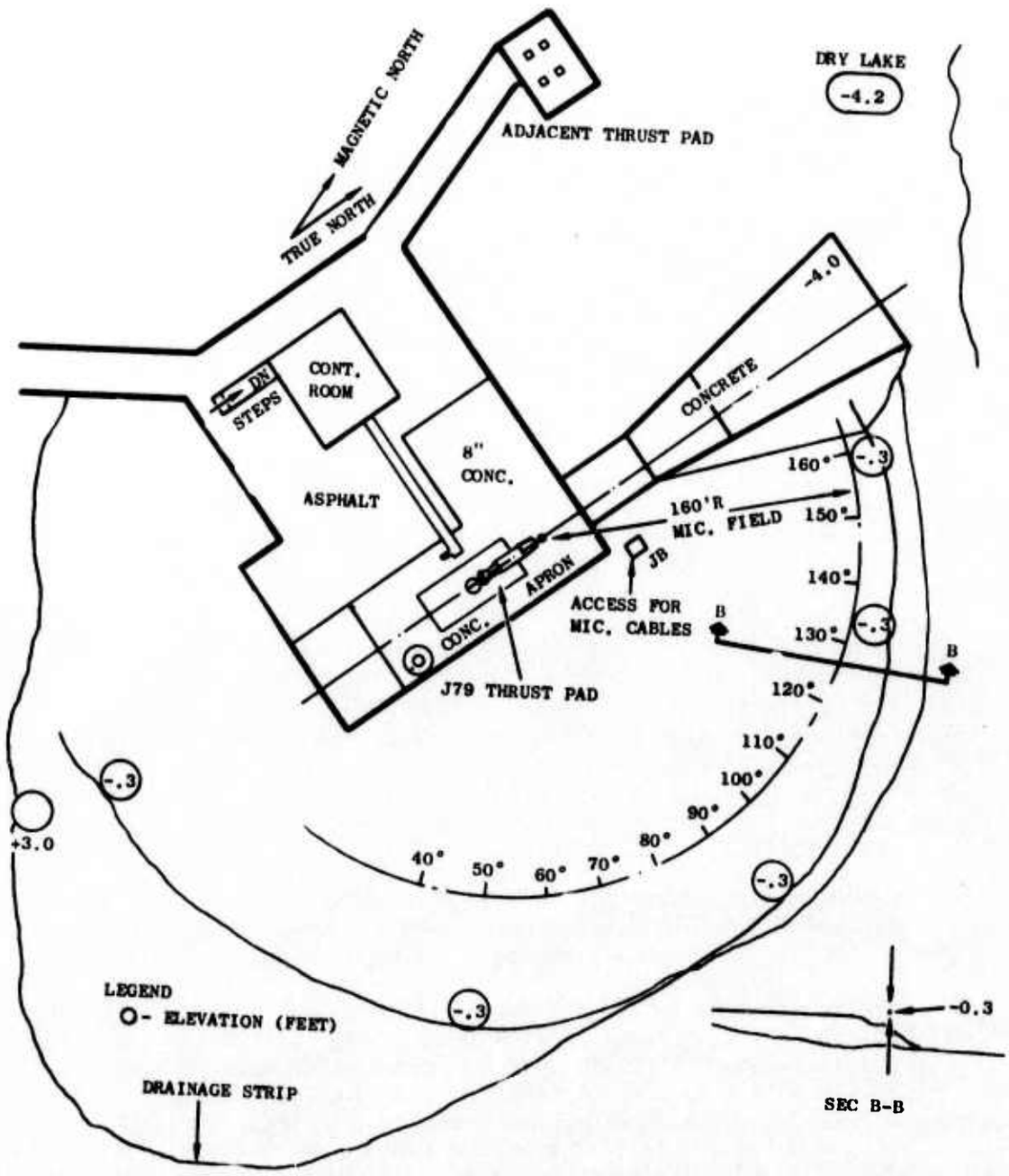

Figure 562. Schematic of the GE/EFTC South Field.

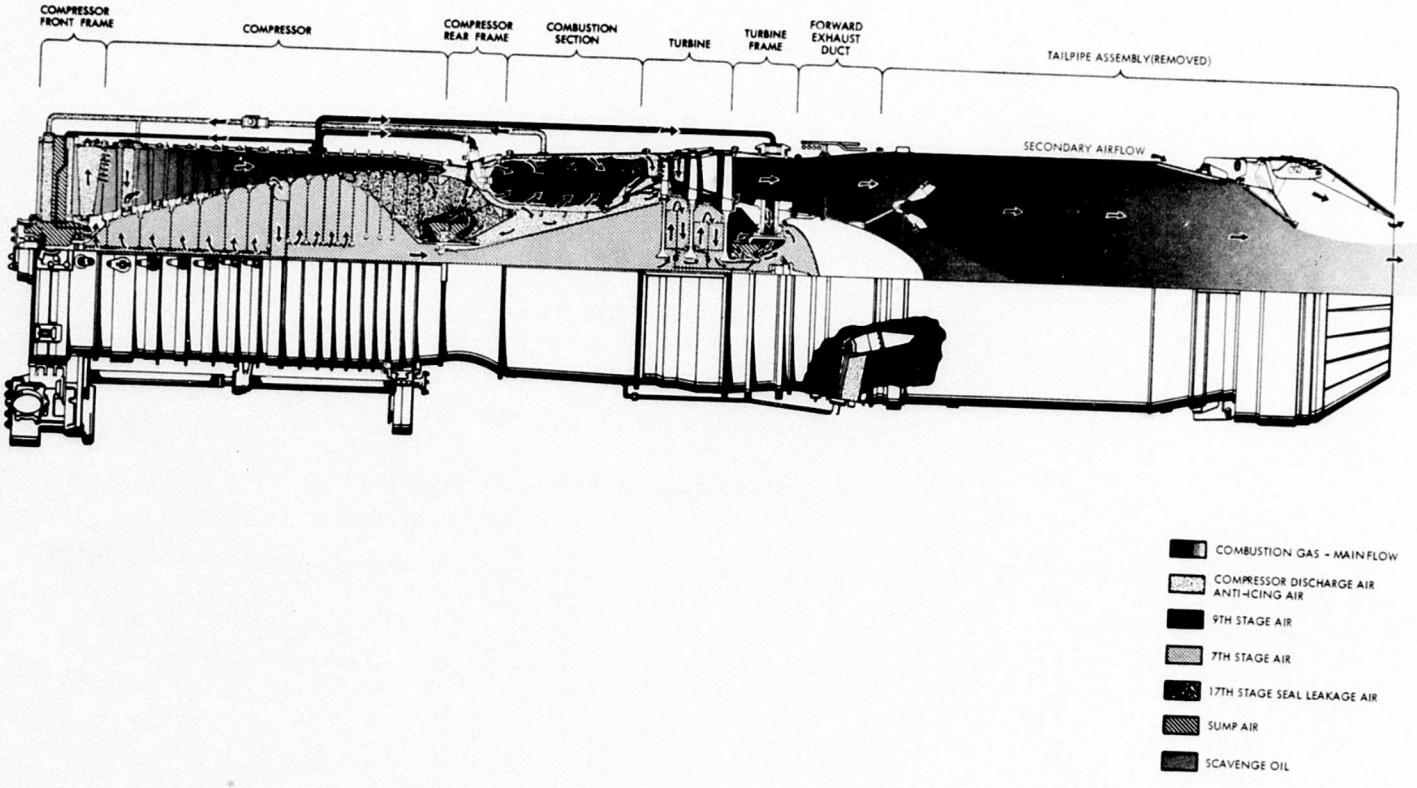

Figure 563. J79-15 Engine Schematic.

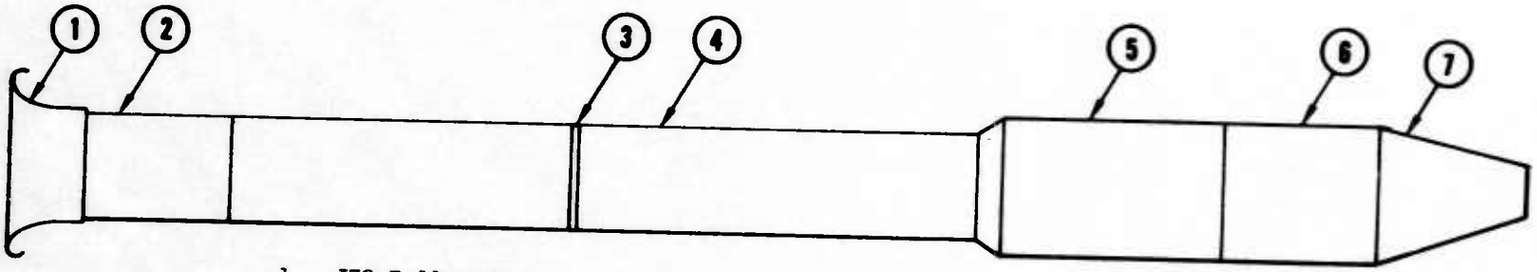

1. J79 Bellmouth
2. Acoustically Treated Inlet Suppressor
3. Slip Joint
4. J79-15 Engine
5. Acoustically Treated Exhaust Suppressor
6. Nozzle Adapter Spool Including Two 4-Element Pt-Tt Combination Exhaust Rakes and Eight Wall Static Taps on Outer Wall
7. Unsuppressed Conic Nozzle: 338-in.^{2}

Figure 564. J79 Engine Stackup Drawing.

Inlet Suppressor

The inlet noise suppressor used for all tests was a 10.5-foot-long cylindrically lined duct with treated inlet splitter as shown in Figure 565. The treatment design was Cerafelt with a porous face plate similar to the exhaust suppressor. The inlet splitter was supported by airfoil-shaped struts placed at 0°, 90°, 180°, 270°. Upstream of the inlet suppressor, a 27-inch-long calibrated J79 bellmouth was attached containing four thermocouples at 0°, 90°, 180°, and 270° and four 4-element rakes at 45, 135, 225, 315°, measuring inlet static and total pressures. The effective inlet area at the inlet plane was 719.63 in^2. The inlet suppressor and bellmouth assembly were mounted separately to the thrust pad and were connected to the engine compressor front frame by a slip-joint flange which was wrapped with a lead vinyl blanket.

Casing Radiation Suppressor

In order to eliminate casing-radiated noise, a lead-lined plywood box was fitted around the engine as shown in Figure 566. The box was 22 feet long, 8 feet high, and 4 feet deep and extended from midway of the inlet suppressor to just forward of the exhaust nozzle. The sides of the box were cut out to fit the contour of the inlet and exhaust suppressors. One side was left open to be able to access the engine, while the side facing the sound field was closed. The lead vinyl blanket was fastened on the exterior of the box and on the inside underneath the engine.

Turbine Exhaust Suppressor

The turbine exhaust suppressor mounted to the turbine rear frame and shown in Figure 567, was available from previous J79 turbomachinery testing. The design consisted of two coannular treated spools forming the inner and outer flowpath walls. The treatment was 1.3 inch thick Cerafelt sandwiched in trays and enclosed by perforated plate with a 23% open area. The suppressor duct length was 54 inches and the duct height 9 inches. The centerbody diameter was 18 inches and was supported by struts midway of the suppressor.

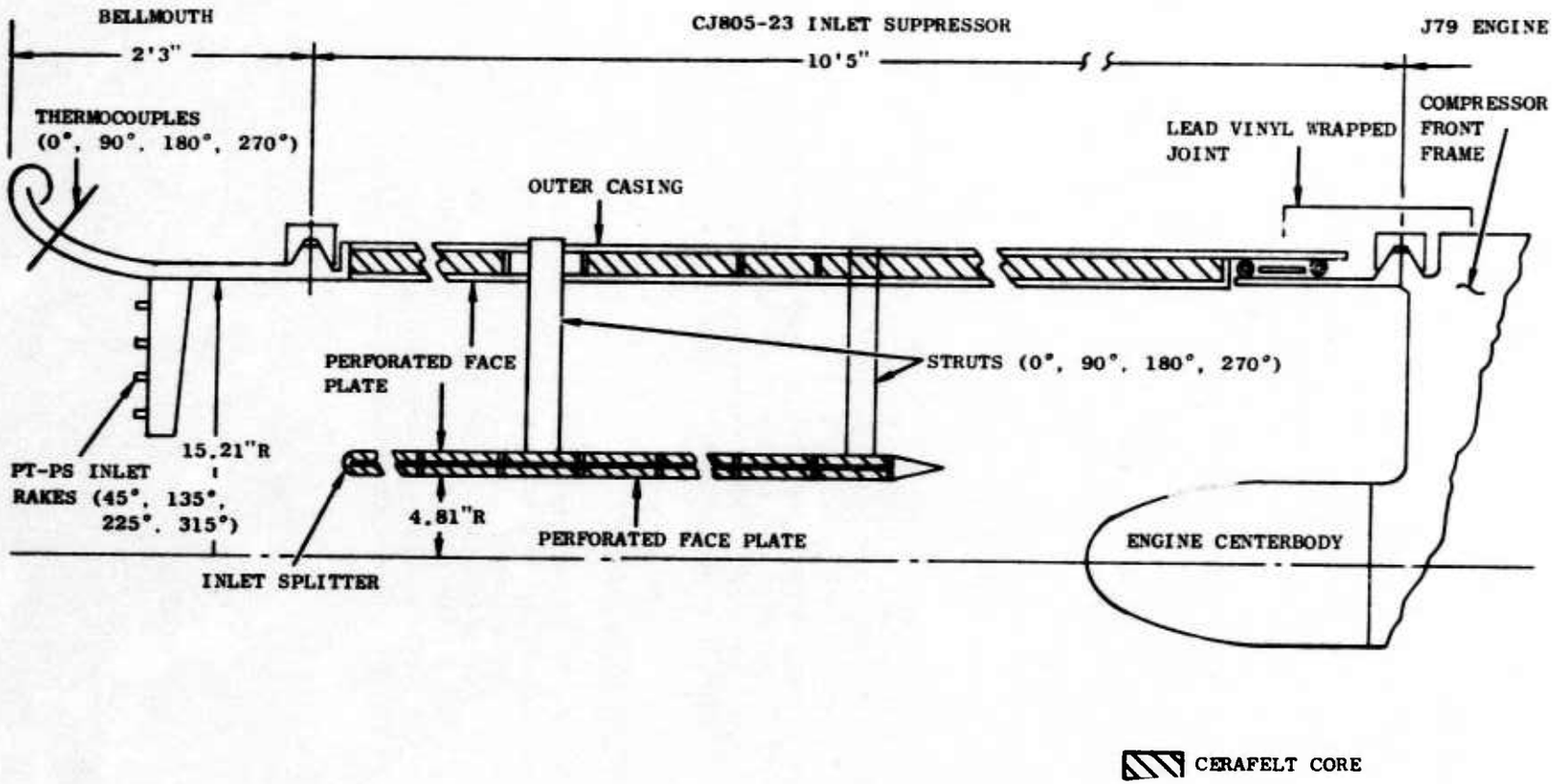

Figure 565. J79 Inlet Suppressor Schematic.

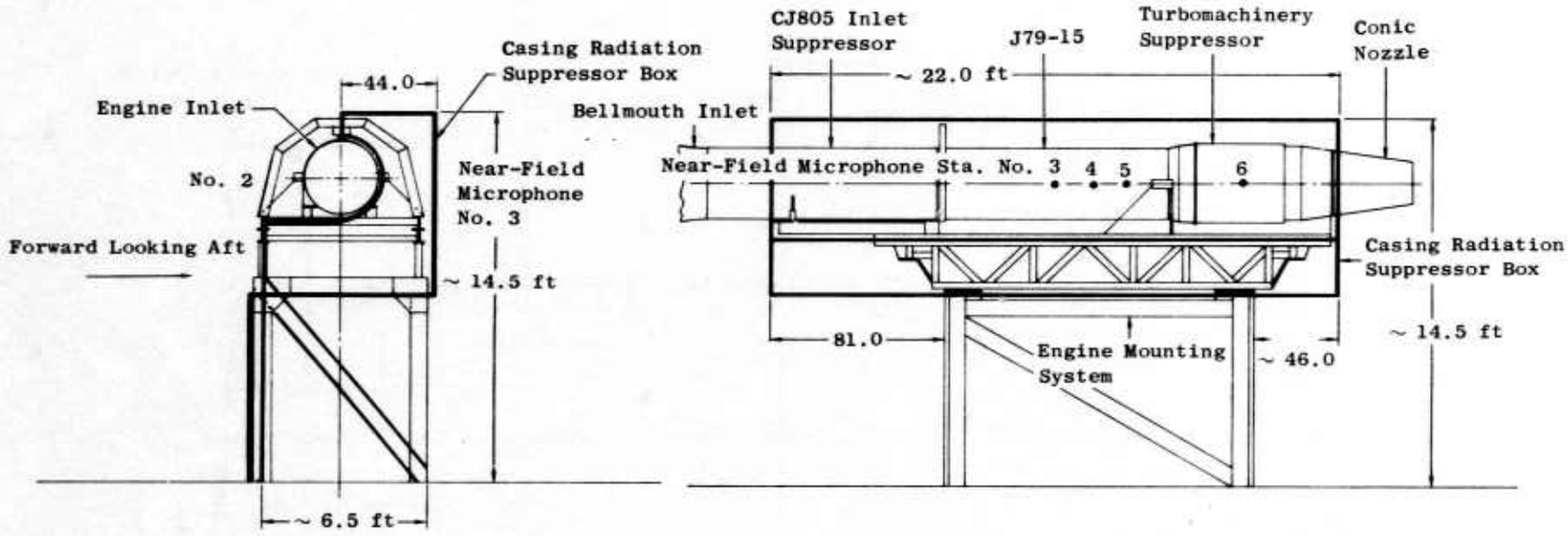

Figure 566. Schematic of Casing Radiation Suppressor Box.

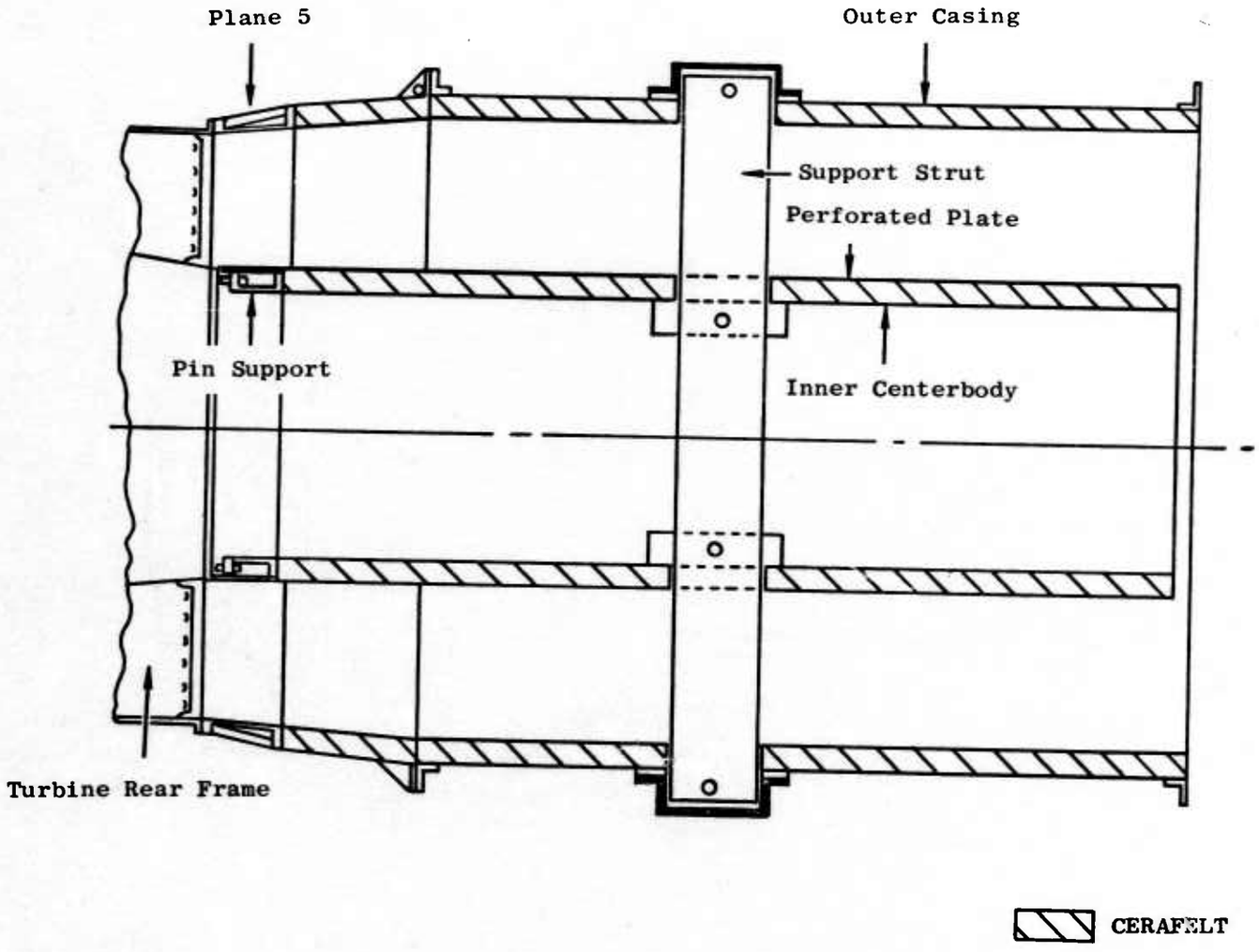

Figure 567. Turbine Exhaust Suppressor.

Adaptor Spool Hardware

Adaptor hardware was required to set the proper nozzle exit plane positions on the engine comparable to those that existed for the conical and multichute nozzle on the JENOTS facility as shown in Figure 568. Two separate adaptor spools were used during the tests, one for the conical nozzle and the other for the suppressed configurations. Allowances in each spool section were made for installation of two 4-element P_T and T_T combination rakes on a common radial plane 4.4 inches aft of the turbine flange at the 30° and 90° positions from top center, aft looking forward. These rakes were used to determine the nozzle exit pressure ratio and total temperature required for calculating the ideal jet velocity.

Unsuppressed Conical Nozzle

The nozzle used for the acoustic baseline for the multichute suppressor tests of the test facility was a conical convergent design with a 20.84-inch discharge diameter for a nominal geometric exhaust area of 341.1 square inches (or an effective exhaust area of 338 in^2) as shown in Figure 569. The nozzle was attached to the exhaust adaptor flange just downstream of the Plane-7 P_T - T_T rakes.

Contamination From Nonjet Noise Sources

To ensure "clean and pure" jet noise emanating from the J79 engine and arriving at the far-field microphones and on the tape recorder, a study of unwanted noise contaminants was conducted. These extraneous sources are composed of:

- Ambient noise from the surroundings
- Electronic noise inherent to data acquisition and reduction systems
- Turbomachinery noise from the J79

A study of the relative levels of these contaminants, how they are minimized and/or removed, and the resulting error and influencing on the full-scale jet noise measurements are included in the next few sections.

Ambient Noise

It is standard practice to record the ambient or background noise (i.e., the noise of the environment without the engine in operation) immediately upon completion of the acoustic testing for that night. This usually occurred around dawn, since testing was restricted to the "quiet" 3am - 8am time period. Three such ambient noise samples were recorded: on 9-26-74 at 5:36, 10-01-74 at 5:28, and 10-04-74 at 7:46 am. The ambient noise OASPL was in the

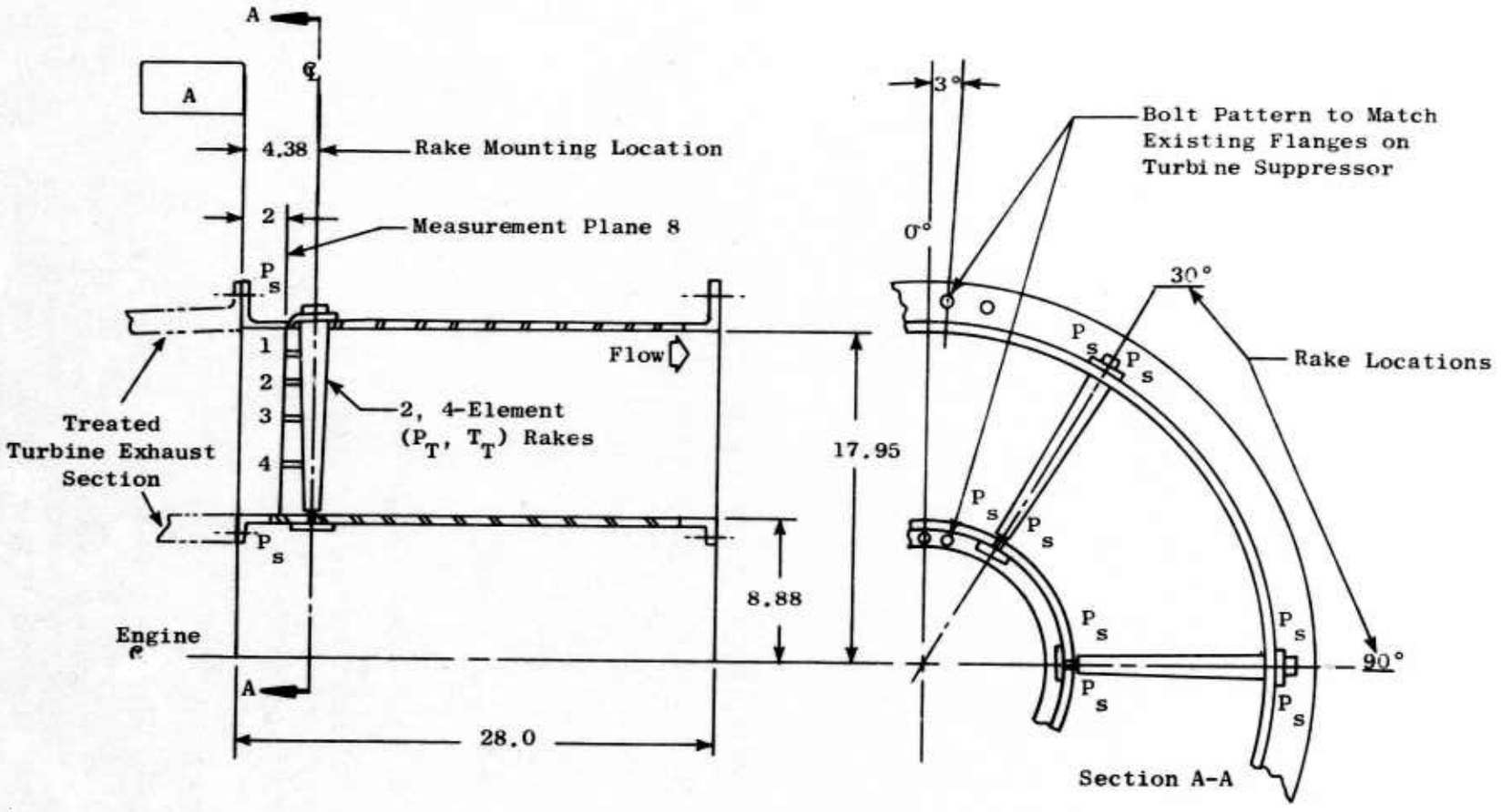

Figure 568. Suppressor Adapter Spool.

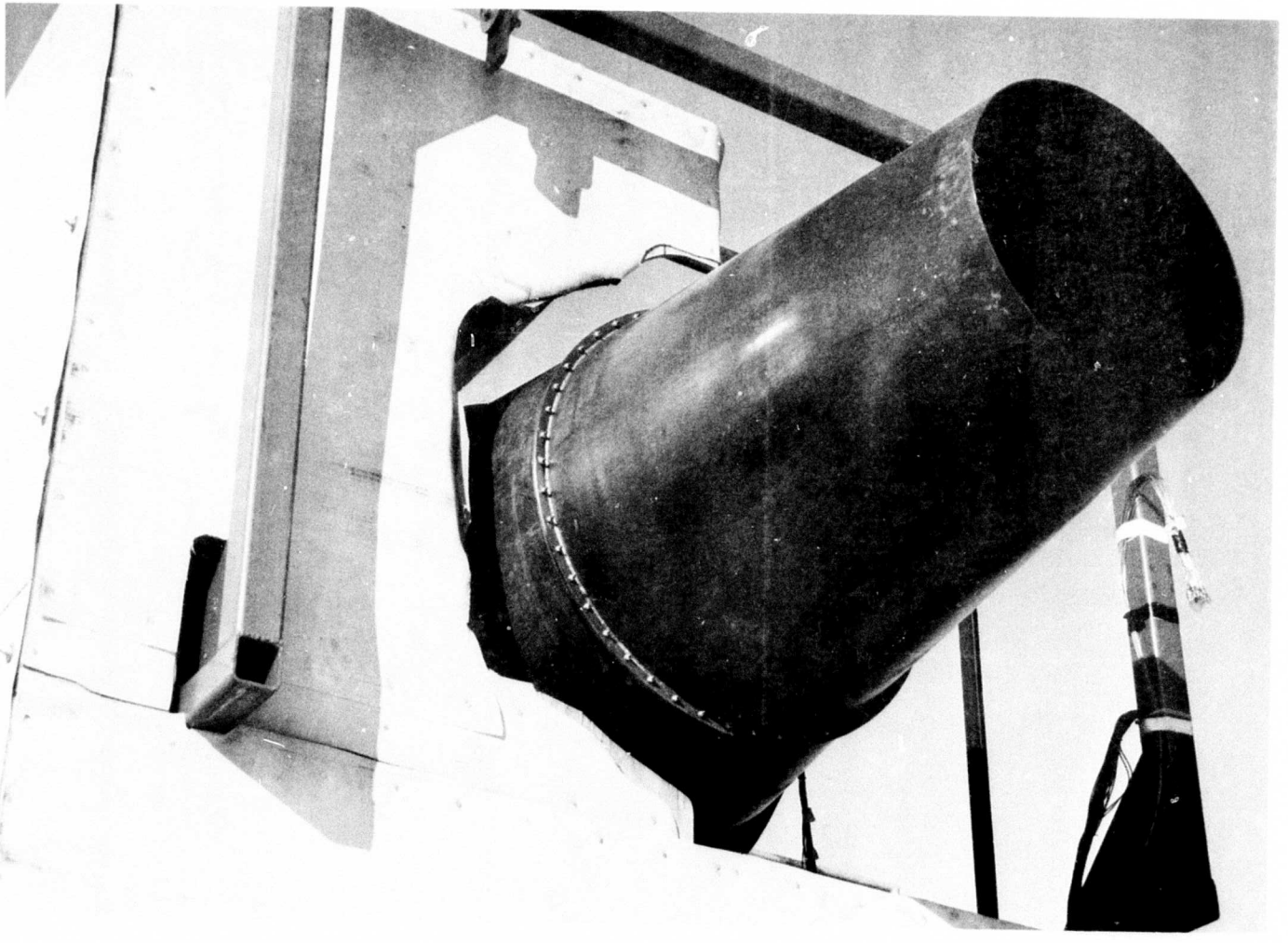

Figure 569. Nozzle Used for Acoustic Baseline Tests of Test Facility.

range of approximately 65 - 70 dB which was indeed quiet conditions.

It is worthwhile, however, to determine if these quiet background noise levels interfere in any way with the data obtained on the certification nozzle. To do this, the most severe case was examined,(i.e., the highest encountered ambient noise levels and the lowest noise levels generated by the conical nozzle). The results, on a 1/3-octave-band (OB) basis are shown in Figure 570, and indicate a difference of 10 dB or more for the 100 Hz - 4000 Hz 1/3-octave bands, implying that true source data were obtained in that frequency region. Below 100 Hz, however, the 1/3 OB's show a difference of less than 10 dB, hence affecting the source level. The required corrections as a function of the difference between source and background noise, are shown in Figure 571. These corrections were applied to reflect the true conical 1/3 OBSPL's, indicated by a dashed line in Figure 570.

It should be pointed out that when the difference between source noise and background noise is less than 3 dB, the source noise is less than the background noise and the corrected source levels should then be regarded only as indicative of the true level and not as an accurate measurement.

In Figure 570 both sets of data are affected by electronic noise floor and dynamic range capability of equipment.

Electronic Noise

All electronic instruments generate small amounts of low energy electrical noise, even those designed with special low noise electrical components such as microphone cartridges, pre- and final-stage amplifiers, tape recorders, and data reduction instrumentation.

An analysis of recording equipment capabilities was undertaken to rank order the major equipment components according to their operational limits (in terms of OASPL). The results are shown in Table 27 and reflect an upper operational limit of 160 dB for the microphone cartridge, while the lower limit is found at 32 dB; this, in essence, is the lowest OASPL that can be detected by the microphone cartridge alone.

The dynamic range of tape recorder and data reduction system combination was verified to be of the order of 46 dB. That is, the tape recorder noise floor was 46 dB below the maximum level being recorded as determined by the amplifier gain settings shown in Table 27. Adding the tape recorder noise floor to the amplifier noise floor will yield a measure of the lowest OASPL signature that can be analyzed without any amplifier electronic noise interference, i.e., acoustic data which register 88-92 dB in OASPL.

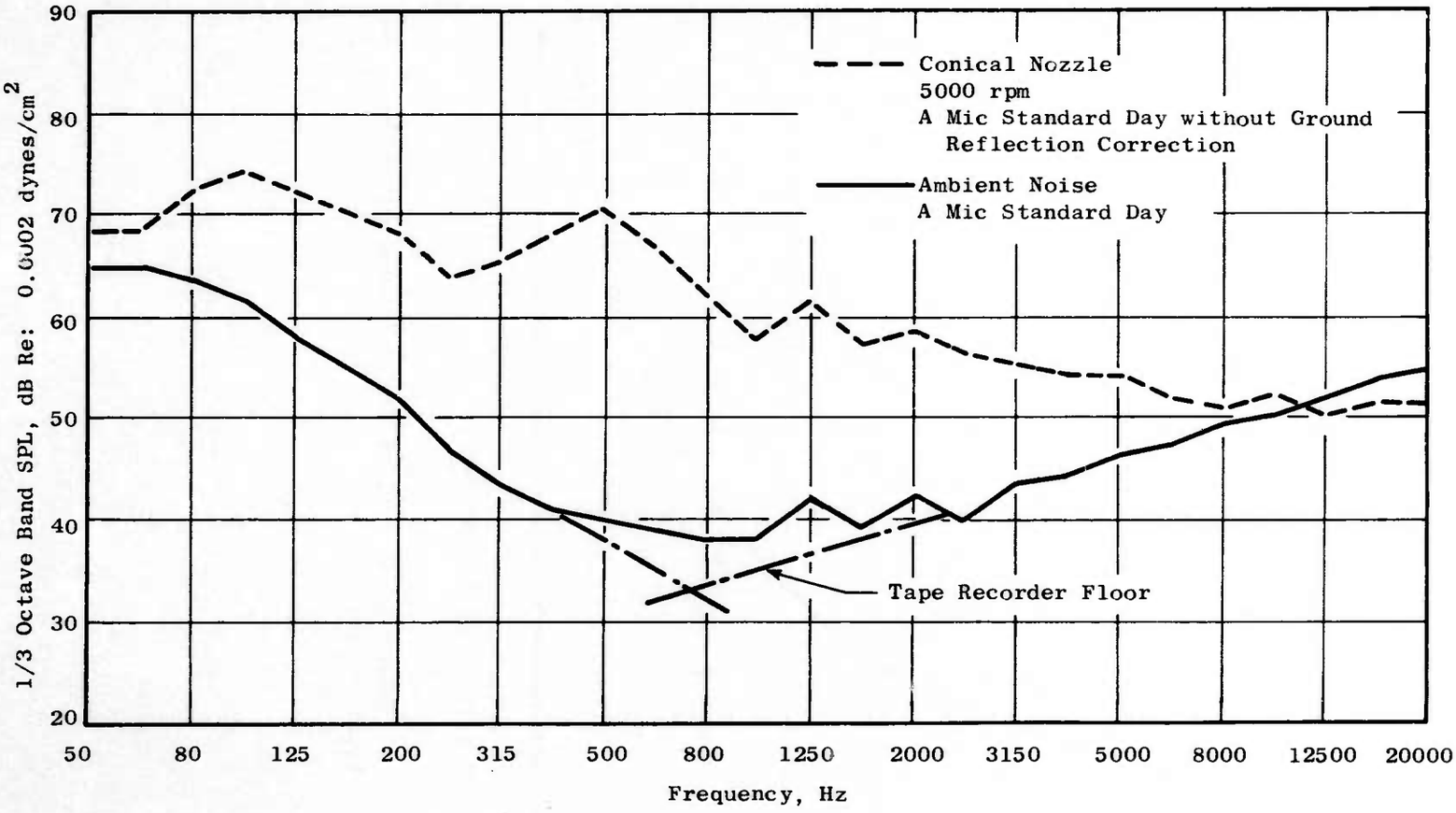

Figure 570. Comparison of the Ambient Noise Level with Recorded Jet Noise.

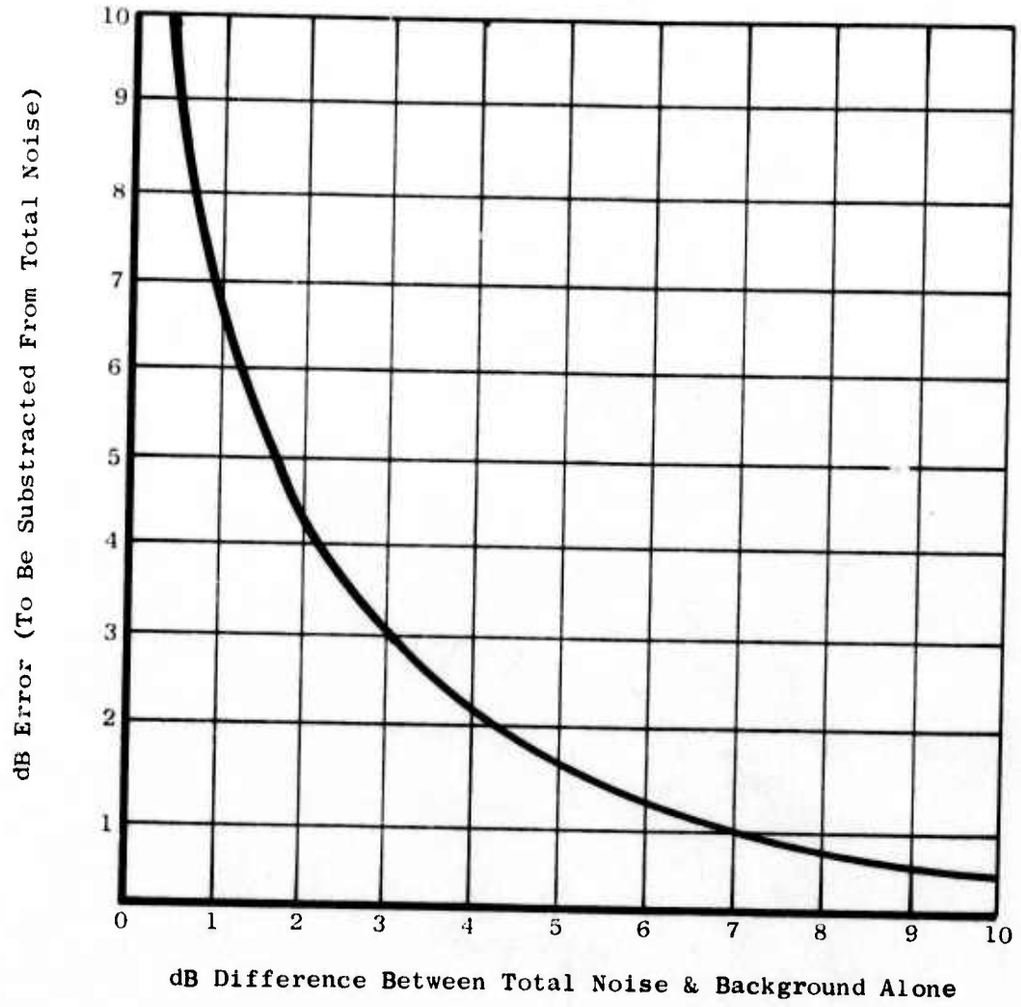

Figure 571. Background Noise Corrections for Sound Level Measurements. Measurements.

Table 27. J79-15 Engine Noise Components.

Component		Engine Speed					
		5040 rpm			6550 rpm		
		Fund.	2nd Harmonic	3rd Harmonic	Fund.	2nd Harmonic	3rd Harmonic
Compressor	1st Stage	1765	3540	5295	2295	4590	6885
	2nd Stage	2270	4540	6810	2950	5900	8850
	3rd Stage	2520	5040	7560	3270	6540	9810
	4th Stage	3275	6550	9825	4260	8520	12780
	5th Stage	3570	7740	11610	5030	10060	15090
	6th Stage	4120	8240	12360	5350	10700	16050
	7th Stage	4860	9720	14580	6320	12640	18960
	8th Stage	5120	10240	15360	6650	13300	19950
	9th Stage	5290	10580	15870	6870	13740	20610
	10th Stage	7810	15620	23430	10150	20300	30450
	11th Stage	7980	15960	---	10370	20740	---
	12th Stage	8140	16280	---	10580	21160	---
	13th Stage	9650	19280	---	12530	25060	---
	14th Stage	9740	19480	---	12660	25320	---
	15th Stage	10150	20300	---	13190	26380	---
	16th Stage	10000	20000	---	13000	26000	---
	17th Stage	10150	20300	---	13190	26380	---
Turbine	1st Stage	6220	12440	18660	8070	16140	24210
	2nd Stage	4790	9580	14370	6230	12460	18690
Inlet Gearbox							
Radial Bevel Gear		1930	3860	5790	2510	5020	7530
Transfer Gearbox							
Radial Bevel Gear		1930	3860	5790	2510	5020	7530
Tach. Gen Gear		1750	3410	5115	2220	4440	6660
Fuel Pump Gear		1705	3410	5115	2220	4440	6660
Cont. Alt. Gear		4080	8160	12240	5300	10600	15900

Turbomachinery Noise

The J79 engine installation at GE/EFTC provided a "jet" noise and air source for future studies in jet mixing noise, jet noise source location, suppressor effects, etc. In order to accurately study these phenomena, the source of jet noise must be essentially free of other jet engine noise sources, such as turbomachinery noise. There are three primary transmission paths for such noise contamination from the engine, namely: 1) out the inlet, 2) out the jet exhaust, and 3) through the engine casing walls. The approach toward eliminating the engine noise contamination was to suppress the sound from the engine using massive inlet and exhaust suppressors on the installation, as shown in Figures 565 and 567 and encasing the engine in a lead box, as shown in Figure 565.

Analysis of the J79 engine far-field 1/3 OB data with the suppressors in place showed the possibility of some turbomachinery tones still present, although their effect for the most part was small. It was determined that correction factors applied to the 1/3 OB data would be adequate to eliminate this contamination. Figures 572 and 573 are typical narrowband plots showing the turbomachinery noise (which was limited to the lowest three rpm's run).

To eliminate the tones the following criteria were used. It was assumed that in a given 1/3 octave band an addition of less than 1 dB due to turbomachinery noise meets the "essentially free" requirement. Figure 574 shows the amount by which a given turbomachinery noise pure tone must exceed the broadband noise in a given 1/3 octave band, as shown on a 40-Hz bandwidth plot, before the limit is exceeded. The J79 rotating parts and their fundamental and harmonic frequencies given in Tables 27 and 28 provide the location (in frequency) of possible turbomachinery tones.

Using the above criteria, the 40-Hz narrowband plots were inspected for turbomachinery tones. The most noticeable tones occurred at low speeds where the jet noise was low. The conical data showed tones at 2000 Hz and 10,000 Hz which appear to be from the radial bevel gear and the 13th through 15th compressor stages, respectively. The 40 Hz narrowband plots showed the presence of 1/rev and 2/rev tones with these tones also affecting surrounding bands. Some unidentifiable tones were found in the 5000 rpm conic nozzle data at 1250 Hz and 2000 Hz which were corrected where it was felt they would severely compromise the accuracy of the PWL (Figure 572).

A.5.2 Edwards Flight Test Center, North Site (J85 Turbine Noise Test)

Testing of the J85 vehicle was performed at the General Electric Flight Test Center at Edwards Air Force Base. The primary acoustic data taken were from far-field microphones located on a 100-foot arc. At the frequencies associated with the J85 turbine tones (above 10 KHz), the atmospheric absorption could potentially eliminate the turbine noise in the far field. As a backup, additional microphones were located on a 30-foot arc. As it turned

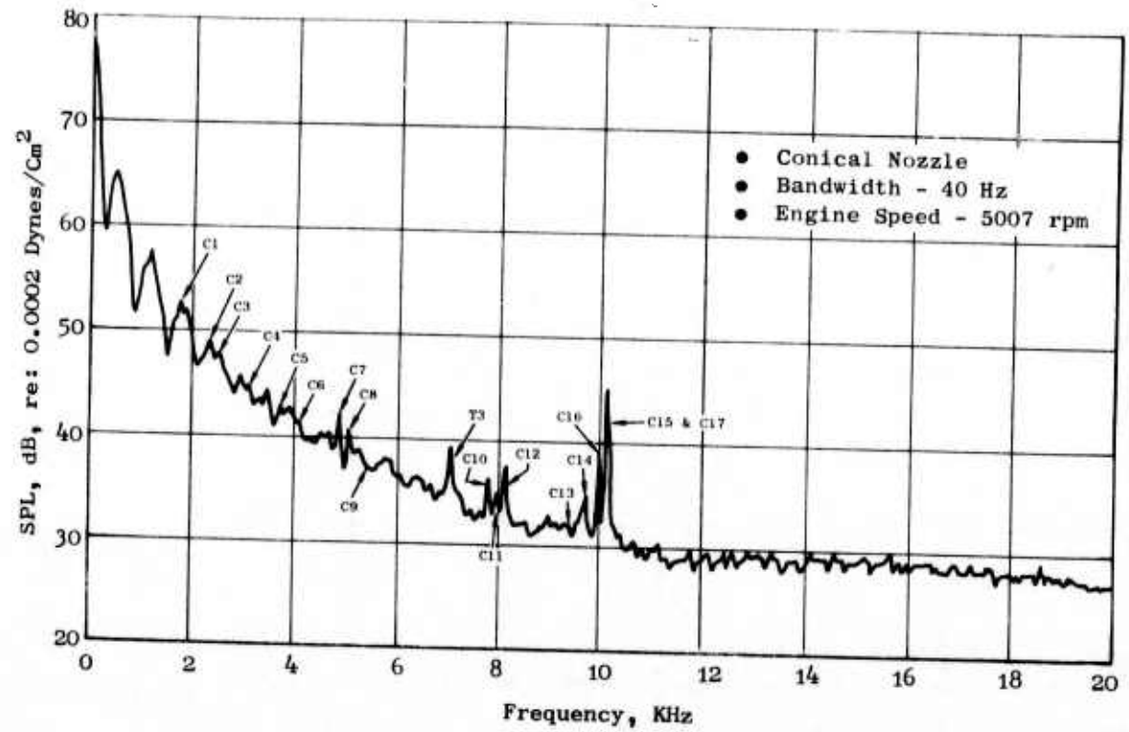

Figure 572. Narrowband of 60° (A" Mic) High Microphones.

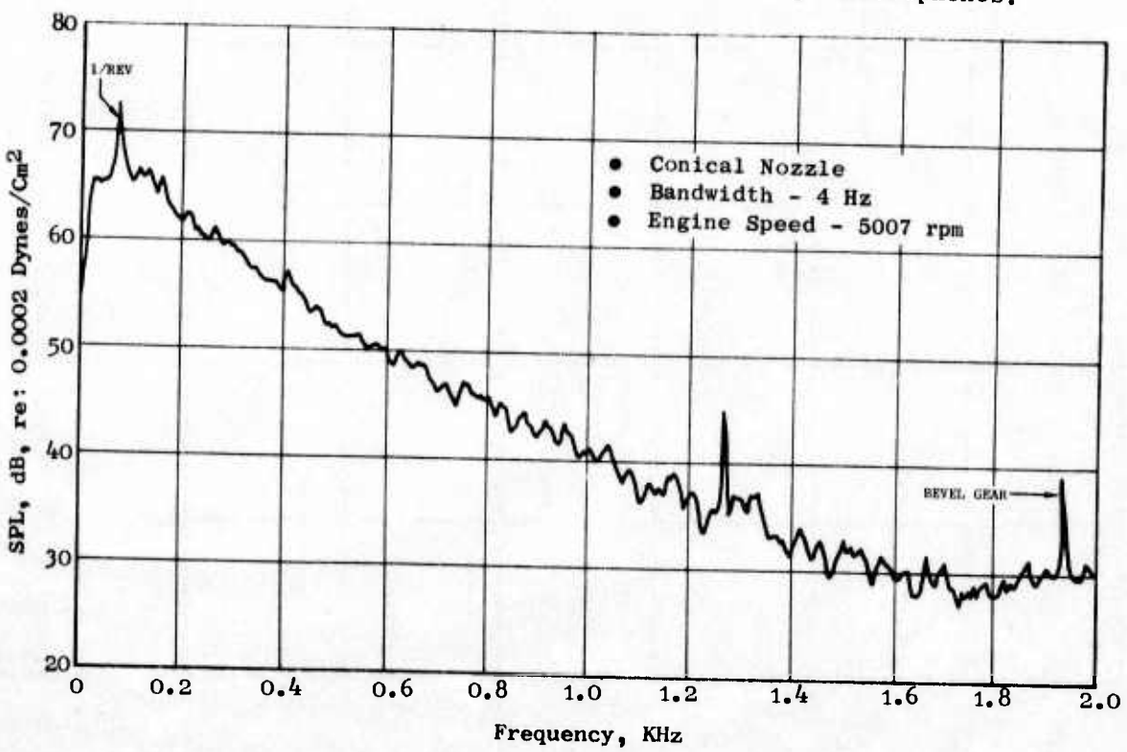

Figure 573. Narrowband of 60° (B" Mic) Low Microphones.

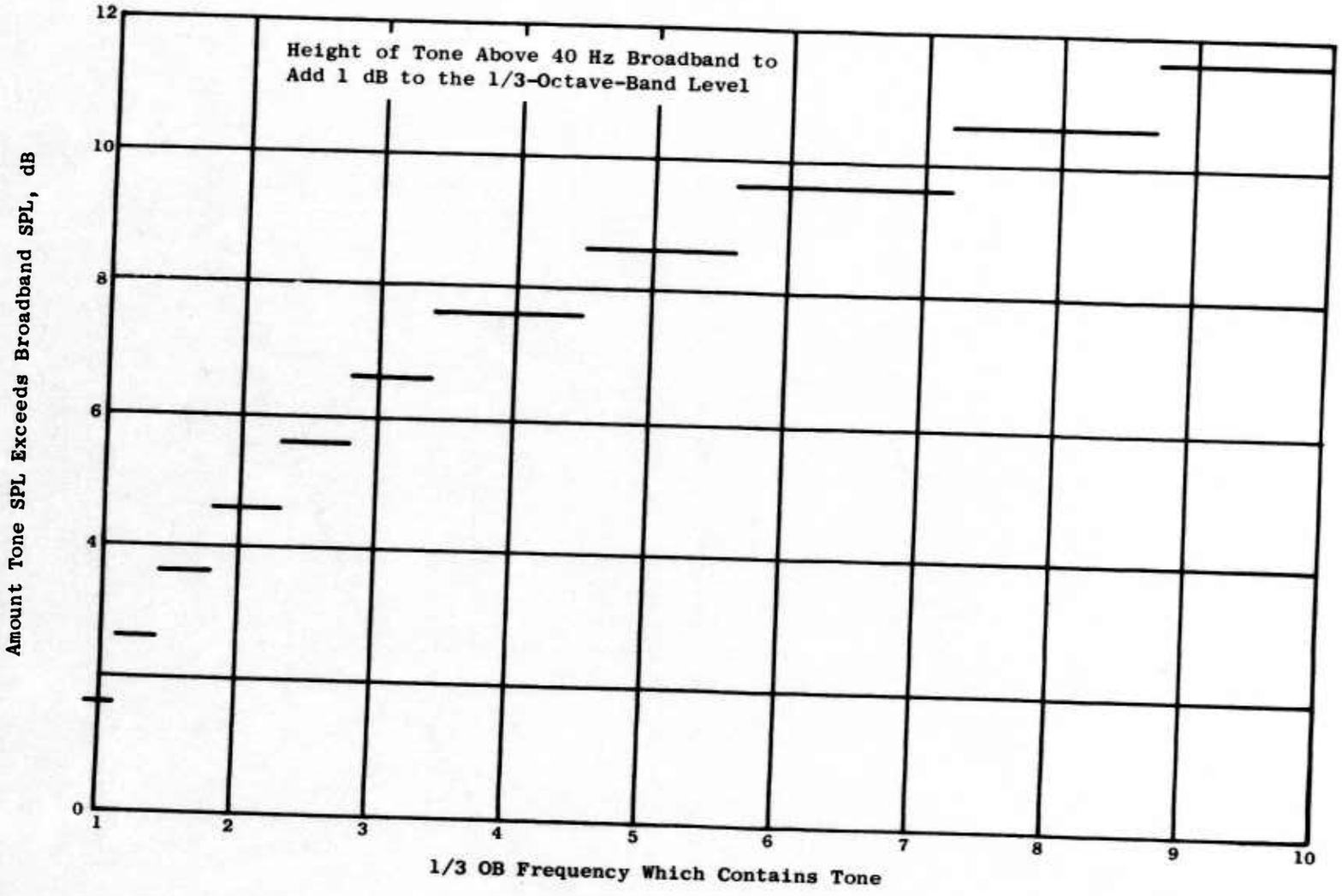

Figure 574. Height of Tone Above 40-Hz Broadband to Add 1 dB to 1/3-Octave Band Level.

Table 28. J79-15 Engine Noise Component Frequency Spectrum for Idle Speed (5040 rpm).

Frequency - cps	Harmonic	Component
37	F	No. 1 Brg f_t
37	F	No. 2 Brg f_t
38.2	F	No. 3 Brg f_t
74	2	No. 1 Brg f_t
74	2	No. 2 Brg f_t
76.4	2	No. 3 Brg f_t
84	F	No. 1, 2, 3 Brg f_r
111	3	No. 1 Brg f_t
111	3	No. 2 Brg f_t
114.6	3	No. 3 Brg f_t
134	F	No. 3 Brg Scav Pump
167	F	Rear Gearbox Scav Pump
168	2	No. 1, 2, 3 Brg f_r
172	F	Main Lube Pump
250	F	Tran Gearbox Scav Pump
252	3	No. 1, 2, 3 Brg f_r
268	2	No. 3 Brg Scav Pump
318	F	Nozzle Pump
334	2	Rear Gearbox Scav Pump
344	2	Main Lube Pump
402	3	No.3 Brg Scav Pump
415	F	Main Fuel Pump
500	2	Tran Gearbox Scav Pump
501	3	Rear Gearbox Scav Pump
516	3	Main Lube Pump
636	2	Nozzle Pump
695	F	No. 2 Brg f_b
750	3	Trans Gearbox Scav Pump
788	F	No. 1 Brg f_b
830	2	Main Fuel Pump
851	F	No. 2 Brg f2
902	F	No. 1 Brg f_2
910	F	No. 3 Brg f_b
954	3	Nozzle Pump
1055	F	RGB Tach Gen Gear
1070	F	No. 3 Brg f_2
1081	F	No. 2 Brg f_1
1115	F	No. 1 Brg f_1

Table 28. J79-15 Engine Noise Component Frequency Spectrum for Idle Speed (5040 rpm) (Continued).

Frequency - cps	Harmonic	Component
1120	F	TGB Scav Pump Gear
1245	3	Main Fuel Pump
1285	F	No. 3 Brg f_1
1390	2	No. 2 Brg f_b
1460	F	RGB Gear-Hor Shaft, Lube Pump, Fuel Control
1545	F	RGB Noz Act Pump Gear
1576	2	No. 1 Brg f_b
1705	F	TGB Hor Shaft, Fuel Pump, Tach Gen Gear
1765	F	Compressor 1st Stage
1800	F	A/B Fuel Pump
1702	2	No. 2 Brg f_2
1804	2	No. 1 brg f_2
1820	2	No. 3 Brg f_b
1930	F	Inlet GB & TGB Radial Bevel Gear
2020	F	Main Fuel Control
2085	F	RGB Scav Pump Gear
2085	3	No. 2 Brg f_b
2110	2	RGB Tach Gen Gear
2140	2	No. 3 Brg f_2
2185	F	TGB Main Drive Gear #1
2230, 2162	2	No. 1 and No. 2 Brg f_1
2240	2	TGB Scav Pump Gear
2270	F	Compressor 2nd Stage
2364	3	No. 1 Brg f_b
2520	F	Compressor 3rd Stage
2570	2	No. 3 Brg f_1
2553	3	No. 2 Brg f_2
2706	3	No. 1 Brg f_2
2730	3	No. 3 Brg f_b
2920	2	RGB Gears Hor Shaft, Lube Pump, Fuel Cont.
3090	2	RGB Noz Act Pump Gear
3165	3	RGB Tach Gen Gear
3210	3	No. 3 Brg f_2
3275	F	Compressor 4th Stage
3345, 3243	3	No. 1 & 2 Brg f_1
3360	3	TGB Scav Pump Gear
3410	2	TGB-Gear Tach Gen, Fuel Pump, Hor Shaft
3445	F	TGB-Main Drive Gear #2
3530	F	Turbine 3 Stage
3530	2	Comp 1 Stage
3600	2	AB, Fuel Pump
3855	3	No. 3 Brg f_1

Table 28. J79-15 Engine Noise Component Frequency Spectrum for Idle Speed (5040 rpm) (Continued).

Frequency - cps	Harmonic	Component
3860	2	TGB & IGB Rad Bev Gear
3865	F	Compressor 5th Stage
4040	2	MF Control
4080	F	TGB Cont Alt Gear
4115	F	Compress 6th Stage
4170	2	RGB Scav Pump Gear
4370	2	Main Drive Gear #1
4380	3	RGB Gear Hor Shaft, Lube Pump, Fuel Cont.
4540	2	Compressor 2nd Stage
4635	3	RGB Noz Act Pump Gear
4790	F	Turbine 2nd Stage
4872	F	Compress 7th Stage
4945	F	TGB A/B Fuel Pump Gear
5040	2	Compress 3rd Stage
5115	3	TGB Gear-Tach Gear, Fuel P and Hor Shaft
5125	F	Comp 8th Stage
5290	F	Comp 9th Stage
5295	3	Comp 1st Stage
5400	3	A/B Fuel Pump
5790	3	IGB & TGB Rad Bev Gear
6060	3	MF Control
6220	F	Turbine 1st Stage
6255	3	RGB Scav Pump Gear
6550	2	Comp 4th Stage
6555	3	TGB Main Dr Gear #1
6810	3	Comp 2nd Stage
6890	2	TGB Main Dr Gear #2
7060	2	Turbine 3rd Stage
7560	3	Comp 3rd Stage
7730	2	Comp 5th Stage
7810	F	Comp 10th Stage
7980	F	Comp 11th Stage
8140	F	Comp 12th Stage
8160	2	TGB, Cont Alt Gear
8230	2	Comp 6th Stage
9580	2	Turbine 2nd Stage
9660	F	Comp 13th Stage
9744	2	Comp 7th Stage
9745	F	Comp 14th Stage
9825	3	Comp 4th Stage
9890	2	TGB AB Fuel Pump Gear
10000	F	Compressor 16th Stage
10165	F	15th and 17th Stage
10250	2	Compressor 8th Stage
10335	3	TGB Main Drive Gear #2
10580	2	Comp 9th Stage

Table 28. J79-15 Engine Noise Component Frequency Spectrum for Idle Speed (5040 rpm) (Concluded).

Frequency - cps	Harmonic	Component
10590	3	Turbine 3rd Stage
11595	3	Comp 5th Stage
12240	3	TGB Cont Alt Gear
12345	3	Comp 6th Stage
12440	2	Turbine 1st Stage
14370	3	Turbine 2nd Stage
14580	3	Comp 7th Stage
14835	3	TGB A/B Fuel Pump Gear
15360	3	Comp 8th Stage
15620	2	Comp 10th Stage
15870	3	Comp 9th Stage
15960	2	Comp 11th Stage
16280	2	Comp 12th Stage
18660	3	Turbine 1st Stage
19280	2	Comp 13th Stage
19480	2	Comp 14th Stage
20000	2	Comp 16th Stage
20300	2	15 and 17th Stage
23430	3	Comp 10th Stage

out, the inlet suppressor and operation at maximum exhaust nozzle setting were successful in unmasking the turbine noise at the 100-foot measuring distance, and the 30-foot data were not used.

Far-field acoustic measurements were made at a 100-foot radial distance, 20° to 160° measured from the inlet axis, in 10° increments and at a 30-foot radial distance for angles of 100° to 140°, in 10° increments, relative to an arc center located on the discharge plane of the exhaust nozzle. The microphone height used was equal to the engine centerline height of 10 feet. The surface of the sound field consisted of leveled, hard-packed sand, with the exception of an asphalt area around the perimeter of the test stand. A lay-out of the test stand and the sound field is shown on Figure 575.

Each far-field microphone system consisted on the following:

Microphone Head	Bruel and Kjaer 4133
Cathode Follower	Bruel and Kjaer 2615
Power Supply	Bruel and Kjaer 2801
Amplifier	Designed and built by GE/Edwards

Since data were required through the 40,000 Hz 1/3 octave band, the 200 Ω power supply option was used to provide optimum response characteristics for measuring high frequency, low amplitude data.

In addition to far-field data, acoustic probe measurements were performed in the turbine exhaust area using two stationary acoustic probes positioned as indicated on Figure 576 with access obtained through unused afterburner spraybar ports. The type microphone used was a Bruel and Kjaer 4136, with the remainder of components the same as for the far-field systems. To improve the signal-to-noise ratio, each probe was also recorded through a high-pass filter, blocking the low frequency (to 2000 Hz) portion of the signal where flow noise was prevalent.

Data were recorded on FM with a Genesco 28-track recorder at a tape speed of 120 ips in order to provide the required recorder response characteristics.

For each test setup, the frequency response of each system was determined by recording a "pink noise" signal, using a Hewlett-Packard Random Noise Generator, for the 50-KHz frequency range and an oscillator for frequencies to 40 KHz. The play-back of these responses was performed using the same equipment as used for acoustic data reduction, thus establishing the response for all components of the system. These responses, along with individual microphone head corrections, were determined for inclusion in the 1/3-octave data processing. If any component of the sound system (with the exception of microphone heads) required replacements, the response of the system was reestablished by the method previously described.

The aerodynamic instrumentation, listed on Table 29, was selected primarily to provide the aerodynamic information necessary to interpret the acoustic results.

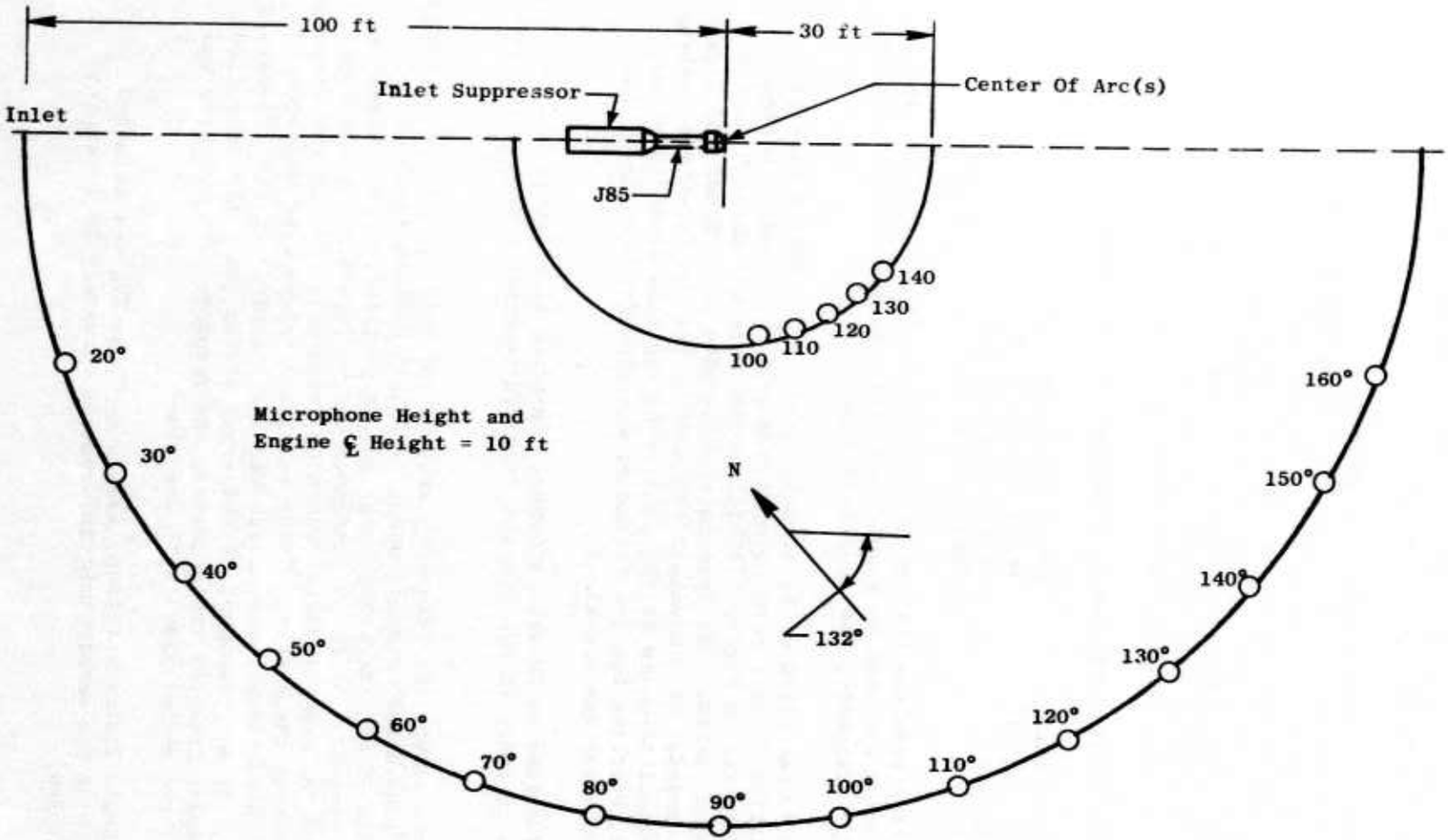

Figure 575. Microphone Locations, J85 Turbine Test.

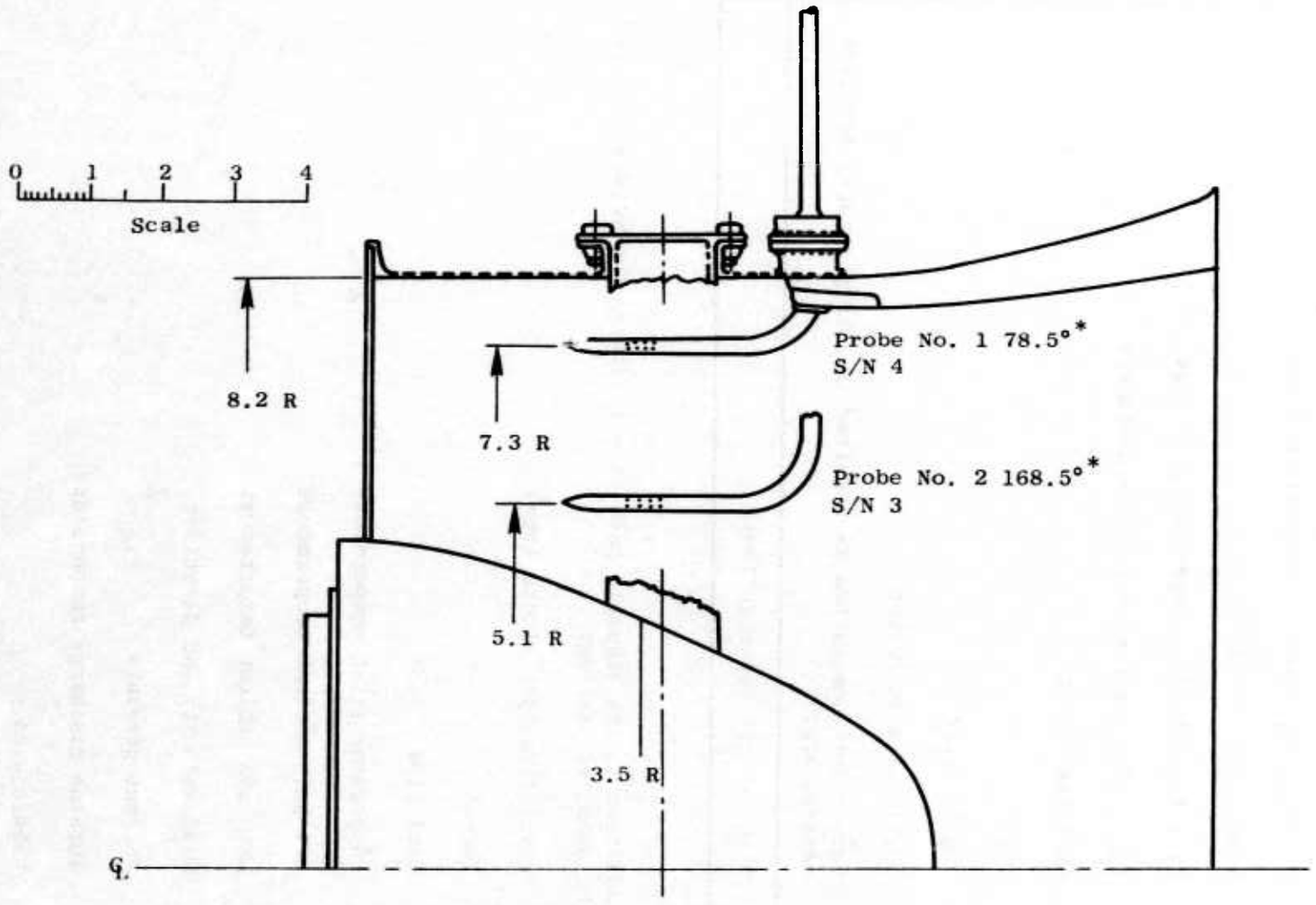

* Measured Clockwise from 12:00 Position Aft Looking Forward

Figure 576. Turbine Exhaust Acoustic Probe Locations.

Table 29. J85 Performance Instrumentation/Measurements

• P_{T_2}/P_{S_2}, T_{T_2} rakes* - compressor inlet
• 4 wall static taps (P_{S_2})
• P_{T_3}, T_{T_3} rakes* - compressor discharge
• $T_{T_{5.1}}$, $P_{T_{5.1}}$ rakes* - turbine discharge
• Fuel flow meter
• Thrust
• Engine speed
• Nozzle area indicator
• Safety instrumentation as required (oil temperature, accelerometers, etc.)
*Removed for Acoustic Tests

In addition to the acoustic data, the following parameters were monitored during the acoustic testing:

- Revolutions per minute (rpm)
- Thrust
- Fuel flow
- Compressor inlet temperature
- Dry bulb ambient temperature
- Wet bulb ambient temperature
- Wind velocity and direction
- Ambient pressure
- Turbine discharge temperature
- Nozzle area

At each test point, two minutes stablization time were allowed before recording acoustic data.

A.6 FLUIDYNE ENGINEERING CORPORATION'S MEDICINE LAKE AERODYNAMIC LABORATORY

A.6.1 Introduction

FluiDyne maintains and operates extensive aerodynamic test facilities which are used by government and industry. The majority of the studies performed in these facilities is related to propulsion system performance and mostly to engine exhaust systems aft of the turbine exit. During the 20 years that FluiDyne has been conducting studies, they have developed special measurement systems and techniques which uniquely apply to their corporate test facilities. These techniques and equipment are continually reviewed and updated to be consistent with new test requirements so that the experiments they conduct and the resulting data are as controlled and accurate as are produced anywhere.

A schematic of FluiDyne's Medicine Lake Aerodynamic Laboratory test facilities is included as Figure 577. Each facility is designed to create uniform and controlled aerodynamic environments for the models being tested. An extreme range of flow properties is available with pressures up to 5000 psi, flow rates of 300 lbs/sec, 10 microns of vacuum, Mach numbers up to 14, and temperatures as high as 4000° F. Nozzle operating conditions for the current program were well within FluiDyne capabilities.

A.6.2 Facility Description

Static Thrust Facilities

The static model tests were performed in FluiDyne's Channels 6, 7, and 12, which are cold-flow, free-jet, static thrust stands designed for nozzle testing over a wide range of pressure ratio simulation. The basic arrangement of these facilities is shown in Figure 578. High pressure dry air from the facility storage system is throttled, metered through an ASME long-radius metering nozzle, and discharged through the test model.

The thrust data are obtained by direct force measurement using a strain gage force balance system. The test nozzles are structurally isolated from the upstream (grounded) portion of the balance system by a thin elastic membrane. The force on the model assembly downstream of the seal is transmitted via the balance strain gage elements to a digital readout system. Calibration of the force balance and seal is described in Section B.6 of Appendix B.

The test data consist of measurements of airflow rate, balance force, nozzle surface static pressures, model total pressure, ambient pressure, meter total temperature, and inlet pressures necessary to calculate the stream

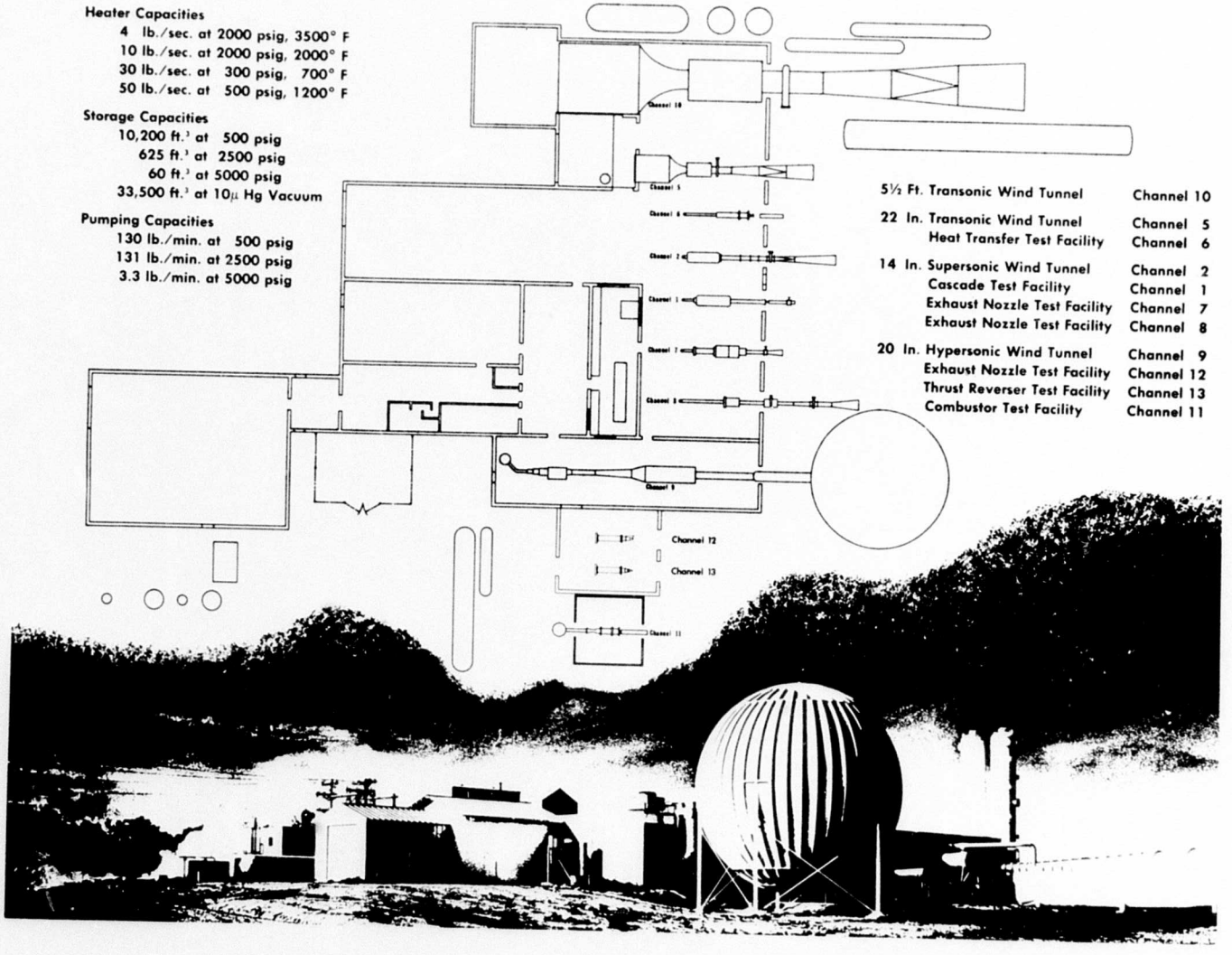

Figure 577. FluiDyne Engineering Corporation's Aerodynamic Facilities.

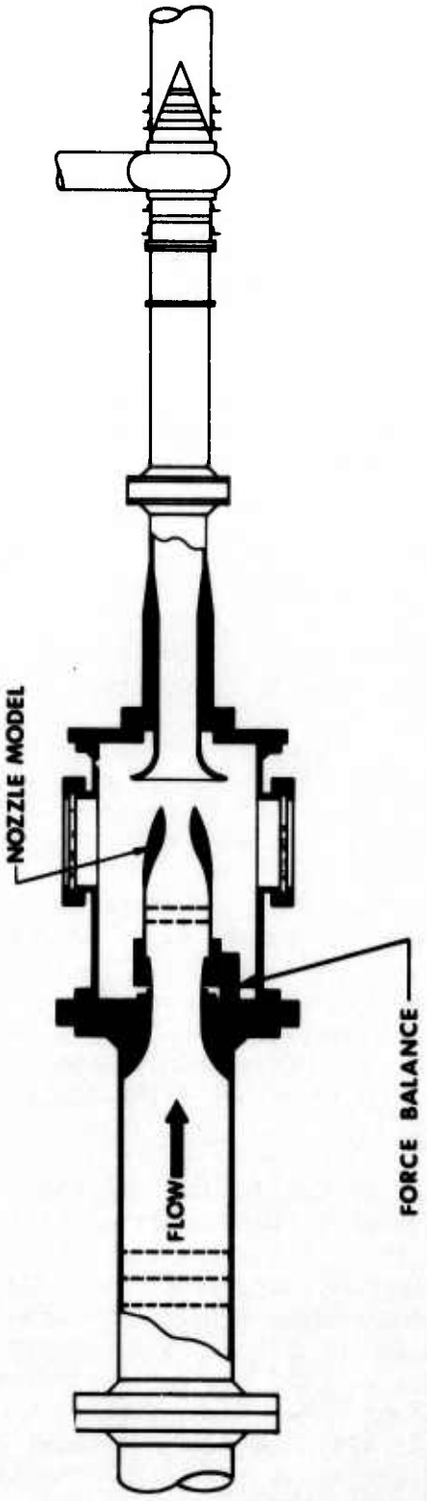

Figure 578. Static Nozzle Test Facilities (Channels 7, 12, and 13).

thrust entering the metric (floating) portion of the model assembly. Pressures are measured with mercury and water manometer banks and bourdon-tube gages, and recorded on Polaroid camera film. Temperatures are measured with iron/constant thermocouples and recorded on chart recorders.

Wind Tunnel Facilities

FluiDyne's Channel 10 Transonic Wind Tunnel facility was used for installed performance tests. A typical installation of an exhaust nozzle in this tunnel is illustrated in Figure 579.

Channel 10 is a transonic wind tunnel having a 66 × 66-inch, slotted-wall test section. It has the capability for achieving an external flow Mach number of 0 to 4.5. This facility is an induction-type tunnel in which atmospheric air is drawn through the test section using air ejectors to reduce downstream pressure. The required Mach number in the test section is obtained by controlling the mass flow to the ejectors. Water condensation in the test section is avoided by burning propane upstream of the inlet.

Static nozzle tests (M=0) are conducted in the tunnel with the ejectors off and with a windscreen to shield the model from local induced flow effects.

The metric break of the model is located some 35 inches downstream of the start of the test section. Suction is used to reduce the boundary layer thickness on the model support tube at an axial position 13 inches downstream of the metric break to approximately 0.6 inch at a Mach number of 0.36.

The test nozzles are mounted on an 8-inch-diameter sting in the tunnel. The model support sting extends from the tunnel inlet to the test section and consists of two concentric pipes. The model air is supplied from a 2500 psi reservoir through the inner pipe; the boundary layer suction is applied through the outer pipe. Thinning of the boundary layer on the support tube is achieved by using the facility vacuum system (35,000 ft^3 sphere) to remove the low energy air adjacent to the tube through a perforated section upstream of the test model.

The thrust-minus-drag data of the exhaust nozzles are determined from a direct force and flow-measuring system located upstream of the test configuration. The internal geometry of the model showing the details of the force-and-flow-measuring section is shown in Figure 580. Nozzle weight flow is determined using a choked ASME, long-radius metering nozzle located in the sting. Since the metering nozzle is choked, it is necessary to measure only total pressure and temperature. Total pressure upstream of the ASME nozzle, P_{t1}, is measured using a four-tube, area-weighted rake. Total temperature, T_{t1}, is measured using two shielded iron-constant thermocouples and a Bristol chart recorder. To determine the actual weight flow of the test nozzle, a meter discharge coefficient is calculated as a function of the meter throat Reynold's number from a semiempirical equation. Real gas effects are accounted for in the weight flow calculation through the critical flow factor (Ref. 56).

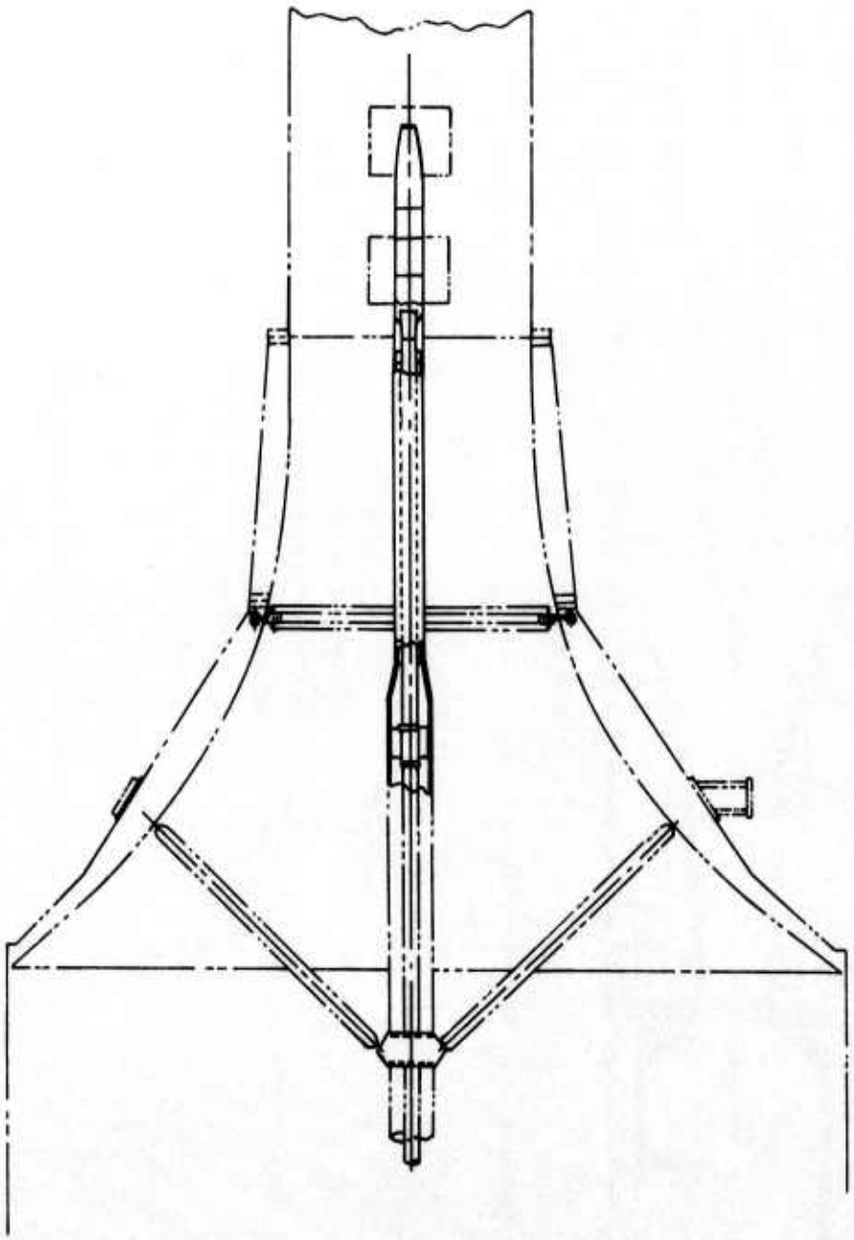

Figure 579. Model Installation in Channel 10 Transonic Tunnel.

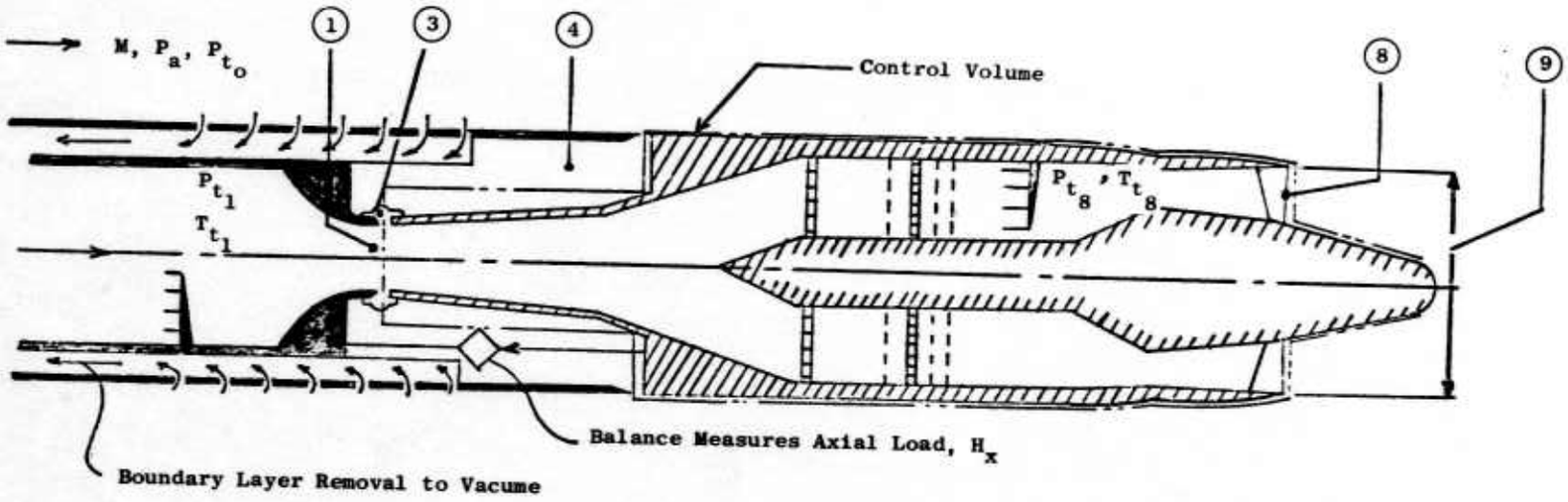

Station	Description
1	ASME Metering Nozzle Throat
3	Flexiable Seal Cavity
4	Balance Cover Sleeve Cavity
8	Nozzle Throat
9	Nozzle Exit

Figure 580. Station Notations.

The metric part of the model is cantilevered directly from the diverging section of the ASME flow-metering nozzle. Two strain gage elements are used to measure the force between the metric nozzle and the ground sting. A flexible seal at the throat of the ASME nozzle is used to separate the metric and grounded sections. The actual thrust-minus-drag of the test nozzle is then determined from the momentum entering the ASME metering nozzle, a balance force obtained from the two strain gage links, and the control volume pressure-area terms. When testing with external flow, the thrust-minus-drag of the test nozzle, as calculated above, is modified to exclude the friction drag on the cylindrical surface from the metric break to the beginning of the test nozzle (approximately 1.3 model diameters). The friction drag on the cylindrical surface is estimated using standard methods.

The nozzle airflow passes through a series of choke plates and screens to provide uniform flow at Station 8. The nozzle total pressure at Station 8, P_{t8}, is determined by using two four-tube, area-weighted rakes. Nozzle total temperature, T_{t8}, is calculated by subtracting the temperature drop due to Joule-Thomson throttling of the flow between Stations 1 and 8. This temperature drop is calculated from a curve fit of tabulated properties of air from Reference 57. The internal and external pressures are measured with bourdon-tube gages and mercury and water manometer banks and recorded on Polaroid camera film.

A.7 NASA-LEWIS 8- × 6-FOOT SUPERSONIC WIND TUNNEL

A.7.1 Introduction

The NASA-Lewis 8 × 6-foot Supersonic Wind Tunnel is capable of attaining test section flow in a Mach number range from 0.36 to 2.0. The change in Mach number is continuous up to 1.3 and in increments of 0.1 between 1.3 and 2.0. The tunnel may be operated in either of two modes: aerodynamic cycle or propulsion cycle.

During the aerodynamic cycle the tunnel is operated as a closed system with dry air added only as required to maintain the desired tunnel conditions. This cycle is used primarily for aerodynamic flow studies where contaminants are not introduced into the airstream. Figure 581 illustrates the airflow path of the aerodynamic cycle.

A.7.2 Facility Description

Major components of the Lewis 8 × 6-foot Supersonic Wind Tunnel are illustrated in Figure 582. These components are an air dryer, a compressor, a flexible-wall nozzle, a test section, an acoustic muffler, and a cooler.

Operating characteristics of the tunnel for both the aerodynamic and propulsion cycles are given in Figure 583, which shows the test section total temperature, total pressure, static pressure, dynamic pressure, altitude,

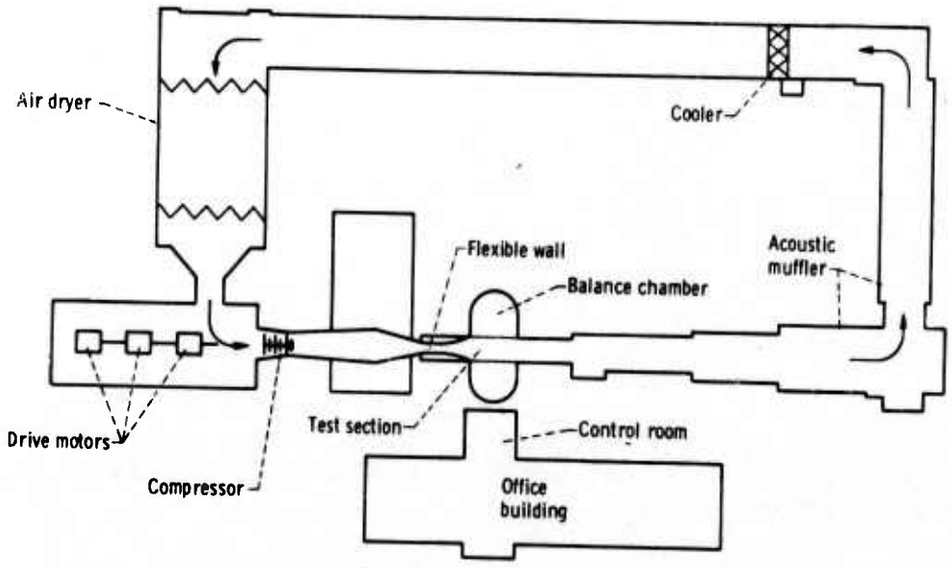

Figure 581. NASA-Lewis 6 x 8-foot Supersonic Wind Tunnel Aerodynamic Cycle.

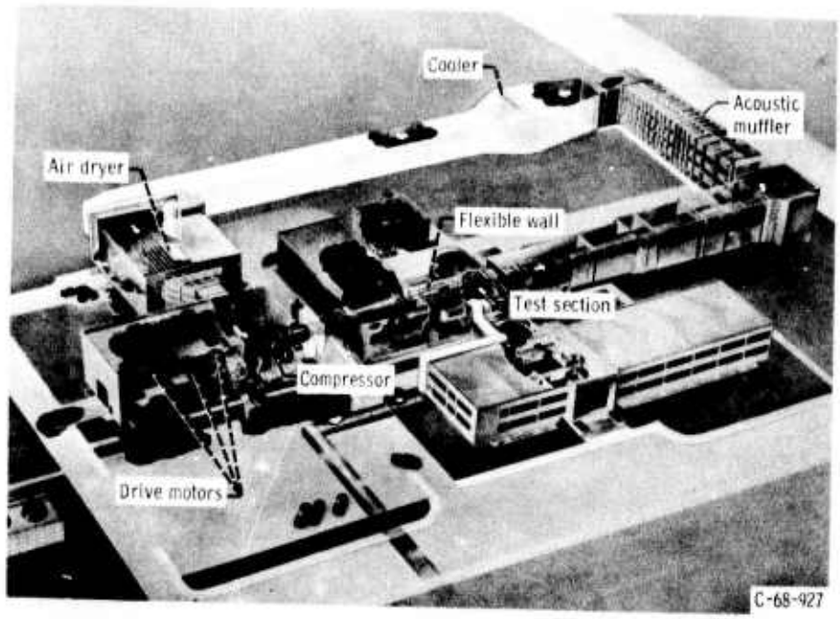

Figure 582. Wind Tunnel Components.

(a) Supersonic Wind Tunnel Total Temperature. Average Temperature Day.

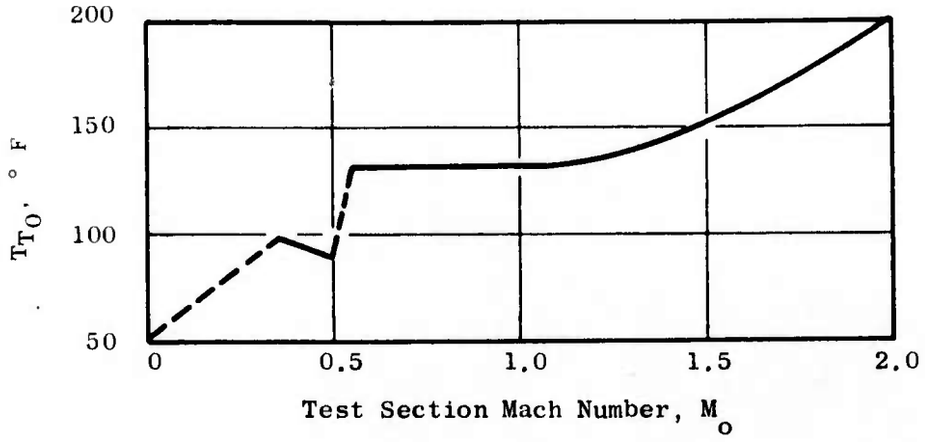

(b) Supersonic Wind Tunnel Total Pressure.

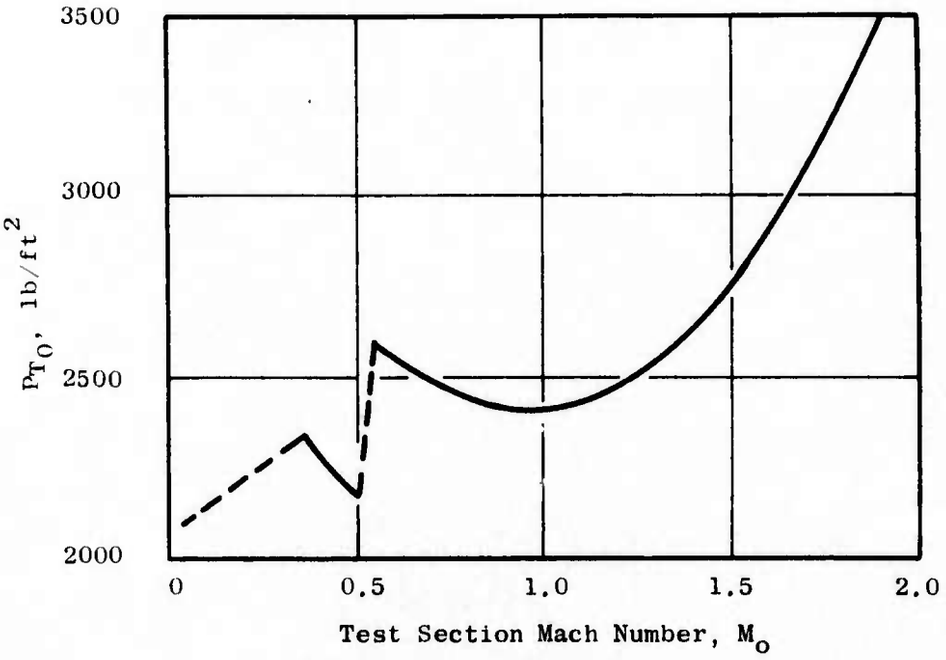

Figure 583. Operating Characteristics of the NASA-Lewis 6 x 8-foot Supersonic Wind Tunnel.

(c) Supersonic Wind Tunnel Static Pressure.

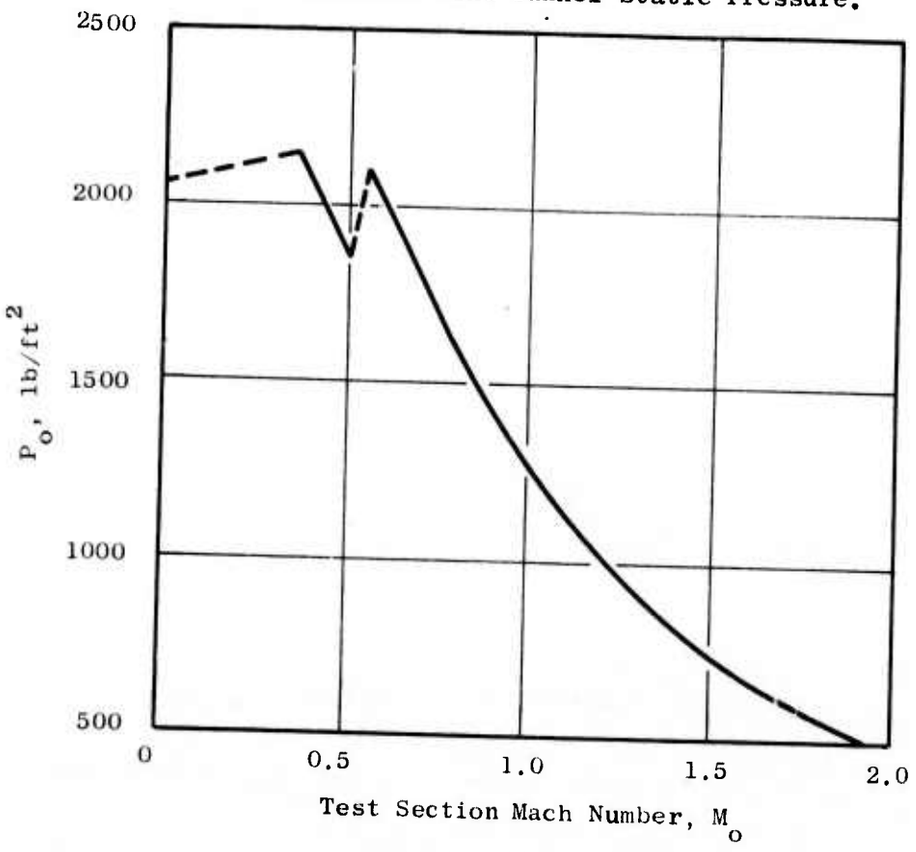

(d) Supersonic Wind Tunnel Dynamic Pressure.

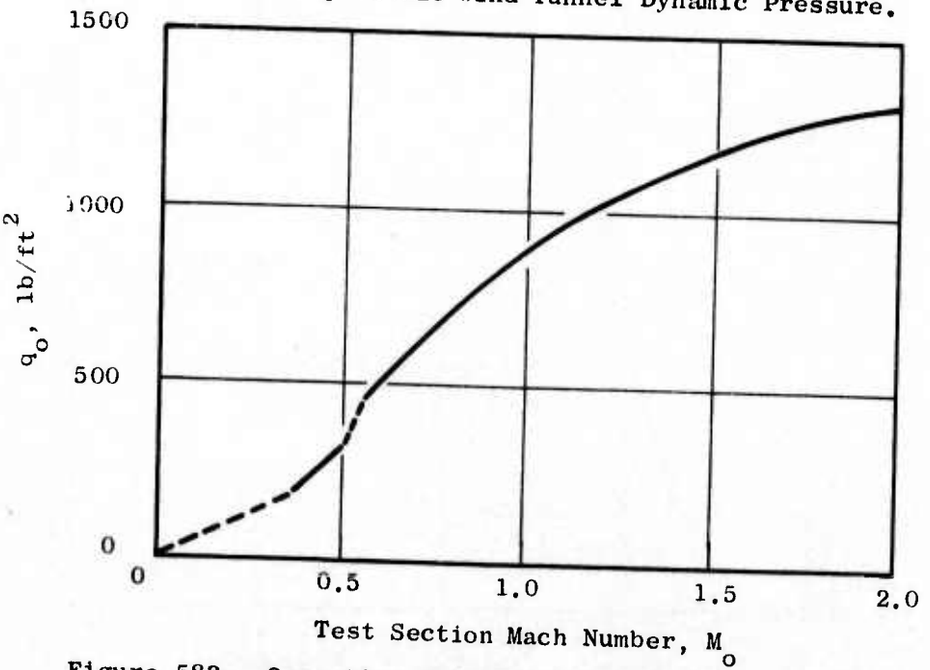

Figure 583. Operating Characteristics of the NASA-Lewis 6 x 8-foot Supersonic Wind Tunnel (Continued).

(e) Supersonic Wind Tunnel Altitude

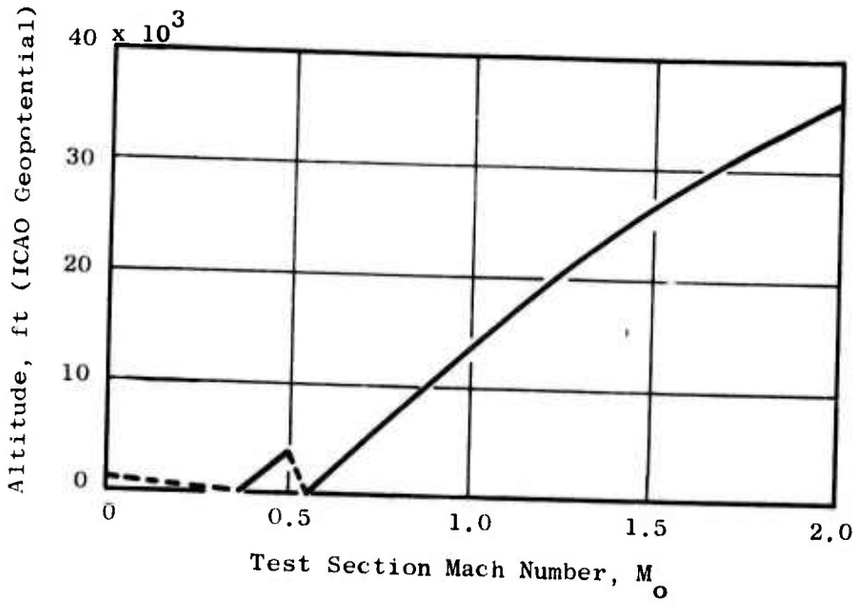

(f) Supersonic Wind Tunnel Reynolds Number.

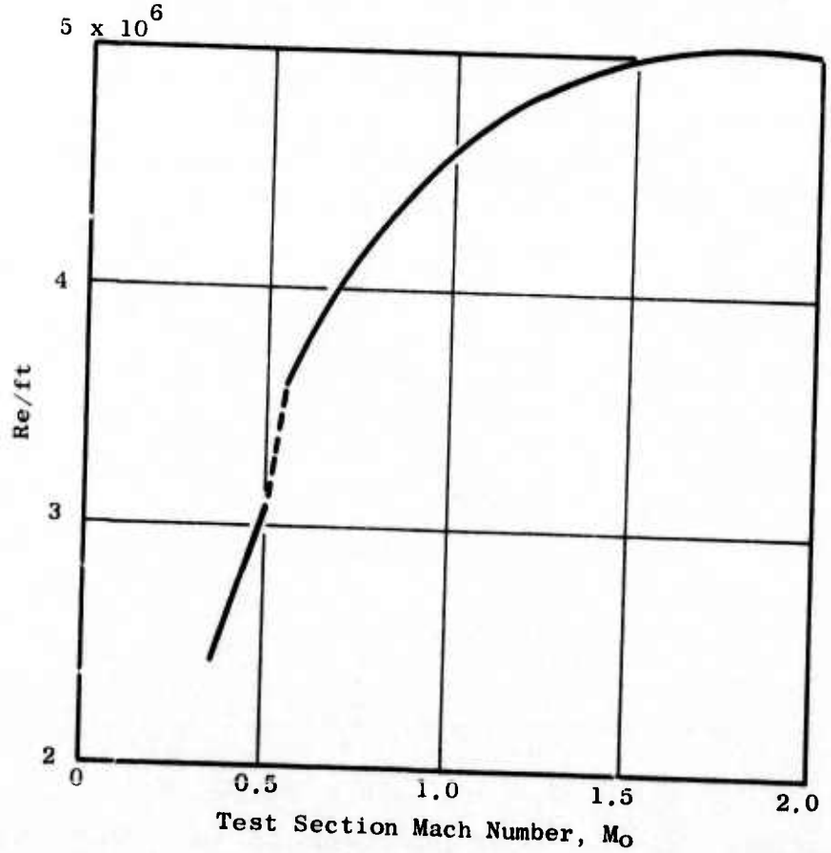

Figure 583. Operating Characteristics of the NASA-Lewis 6 x 8-foot Supersonic Wind Tunnel (Continued).

(g) Supersonic Wind Tunnel Mass Flow.

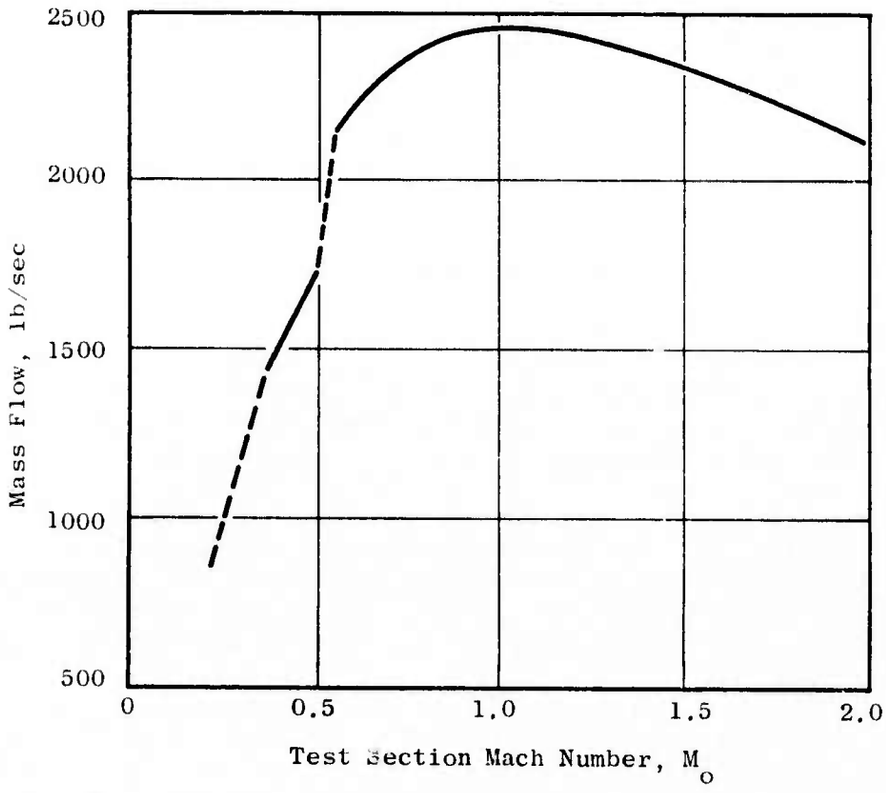

Figure 583. Operating Characteristics of the NASA-Lewis 6 x 8-foot Supersonic Wind Tunnel (Concluded).

Reynolds number, and mass flow versus the test section Mach number over the tunnel operating range. The discontinuity between Mach 0.50 and 0.55 is caused by varying compressor speeds to avoid overpressurization of the balance chamber surrounding the test section.

The test section is 8 feet high and 6 feet wide with parallel side walls for a total length of 23 feet 6 inches. For 2 feet 3 inches downstream of the test section, the side walls diverge to 6 feet 4 inches to compensate for the blockage of the transonic strut. The top and bottom plates are parallel to each other. The walls and top and bottom plates are made of 1.00-inch-thick stainless steel.

The test section is perforated on four sides. Perforations start 9 feet 1 inches from the upstream end of the test section and extend 14 feet 5 inches downstream. These perforations provide approximately 6 percent porosity; however, this can be reduced and varied along the length of the test section by selective use of inserts in the 1.0-inch-diameter perforations.

Models are installed through an access door in the bottom of the tunnel diffuser downstream of the test section. The opening is 16 feet long and 6 feet wide. Two 2-ton overhead cranes are provided in the ceiling of the diffuser section. Models, on special dollies, are lifted into the diffuser section and rolled to the test section for installation.

The top and bottom plates of the test section are removable for installation of small model supports and auxiliary apparatus. The opening may vary up to 10 feet long by 12 inches wide depending upon the selection of insert plates and location in the test section. The tunnel insert plates cannot be altered, therefore new inserts are required if modifications are necessary.

Typical model installations in the wind-tunnel employ single strut mountings (0° or 30° swept struts) as shown in Figure 584. The model suppressors for the performance tests were approximately 8 inches in diameter. Transition sections are used to adapt the model nozzles to the facility.

The thrust-minus-drag data are determined with the direct force-and flow-measuring systems, which are located just downstream of the transition sections. The force-and-flow measuring systems consisted of the same FluiDyne hardware as the systems used in FluiDyne's Channel 10, which was described in Section A.6.

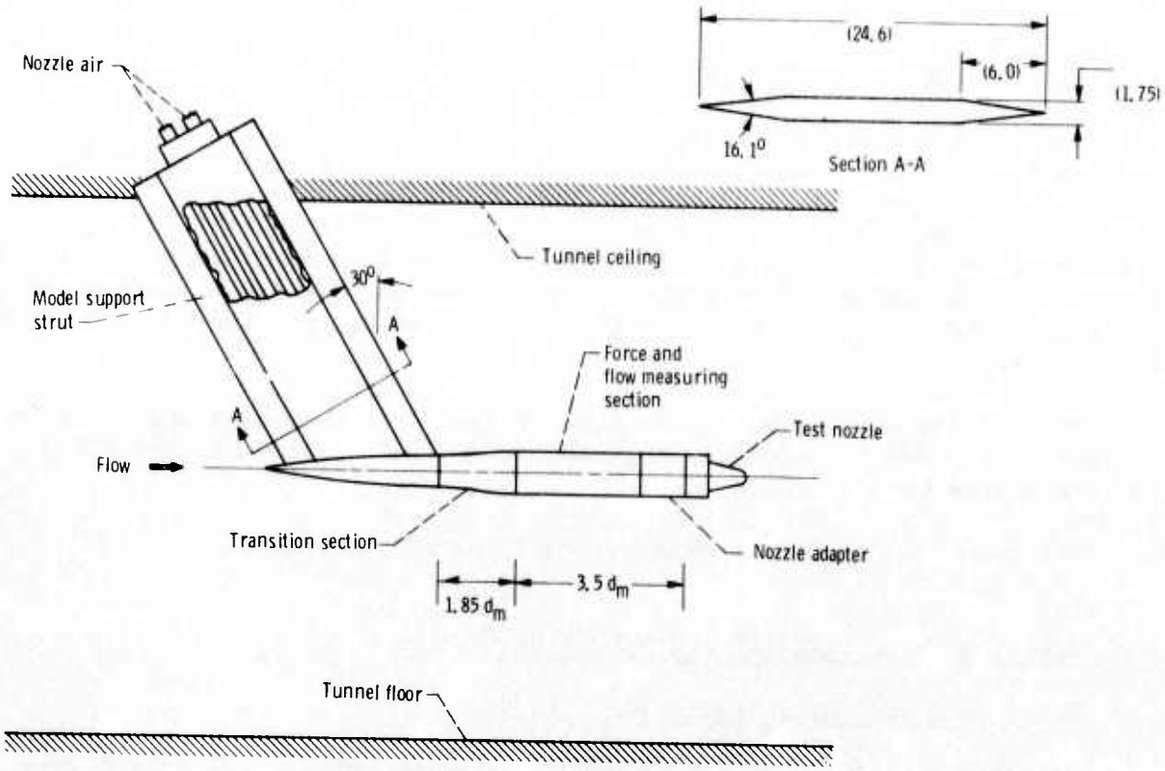

Figure 584. Model Installed in 6 X 8-foot Supersonic Wind Tunnel.

APPENDIX B

DATA ACQUISITION AND REDUCTION METHODS

B.1 FACILITY DATA ACQUISITION AND REDUCTION SUMMARY

The acoustic and aerodynamic performance data acquisition and reduction systems for the test facilities described in Appendix A are summarized in the following sections of this appendix. The JENOTS acoustic data systems are described in Section B.2. The Peebles facility acoustic data reduction systems are described in Section B.3. Separate data acquisition and reduction systems for the turbomachinery tests with the J85 engine and the jet noise suppression tests with the J79 engine are described in Section B.4 for the Edwards Flight Test Center.

Aerodynamic performance reduction and analysis procedures are described in Section B.5 for the FluiDyne Engineering Facilities, and for the NASA-Lewis 6 x 8 ft wind-tunnel.

The laser velocimeter system is described in Section B.6.

B.2 JENOTS DATA ACQUISITION AND REDUCTION SYSTEMS

B.2.1 Acoustic Data Acquisition System

The data collection system at JENOTS is shown schematically in Figure 585. It is composed of a Bruel and Kjaer (B&K) microphone/cathode follower powered and conditioned by a B&K 2801 power supply followed by three feet of line to a specially designed 10 dB fixed-gain preamplifier which drives 150 feet of cable terminating at the variable gain differential input amplifiers to the Sangamo Saber IV tape recorder. The signal is recorded on tape for future playback in the data reduction room.

The most commonly used microphones are the B&K 4135 (1/4 inch) and the B&K 4133 (1/2 inch) free-field microphones. The cathode follower used most often is the B&K 2615 preamplifier, although B&K 2619's are also used. The B&K 2801 power supply is operated in the direct output mode to avoid sensitivity loss. The frequency response of the various preamplifiers is not influenced by the power supply when used in this position.

The amplifier at the tape recorder was designed by GE and built by Random Electronics. It has a variable gain from -10 dB to +60 dB. The amplifier delivers a 4-volt, peak-to-peak signal to the tape recorder electronics at the normal calibration signal level. This setting will allow 6 dB over range without distortion. The amplifiers are flat within 5% from 5 Hz to 100 Hz. Each amplifier has an adjustable vernier attenuator which can give any desired measure of attenuation between 0 and 10 dB. During test calibration this vernier is usually adjusted to make the 124 dB piston phone calibra-

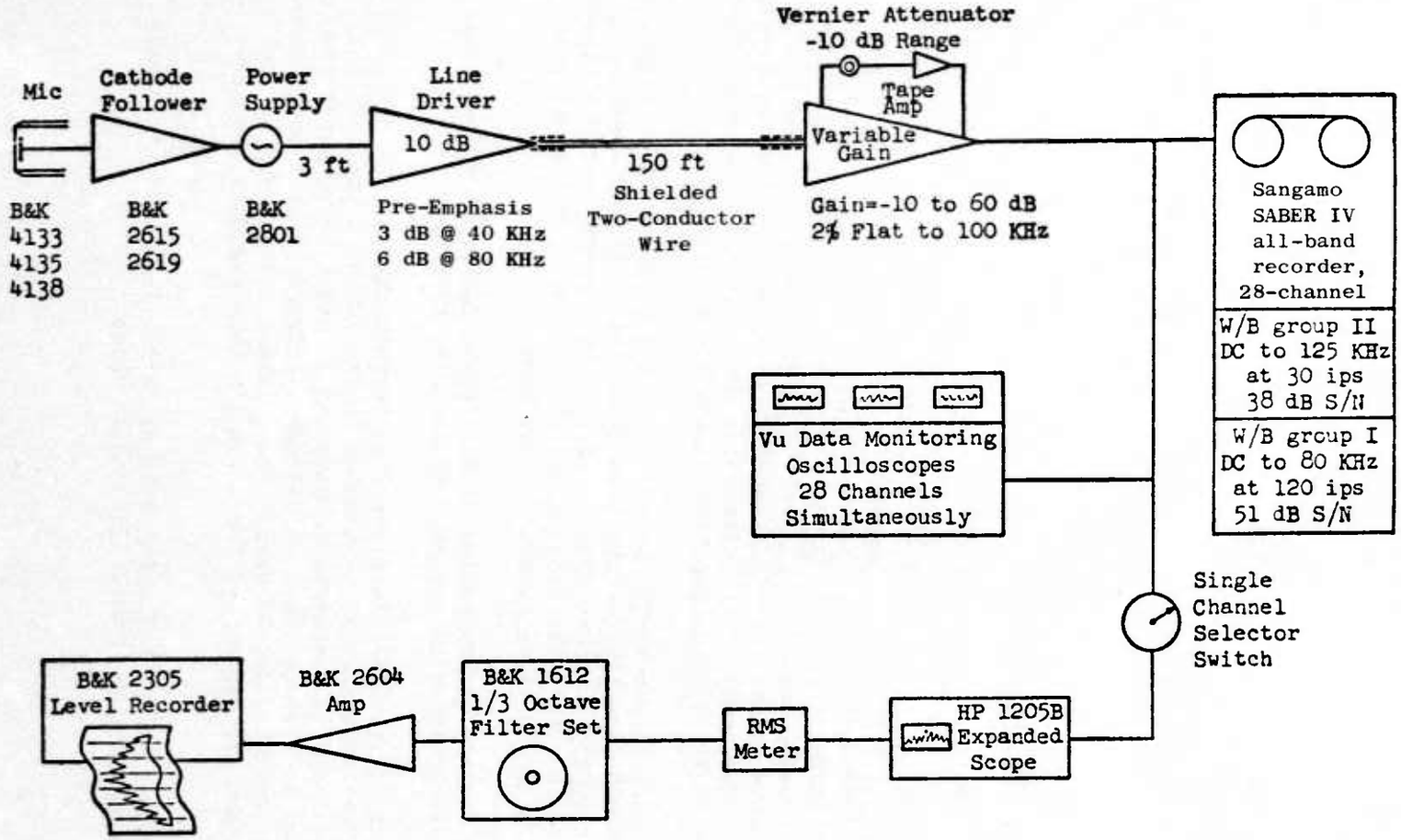

Figure 585. JENOTS Data Acquisition System.

tion signal the full-scale (1.4 Vrms) input to the tape recorder. The 10-dB steps in the tape recorder amplifier then directly correspond to 10-dB steps in OASPL from 124 dB. The output of each amplifier channel has a Vu-Data monitoring oscilloscope for continual inspection of all signals for any clipping or deterioration of the signal due to excessive crest factor (Peak Value/RMS).

The Sangamo Sabre IV, 4930 magnetic tape recorder/reproducer has IRIG wideband, RM wideband Group I and Group II capability. In normal JENOTS operation all data are recorded on one-inch magnetic tape in Wideband Group II at 30 ips, having a flat frequency response in excess of 100 KHz when used in conjunction with the B&K 4135 microphone. The voice channel is recorded direct.

B.2.2 Acoustic Calibration Technique

To ascertain that valid acoustic data were obtained from each acoustic test, rigid procedures are followed for equipment calibration prior to test. The calibration of all microphones is checked periodically using an acoustic calibration system built by General Electric and available at the Evendale facilities. All microphones whose voltage outputs deviate more than ± 1 dB, as compared to manufacturer specifications during field/laboratory calibration procedures, are not used until a recalibration is done using this facility and until new absolute sensitivity and frequency response characteristic values are assigned, where applicable. Any microphone output deviating by more than ± 2 dB is returned to the manufacturer for repair and recalibration.

The acoustic calibration system provides for the calibration of 1-inch, 1/2-inch, and 1/4-inch capacitance-type microphones to establish absolute sensitivity and frequency response characteristics by electrostatic and free-field comparison techniques. Traceability of calibration to NBS is by means of the piston phone and a 1-inch standard microphone.

Capabilities for the determination of microphone cartridge open circuit sensitivity and cathode follower attenuation are also provided.

In addition to the periodic laboratory microphone checks, the entire acoustic data acquisition system is calibrated in the field in the following manner. The overall system frequency response is obtained by removing the microphone head and applying a constant voltage oscillator signal at the center frequency of each one-third octave band. The response corrections in each one-third octave band are determined for inclusion into the data reduction program.

Immediately prior to and following each day's testing, each microphone system is calibrated using the Model 4220 piston phone.

B.2.3 Facility Data Acquisition System

All of the facility data and additional pressure and temperatures for various test model instrumentation requirements are recorded on a digital data acquisition system.

A total of 125 pressure lines, 96 CA T/C circuits, and 21 IR T/C circuits are available for use with the digital system.

One hundred pressure lines out of the 125 connect to a bank of 8 scanner valves containing 25 psia transducers. Each scanner valve can measure eleven pressures per transducer for a total of 88 pressures in the 0 - 25 psia range. Twenty-five pressure lines are routed to a cabinet containing five individual tranducers that handle pressures (0, 50, 100, and 500 psia) but can be changed to meet specific requirements. The 8 scanners are used for measuring model pressures, while the individual transducers measure facility airflow data.

The CA T/C's are used to measure main airflow temperature and various skin temperatures on the models. The IR T/C's are used to measure flame tunnel temperature. These signals are then fed into an automatic switching unit in an ordered manner and conducted through digital amplifiers to a digital printer and a digital punch.

B.2.4 Acoustic Data Reduction

On-line data reduction and monitoring capability is available in the JENOTS control room. As shown in Figure 585, a single-channel selector switch can route any microphone signal parallel to the tape recorder for expanded waveform presentation on a HP1205 B oscilloscope. Overall sound level of the selected channel can be read out on a calibrated RMS meter. The signal can then be passed through a B&K 1612 band pass filter set, amplified by a B&K 2604 amplifier, and recorded on a B&K 2305 level recorder. The filter set can be dialed to 1/3 octave frequencies from 12.5 Hz to 40 KHz, octave frequencies from 16 Hz to 31.5 KHz, linear, "A", "B" and "C" weighted networks from 20 Hz to 45 KHz.

Standard data reduction is conducted in the General Electric AEG Instrumentation and Data Room (IDR). As shown in Figure 586, the data tapes are played back on CEC3700B tape deck with electronics capable of reproducing signal characteristics within the specifications indicated for Wideband Group I and Group II.

All 1/3 octave analysis is performed on a General Radio 1921 1/3 octave analyzer. Normal integration time is set for 32 seconds to ensure good interaction for the frequency content. Each data channel is passed through an interface to the GEPAC 30 computer where the data are corrected for the frequency response of the microphone and the data acquisition system corrected to Standard day (59° F, 70% RH) atmospheric attenuation conditions per SAE ARP866 Standards, and processed to calculate the perceived noise level and OASPL from the spectra. For calculation of acoustic power, corrections for ground

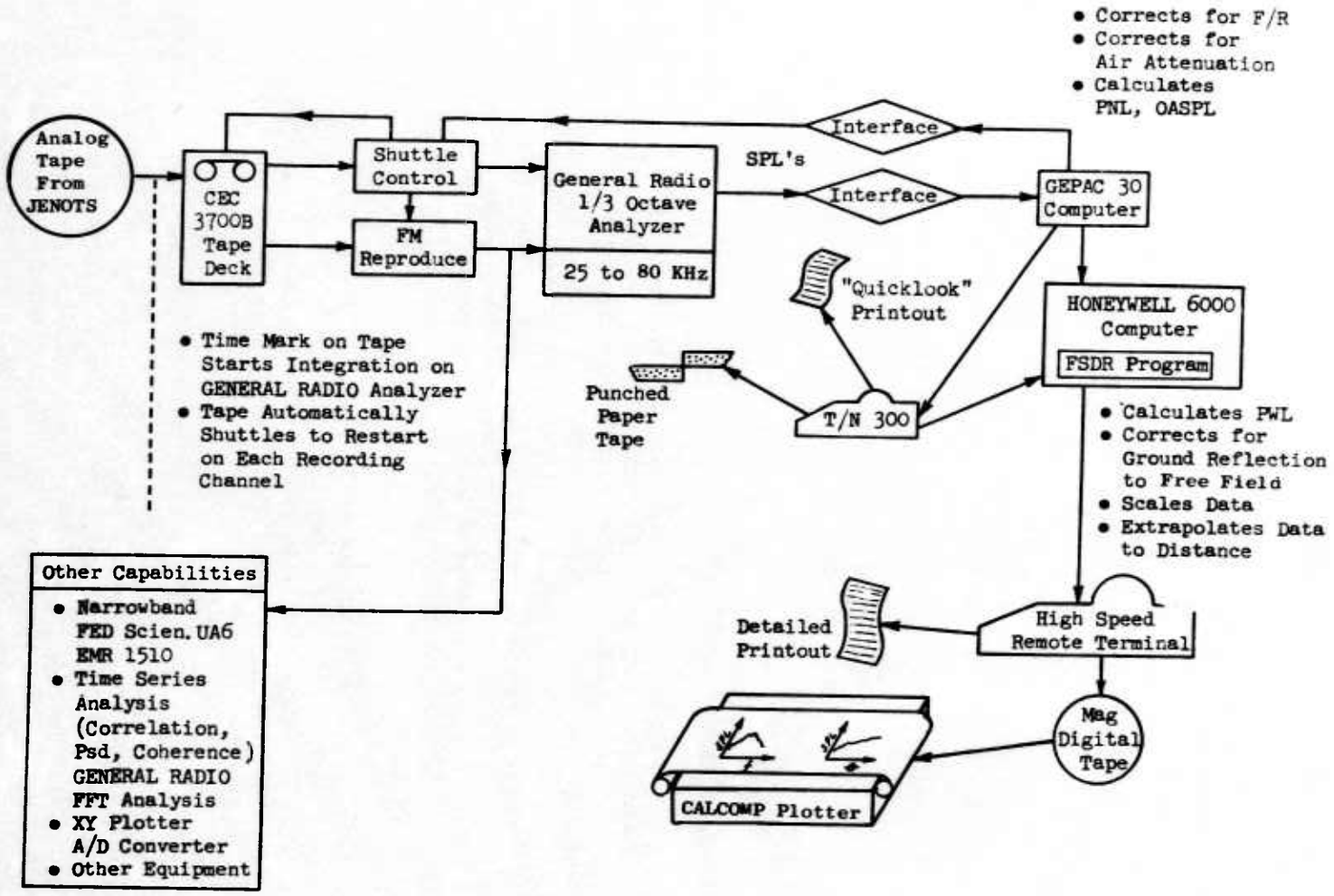

Figure 586. Data Reduction System, JENOTS.

reflections to the free field, scaling to other nozzle sizes, or extrapolations to different far-field distances, the data are sent to the Honeywell 6000 computer for data processing.

Other data reduction techniques are available in IDR. Constant narrow-band spectra can be reduced on the Federal Scientific UA6 or the EMR (Schlumberger) 1510 analyzer. Complex Time Series analysis such as cross correlation cross PSD, coherence functions on probability density can be processed through the (General Radio) Time Data System (computer based system incorporating analysis techniques in both the time & frequency domain).

Many other capabilities such as tracking filters and high speed "Fiber Optics" are also available.

B.2.5 Acoustic Data Scaling Technique

Continuous frequency data through 80 KHz were recorded using the 40-foot hemispherical arc microphones at the 15.93 foot height at each 10° incremental position from 20° through 160° from the inlet axis. Far-field arc acoustic measurements were reduced in 1/3-octave-band form, corrected to standard day conditions of 59° F, 70% relative humidity, and scaled to full engine size using a scale factor of 8:1 (40-foot model arc = 320 ft engine arc, and model 400 Hz thru 80 KHz = engine 50 Hz thru 10 KHz).

The basis on which the model acoustic data were scaled to engine size came from consideration of constant Strouhal number at a given jet velocity. the full-scale engine frequency, f_e, was related to the measured model frequency, f_m, by the following:

$$f_e \times D8_e = f_m \times D8_m$$

where $D8_m$ is the equivalent physical exit diameter of the model, and $D8_e$ is the equivalent physical exit diameter of the engine. The above relationship assigns the engine jet velocity as that of the model. The scale factor for nozzle diameter, measuring arc, and frequency range thus was defined as the ratio of the engine equivalent physical exit diameter to the model equivalent physical exit diameter and was set at 8:1 for nearly all JENOTS model tests.

Data were presented as model frequency on the 40-foot arc and as scaled frequencies on the 320-foot arc. Extrapolations were done to 300, 1500, and 2128-foot sideline distances using 59° F, 70% relative humidity air absorption and without EGA.

All data were corrected for calibration level response and for system frequency response of the record/playback system through the entire frequency range.

B.3 CORPORATE RESEARCH AND DEVELOPMENT CENTER

B.3.1 Data Acquisition and Reduction System

Data acquisition is controlled by a HP 2100 series mini-computer that obtains the acoustic signals from a GR 1921 real-time 1/3-octave-band analyzer and samples the temperatures and pressure signals. By the use of a scanning multichannel amplifier, GR 1566, each microphone signal is sequentially analyzed; the signal level of each 1/3 octave band (100 Hz to either 40 KHz or 80 KHz depending on the type microphone utilized) is stored on magnetic tape. For operational monitoring, a three-dimensional plot of SPL, 1/3 octave frequency, and acoustic angle from each microphone is displayed on an oscilloscope as the microphone array is sampled. For backup and when longer averaging times are necessary, the acoustic signals are recorded simultaneously on a Sangamo Sabre IV, wide band, Group II tape recorder. After all the signals have been accumulated, the computer corrects the data for nonuniform response of the microphone cartridge. Using these corrected values of the sound pressure levels for each microphone, the 1/3-octave-band acoustic power levels and the overall acoustic power level are computed. The raw and calculated data are then stored on magnetic tape.

While the computer is processing the acoustic data, simultaneous measurement and calculation of all the pertinent parameters for determination of the nozzle exit conditions and ambient conditions are also carried out and recorded on magnetic tape. As all the pertinent data exist on one magnetic tape, the acoustic information is readily normalized immediately following the test on the mini-computer.

B.4 PEEBLES DATA ACQUISITION AND REDUCTION METHODS

Standard acoustic data reduction is conducted in the General Electric AEG Instrumentation and Data Room (IDR). As shown in Figure 587, the data tapes are played back on a CEC3700B tape deck with electronics capable of reproducing signal characteristics within the specifications indicated for Wideband Group I and Group II. An automatic shuttling control is incorporated in the system. In normal operation a tone is inserted on the recorder and the time slot designed for data analysis. Tape control automatically shuttles the tape initiating an integration start signal to the analyzer at the tone as the tape moves in its forward motion. This motion continues until an integration complete is received from the analyzer, at which time the tape direction is reversed and, at the tone, the tape restarts in the forward direction advancing the channel to be analyzed until all the channels have been processed. A time code generator is also utilized to signal tape position of the readings as directed by the computer program control. After each total reading is completed, the number of tape channels at each point is advanced to the next reading.

All 1/3-octave analysis is performed on a General Radio 1921 1/3-octave analyzer. Normal integration time is set for 32 seconds to ensure good interaction for the low frequency content. The analyzer has a 1/3-octave filter

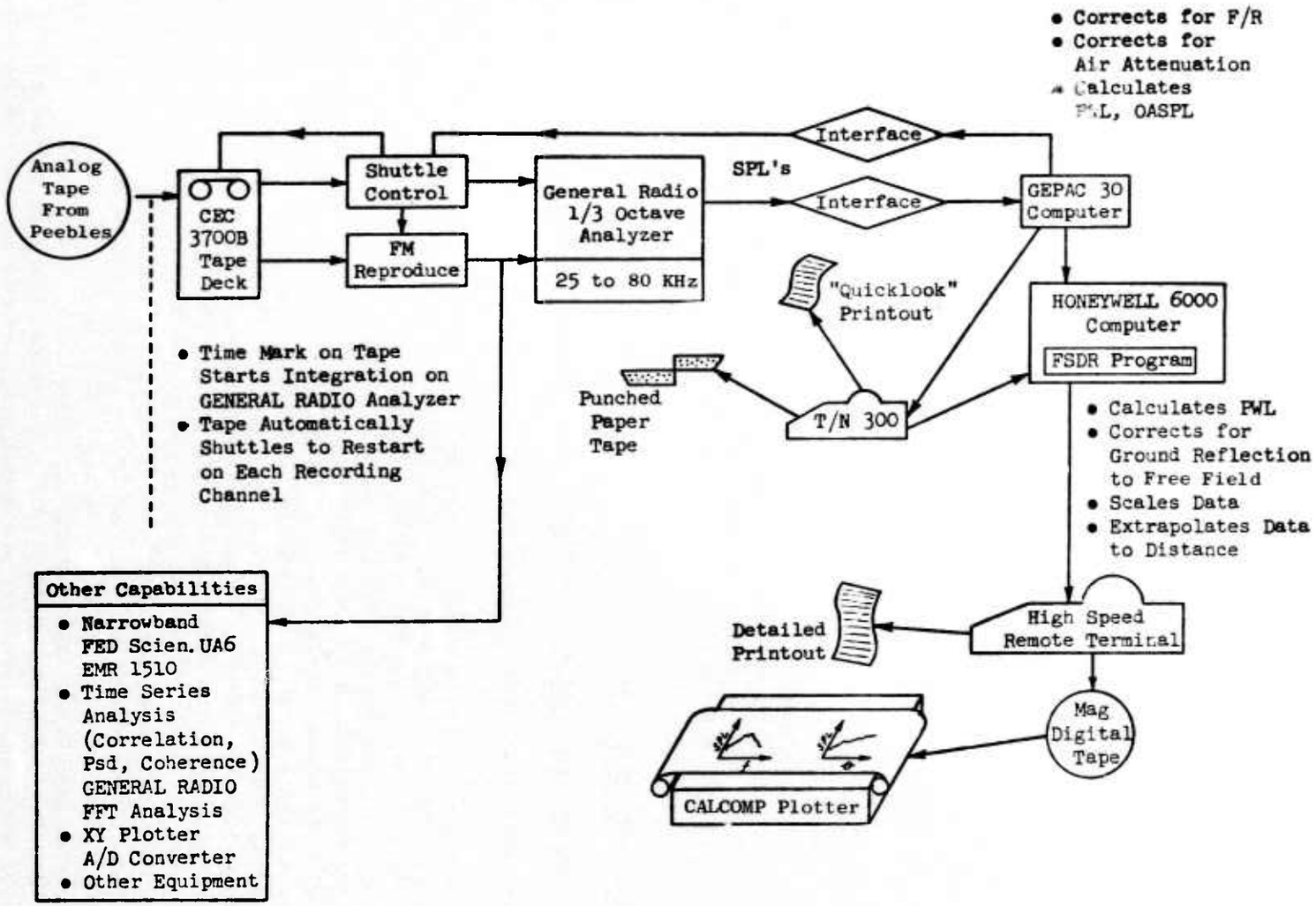

Figure 587. Data Reduction System, Peebles.

set for 12.5 Hz to 100 Hz and has a rated accuracy of ± 1/4 dB in each band. Each data channel is passed through an interface to the GFPAC 30 computer where the data are corrected for the frequency response of the microphone and the data acquisition system; corrected to Standard day (59° F, 70% RH) atmospheric attenuation conditions per SAE ARP866 Standards (Reference 583), and processed to calculate the perceived noise level and OASPL from the spectra. The output of the computer is passed to a Terminet 300 console where the corrected SPL's can be punched out on paper tape and printed out on sheets for "quick look" analysis. For calculation of acoustic power or extrapolations to different far-field distances, the data are sent to the Honeywell 6000 computer for data processing. This step can either be accomplished by storing the SPL's on punched paper tape and/or transmitting via direct time share link to the 6000 computer through a 1200 band modem. In the 6000 computer, the data are processed through the Full-Scale Data Reduction (FSDR) Program where the appropriate calculations are performed. The data printout is accomplished on a high speed "remote" terminal. A magnetic type can be written for CALCOMP plotting of the data.

Other data reduction techniques are available in IDR. Constant narrowband spectra can be reduced on the Federal Scientific UA6 or the EMR (Schlumberger) 1510 analyzer. Complex Time Series analysis such as cross correlation cross PSD, coherence functions on probability density can be processed through the (General Radio) Time Data System (computer based system incorporating analysis techniques in both the time and frequency domain).

B.5 EDWARDS FLIGHT TEST CENTER

B.5.1 Data Systems for the J79 Engine Jet Suppression Tests

Aero Data Acquisition System and Data Reduction

Aero data were obtained on the J79 engine with the three jet exhaust nozzle configurations. For all test points, sufficient aero data were collected to determine inlet airflow, ideal fully expanded isentropic jet velocity, nozzle pressure ratio, exit gas temperature and thrust. To accomplish this the instrumentation signals from the bellmouth inlet static and total pressures, the total pressures sensed on two rakes located in the extension spool piece, and wall static taps located in the extension spool piece, were fed into four transducer heads. Other pressures such as compressor discharge static pressure, etc., were hooked up to individual pressure transducers. The output of all the pressure transducers was wired into a scanivalve which could complete a full cycle scan of these individual pressures in 4.8 seconds. Thermocouples sensing temperatures in the inlet, turbine discharge, etc., were connected into a CATS block. The output of the scanivalve together with some direct instrumentation readouts (e.g., fuel flow, rpm, etc.) were fed into a PCM System (pulse code modulator) and recorded on magnetic tape via an Ampex FR-100 tape recorder operating at 30 ips. In the data reduction center the tape was played back, amplified, and via a computer decoded to count units and scaled to translate the measurements into engineering units. Next, the aero data were printed out on a 10-per-second basis for all measured parameters

and also printed using a 30-second averaging time. Selected averaged parameters were then used as input to an aero performance computer program which printed the as-measured, calculated, and corrected to standard day (59° F, 14.7 psia) parameters.

Acoustic Data Acquisition and Processing

Acoustic data acquisition for all configurations was made through the use of Bruel and Kjaer microphone systems attached to vertical poles. Two microphones per station were used on the 160-foot radius: one high microphone, called A, which was at engine centerline and a low microphone, called B, which was 2 feet above the ground. The far-field microphones were 1/2-inch Model 4133 cartridges connected to a cathode follower Model 2615. Each microphone was operated from a Microphone Power Supply Type 2801 which provided the necessary voltage to the cathode follower. The output of the microphone was fed via a signal amplifier onto the magnetic tape using an Ampex FR-100 tape recorder, operating at 60 in./sec with a carrier frequency a 108 KHz. Each signal was monitored by an oscilloscope and RMS voltmeter. A sketch of this data acquisition system is shown in Figure 588.

The frequency response of each data channel (without microphone head) was performed by inserting a Hewlet-Packard Model 8057A Pseudo-Random Pink Noise Generator signal into each cathode follower, the signal of which was preserved on tape for response determination (pink noise contains all frequencies of interest and has equal energy in each 1/3 OB).

Each day's acoustic data acquisition was started and finished with a system calibration. This was accomplished by inserting a B&K piston phone, type 2440, on each microphone head and recording its signal output on tape. Any microphone voltage output found to deviate more than ± 1.5 dB, from laboratory microphone calibration, with the piston phone applied, was replaced. All data points were recorded for a minimum of 1.5 minutes to allow enough sample length for data reduction. No acoustic data were taken above 10 mph or during gusty winds.

Acoustic Data Processing

In this section a description is given of the data reduction process, instrumentation, and the corrections applied to the tape recorded data for obtaining:

- "As-measured data," which are the recorded (raw) data corrected for the nonlinear frequency response of the data acquisition equipment.
- "Standard day data" which are the as-measured data to which humidity absorption corrections were added to obtain sound data at standard day conditions of 59° F, 70% relative humidity per SAE ARP 866.

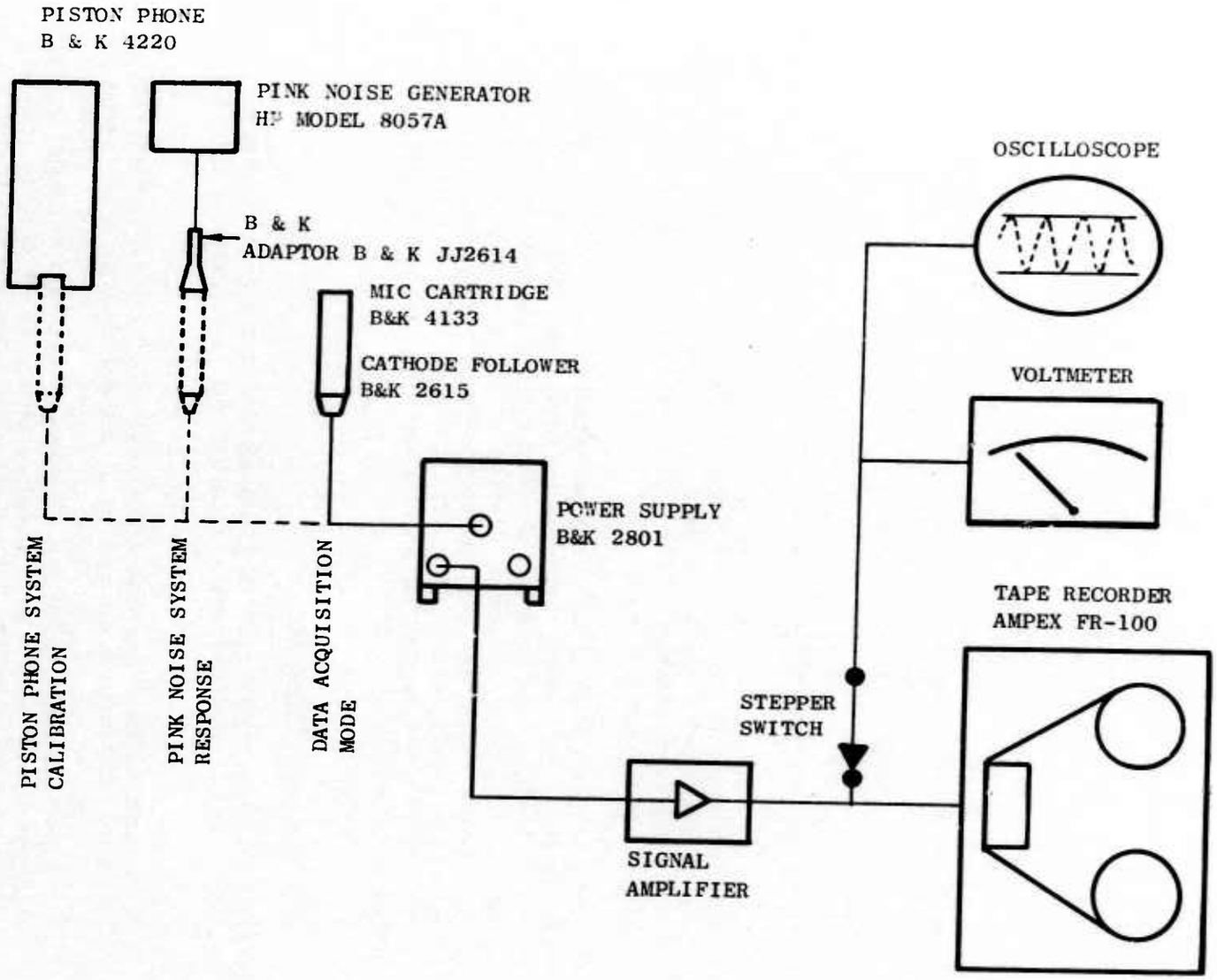

Figure 588. Sketch of Edwards Acoustic Data Acquisition Equipment.

- "Free-field data" which are the standard day corrected for test site characteristics.

In order to obtain 1/3-octave-band spectra, the data reduction started by playing back the speed tapes into a General Radio Real Time Analyzer, Model 1921. These data were sampled over a 32-second integration time. The same portion of the data tape was shuttled back and forth for all data channels (microphone stations) and analyzed by the General Radio 1/3 OB analyzer as shown in Figure 589. The output of the analyzer went into a Honeywell H-316 computer (A-D conversion) which, in turn, generated a computer formated tape (digital tape) which contained the 1/3 OB raw data. To obtain the "as-measured" data, the total frequency response system corrections of each data channel were added to the raw data. To obtain these corrections the frequency response tape recording of the pink noise was analyzed by the General Radio analyzer for each channel through the same process as the data described above (shown on the right-hand side of Figure 588, yielding pink noise response levels for each channel and 1/3 OB of interest). These were fed into the XDS computer where they were normalized to the 250 Hz band to obtain the necessary corrections. The response correction for the pink noise generator itself and the microphone cartridge response were added to provide the complete system response correction. The system correction breakdown was printed out on a hard copy and on punched cards and added together with other nonsystem correction factors to the raw data to provide the measured, standard day, and free-field sound data.

B.5.2 Edwards Data Acquisition and Reduction Method (J85 Turbine Noise Test)

For the J85 turbine noise test all 1/3-octave spectrum analysis and data processing included in this report was performed at GE/Edwards Flight Test Center, using a General Radio 1/3-octave Realtime-Analyzer, Model 1921. Data are sampled over a 32-second integration time, with all frequencies sampled simultaneously. Through the use of a tape marking system, the same portion of the data tape was sampled for all data channels. The flow diagram of the data handling sequence(s) employed for generating 1/3-octave data is indicated on Figure 58a.

All 1/3-octave-band data are corrected for 59° F/70% relative humidity standard day atmospheric absorption via SAE ARP 866 (Reference 58). Extrapolations are performed taking into account spherical divergence, atmospheric absorptions, and Extra Ground Absorption (EGA) from SAE AIR 923 (Reference 60). Perceived Noise Level (PNL) is calculated per SAE ARP 865 (1969 Revision), Reference 49.

Narrowband spectrum analysis was performed at GE/Evendale and GE/EFTC using Federal Scientific Ubiquitous Spectrum Analyzers, models UA-6A and UA-500. The frequency range was 40-20,000 Hz using a 40-Hz filter bandwidth, with 256 scans over a 12.8-second integration period. Successive spectra for each scan are summed digitally over the selected integration period and the resultant average is displayed using an X-Y Plotter.

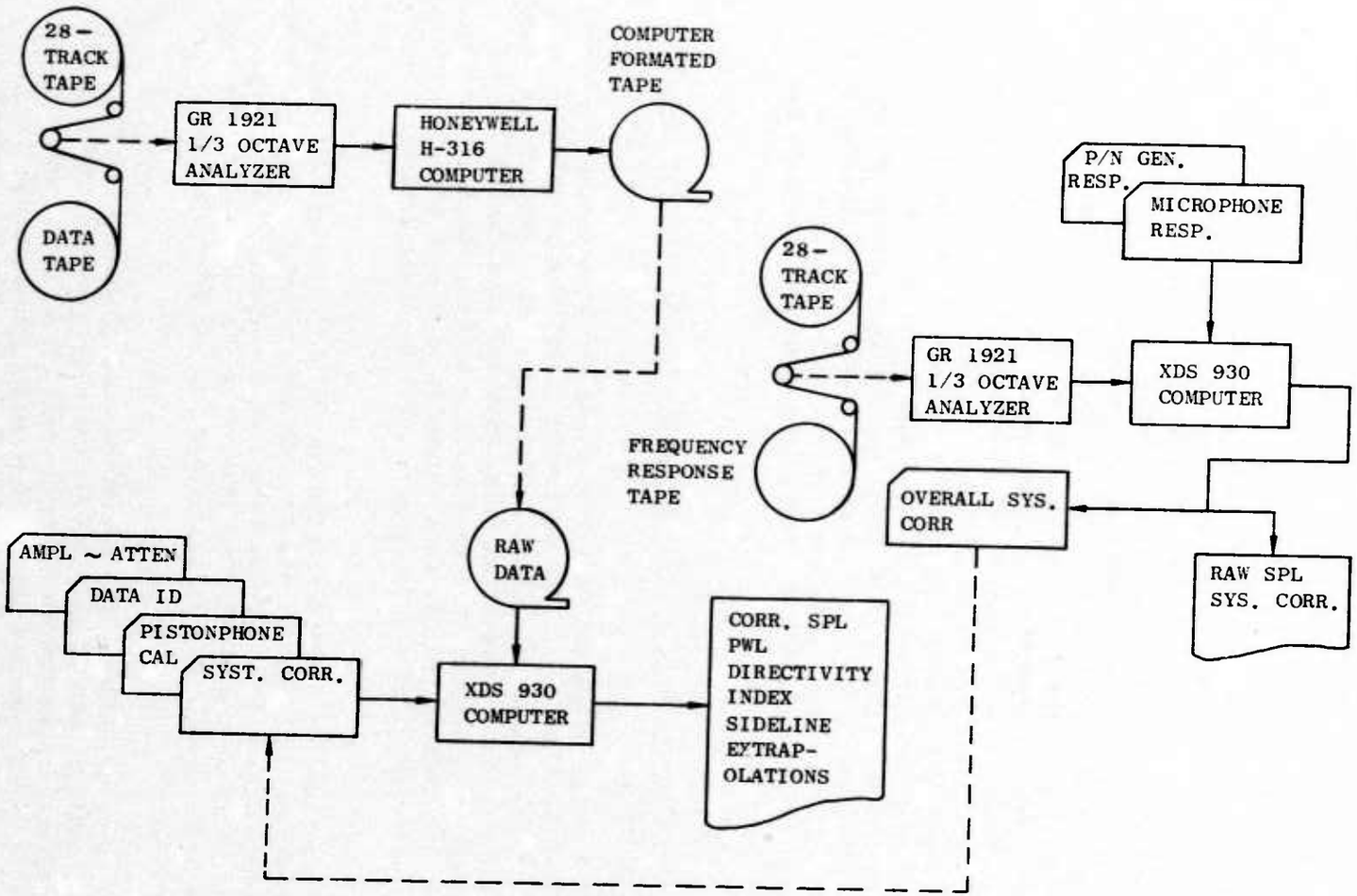

Figure 589. GE/EFTC Acoustic Data Processing System.

The aerodynamic performance measurements were utilized to calculate the weight flow, turbine inlet temperature, exit velocity, and specific fuel consumption (sfc) using standard cycle analysis equations. A pitchline analysis was performed to calculate the turbine inlet pressure by maintaining continuity and iterating on turbine exit pressure.

B.6 AERODYNAMIC TEST FACILITY DATA ACQUISITION AND REDUCTION METHODS

Aerodynamic Data Analysis Procedures

Introduction

The force- and flow-measuring systems used for this aerodynamic program were common for both the FluiDyne and NASA-Lewis test series. Therefore, the data analysis procedures presented below were the same for both facilities.

Flow Rates and Discharge Coefficient

The actual mass flow rate through the test nozzle was determined with a choked ASME long-radius metering nozzle at Station 1.

$$W_1 = \frac{K_{cr} C_{D1} A_1 P_{t1}}{\sqrt{T_{t1}}}$$

The meter discharge coefficient (C_{D1}) was calculated as a function of throat Reynolds number, using a semiempirical equation.

$$C_{D1} = 1 - 0.184 R_{N1}^{-0.2}$$

C_{D1} varied between 0.992 and 0.994 for the present tests.

The critical flow factor, K, was calculated as a function of total pressure and total temperature. The equation for K, applicable to the range of P_t and T_t normally encountered in the present test facility, was obtained from Reference 1.

$$K_{cr} = 0.53160 + (P_t + 16.9)\left[1.581 - 0.00834\ (T_t - 520)\right] \times 10^{-5}$$

P_t is in units of psia, and T_t is in ° R.

A_1, the meter geometric throat area, was 3.4636 in^2. Meter total pressure, P_{t1}, was measured with total-pressure tubes, as indicated in Figure 565 of Section A.6, Appendix A. Meter total temperature, T_{t1}, was measured using two shielded iron-constantane thermocouple probes.

The discharge coefficient of the test nozzle is defined as the ratio of actual mass flow rate through the nozzle to the ideal isentropic mass flow rate at the nozzle pressure ratio. the actual mass flow rate was determined as described above. The ideal flow rate at a particular nozzle pressure ratio ($\lambda_8 = P_{t8}/P_o$) is:

$$W_{8i} = \frac{K_{cr8}\ A_8\ P_{t8}\ (A^*/A)_8}{\sqrt{T_{t8}}}$$

A^*/A, the isentropic area ratio, is a function of λ and γ. For the present tests, A^*/A was evaluated at $\gamma = 1.4$.

$$A^*/A = 3.86393\ \lambda^{-0.71429}\sqrt{1 - \lambda^{-0.28571}} \quad \text{for} \quad \lambda \leq 1.8929;$$

$$A^*/A = 1 \quad \text{for} \quad \lambda \geq 1.8929$$

The nozzle discharge coefficient is then:

$$C_{D8} = \frac{W_1}{W_{8i}} = \frac{K_{cr1}\ C_{D1}\ A_1\ P_{t1}}{K_8\ A_8\ P_{t8}\ (A^*/A)_8}\sqrt{\frac{T_{t8}}{T_{t1}}}$$

P_{t8} was defined as the numerical average of eight equal-area-weighted probes. T_{t8} was calculated from T_{t1} by subtracting the temperature drop due to Joule-Thomson throttling between Stations 1 and 8. This temperature drop varied between 3° F and 7° F.

K_8 was evaluated using a previous equation as a function of P_{t8} and T_{t8}. The geometric throat area, A_8, was calculated from inspected dimensions.

Throat Coefficient

The net static axial thrust of an exhaust nozzle is defined as the axial exit momentum of the exhaust flow, plus the excess of exit pressure over ambient pressure times the exit area:

$$H = m\ v_e + (P_e - P_o)\ A_e$$

The net static thrust of an exhaust nozzle model was determined for the current test program by applying the momentum equation to the control volume shown in Figure 565 of Section A.6. The analysis of forces applied to the control volume includes entering stream thrust (F_1), a balance force (H_2), various pressure-area terms and seal tare forces, and the axial exit stream thrust, ($H + P_oA_e$). Summing axial forces:

$$H = F_1 + P_3\ (A_3 + \Delta A - A_1) - P_o\ (A_3 - \Delta A) - H_2$$

The stream thrust at Station 1 is the exit stream thrust of a choked long-radius ASME nozzle, and is calculated as:

$$F_i = G_1 \ (1 + 1.4 \ C_{D1} \ C_{fg1}) \times 0.52828 \ P_{t1} \ A_1$$

Use of $\gamma = 1.4$ and $P^*/P_t = 0.52828$ in the above equation implies an ideal gas. The factor G, derived from tabulated values in References 56 and 57, corrects the stream thrust from that of an ideal gas to that of a real gas:

$$G = 1.00012 + 6.8338 \times 10^{-6} \times P_t \quad \text{(psia)}$$

C_{D1} has already been discussed; C_{fg1} was calculated in an analogous manner,

$$C_{fg1} = 1 - 0.109 \ R_{N1}^{-0.2}$$

This equation is a semiempirical expression of the thrust coefficient of an ASME nozzle at a pressure ratio of $\lambda = 1.8929$ (corresponding to $P^*/P_t = 0.52828$). For the present tests, G_1 varied from 1.001 to 1.002, and C_{fg1} varied between 0.995 and 0.996.

P_3 is the seal cavity static pressure which acts over an area determined partly by the seal extrusion, ΔA. ΔA is a change in effective seal area determined by calibration. A_3 is the geometric area of the seal (used as a reference area to define ΔA).

The thrust coefficient (Cfg) is defined in this report as the ratio of the measured net nozzle thrust to the ideal thrust of the actual mass flow expanded to ambient pressure.

The ideal thrust, $m_a v_i$, is calculated from the actual mass flow and the dimensionless ideal thrust function based on nozzle pressure ratio. The dimensionless ideal thrust, $m_i v_i / P_t A^*$, is a function of only the nozzle overall pressure ratio, λ (for a given γ). The denominator of Cfg thus is calculated using the ideal dimensionless thrust and the model throat conditions:

$$m_a v_i = (A^*/A) \ C_{D8} \ A_8 \ P_{t8} \left[\frac{m_i v_i}{P_t \ A^*} \right]_8$$

where,

$$\frac{m_i v_i}{P_t \ A^*} = 1.81162 \left[1 - (1/\lambda)^{0.2857} \right]^{1/2} \quad \text{for } \gamma = 1.4$$

The thrust coefficient is the ratio of actual net thrust to ideal thrust:

$$C_{fg} = \frac{H}{m_a v_i}$$

The nozzle thrust data were also expressed in terms of the dimensionless exit stream thrust parameter, f_9, calculated as:

$$f_9 = \frac{H + P_o A_9}{A_8 P_{t8}}$$

Force Balance Calibration

The balance is first loaded with known weights to obtain a curve of axial downstream force divided by readout (H_2/C_2) versus C_2 for no pressure difference across the seal. The balance interior is next pressurized to produce seal pressure differentials, ΔP. Since this pressure loading produces a downstream force on the balance (indicated by the readout), upstream loads (L) are applied to decrease the net load to simulate actual test conditions of load and ΔP. The sum of the indicated flexure load and the reverse load must equal the downstream pressure load, $\Delta P(A_3 + \Delta A)$. Since H_2, L, ΔP and A_3 are known, the effective seal area (ΔA) may be calculated. Plotting of $\Delta 4$ as a function of balance output and differential pressure completes the calibration.

Instrumentation

Although the internal and external instrumentation on the models and in the force- and flow-metering systems was the same for both the FluiDyne and NASA-Lewis test series, the data acquisition and processing equipment was different. At FluiDyne the model pressures were measured on multiple-tube mercury and water manometers. The stagnation pressure (P_{t1}) and the seal cavity static pressure (P_3) were measured with bourdon-tube pressure gages. The pressures were recorded on Polaroid film. The stagnation temperature (T_{t1}) was recorded on a Bristol chart recorder. The pressures and temperatures were read from the film and chart by the FluiDyne test engineer, and these measurements were used in the data reduction computer program.

The data acquisition and processing systems at NASA-Lewis were fully automated and were physically linked for on-line data reduction. The high and low pressures in the test setup were read by transducers and scanivalves, respectively. The thermocouples were electronically recorded. A schematic diagram of the NASA-Lewis data recording and processing system is presented in Figure 590. The heart of this system is CADDE II (Central Automatic Digital Data Encoder). The CADDE II data recording system is a low speed voltage scanner and digitizer designed to convert steady-state direct current signals to digital numbers at a rate of 25 samples per second. The raw data are recorded on digital magnetic tape, which becomes the permanent data record. Optionally, the raw data can be sent to the central computing facility for further processing.

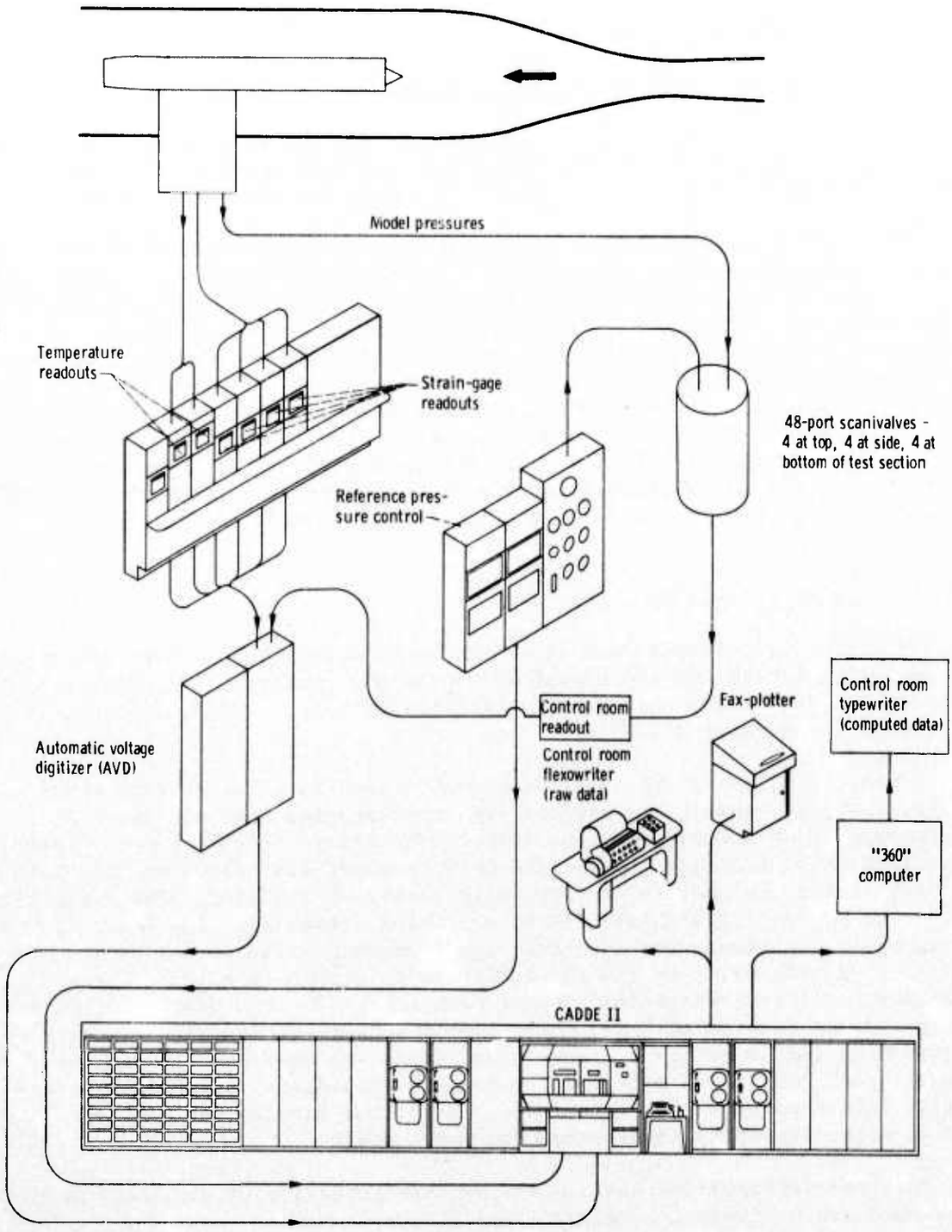

Figure 590. Automatic Data Recording and Processing System.

B.7 LASER VELOCIMETER SYSTEM

B.7.1 Laser Velocimeter Technical Background

The laser velocimeter offers the means of obtaining mean and turbulence velocity measurements at Mach numbers limited primarily by the tracking particle dynamics. Further, no penetration into the flow is required.

The laser velocimeter used in the testing and evaluation at the GE Evendale jet noise outdoor site (JENOTS) is of the differential Doppler type, as developed by C.M. Penny (Reference 62) and W.B. Jones (Reference 63) of the General Electric R&D Center. It was adapted to jet noise evaluation use at the General Electric JENOTS facility under the Air-Force-sponsored Supersonic Jet Noise Program, details to be found in Reference 5. The equipment is basically a two-part package consisting of the laser velocimeter head and the laser velocimeter signal processing equipment. The laser velocimeter head is specifically designed for remote operation in a high-noise, high-vibration environment. The laser velocimeter signal processor is located in the JENOTS control room along with recording and display equipment.

Laser Velocimeter Head

The laser velocimeter head is of the backscatter type. Both transmitting and receiving subsystems are contained within one housing. The housing is mounted on a two-direction, remotely operated actuator, which, in turn, is mounted on a pneumatic dolly.

A cross section of the laser velocimeter head is shown in Figure 591. The design is a coaxial, backscatter type that permits both the laser and photosensor to be contained in one frame. The design objective was a laser velocimeter head that was insensitive to both sound and vibration, and sufficiently stable to require no field adjustments of any kind. The laser light source was chosen for high stability, hands-off operation. The laser is contained in the square cross section lower housing. The optics components consist of a beam splitter and three mirrors to provide the laser beams necessary for the differential Doppler technique. The two upper mirrors in Figure 591 are mounted on thin, three-legged spiders to minimize blockage of returning (backscattered) light. Two lenses are used as shown in the figure. Each lens is an air-speed, coated, 6-inch-diameter, 30-inch-focal-length, telescope-type objective lens. The actual working distance (front lens to measuring spot) is dependent on model scale.

Both the vertical and horizontal traverse actuation of the laser velocimeter head are controlled remotely.

Laser Velocimeter Signal Processor

The laser velocimeter signal processor used is based on the precision Doppler burst counter-timer as developed by Jones (Reference 53). This

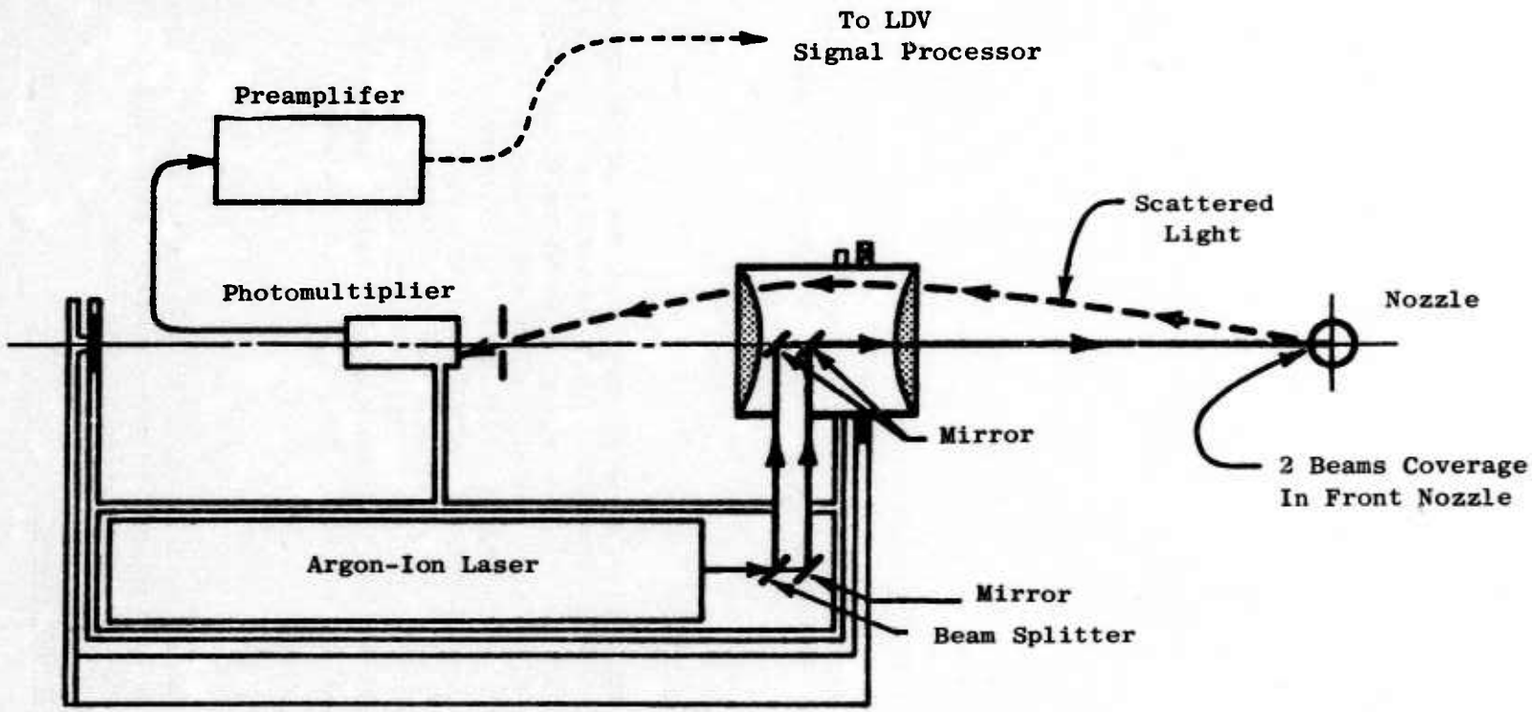

Figure 591. Cross Section of Laser Velocimeter Head for Backscatter Operation.

concept, which accurately determines the elapsed time for a preset number of Doppler burst cycles, avoids the so-called ambiguity that is inherent in the frequency spectrum type of laser velocimeter analyser. Because of this lack of ambiguity, measurements of both high and low turbulence may be made with very low instrumental broadening. The precision counter-timer concept has another advantage; i.e., full information is obtained from single particle traverses, requiring very low seeding density in the test gas.

Data Acquisition Equipment

Figure 592 shows the arrangement of data acquisition equipment used for the laser velocimeter. The oscilloscope and camera are used to record plume turbulent velocity special profiles by applying either horizontal or vertical actuator position signals to the scope "H" input. A high speed tape recording (FM mode) is made of representative points in the plume for later analysis of the turbulent velocity frequency spectrum. A pulse height analyser (256 channel) is used to acquire the turbulent velocity power spectrum; histograms and the results are displayed on an X-Y plotter. The chart recorder is used to display mean velocity as a system check. Two frequency counters are used. One counter displays the validated measurement rate integrated over a one second time period; the second counter displays the total number of resets per second. The ratio of these two counter displays is monitored continuously as an indication of laser velocimeter system efficiency.

Laser Velocimeter Seeder

The hot jet is seeded with aluminum oxide powder of one micron nominal diameter. A photograph of the fluidized bed powder feeder is shown installed at JENOTS, Figure 593. A schematic of the feeder is shown as Figure 594. An air pressure of 4 to 20 inches of water is applied to the powder (upward) causing it to become fluidized. The gentle flow of air readily entrains single particles, which are then carried to a dilution zone where additional shop air is mixed in. The diluted suspension is split to two injection points. The majority of powder (about 80%) is seeded into the air supply for the hot jet burner. The remainder, about 20%, is injected just below the nozzle for seeding the secondary (entrained) air in a limited sector of plume.

Calibration

The laser velocimeter calibration consists of two parts; the spacing of the interference planes is determined at the measurement volume, and the signal processor is calibrated as volts out versus burst frequency in.

- Spacing of Interference Planes

  The spacing, s, of interference planes (fringes) is determined indirectly by measurement of included beam angle, α, as follows:

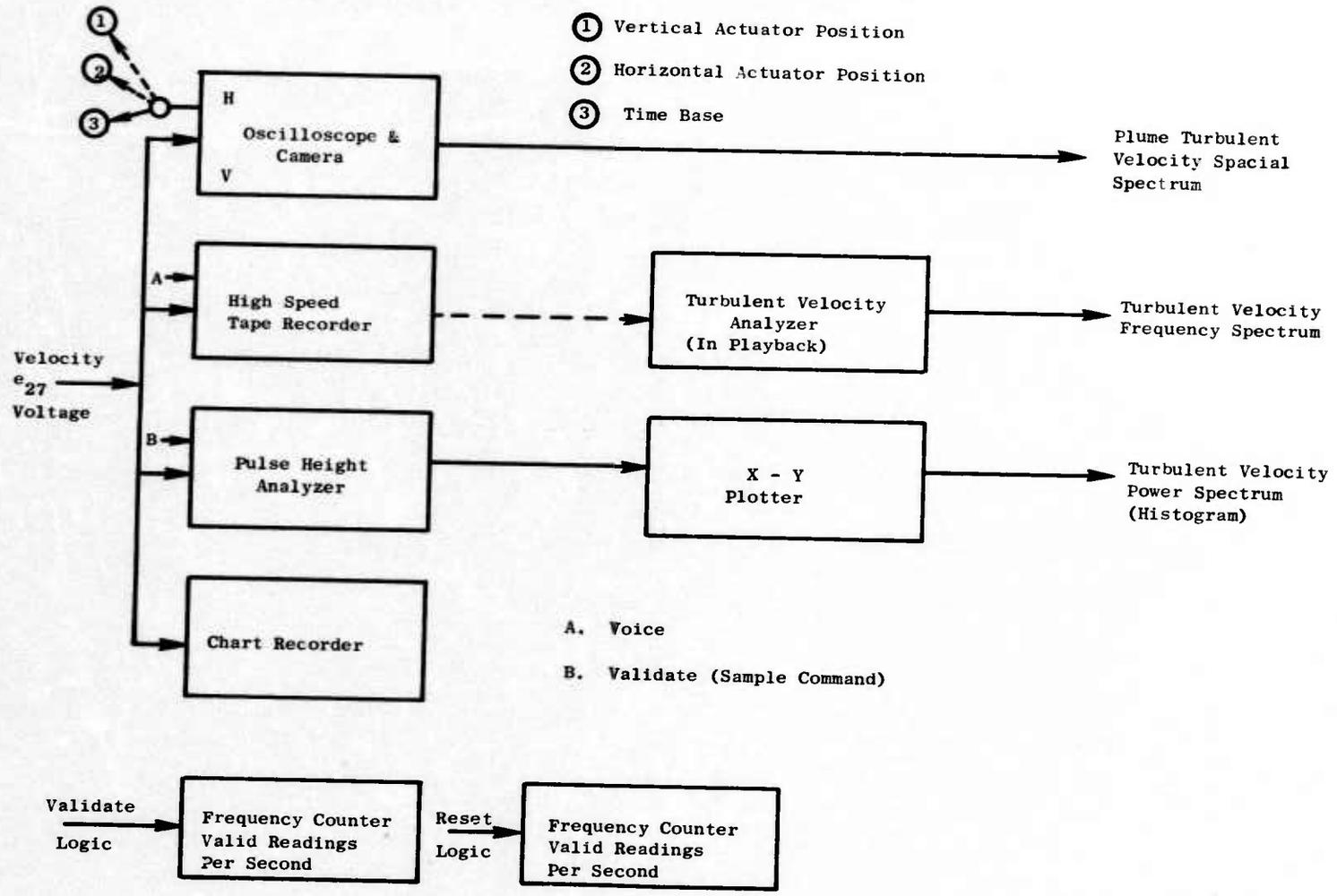

Figure 592. Data Acquisition - Laser Velocimeter.

Figure 593. View of the Fluidizer Bed LV Seeder.

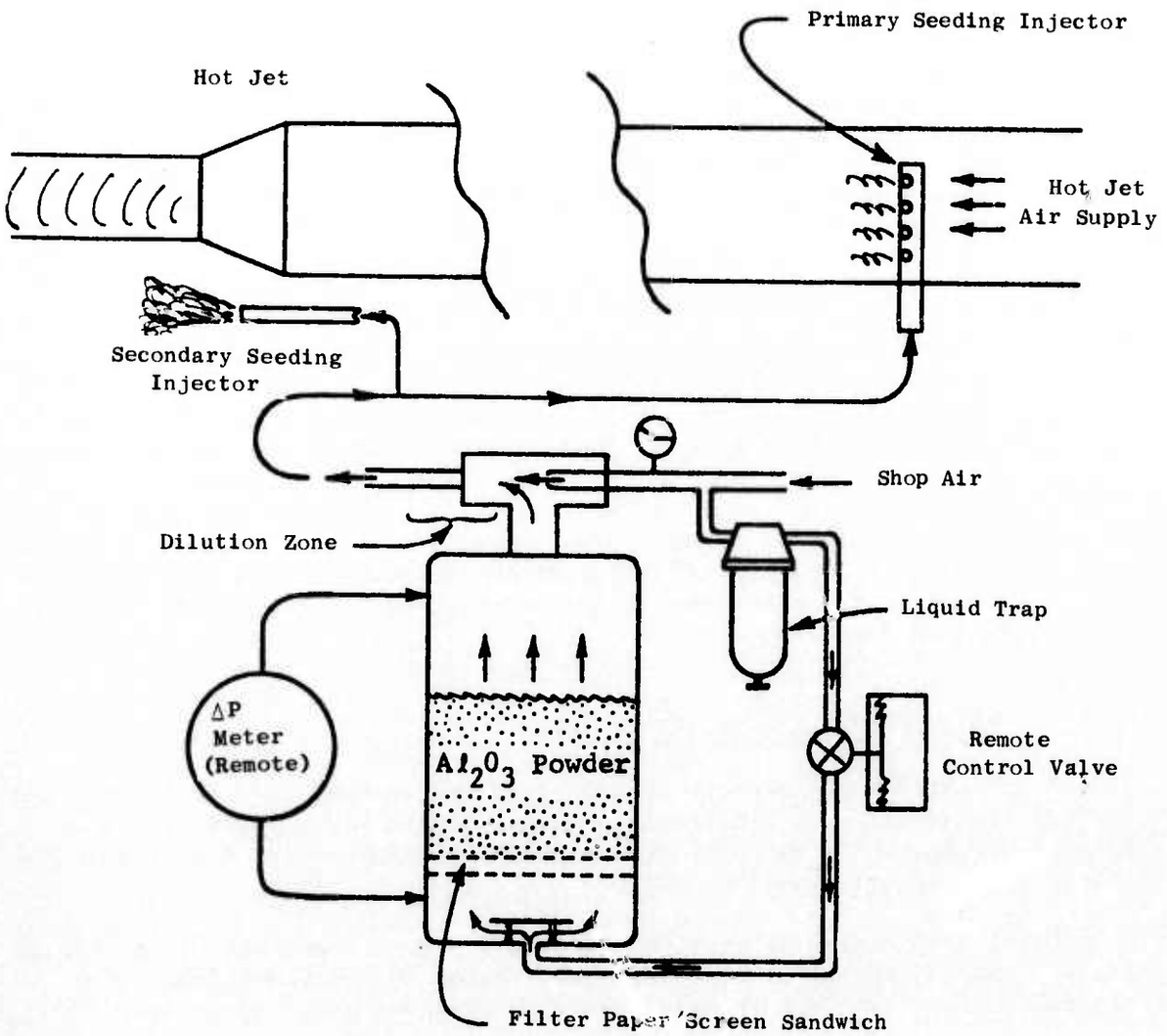

Figure 594. Fluidized Bed Powder Feeder and Injectors.

$$\text{Spacing, } S = \frac{\text{Laser Wavelength, } \lambda}{2 \sin (\alpha/2)}$$

The angle, α, is determined by finding the tangent of α as follows: The laser beams are allowed to cross and fall on a distant target (whose surface is normal to the bisector). The spacing of the two spots and the distance of the target to the measurement volume center are determined by machinist's scale and steel tape, respectively.

- Signal Processor Frequency Calibration

A variable frequency oscillator and precision frequency counter (quartz crystal-controlled time base) are used to provide calibration of the signal processor. The pure Doppler burst wave form is simulated closely by use of an amplitude modulator made with an FET analog gate. The burst envelope shape, which is essentially due to the Gaussian distribution of light in a focused TEM_{∞} laser beam, is obtained by modifying the output of a laboratory triangular waveform generator. Flexibility in the equipment is also provided to adjust the simulated fringe contrast in the test burst from 10% to 100% contrast.

Environmental Sensitivity Checks

Ambient temperature effects on the laser velocimeter head are controlled to ensure that laser beam alignment is always within specifications. Beam alignment checks made between test runs at JENOTS have proven the accuracy of the beam intersection and alignment.

Minimal temperature effects on the velocity output voltage of the signal processor are considered to be no problem. Acoustic and vibration checks conducted on the laser velocimeter have also shown no adverse results.

APPENDIX C

JET NOISE REDUCTION TEST SUMMARIES

Table 30. Test Summary, 5.7" I.D. Water-Cooled Conical Nozzle.

- (Not) Corrected to Free Field
- Angle Referenced from Jet Axis, degrees

Model: 5.7" ID WATER COOLED CONICAL NOZZLE

Scale Model A_8 = 25.63 in^2

Test Date(s): 1-26-73

Scale Factor: 8:1

Full Scale A_8 = 11.392 ft^2

TEST CONDITIONS						FULL-SCALE ACOUSTIC TEST RESULTS								
							320-foot Arc		300-foot Sideline		1500-ft Sideline		2128-ft Sideline	
Rdg No.	P_o (psia)	P_{T8}/P_o	T_{T8} (° R)	Ideal V_j (ft/sec)	W_B (lb/sec)	10 Log ρA	Peak (PNdB)	Maximum Angle (degrees)	Peak (PNdB)	Maximum Angle (degrees)	Peak (PNdB)	Maximum Angle (degrees)	Peak (PNdB)	Maximum Angle (degrees)
1	14.459	1.502	1246	1288	8.33	-4.1	117.0	130°/140°	115.1	130°	99.3	130°	95.4	130°
2	14.455	1.675	1300	1473	9.10	-4.1	123.5	150°	120.5	130°	104.5	130°	100.6	130°
3	14.450	1.820	1331	1598	9.60	-4.2	127.3	150°	123.5	140°	107.7	140°	103.9	140°
4	14.435	2.053	1454	1818	10.12	-4.4	134.1	140°	130.6	140°	114.6	140°	110.7	140°
5	14.429	2.258	1523	1970	10.92	-4.4	137.7	140°	134.2	140°	118.1	140°	114.2	140°
6	14.424	2.449	1591	2102	11.46	-4.5	139.7	140°	136.3	130°	120.0	130°	116.1	130°
7	14.421	2.695	1659	2246	12.47	-4.4	140.8	140°	138.8	130°	122.3	130°	118.4	130°
8	14.417	3.003	1775	2431	13.44	-4.4	147.4	130°/140°	145.6	130°	129.6	130°	125.7	130°
9	14.411	3.308	1860	2582	14.36	-4.4	146.2	130°	144.3	130°	128.1	130°	124.2	130°
10	14.408	3.594	2017	2768	14.88	-4.5	145.8	130°	143.8	130°	126.9	130°	122.9	130°
11	14.406	3.906	2136	2926	15.72	-4.5	146.1	130°	144.1	130°	127.3	130°	123.3	130°
12	14.406	3.523	2363	2976	13.66	-5.3	145.7	130°	143.7	130°	126.9	120°/130°	122.9	120°/130°
13	14.398	3.553	2130	2834	14.44	-4.8	145.7	130°	143.7	130°	126.7	130°	122.5	130°
14	14.389	3.568	1929	2701	15.31	-4.3	145.5	130°	143.5	130°	126.5	130°	122.5	130°
2-12-73														
1	14.556	2.034	1354	1744	10.57	-4.1	132.9	140°	129.4	140°	113.6	140°	109.2	140°
2	14.555	2.038	1579	1886	9.72	-4.7	135.2	140°	131.7	140°	115.7	140°	111.8	140°
3	14.552	2.037	1728	1972	9.18	-5.1	136.3	140°	132.9	140°	116.8	140°	112.9	140°
4	14.550	2.032	1979	2107	9.00	-5.7	137.2	140°	134.7	130°	118.7	130°	114.8	130°
5	14.547	2.529	1411	2011	12.82	-3.8	139.1	140°	135.6	140°	119.4	140°	115.5	140°
6	14.546	2.532	1580	2129	12.08	-4.3	140.0	140°	137.1	130°	120.8	130°	116.8	130°
7	14.544	2.542	1757	2249	11.52	-4.8	140.6	130°	138.6	130°	122.2	130°	118.3	130°
8	14.543	2.539	1971	2381	10.77	-5.3	141.7	130°	139.8	130°	123.3	130°	119.4	130°
9	14.541	3.030	1416	2179	14.73	-3.4	143.7	150°	140.1	140°	124.1	130°	120.2	130°
10	14.538	3.037	1578	2303	14.53	-3.9	415.4	140°	142.9	130°	126.9	130°	123.0	130°
11	14.533	3.030	1752	2424	13.65	-4.3	147.3	130°	145.5	130°	129.6	130°	125.8	130°
12	14.533	3.043	1945	2559	13.04	-4.8	147.8	130°	145.9	130°	130.1	130°	126.3	130°
13	14.531	3.499	1430	2310	1765	-3.1	143.9	130°	141.9	130°	124.5	130°	120.5	130°
14	14.531	2.570	1584	2447	17.02	-3.4	145	130°	143.0	130°	125.9	130°	121.9	130°
15	14.529	3.564	1761	2579	16.06	-3.9	145.1	130°	143.1	130°	126.5	130°	122.5	130°
16	14.530	3.595	1956	2726	15.32	-4.3	145.5	130°	143.5	130°	126.7	130°	122.8	130°
17	14.531	1.836	1417	1660	9.62	-4.4	129.6	150°	125.6	140°	109.8	140°	106.0	140°
18	14.531	1.679	1284	1467	8.93	-4.1	124.0	150°	120.5	150°	120.5	130°	100.8	130°
19	14.531	1.487	1254	1277	7.85	-4.1	118.0	150°	115.8	130°	100.0	130°	96.2	130°

Table 31. Test Summary, 40-Chute/Plug Nozzle Suppressor.

- (Not) Corrected to Free Field
- Angle Referenced from Jet Axis, degrees

Model: 40-CHUTE/PLUG NOZZLE SUPPRESSOR

Scale Model A_8 = 28.62 in^2

Test Date(s): 2-13-73

Scale Factor: 8:1

Full Scale A_8 = 12.72 ft^2

TEST CONDITIONS						FULL-SCALE ACOUSTIC TEST RESULTS								
							320-foot Arc		300-foot Sideline		1500-ft Sideline		2128-ft Sideline	
Rdg No.	P_o (psia)	P_{T8}/P_o	T_{T8} (° R)	Ideal V_j (ft/sec)	W_B (lb/sec)	10 Log ρA	Peak (PNdB)	Maximum Angle (degrees)	Peak (PNdB)	Maximum Angle (degrees)	Peak (PNdB)	Maximum Angle (degrees)	Peak (PNdB)	Maximum Angle (degrees)
1	14.521	1.538	1250	1326	8.65	-3.7	120.5	110°	120.5	110°	102.4	110°	97.7	110°
2	14.521	1.680	1347	1503	9.46	-3.9	122.8	110°	122.8	110°	104.7	110°	100.0	110°
4	14.519	1.842	1427	1670	9.93	-4.1	124.6	110°	124.7	110°	106.8	110°	102.2	110°
5	14.518	2.061	1473	1835	10.79	-4.1	126.0	110°	126.0	110°	108.6	110°	103.9	110°
6	14.513	2.254	1579	2003	11.36	-4.2	126.5	110°	126.5	110°	109.2	110°	104.5	110°
7	14.511	2.462	1609	2119	12.24	-4.1	127.7	130°	127.5	110°	110.0	110°	105.5	110°
8	14.506	2.700	1744	2304	13.11	-4.3	129.7	130°	128.9	110°	111.4	110°	106.8	110°
2-19-73														
1	14.519	2.983	1867	2487	14.09	-4.3	131.6	130°	129.6	130°	111.9	110°/120°/130°	107.5	120°
2	14.509	3.291	1932	2627	15.44	-4.2	133.1	140°	130.9	130°	113.9	120°	109.6	120°
3	14.509	3.612	2020	2775	16.24	-4.1	137.3	140°	134.3	130°	117.6	140°	113.7	140°
4	14.501	3.941	2171	2959	17.10	-4.2	140.2	140°	137.1	130°	120.9	130°	116.9	130°/140°
5	14.499	3.539	2016	2753	16.04	-4.2	136.1	140°	133.1	130°	116.2	130°/140°	112.2	130°/140°
6	14.497	3.531	1818	2613	16.85	-3.7	134.3	150°	131.6	130°	114.5	120°	110.1	120°/130°
7	14.494	3.558	1581	2442	18.25	-3.1	133.0	150°	130.6	120°	113.4	120°	109.0	120°
8	14.494	3.553	1415	2310	19.40	-2.6	132.2	130°/150°	130.2	130°	112.8	120°	108.3	120°
9	14.493	3.069	1989	2596	14.14	-4.5	132.1	130°	130.3	110°	112.9	110°	108.4	110°
10	14.493	3.089	1720	2420	15.29	-3.9	131.2	130°	129.8	110°	112.3	110°	107.7	110°
11	14.494	3.039	1598	2318	15.57	-3.6	130.5	130°	128.9	110°	111.4	120°	106.9	120°
12	14.493	3.045	1412	2180	16.53	-3.1	129.5	130°	127.5	120°/130°	110.0	120°	105.5	120°
13	14.491	2.552	1983	2394	11.85	-5.0	129.4	130°	128.6	110°	111.2	110°	106.7	110°
14	14.489	2.557	1777	2268	12.96	-4.5	128.2	130°	127.4	110°	109.9	110°	105.5	110°
15	14.490	2.549	1604	2152	13.39	-4.0	127.9	130°	127.2	110°	109.5	110°	104.8	110°
16	14.489	2.637	1424	2060	13.74	-3.5	127.1	130°	126.3	110°	108.5	110°	103.8	110°
18	14.489	2.057	1786	2017	10.14	-4.9	125.8	110°	125.8	110°	108.5	110°	103.8	110°
19	14.489	2.062	1610	1919	10.20	-4.5	125.3	110°	125.3	110°	107.8	110°	103.1	110°
20	14.489	2.054	1421	1798	11.15	-3.9	124.4	110°	124.4	110°	106.6	110°	101.9	110°

Table 32. Test Summary, 40-Spoke Low-C_D Plug Nozzle Suppressor.

- (Not) Corrected to Free Field
- Angle Referenced from Jet Axis, degrees

Model: 40 SPOKE LOW-C_D PLUG NOZZLE SUPPRESSOR

Test Date(s): 2-23-74

Scale Factor: 8:1

Scale Model A_8 = 34.627 in^2

Full Scale A_8 = 15.39 ft^2

TEST CONDITIONS						FULL-SCALE ACOUSTIC TEST RESULTS								
							320-foot Arc		300-foot Sideline		1500-ft Sideline		2128-ft Sideline	
Rdg No.	P_o (psia)	P_{T8}/P_o	T_{T8} (° R)	Ideal V_j (ft/sec)	W_B (lb/sec)	10 Log ρA	Peak (PNdB)	Maximum Angle (degrees)	Peak (PNdB)	Maximum Angle (degrees)	Peak (PNdB)	Maximum Angle (degrees)	Peak (PNdB)	Maximum Angle (degrees)
1	14.354	1.550	1334	138.1	9.17	-4.0	120.3	110°	120.3	110°	102.6	110°	98.0	110°
2	14.353	1.703	1366	1532	10.38	-4.0	122.3	110°	122.3	110°	105.0	110°	100.5	110°
3	14.354	1.862	1469	1708	10.80	-4.3	124.3	110°	124.3	110°	106.9	110°	102.4	110°
4	14.353	2.077	1543	1887	12.12	-4.3	126.0	110°	126.0	110°	108.7	110°	104.2	110°
5	14.352	2.270	1606	2028	12.81	-4.3	127.3	110°/130°	127.3	110°	109.7	110°	105.3	110°
6	14.352	2.480	1641	2148	13.88	-4.3	129.4	150°	128.4	110°	111.3	110°	107.0	110°
7	14.352	2.732	1763	2329	14.72	-4.3	132.4	150°	129.9	110°	113.2	110°	109.2	110°
8	14.352	3.045	1802	2464	16.00	-4.2	135.4	140°	133.1	130°	116.4	130°	112.4	130°
9	14.352	3.336	1952	2654	16.79	-4.3	139.4	140°	136.9	130°	120.5	130°	116.5	130°
10	14.352	3.634	2080	2822	17.57	-4.3	141.7	130°	139.7	130°	123.2	130°	119.3	130°
11	14.354	3.968	2181	2972	18.69	-4.2	143.9	130°	141.9	130°	125.7	130°	121.8	130°
2-28-73														
1	14.617	2.038	1463	1815	12.21	-4.0	125.6	130°	125.3	110°	107.9	110°	103.3	110°
2	14.617	2.050	1597	1904	11.62	-4.4	126.4	110°	126.4	110°	109.2	110°	104.7	110°
3	14.617	2.046	1800	2019	10.68	-4.9	127.1	110°	127.1	110°	109.8	110°	105.3	110°
4	14.617	2.038	1989	2113	10.36	-5.4	127.7	110°	127.7	110°	110.5	110°	106.0	110°
5	14.631	2.546	1427	2029	15.35	-3.5	129.3	150°	127.9	110°	110.3	110°	105.9	110°
6	14.618	2.537	1620	2158	14.36	-4.1	130.5	150°	128.6	110°	11.3	110°	107.1	110°
7	14.618	2.543	1786	2269	13.65	-4.5	131.8	150°	129.8	110°	112.5	110°	108.5	110°
8	14.617	2.543	2018	2411	12.78	-5.0	132.9	150°	130.2	110°/130°	113.2	110°	109.1	110°
9	14.613	3.052	1441	2205	18.43	-3.1	133.9	150°	130.9	130°	113.7	130°	109.6	130°
10	14.613	3.031	1578	2301	17.38	-3.5	135.4	150°	131.5	130°	114.7	130°	110.6	130°
11	14.613	3 036	1785	2449	16.33	-4.0	136.0	150°	133.4	130°	116.3	130°	112.2	130°
12	14.612	3.036	2004	2595	15.16	-4.6	138.9	150°	135.3	130°	118.3	130°	114.2	130°
13	14.609	3.578	1449	2343	21.36	-2.7	138.2	140°	134.8	130°	118.2	140°	114.2	140°
14	14.607	3.578	1804	2614	19.09	-3.6	140.6	140°	137.9	130°	121.4	130°	117.4	130°
15	14.604	3.584	1608	2470	20.28	-3.1	139.5	140°	136.0	140°	119.7	140°	115.7	140°
16	14.603	3.583	2024	2770	17.78	-4.1	141.8	130°/140°	139.8	130°	123.2	130°	119.2	130°

Table 33. Test Summary, Baseline 5.7" I.D. Conical Nozzle.

- (Not) Corrected to Free Field
- Angle Referenced from Jet Axis, degrees

Model: BASELINE; 5.7" I.D. CONICAL NOZZLE — Scale Model A_8 = 25.63 in^2

Test Date(s): 5-9-74 — Scale Factor: 8:1 — Full Scale A_8 = 11.391 ft^2

TEST CONDITIONS						FULL-SCALE ACOUSTIC TEST RESULTS								
							320-foot Arc		300-foot Sideline		1500-ft Sideline		2128-ft Sideline	
Rdg No.	P_o (psia)	P_{T8}/P_o	T_{T8} (° R)	Ideal V_j (ft/sec)	W_B (lb/sec)	10 Log ρA	Peak (PNdB)	Maximum Angle (degrees)	Peak (PNdB)	Maximum Angle (degrees)	Peak (PNdB)	Maximum Angle (degrees)	Peak (PNdB)	Maximum Angle (degrees)
1	14.376	1.59	1008	1230	8.61	-3.0	117.4	150°	115.3	120°	99.19	130°	95.35	130°
2	14.376	1.488	1097	1196	7.61	-3.5	117.7	140°	115.6	120°	99.52	120°	95.69	130°
3	14.375	2.528	1585	2130	11.63	-4.5	139.9	140°	137.5	130°	121.1	130°	117.2	130°
4	14.375	2.424	1662	2137	10.94	-4.7	139.5	130°	137.2	130°	120.8	130°	116.9	130°
*5	14.516	2.065	1381	1778	9.81	-4.1	135.1	140°	131.5	140°	115.1	140°	111.2	140°
5	14.375	2.656	1820	2337	11.47	-5.0	141.6	130°	139.7	130°	123.3	130°	119.4	130°
6	14.375	3.053	1934	2554	12.69	-5.2	148.3	130°	146.3	130°	130.1	130°	126.2	130°
7	14.375	2.407	1495	2019	11.56	-4.3	139.3	140°	135.7	140°	119.2	130°	115.3	130°
8	14.375	2.020	1311	1710	10.56	-3.9	131.8	150°	126.8	140°	110.9	140°	107.2	140°

*Note: Run 2 Try 1 Test Pt.

Table 34. Test Summary, 36-Deep-Chute Suppressor.

• (Not) Corrected to Free Field

• Angle Referenced from Jet Axis, degrees

Model: 36 DEEP CHUTE SUPPRESSOR

Scale Model A_8 = 25.606 in^2

Test Date(s): 5-21-74

Scale Factor: 8:1

Full Scale A_8 = 11.58 ft^2

TEST CONDITIONS						FULL-SCALE ACOUSTIC TEST RESULTS								
							320-foot Arc		300-foot Sideline		1500-ft Sideline		2128-ft Sideline	
Rdg No.	P_o (psia)	P_{T8}/P_o	T_{T8} (° R)	Ideal V_j (ft/sec)	W_B (lb/sec)	10 Log ρA	Peak (PNdB)	Maximum Angle (degrees)	Peak (PNdB)	Maximum Angle (degrees)	Peak (PNdB)	Maximum Angle (degrees)	Peak (PNdB)	Maximum Angle (degrees)
1	14.453	1.474	1124	1196	7.53	-3.6	116.0	110°/120°	116.1	110°	98.75	110°	94.15	110°
2	14.452	1.490	1252	1280	7.14	-4.0	116.7	120°	116.6	110°	99.27	110°	94.69	110°
3	14.452	2.018	1301	1701	9.78	-3.8	122.9	130°	122.6	110°	105.0	110°	100.3	110°
4	14.444	1.813	1389	1628	8.38	-4.3	122.6	120°	122.5	110°	104.8	110°	100.2	110°
5	14.440	2.015	1455	1797	9.07	-4.4	124.7	110°	124.7	110°	106.9	110°	102.4	110°
6	14.434	2.436	1474	2017	11.05	-4.2	128.5	150°	127.7	110°	110.3	110°	105.7	110°
7	14.430	2.219	1534	1957	9.83	-4.5	126.8	150°	126.4	110°	109.1	110°	104.6	110°
8	14.426	2.528	1570	2120	11.14	-4.4	129.4	150°	128.7	110°	111.3	110°	106.9	110°
9	14.425	2.402	1608	2092	10.46	-4.6	129.2	140°	128.4	110°	110.6	110°	106.2	110°
10	14.423	2.669	1748	2295	11.06	-4.8	131.9	140°	130.8	110°	113.5	110°	109.1	110°
11	14.421	2.984	1920	2523	11.76	-5.2	135.9	140°	133.2	130°	116.9	130°	113.1	130°
12	14.420	3.239	1996	2655	12.53	-5.2	138.1	140°	136.1	130°	120.1	130°	116.3	130°
13	14.417	3.540	2114	2820	13.28	-5.4	141.1	130°	139.1	130°	122.9	130°	119.1	130°
14	14.418	2.982	1832	2453	12.17	-4.9	135.5	140°	132.5	130°	116.2	130°	112.4	130°
19	14.403	2.036	1332	1731	9.94	-4.0	124.5	140°	124.5	140°	106.4	110°	101.9	110°

Table 35. Test Summary, 36-Chute Suppressor with Hardwall Ejector No. 1.

- (Not) Corrected to Free Field
- Angle Referenced from Jet Axis, degrees

Model: 36 CHUTE/W H.W. EJECTOR NO. 1

Scale Model A_8 = 25.606 in^2

Test Date(s): 5-23-74

Scale Factor: 8:1

Full Scale A_8 = 11.58 ft^2

TEST CONDITIONS						FULL-SCALE ACOUSTIC TEST RESULTS								
							320-foot Arc		300-foot Sideline		1500-ft Sideline		2128-ft Sideline	
Rdg No.	P_o (psia)	P_{T8}/P_o	T_{T8} (° R)	Ideal V_j (ft/sec)	W_B (lb/sec)	10 Log ρA	Peak (PNdB)	Maximum Angle (degrees)	Peak (PNdB)	Maximum Angle (degrees)	Peak (PNdB)	Maximum Angle (degrees)	Peak (PNdB)	Maximum Angle (degrees)
1	14.382	1.480	1162	1219	7.66	-3.7	112.9	100° & 120°	114.2	110°	96.9	110°	92.3	110°
2	14.381	1.491	1292	1301	7.24	-4.2	115.8	110°	115.9	100°	98.8	100°	94.3	100°
3	14.381	1.898	1322	1591	8.65	-4.1	119.4	110°	119.5	110°	101.7	110°	97.1	110°
4	14.381	2.008	1314	1703	9.77	-3.9	121.3	110°	121.3	110°	103.7	110°	99.1	110°
5	14.379	2.020	1384	1755	9.5	-4.1	122.3	110°	122.3	110°	104.3	110°	99.7	110°
6	14.379	2.239	1444	1908	10.18	-4.2	123.8	110°	123.8	110°	106.2	110°	101.5	110°
7	14.376	2.428	1384	1951	11.48	-3.9	125.4	110°	125.4	110°	107.7	110°	103.1	110°
8	14.374	2.403	1525	2038	10.72	-4.4	125.4	110°	125.4	110°	107.9	110°	103.4	110°
9	14.376	2.517	1496	2065	11.39	-4.2	125.7	110°	125.7	110°	108.1	110°	103.7	110°
10	14.376	2.678	1626	2217	11.61	-4.5	131.1	120°	130.2	120°	111.4	120°	107.2	120°
11	14.376	2.986	1850	2477	12.17	-5.0	133.9	140°	130.4	130°& 140°	114.3	140°	110.6	140°
12	14.376	3.233	1936	2613	12.72	-5.1	136.5	140°	133.6	130°	117.4	130°	113.7	130°
13	14.376	3.545	2024	2760	13.62	-5.7	139.1	130°	137.2	130°	120.9	130°	117.1	130°
7-17-74														
17	14.504	2.519	1575	2120	11.54	-4.4	126.2	150°	125.4	110°	108.0	110°	103.5	110°
18	14.504	2.392	1598	2081	10.80	-4.6	124.8	110°/150°	124.8	110°	107.4	110°	102.8	110°
19	14.504	2.646	1681	2241	11.76	-4.6	128.0	150°	126.9	110°	109.6	110°	105.4	130°
20	14.499	3.018	1925	2537	12.28	-5.1	133.4	140°	129.8	140°	115.0	130°	111.3	130°
21	14.499	3.251	1989	2653	13.00	-5.2	136.2	130°	134.4	130°	118.3	130°	114.6	130°
22	14.499	3.532	2087	2800	13.74	-5.3	139.6	130°	137.7	130°	121.4	130°	117.5	130°
25	14.502	1.992	1526	1826	9.22	-4.6	122.1	110°	122.1	110°	104.2	110°	99.5	110°
26	14.502	1.469	1227	1244	7.44	-4.0	114.8	110°	114.9	110°	97.6	110°	93.0	110°

Table 36. Test Summary, 36-Deep-Chute Suppressor with Hardwall Ejector No. 2.

- (Not) Corrected to Free Field
- Angle Referenced from Jet Axis, degrees

Model: 36 DEEP CHUTE/W H.W. EJECTOR NO. 2

Test Date(s): 6-3-74

Scale Factor: 8:1

Scale Model A_8 = 25.606 in^2

Full Scale A_8 = 11.58 ft^2

TEST CONDITIONS						FULL-SCALE ACOUSTIC TEST RESULTS								
							320-foot Arc		300-foot Sideline		1500-ft Sideline		2128-ft Sideline	
Rdg No.	P_o (psia)	P_{T8}/P_o	T_{T8} (° R)	Ideal V_j (ft/sec)	W_B (lb/sec)	10 Log ρA	Peak (PNdB)	Maximum Angle (degrees)	Peak (PNdB)	Maximum Angle (degrees)	Peak (PNdB)	Maximum Angle (degrees)	Peak (PNdB)	Maximum Angle (degrees)
1	14.477	1.475	1154	1212	7.88	-3.7	115.2	110°	115.3	110°	97.9	110°	93.1	110°
2	14.477	1.491	1260	1283	7.53	-4.1	116.6	110°	116.6	110°	99.3	110°	98.9	110°
3	14.476	1.822	1374	1624	8.68	-4.2	121.5	110°	121.6	110°	103.8	110°	99.2	110°
4	14.474	2.014	1329	1717	9.92	-3.9	122.8	120°	122.4	110°	104.7	110°	100.1	110°
7	14.467	2.395	1719	2159	10.09	-4.9	127.3	110°/150°	127.3	110°	109.5	110°	104.9	110°
8	14.467	2.424	1579	2082	10.77	-4.5	126.9	110°/120°/130°	126.9	110°	109.1	110°	104.5	110°
9	14.467	2.520	1700	2203	10.80	-4.8	128.5	140°/150°	128.3	110°	110.6	110°	105.9	110°
10	14.465	2.636	1885	2370	10.60	-5.2	130.5	140°	129.3	110°	111.8	110°/130°	107.9	130°
11	14.465	2.210	1659	2031	9.68	-4.8	125.7	130°	125.7	110°	108.1	110°	103.6	110°
14	14.465	3.027	1950	2544	11.99	-5.2	134.4	140°	131.7	130°	115.0	130°	111.1	130°
15	14.462	3.204	1916	2576	12.56	-5.1	136.6	130°/140°	134.7	130°	118.3	130°	114.5	130°
16	14.502	1.469	1226	1244	7.66	-4.0	115.6	110°	115.6	110°	98.5	110°	93.9	110°
16	14.462	3.541	1957	2714	14.06	-5.0	139.5	130°	139.6	130°	121.2	130°	117.4	130°
17	14.503	2.018	1303	1702	10.35	-3.8	122.1	130°	121.8	110°	104.1	110°	99.5	110°
18	14.503	2.420	1458	1999	11.61	-4.1	126.5	130°	125.1	110°	107.6	110°	103.0	110°
19	14.503	2.519	1576	2121	11.59	-4.4	127.8	130°	126.6	110°	109.1	110°	104.7	110°
20	14.503	2.664	1693	2257	16.78	-4.7	129.0	130°/140°/150°	127.8	110°	110.4	110°/130°	106.4	130°
21	14.500	3.002	1867	2494	12.50	-5.0	133.1	130°/140°	131.0	130°	114.8	130°	100.9	130°
22	14.500	3.252	1932	2616	13.30	-5.1	135.9	130°	133.9	130°	117.9	130°	114.1	130°
23	14.500	3.529	2044	2770	13.96	-5.2	139.1	130°	137.2	130°	121.1	130°	117.3	130°
24	14.498	2.859	1809	2406	12.17	-4.9	131.6	140°	129.3	110°/130°	113.0	130°	109.1	130°
25	14.497	2.514	1653	2170	11.19	-4.6	127.9	130°	127.2	110°	109.6	110°	105.1	110°

Table 37. Test Summary, 36-Chute Suppressor with Treated Ejector No. 1 (Packing 1).

- (Not) Corrected to Free Field
- Angle Referenced from Jet Axis, degrees

Model: 36 CHUTE SUPPRESSOR WITH TREATED EJECTOR NO. 1 (PACKING 1)

Scale Model A_8 = 25.606 in^2

Test Date(s): 7-17-74

Scale Factor: 8:1

Full Scale A_8 = 11.58 ft^2

TEST CONDITIONS						FULL-SCALE ACOUSTIC TEST RESULTS								
							320-foot Arc		300-foot Sideline		1500-ft Sideline		2128-ft Sideline	
Rdg No.	P_o (psia)	P_{T8}/P_o	T_{T8} (° R)	Ideal V_j (ft/sec)	W_B (lb/sec)	10 Log ρA	Peak (PNdB)	Maximum Angle (degrees)	Peak (PNdB)	Maximum Angle (degrees)	Peak (PNdB)	Maximum Angle (degrees)	Peak (PNdB)	Maximum Angle (degrees)
2	14.524	1.461	1089	1164	8.16	-3.4	110.5	110°	110.6	110°	93.2	110°	88.6	110°
3	14.524	1.467	1220	1239	7.62	-3.9	112.4	110°	112.5	110°	95.1	110°	90.5	110°
5	14.523	2.012	1319	1709	10.10	-3.9	119.0	110°	119.0	110°	101.4	110°	96.7	110°
6	14.519	2.001	1460	1792	9.43	-4.4	119.9	110°	120.0	110°	102.5	110°	97.9	110°
7	14.519	2.204	1527	1945	10.27	-4.4	122.3	110°	122.3	110°	104.6	110°	100.1	110°
8	14.519	2.423	1471	2010	11.47	-4.1	123.6	110°	123.6	110°	106.2	110°	101.7	110°
9	14.519	2.391	1633	2103	10.67	-4.6	124.1	140°/150°	123.8	110°	106.4	110°	101.9	110°
10	14.514	2.519	1588	2129	11.30	-4.5	125.2	140°	124.3	110°	106.9	110°	102.7	110°
11	14.511	2.653	1740	2284	11.42	-4.8	128.2	140°	126.2	110°	109.5	130°	105.8	130°
12	14.511	2.997	1871	2494	12.32	-5.0	132.8	130°/140°	130.9	130°	114.9	130°	111.2	130°
13	14.510	3.244	1937	2617	13.18	-5.1	135.1	130°	133.2	130°	117.2	130°	113.5	130°
14	14.509	3.530	2037	2765	13.89	-5.2	138.7	130°	136.8	130°	120.6	130°	116.9	130°
15	14.509	2.857	1802	2400	12.08	-4.9	131.1	140°	128.6	130°	112.5	130°	108.7	130°

Table 38. Test Summary, 36-Chute Suppressor with Treated Ejector No. 1 (Packing 2).

- (Not) Corrected to Free Field
- Angle Referenced from Jet Axis, degrees

Model: 36 CHUTE W/TREATED EJECTOR NO. 1 (PACKING 2)

Scale Model A_8 = 25.606 in^2

Test Date(s): 8-7-74 Scale Factor: 8:1

Full Scale A_8 = 11.58 ft^2

TEST CONDITIONS						FULL-SCALE ACOUSTIC TEST RESULTS								
							320-foot Arc		300-foot Sideline		1500-ft Sideline		2128-ft Sideline	
Rdg No.	P_o (psia)	P_{T8}/P_o	T_{T8} (° R)	Ideal V_j (ft/sec)	W_B (lb/sec)	10 Log ρA	Peak (PNdB)	Maximum Angle (degrees)	Peak (PNdB)	Maximum Angle (degrees)	Peak (PNdB)	Maximum Angle (degrees)	Peak (PNdB)	Maximum Angle (degrees)
2	14.489	3.478	1983	2715	14.12	-5.1	138.1	130°	136.2	130°	120.2	130°	116.4	130°
3	14.479	2.507	1679	2184	10.89	-4.7	126.5	140°	125.5	110°	108.5	110°/130°	104.7	130°
4	14.479	2.379	1457	1981	11.20	-4.1	123.3	110°/140°/150°	123.2	110°	105.9	110°	101.4	110°
5	14.477	1.987	1302	1684	10.08	-3.9	119.2	110°	119.3	110°	101.7	110°	97.0	110°
6	14.479	1.481	1185	1235	8.01	-3.8	113.1	110°	113.1	110°	95.89	110°	91.34	110°
7	14.479	3.005	1837	2474	12.78	-4.9	132.9	140°	130.2	130°	114.3	130°	110.6	130°

Table 39. Test Summary, 36-Chute Suppressor with Treated Ejector No. 2.

- (Not) Corrected to Free Field
- Angle Referenced from Jet Axis, degrees

Model: 36 CHUTE SUPPRESSOR/W TREATED EJECTOR NO. 2

Test Date(s): 7-18-74

Scale Factor: 8:1

Scale Model A_8 = 25.906 in^2

Full Scale A_8 = 11.58 ft^2

TEST CONDITIONS						FULL-SCALE ACOUSTIC TEST RESULTS									
							320-foot Arc		300-foot Sideline		1500-ft Sideline		2128-ft Sideline	
Rdg No.	P_o (psia)	P_{T8}/P_o	T_{T8} (° R)	Ideal V_j (ft/sec)	W_B (lb/sec)	10 Log ρA	Peak (PNdB)	Maximum Angle (degrees)	Peak (PNdB)	Maximum Angle (degrees)	Peak (PNdB)	Maximum Angle (degrees)	Peak (PNdB)	Maximum Angle (degrees)
1	14.507	1.472	1274	1271	7.48	-4.1	113.4	110°	113.4	110°	96.3	110°	91.8	110°
2	14.506	3.001	1873	2497	12.56	-5.0	132.7	140°	130.2	130°	114.4	130°	110.6	130°
3	14.506	3.252	1943	2623	13.27	-5.1	135.4	130°/140°	133.6	130°	117.7	130°	113.9	130°
4	14.505	2.860	1788	2392	12.32	-4.8	130.4	140°	128.0	130°	112.1	130°	108.3	130°
5	14.505	2.648	1675	2239	11.72	-4.6	127.5	150°	125.9	110°	109.1	130°	105.3	130°
6	14.505	2.518	1642	2164	11.33	-4.6	125.9	150°	124.7	110°	107.5	110°/130°	103.6	130°
7	14.505	3.532	2034	2763	14.00	-5.4	138.6	130°	136.7	130°	120.8	130°	117.0	130°
8	14.505	2.515	1548	2100	11.74	-4.3	125.1	150°	124.5	110°	107.5	110°	103.2	110°
9	14.505	2.420	1440	1987	11.69	-4.0	123.5	150°	122.5	110°	105.5	110°	101.1	110°
10	14.505	2.394	1617	2094	10.87	-4.6	124.3	150°	123.7	110°	106.6	110°	102.3	110°
11	14.505	2.206	1495	1926	10.41	-4.3	121.7	110°	121.7	110°	104.5	110°	100.1	110°
12	14.505	1.994	1442	1776	9.61	-4.3	119.2	110°	119.2	110°	101.9	110°	97.5	110°
13	14.505	2.009	1288	1687	10.37	-3.8	118.7	110°	118.7	110°	101.3	110°	96.8	110°
14	14.505	1.767	1325	1557	8.87	-4.1	115.9	110°	115.9	110°	98.6	110°	94.1	110°
15	14.505	1.459	1081	1158	8.11	-3.4	111.0	110°	111.1	110°	93.9	110°	89.3	110°

Table 40. Test Summary, 36-Deep-Chute Suppressor.

- (Not) Corrected to Free Field
- Angle Referenced from Jet Axis, degrees

Model: 36-DEEP-CHUTE SUPPRESSOR

Scale Model A_8 = 25.606 in^2

Test Date(s): 6-4-74

Scale Factor: 8:1

Full Scale A_8 = 11.88 ft^2

TEST CONDITIONS						FULL-SCALE ACOUSTIC TEST RESULTS							
							320-foot Arc		300-foot Sideline		1500-ft Sideline		2128-ft Sideline	
Rdg No.	P_o (psia)	P_{T8}/P_o	T_{T8} (° R)	Ideal V_j (ft/sec)	W_B (lb/sec)	10 Log ∫A	Peak (PNdB)	Maximum Angle (degrees)	Peak (PNdB)	Maximum Angle (degrees)	Peak (PNdB)	Maximum Angle (degrees)	Peak (PNdB)	Maximum Angle (degrees)
1	14.469	2.663	1726	2278	11.30	-4.8	130.6	140	129.3	110	111.7	110	107.2	110
2	14.465	2.980	1862	2482	12.00	-5.0	135.1	140	132.0	130	115.4	130	111.5	130
3	14.465	3.330	1968	2664	15.17	-5.1	137.3	140	134.8	130	118.4	130	114.6	130
4	14.461	3.540	2040	2769	13.67	-5.2	139.7	130	137.8	130	121.5	130	117.7	30
5	14.461	2.877	1713	2347	13.61	-4.6	133.1	140	129.9	110	112.8	130	108.9	130
6	14.445	2.538	1646	2175	12.35	-4.6	130.1	140	127.9	110	110.3	110	105.8	110
7	14.455	2.028	1475	1810	9.26	-4.4	124.5	140	123.2	110	105.5	110	101.0	110

Table 41. 32-Chute Suppressor, A_8 = 30.828 $in.^2$.

- (Not) Corrected to Free Field
- Angle Referenced from Jet Axis, degrees

Model: 32-CHUTE SUPPRESSOR

Scale Model A_8 = 30.828 in^2

Test Date(s): 6-14-74

Scale Factor: 8:1

Full Scale A_8 = 12.701 ft^2

TEST CONDITIONS						FULL-SCALE ACOUSTIC TEST RESULTS							
							320-foot Arc		300-foot Sideline		1500-ft Sideline		2128-ft Sideline	
Rdg No.	P_o (psia)	P_{T8}/P_o	T_{T8} (° R)	Ideal V_j (ft/sec)	W_B (lb/sec)	10 Log ρA	Peak (PNdB)	Maximum Angle (degrees)	Peak (PNdB)	Maximum Angle (degrees)	Peak (PNdB)	Maximum Angle (degrees)	Peak (PNdB)	Maximum Angle (degrees)
1	14.347	1.480	1092	1181	9.60	-2.7	116.6	110°	116.7	110°	98.7	110°	98.9	110°
2	14.347	1.490	1270	1289	8.94	-3.3	117.9	110°	117.9	110°	99.8	110°	95.1	110°
5	14.450	2.042	1389	1771	11.46	-3.3	124.8	110°	124.8	110°	107.2	110°	102.6	110°
6	14.431	2.255	1528	1971	12.07	-3.6	126.9	110°	127.0	110°	109.3	110°	104.7	110°
7	14.429	2.436	1595	2098	12.68	-3.7	127.9	110°/140°/150°	128.0	110°	110.3	110°	105.8	110°
8	14.426	2.453	1461	2015	13.46	-3.3	129.6	150°	127.3	110°	109.4	110°	104.8	110°
9	14.426	2.557	1559	2124	13.48	-3.6	128.9	150°	128.7	110°	111.0	110°	106.5	110°
10	14.425	2.699	1713	2283	13.60	-3.9	130.3	150°	129.7	110°	112.1	110°	107.6	110°
11	14.423	3.033	1872	2507	14.61	-4.2	134.8	150°	131.5	110°	114.1	110°	109.7	110°
12	14.421	3.284	1925	2620	15.54	-4.2	136.9	150°	132.6	110°	116.3	140°	112.4	140°
13	14.418	3.585	2038	2780	16.44	-4.4	140.5	140°	136.7	130°	120.4	130°	116.5	130°
14	14.416	2.914	1791	2413	14.39	-4.1	133.4	150°	131.1	110°	113.7	110°	109.2	110°
15	14.416	2.566	1636	2180	13.31	-3.8	129.5	150°	129.4	110°	111.9	110°	107.4	110°
16	14.416	2.049	1302	1718	12.06	-3.0	125.2	110°	125.2	110°	107.4	110°	102.9	110°

Table 42. Test Summary, 40-Chute Suppressor.

- (Not) Corrected to Free Field
- Angle Referenced from Jet Axis, degrees

Model: 40-CHUTE SUPPRESSOR

Test Date(s): 6-5-74

Scale Factor: 8:1

Scale Model A_8 = 28.62 in^2

Full Scale A_8 = 12.92 ft^2

TEST CONDITIONS						FULL-SCALE ACOUSTIC TEST RESULTS									
							320-foot Arc		300-foot Sideline		1500-ft Sideline		2128-ft Sideline	
Rdg No.	P_o (psia)	P_{T8}/P_o	T_{T8} (° R)	Ideal V_j (ft/sec)	W_8 (lb/sec)	10 Log ρA	Peak (PNdB)	Maximum Angle (degrees)	Peak (PNdB)	Maximum Angle (degrees)	Peak (PNdB)	Maximum Angle (degrees)	Peak (PNdB)	Maximum Angle (degrees)
1	14.445	2.689	1709	2279	12.50	-4.2	128.7	130°	127.9	110°	110.3	110°	105.7	110°
2	14.445	2.850	1914	2472	14.91	-4.7	131.6	140°	129.7	110°	112.3	110°	107.8	110°
1	14.441	3.275	2014	2679	13.78	-4.8	134.2	140°	131.4	110°	114.3	110°	110.0	120°
2	14.440	3.562	2115	2826	14.66	-4.9	137.7	140°	134.0	120°/130°	117.7	130°	113.7	130°/140°
3	14.439	2.543	1635	1170	12.11	-4.11	130.4	150°	127.7	110°	110.2	110°	105.6	110°
4	14.438	2.889	1801	2411	13.08	-4.4	131.8	150°	129.5	110°	112.1	110°	107.5	110°
5	14.435	2.435	1505	2038	12.20	-3.8	129.8	150°	126.8	110°	109.2	110°	104.5	110°

Table 43. Test Summary, 5.7" I.D. Conical Nozzle (Baseline).

- (Not) Corrected to Free Field
- Angle Referenced from Jet Axis, degrees

Model: 5.7" I.D. CONICAL NOZZLE (BASELINE)

Test Date(s): 8-17-73

Scale Factor: 8:1

Scale Model A_8 = 25.63 in^2

Full Scale A_8 = 11.391 ft^2

TEST CONDITIONS						FULL-SCALE ACOUSTIC TEST RESULTS								
							320-foot Arc		300-foot Sideline		1500-ft Sideline		2128-ft Sideline	
Rdg No.	P_o (psia)	P_{T8}/P_o	T_{T8} (° R)	Ideal V_j (ft/sec)	W_B (lb/sec)	10 Log ρA	Peak (PNdB)	Maximum Angle (degrees)	Peak (PNdB)	Maximum Angle (degrees)	Peak (PNdB)	Maximum Angle (degrees)	Peak (PNdB)	Maximum Angle (degrees)
1	14.49	1.48	1272	1279	7.6	-4.2	117.3	130°	115.4	130°	99.5	130°	95.7	130°
2	14.49	1.62	1335	1446	8.1	-4.3	121.2	140°/150°	119.2	130°	103.4	130°	99.6	130°
3	14.49	1.79	1400	1621	8.9	-4.4	126.8	140°	123.9	130°	108.2	130°	104.5	130°
4	14.49	1.98	1483	1794	9.6	-4.5	133.2	140°	129.7	140°	113.5	140°	109.7	140°
5	14.48	2.18	1538	1939	10.2	-4.5	136.7	140°	133.4	130°	117.1	130°	113.3	130°
6	14.48	2.38	1661	2115	10.7	-4.7	139.2	130°	137.3	130°	120.8	130°	116.9	130°
7	14.48	2.61	1714	2248	11.3	-4.6	141.5	130°	139.6	130°	123.0	130°	119.0	130°
8	14.48	2.98	1885	2497	12.4	-4.7	144.7	130°	142.8	130°	126.4	130°	122.6	130°

Table 44. Test Summary, 72-Tube Annular Plug Suppressor (Model 1).

- (Not) Corrected to Free Field
- Angle Referenced from Jet Axis, degrees

Model: 72-TUBE ANNULAR PLUG SUPPRESSOR (MODEL 1)

Scale Model A_8 = 30.8694 in^2

Test Date(s): 8-16-73

Scale Factor: 8:1

Full Scale A_8 = 13.7197 ft^2

TEST CONDITIONS						FULL-SCALE ACOUSTIC TEST RESULTS								
							320-foot Arc		300-foot Sideline		1500-ft Sideline		2128-ft Sideline	
Rdg No.	P_o (psia)	P_{T8}/P_o	T_{T8} (° R)	Ideal V_j (ft/sec)	W_B (lb/sec)	10 Log ρA	Peak (PNdB)	Maximum Angle (degrees)	Peak (PNdB)	Maximum Angle (degrees)	Peak (PNdB)	Maximum Angle (degrees)	Peak (PNdB)	Maximum Angle (degrees)
3	14.48	1.81	1368	1616	10.4	-3.5	123.7	110°/130°	123.8	110°	105.8	110°	101.0	110°
4	14.48	2.00	1464	1795	11.1	-3.6	126.7	110°	126.8	110°	108.7	110°	103.9	110°
5	14.48	2.19	1530	1942	11.8	-3.7	128.2	130°	128.1	110°	110.1	110°	105.4	110°
6	14.48	2.38	1655	2114	12.2	-3.9	129.0	130°	128.8	110°	111.0	110°	106.4	110°
7	14.48	2.62	1745	2272	12.9	-3.9	130.5	130°	129.7	110°	111.9	100°	107.4	100°
8	14.48	2.98	1871	2490	14.1	-3.9	1366	140°	130.9	110°	113.1	110°	108.5	110°
9	14.48	3.22	2033	2673	14.6	-4.0	132.7	130°	132.4	110°	114.8	110°	110.3	110°
10	14.48	3.51	2080	2790	15.8	-3.9	133.9	140°	133.2	110°	115.5	110°	110.9	110°
11	14.48	3.85	2190	2949	16.8	-3.8	134.9	130°/140°	133.9	110°	116.2	110°	111.6	110°
12	14.48	1.63	1328	1450	9.2	-3.4	122.3	110°	122.3	110°	104.3	110°	99.6	110°
13	14.48	1.47	1274	1270	8.4	-3.4	119.1	110°	119.1	110°	101.3	110°	96.6	110°

Table 45. Test Summary, 66-Tube Annular Plug Suppressor (Model 2).

- (Not) Corrected to Free Field
- Angle Referenced from Jet Axis, degrees

Model: 66-TUBE ANNULAR PLUG SUPPRESSOR (MODEL 2)

Scale Model A_8 = 31.3157 in^2

Test Date(s): 8-15-73

Scale Factor: 8:1

Full Scale A_8 = 13.9181 ft^2

TEST CONDITIONS						FULL-SCALE ACOUSTIC TEST RESULTS							
							320-foot Arc		300-foot Sideline		1500-ft Sideline		2128-ft Sideline	
Rdg No.	P_o (psia)	P_{T8}/P_o	T_{T8} (° R)	Ideal V_j (ft/sec)	W_B (lb/sec)	10 Log ρA	Peak (PNdB)	Maximum Angle (degrees)	Peak (PNdB)	Maximum Angle (degrees)	Peak (PNdB)	Maximum Angle (degrees)	Peak (PNdB)	Maximum Angle (degrees)
2	14.42	1.48	1219	1252	8.5	-3.1	119.4	110°	119.5	110°	101.4	110°	96.7	110°
3	14.42	1.63	1280	1421	3.7	-3.2	122.1	110°	122.2	110°	104.1	110°	99.4	110°
4	14.42	1.82	1315	1586	10.8	-3.2	124.6	130°	124.4	110°	106.4	110°	101.7	110°
5	14.42	1.99	1405	1753	11.8	-3.4	126.8	110°	126.8	110°	108.9	110°	104.1	110°
6	14.42	2.20	1489	1918	11.6	-3.5	128.9	130°	128.7	110°	110.5	110°	105.8	110°
7	14.42	2.39	1645	2112	12.8	-3.8	129.9	110°	129.9	110°	111.9	110°	107.1	110°
8	14.42	2.63	1720	2262	12.8	-3.8	131.1	130°	130.9	110°	113.1	110°	108.4	110°
9	14.42	2.98	1851	2478	13.5	-3.8	132.2	110°	132.4	110°	114.6	110°	109.9	110°
10	14.42	3.22	1935	2609	14.6	-3.8	133.6	110°	133.6	110°	115.9	110°	111.3	110°
11	14.42	3.52	2017	2750	15.6	-3.7	134.4	110°	134.4	110°	116.5	110°	111.9	110°
12	14.42	3.85	2154	2925	16.5	-3.7	134.9	110°/130°	134.9	110°	117.0	110°	112.5	110°
13	14.42	2.99	1883	2499	13.7	-3.8	133.1	110°	133.2	110°	115.1	110°	110.5	110°
14	14.42	2.21	1512	1941	11.6	-3.6	129.1	110°	129.1	110°	111.1	110°	106.4	110°
15	14.42	1.79	1386	1609	9.7	-3.5	125.5	110°	125.5	110°	107.4	110°	102.7	110°
16	14.42	1.47	1246	1259	8.4	-3.2	120.5	110°	120.5	110°	102.5	110°	97.7	110°
17	14.42	3.53	2108	2812	15.3	-3.9	134.4	110°	134.3	110°	116.7	110°	112.1	110°

Table 46. Test Summary, 66-Tube Annular Plug Suppressor with Hardwall Ejector No. 2 (Model 2).

- (Not) Corrected to Free Field
- Angle Referenced from Jet Axis, degrees

Model: 66-TUBE ANNULAR PLUG SUPPRESSOR WITH HARDWALL EJECTOR NO. 2 (MODEL 2)

Scale Model A_8 = 31.3157 in^2

Test Date(s): 5-13-74

Scale Factor: 8:1

Full Scale A_8 = 13.9181 ft^2

TEST CONDITIONS						FULL-SCALE ACOUSTIC TEST RESULTS								
							320-foot Arc		300-foot Sideline		1500-ft Sideline		2128-ft Sideline	
Rdg No.	P_o (psia)	P_{T8}/P_o	T_{T8} (° R)	Ideal V_j (ft/sec)	W_B (lb/sec)	10 Log ρA	Peak (PNdB)	Maximum Angle (degrees)	Peak (PNdB)	Maximum Angle (degrees)	Peak (PNdB)	Maximum Angle (degrees)	Peak (PNdB)	Maximum Angle (degrees)
1	14.41	1.49	1046	1174	9.3	-2.4	118.2	110°	118.3	110°	100.3	110°	95.5	110°
2	14.41	1.49	1149	1224	8.6	-2.8	118.8	110°	118.9	110°	101.0	110°	96.4	110°
4	14.41	1.80	1375	1613	9.4	-3.4	124.7	110°	124.7	110°	106.6	110°	101.8	110°
5	14.41	2.00	1440	1780	10.3	-3.4	127.6	110°	127.6	110°	109.0	110°	104.1	110°
6	14.40	2.45	1480	2026	12.4	-3.3	130.2	110°	130.3	110°	111.8	110°	107.0	110°
7	14.40	2.20	1542	1951	10.9	-3.6	129.6	110°	129.6	110°/120°	111.4	110°	106.7	110°
8	14.40	2.51	1609	2141	12.2	-3.7	131.2	110°	131.3	110°	113.1	110°	108.3	110°
9	14.40	2.40	1651	2119	11.5	-3.8	131.2	110°	131.3	110°	113.1	110°	108.3	110°
10	14.38	2.65	1793	2315	12.1	-4.1	132.2	110°	132.2	110°	114.0	110°	109.4	110°
11	14.37	2.98	1832	2465	13.6	-4.1	132.8	110°	132.8	110°	114.8	110°	110.0	110°
14	14.37	2.03	1327	1725	11.0	-3.1	127.3	110°	127.4	110°	108.9	110°	104.1	110°
15	14.37	3.25	1957	2631	14.6	-4.3	133.5	110°	133.5	110°	115.5	110°	110.8	110°
16	14.36	3.53	2068	2786	15.4	-4.4	134.2	110°	134.3	110°	116.0	110°	111.2	110°

Table 47. Test Summary, 66-Tube Annular Plug Suppressor with Treated Ejector No. 2 (Model 2).

- (Not) Corrected to Free Field
- Angle Referenced from Jet Axis, degrees

Model: 66-TUBE ANNULAR PLUG SUPPRESSOR WITH TREATED EJECTOR NO. 2 (MODEL 2)

Scale Model A_8 = 31.3157 in^2

Test Date(s): 8-5-74

Scale Factor: 8:1

Full Scale A_8 = 13.9881 ft^2

TEST CONDITIONS						FULL-SCALE ACOUSTIC TEST RESULTS								
							320-foot Arc		300-foot Sideline		1500-ft Sideline		2128-ft Sideline	
Rdg No.	P_o (psia)	P_{T8}/P_o	T_{T8} (° R)	Ideal V_j (ft/sec)	W_B (lb/sec)	10 Log ρA	Peak (PNdB)	Maximum Angle (degrees)	Peak (PNdB)	Maximum Angle (degrees)	Peak (PNdB)	Maximum Angle (degrees)	Peak (PNdB)	Maximum Angle (degrees)
3	14.46	1.99	1261	1661	11.7	-2.8	124.2	110°	124.2	110°	106.2	110°	101.5	110°
4	14.46	2.00	1479	1801	10.7	-3.5	125.5	110°	125.5	110°	102.6	110°	102.9	110°
5	14.46	2.39	1470	1996	12.8	-3.3	128.2	110°	128.2	110°	110.3	110°	105.5	110°
6	14.46	2.49	1528	2076	13.0	-3.4	128.9	110°	128.9	110°	111.0	110°	106.3	110°
8	14.45	2.96	1805	2437	13.9	-4.0	131.8	110°	131.8	110°	113.8	110°	109.1	110°
9	14.45	3.22	1866	2562	14.1	-4.0	132.0	110°	132.1	110°	114.3	110°	109.7	110°
10	14.45	3.54	2017	2756	15.5	-4.3	133.1	110°	133.1	110°	115.3	110°	110.7	110°
11	14.45	2.92	1751	2388	13.9	-3.9	131.3	110°	131.3	110°	113.5	110°	108.5	110°
12	14.45	2.54	1669	2193	12.5	-3.8	129.9	110°	129.9	110°	112.1	110°	107.4	110°
13	14.45	2.67	1707	2268	12.8	-3.8	130.4	110°	130.4	110°	112.6	110°	108.0	110°

Table 48. Test Summary, Unsuppressed 2-D Nozzle (Sideline Orientation).

- (Not) Corrected to Free Field
- Angle Referenced from Jet Axis, degrees

Model: UNSUPPRESSED 2-D NOZZLE (SIDELINE ORIENTATION)

Scale Model A_8 = 28.13 $in.^2$

Test Date(s): 1973 Scale Factor: 8:1

Full Scale A_8 = 12.5 ft^2

TEST CONDITIONS						FULL-SCALE ACOUSTIC TEST RESULTS									
							320-foot Arc		300-foot Sideline		1500-ft Sideline		2128-ft Sideline	
Rdg No.	P_o (psia)	P_{T8}/P_o	T_{T8} (° R)	Ideal V_j (ft/sec)	W_B (lb/sec)	10 Log ρA	Peak (PNdB)	Maximum Angle (degrees)	Peak (PNdB)	Maximum Angle (degrees)	Peak (PNdB)	Maximum Angle (degrees)	Peak (PNdB)	Maximum Angle (degrees)
1	14.48	1.47	1322	1298	8.4	-3.9	123.6	130°	121.7	130°	106.1	130°	102.4	130°
2	14.48	1.64	1394	1499	8.9	-4.1	127.3	130°	125.4	130°	109.7	130°	106.0	130°
3	14.48	1.80	1453	1656	9.4	-4.1	131.0	130°	129.2	130°	113.4	130°	109.7	130°
4	14.48	1.99	1541	1835	10.1	-4.3	134.5	130°	132.7	130°	116.8	130°	112.9	130°
5	14.48	2.21	1551	1961	11.1	-4.1	137.2	130°	135.3	130°	119.2	130°	115.5	130°
6	14.48	2.40	1626	2104	11.8	-4.2	139.1	130°	137.2	130°	121.0	130°	117.2	130°
7	14.48	2.63	1718	2262	12.4	-4.2	140.9	130°	139.1	130°	122.7	130°	118.8	130°
8	14.48	2.99	1786	2434	13.9	-4.1	143.0	130°	141.1	130°	124.8	130°	120.9	130°
9	14.48	2.98	1844	2472	13.6	-4.2	142.7	130°	140.8	130°	124.5	130°	120.6	130°
10	14.48	3.22	1935	2608	14.4	-4.2	143.6	130°	141.7	130°	125.3	130°	121.4	130°
11	14.48	3.50	2046	2764	15.3	-4.2	142.7	120	142.1	110°	125.7	120°	121.8	120°

Table 49. Test Summary, Unsuppressed 2-D Over-the-Wing Nozzle with Sidewalls (Sideline Orientation).

- (Not) Corrected to Free Field
- Angle Referenced from Jet Axis, degrees

Model: UNSUPPRESSED 2-D OVER-THE-WING NOZZLE SIDEWALLS (SIDELINE ORIENTATION) Scale Model A_8 = 28.13 in.^{2}

Test Date(s): 1973 Scale Factor: 8:1 Full Scale A_8 = 12.5 ft^2

TEST CONDITIONS						FULL-SCALE ACOUSTIC TEST RESULTS									
							320-foot Arc		300-foot Sideline		1500-ft Sideline		2128-ft Sideline	
Rdg No.	P_o (psia)	P_{T8}/P_o	T_{T8} (° R)	Ideal V_j (ft/sec)	W_B (lb/sec)	10 Log ρA	Peak (PNdB)	Maximum Angle (degrees)	Peak (PNdB)	Maximum Angle (degrees)	Peak (PNdB)	Maximum Angle (degrees)	Peak (PNdB)	Maximum Angle (degrees)
12	14.48	2.65	1651	2223	13.0	-4.0	137.3	120°	136.6	120°	120.4	120°	116.6	120°
13	14.48	2.97	1808	2444	13.8	-4.1	140.1	120°	139.4	120°	123.1	120	119.2	120°
14	14.48	2.98	1849	2476	13.8	-4.2	1400	120°	139.3	120°	122.9	120°	119.1	120°
15	14.48	3.24	1904	2592	14.7	-4.1	143.9	130	141.9	130°	125.6	130°	121.7	130°
15	14.48	2.98	1732	2395	14.3	-3.9	142.5	130°	140.6	130°	124.2	130°	120.3	130°

Table 50. Test Summary, Unsuppressed 2-D Over-the-Wing Nozzle with Sidewalls and Wing (Flush-Mounted - Sideline Orientation).

• (Not) Corrected to Free Field

• Angle Referenced from Jet Axis, degrees

Model: UNSUPPRESSED 2-D OVER-THE-WING NOZZLE WITH SIDEWALLS AND WING (FLUSH MOUNTED) (SIDELINE ORIENTATION)

Test Date(s): 1973

Scale Factor: 8:1

Scale Model A_8 = 28.13 in.^{2}

Full Scale A_8 = 12.5 ft^2

TEST CONDITIONS						FULL-SCALE ACOUSTIC TEST RESULTS								
							320-foot Arc		300-foot Sideline		1500-ft Sideline		2128-ft Sideline	
Rdg No.	P_o (psia)	P_{T8}/P_o	T_{T8} (° R)	Ideal V_j (ft/sec)	W_B (lb/sec)	10 Log PA	Peak (PNdB)	Maximum Angle (degrees)	Peak (PNdB)	Maximum Angle (degrees)	Peak (PNdB)	Maximum Angle (degrees)	Peak (PNdB)	Maximum Angle (degrees)
1	14.49	1.49	1285	1291	8.6	-3.8	115.1	130°	113.2	130°	97.4	130°	93.7	130°
2	14.49	1.65	1325	1463	9.1	-3.8	119.7	130°	117.9	130°	102.2	130°	98.5	130°
3	14.49	1.80	1427	1641	9.6	-4.1	124.3	130°	122.4	130°	107.1	130°	103.5	130°
4	14.49	2.00	1336	1710	10.5	-3.6	130.2	130°	128.4	130°	113.1	130°	109.6	130°
5	14.49	2.20	1564	1965	11.4	-4.2	130.6	130°	128.7	130°	112.9	130°	109.2	130°
6	14.49	2.41	1629	2109	11.9	-4.2	133.8	130°	131.9	130°	116.0	130°	112.2	130°
7	14.49	2.64	1747	2282	12.5	-4.3	136.6	130°	134.7	130°	118.7	130°	114.9	130°
8	14.49	2.99	1774	2426	14.5	-4.0	141.3	130°	136.6	140°	120.3	140°	116.4	140°
9	14.49	2.97	1860	2479	13.6	-4.3	139.2	130°	137.3	130°	121.1	130°	117.3	130°
10	14.49	3.24	1927	2609	14.6	-4.2	140.7	130°	138.8	130°	122.6	130°	118.7	130°
11	14.49	3.51	2065	2779	16.7	-4.3	142.6	130°	140.7	130°	124.3	130°	120.3	130°

Table 51. Test Summary, Unsuppressed 2-D Over-the-Wing Nozzle with Sidewalls and Ejector, No Wing (Sideline Orientation).

- (Not) Corrected to Free Field
- Angle Referenced from Jet Axis, degrees

Model: UNSUPPRESSED 2-D OVER-THE-WING NOZZLE WITH SIDEWALLS AND EJECTOR, NO WING (SIDELINE, ORIENTATION)

Scale Model A_8 = 28.13 in.^{2}

Test Date(s): 1973

Scale Factor: 8:1

Full Scale A_8 = 12.5 ft^2

TEST CONDITIONS						FULL-SCALE ACOUSTIC TEST RESULTS								
							320-foot Arc		300-foot Sideline		1500-ft Sideline		2128-ft Sideline	
Rdg No.	P_o (psia)	P_{T8}/P_o	T_{T8} (° R)	Ideal V_j (ft/sec)	W_B (lb/sec)	10 Log pA	Peak (PNdB)	Maximum Angle (degrees)	Peak (PNdB)	Maximum Angle (degrees)	Peak (PNdB)	Maximum Angle (degrees)	Peak (PNdB)	Maximum Angle (degrees)
1	14.41	1.49	1287	1298	8.8	-3.8	120.7	130°	119.1	120°	103.8	120°	100.2	120°
2	14.41	1.66	1316	1466	9.5	-3.8	123.8	130°	122.1	120°	106.8	120°	103.2	120°
3	14.41	1.8	1418	1637	9.8	-4.1	130.0	130°	128.2	130°	128.2	130°	109.3	130°
4	14.41	2.01	1483	1812	10.7	-4.1	131.6	130°	129.8	130°	114.2	130°	110.5	140°
5	14.41	2.21	1560	1971	11.3	-4.2	134.4	130°	132.6	120°	116.8	130°	113.2	130°
6	14.41	2.42	1632	2115	12.1	-4.2	135.3	140°	133.2	130°	117.3	130°	113.6	130°
7	14.41	2.65	1745	2286	12.8	-4.3	136.8	130°	135.3	120°	119.3	120°	115.5	120°
8	14.40	3.00	1654	2345	15.3	-3.7	138.9	130°	137.3	120°	121.2	120°	117.3	120°
9	14.40	3.01	1859	2491	15.4	-4.2	138.9	120°	138.2	120°	122.0	120°	118.2	120°
10	14.40	3.25	1942	2621	14.6	-4.2	140.2	120°	139.4	120°	123.3	120°	119.4	120°
11	14.40	3.52	2068	2784	15.4	-4.3	141.4	120°	140.7	120°	124.4	120°	120.6	120°
12	14.39	2.65	1769	2302	12.6	-4.3	133.2	150°	130.5	120°	114.6	120°	110.8	120°
13	14.39	3.00	1835	2468	13.9	-4.2	136.3	150°	133.4	120°	117.4	120°	113.6	120°

Table 52. Test Summary, Unsuppressed 2-D Nozzle, No Wing (Flyover Position).

- (Not) Corrected to Free Field
- Angle Referenced from Jet Axis, degrees

Model: UNSUPPRESSED 2-D NOZZLE - NO WING (FLYOVER POSITION)

Test Date(s): 1973

Scale Factor: 8:1

Scale Model A_8 = 28.13 $in.^2$

Full Scale A_8 = 12.5 ft^2

TEST CONDITIONS						FULL-SCALE ACOUSTIC TEST RESULTS								
							320-foot Arc		300-foot Sideline		1500-ft Sideline		2128-ft Sideline	
Rdg No.	P_o (psia)	P_{T8}/P_o	T_{T8} (° R)	Ideal V_j (ft/sec)	W_8 (lb/sec)	10 Log ρA	Peak (PNdB)	Maximum Angle (degrees)	Peak (PNdB)	Maximum Angle (degrees)	Peak (PNdB)	Maximum Angle (degrees)	Peak (PNdB)	Maximum Angle (degrees)
1	14.36	1.5	1288	1307	8.6	-3.8	119.4	130°	118.9	100°	103.3	120°	99.7	120°
2	14.36	1.66	1328	1474	9.4	-3.9	122.4	120°	121.8	110°	106.2	120°	102.5	120°
3	14.36	1.81	1411	1637	9.7	-4.0	126.8	120°	126.1	120°	110.6	120°	106.9	120°
4	14.36	2.0	1491	1816	10.8	-4.2	132.1	120°	131.4	120°	115.7	120°	111.9	120°
5	14.37	2.22	1547	1965	11.3	-4.1	135.5	120°	134.8	120°	118.9	120°	115.1	120°
6	14.37	2.41	1653	2125	11.8	-4.3	138.1	110°	138.1	110°	121.7	110°	117.8	110°
7	14.37	2.66	1765	2301	12.6	-4.3	140.6	110°	140.6	110°	124.2	110°	120.3	110°
8	14.37	3.01	1628	2329	14.8	-3.7	142.1	110°	142.1	110°	125.5	110°	121.6	110°
9	14.37	3.02	1858	2493	13.9	-4.2	141.7	[illegible]	141.7	110°	125.2	110°	121.2	110°
10	14.37	3.24	1952	2625	14.6	-4.3	142.9	110°	142.9	110°	126.4	110°	122.5	110°
11	14.37	3.53	2077	2791	15.4	-4.3	144.0	110°	144.0	110°	127.6	110°	123.6	110°

Table 53. Test Summary, Unsuppressed 2-D Nozzle with Wing at y/h ~ 1 (Flyover Position).

- (Not) Corrected to Free Field
- Angle Referenced from Jet Axis, degrees

Model: UNSUPPRESSED 2-D NOZZLE WITH WING AT y/h~1 (FLYOVER POSITION) Scale Model A_8 = 28.13 in.^{2}

Test Date(s): 1973 Scale Factor: 8:1 Full Scale A_8 = 12.5 ft^2

TEST CONDITIONS						FULL-SCALE ACOUSTIC TEST RESULTS								
							320-foot Arc		300-foot Sideline		1500-ft Sideline		2128-ft Sideline	
Rdg No.	P_o (psia)	P_{T8}/P_o	T_{T8} (° R)	Ideal V_j (ft/sec)	W_B (lb/sec)	10 Log ρA	Peak (PNdB)	Maximum Angle (degrees)	Peak (PNdB)	Maximum Angle (degrees)	Peak (PNdB)	Maximum Angle (degrees)	Peak (PNdB)	Maximum Angle (degrees)
1	–	–	–	–	–	–	–	–	–	–	–	–	–	–
2	14.45	1.64	1315	1454	9.4	-3.8	114.9	130°	113.1	130°	97.6	130°	93.9	130°
3	14.45	1.79	1435	1640	9.0	-4.1	118.4	130°	116.6	130°	101.1	130°	97.5	130°
4	14.45	2.00	1488	1806	10.6	-4.1	122.1	130°	120.3	130°	104.9	130°	101.3	130°
5	14.45	2.21	1578	1979	10.6	-4.2	125.9	130°	124.0	130°	108.6	130°	104.9	130°
6	14.45	2.41	1666	2131	12.4	-4.3	129.4	130°	127.5	130°	111.9	130°	108.2	130°
7	14.45	2.64	1769	2297	13.6	-4.3	133.3	130°	131.5	130°	115.7	130°	111.9	130°
8	14.45	2.99	1659	2348	15.0	-3.8	135.2	130°	133.3	130°	117.4	130°	113.7	130°
9	14.45	2.99	1846	2476	14.1	-4.2	136.5	130°	134.6	130°	118.6	130°	114.8	130°
10	14.45	3.24	1930	2610	14.9	-4.2	138.6	130°	136.7	130°	120.6	130°	116.8	130°
11	14.45	3.51	2062	2775	15.7	-4.3	140.2	130°	138.6	120°	122.4	120°	118.6	120°
12	14.45	1.48	1287	1284	8.7	-3.8	112.2	130°	110.3	130°	94.8	130°	91.0	130°

Table 54. Test Summary, Unsuppressed 2-D Nozzle with Wing (Flush) at y/h = 0 (Flyover Position).

- (Not) Corrected to Free Field
- Angle Referenced from Jet Axis, degrees

Model: UNSUPPRESSED 2-D NOZZLE WITH WING (FLUSH) AT y/h = 0 (FLYOVER POSITION)

Scale Model A_8 = 28.13 in.^{2}

Test Date(s): 1973

Scale Factor: 8:1

Full Scale A_8 = 12.5 ft^2

TEST CONDITIONS						FULL-SCALE ACOUSTIC TEST RESULTS									
							320-foot Arc		300-foot Sideline		1500-ft Sideline		2128-ft Sideline	
Rdg No.	P_o (psia)	P_{T8}/P_o	T_{T8} (° R)	Ideal V_j (ft/sec)	W_B (lb/sec)	10 Log ρA	Peak (PNdB)	Maximum Angle (degrees)	Peak (PNdB)	Maximum Angle (degrees)	Peak (PNdB)	Maximum Angle (degrees)	Peak (PNdB)	Maximum Angle (degrees)
1	14.44	1.49	1293	1295	8.7	-3.8	112.2	130°	110.3	130°	94.5	130°	90.6	130°
2	14.44	1.64	1315	1456	9.3	-3.8	115.0	130°	113.2	130°	97.5	130°	93.7	130°
3	14.44	1.80	1425	1638	9.8	-4.1	118.5	130°	116.6	130°	101.0	130°	97.3	130°
4	14.44	2.01	1474	1803	10.8	-4.1	122.6	130°	120.7	130°	105.1	130°	101.4	130°
5	14.44	2.20	1546	1956	11.5	-4.1	127.3	130°	125.4	130°	109.6	130°	105.9	130°
6	14.44	2.41	1637	2114	12.1	-4.2	131.5	130°	129.6	130°	113.6	130°	109.8	130°
7	14.44	2.65	1742	2283	12.9	-4.3	134.9	130°	133.3	120°	117.2	120°	113.4	120°
8	14.44	2.99	1655	2343	14.9	-3.7	137.4	130°	135.6	120°	119.4	120°	115.5	120°
9	14.43	3.00	1845	2479	14.1	-4.2	138.4	130°	136.8	120°	120.5	120°	116.5	120°
10	14.43	3.23	1945	2617	14.8	-4.2	139.3	130°	138.5	120°	122.1	120°	118.2	120°
11	14.43	3.51	2064	2778	15.7	-4.3	141.1	120°	140.3	120°	123.9	120°	119.9	120°

Table 55. Test Summary, Suppressed 2-D Nozzle with Wing at y/h ≈ 1 (Flyover Position).

- (Not) Corrected to Free Field
- Angle Referenced from Jet Axis, degrees

Model: SUPPRESSED 2-D NOZZLE WITH WING AT Y/h≈1 (FLYOVER POSITION)

Scale Model A_8 = 28.13 in.^{2}

Test Date(s): 1973

Scale Factor: 8:1

Full Scale A_8 = 12.5 ft^2

TEST CONDITIONS						FULL-SCALE ACOUSTIC TEST RESULTS								
							320-foot Arc		300-foot Sideline		1500-ft Sideline		2128-ft Sideline	
Rdg No.	P_o (psia)	P_{T8}/P_o	T_{T8} (° R)	Ideal V_j (ft/sec)	W_B (lb/sec)	10 Log ρA	Peak (PNdB)	Maximum Angle (degrees)	Peak (PNdB)	Maximum Angle (degrees)	Peak (PNdB)	Maximum Angle (degrees)	Peak (PNdB)	Maximum Angle (degrees)
1	14.50	1.48	657	918	14.0	-0.7	116.3	150°	111.9	130°	93.9	130°	89.0	130°
2	14.49	2.01	644	1193	18.9	-0.3	109.8	140°	107.9	120°	90.0	120°	85.6	120°
3	14.49	2.95	579	1377	27.8	1.0	114.8	150°	113.7	120°	98.1	120°	94.3	120°
4	14.49	1.48	1230	1254	9.4	-3.5	113.8	150°	111.5	120°	93.9	120°	89.1	120°
5	14.49	1.65	1253	1424	11.0	-3.4	112.9	150°	109.7	120°	93.0	120°	89.0	120°
6	14.49	1.80	1350	1592	11.4	-3.7	113.6	150°	111.9	120°	96.0	120°	92.1	120°
7	14.49	2.00	1432	1773	11.5	-3.8	115.8	120°	115.1	120°	99.5	120°	95.8	120°
8	14.49	2.20	1483	1913	12.4	-3.8	118.2	120°	117.5	120°	102.1	120°	98.6	120°
9	14.49	2.40	1577	2070	12.9	-3.9	120.9	120°	120.3	120°	104.9	120°	101.3	120°

Table 56. Test Summary, Suppressed 2-D Nozzle with Wing (Flush) at y/h = 0 (Flyover Position).

- (Not) Corrected to Free Field
- Angle Referenced from Jet Axis, degrees

Model: SUPPRESSED 2-D WITH WING (FLUSH) AT y/h = 0 (FLYOVER POSITION)

Scale Model A_8 = 28.13 in.^{2}

Test Date(s): 1973

Scale Factor: 8:1

Full Scale A_8 = 12.5 ft^2

TEST CONDITIONS						FULL-SCALE ACOUSTIC TEST RESULTS								
							320-foot Arc		300-foot Sideline		1500-ft Sideline		2128-ft Sideline	
Rdg No.	P_o (psia)	P_{T8}/P_o	T_{T8} (° R)	Ideal V_j (ft/sec)	W_B (lb/sec)	10 Log ρA	Peak (PNdB)	Maximum Angle (degrees)	Peak (PNdB)	Maximum Angle (degrees)	Peak (PNdB)	Maximum Angle (degrees)	Peak (PNdB)	Maximum Angle (degrees)
1	14.48	1.49	1214	1257	9.3	-3.4	112.9	130°	112.1	110°	94.5	110°	89.8	110°
2	14.48	1.65	1278	1438	10.1	-3.5	111.7	130°	110.3	120°	92.9	120°	88.3	110°
3	14.47	1.79	1369	1598	10.4	-3.7	112.7	130°	112.2	110°	94.9	110°	90.7	120°
4	14.47	1.98	1426	1760	11.2	-3.8	115.5	130°	113.7	120°	97.9	120°	94.1	120°
5	14.47	2.20	1496	1923	12.2	-3.8	118.2	130°	116.5	120°	100.9	120°	92.2	120°
6	14.47	2.39	1556	2052	12.9	-3.8	121.5	130°	119.7	130°	1043	120°	100.7	130°

Table 57. Test Summary, Suppressed 2-D Nozzle, No Wing (Flyover Position).

- (Not) Corrected to Free Field
- Angle Referenced from Jet Axis, degrees

Model: SUPPRESSED 2-D NOZZLE, NO WING (FLYOVER POSITION)

Scale Model A_8 = 28.13 in.^{2}

Test Date(s): 1973

Scale Factor: 8:1

Full Scale A_8 = 12.5 ft^2

TEST CONDITIONS						FULL-SCALE ACOUSTIC TEST RESULTS								
							320-foot Arc		300-foot Sideline		1500-ft Sideline		2128-ft Sideline	
Rdg No.	P_o (psia)	P_{T8}/P_o	T_{T8} (° R)	Ideal V_j (ft/sec)	W_B (lb/sec)	10 Log ρA	Peak (PNdB)	Maximum Angle (degrees)	Peak (PNdB)	Maximum Angle (degrees)	Peak (PNdB)	Maximum Angle (degrees)	Peak (PNdB)	Maximum Angle (degrees)
1	14.46	1.49	1232	1264	9.2	-3.5	126.6	110°	126.6	110°	108.3	110°	103.4	110°
2	14.46	1.64	1263	1423	10.0	-3.5	123.0	110°	123.1	110°	104.4	110°	99.3	110°
3	14.46	1.79	1370	1597	10.4	-3.7	123.7	110°	123.7	110°	105.3	110°	100.4	110°
4	14.46	1.99	1434	1766	11.2	-3.8	123.6	110°	123.6	110°	106.9	120°	103.3	120°
5	14.46	2.20	1511	1933	12.1	-3.9	1255	120°	124.8	120°	109.4	120°	105.8	120°
6	14.46	2.38	1574	2062	12.2	-3.9	130.9	120°	130.5	110°	115.0	120°	111.5	120°
7	14.46	2.65	1674	2237	13.6	-3.9	134.9	110°	118.9	110°	115.2	110°	115.2	110°
8	14.45	2.99	1580	2291	15.9	-3.4	135.6	120°	134.8	120°	118.6	120°	114.7	120°
9	14.45	2.98	1774	2424	14.9	-3.9	1368	120°	136.0	120°	119.8	120°	115.9	120°

Table 58. Test Summary, Dual-Flow Exhaust Nozzle, Core and Fan.

A_{Core} = 17.856 in.^{2} (1143 in.^{2})

A_{Fan} = 13.52 in.^{2} (865 in.^{2})

- Not corrected for free field
- Angles from inlet

Test Date: 10-3-73

Scale Factor: 8:1

	TEST CONDITIONS										ACOUSTIC TEST RESULTS								
	CORE					FAN						320-ft Arc		300-ft SL		1500-ft SL		2128-ft SL	
Reading	P_o	P_{T8}/P_o	T_{T8}	V_C	W_8	P_o	P_{T18}/P_o	T_{T18}	V_F	W_{18}	10 Log ρA	Peak PNdB	Max. Angle (°)	Peak PNdB	Max. Angle (°)	Peak PNdB	Max. Angle (°)	Peak PNdB	Max. Angle (°)
11	14.46	1.09	1210	595	2.2	---	---	---	---	---	-5.8	99.6	40	96.7	110	78.9	110	74.5	110
12	14.46	1.51	1467	1400	4.6	---	---	---	---	---	-6.3	117.7	120	118.1	80	100.6	100	96.1	100
13	14.46	1.76	1607	1705	5.2	---	---	---	---	---	-6.5	123.5	110	123.5	110	105.8	110	101.3	110
14	14.46	2.31	1599	2031	7.1	---	---	---	---	---	-6.2	126.2	110	126.3	110	108.9	110	104.3	110
15	14.43	3.00	1609	2294	8.9	---	---	---	---	---	-5.9	130.3	140	127.5	{110 / 130}	111.7	130	107.9	130
16	14.44	3.48	1604	2418	10.5	---	---	---	---	---	-5.7	135.5	140	131.9	140	115.7	140	111.8	140
21	---	---	---	---	---	14.40	1.21	626	636	3.6	-4.0	98.5	150	97.5	110	81.1	110	76.9	110
23	---	---	---	---	---	14.40	2.36	771	1420	7.7	-4.1	122.5	{110 / 150}	122.6	110	104.7	110	100.4	110
25	---	---	---	---	---	14.41	3.00	799	1610	10.9	-4.0	124	60	124	90	106.9	90	102.4	90

Table 59. Test Summary, Dual-Flow Exhaust Nozzle, Core and Fan, A_8/A_{18} = 1.32.

A_{Core} = 17.856 in.^{2} (7.936 ft^2)

A_{Fan} = 13.52 in.^{2} (6.009 ft^2)

- Not corrected for free field
- Angles from inlet

A_8/A_{18} = 1.32

Test Date: 10-4-73

Scale Factor: 8:1

	TEST CONDITIONS										ACOUSTIC TEST RESULTS								
	CORE					FAN						320-ft Arc		300-ft SL		1500-ft SL		2128-ft SL	
Reading	P_o	P_{T8}/P_o	T_{T8}	V_C	W_8	P_o	P_{T18}/P_o	T_{T18}	V_F	W_{18}	10 Log ρA	Peak PNdB	Max. Angle (°)	Peak PNdB	Max. Angle (°)	Peak PNdB	Max. Angle (°)	Peak PNdB	Max. Angle (°)
32	14.43	1.49	1466	1384	5.0	14.43	1.95	756	1255	7.3	-2.2	121.5	110	121.5	110	103.7	110	99.1	110
33	14.43	1.77	1612	1712	5.9	14.43	2.36	758	1409	8.7	-2.3	124.7	110	124.7	110	107.2	110	102.7	110
34	14.43	2.30	1598	2029	7.6	14.43	2.76	807	1564	9.4	-2.2	127.0	110	127.1	110	109.4	110	104.8	110
35	14.42	3.00	1604	2293	9.2	14.43	3.01	803	1615	10.0	-2.1	129.5	{140 150}	127.1	110	110.9	130	107.2	130
36A	14.42	3.49	1605	2422	10.2	14.42	3.49	798	1698	11.1	-1.9	134	150	130.9	130	115.1	130	111.4	130
36	14.40	3.48	1599	2413	10.1	14.40	3.01	803	1615	10.0	-2.0	132.9	140	130.1	130	114.4	130	110.7	130
37	14.40	1.79	556	1011	10.4	14.40	3.50	791	1692	11.2	.2	127.1	80	128	110	110.1	80	105.4	80
38	14.41	1.39	696	867	6.6	14.41	3.50	799	1701	11.1	-0.3	127.4	110	127.4	110	109.5	80	104.9	80
39	14.41	1.64	762	1101	8.0	14.41	3.49	805	1768	10.7	-0.6	127.8	110	127.8	110	109.8	80	105.2	80
40	14.41	1.57	1005	1207	6.6	14.41	3.49	791	1690	11.1	-1.0	127.7	110	127.8	110	109.8	80	105.1	80
41	14.41	1.53	1230	1305	5.7	14.41	3.50	797	1698	11.1	-1.4	127.6	110	127.9	80	110.5	80	105.8	80
42	14.42	1.49	1466	1379	5.0	14.42	3.49	794	1694	11.1	-1.7	127.7	110	127.8	110	110.5	80	105.8	80
43	14.42	1.76	1611	1707	5.9	14.42	3.49	803	1704	11.1	-2.9	127.5	150	127.7	80	110.3	80	105.7	80

Table 60. Test Summary, Dual-Flow Exhaust Nozzle, Suppressed Core Flow, A_{Core} = 17.856 in.^{2}.

A_{Core} = 17.856 in.^{2} (1142.8 in.^{2})

Test Date: 4-2-74 & 4-10-74

Scale Factor: 8:1

Reading	TEST CONDITIONS										ACOUSTIC TEST RESULTS								
	CORE					FAN						320-ft Arc		300-ft SL		1500-ft SL		2128-ft SL	
	P_o	P_{T8}/P_o	T_{T8}	V_C	W_8	P_o	P_{T18}/P_o	T_{T18}	V_F	W_{18}	10 Log ΔA	Peak PNdB	Max. Angle (°)	Peak PNdB	Max. Angle (°)	Peak PNdB	Max. Angle (°)	Peak PNdB	Max. Angle (°)
4/2/74																			
15	14.35	1.19	1388	903	---	---	---	---	---	---	-6.3	108.2	120	107.9	110	90.0	110	85.2	110
16	14.35	1.51	1470	1403	---	---	---	---	---	---	-6.3	119.8	110	119.8	110	110.8	110	97.1	110
17	14.35	1.77	1613	1715	---	---	---	---	---	---	-6.6	123.8	120	123.5	110	105.6	110	100.9	110
18	14.35	2.31	1618	2047	---	---	---	---	---	---	-6.3	127.1	140	125.8	110	108.4	110	103.8	110
First Reading 20	14.34	3.02	1614	2305	---	---	---	---	---	---	-5.9	133.0	140	129.8	130	113.7	130	109.8	130
Rerun 20	14.32	3.02	1614	2305	---	---	---	---	---	---	---	132.0	140	129.3	130	112.9	130	109.1	130
21	14.35	3.52	1605	2428	---	---	---	---	---	---	-5.7	137.6	140	134.1	130	117.7	130	113.8	130
4/10/74																			
15	14.56	1.18	1385	879	---	---	---	---	---	---	-6.3	107.8	110	107.8	110	89.8	110	85.0	110
17	14.56	1.76	1602	1699	---	---	---	---	---	---	-6.5	124.5	130	124.3	110	106.1	110	101.4	110
19	14.56	2.64	1599	2172	---	---	---	---	---	---	-6.0	128.6	140	126.9	120	109.9	130	105.9	130
21	14.56	3.45	1606	2412	---	---	---	---	---	---	-5.7	136.9	140	133.5	130	117.1	130	113.3	130

Table 61. Test Summary, Dual-Flow Noncoplanar Exhaust Nozzle, Suppressed Core, Unsuppressed Fan, A_8/A_{18} = 1.0.

A_{Core} = 17.856 in.^{2} (1142.8 in.^{2})

A_{Fan} = 17.856 in.^{2} (1142.8 in.^{2})

- Suppressed Core
- Unsuppressed Fan

A_8/A_{18} = 1.0

Test Date: 4-2-74

Scale Factor: 8:1

	TEST CONDITIONS										ACOUSTIC TEST RESULTS								
	CORE					FAN						320-ft Arc		300-ft SL		1500-ft SL		2128-ft SL	
Reading	P_o	P_{T8}/P_o	T_{T8}	V_C	W_8	V_F/V_C	P_{T18}/P_o	T_{T18}	V_F	W_{18}	10 Log ρA	Peak PNdB	Max. Angle (°)	Peak PNdB	Max. Angle (°)	Peak PNdB	Max. Angle (°)	Peak PNdB	Max. Angle (°)
22	14.35	1.19	1384	903	---	1.05	1.50	689	950	---	-1.4	115.2	140	112.3	130	95.8	130	91.8	130
23	14.35	1.51	1480	1404	---	.89	1.95	743	1245	---	-1.4	122.3	110	122.3	110	104.1	110	99.3	110
24	14.35	1.78	1611	1723	---	.82	2.37	765	1417	---	-1.4	124.9	110	125.3	80	107.0	110	102.3	110
25	14.35	2.29	1616	2037	---	.75	2.74	781	1532	---	-1.3	132.8	150	130.0	130	113.1	130	108.9	130
26	14.35	2.68	1608	2189	---	.74	2.99	813	1621	---	-1.4	130.9	150	129.6	80	111.8	80	107.1	80
27	14.35	3.00	1627	2308	---	.70	2.99	814	1623	---	-1.3	133.1	150	129.9	130	113.2	130	109.2	130
28	14.34	3.02	1606	2300	---	.74	3.49	812	1713	---	-1.1	136.7	150	131.3	110	114.3	130	110.3	130
29	14.34	3.52	1616	2436	---	.70	3.50	813	1714	---	-1.1	137.8	150	134.1	140	117.4	140	113.5	140
30	14.34	1.73	1595	1675	---	1.02	3.49	815	1716	---	-1.2	132.6	140	132.5	80	114.0	80	109.3	80

Table 62. Test Summary, Dual-Flow Noncoplanar Exhaust Nozzle, Suppressed Core, Unsuppressed Fan, A_8/A_{18} = 1.5.

A_{Core} = 17.856 in.^{2} (1142.8 in.^{2})

A_{Fan} = 11.904 in.^{2} (761.8 in.^{2})

- Suppressed Core
- Unsuppressed Fan

A_8/A_{18} = 1.5

Test Date: 4-10-74

Scale Factor: 8:1

	TEST CONDITIONS										ACOUSTIC TEST RESULTS								
	CORE					FAN						320-ft Arc		300-ft SL		1500-ft SL		2128-ft SL	
Reading	P_o	P_{T8}/P_o	T_{T8}	V_C	W_8	V_F/V_C	P_{T18}/P_o	T_{T18}	V_F	W_{18}	10 Log ρA	Peak PNdB	Max. Angle (°)	Peak PNdB	Max. Angle (°)	Peak PNdB	Max. Angle (°)	Peak PNdB	Max. Angle (°)
22	14.56	1.19	1370	894	1.03	1.10	1.49	745	981	---	-2.6	112.6	140	110.9	110	93.6	110	89.4	110
23	14.56	1.49	1455	1373	.88	.90	1.94	732	1232	---	-2.4	120.7	110	120.8	110	102.8	110	98.1	110
24	14.55	1.74	1611	1691	.83	.84	2.36	770	1418	---	-2.5	124.4	110	124.4	110	106.5	110	101.8	110
25	14.55	2.28	1609	2027	.77	.77	2.75	806	1560	---	-2.4	127.9	150	126.5	80	108.7	110	104.2	110
26	14.55	2.62	1607	2168	.74	.75	2.99	811	1619	---	-2.3	129.7	150	127.9	80	109.8	130	105.9	130
27	14.54	2.95	1603	2278	.70	.71	2.98	820	1626	---	-2.3	132.1	150	128.7	130	112.5	130	108.7	130
28	14.54	2.96	1595	2275	.74	.75	3.48	805	1705	---	-2.1	133.5	150	130.1	80	113.0	130	109.1	130
29	14.54	3.46	1605	2414	.70	.71	3.48	817	1717	---	-2.1	133.5	150	130.1	80	113.0	130	109.1	130
30	14.54	1.74	1607	1687	1.00	1.01	3.49	807	1707	---	-2.3	132.0	140	130.3	80	112.4	80	107.7	80

Table 63. Test Summary, Dual-Flow Coplanar Exhaust Nozzle, Suppressed Core, Unsuppressed Fan, A_8/A_{18} = 1.5.

A_{Core} = 17.856 in.^{2} (1142.8 in.^{2})

A_{Fan} = 11.904 in.^{2} (761.86 in.^{2})

- Suppressed Core
- Unsuppressed Fan

A_8/A_{18} = 1.5

Test Date: 4-10-74

Scale Factor: 8:1

	TEST CONDITIONS										ACOUSTIC TEST RESULTS								
	CORE					FAN						320-ft Arc		300-ft SL		1500-ft SL		2128-ft SL	
Reading	P_o	P_{T8}/P_o	T_{T8}	V_C	W_8	V_F/V_C	P_{T18}/P_o	T_{T18}	V_F	W_{18}	10 Log ρA	Peak PNdB	Max. Angle (°)	Peak PNdB	Max. Angle (°)	Peak PNdB	Max. Angle (°)	Peak PNdB	Max. Angle (°)
22	14.53	1.19	1368	892	---	1.10	1.49	739	980	---	-2.6	110.2	120	110.0	110	92.6	110	88.0	110
23	14.53	1.48	1469	1366	---	.88	1.94	700	1204	---	-2.3	120.9	120	120.6	110	102.9	110	98.3	110
24	14.52	1.72	1614	1678	---	.85	2.35	781	1425	---	-2.5	125.4	110	125.7	80	107.4	110	102.7	110
25	14.52	2.28	1604	2020	---	.77	2.74	796	1547	---	-2.4	128.3	120	128.7	80	110.3	80	105.4	80
26	14.52	2.62	1604	2168	---	.74	2.98	798	1604	---	-2.3	129.7	150	129.6	80	111.6	80	106.7	80
27	14.52	2.95	1607	2279	---	.70	2.98	797	1603	---	-2.3	132.2	140	129.8	80	112.9	130	109.1	130
28	14.52	3.00	1603	2278	---	.74	3.44	799	1690	---	-2.1	133.9	150	131.5	80	113.8	130	109.8	130
29	14.52	3.44	1604	2410	---	.70	3.47	786	1682	---	-2.0	137.8	150	133.9	140	117.4	140	113.5	130 140
30	14.52	1.73	1595	1673	---	1.02	3.47	807	1705	---	-2.3	130.9	80	131.5	80	113.5	80	108.7	80

Table 64. Test Summary, Unsuppressed 2-D Over-the-Wing Exhaust Nozzle.

- (Not) Corrected to Free Field
- Angle Referenced from Jet Axis, degrees

Model: UNSUPPRESSED 2-D OVER-THE-WING NOZZLE

Test Date(s): 11-22-74

Scale Factor: 8:1

Scale Model A_8 = 28.13 in^2

Full Scale A_8 = 12.5 ft^2

TEST CONDITIONS						FULL-SCALE ACOUSTIC TEST RESULTS								
							320-foot Arc		300-foot Sideline		1500-ft Sideline		2128-ft Sideline	
Rdg No.	P_o (psia)	P_{T8}/P_o	T_{T8} (° R)	Ideal V_j (ft/sec)	W_B (lb/sec)	10 Log ρA	Peak (PNdB)	Maximum Angle (degrees)	Peak (PNdB)	Maximum Angle (degrees)	Peak (PNdB)	Maximum Angle (degrees)	Peak (PNdB)	Maximum Angle (degrees)
1	14.52	1.48	1282	1280	9.1	-3.7	121.1	120°	120.4	120°	104.4	120°	100.4	120°
2	14.52	1.62	1328	1437	9.6	-3.8	124.3	120°	123.6	120°	107.4	120°	103.5	120°
3	14.51	1.76	1389	1589	10.3	-3.9	127.9	120°	127.2	120°	111.1	120°	110.6	120°
4	14.51	1.76	1466	1771	11.2	-4.0	131.4	120°	130.6	120°	114.5	120°	110.6	120°
5	14.50	2.18	1534	1936	12.1	-4.1	134.4	130°	133.6	120°	116.9	120°	113.0	120°
6	14.50	2.38	1605	2082	13.0	-4.2	136.9	120°	136.3	120°	119.6	120°	115.6	120°
7	14.50	2.61	1687	2229	13.9	-4.3	139.5	120°	1387	130°	121.8	120°	117.8	120°
8	14.50	2.98	1846	2472	15.1	-4.6	142.6	120°	141.9	120°	124.8	120°	120.8	120°
9	14.50	2.63	1742	2277	13.8	-4.4	140.6	120°	139.8	120°	122.8	120°	118.9	120°
10	14.50	2.20	1562	1964	12.2	-4.2	135.3	120°	134.6	120°	118.2	120°	114.3	120°
11	14.50	3.20	1938	2604	15.8	-4.7	144.1	120°	143.3	120°	126.3	120°	122.3	120°
12	14.50	3.49	2043	2761	16.8	-4.8	145.2	120°	144.5	120°	127.4	120°	123.4	120°
13	14.50	1.80	1418	1636	10.5	-3.9	128.7	120°	128.0	120°	111.9	120°	108.0	120°
14	14.50	1.49	1260	1281	9.3	-3.6	121.0	120°	120.3	120°	104.2	120°	100.3	120°

Table 65. Test Summary, Unsuppressed 2-D Over-the-Wing Exhaust Nozzle with Hardwall Ejector.

- (Not) Corrected to Free Field
- Angle Referenced from Jet Axis, degrees

Model: UNSUPPRESSED 2-D OVER-THE-WING NOZZLE WITH HARDWALL EJECTOR

Scale Model A_8 = 28.13 in^2

Test Date(s): 7-9-74

Scale Factor: 8:1

Full Scale A_8 = 12.5 ft^2

TEST CONDITIONS						FULL-SCALE ACOUSTIC TEST RESULTS								
							320-foot Arc		300-foot Sideline		1500-ft Sideline		2128-ft Sideline	
Rdg No.	P_o (psia)	P_{T8}/P_o	T_{T8} (° R)	Ideal V_j (ft/sec)	W_B (lb/sec)	10 Log ρA	Peak (PNdB)	Maximum Angle (degrees)	Peak (PNdB)	Maximum Angle (degrees)	Peak (PNdB)	Maximum Angle (degrees)	Peak (PNdB)	Maximum Angle (degrees)
1	14.43	2.40	1671	2130	11.8	-4.4	136.2	140°	133.6	130°	117.5	130°	113.6	130°
2	14.43	2.20	1575	1976	11.2	-4.2	134.5	140°	132.3	130°	116.2	130°	112.4	130°
3	14.43	2.00	1458	1788	10.6	-4.0	133.1	140°	131.2	130°	115.3	130°	111.6	130°
4	14.43	2.64	1747	2284	12.7	-4.4	137.9	140°	135.9	130°	119.7	130°	115.8	130°
5	14.42	2.99	1780	2430	14.1	-4.4	139.7	130°	137.8	130°	121.4	120°/130°	117.5	120°/130°
6	14.42	2.99	1894	2507	13.7	-4.7	139.8	130°	138.4	120°	122.1	120°	118.2	120°
*7	14.42	3.23	1958	2626	14.5	-4.7	140.9	130°	139.8	120°	123.4	120°	119.5	120°
8	14.42	3.60	2056	2797	15.7	-4.8	142.3	120°	141.5	120°	125.2	120°	121.3	120°
9	14.42	1.80	1379	1615	9.9	-3.8	130.4	140°	128.2	130°	112.7	130°	109.2	130°
10	14.42	1.64	1314	1455	9.3	-3.7	124.1	130°	122.3	130°	106.7	130°	103.0	130°
11	14.42	1.48	1257	1271	8.9	-3.7	119.8	130°	117.9	130°	102.0	130°	98.3	130°

Table 66. Test Summary, Unsuppressed 2-D Over-the-Wing Exhaust Nozzle with Treated Ejector.

- (Not) Corrected to Free Field
- Angle Referenced from Jet Axis, degrees

Model: UNSUPPRESSED 2-D OVER-THE-WING NOZZLE WITH TREATED EJECTOR

Scale Model A_8 = 28.13 in^2

Test Date(s): 7-11-74

Scale Factor: 8:1

Full Scale A_8 = 12.5 ft^2

TEST CONDITIONS						FULL-SCALE ACOUSTIC TEST RESULTS								
							320-foot Arc		300-foot Sideline		1500-ft Sideline		2128-ft Sideline	
Rdg No.	P_o (psia)	P_{T8}/P_o	T_{T8} (° R)	Ideal V_j (ft/sec)	W_B (lb/sec)	10 Log ρA	Peak (PNdB)	Maximum Angle (degrees)	Peak (PNdB)	Maximum Angle (degrees)	Peak (PNdB)	Maximum Angle (degrees)	Peak (PNdB)	Maximum Angle (degrees)
1	14.43	2.85	1728	2273	13.0	-4.4	137.1	130°	135.3	120°/130°	118.9	120°/130°	114.9	120°/130°
2	14.43	2.99	1769	2434	14.5	-4.3	139.1	130°	138.1	120°	121.8	120°	117.8	120°
3	14.43	2.99	1867	2491	14.1	-4.6	139.4	120°/130°	138.6	120°	122.2	120°	118.3	120°
4	14.43	3.26	1936	2621	14.9	-4.7	140.8	120°/130°	140.1	120°	123.6	120°	119.7	120°

Table 67. Test Summary, Asymmetric 2-D Suppressed Exhaust Nozzle with Hardwall Ejector, Scale Factor = 10:1.

- (Not) Corrected to Free Field
- Angle Referenced from Jet Axis, degrees

Model: ASYMMETRIC 2-D SUPPRESSED NOZZLE WITH HARDWALL

Test Date(s): 7/16/74

Scale Factor: 8:1

Scale Model A_8 = 17.85 in^2

Full Scale A_8 = 12.40 ft^2

TEST CONDITIONS						FULL-SCALE ACOUSTIC TEST RESULTS									
							320-foot Arc		300-foot Sideline		1500-ft Sideline		2128-ft Sideline	
Rdg No.	P_o (psia)	P_{T8}/P_o	T_{T8} (° R)	Ideal V_j (ft/sec)	W_B (lb/sec)	10 Log ρA	Peak (PNdB)	Maximum Angle (degrees)	Peak (PNdB)	Maximum Angle (degrees)	Peak (PNdB)	Maximum Angle (degrees)	Peak (PNdB)	Maximum Angle (degrees)
1	14.47	1.49	1294	1280	5.4	-3.8	111.7	110°	113.8	110°	97.54	110°	93.41	110°
2	14.47	1.77	1409	1606	6.2	=4.0	115.4	110°	117.5	110°	100.9	110°	96.73	110°
3	14.47	2.17	1560	1950	7.2	-4.2	121.3	130°	121.5	130°	105.6	130°	101.8	130°
4	14.47	2.63	1738	2274	8.4	-4.4	127.8	130°	128.0	130°	112.1	130°	108.3	130°
5	14.47	2.98	1779	2425	9.3	-4.4	130.9	130°	131.1	130°	115.2	130°	111.4	130°
6	14.47	2.98	1849	2475	9.1	-4.6	131.6	130°/140°	131.8	130°	115.9	130°	112.1	130°
7	14.47	3.23	1910	2593	9.7	-4.6	134.3	130°	134.5	130°	118.3	130°	114.5	130°
17	14.46	3.52	2047	2768	10.3	-4.9	137.3	130°	137.6	120°/120°	121.5	120°/130°	117.6	120°/130°
18	14.46	.243	1647	2130	8.6	-4.3	125.2	130°	125.3	120°/130°	109.5	120°/130°	105.8	120°/130°
19	14.46	2.03	1509	1838	7.2	-4.1	118.5	130°	120.1	110°	103.7	110°	99.74	110°

Table 68. Test Summary, Suppressed 2-D Over-the-Wing Exhaust Nozzle with Treated Ejector, Scale Factor = 10:1.

- (Not) Corrected to Free Field
- Angle Referenced from Jet Axis, degrees

Model: SUPPRESSED 2-D OVER-THE-WING NOZZLE WITH TREATED EJECTOR

Test Date(s): 7/12/74

Scale Factor: 10:1

Scale Model A_8 = 17.85 in^2

Full Scale A_8 = 12.40 ft^2

TEST CONDITIONS						FULL-SCALE ACOUSTIC TEST RESULTS								
							320-foot Arc		300-foot Sideline		1500-ft Sideline		2128-ft Sideline	
Rdg No.	P_o (psia)	P_{T8}/P_o	T_{T8} (° R)	Ideal V_j (ft/sec)	W_B (lb/scc)	10 Log ρA	Peak (PNdB)	Maximum Angle (degrees)	Peak (PNdB)	Maximum Angle (degrees)	Peak (PNdB)	Maximum Angle (degrees)	Peak (PNdB)	Maximum Angle (degrees)
1	14.51	1.47	1284	1278	5.5	-3.8	110.0	50°	110.3	50°	93.27	50°	88.92	50°
2	14.51	1.74	1379	1571	6.3	-3.9	111.6	130°	111.8	110°/130°	95.96	110°	92.2	110°
3	14.51	2.14	1517	1908	7.3	-4.1	119.4	130°	119.6	130°	103.9	130°	100.3	130°
4	14.51	2.58	1659	2201	8.5	-4.2	125.5	130°	125.4	120°/130°	109.5	130°	105.8	130°
5	14.51	2.91	1741	2378	9.1	-4.3	128.6	130°	128.8	130°	112.9	130°	109.2	130°
7	14.50	3.19	1987	2632	9.3	-4.8	132.4	130°	132.7	120°/130°	116.8	120°	113.0	120°
8	14.50	2.96	1925	2520	8.8	-4.8	130.2	130°	130.4	130°	114.2	120°/130°	110.6	120°/130°
						WITH VENTED SIDEWALLS								
9	14.50	2.64	1809	2322	8.2	-4.6	126.6	140°	126.5	120°	110.5	120°	106.7	120°
10	14.50	2.98	1828	2459	9.2	-4.5	129.5	130°	129.7	130°	113.7	120°/130°	109.9	120°/130°
11	14.50	2.98	1865	2483	9.0	-4.6	129.7	130°	129.9	130°	113.9	130°	110.1	120°/130°
12	14.50	3.22	1970	2632	9.4	-4.8	132.6	130°	132.8	120°/130°	116.8	120°/130°	112.9	120°/130°

Table 69. Test Summary, 5.7" I.D. Unsuppressed Conical Nozzle.

- (Not) Corrected to Free Field
- Angle Referenced from Jet Axis, degrees

Model: 5.7" I.D. UNSUPPRESSED CONICAL NOZZLE

Test Date(s): 12-3-74

Scale Factor: 8:1

Scale Model A_8 = 25.63 in^2

Full Scale A_8 = 11.392 ft^2

TEST CONDITIONS						FULL-SCALE ACOUSTIC TEST RESULTS								
							320-foot Arc		300-foot Sideline		1500-ft Sideline		2128-ft Sideline	
Rdg No.	P_o (psia)	P_{T8}/P_o	T_{T8} (° R)	Ideal V_j (ft/sec)	W_B (lb/sec)	10 Log ρA	Peak (PNdB)	Maximum Angle (degrees)	Peak (PNdB)	Maximum Angle (degrees)	Peak (PNdB)	Maximum Angle (degrees)	Peak (PNdB)	Maximum Angle (degrees)
1	14.49	1.09	1067	556	3.8	-3.7	91.2	120°	90.4	120°	73.4	120°	69.1	120°
2	14.48	1.29	1089	967	6.8	-3.6	107.6	120°	106.8	120°	90.6	120°	86.6	120°
3	14.48	1.48	1113	1193	8.5	-3.5	115.2	140°	114.3	120°	98.1	120°	94.1	120°
4	14.48	1.48	1288	1283	7.8	-4.2	118.6	150°	116.7	120°	100.6	120°	96.6	120°
5	14.48	1.90	1247	1598	10.7	-3.7	128.9	150°	124.1	140°	108.5	140°	104.8	140°
6	14.48	1.18	1067	762	5.3	-3.6	100.2	120°	99.5	120°	82.9	120°	78.7	120°
7	14.47	2.05	1318	1728	11.2	-3.9	132.6	150°	128.2	140°	112.5	140°	108.7	140°
8	14.48	2.05	1096	1578	12.6	-3.0	127.8	150°	123.3	140°	107.6	140°	103.9	140°
9	14.48	2.05	1704	1967	9.7	-5.0	136.7	140°	133.1	140°	116.9	140°	113.1	130°/140°
10	14.48	2.28	1385	1890	12.1	-4.0	135.9	140°	132.5	140°	116.4	140°	112.5	140°
11	14.48	2.45	1460	2015	12.6	-4.1	138.3	140°	134.7	140°	118.6	140°	114.7	140°
12	14.48	2.51	1473	2049	12.9	-4.1	138.4	140°	135.5	130°	119.4	130°	115.6	130°
13	14.48	2.46	1078	1732	15.3	-2.7	135.4	150°	131.0	140°	115.2	140°	111.5	140°
14	14.48	2.46	1846	2270	11.0	-5.2	141.3	130°	139.5	130°	123.3	130°	119.5	130°
15	14.48	2.60	1582	2155	12.9	-4.4	140.1	130°	138.2	130°	122.1	130°	118.3	130°
16	14.48	2.60	1688	2226	12.3	-4.7	140.9	130°	139.0	130°	122.9	130°	119.1	130°
17	14.49	2.95	1806	2434	13.4	-4.9	146.2	130°	144.3	130°	128.4	130°	124.6	130°
18	14.49	2.94	1552	2255	14.8	-4.2	145.6	140°	143.2	130°	127.2	130°	123.5	130°

Table 70. Test Summary, 32-Chute Suppressor, A_8 = 26.15 in.^{2}.

- (Not) Corrected to Free Field
- Angle Referenced from Jet Axis, degrees

Model: 32 CHUTE SUPPRESSOR

Test Date(s): 12-6-74 Scale Factor: 8:1

Scale Model A_8 = 26.15 in^2

Full Scale A_8 = 11.60 ft^2

TEST CONDITIONS						FULL-SCALE ACOUSTIC TEST RESULTS								
							320-foot Arc		300-foot Sideline		1500-ft Sideline		2128-ft Sideline	
Rdg No.	P_o (psia)	P_{T8}/P_o	T_{T8} (° R)	Ideal V_j (ft/sec)	W_B (lb/sec)	10 Log ρA	Peak (PNdB)	Maximum Angle (degrees)	Peak (PNdB)	Maximum Angle (degrees)	Peak (PNdB)	Maximum Angle (degrees)	Peak (PNdB)	Maximum Angle (degrees)
1	14.53	1.08	1100	544	3.6	-3.7	94.1	130°	93.7	110°	75.0	120°	70.4	120°
2	14.53	1.22	1034	822	6.1	-3.3	105.6	120°/130°	104.8	120°	86.7	120°	82.0	120°
3	14.52	1.67	1184	1402	9.3	-3.5	120.7	120°	119.9	120°	101.8	120°	97.1	120°
4	14.52	1.86	1266	1584	9.9	-3.7	124.0	120°	123.2	120°	104.9	120°	100.1	120°
5	14.52	1.79	1380	1603	9.1	-4.2	124.1	120°	123.3	120°	105.2	120°	100.4	120°
6	14.52	1.48	1259	1277	7.9	-4.0	119.0	120°	118.3	110°	100.4	120°	96.1	120°
7	14.52	1.53	1122	1247	8.6	-3.4	117.4	130°	116.5	120°	98.5	120°	93.7	120°
8	14.51	1.19	1110	804	5.4	-3.7	104.8	120°	104.0	120°	86.3	120°	81.9	120°
9	14.48	2.04	1348	1740	10.5	-3.9	125.8	120°	124.9	120°	106.9	120°	102.2	120°
10	14.48	2.26	1446	1920	11.2	-4.1	127.6	120°	126.8	120°	108.8	120°	104.0	120°
11	14.48	2.38	1505	2014	11.5	-4.2	128.5	120°	127.9	110°	109.9	110°	105.3	110°
12	14.48	2.46	1597	2108	11.5	-4.4	128.9	120°/130°	128.1	120°	110.2	120°	105.5	120°
13	14.47	2.65	1685	2246	12.1	-4.6	130.3	140°	129.6	110°	111.5	120°	106.9	120°
14	14.47	3.00	1870	2494	13.1	-4.9	133.2	150°	131.5	110°	113.6	120°	109.1	120°
15	14.47	3.22	1885	2574	13.9	-4.9	134.6	150°	132.3	120°	114.6	120°	110.3	120°
16	14.46	3.52	1998	2735	14.6	-5.0	135.1	140°	133.9	120°/130°	116.9	140°	113.0	140°
17	14.46	3.85	2116	2899	15.6	-5.2	140.0	140°	136.5	140°	119.9	140°	115.9	140°
18	14.46	3.23	1941	2615	13.6	-5.0	134.9	140°/150°	132.5	120°	114.9	120°	110.4	120°
19	14.46	3.00	1860	2487	13.0	-4.9	133.6	150°	131.9	110°	113.9	110°/120°	109.5	120°
20	14.46	2.49	1587	2116	11.7	-4.4	129.2	130°/150°	128.4	110°	110.3	110°/120°	105.7	110°/120°
21	14.46	2.29	1467	1949	11.2	-4.1	128.0	120°	127.2	120°	109.1	120°	104.4	120°
22	14.46	1.89	1270	1607	10.0	-3.7	124.2	130°	123.3	120°	105.1	120°	100.4	120°
24	14.45	1.22	1012	820	6.1	-3.2	105.2	120°	104.4	120°	86.1	120°	81.4	120°
25	14.45	1.70	1190	1426	9.2	-3.6	121.2	120°	120.4	120°	101.9	120°	97.3	120°
26	14.45	2.12	1804	2067	9.2	-5.2	128.4	120°	127.9	110°	110.1	110°	105.4	110°
27	14.45	2.11	1292	1742	11.1	-3.7	126.1	120°	125.3	120°	106.9	120°	102.1	120°
28	14.45	2.40	1136	1757	13.6	-2.9	126.9	120°	126.1	120°	108.4	120°	103.7	120°
29	14.45	2.55	1038	1731	15.4	-2.4	126.3	130°	125.4	120°	107.1	120°	102.2	120°
30	14.45	2.55	1841	2304	11.0	-5.1	130.9	140°	130.3	110°	112.5	110°	107.9	110°
31	14.45	3.03	1587	2307	14.2	-4.2	132.3	140°	130.9	110°	113.1	120°	108.6	120°
32	14.45	3.04	1877	2511	13.1	-4.9	134.2	140°	132.0	120°	114.5	120°	110.1	120°
33	14.45	3.03	954	1790	19.4	-1.8	128.6	150°	127.9	90°	109.2	90°	104.1	90°

Table 71. Test Summary, 32-Chute Suppressor with Hardwall Ejector.

- (Not) Corrected to Free Field
- Angle Referenced from Jet Axis, degrees

Model: 32 CHUTE SUPPRESSOR WITH HARDWARE EJECTOR

Scale Model A_8 = 26.15 in^2

Test Date(s): 12/5/74 Scale Factor: 8:1 Full Scale A_8 = 11.60 ft^2

TEST CONDITIONS						FULL-SCALE ACOUSTIC TEST RESULTS								
							320-foot Arc		300-foot Sideline		1500-ft Sideline		2128-ft Sideline	
Rdg No.	P_o (psia)	P_{T8}/P_o	T_{T8} (° R)	Ideal V_j (ft/sec)	W_B (lb/sec)	10 Log ρA	Peak (PNdB)	Maximum Angle (degrees)	Peak (PNdB)	Maximum Angle (degrees)	Peak (PNdB)	Maximum Angle (degrees)	Peak (PNdB)	Maximum Angle (degrees)
1	14.56	1.08	1090	531	3.6	-3.7	92.2	120°	91.6	110°	73.4	110°	68.8	120°
2	14.56	1.22	1066	851	6.1	-3.4	105.9	120°	105.3	110°	87.4	110°	82.7	110°
3	14.56	1.70	1213	1439	9.4	-3.6	120.6	110°	120.6	110°	102.8	110°	98.1	110°
4	14.55	1.90	1286	1622	10.2	-3.7	123.3	110°	123.4	110°	105.3	110°	100.5	110°
5	14.55	2.10	1357	1784	10.9	-3.9	124.6	110°	124.6	110°	106.5	110°	101.8	110°
6	14.55	2.31	1437	1939	11.7	-4.0	125.5	110°	125.5	110°	107.4	110°	102.6	100°/110°
7	14.54	2.49	1568	2103	11.9	-4.3	127.5	110°	127.5	110°	109.5	110°	104.9	110°
8	14.54	2.95	1815	2441	13.1	-4.8	131.7	150°	130.5	110°	112.9	110°	108.4	110°
9	14.54	3.19	1895	2570	13.8	-4.9	135.0	150°	131.5	130°	114.2	120°	110.4	130°

Table 72. Test Summary, 32-Chute Suppressor with Treated Ejector.

- (Not) Corrected to Free Field
- Angle Referenced from Jet Axis, degrees

Model: 32 CHUTE SUPPRESSOR WITH TREATED EJECTOR

Test Date(s): 12-5-74

Scale Factor: 8:1

Scale Model A_8 = 26.15 in^2

Full Scale A_8 = 11.60 ft^2

TEST CONDITIONS						FULL-SCALE ACOUSTIC TEST RESULTS								
							320-foot Arc		300-foot Sideline		1500-ft Sideline		2128-ft Sideline	
Rdg No.	P_o (psia)	P_{T8}/P_o	T_{T8} (° R)	Ideal V_j (ft/sec)	W_B (lb/sec)	10 Log ρA	Peak (PNdB)	Maximum Angle (degrees)	Peak (PNdB)	Maximum Angle (degrees)	Peak (PNdB)	Maximum Angle (degrees)	Peak (PNdB)	Maximum Angle (degrees)
1	14.53	1.08	1000	504	3.6	-3.3	96.4	130°	89.4	130°	71.0	120°	66.4	120°
2	14.53	1.27	1028	835	6.2	-3.3	102.9	120°	102.2	120°	84.0	120°	79.6	120°
3							117.9	120°	117.6	110°	99.6	110°	94.8	110°
4	14.53	1.90	1287	1625	10.1	-3.8	120.8	110°	120.8	110°	102.7	110°	98.0	110°
5	14.53	2.10	1355	1782	11.0	-3.9	112.9	110°	122.9	110°	104.9	110°	100.1	110°
6	14.53	2.32	1442	1945	11.6	-4.0	124.5	110°	124.5	110°	106.4	110°	101.8	110°
7	14.53	2.41	1490	2017	11.9	-4.1	125.4	110°	125.4	110°	107.4	110°	102.7	120°
8	14.53	2.49	1578	2109	11.9	-4.4	126.5	110°	126.5	110°	108.5	110°	103.9	110°
9	14.53	1.48	1282	1286	7.7	-4.0	114.5	120°	114.4	110°	96.3	110°	91.7	110°
10	14.53	1.79	1393	1611	9.0	-4.2	120.4	110°	120.4	110°	120.4	110°	91.7	110°
11	14.53	2.61	1696	2238	12.0	-4.6	127.1	110°	127.1	110°	109.3	110°	104.9	110°
12	14.53	2.95	1820	2444	13.0	-4.8	131.4	150°	129.6	110°	112.2	110°	94.8	110°
13	14.53	3.19	1898	2574	13.8	-4.9	133.9	150°	131.3	130°	114.1	130°	110.1	130°
14	14.53	3.48	1986	2718	14.7	-5.0	137.0	140°	133.5	140°	117.0	140°	113.1	140°
15	14.53	3.82	2112	2890	15.7	-5.2	140.9	140°	137.9	130°	121.4	130°	117.5	130°
16	14.53	2.97	1878	2490	13.0	-4.9	134.4	140°	130.9	140°	114.4	140°	110.5	140°
17	14.53	2.51	1585	2124	12.0	-4.4	126.5	110°	126.5	110°	108.5	110°	103.9	110°
18	14.53	2.33	1458	1960	11.5	-4.1	125.0	110°	125.0	110°	106.9	110°	102.2	110°
19	14.53	1.90	1290	1626	10.1	-3.8	121.0	110°	121.0	110°	103.2	110°	98.4	110°
20	14.53	1.70	1210	1439	9.4	-3.6	117.6	110°/120°	117.6	110°	99.4	110°	94.8	110°
21	14.53	2.44	1496	2034	11.9	-4.1	125.7	110°	125.7	110°	107.8	110°	103.2	110°

Table 73. Test Summary, Engine Aerodynamic Performance Data, Baseline Conical Nozzle.

J79-15 Engine S/N 439-012 Test Date: 10-4-74 Test Location: GE/EFTC-North Base

Test Configuration: Conical Nozzle (Baseline), CJ805-23 Inlet Suppressor, Turbine Exhaust Suppressor

RUN	SPM	NK	Pcnt NK	BAR	HUM	T_2	P_{T2}	P_{S2}	W_2	W_{2K}	W_F	P_{T7}	P_{S7}	T_{T7}	T_{T7K}
5.01	4998	5055	65.83	27.56	50	506.9	13.55	13.44	42.8	45.8	1289	14.55	13.55	1050	1074
5.02	5930	5999	78.12	27.56	50	506.7	13.55	13.20	75.8	80.8	2025	16.81	13.51	1020	1044
5.03	6726	6810	88.68	27.56	50	505.8	13.55	12.55	124.5	133.0	4720	24.40	13.55	1214	1244
5.04	6935	7024	91.47	27.56	50	505.5	13.55	12.31	137.2	146.5	6018	27.74	13.54	1321	1355
5.05	7096	7185	93.56	27.56	50	505.8	13.55	12.15	144.7	154.8	6935	30.00	13.50	1390	1425
5.06	7204	7355	95.78	27.56	52	505.8	13.55	11.98	152.1	162.5	8090	32.58	13.47	1484	1521
5.07	7465	7561	98.46	27.56	52	505.5	13.55	11.92	154.6	165.1	8846	33.85	13.59	1548	1586
5.08	7618	7714	100.44	27.56	52	505.8	13.55	11.89	155.8	166.4	9461	34.80	13.58	1609	1649
5.09	4998	5058	65.86	27.56	52	506.4	13.55	13.44	42.8	45.8	1239	14.55	13.55	1039	1064
5.10	7602	7708	100.34	27.56	53	504.8	13.55	11.88	156.3	168.8	9461	34.90	13.46	1608	1652
5.11	7482	7583	98.74	27.56	53	505.0	13.55	11.90	155.5	168.0	8915	34.04	13.54	1563	1605
5.12	7289	7364	95.89	27.56	53	508.2	13.55	11.97	152.2	162.9	8108	32.58	13.57	1489	1519
5.13	7088	7164	93.29	27.56	53	507.6	13.55	12.13	145.4	155.6	7011	30.15	13.55	1409	1439
5.14	6903	8977	90.88	27.57	52	507.6	13.56	12.35	135.5	144.9	5818	27.22	13.62	1305	1333
5.15	8702	8778	88.26	27.57	50	507.1	13.55	12.55	124.3	133.0	4824	24.14	13.58	1205	1232
5.16	5962	6025	78.46	27.57	50	507.8	13.56	13.21	75.5	80.8	2022	16.91	13.53	996	1017
5.17	5006	5059	65.88	27.57	51	507.8	13.56	13.45	42.8	45.7	1262	14.54	13.55	1039	1061

RUN	RPM	NK	W_8	A_8	P_{T7}/P_o	V_7	GAMMA	CP GAS	R	F/A RATIO	FG	FGK	FGX	FGXK	FO/FGX
5.01	4998	5055	42.6	338.0	1.078	516	1.374	.252	53.37	.0084	858	717	684	746	.961
5.02	5930	5999	75.2	338.0	1.245	883	1.376	.251	53.37	.0075	1960	2135	2019	2200	.971
5.03	6726	6810	124.3	338.0	1.807	1510	1.363	.258	53.37	.0106	5691	6202	5836	6360	.975
5.04	6935	7024	137.2	338.0	2.055	1615	1.355	.262	53.37	.0123	7172	7816	7360	8021	.974
5.05	7096	7185	144.9	338.0	2.222	1656	1.351	.264	53.37	.0134	8187	8922	8356	9107	.980
5.06	7264	7355	152.5	338.0	2.413	1709	1.345	.267	53.38	.0149	9297	10131	9504	10358	.978
5.07	7465	7561	155.2	338.0	2.507	1744	1.341	.270	53.38	.0160	9901	10790	10065	10969	.984
5.08	7618	7714	156.5	338.0	2.578	1778	1.338	.272	53.38	.0170	10285	11208	10497	11439	.980
5.09	4998	5058	42.6	338.0	1.078	514	1.375	.252	53.37	.0061	658	717	681	742	.965
5.10	7602	7706	157.1	336.0	2.585	1777	1.338	.272	53.38	.0170	10367	11297	10545	11492	.983
5.11	7482	7583	158.1	338.0	2.521	1753	1.340	.270	53.38	.0181	10038	10939	10208	11124	.983
5.12	7289	7384	152.8	338.0	2.413	1712	1.345	.268	53.38	.0149	9380	10222	9525	10381	.985
5.13	7088	7164	145.8	336.0	2.233	1667	1.350	.265	53.37	.0135	8324	9071	8478	9239	.982
5.14	8903	6977	135.5	338.0	2.016	1806	1.357	.281	53.37	.0120	7021	7848	7133	7770	.984
5.15	6702	6778	124.1	338.0	1.787	1492	1.363	.257	53.37	.0104	5649	6154	5755	6270	.981
5.18	5982	6025	75.2	338.0	1.252	863	1.378	.250	53.37	.0075	2029	2210	2018	2198	1.005
5.17	5006	5059	42.8	338.0	1.077	510	1.375	.252	53.37	.0083	671	730	876	736	.992

RUN	RPM	NK	P_7/P_{S7}	P_{S7}/P_o		W_7	V_9	V_{9K}	RUN	RPM	WIND (mph)	DIR (°)	T DRY (° F)	T WET (° F)	
5.01	4998	5055	1.074	1.005	---	42.0	516	522	5.01	4998	8	180	54	51	
5.02	5930	5999	1.244	1.002	---	76.6	863	873	5.02	5930	8	180	54	51	
5.03	6726	6810	1.801	1.005	---	124.6	1510	1530	5.03	6726	8	160	54	51	
5.04	6935	7024	2.049	1.004	---	134.9	1725	1747	5.04	6935	12	180	54	51	
5.05	7096	7185	2.222	1.001	---	140.4	1855	1878	5.05	7096	10.5	180	54	51.5	
5.06	7264	7355	2.419	.999	---	144.7	2004	2030	5.06	7264	9	170	54	51.5	
5.07	7465	7561	2.491	1.008	---	146.0	2086	2113	5.07	7465	9	175	54	51.5	
5.08	7618	7714	2.563	1.007	---	145.8	2157	2184	5.08	7618	9	180	54	51.5	
5.09	4998	5058	1.074	1.005	---	42.2	514	520	5.09	4998	0	0	53.5		
5.10	7602	7706	2.593	.998	---	145.8	2159	2189	5.10	7602	5	110	53.5	51.0	
5.11	7482	7583	2.514	1.004	---	145.6	2103	2131	5.11	7482	6	180	53.5	51.0	
5.12	7289	7364	2.401	1.006	---	144.7	2008	2028	5.12	7289	2	200	53.5	51.0	
5.13	7088	7184	2.225	1.005	---	140.1	1873	1893	5.13	7088	5	130	54	51.5	
5.14	8903	6977	1.999	1.010	---	133.8	1693	1712	5.14	8903	4.5	180	54.5	51	
5.15	8702	6778	1.780	1.005	---	123.6	1492	1509	5.15	8702	2.5	300	54.5	51	
5.16	5982	6025	1.250	1.003	---	78.7	883	872	5.18	5962	1.5	310	55	51.5	
5.17	5008	5059	1.073	1.004	---	42.0	510	516	5.17	5006	8	110	55	51	

Table 74. Test Summary, Unsuppressed Conical Nozzle, 20.82" Diameter A_8.

- Corrected to Free Field
- Angle Referenced from Jet Axis, degrees

Model: UNSUPPRESSED CONICAL NOZZLE, 20.82" DIAMETER$_8$ (J79)

Scale Model A_8 = 341.0 in^2

Test Date(s): 10/4/74

Scale Factor: 2:1

TEST CONDITIONS						FULL-SCALE ACOUSTIC TEST RESULTS								
							320-foot Arc		300-foot Sideline		1500-ft Sideline		2128-ft Sideline	
Rdg No.	P_o (psia)	P_{T8}/P_o	T_{T8} (° R)	Ideal V_j (ft/sec)	W_B (lb/sec)	10 Log ρA	Peak (PNdB)	Maximum Angle (degrees)	Peak (PNdB)	Maximum Angle (degrees)	Peak (PNdB)	Maximum Angle (degrees)	Peak (PNdB)	Maximum Angle (degrees)
1	13.52	1.08	1050	516	42.0	-4.7	89.5	120°	88.7	120°	70.6	110°/120°	66.3	110°
2	13.52	1.24	1020	863	76.8	-4.4	103.1	120°	102.3	120°	83.9	120°	79.6	120°
3	13.52	1.81	1214	1510	124.6	-4.8	125.1	150°	120.2	130°	103.0	130°/140°	99.0	140°
4	13.52	2.06	1321	1725	134.9	-5.0	132.9	150°	127.3	140°	110.1	140°	106.1	140°
5	13.52	2.22	1390	1855	140.4	-5.1	135.3	150°	131.3	140°	113.9	140°	109.8	140°
6	13.52	2.41	1484	2004	144.7	-5.3	137.5	140°	133.8	140°	116.5	140°	112.3	140°
7	13.52	2.51	1546	2086	146.0	-5.5	138.2	140°	134.8	130°	117.3	140°	113.2	140°
8	13.52	2.58	1609	2157	145.8	-5.0	138.4	140°	135.8	130°	118.2	130°	114.0	130°
9	13.52	1.08	1039	514	42.2	-4.7	89.6	120°	88.8	120°	70.9	120°	66.6	120°
10	13.52	2.58	1608	2159	145.8	-5.6	138.3	140°	136.3	130°	119.1	130°	115.0	130°
11	13.52	2.52	1563	2103	145.6	-5.5	138.1	140°	135.3	130°	118.1	130°	114.0	130°
12	13.52	2.41	1489	2008	144.7	-5.3	137.1	140°	133.4	130°/140°	116.1	140°	111.9	140°
13	13.52	2.23	1409	1873	140.1	-5.2	135.5	150°	131.2	140°	113.9	140°	109.8	140°
14	13.52	2.02	1305	1693	133.6	-4.9	133.2	150°	126.9	150°	109.3	140°	105.4	140°
15	13.52	1.79	1205	1492	123.6	-4.7	125.4	150°	120.6	130°	103.5	130°	99.4	130°
16	13.52	1.25	996	863	42.0	-4.7	89.7	120°	88.9	120°	71.3	120°	67.0	120°

Table 75. Test Summary, Engine Aerodynamic Performance Data, 32-Chute Suppressor.

J79-15 Engine S/8 439-012 Test Date: 9-26-74 Test Location: GE/EFTC-North Base

Test Configuration: 32-Chute Compressor, CJ805-23 Inlet Suppressor, Turbine Exhaust Suppressor

RUN	RFM	NK	Pent 8K	BAR	HUM	T_2	P_{T2}	P_{S2}	W_2	W_{2K}	W_F	P_{T7}	P_{S7}	T_{T7}	T_{T7K}
3.01	4998	4969	64.70	27.58	54	524.7	13.56	13.46	40.1	43.6	1257	14.61	13.57	1068	1055
3.02	5938	5907	76.92	27.58	54	524.0	13.58	13.26	71.3	77.3	1894	16.47	13.54	1029	1018
3.03	5022	4994	65.03	27.58	54	524.4	13.56	13.46	40.1	43.8	1236	14.60	13.56	1057	1045
3.04	5938	5906	76.91	27.58	54	524.2	13.56	13.28	71.2	77.3	1885	16.46	13.52	1025	1014
3.05	6710	6679	86.97	27.58	53	523.5	13.56	12.67	117.3	127.2	4197	22.77	13.55	1187	1176
3.06	6903	6879	89.57	27.58	53	522.3	13.56	12.48	128.1	136.7	5234	25.46	13.61	1276	1267
3.07	7064	7039	91.86	27.58	53	522.3	13.58	12.29	137.6	149.0	6270	28.06	13.58	1355	1345
3.08	7256	7234	94.20	27.58	54	521.8	13.58	12.08	147.1	159.2	7582	31.21	13.48	1464	1455
3.09	7449	7425	96.69	27.58	54	521.9	13.58	11.98	151.2	163.6	8465	32.83	13.56	1533	1523
3.10	7674	7651	99.63	27.58	54	521.8	13.56	11.91	153.1	165.9	9296	34.04	13.57	1606	1596
3.11	5006	4987	64.94	27.58	52	522.6	13.58	13.46	40.2	43.6	1213	14.59	13.54	1055	1047
3.12	5954	5935	77.29	27.58	52	521.9	13.56	13.23	72.4	78.5	1888	16.51	13.51	1012	1005
3.13	6710	6692	87.14	27.58	52	521.4	13.56	12.64	118.1	127.9	4211	22.84	13.57	1178	1171
3.14	6895	6884	89.64	27.58	52	520.3	13.58	12.47	128.9	139.3	5246	25.51	13.87	1288	1263
3.15	7088	7071	92.08	27.58	53	521.0	13.56	12.25	138.8	150.1	6414	28.43	13.56	1363	1356
3.16	7264	7248	94.39	27.58	53	520.9	13.56	12.05	147.5	159.7	7667	31.36	13.49	1463	1456
3.17	7449	7433	96.79	27.58	53	520.9	13.56	11.96	151.2	163.8	8462	32.66	13.62	1522	1515
3.18	7690	7669	99.67	27.58	53	521.4	13.56	11.91	153.1	165.9	9316	33.95	13.66	1604	1595

RUN	RPM	NK	W_6	A_8	P_{T7}/P_o	V_7	GAMMA	CP GAS	R	F/A RATIO	FG	FGK	FGX	FGXK	FG/FGX
3.01	4998	4969	40.0	336.0	1.062	533	1.373	.253	53.37	.0066	653	711	663	722	.984
3.02	5938	5907	70.9	338.0	1.219	825	1.376	.251	53.37	.0074	1750	1906	1620	1983	.981
3.03	5022	4994	40.0	336.0	1.081	528	1.373	.252	53.37	.0086	653	711	657	715	.994
3.04	5938	5906	70.9	338.0	1.219	823	1.376	.251	53.37	.0074	1723	1676	1814	1975	.950
3.05	6710	6679	117.1	338.0	1.686	1409	1.365	.257	53.37	.0100	4905	5342	5129	5588	.956
3.06	6903	6879	128.0	338.0	1.685	1588	1.359	.260	53.37	.0114	8084	6628	8363	6930	.956
3.07	7064	7039	137.7	338.0	2.079	1635	1.353	.263	53.37	.0128	7238	7661	7533	6205	.960
3.08	7256	7234	147.4	338.0	2.311	1698	1.346	.267	53.38	.0144	6525	9285	6917	9712	.956
3.09	7449	7425	151.7	338.0	2.430	1737	1.342	.269	53.38	.0157	9293	10121	9646	10506	.963
3.10	7874	7651	153.8	336.0	2.520	1776	1.338	.272	53.38	.0170	9342	10719	10194	11104	.965
3.11	5006	4987	40.1	338.0	1.080	525	1.374	.252	53.37	.0065	653	711	654	713	.998
3.12	5954	5935	72.1	336.0	1.222	623	1.377	.251	53.36	.0073	1792	1951	1845	2010	.971
3.13	6710	6892	117.8	336.0	1.691	1407	1.365	.256	53.37	.0100	5001	5447	5155	5615	.970
3.14	6895	6884	126.8	338.0	1.669	1563	1.359	.260	53.37	.0114	6153	6701	6389	8959	.963
3.15	7088	7071	138.7	338.0	2.105	1840	1.353	.263	53.37	.0130	7401	6061	7670	8354	.965
3.18	7284	7248	147.8	338.0	2.322	1698	1.346	.267	53.36	.0146	6821	9390	6983	9782	.962
3.17	7449	7433	151.7	336.0	2.419	1730	1.343	.269	53.38	.0157	9279	10106	9569	10445	.968
3.18	7690	7669	153.9	338.0	2.513	1775	1.338	.272	53.38	.0170	9655	10734	10176	11086	.968

RUN	RPM	NK	P_7/P_{S7}	P_{67}/P_o		W_7	V_9	V_{9K}	RUN	RPM	WIND (mph)	DIR (°)	T DRY (° F)	T WET (° F)	
3.01	4998	4969	1.077	1.006	---	42.5	533	530	3.01	4998	8	160	67.0	54.5	
3.02	5938	5907	1.216	1.004	---	72.2	825	821	3.02	5938	7	170	66.0	54.0	
3.03	5022	4994	1.077	1.005	---	42.7	526	525	3.03	5022	6	160	66.0	54.0	
3.04	5936	5906	1.217	1.002	---	72.4	823	816	3.04	5936	7	160	66.0	54.0	
3.05	6710	6679	1.660	1.004	---	116.7	1409	1403	3.05	6710	6	160	65.0	53.5	
3.06	6903	6879	1.671	1.009	---	126.7	1599	1593	3.06	6903	7	180	65.0	53.5	
3.07	7064	7039	2.068	1.006	---	134.6	1760	1754	3.07	7064	7	180	65.0	53.5	
3.08	7258	7234	2.315	.999	---	141.0	1946	1940	3.08	7258	6	180	65.0	54.0	
3.09	7449	7425	2.421	1.005	---	143.3	2045	2039	3.09	7449	8	170	65.0	54.0	
3.10	7674	7651	2.508	1.006	---	143.6	2132	2126	3.10	7674	9	160	65.0	54.0	
3.11	5006	4987	1.078	1.004	---	42.9	525	523	3.11	5006	7	170	64.0	52.5	
3.12	5954	5935	1.222	1.001	---	73.8	823	821	3.12	5954	7	180	64.0	52.5	
3.13	6710	6692	1.663	1.006	---	117.6	1407	1404	3.13	6710	8	120	84.0	52.5	
3.14	6895	6884	1.866	1.013	---	127.4	1598	1593	3.14	8895	8	170	64.0	52.5	
3.15	7088	7071	2.094	1.006	---	135.7	1779	1775	3.15	7086	8	170	84.0	53.0	
3.16	7204	7248	2.325	1.000	---	141.6	1950	1946	3.16	7284	9	150	64.0	53.0	
3.17	7449	7433	2.399	1.009	---	143.5	2033	2029	3.17	7449	12	170	64.0	53.0	
3.18	7690	7669	2.482	1.014	---	143.7	2128	2122	3.18	7690	8	170	64.0	53.0	

Table 76. Test Summary, 32-Chute Suppressor, A_8 = 344.28 in.^{2}.

• Corrected to Free Field

• Angle Referenced from Jet Axis, degrees

Model: 32-CHUTE SUPPRESSOR (J79)

Scale Model A_8 = 344.28 in^2

Test Date(s): 9/26/74

Scale Factor: 2:1

TEST CONDITIONS						FULL-SCALE ACOUSTIC TEST RESULTS								
							320-foot Arc		300-foot Sideline		1500-ft Sideline		2128-ft Sideline	
Rdg No.	P_o (psia)	P_{T8}/P_o	T_{T8} (° R)	Ideal V_j (ft/sec)	W_B (lb/sec)	10 Log ρA	Peak (PNdB)	Maximum Angle (degrees)	Peak (PNdB)	Maximum Angle (degrees)	Peak (PNdB)	Maximum Angle (degrees)	Peak (PNdB)	Maximum Angle (degrees)
1	13.51	1.08	1068	533	42.5	-4.8	92.6	130°	90.9	120°	72.8	120°	68.5	120°
2	13.51	1.22	1029	825	72.2	-4.5	103.1	130°	102.2	120°	83.5	110°	78.6	110°
3	13.51	1.08	1057	528	42.7	-4.7	91.9	130°	90.5	110°	72.9	120°	68.7	120°
4	13.51	1.22	1025	823	72.4	-4.4	103.2	130°	102.0	120°	83.4	110°	78.5	110°
5	13.51	1.69	1187	1409	116.7	-4.7	118.6	150°	117.6	120°	98.5	110°	93.5	110°/120°
6	13.51	1.88	1276	1599	126.7	-4.9	122.4	150°	120.7	120°	101.8	110°	96.8	110°
7	13.51	2.08	1355	1760	134.6	-5.0	125.9	160°	122.9	110°	104.2	110°	99.2	110°
8	13.51	2.31	1464	1946	141.0	-5.3	127.7	160°	126.9	110°	108.5	110°	103.7	110°
9	13.51	2.43	1533	2045	143.1	-5.4	128.3	150°	126.0	110°	107.7	110°	102.9	110°
10	13.51	2.52	1606	2132	143.6	-5.6	129.1	150°	126.6	110°	108.3	110°	103.5	110°
11	13.51	1.08	1055	525	42.9	-4.7	92.0	130°	91.1	120°	73.0	120°	68.6	120°
12	13.51	1.22	1012	823	73.6	-4.4	103.6	130°	102.6	120°	83.8	120°	78.9	110°/120°
13	13.51	1.69	1178	1407	117.6	-4.7	119.3	120°	118.5	120°	99.4	120°	94.3	120°
14	13.51	1.89	1268	1596	127.4	-4.9	122.5	150°	120.9	120°	101.9	120°	96.9	120°
15	13.51	2.10	1363	1779	135.7	-5.1	125.7	150°	123.2	110°	104.8	110°	99.8	110°
16	13.51	2.32	1463	1950	141.6	-5.3	128.2	160°	126.6	110°	108.3	110°	103.5	110°
17	13.51	2.42	1522	2033	143.5	-5.4	128.2	150°	125.9	110°	107.5	110°	102.7	110°
18	13.51	2.51	1604	2128	143.7	-5.6	129.3	150°	126.9	110°	108.5	110°	103.7	110°

Table 77. Test Summary, Engine Aerodynamic Performance Data, 32-Chute Plug Suppressor with Ejector.

J79-15 Engine 6/N 439-012 Test Date: 10-1-74 Test Location: GE/EFTC-North Base

Test Configuration: 32-Chute Plug Suppressor with Ejector, CJ805-23 Inlet Suppressor, Turbine Exhaust Suppressor

RUN	RPM	NK	Pcnt NK	RAI	HUM	T_2	P_{T2}	P_{S2}	W_2	W_{2K}	W_F	P_{T7}	P_{S7}	T_{T7}	T_{T7K}
4.01	5022	5054	85.81	27.65	25	512.1	13.61	13.50	42.6	45.7	1261	14.56	13.61	1039	1052
4.02	5946	5987	77.96	27.65	25	511.5	13.61	13.26	75.3	80.7	1970	16.58	13.57	1009	1023
4.03	6718	6763	88.07	27.65	26	511.7	13.61	12.63	122.8	131.5	4443	23.40	13.62	1191	1207
4.04	6903	6947	90.46	27.65	26	512.0	13.61	12.44	133.0	142.5	5419	25.98	13.69	1278	1294
4.05	7088	7133	92.89	27.65	25	512.0	13.61	12.24	142.7	152.8	6600	28.91	13.66	1367	1384
4.06	7256	7309	95.17	27.85	27	511.2	13.61	12.05	151.1	161.7	7806	31.64	13.68	1459	1480
4.07	7449	7503	97.70	27.65	27	511.2	13.81	11.96	154.8	165.7	8565	32.95	13.75	1520	1542
4.08	7682	7745	100.85	27.65	27	510.3	13.61	11.92	156.5	167.3	9145	34.27	13.75	1605	1631
4.09	4990	5028	65.47	27.65	27	510.0	13.61	13.50	42.7	45.7	1202	14.51	13.60	1038	1054
4.10	5954	5989	77.99	27.65	27	512.6	13.61	13.26	75.2	80.7	1912	16.58	13.56	997	1008
4.11	6702	6748	87.84	27.65	30	511.9	13.61	12.65	121.6	130.2	4311	23.10	13.69	1176	1191
4.12	6911	6958	90.60	27.86	30	511.7	13.61	12.43	133.6	143.0	5504	28.18	13.73	1280	1297
4.13	7088	7137	92.94	27.68	30	511.5	13.61	12.24	142.8	152.8	6576	28.86	13.65	1361	1380
4.14	7264	7317	85.28	27.66	30	511.2	13.61	12.05	151.1	161.7	7830	31.74	13.59	1461	1482
4.15	7465	7521	97.93	27.86	30	511.0	13.61	11.96	154.8	165.7	6589	33.05	13.68	1525	1547
4.16	7690	7747	100.88	27.66	30	511.0	13.61	11.92	158.4	167.3	9421	34.18	13.75	1605	1828

RUN	RPM	NK	W_8	A_8	P_{T7}/P_o	V_7	GAMMA	CP GAS	R	F/A RATIO	FG	FGK	FGX	FGXK	FG/FGX
4.01	5022	5054	42.4	338.0	1.075	505	1.375	.252	53.37	.0083	844	699	666	724	.968
4.02	5946	5987	75.0	338.0	1.224	825	1.377	.251	53.36	.0073	1837	1995	1923	2089	.955
4.03	6718	6763	122.5	338.0	1.728	1442	1.364	.257	53.37	.0102	5197	5645	5492	5986	.948
4.04	6903	6947	132.9	338.0	1.918	1589	1.358	.260	53.37	.0114	8308	6852	6694	7271	.942
4.05	7088	7133	142.8	338.0	2.134	1642	1.352	.263	53.37	.0130	7542	8192	7975	8863	.946
4.06	7256	7309	151.4	338.0	2.336	1695	1.347	.266	53.37	.0145	8668	9413	9198	9992	.942
4.07	7449	7503	155.3	338.0	2.433	1729	1.343	.269	53.36	.0155	9258	10054	9834	10682	.941
4.08	7682	7745	157.2	338.0	2.530	1776	1.338	.272	53.38	.0169	9791	10835	10438	11337	.938
4.09	4990	5028	42.5	338.0	1.071	493	1.375	.252	53.37	.0079	617	670	651	707	.948
4.10	5954	5989	74.9	338.0	1.224	820	1.378	.250	53.36	.0071	1796	1950	1909	2074	.940
4.11	6702	6746	121.3	338.0	1.706	1417	1.365	.256	53.37	.0099	5060	5496	5345	5806	.947
4.12	6911	6958	133.5	338.0	1.932	1591	1.356	.280	53.37	.0116	8363	6909	6764	7345	.941
4.13	7088	7137	142.9	338.0	2.130	1639	1.353	.263	53.37	.0129	7501	8144	7953	8635	.943
4.14	7264	7317	151.5	338.0	2.343	1696	1.346	.267	53.37	.0145	8653	9395	9220	10012	.938
4.15	7465	7521	155.3	338.0	2.439	1732	1.343	.269	53.36	.0156	9229	.0021	9867	10714	.835
4.16	7690	7747	157.1	338.0	2.521	1776	1.338	.272	53.38	.0169	9750	10587	10413	11307	.938

RUN	RPM	NK	P_7/P_{97}	P_{S7}/P_o		W_7	V_9	V_{9K}	RUN	RPM	WIND (mph)	DIR (°)	T DRY (° F)	T WET (° F)	
4.01	5022	5054	1.070	1.008	---	41.3	505	508	4.01	5022	0	0	57	45	
4.02	5946	5987	1.222	1.003	---	74.0	825	631	4.02	5948	4	340	57	45	
4.03	6718	6783	1.716	1.007	---	120.1	1442	1452	4.03	8718	4	340	56.5	45	
4.04	6903	6947	1.898	1.012	---	129.2	1620	1631	4.04	8903	4	315	56.5	45	
4.05	7068	7133	2.116	1.010	---	137.6	1797	1808	4.05	7088	4	280	57	45.5	
4.06	7256	7309	2.318	1.010	---	143.2	1954	1866	4.06	7256	8	275	57	45.5	
4.07	7449	7503	2.396	1.018	---	144.8	2037	2052	4.07	7449	5	300	57	45.5	
4.08	7682	7745	2.492	1.016	---	144.9	2135	2153	4.08	7682	6	280	57	45.5	
4.09	4990	5028	1.087	1.005	---	40.4	493	496	4.09	4990	5	280	57	45.5	
4.10	5954	5989	1.223	1.002	---	74.5	820	825	4.10	5954	8	280	57	45.5	
4.11	6702	6746	1.687	1.012	---	119.1	1417	1426	4.11	6702	7	280	57.5	46.5	
4.12	6911	6958	1.907	1.014	---	130.1	1630	1641	4.12	6911	6	280	57.5	46.5	
4.13	7088	7137	2.114	1.009	---	137.7	1790	1803	4.13	7086	7	280	57.5	46.5	
4.14	7284	7317	2.338	1.004	---	143.3	1958	1972	4.14	7264	8	270	57.5	46.5	
4.15	7485	7521	2.416	1.011	---	144.7	2043	2059	4.15	7465	6	275	57.5	46.5	
4.16	7690	7747	2.484	1.018	---	144.5	2132	2148	4.16	7690	8	280	57.5	46.5	

Table 78. Test Summary, 32-Chute Suppressor with Ejector.

• Corrected to Free Field

• Angle Referenced from Jet Axis, degrees

Model: 32-CHUTE SUPPRESSOR WITH EJECTOR (J79)

Scale Model A_8 = 344.28 in^2

Test Date(s): 10-1-74

Scale Factor: 2:1

TEST CONDITIONS						FULL-SCALE ACOUSTIC TEST RESULTS								
							320-foot Arc		300-foot Sideline		1500-ft Sideline		2128-ft Sideline	
Rdg No.	P_o (psia)	P_{T8}/P_o	T_{T8} (° R)	Ideal V_j (ft/sec)	W_8 (lb/sec)	10 Log ρA	Peak (PNdB)	Maximum Angle (degrees)	Peak (PNdB)	Maximum Angle (degrees)	Peak (PNdB)	Maximum Angle (degrees)	Peak (PNdB)	Maximum Angle (degrees)
1	13.57	1.08	1039	505	41.3	-4.6	89.9	130°	88.4	120°	70.3	80°/110°	66.2	80°
2	13.57	1.22	1009	825	74.0	-4.4	100.9	120°	100.1	120°	81.9	120°	76.7	110°
3	13.57	1.73	1191	1442	120.1	-4.7	116.0	110°	116.0	110°	96.8	110°	91.9	110°
4	13.57	1.92	1278	1620	129.2	-4.9	119.0	110°	119.0	110°	99.5	110°	94.6	110°
5	13.57	2.13	1367	1797	137.6	-5.0	121.4	150°	121.6	110°	102.3	110°	97.4	110°
6	13.57	2.34	1459	1954	143.2	-5.2	120.9	150°	123.4	110°	105.0	110°	100.1	110°
7	13.57	2.43	1520	2037	144.8	-5.9	124.2	110°	124.2	110°	105.9	110°	101.0	110°
8	13.57	2.53	1605	2135	144.9	-5.6	125.2	110°	125.2	110°	106.8	110°	102.1	110°
9	13.57	1.07	1038	493	40.4	-4.6	90.4	130°	88.7	110°	71.0	110°	66.6	110°
10	13.57	1.22	997	820	74.5	-4.3	101.3	110°	101.3	110°	83.4	110°	78.8	110°
11	13.57	1.71	1176	1417	119.1	-4.6	117.3	110°	117.3	110°	98.9	110°	93.9	110°
12	13.57	1.93	1280	1630	130.1	-4.9	120.6	110°	120.7	110°	100.9	110°	95.4	110°
13	13.57	2.13	1361	1790	137.7	-5.0	123.1	110°	123.1	110°	103.9	110°	98.9	110°
14	13.57	2.34	1461	1958	143.3	-5.2	123.2	110°	123.2	110°	104.9	110°	100.0	110°
15	13.57	2.44	1525	2043	144.7	-5.4	125.3	110°	125.4	110°	107.0	110°	102.1	110°
16	13.57	2.52	1605	2132	144.5	-5.6	125.3	110°	125.3	110°	107.1	110°	102.3	110°

APPENDIX D

SUMMARY OF TEST POINTS FOR J85 TURBINE NOISE TEST

A summary of the actual nozzle settings and speeds tested, along with the ambient conditions for the J85 test, is presented in Tables 79 through 87.

Table 79. Far-Field Acoustic Tests - Baseline, Bellmouth Inlet, Nominal A_8 Schedule.

Rdg	$N/\sqrt{\theta}$ (%)	A_8 ($in.^2$)	P_{amb} (in. Hg)	T_{dry} (° F)	T_{wet} (° F)	R.H. (%)	Wind		SPL† (110°)
							Dir (deg)	Vel (kts)	
7.1	70.4	139.2	27.79	55.0	48.0	60.8	50	3.0	81.4
7.2	75.3	130.3	27.79	53.0	47.0	64.9	340	2.0	79.9
7.3	80.1	130.2	27.79	53.0	47.0	64.9	330	1.5	81.7
7.4	85.1	130.2	27.79	49.5	46.5	80.8	360	1.0	82.9
7.5	90.1	130.2	27.79	49.5	46.5	80.8	340	2.5	85.1
7.6	95.2	112.4	27.80	52.0	48.5	78.7	30	4.5	85.2
7.7	100.2	112.3	27.80	52.0	48.5	78.7	20	4.0	86.6
7.8	70.1	139.9	27.80	52.0	48.5	78.7	10	5.0	82.4
7.9	75.0	131.1	27.80	52.0	48.5	78.7	360	2.5	79.5
7.10	80.2	131.1	27.80	50.5	47.0	78.1	360	2.0	80.9
7.11	85.2	131.1	27.80	50.5	47.0	78.1	360	2.0	83.7
7.12	90.1	131.0	27.80	50.0	48.5	90.3	350	3.0	84.6
7.13	94.9	113.3	27.80	50.0	48.5	90.3	20	3.0	84.9
7.14	99.8	113.1	27.81	51.5	49.0	84.5	360	5.0	85.8

† 1/3-Octave Band Nearest 2nd Stage BPF

Table 80. Far-Field Acoustic Tests - Baseline, Bellmouth Inlet, Maximum A_8.

Rdg	$N/\sqrt{\theta}$ (%)	A_8 ($in.^2$)	P_{amb} (in. Hg)	T_{dry} (° F)	T_{wet} (° F)	R.H. (%)	Wind		SPL† (110°)
							Dir (deg)	Vel (kts)	
7.15	69.8	198.8	27.81	51.5	49.0	84.5	40	2.5	84.0
7.16	80.1	198.8	27.81	54.5	50.0	74.0	40	3.0	83.0
7.17	90.0	198.8	27.81	54.5	50.0	74.0	40	2.5	90.7
7.18	99.8	153.0	27.82	54.5	50.0	74.0	20	4.0	89.4
7.19	69.8	198.1	27.82	57.0	52.0	72.5	20	4.5	83.8
7.20	79.9	198.1	27.82	57.0	52.0	72.5	70	4.5	82.6
7.21	90.1	198.1	27.82	57.0	51.5	69.8	50	4.0	91.0
7.22	99.8	153.1	27.82	57.0	51.5	69.8	60	3.0	89.1

† 1/3-octave Band Nearest 2nd Stage BPF

Table 81. Far-Field Acoustic Tests - Baseline, Suppressor Inlet, Nominal A_8 Schedule.

Rdg	$N/\sqrt{\theta}$ (%)	A_8 ($in.^2$)	P_{amb} (in. Hg)	T_{dry} (° F)	T_{wet} (° F)	R.H. (%)	Wind		SPL† (110°)
							Dir (deg)	Vel (kts)	
8.1	70.1	138.3	27.73	55.5	53.0	85.6	290	4.0	81.1
8.2	80.3	131.0	27.74	55.5	53.0	85.6	290	3.0	82.6
8.3	90.1	131.0	27.74	55.5	53.0	85.6	290	4.0	85.9
8.4	100.0	112.2	27.74	55.0	53.0	88.3	290	4.5	86.4
8.5	69.9	139.6	27.74	55.0	53.0	88.3	320	2.5	81.3
8.6	80.0	139.1	27.74	55.0	53.0	88.3	340	6.0	83.3
8.7	90.1	130.9	27.74	56.0	53.0	82.9	290	5.0	86.2
8.8	100.0	112.3	27.74	56.0	53.0	82.9	300	7.0	87.6

† 1/3-octave band nearest 2nd stage BPF

Table 82. Far-Field Acoustic Tests - Baseline, Suppressor Inlet, Maximum A_8.

Rdg	$N/\sqrt{\theta}$ (%)	A_8 ($in.^2$)	P_{amb} (in. Hg)	T_{dry} (° F)	T_{wet} (° F)	R.H. (%)	Wind Dir (deg)	Wind Vel (kts)	SPL† (110°)	PWL‡	OAPWL§ (Turbine)
8.9	69.6	197.7	27.74	56.0	53.0	82.9	300	2.5	82.9	129.6	133.2
8.10	75.1	197.7	27.75	57.0	53.5	80.5	310	5.0	80.2	128.8	134.0
8.11	79.8	197.7	27.75	58.5	53.5	73.2	310	5.0	85.9	131.8	135.8
8.12	84.9	197.7	27.75	58.5	53.5	73.2	20	5.0	89.9	135.7	138.5
8.13	89.8	197.7	27.75	58.5	53.5	73.2	40	2.0	92.4	138.5	141.3
8.14	95.1	197.7	27.75	58.5	53.5	73.2	40	4.5	92.4	139.4	144.2
8.15	100.1	153.6	27.75	59.0	53.5	70.8	20	5.0	91.8	138.7	143.1
8.16	70.2	197.7	27.75	59.0	53.5	70.8	40	3.0	83.4	129.6	133.2
8.17	75.2	197.7	27.75	59.0	53.5	70.8	50	1.0	82.5	129.3	134.2
8.18	80.0	197.7	27.76	60.5	54.0	66.8	350	1.0	86.1	131.8	135.7
8.19	85.0	197.7	27.76	60.5	54.0	66.7	60	1.0	89.8	135.5	138.3
8.20	89.8	197.7	27.76	60.5	54.0	66.7	50	0.5	91.8	137.9	141.0
8.21	94.5	197.7	27.76	60.5	54.0	66.7	70	0.5	91.3	138.2	142.9
8.22	99.9	152.3	27.76	60.5	54.0	66.7	50	0.5	91.2	138.1	142.5

† 1/3-octave band nearest 2nd stage BPF

‡ 1/3-octave band nearest 2nd stage BPF; 40° - 160°

§ 8 KHz - 40 KHz

Table 83. Far-Field Acoustic Tests - Spacing, Maximum A_8.

Rdg	$N/\sqrt{\theta}$ (%)	A_8 ($in.^2$)	P_{amb} (in. Hg)	T_{dry} (° F)	T_{wet} (° F)	R.H. (%)	Wind Dir (deg)	Wind Vel (kts)	SPL† (110°)	PWL‡	OAPWL§ (Turbine)
20.1	69.9	199.0	27.56	60.5	52.0	57.4	190	4.0	79.1	125.8	130.5
20.2	75.1	199.0	27.56	58.5	52.0	65.7	160	4.0	79.1	125.7	131.4
20.3	80.1	199.0	27.56	58.5	52.0	65.7	180	4.0	80.8	127.8	133.0
20.4	85.1	199.0	27.56	58.5	52.0	65.7	190	4.0	83.3	130.2	135.1
20.5	90.2	199.0	27.56	57.5	51.5	67.6	200	4.0	83.5	130.7	136.4
20.6	95.1	199.0	27.56	57.5	51.5	67.6	190	3.0	83.8	131.3	137.7
20.7	100.1	160.4	27.56	59.0	52.0	63.6	190	3.0	81.3	131.2	139.7
20.8	70.1	200.6	27.56	59.0	52.0	63.5	190	4.0	78.7	125.5	130.2
20.9	75.1	200.6	27.57	59.0	52.0	63.5	130	2.0	79.1	126.0	131.6
20.10	80.2	200.6	27.57	59.0	52.0	63.5	160	2.0	79.9	127.1	132.5
20.11	85.2	200.6	27.57	58.0	52.0	67.9	130	3.0	82.2	129.5	134.6
20.12	90.2	200.6	27.57	58.0	52.0	67.9	170	4.0	83.2	130.7	136.4
20.13	95.1	200.6	27.57	58.0	52.0	67.9	170	3.0	84.2	131.9	138.4
20.14	100.2	159.2	27.57	57.0	51.5	69.9	180	5.0	82.5	131.9	140.1

† 1/3-octave band nearest 2nd stage BPF

‡ 1/3-octave band nearest 2nd stage BPF; 40° - 160°

§ 8 KHz - 40 KHz

Table 84. Far-Field Acoustic Tests - Spacing and Treatment, Maximum A_8.

Rdg	$N/\sqrt{\theta}$ (%)	A_8 ($in.^2$)	P_{amb} (in. Hg)	T_{dry} (° F)	T_{wet} (° F)	R.H. (%)	Wind Dir (deg)	Wind Vel (kts)	SPL† (110°)	PWL‡	OAPWL§ (Turbine)
24.1	70.3	200.0	27.72	37.0	34.5	79.1	290	4.0	65.1	115.5	122.7
24.2	74.4	200.0	27.72	37.0	34.5	79.1	310	3.0	66.6	117.9	124.7
24.3	80.0	200.0	27.72	37.0	34.5	79.1	280	5.0	68.3	119.6	126.4
24.4	84.9	200.0	27.72	37.5	35.0	79.3	280	6.0	70.5	120.6	127.8
24.5	89.7	200.0	27.72	37.5	35.0	79.3	270	6.0	73.0	122.0	130.3
24.6	94.9	200.0	27.72	37.5	35.0	79.3	270	7.0	79.0	127.3	135.5
24.7	99.9	160.0	27.72	37.5	35.0	79.3	270	6.0	80.5	130.5	139.9
24.8	70.1	200.0	27.72	37.0	34.5	79.1	270	6.0	65.6	116.3	123.5
24.9	74.9	200.0	27.72	37.0	34.5	79.1	270	5.0	66.6	118.2	125.3
24.10	79.8	200.0	27.72	37.0	34.5	79.1	270	7.0	68.6	119.5	126.9
24.11	84.9	200.0	27.72	37.0	34.5	79.1	270	5.0	71.8	121.5	128.3
24.12	90.0	200.0	27.72	37.0	35.0	83.2	290	6.0	73.1	122.0	130.4
24.13	95.0	200.0	27.72	37.0	35.0	83.2	270	4.0	79.9	127.7	135.6
24.13	95.0	200.0	27.72	37.0	35.0	83.2	270	4.0	79.9	127.7	135.6
24.14	99.9	160.0	27.72	37.0	35.0	83.2	270	2.0	79.8	129.7	139.6

† 1/3-octave band nearest 2nd stage BPF

‡ 1/3-octave band nearest 2nd stage BPF; 40° - 160°

§ 8 KHz - 40 KHz

Table 85. Acoustic Probe Tests - Baseline, Maximum A_8.

Rdg	$N/\sqrt{\theta}$ (%)	A_8 ($in.^2$)	P_{amb} (in. Hg)	T_{dry} (° F)	Turbine 2nd Stage Tone PWL, (NB)
9.5	69.9	198.0	27.64	63.0	134.5
9.6	75.1	198.0	27.64	63.0	129.1
9.7	80.0	198.0	27.64	63.0	136.6
9.8	85.1	198.0	27.64	64.0	140.9
9.9	90.0	198.0	27.64	64.0	136.2
9.10	94.8	198.0	27.64	65.5	133.4
9.11	100.0	152.0	27.64	67.0	135.9
May 18, 1973					

Table 86. Acoustic Probe Tests - Spacing, Maximum A_8.

Rdg	$N/\sqrt{\theta}$ (%)	A_8 ($in.^2$)	P_{amb} (in. Hg)	T_{amb} (° F)	Turbine 2nd Stage Tone PWL, (NB)
21.1	70	200.2	27.62	60.0	133.9
21.2	75	200.2	27.62	60.0	127.5
21.3	80	200.2	27.62	61.5	138.2
21.4	85	200.2	27.63	61.5	130.6
21.5	90	200.2	27.63	61.5	126.3
21.6	95	200.2	27.63	63.0	128.2
21.7	100	160.0	27.63	63.0	125.1
September 22, 1973					

Table 87. Acoustic Probe Tests - Spacing and Treatment, Maximum A_8.

Rdg	$N/\sqrt{\theta}$ (%)	A_8 ($in.^2$)	P_{amb} (in. Hg)	T_{amb} (° F)	Turbine 2nd Stage Tone PWL, (NB)
25.1	70	200.0	27.67	43.0	111.0
25.2	75	200.0	27.67	43.0	98.5
25.3	80	200.0	27.67	43.0	104.8
25.4	85	200.0	27.67	43.0	105.0
25.5	90	200.0	27.67	43.0	105.8
25.6	95	200.0	27.67	44.5	112.6
25.7	100	160	27.62	44.5	111.4
October 24, 1973					

REFERENCES

1. Brausch, J.F. and Doyle, V.L. "Summary of GE4/SST Acoustic Suppression Research," Supersonic Transport Noise Reduction Technology Program, Phase I, General Electric Company, FAA-SS-72-42, December 1972.

2. Brausch, J.F., "Flight Velocity Influence on Jet Noise of Conical Ejector, Annular Plug and Segmented Suppressor Nozzles," General Electric Company, NASA CR-120961, 1972.

3. Fisk, W.S., et al., "Supersonic Transport Noise Reduction Technology Summary - Phase I," Final Report, General Electric Company, FAA-SS-72-43, December, 1972.

4. Szeliga, R. and Allan, R.D., "Advanced Supersonic Technology Propulsion System Study," Final Report, General Electric Company, NASA CR-143634, July 1974.

5. Benzakein, M.J., and Knott, P.R., "Supersonic Jet Noise," General Electric Company, AFAPL-TR-72-52, August 1972.

6. Savell, C.T., "Task 1 - Activation of Facilities and Validation of Source Location Techniques," High Velocity Jet Noise Source Location and Reduction, (Contract DOT-OS-30034), 1975.

7. Heck, P.H., Latham, D., et al., "Acoustic Tests of Duct-Burning Turbofan Jet Noise Simulation Program," Final Report.

8. Smith, M.J.T., and Bushell, K.W., "Turbine Noise - Its Significance in the Civil Aircraft Noise Problem," Trans. ASME, 69-WA/GT-12 November, 1969.

9. Harrington, Douglas E., and Schloemer, James J., "Thrust Performance of Isolated Plug Nozzles with Two Types of 40-Spoke Noise Suppressors at Mach Numbers from 0 to 0.45," NASA TM X-2951, 1974.

10. "SST Technology Follow-on Program - Phase II," Quarterly Report, the Boeing Company, July - September 1974.

11. Harrington, Douglas E., Schloemer, James J., And Shebe, Stanley A., "Thrust Performance of Isolated 36-Chute Suppressor Plug Nozzles with and without Ejectors at Mach Numbers from 0 to 0.45," NASA TM X, 3298, 1975.

12. "SST Technology Follow-on Program - Phase I, A Summary of the SST Noise Suppression Test Program," Final Report, The Boeing Company, FAA-SS-72-41, 1972

13. Smith, M.J.T., "The Noise Performance of a Supersonic Plug Nozzle," ARC 29-427, 1967.

14. Scharton, T.D., Pinkel, B., and Tomooka, S., "Exploratory Investigation of Jet Engine Silencing with Plug Nozzle Configurations," AIAA Paper No. 72-160, 1972.

15. Dosanjh, D.S., et. al., "Noise Reduction from Supersonic Jet Flows," Quarterly Reports on Contract No. DOT-OS-20094, 1972-1973.

16. Hardin, J.C., "Analysis of Noise Produced by an Orderly Structure of Turbulent Jets," NASA TND-7242, April 1973.

17. Crow, S.C., Champagne, F.H., "Orderly Structure in Jet Turbulence," J. Fluid Mech., Vol. 48, pt. 3, August 16, 1971, pp. 547-591.

18. Wooldridge, C.E., Wooten, D.C., "A Study of the Large-Scale Eddies of Jet Turbulence Producing Jet Noise," AIAA Paper No. 71-154, January 1971.

19. Beavers, G.S., Wilson, T.A., "Vortex Growth in Jets," J. Fluid Mech., Vol. 44, pt. 1, October 21, 1970, pp. 97-112.

20. Michalke, A., "A Wave Model for Sound Generation in Circular Jets," DLR FB 70-57, November 1970.

21. Tam, C.K.W., "Supersonic Jet Noise Generated by Large Scale Disturbances," AIAA, 1974.

22. Sedelnikov, T.Kh., "The Frequency Spectrum of the Noise of Supersonic Jet," NASA TTF-538, 1967.

23. Bishop, K.A., Ffowcs-Williams, J.E. Smith, "On the Noise Sources of the Unsuppressed High Speed Jet," Turbulent Jet Flows (Von Kasman Inst. for Fluid Dynamics), 1971.

24. Fuchs, H.W., "Space Correlations of the Fluctuating Pressure in Subsonic Turbulent Jets," JSV, 23, 1, 77-99, 1972.

25. Laufer, J., Kaplan, R.E., Chue, W.T., "On the Generation of Jet Noise," JASA, 1973.

26. Hardin, J.C., "Noise Produced by the Large-Scale Transition Region Structure of Turbulent Jets," AIAA - 74.

27. Kazin, S.B., Matta, R.K., et al., "Core Engine Noise Control Program, Vol. I - Identification of Component Noise Sources," General Electric Company, DOT/FAA Report No. FAA-RD-74-125, I, August, 1975.

28. Kazin, S.B., Matta, R.K., et al., "Core Engine Noise Control Program, Vol. II - Identification of Noise Generation and Suppression Mechanisms," FAA-RD-74-125, II, August.

29. Kazin, S.B., Matta, R.K., et al., "Core Engine Noise Control Program, Vol. III - Prediction Methods," General Electric Company, DOT/FAA Report No. FAA-RD-740125, III, August.

30. "SST Technology Follow-on Program - Phase II," Quarterly Report, The Boeing Company, October - December 1974.

31. Kantola, R., "Jet and Suppressor Correlation Measurements," AIAA Paper 75-504, AIAA 2nd Aero-Acoustics Conference, 1975.

32. Harper-Bourne, M., and Fisher, M.T., "The Noise from Shock Waves in Supersonic Jets," Preprint 131, AGARD Conference on Noise Mechanisms, 1973.

33. Quarterly Progress Report, SST Follow-on Program, Phase II, The Boeing Commercial Airplane Company, July - September 1974.

34. Rakl, R., "Two Causality Correlation Techniques Applied to Jet Noise," Ph.D. Thesis, University of British Columbia, April 1973.

35. Lee, H.K. and Ribner, H.S., Journal of the Acoustical Society of America, 52, pp. 1280-1290, 1972.

36. Scharton, T.D., and White, P.H., JASA, Volume 52, No. 1, (Part 2), pp. 399-412, 1972.

37. Meecham, W.C., and Hurdle, P.M., AGARD Conference Pre-Print No. 131, pp. 8-1 to 8-12, Brussels, September 1973.

38. Siddon, T.E., and Rakl, R., "Cross-correlation Analysis of Flow Noise with Fluid Dilation as a Source Fluctuation," Presented at the 82nd Meeting of the Acoustical Society of America, Denver, Colorado, October 1971.

39. McGregor, G.R. and Simcox, C.R., "The Location of Acoustic Sources in Jet Flows by Means of the Wall Isolation Technique," AIAA 73-1041, October 1973.

40. Powell, A., "On The Mechanism of Choked Jet Noise," Proc. Phys. Soc. B (1953), Volume 66, 1039-1056.

41. Evans, T., "Prediction of Single Stream Shock Cell Noise," SAE Committee Correspondence, September 25, 1974.

42. Hoch, Cocking, et al., "Studies of The Influence of Density on Jet Noise," SNECMA - GTE, June 1973.

43. Benzakein, M.J., Kazin, S.B., "Theoretical Prediction of Aerodynamically Generated Noise in Fans and Compressors," Paper presented at ASA Conf., Cleveland, Ohio, November 1968.

44. Society of Automotive Engineers, "Jet Noise Prediction," SAE AIR 876, July 1965.

45. DuBois, C.E., "Air Induction Subsystem Specifications," (Model 2707-300), The Boeing Company Document No. D6A10114-1, 1969.

46. Vier, W.F., and Younghans, J.L., "SST Inlet Performance for the Peebles GE4 Block I Engine/Boeing Inlet Compatibility Test," TM-68-544, September 6, 1968.

47. Keith, J.S., et al., "Analytical Method for Predicting the Pressure Distribution About a Nacelle," NASA CR-2217, July 1973.

48. Ferguson, D.L., "Computer Program for the Analysis of Laminar and Turbulent Boundary Layers," General Electric, R70AEG197, June 1970.

49. Society of Automotive Engineers, "Definition and Procedures for Computing the Perceived Noise Level of Aircraft Noise," SAE ARP 865, August 1969.

50. Benzakein, M.J., Claes, H.P., et al., "Fan/Compressor Noise Research, Vol. I - Detailed Discussion," General Electric Company, DOT/FAA Report No. FAA-RD-71-85, I, March 1972.

51. Cumpsty and Lowrie, "The Cause of Tone Generation by Aero-Engine Fans at High Subsonic Tip Speeds and the Effect of Forward Speed," ASME Paper 73-WA/GT-4, 1973.

52. Bushell, K.W., "Measurement and Prediction of Jet Noise in Flight," AIAA Paper No. 75-461, March 1975.

53. Brooks, J.R., and Woodrow, R.J., "The Effects of Forward Speed on a Number of Turbojet Exhaust Silencers," AIAA Paper No. 75-506, March 1975.

54. Packman, A.B., et al., "Effect of Simulated Forward Flight on Subsonic Jet Exhaust Noise," AIAA Paper No. 75-869, June 1975.

55. Atencio, A., Jr., "Wind Tunnel Measurements of Forward Speed Effects on Jet Noise From Suppressor Nozzles and Comparison with Flight Data," AIAA Paper No. 75-870, June 1975.

56. Johnson, R.C., "Real-Gas Effects in Critical-Flow-Through Nozzles and Tabulated Thermodynamic Properties," NASA TN D-2565. 1965.

57. Jordan, D.P., and Mintz, M.D., "Air Tables," McGraw-Hill Book Company, New York, 1965.

58. Society of Automotive Engineers, "Standard Values of Atmospheric Absorption as a Function of Temperature and Humidity for Use in Evaluating Aircraft Flyover Noise," SAE ARP 866, August 1964.

59. Ames Research Staff, "Equations, Tables, and Charts for Compressible Flow," NACA Report 1135. 1953.

60. Society of Automotive Engineers, "Method for Calculating the Attenuation of Aircraft Ground to Ground Noise Propagation During Takeoff and Landing," SAE AIR 923, August, 1966.

61. Reimer, R.M., "Computation of the Critical Flow Function, Pressure Ratio, and Temperature Ratio for Real Air," ASME Paper #62-WA-177, 1962.

62. Penney, C.M. "Differential Doppler Velocity Measurements," Paper No. 1.6 presented at the 1969 Institute of Electrical and Electronics Engineers Conference on Laser Engineering and Application, Washington, D.C. (May 26-28, 1969).

63. Jones, W.B., "Laser Fluid Velocity Sensor," paper presented at the Fluid Flow Symposium, Pittsburgh, Pennsylvania (May 1971) and General Electric Company Report No. 70-C-101 (March 1970).

64. Emmerling, J.J., "Core Engine Noise Control Program," Volume IV, "Extension of Low Frequency Core Noise Prediction," FAA-RD-74-125 IV.